

Slippery surfaces from lipid-lubricated hydrogels pp. 288 & 335

The nucleus measures cell confinement pp. 295, 310, & 311

Metabolomics of healthy and failing hearts p. 364

Science

\$15
16 OCTOBER 2020
sciencemag.org

AAAS

VOTING IN A MAELSTROM

Science looms large in
crises facing U.S. voters pp. 267 & 278



CONTENTS

16 OCTOBER 2020 • VOLUME 370 • ISSUE 6514

U.S. ELECTIONS

FEATURES

278 Weathering the storm

As president, Donald Trump has battered science. But increased spending by Congress and some supportive agency heads have provided relief *By J. Mervis*

283 Scientists and science are on the ballot *By J. Mervis*

284 What if Biden wins?

A new president will have vast authority to rapidly shift science policy, but will confront obstacles beyond his control *By D. Malakoff*

ON THE COVER

Donald Trump's presidency has been marked by a dismissal of science and evidence. Now, voters are deciding who will occupy the White House amid a host of science-related crises, including the COVID-19 pandemic, forest fires and climate change, and fierce debates over immigration and racial justice. See pages 267 and 278. *Illustration: Zoë van Dijk*



SEE ALSO: EDITORIAL p. 267

NEWS

IN BRIEF

268 News at a glance

IN DEPTH

270 Lava lake rises at dangerous African volcano

Funding for volcano's lone monitoring station lost as warning signs flash *By R. Pease*

271 A cut above: pair that developed CRISPR earns historic award

Chemistry Nobel honors biology's powerful genome editor *By J. Cohen*

272 U.S. faculty job market tanks

As COVID-19 upends university finances, postdocs worry about their future *By K. Langin*

273 At last, room temperature superconductivity achieved

But the hydrogen-based material requires high pressure *By R. F. Service*

274 Satellite swarm threatens radio array

"Megaconstellations" already bedevil optical telescopes. Now, radio astronomers are concerned *By D. Clery*

275 Found: genes that sway the course of the coronavirus

Host variants boost severity risk, may point to drug options *By J. Kaiser*

276 The United Kingdom's mask crusader

Trisha Greenhalgh argues COVID-19 shows that health policy need not wait for perfect evidence *By E. Ruppel Shell*

INSIGHTS

PERSPECTIVES

286 COVID-19 in children and young people

Children have a low risk of COVID-19 and are disproportionately harmed by precautions *By M. D. Snape and R. M. Viner*

288 Lubricating lipids in hydrogels

A self-renewing lipid layer substantially reduces friction and wear of a hydrogel surface *By T. A. Schmidt*
REPORT p. 335

290 Advancing limb neural prostheses

Neurotechnology can overcome communication difficulties between prostheses and amputees *By S. Raspopovic*

292 Reconstituting tissue patterning

A synthetic morphogen reveals quantitative principles of tissue patterning *By N. Barkai and B.-Z. Shilo*
RESEARCH ARTICLE p. 321; REPORT p. 327

294 Immiscible immunity

Mammalian metabolism meets immunity at mitochondria-adjacent lipid droplets *By D. R. Green*
RESEARCH ARTICLE p. 309

295 A cellular sense of space and pressure

The nucleus measures cell confinement with a mechanosensitive phospholipase *By Z. Shen and P. Niethammer*
RESEARCH ARTICLES pp. 310 & 311

297 Joe L. Martinez Jr. (1944–2020)

Neuroscientist and advocate of inclusion *By K. A. Trujillo et al.*

POLICY FORUM

298 COVID-19 recovery funds dwarf clean energy investment needs

A modest fraction of current global stimulus funds can put the world on track to achieve Paris Agreement goals *By M. Andrijevic et al.*

BOOKS ET AL.

301 Experiments in creativity

Artists and engineers joined forces in the 1960s, blurring the line between art and technology *By I. Ockert*

302 Tales from times long past

Field adventures and human origin stories combine in a paleoanthropologist's compelling new memoir *By B. J. King*

LETTERS

303 Save Kazakhstan's shrinking Lake Balkhash

By A. Ussenaliyeva

303 Airborne transmission of SARS-CoV-2

By K. A. Prather et al.

304 Deliberate poisoning of Africa's vultures

By M. Henriques et al.

RESEARCH

IN BRIEF

305 From *Science* and other journals

REVIEW

308 Neurodevelopment

Transient cortical circuits match spontaneous and sensory-driven activity during development Z. Molnár et al.

REVIEW SUMMARY; FOR FULL TEXT:
DX.DOI.ORG/10.1126/SCIENCE.ABB2153

RESEARCH ARTICLES

309 Innate immunity

Mammalian lipid droplets are innate immune hubs integrating cell metabolism and host defense M. Bosch et al.

RESEARCH ARTICLE SUMMARY; FOR FULL TEXT:
DX.DOI.ORG/10.1126/SCIENCE.AAY8085
PERSPECTIVE p. 294**Cell biology****310** The nucleus acts as a ruler tailoring cell responses to spatial constraints

A. J. Lomakin et al.

RESEARCH ARTICLE SUMMARY;
FOR FULL TEXT:

DX.DOI.ORG/10.1126/SCIENCE.ABA2894

311 The nucleus measures shape changes for cellular proprioception to control dynamic cell behavior V. Venturini et al.RESEARCH ARTICLE SUMMARY;
FOR FULL TEXT:

DX.DOI.ORG/10.1126/SCIENCE.ABA2644

PERSPECTIVE p. 295

312 Developmental biology

Apical stress fibers enable a scaling between cell mechanical response and area in epithelial tissue J. M. López-Gay et al.

RESEARCH ARTICLE SUMMARY; FOR FULL TEXT:
DX.DOI.ORG/10.1126/SCIENCE.ABB2169**313 Neuroscience**

Behavioral state coding by molecularly defined paraventricular hypothalamic cell type ensembles S. Xu et al.

RESEARCH ARTICLE SUMMARY; FOR FULL TEXT:
DX.DOI.ORG/10.1126/SCIENCE.ABB2494**314 Microbiota**Microbiota-modulated CART⁺ enteric neurons autonomously regulate blood glucose P. A. Muller et al.**321 Morphogens**

Patterning and growth control in vivo by an engineered GFP gradient K. S. Stapornwongkul et al.

PERSPECTIVE p. 292; REPORT p. 327

REPORTS

327 Morphogens

Engineering synthetic morphogen systems that can program multicellular patterning S. Toda et al.

PERSPECTIVE p. 292; RESEARCH ARTICLE p. 321

331 Ultracold chemistry

Coherently forming a single molecule in an optical trap X. He et al.

335 Hydrogels

Cartilage-inspired, lipid-based boundary-lubricated hydrogels W. Lin et al.

PERSPECTIVE p. 288

339 Spectroscopy

Zeptosecond birth time delay in molecular photoionization S. Grundmann et al.

342 Thermogalvanics

Thermosensitive crystallization-boosted liquid thermocells for low-grade heat harvesting B. Yu et al.

346 Ecology

Species richness and redundancy promote persistence of exploited mutualisms in yeast M. C. Vidal et al.

351 Signal transduction

The GATOR–Rag GTPase pathway inhibits mTORC1 activation by lysosome-derived amino acids G. G. Hesketh et al.

356 Inorganic chemistry

Structural and spectroscopic characterization of an Fe(VI) bis(imido) complex J. L. Martinez et al.

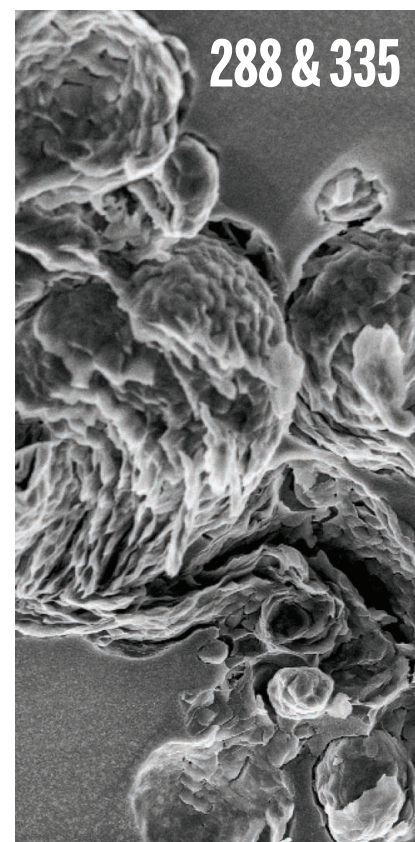
360 Structural biology

Structural and mechanistic bases for a potent HIV-1 capsid inhibitor S. M. Bester et al.

364 Physiology

Comprehensive quantification of fuel use by the failing and nonfailing human heart D. Murashige et al.

PODCAST



DEPARTMENTS

266 EditorialNot throwing away our shot
By H. Holden Thorp**267 Editorial**Speed and American elections
By Jill Lepore
U.S. ELECTIONS SECTION p. 278**374 Working Life**My last drop
By John C. AyersNew Products..... 369
Science Careers.....370

Not throwing away our shot



H. Holden Thorp
Editor-in-Chief,
Science journals.
hthorp@aaas.org;
@hholdenthorp

Over the past few weeks, prominent scientific publications have condemned President Donald Trump's record on science. This is unprecedented. Although my predecessors at *Science* have always held elected U.S. officials accountable (but could not make a formal political endorsement because of the nonprofit status of the American Association for the Advancement of Science, the publisher of *Science*), many of these publications are now clearly denouncing the U.S. president, administration, and federal agency leaders as the nation approaches a highly consequential presidential election. To paraphrase lyrics by Lin-Manuel Miranda in "Hamilton" about another set of political essays, why do we write like we're running out of time? Because recent events show that the voice of the scientific community can lead to positive change.

I have been supportive and then critical of Stephen Hahn, commissioner of the U.S. Food and Drug Administration (FDA). When he granted the emergency use authorization (EUA) for hydroxychloroquine to treat coronavirus disease 2019 (COVID-19), much of the biomedical community lost trust in him, but I maintained that if he stuck to the science on the COVID-19 vaccine, the nation should support him. When he botched the announcement of the EUA for convalescent plasma to treat the disease, I lost confidence in him again and wrote that society was on its own to tackle COVID-19 without help from the FDA. At the same time, Eric Topol, editor-in-chief of *Medscape* and a prominent scientist and public health advocate, called for Hahn to resign.

Topol got Hahn's attention. After Topol's editorial appeared, the commissioner reached out to him, which, as Topol told me, started a series of conversations about their differences. Hahn confirmed to Topol that he had been instructed by the White House to extoll the benefits of convalescent plasma beyond his scientific judgment. Subsequently, the FDA proposed to the White House a more stringent protocol for approving a COVID-19 vaccine. In the case of the two leading vaccine candidates (Moderna and Pfizer), a 2-month delay would be required for half of the volunteers that received a second shot, which must be delivered 3 to 4 weeks after the

first immunization. This meant that an EUA for a vaccine would not be approved before the election. Trump attacked Hahn and criticized this logical move for patient safety as being politically motivated. Surprisingly, a few days later, the White House agreed to the FDA guidelines. Hahn had stood up for science and stood up to Trump. In an interview with Topol, Hahn pledged to stand up for sound scientific judgement.

The pressure put on Hahn by the scientific community played a big role in stiffening his spine. Topol told me that Hahn said he was "profoundly dejected" after the convalescent plasma debacle and realized that the subsequent vaccine drama posed an "existential crisis"—either he would be fired by Trump or permanently lose his standing in the scientific community.

Ultimately, he decided that doing what was right for the success of the COVID-19 vaccine trials and the safety of the public—while also repairing his reputation in medical science—was more important than keeping his job at the FDA. We can hope that it's too much trouble for Trump to fire him this close to the election. I'm now back to supporting Hahn knowing that scientists will decide whether to approve the COVID-19 vaccines and provided he continues to support science.

With his apparent recovery from COVID-19 due perhaps in part to receiving an experimental monoclonal antibody cocktail from Regeneron, Trump's attention has turned to tout-

ing this treatment as a "cure" and promising its availability to all Americans. An antibody-based treatment does deserve more scientific attention, but a therapeutic is not a cure. If an EUA for this treatment is announced, the scientific community needs Hahn to resist Trump's pressure to exaggerate and declare the pandemic over. These antibodies are helpful but currently in very limited supply and not something that will "get everybody out of the hospitals," as Trump said recently. The scientific community must keep the pressure on Hahn to state the science clearly.

Readers who don't think *Science* and its publishing peers should write about politics often tell us to "stick to science." We are sticking to science, but more importantly, we're sticking up for science.

—H. Holden Thorp

"The pressure put on Hahn by the scientific community played a big role in stiffening his spine."

Speed and American elections

As you love your country, fly to your polls,” the *Gazette of the United States* urged voters in 1800, in a presidential election that pitted Thomas Jefferson against John Adams. But voters hardly raced to the polls that year: Balloting began in March and ended in November and the winner was declared only weeks before inauguration. In the centuries since, both voting and counting in the United States have gotten faster, if not always more fair, and this year, the communication of results long before they can possibly be known threatens to undermine not only the election but democracy itself.

Republicans have raised alarms about old-fashioned, well-regulated technologies: the paper ballot and the post office. But the real danger this election comes from new-fangled, unregulated social media companies. “What’s the Plan if Trump Tweets that He’s Won Re-election?” *The New York Times* asked last month. Twitter plans to slow down communications on its platform beginning 20 October. That may be too little, too late.

The push for speed came, first, from newspapers. In 1852, *The New York Times* promised that a new technology of communication, the telegraph, would “enable the Press of the entire country to announce the result of the national election on the morning after the closing of the polls.” But as late as 1896, newspapers were still using homing pigeons to collect returns although, by 1904, electricity allowed big-city newspapers headquartered in tall buildings to speed results to the public by way of lights that could be seen for miles (that’s what’s meant by a “news flash”): Steady light to the west meant a Democratic victory; steady light to the east a Republican one.

The emergence of radio in the 1920s and modern polling in the 1930s made election reporting more frantic and, equally, more prone to error. In 1948, the *Chicago Daily Tribune* famously went to press with the dead-wrong headline, DEWEY DEFEATS TRUMAN. But the real turn came in 1952 when CBS Television News brought in a UNIVAC computer to predict the outcome of the contest between Dwight Eisenhower and Adlai Stevenson. With the introduction of “giant electronic brains” into election-night television coverage, Americans came to expect to learn of the outcome of a presidential election before turning in for the night.

“Haste...has also not infrequently undermined the democratic process.”

In 1960, all three television networks used computers to make projections in the contest between John F. Kennedy and Richard M. Nixon, which proved to be one of the closest elections in American history. On CBS, an IBM 7090 predicted a Kennedy victory at 8:12 p.m. Eastern Standard Time, while polls remained open in much of the country. Republicans pushed for a recount; Nixon decided to concede. Afterward, IBM published a promotional brochure called “The Fastest Reported Election,” boasting, “For waiting millions on election night, the computer cut down the time of waiting.” Newspapers soon began commissioning computers, too. In 1962, *The New York Times* hired the Simulmatics Corporation, a pioneering predictive analytics company. Simulmatics promised that it could help the newspaper report the results of the mid-term elections in “real time,” a term that had been coined by the U.S. Department of Defense, at the height of the Cold War, to explain how computers predicted, by way of simulation, the path and velocity of missiles.

Ballots aren’t bombs. Honestly, what’s the hurry? Haste is not in the public interest. It has also not infrequently undermined the democratic process. In 1980, NBC Television News called Ronald Reagan the presidential winner at 8:15 p.m. At 10 p.m., Jimmy Carter conceded. Polls hadn’t closed yet in the West, and down-ticket Democrats who lost their races blamed Carter. But, really, NBC was to blame. As a consequence, television networks adopted new rules, barring the calling of elections before the polls close. In 2000, every television network, relying on computer projections, called the presidential election for George W. Bush over Al Gore, leading Gore to concede, prematurely. Again, television networks established new rules.

Media companies fix their mistakes. Journalists work in the public interest. “We are not a media company,” Mark Zuckerberg insisted after the 2016 election, deflecting blame. For 2020, Facebook has established a Voting Information Center; one of its purposes, Zuckerberg says, is “to prepare people for the possibility that it may take a while to get official results.” That might work. Or, it might not. Either way, after the 3 November election, control of the nation’s election reporting needs to be wrested out of Zuckerberg’s clutches and returned to journalists.

—Jill Lepore



Jill Lepore is the David Woods Kemper ‘41 Professor of American History, Harvard College Professor, and Affiliate Professor of Law at Harvard University, Cambridge, MA, USA.

“Allowing a dangerous virus that we don’t fully understand to run free is simply unethical. It’s not an option.”

Tedros Adhanom Ghebreyesus, head of the World Health Organization, on claims that populations will develop “herd immunity” to the pandemic coronavirus if lockdowns end.

IN BRIEF

Edited by **Jeffrey Brainard**



Scientists consider the skull of an auctioned *Tyrannosaurus rex* to be among the most pristine ever found.

PALEONTOLOGY

Top dino fetches top dollar at auction

An unusually complete *Tyrannosaurus rex* fossil was sold last week for a record-breaking \$31.8 million at an auction, dismay- ing many paleontologists. They worry such sales will encourage more private trade of fossils, leaving important specimens off- limits to researchers. The auctioned fossil, officially called BHI 3033, is popularly known as Stan, after its discoverer, amateur paleontologist Stan Sacrison, who found it in 1987 in South Dakota’s Hell Creek Formation. The sale price dwarfs the \$8.4 million that the Field Museum in Chicago paid in 1997 for the *T. rex* fossil named Sue. Stan’s buyer has not been identified. In September, the Society of Vertebrate Paleontology asked Christie’s, the auction house, to sell Stan only to “institutions committed to curating specimens for the public good and in perpetuity, or those bidding on behalf of such institutions.”

China joins global vaccine plan

PUBLIC HEALTH | China announced last week it is joining a global initiative to distribute COVID-19 vaccines fairly and affordably. The country, which has developed several vaccine candidates, was one of the last big nations that had not signed on to the COVID-19 Vaccines Global Access (COVAX) Facility, developed by the World Health Organization (WHO) and partners. It aims to shepherd approximately a dozen vaccines to market and distribute 2 billion doses to partic- ipating countries by the end of 2021. Each country would receive enough to inoculate at least 20% of its population. But China said it will buy vaccines through COVAX for only 1% of its people, a pledge that could limit its draw on the project’s vaccine supplies. A total of 180 countries representing approximately 90% of the world’s population have now joined the plan, WHO said at a 12 October press briefing. The United States is not one of them.

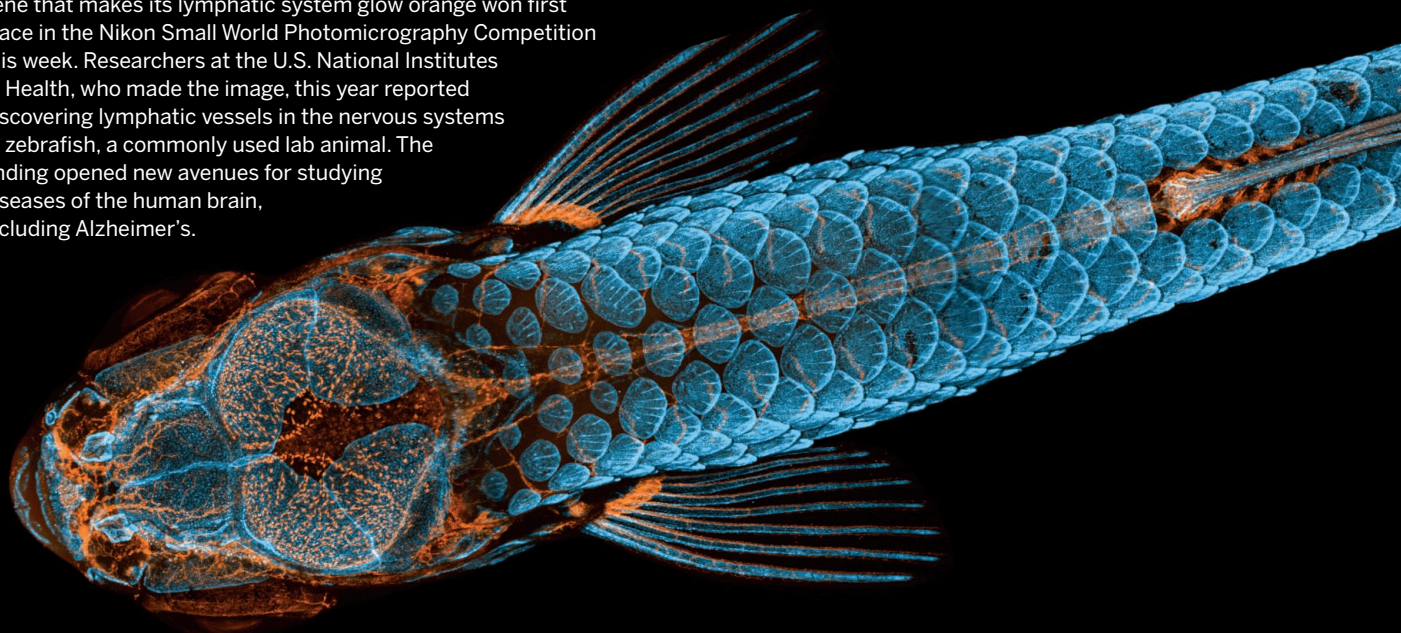
Tasmanian devil reintroduced

CONSERVATION | Though an icon of the Down Under continent, the fierce-looking Tasmanian devil had been missing from Australia’s mainland for at least 3000 years, probably wiped out by people. But a comeback has begun: Between March and September, Aussie Ark and two other con- servation organizations released 26 of these Boston terrier-size carnivorous marsupials into a fenced 160-hectare preserve north of Sydney. In modern times, the devil has been endemic only to Tasmania, and since 1995, lethal, transmissible cancers have reduced its populations there by 90% to about 25,000. The newly released animals come from a group of almost 400 cancer-free devils raised in captivity by Aussie Ark; it plans to place 40 more in two other mainland locations by 2023. The organization views the reintroduc- tions as a step toward “rewilding” parts of Australia with other native species as well.

Nobel honors auction theory

AWARDS | The Nobel Memorial Prize in Economic Sciences was awarded on 12 October for research on auction formats now used to sell goods and services such as

IN FOCUS An image of a juvenile zebrafish carrying an inserted gene that makes its lymphatic system glow orange won first place in the Nikon Small World Photomicrography Competition this week. Researchers at the U.S. National Institutes of Health, who made the image, this year reported discovering lymphatic vessels in the nervous systems of zebrafish, a commonly used lab animal. The finding opened new avenues for studying diseases of the human brain, including Alzheimer's.



internet ads, fishing quotas, and electricity. The prize is shared by Paul Milgrom and Robert Wilson, both of Stanford University. (Wilson delivered the news to Milgrom, his neighbor, via a doorbell camera because Milgrom had ignored the early morning phone calls from Sweden.) In the 1960s and '70s, Wilson used game theory to show how the risk of the "winner's curse"—winning an auction at too high a price—leads to low bids and lower revenue auctions. Milgrom, Wilson's graduate student, showed how auctions that give bidders more information about an item's value are better at avoiding the winner's curse. In the 1990s, the U.S. Federal Communications Commission (FCC) put their theories to work in its allocation of radio spectrum to telecom companies. FCC switched from giving away bandwidth in a random lottery to an auction format designed by Milgrom and Wilson, raising more than \$120 billion over the next 20 years. Other countries have used similar auctions for other assets, such as carbon emission allowances.

Co-discoverer of ozone threat dies

ENVIRONMENT | Mario Molina, an atmospheric chemist and Nobel laureate who helped identify and reduce threats to Earth's ozone layer, died last week at age 77. With F. Sherwood Rowland, Molina showed in 1974 that ultraviolet (UV) light could break down

chlorofluorocarbons (CFCs), supposedly inert chemicals widely used in aerosol cans and refrigeration, when they reached the upper atmosphere. Chlorine freed by the reaction, they showed, could destroy large amounts of UV-blocking ozone. The insight, validated by the discovery in 1985 of the ozone hole above Antarctica, led to the 1987 Montreal Protocol, an international agreement that required phasing out use of CFCs and similar pollutants. Molina worked behind the scenes to support its creation. Many of these products are also potent greenhouse gases, which has made the Montreal Protocol perhaps the most effective global step taken so far to curb global warming.

São Paulo science spared

FUNDING | The academic community in Brazil's São Paulo state breathed a sigh of relief last week after its government abandoned a plan to take control of the financial reserves of three state universities and the São Paulo Research Foundation (FAPESP). The move, part of a bill to balance state finances, would have crippled research in São Paulo, which accounts for 40% of Brazil's scientific output, scientists said (*Science*, 4 September, p. 1152). But another threat is looming for FAPESP. A new bill would allow the government to withhold 30% of the agency's funds, which are a fixed share of the state's tax revenues, in 2021.

BY THE NUMBERS

\$200,000

Estimated loss on average for a U.S. family of four from COVID-19 during the next decade. About half is from lost income; the rest reflects the costs of health impairments and premature deaths. The price of countering the pandemic by testing people and tracing their contacts would be only one-thirtieth of those losses, economists estimate. (JAMA)

\$42,000

Total cost of 51 disinformation ads on Facebook, viewed at least 8 million times this year in the United States, that called findings of climate change science a "hoax." Facebook says it prohibits ads that include claims debunked by third-party fact-checkers and started a web page to connect people with factual information about climate science; critics call its efforts inadequate. (InfluenceMap)



In a 2002 eruption, a lava lake within the crater of Nyiragongo volcano drained in hours.

NATURAL HAZARDS

Lava lake rises at dangerous African volcano

Funding for volcano's lone monitoring station lost as warning signs flash

By **Roland Pease**

In 2002, the last time Nyiragongo volcano erupted, lava raced down its flanks into the crowded city of Goma, on the border between the Democratic Republic of the Congo and Rwanda. About 250 people died, 20% of the city was destroyed, and hundreds of thousands fled. Since then, the at-risk population living in the shadow of the 3470-meter-tall volcano has more than doubled to 1.5 million.

Now, conditions are ripe for another disaster, says Dario Tedesco, a volcanologist at the Luigi Vanvitelli University of Campania, who earlier this year led a campaign into the volcano's roiling crater. He and his colleagues found the lava lake there filling at an alarming rate, raising the risk that the molten rock could burst through the crater walls once again. Their analysis suggests peak hazard will arrive in 4 years, although they believe an earthquake could trigger a crisis earlier. Adding to the concerns, the Goma Volcano Observatory (GVO), the only monitoring station in the region, is losing its financial support from the World Bank. Tedesco's assessment is blunt. "This is the most dangerous volcano in the world!"

Tedesco began to watch the volcano in the mid-1990s, when refugees, fleeing the genocide in nearby Rwanda, swelled Goma's population. The United Nations sought his

advice on the dangers of the volcano, so he monitored Nyiragongo's moods in the years before the 2002 eruption. He is alarmed by parallels to today.

The 2002 eruption began after an earthquake opened up fissures in the southern flank of the volcano. The 200-meter-wide lava lake, the largest in the world, drained in a matter of hours, releasing low-silica, runny lava that flowed as fast as 60 kilometers per hour. The lava piled up in layers up to 2 meters deep in Goma and created a new delta 800 meters wide in nearby Lake Kivu.

As soon as the fissures healed, however, fresh lava began to bubble up and refill the crater lake. Activity accelerated in 2016 when a second vent began to fountain within the crater. In February, on their most recent inspection, Tedesco and his colleagues—flown in by U.N. peacekeepers to avoid the rebels active in the area—found the lake rising faster than ever. The second vent was gushing an estimated 4 cubic meters of lava per second, enough to fill an Olympic swimming pool every 10 minutes. "As long as the volume is increasing, it increases the chances of a volcanic eruption onto Goma," says GVO Director General Katcho Karume, who also took part in the campaign.

Pierre-Yves Burgi, a geophysical modeler at the University of Geneva, says the lava lake level is effectively a pressure gauge for the volcano's internal plumbing, like mer-

cury in a barometer. His model suggests the internal pressure is 20 atmospheres, well beyond the mechanical strength of the volcano's rocky flanks, Burgi and colleagues reported in August in *Geophysical Research Letters*. "This situation is unstable," he says. "The danger is of a tremor opening up a new fissure."

They believe the system may be reaching a critical point, as it did before the 2002 eruption and an earlier one in 1977. In both cases lava lake levels stabilized several years before the eruption, they argue, as the mass of molten rock weighed down on the magma below. The eruptions lagged because magma takes time to force open existing fractures, explains Andrew Bell, an expert on rock mechanics at the University of Edinburgh who developed a model to explain the collapse of Mount St. Helens in 1982. Burgi expects the lava lake to stop rising soon, in which case the period of peak danger for Goma would be from 2024 to 2027.

"They are right to be concerned," Bell says. "Nyiragongo is dangerous in a way a lot of volcanoes aren't." He adds, however, that the behavior of the lava lake doesn't say much about the immediate risk of eruption. Swarms of small earthquakes or ground deformation are clearer warning signs of restless magma, he says. Cynthia Ebinger, an expert on Rift Valley geology at Tulane University, also has issues with Burgi's model,

which assumes the magma plumbing feeding Nyiragongo's lava lake is the main factor controlling an eruption. She says the stretching of tectonic plates in the region leads to earthquakes and fresh intrusions of magma that can also trigger eruptions.

A network of seismometers around the volcano, operated by GVO and installed in recent years with assistance from researchers in Belgium and Luxembourg, shows high earthquake activity and several deep swarms, says François Kervyn, director of the natural hazards division at the Royal Museum for Central Africa in Belgium. He doesn't know how unusual the activity is because his team lacks comparable, older data. But he says sustained, rumbling tremors were recorded months before the 2002 eruption. "Nothing like that is detected for the moment," he wrote in an email.

Kervyn says the network requires constant maintenance, because of vandalism, theft, and lightning damage. Several seismometers are currently out of action. But the civil unrest in the area makes repairs dangerous. Earlier this year 13 park rangers were killed in an ambush in the surrounding Virunga National Volcano Park.

The threat of violence is only one of GVO's problems. Established in 1986, the observatory is set to lose the funding it has relied on for the past 5 years. With a staff of about 40, the observatory maintains the seismic stations and monitors the lake and the potentially deadly gases emitted by the volcano. It also plans for Goma's evacuation, and will issue the alarm if an eruption occurs.

Since 2015, the World Bank has given the observatory \$2.3 million, as part of an aid package primarily intended to rebuild and protect the city airport, which was seriously damaged in the 2002 eruption. But that project has ended. In an email, a spokesperson for the World Bank Group confirmed that "no follow-up activities are envisioned by the WBG so far."

The U.N. peacekeeping force is concerned. At the end of September, it flew Tedesco back to the city for more talks with the World Bank and other development agencies. A U.N. spokesperson says the peacekeepers are considering supporting GVO in the short term. "We are conscious of the importance of keeping the volcanoes monitored as a way to protect civilians and save lives."

As *Science* went to press, there was no news of a resolution. Tedesco planned to inspect Nyiragongo's crater again, but bad weather forced the cancellation of a helicopter flight. "If things remain like this, there is little to be optimistic about," he says. ■

Roland Pease is a journalist in Swindon, U.K.

NOBEL PRIZES

A cut above: pair that developed CRISPR earns historic award

Chemistry Nobel honors biology's powerful genome editor

By Jon Cohen

Decades typically pass before a discovery leads to a Nobel Prize, but the chemistry award last week celebrated two scientists who, a short 8 years ago, described how to transform an obscure bacterial immune mechanism into the most powerful genome editor ever devised: CRISPR.

The award, to Emmanuelle Charpentier of the Max Planck Unit for the Science of Pathogens and Jennifer Doudna of the University of California (UC), Berkeley, marks the first time a Nobel Prize in science has gone to an all-female team. It also comes amid a high-stakes patent fight over the revolutionary genetic "scissors"—which promise to have an impact on medicine, crops, livestock, pest control, and even climate change. Few doubted it would one day merit a Nobel, but who would receive it, and when, was anyone's bet. Both scientists said they were stunned by the award. "I'm just floating," Doudna said the next day. "It feels unreal."

The pair built on other scientists' discovery that bacteria have distinctive stretches of DNA—so-called clustered regularly interspaced short palindromic repeats, or CRISPR—embedded in their genomes. Retained from viruses that have infected the microbes in the past, the DNA allows them to recognize and defend themselves against future invasions. In a paper published online in *Science* on 28 June 2012, they reconfigured CRISPR to turn it into a tool that could edit DNA in a cell-free system.

Doudna and Charpentier, who is originally from France and at the time of the discovery worked at Umeå University in Sweden, programmed a short "guide RNA" to carry a bacterial CRISPR-associated enzyme to exact DNA locations, allowing them to target specific genes for the enzyme to cut. As the cell attempts to repair the damage, it often makes mistakes, which can cripple a gene—an effective way to study its normal role or eliminate a harmful mutant. CRISPR also makes it possible to insert a new stretch of DNA at the cut site.

Many other groups soon built on the findings, making CRISPR a common tool in labs around the world and spawning dozens of companies in agriculture and medicine pursuing potential markets worth many billions of dollars. One CRISPR application has already cured a person of sickle cell disease.

Many scientists expected that Feng Zhang of the Broad Institute, whose team in January 2013 published the first evidence that CRISPR worked in mammalian cells, would share the prize. The institutions of the three scientists are locked in a patent battle over who deserves the intellectual property rights to CRISPR's discovery, which could be worth billions of dollars. Zhang had not yet commented on the Nobel Prize as *Science* went to press, but Erik Sontheimer, a CRISPR researcher at the University of Massachusetts Medical School, endorses the decision. "The prize is not based on anything related to patent law," he says.

Harvard University chemist George Church published a study showing CRISPR



Emmanuelle Charpentier (left) and Jennifer Doudna were honored for changing how scientists edit DNA.

could edit mammalian cells at the same time as Zhang, who had been a postdoc in his lab. But Church doesn't think either of them was slighted. As he sees it, Charpentier and Doudna made a discovery, which is what the Nobel Committee prefers to reward, and he and Zhang were inventors who showed how to apply it. "If anyone wants any tips on how not win a Nobel Prize, it's pretty easy," Church says. "I've carefully avoided all this kind of brouhaha by focusing on inventions." And, he says, Zhang, who is 38, is young. "Feng Zhang is so full of creative ideas that I have no doubt that he will get one or two in the future."

Doudna would not directly address whether the Broad scientist should have shared the Nobel and dismissed the idea it might affect any patent decisions. "We could see this prize as acknowledging the importance of the field overall," she adds, noting many scientists developed the CRISPR tool.

The editor is both cheap and easy to use, stoking fears it could be misused in ways that threaten the environment or the human species itself. CRISPR-powered "gene drives," for example, can rapidly spread altered DNA through a species. Researchers have already shown how the technology can sterilize and wipe out populations of disease-carrying mosquitoes—but critics worry that entirely eliminating an organism from an ecosystem could have an unintended negative impact.

And in one of the most controversial biomedical experiments of the past decade, researcher He Jiankui used CRISPR to edit the genomes of human embryos in China, resulting in the birth of three babies. He was widely condemned by the scientific community and eventually jailed in China, a country that has become a leader in other areas of CRISPR research.

Doudna says her status as a Nobel laureate will allow her to become something of an ambassador for science, and she plans to devote the award money to a program her husband, UC Berkeley chemist Jamie Cate, runs for science, technology, engineering, and math students from underrepresented groups. "I feel a real sense of responsibility to making sure that girls and young women in particular feel welcomed into our field and that their work will be valued."

Fyodor Urnov, a CRISPR researcher who works with Doudna, calls it "the most deserved Nobel Prize of the past 20 years." The discovery "changed everything for the better," says Urnov, who previously worked on a more cumbersome gene editor called zinc fingers. "We can improve the world around us in extraordinary ways," he says. "The 21st century will be the age of CRISPR—thanks to Jennifer and Emmanuelle." ■



The coronavirus pandemic has further disrupted the already precarious academic employment landscape.

WORKFORCE

U.S. faculty job market tanks

As COVID-19 upends university finances, postdocs worry about their future

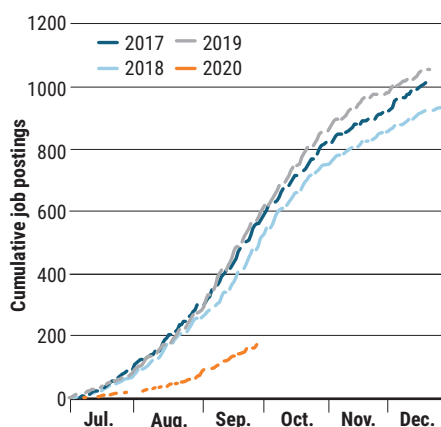
By Katie Langin

In February, Ashley Ingiosi was excited to finally interview for a faculty position after spending 10 years in training as a grad student and postdoc. "Then COVID came around," the Washington State University, Spokane, neuroscientist says, and the job opening was eliminated. "That was the end of my job search last year."

Now, Ingiosi is preparing applications for the 2020–21 academic cycle and is encountering a new problem: a dearth of faculty job openings. This year, the job posting website she follows—NeuroRumbl—had only listed 50 faculty positions by the end of September.

A slow start

U.S. faculty openings are down 70%, according to an analysis of the *Science Careers* job board. (Gaps reflect days with no new postings.)



Last year, 108 positions had been posted by that time. It's "depressing," she says.

The scarcity of academic jobs is a perennial problem for U.S. science trainees. But this year, faculty job openings at U.S. institutions are down 70% compared with last year, according to an analysis of job advertisements on the *Science Careers* job board. (*Science's* news team operates independently from the job board.) Only 173 U.S.-based jobs were posted from July to September, compared with 571 during the same period last year. Non-U.S. job postings dropped by 8%.

"It's about double-worse than I imagined," says Andrew Spaeth, an industrial chemist and co-creator of a popular online faculty job list for chemists. "I thought we'd see a hit—maybe 30%," he says, but his site lists roughly 70% fewer openings compared with last year. An ecology and evolution job list reveals a similar drop, with 65% fewer openings this year.

The dismal numbers reflect anxiety about university finances amid the pandemic, says Robert Zemsky, a professor of education at the University of Pennsylvania who studies university finances. Big public universities, in particular, are a "total mess," he says. "They are losing enrollment, they are losing revenue, and they don't know what to do, so they have hiring freezes everywhere." Even universities that are financially stable now are concerned about the future. "Everybody is sitting on their hands and nobody wants to make bets at all right now," he says.

Given the hiring slowdown, many postdocs will probably try to stay in their positions

for longer than they would have otherwise, says Paula Stephan, an economics professor at Georgia State University who studies the scientific workforce. A letter in *Science* (29 May, p. 957) argued that institutions should take steps to extend postdoc appointments. But because postdoc salaries are funded by a variety of mechanisms, co-author Amir Behbahani acknowledges, finding money to extend everyone's salary would be challenging. "This is not an easy problem to fix," says Behbahani, a postdoc at the California Institute of Technology.

Stephan notes, "There hasn't been a huge increase in funding, so it's not clear where those dollars will come from, but maybe they'll come from [principal investigators] not taking on new postdocs." Yet if postdoc appointments are extended, she points out, that could lead to downstream impacts on another group: soon-to-be Ph.D. graduates. "It really worries me that if we help people stay on for ... longer, it's just going to kick the can down the road and it doesn't help people to get the message that there are not a lot of [faculty] jobs out there." But these are exceptional times, she adds. "We really need to think about how to provide some kind of lifeline ... and not lose a group of people that we put a lot of resources into training."

As tough as the situation is, it could serve as an opportunity, says Cynthia Fuhrmann, an assistant dean of career and professional development at the University of Massachusetts Medical School. "The reality is Ph.D. scientists move on to many different career paths and have for a long time," she points out. The academic hiring freezes could spur more young scientists to look into non-academic options, and Ph.D. and postdoc training programs to think more carefully about "preparing scientists who can nimbly adapt across a breadth of roles and across a breadth of sectors in science," Fuhrmann says.

If and when academic jobs rebound, Fuhrmann hopes the way will be open for scientists who took nonacademic jobs and would like to return. Academic search committees should be open to interviewing scientists "who have taken a different route right now, out of necessity in part, and to recognize what really interesting perspectives ... [they] could bring if they move their science back into an academic setting," she says.

As for Ingiosi, she isn't considering non-academic positions just yet. She already has one faculty job interview lined up this year and is busy applying for other positions. But if she doesn't land a job offer during this application cycle, her plans may change. "I always told myself that I wouldn't do this to myself 3 years in a row." ■

HIGH-PRESSURE PHYSICS

At last, room temperature superconductivity achieved

But the hydrogen-based material requires high pressure

By **Robert F. Service**

Fulfilling a decades-old quest, this week researchers report creating the first superconductor that does not have to be cooled for its electrical resistance to vanish. There's a catch: The new room temperature superconductor only works at a pressure equivalent to about three-quarters of that at the center of Earth. But if researchers can stabilize the material at ambient pressure, dreamed-of applications of superconductivity could be within reach, such as low-loss power lines and ultrapowerful superconducting magnets that don't need refrigeration, for MRI machines and maglev trains.

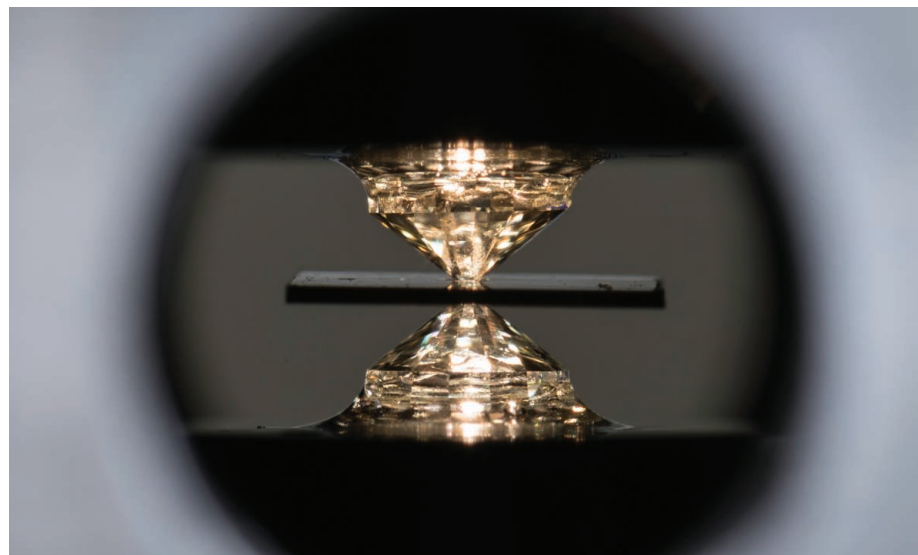
"This is a landmark," says Chris Pickard, a physicist at the University of Cambridge. But the extreme conditions of the experiment mean that even though it was "pretty spectacular," says Brian Maple, a physicist at the University of California, San Diego, "this is certainly not going to be useful in making a device."

The announcement, by a team led by physicist Ranga Dias of the University of Rochester, culminates a long march up the thermometer. Superconductivity was first discovered in 1911 by Dutch physicist Heike Kamerlingh Onnes in a mercury wire chilled to 4.2° above absolute zero,

or 4.2 K. In 1957, physicists John Bardeen, Leon Cooper, and Robert Schrieffer explained the phenomenon: Their "BCS theory" suggested an electron zipping through a superconductor temporarily deforms the material's structure, pulling another electron behind in its wake without resistance.

In 1986, a pair of physicists found that in different materials, copper oxide ceramics, superconductivity set in at a higher "critical temperature," or T_c , of 30 K. Other groups quickly cooked up related ceramic recipes; by 1994, they pushed the T_c up to 164 K in a mercury-based copper oxide under pressure. Electrons also pair up in cuprate superconductors, but just how they superconduct remains murky.

In 1968, Neil Ashcroft, a theorist at Cornell University, had suggested a different type of material should display BCS superconductivity above room temperature: hydrogen under intense pressure. Numerous groups have claimed to make such metallic hydrogen, using diamond anvil cells, palm-size devices in which a target substance gets crushed to enormous pressure between the tips of two diamonds. But the results remain controversial, in part because the pressures—exceeding those at the center of Earth—are so high they typically crack the diamonds (*Science*, 27 January 2017, p. 332). In 2004, Ashcroft suggested binding hydro-



Crushed between two diamonds, a compound of hydrogen, sulfur, and carbon superconducts at room temperature.

gen to another element might add a sort of “chemical precompression” that could make higher temperature superconductivity possible at lower pressures.

The strategy worked. In 2015, researchers led by Mikhail Eremets at the Max Planck Institute for Chemistry reported in *Nature* that they discovered superconductivity at 203 K in H_3S compressed to 155 gigapascals (GPa), more than 1 million times Earth’s atmospheric pressure. Over the next 3 years, Eremets and others boosted the T_c as high as 250 K in hydrogen-rich compounds containing lanthanum. But release the pressure, and all those compounds disintegrate.

Dias and his colleagues thought they could push the T_c up even higher by adding a third element: carbon, which forms strong bonds with neighboring atoms. “We were flying blind,” says team member Ashkan Salamat, a physicist at the University of Nevada, Las Vegas.

They loaded their diamond anvil cell with tiny solid particles of carbon and sulfur milled together, and then piped in three gases: hydrogen, hydrogen sulfide, and methane. They then shined a green laser through the diamond, triggering a chemical reaction that turned the mixture into transparent crystals.

When they then cranked up the pressure to 148 GPa and checked the conductivity of the sample via electrical leads, they found that the crystals became superconducting at 147 K. By increasing the pressure to 267 GPa, the team reached a T_c of 287 K, the temperature of a chilly room or an ideal wine cellar. Magnetic field measurements also indicated the sample had become superconductive, Dias and his colleagues report this week in *Nature*.

“The results look believable,” Eremets says. He notes, however, that the Rochester team has not yet been able to determine the precise structure of the compound that’s superconducting. Researchers will soon set to work on that question, and they will likely also start to substitute other elements into three-component hydrogen-based mixtures in hopes of even higher temperature superconductors. “That’s the next thing everyone is going to be doing,” says Eva Zurek, a theorist at the University at Buffalo.

The ultimate aim, Eremets adds, is to find a room temperature superconductor that is stable when the pressure is released. If researchers pull that off, the results could transform daily life. Dias says: “I think this is actually possible.” But theory doesn’t yet suggest a way to make hydrogen-based materials work at ambient pressures. Zurek adds, “We don’t necessarily have a clear path forward.” ■

ASTRONOMY

Satellite swarm threatens radio array

“Megaconstellations” already bedevil optical telescopes. Now, radio astronomers are concerned

By Daniel Clery



Companies hope to put tens of thousands of communications satellites in orbit.

When complete, the 197 radio astronomy dishes of the Square Kilometre Array (SKA) in South Africa will sit within a radio-quiet zone the size of Pennsylvania where even a cell-phone is forbidden, to safeguard signals from the heavens. Yet that precaution won’t save the array, due to be completed in the late 2020s, from what may soon be overhead: tens of thousands of communications satellites beaming radio signals straight down. “The sky will be full of these things,” says SKA Director General Phil Diamond.

The rocket company SpaceX has already launched hundreds of Starlink satellites, the first “megaconstellation” intended to provide internet service to remote areas. The satellites have aroused the ire of optical astronomers because of the bright streaks they leave across telescopes’ fields of view. Now, radio astronomers are worried, too. Last week, SKA released an analysis of the impact that Starlink and other constellations would have on the array. It finds they would interfere with one of the radio channels SKA plans to use, hampering searches for organic molecules in space as well as water molecules used as a key marker in cosmology.

SpaceX is promising to address the concern. But radio astronomers are also seeking regulations. The United Nations Office for Outer Space Affairs (UNOOSA), which discussed the SKA analysis at a workshop last week, is considering ways to prevent pollution of the night sky, for the benefit not just of astronomy, but also wildlife and the public. Astronomers also hope the International

Telecommunication Union (ITU), a U.N. organization, will step in. “The radio spectrum is a resource that is being consumed by private companies that typically have no regard for science,” says radio astronomer Michael Garrett, director of the Jodrell Bank Centre for Astrophysics in the United Kingdom. “It’s only government intervention that can stop this state of affairs in my view.”

So far, SpaceX has launched more than 700 Starlinks out of an initial goal of 1440, and it has won approval for 12,000. Operators such as OneWeb and Amazon’s Project Kuiper have similar ambitions. Studies suggest wide-field optical surveys will be worst affected, with satellite tracks marring most images. The team building the Vera C. Rubin Observatory, a survey telescope in Chile due to see first light next year, is working with SpaceX to reduce the impact. The company has changed the orientation of satellites as they rise in orbit, painted them darker, and fitted “visors” to reduce reflections. All Starlink satellites launched since August have visors, SpaceX’s Patricia Cooper, vice president for satellite government affairs, told the UNOOSA workshop last week. “We’re trying to look for a path where we can coexist,” she said.

The analysis from SKA, which when complete will be the world’s largest radio observatory, highlights the new concern. The band that Starlink uses to beam down internet signals takes up a sizable chunk of frequencies from 10.7 to 12.7 gigahertz, within a range known as band 5b that is one of seven bands SKA’s South African dishes will target. The

IMAGE: ESA/SCIENCE OFFICE

SKA analysis calculated the impact of 6400 satellites, taking into account both direct signals and leakage called “side lobes.”

The SKA team finds that satellite transmissions will lead to a 70% loss in sensitivity in the downlink band. If the number of satellites in megaconstellations reaches 100,000, as predicted by many, the entire band 5b would be unusable. SKA would lose its sensitivity to molecules such as glycine, a protein component. “If it was detected in a planetary system that was forming, that would be a very interesting piece of information,” Diamond says. “This is a new area that SKA is opening up.” The band could also contain the fingerprints of water molecules in distant galaxies, a tracer that cosmologists use to study how dark energy is accelerating the expansion of the universe.

Since 1959, ITU has protected a number of narrow frequency bands for astronomy. But in recent decades, digital receivers have allowed telescopes to “operate over the whole spectrum,” Diamond says. “We’ve learned to coexist with transmitters,” typically by excluding them from a radio quiet zone or siting telescopes in remote areas. But they have no control over transmitters flying overhead.

Radio astronomers want the satellite operators to turn off their transmitters, move to other bands, or point them away when they are flying over an observatory. Tony Beasley, director of the U.S. National Radio Astronomy Observatory, says they have been discussing these options with SpaceX. “In the next year or two, we will be doing tests where we’re going to be trying to coordinate in real time, technically, with them,” Beasley says this is a reflection of SpaceX’s corporate culture: “They want to do cool stuff; they don’t want to do any harm.”

Other astronomers don’t want to count on corporate goodwill. At the UNOOSA workshop, they pushed for two recommendations: that all future satellites in low-Earth orbit be designed to avoid beaming at radio telescopes and radio quiet zones, and that satellites control the leakage from their side lobes. Those recommendations, along with others that would protect optical observatories, will be debated next year in U.N. subcommittees before going to UNOOSA and, ultimately, the U.N. General Assembly for approval.

Beasley is philosophical about the situation. “SpaceX is legally transmitting inside one of their bands and there are going to be impacts for anyone trying to do radio astronomy,” he says. “These spectrum allocations represent the goals and intent of society. We make [them] to enable commerce and to enable defense and all kinds of activities. We have to come to a solution that satisfies all these to some extent.” ■

COVID-19

Found: genes that sway the course of the coronavirus

Host variants boost severity risk, may point to drug options

By Jocelyn Kaiser

It’s one of the pandemic’s puzzles: Most people infected by SARS-CoV-2 never feel sick, whereas others develop serious symptoms or even end up in an intensive care unit clinging to life. Age and preexisting conditions, such as obesity, account for much of the disparity. But geneticists have raced to see whether a person’s DNA also explains why some get hit hard by the coronavirus, and they have uncovered tantalizing leads.

Now, a U.K. group studying more than 2200 COVID-19 patients has pinned down common gene variants that are linked to the most severe cases of the disease, and that point to existing drugs that could be repurposed to help. “It’s really exciting. Each one provides a potential target” for treatment, says genetic epidemiologist Priya Duggal of Johns Hopkins University.

Kenneth Baillie of the University of Edinburgh, an intensive care physician and geneticist, led the new study, which he discussed on 2 October at an online meeting of a data-pooling effort called the COVID-19 Host Genetics Initiative. He’s hoping the results, also posted as a pre-

print on medRxiv, will speed treatments, although he cautions that any clinical trial inspired by the findings should wait for the study’s acceptance in a peer-reviewed journal. “Because the epidemic is progressing at such an alarming rate, even a few months of time saved will save lots of lives,” Baillie says.

In a standard approach to finding genes that influence a condition, geneticists scan the DNA of large numbers of people for millions of marker sequences, looking for associations between specific markers and cases of the disease. In June, one such genome-wide association study in *The New England Journal of Medicine (NEJM)* found two “hits” linked to respiratory failure in 1600 Italian and Spanish COVID-19 patients: a marker within the *ABO* gene, which determines a person’s blood type, and a stretch of chromosome 3 that holds a half-dozen genes. Those two links have also emerged in other groups’ data, including some from the DNA testing company 23andMe.

The new study confirmed the chromosome 3 region’s involvement. And because 74% of its patients were so sick that they needed invasive ventilation, it had the statistical strength to reveal other mark-



A study of some of the sickest COVID-19 patients, such as those placed on ventilators, has identified gene variants that put people at greater risk of severe disease.

ers, elsewhere in the genome, linked to severe COVID-19. One find is a gene called *IFNAR2* that codes for a cell receptor for interferon, a powerful molecular messenger that rallies the immune defenses when a virus invades a cell. A variant of *IFNAR2* found in one in four Europeans raised the risk of severe COVID-19 by 30%. Baillie says the *IFNAR2* hit is “entirely complementary” to a finding reported in *Science* last month: Very rare mutations that disable *IFNAR2* and seven other interferon genes may explain about 4% of severe COVID-19 cases (25 September, p. 155). Both studies raise hopes for ongoing trials of interferons as a COVID-19 treatment.

A more surprising hit from the U.K. study points to *OAS* genes, which code for proteins that activate an enzyme that breaks down viral RNA. A change in one of those genes might impair this activation, allowing the virus to flourish. The U.K. data suggest there is a variant as common and influential on COVID-19 as the interferon genetic risk factor.

Other genes identified by Baillie's team could ramp up the inflammatory responses to lung damage triggered by SARS-CoV-2, reactions that can be lethal to some patients. One, *DPP9*, codes for an enzyme known to be involved in lung disease; another, *TYK2*, encodes a signaling protein involved in inflammation. Drugs that target those two genes' proteins are already in use—inhibitors of *DPP9*'s enzyme for diabetes and baricitinib, which blocks *TYK2*'s product, for arthritis. Baricitinib is in early clinical testing for COVID-19, and the new data could push it up the priority list, Baillie says.

The chromosome 3 region still stands out as the most powerful genetic actor: A single copy of the disease-associated variant more than doubles an infected person's odds of developing severe COVID-19. Evolutionary biologists reported last month in *Nature* that this suspicious region actually came from Neanderthals, through interbreeding with our species tens of thousands of years ago. It is now found in about 16% of Europeans and 50% of South Asians.

But the specific chromosome 3 gene or genes at play remain elusive. By analyzing gene activity data from normal lung tissue of people with and without the variant, the U.K. team homed in on *CCR2*, a gene that encodes a receptor for cytokine proteins that play a role in inflammation. But other data discussed at last week's meeting point to *SLC6Z20*, which codes for a protein that interacts with the main cell receptor used by SARS-CoV-2 to enter cells. “I don't think

anyone at this point has a clear understanding of what are the underlying genes” for the chromosome 3 link, says Andrea Ganna of the University of Helsinki, who co-leads the COVID-19 Host Genetics Initiative.

The U.K. genetics study did not confirm that the *ABO* variants affect the odds of severe disease. Some studies looking directly at blood type, not genetic markers, have reported that type O blood protects against COVID-19, whereas A blood makes a person more vulnerable. It may be that blood type influences whether a person gets infected, but not how sick they get, says Stanford University geneticist Manuel Rivas. In any case, O blood offers at best modest protection. “There are a lot of people with O blood that have died of the disease. It doesn't really help you,” says geneticist Andre Franke of the Christian-Albrecht University of Kiel, a co-leader of the *NEJM* study.

Researchers expect to pin down more COVID-19 risk genes—already, after folding in the U.K. data plumbed by Baillie's team, the COVID-19 Host Genetics Initiative has found another hit, a gene called *FOXP4* implicated in lung cancer. And in a new medRxiv preprint posted last week, the company Ancestry.com reports that a gene previously connected to the effects of the flu may also boost COVID-19 susceptibility only in men, who are more likely to die of the disease than women.

Geneticists have had little luck so far identifying gene variants that explain why COVID-19 has hit Black people in the United States and United Kingdom particularly hard. The chromosome 3 variant is absent in most people of African ancestry. Researchers suspect that socioeconomic factors and preexisting conditions may better explain the increased risks. But several projects, including Baillie's, are recruiting more people of non-European backgrounds to bolster their power to find COVID-19 gene links. And in an abstract for an online talk later this month at the American Society of Human Genetics annual meeting, the company Regeneron reports it has found a genome region that may raise the risk of severe disease mainly in people of African ancestry.

Even as more genetic risk factors are identified, their overall effect on infected people will be modest compared with other COVID-19 factors, Duggal says. But studies like the U.K. team's could help reveal the underlying biology of the disease and inspire better treatments. “I don't think genetics will lead us out of this. I think genetics may give us new opportunities,” Duggal says. ■

VOICES OF THE PANDEMIC

The United Kingdom's mask crusader

Trisha Greenhalgh argues COVID-19 shows that health policy need not wait for perfect evidence

By Ellen Ruppel Shell

In May, when several prominent U.K. scientists pushed back against a Royal Society report recommending face masks to help control the spread of COVID-19, Trisha Greenhalgh was furious. The scientists argued there was insufficient support in the scientific literature for the efficacy of masks, and the U.K. government, following their lead, declined to mandate masks for the general public.

“The search for perfect evidence may be the enemy of good policy,” Greenhalgh, a physician and expert in health care delivery at the University of Oxford, fumed in the *Boston Review*. “As with parachutes for jumping out of airplanes, it is time to act without waiting for randomized controlled trial evidence.”

Greenhalgh is a firm believer in evidence-based medicine. She wrote a best-selling book on the topic, and her research has earned some of her nation's highest honors. But in recent years, she has grown critical of what she believes is the privileging of randomized controlled studies over clinical experience and close observation. COVID-19, she argues, has revealed the limits of evidence-based medicine—masks being a potent case in point.

“The real tension in public health is, in the absence of strong evidence, whether it's appropriate to take action,” says Tom Inglesby, director of Johns Hopkins University's Center for Health Security. “And a large-scale intervention like masks is extremely difficult to study.” Yet the limited evidence available suggested masks could reduce the amount of virus transmitted from one person to another by more than 90%. And that, Greenhalgh insists, should have been enough to motivate an inexpensive and largely risk-free public health intervention. “Hundreds of thousands of lives were lost before many governments introduced mandatory masking,” she says.

Science's
COVID-19
reporting is
supported by the
Pulitzer Center
and the
Heising-Simons
Foundation.

Even more lives might have been lost if not for Greenhalgh's tireless promotion of masks, which ultimately helped win over policymakers, says Chas Bountra, a professor of translational medicine and pro vice-chancellor of innovation at Oxford. She faced powerful opposition, he says. "Not every scientist would have had the courage."

Greenhalgh says she was born with an insatiable appetite for academic challenges—and a distaste for following the rules. "I nearly got kicked out of secondary school for stealing a dog and bringing him to class," she says.

Warned by a teacher that the University of Cambridge did not admit outspoken young women of "her sort," she applied nonetheless and was granted an interview. "I didn't have the proper clothes, so I made myself a suit," she recalls. Her interlocutor, Tim Hunt, a biochemist who would go on to win the Nobel Prize in Physiology or Medicine (and in 2015 became notorious for disparaging comments he made about women in science), didn't seem to notice. "He kept his head down and asked me seven questions," she says. When he told Greenhalgh she'd gotten every answer wrong, she asked him to explain, and together they reviewed the problems one by one, until she fully understood her errors. "I got my place at Cambridge because research isn't knowing the right answers before you start," she says. "It's about how you ask the questions and how systematically you go about finding the answers."

After studying social and political science at Cambridge, Greenhalgh qualified in medicine at Oxford and then embarked on a career in primary care, with a research focus in endocrinology and a passion for teaching. In 1999, noting that disadvantaged students could not afford to attend her course in international primary health care, she designed—and, for 10 years, ran—the United Kingdom's first fully online master's degree program, attended by hundreds of doctors and nurses from all over the world. "I was humbled by their passion to improve quality of care in what are often staggeringly difficult circumstances," she says.

Greenhalgh has no fear of challenging conventional wisdom. For example, in a 2014 paper that became one of the most read and shared in the history of *The BMJ*,

she posed a hypothetical case of a 74-year-old woman prescribed a high dose of statins to lower her cholesterol, who then suffers muscle pains—a common side effect of statins—that interfere with her hobbies and ability to exercise. Greenhalgh's point was that the prescribing physician had followed protocol but had not accounted for how the patient lived her life. Such scenarios, Greenhalgh wrote, offer "a good example of the evidence-based tail wagging the clinical dog."

"She refutes any mechanical form of reasoning, be it an automatic use of guidelines or a specific research design, as unscholarly," says philosopher Eivind Engbreetsen of the University of Oslo, who has collabo-



"As scientists, our goal must be to cut through the rubbish."

Trisha Greenhalgh, University of Oxford

rated with Greenhalgh for several years. "And she categorically opposes what she calls the most overused and underanalyzed statement in the academic vocabulary: that 'more research is needed.' What we need, she says, is more thinking."

As the mask debate was raging late this spring, Greenhalgh joined data scientist Jeremy Howard at the University of San Francisco to launch a website aimed at turning the tide of public opinion around the world (www.masks4all.co). Their accompanying blog got millions of views and was translated into 21 languages. "Jeremy

came up with the slogan 'It's a piece of cloth, not a land mine,' which drew attention to the quite absurd framing that some anti-maskers had cooked up," Greenhalgh says. After that, the media—and policymakers—came calling.

In one TV appearance, a politician insisted masks were unnecessary because the best barrier to COVID-19 was a front door. Greenhalgh agreed that was true, but added that if people don't want to be on lockdown forever, "I suggest we take that front door, turn it on its side, shrink it down to the size of your hand, and make it out of a double layer of cloth."

Greenhalgh, whom one critic dubbed "the high priestess" of England's masking campaign, joined a World Health Organization (WHO) committee studying the behavioral aspects of mask wearing, such as whether it has an impact on other risky behaviors. "What was apparent was that the people on the WHO committee did not appear to understand the full evidence base," she says. But Greenhalgh persisted, and in early June, WHO, along with the U.S. Centers for Disease Control and Prevention and Public Health England, shifted from claiming masks are potentially harmful to endorsing them. "I think the lesson here is don't give up," she says.

Greenhalgh contends that COVID-19 has made the collaboration of science with the humanities and social sciences all the more vital. Take vaccines, for example. Greenhalgh has enrolled as a test subject for Oxford's promising vaccine candidate and insists that carefully controlled studies are essential before any vaccine is released to the general public. Unlike masks, she notes, vaccines and treatments can have dangerous downsides.

But she's well aware of the human factor: Even the best vaccine will not work if people are too frightened to use it, and she is determined to help mitigate that problem through advocacy and public speaking. Technological innovation, she says, is not enough. Empathy, too, plays a vital role. "Science sits awkwardly in a society where truth no longer matters," she says. "As scientists, our goal must be to cut through the rubbish." ■

Ellen Ruppel Shell, professor of science journalism at Boston University, is author most recently of *The Job: Work and Its Future in a Time of Radical Change*.

WEATHERING THE STORM

As president, Donald Trump has battered science.
But increased spending by Congress and
some supportive agency heads have provided relief

By **Jeffrey Mervis**, with reporting by Adrian Cho,
Warren Cornwall, Jocelyn Kaiser, Robert F. Service, Erik Stokstad, and Paul Voosen



Disastrous. Damaging. Catastrophic. Those are just some of the more polite terms that many U.S. scientists use to describe the policies of President Donald Trump. His handling of the COVID-19 pandemic, his repeated public dismissals of scientific expertise, and his disdain for evidence have prompted many researchers to label him the most antisocial president in living memory.

Last month, that sense of betrayal led two of the nation's preeminent scientific bodies, the U.S. National Academy of Sciences and the National Academy of Medicine, to issue an uncharacteristically harsh rebuke. Although the 24 September statement did not name Trump, it was clearly aimed at the president.

"Policymaking must be informed by the best available evidence without it being distorted, concealed, or otherwise deliberately miscommunicated," the leaders of the two academies wrote. "We find reports and incidents of the politicization of science, particularly the overriding of evidence and advice from public health officials and derision of government scientists, to be alarming."

Although many U.S. scientists share those sentiments, other aspects of the administration's overall record elicit a more positive response. Ask researchers how federal funding for their fields has fared since Trump took office in January 2017, and they might acknowledge sustained support and even mention new opportunities in some areas. Inquire about what they think of the appointees leading the federal agencies that fund their work, and they will offer some good—even glowing—reviews.

Those seemingly contradictory responses reflect the complexity of an \$80-billion-a-year system that remains the envy of the world. Any president trying to alter that behemoth has three levers to press—policies, budget requests, and leadership appointments.

To analyze Trump's record in each area, *Science* has talked to dozens of researchers, administrators, and lobbyists. Many asked to remain anonymous because they have ongoing interactions with the administration.

Most scientists give Trump exceedingly low marks in an arena where he has perhaps the greatest authority: foreign affairs. His unilateral decisions to pull out of the Paris climate treaty, the Iran nuclear deal, and the World Health Organization are widely seen as damaging not just to global scientific cooperation, but also to the continued health, safety, and prosperity of the planet. Similarly, most scientists think the administration's ag-

gressive efforts to restrict immigration pose a serious threat to the nation's ability to attract scientific talent from around the world.

In the domestic arena, Trump's efforts to impose new policies by executive order and rewrite regulations have also drawn sharp criticism from scientists. They say the administration has routinely ignored or suppressed evidence that doesn't support its efforts to roll back environmental regulations, including those aimed at limiting emissions of greenhouse gases. Trump has also threatened the reliability of key demographic data by interfering with the orderly completion of the 2020 census, and by telling the Department of Commerce to exclude undocumented residents from the final count.



President Donald Trump has often ignored expert advice on COVID-19.

Biomedical researchers, meanwhile, have been appalled by what they say is a de facto ban on the use of tissue derived from elective abortions in research, as well as orders to cancel a grant that Trump disliked. Such moves, many researchers believe, are designed to advance the president's political agenda at the expense of national interests.

Fewer scientists complain about the Trump administration's record on spending. But that's largely because Congress has ignored the deep cuts the White House has proposed in its annual budget requests to Congress (see graphic, p. 280).

For example, the National Institutes of Health (NIH), the biggest federal supporter of academic research, has seen its budget rise by 39% in the past 5 years despite deep cuts proposed by Trump. The budget of the National Science Foundation (NSF) has gone up by 17% over the past 3 years, reversing the downward direction that Trump has requested and rising more than twice as fast as it did under former President Barack Obama.

Researchers working on artificial intelligence (AI) and in quantum information science are enjoying an even more rapid growth

rate. In a rare embrace of large spending increases, the Trump administration has thrown its weight behind a 2-year doubling of those fields, which fuel what it calls "industries of the future." And Congress seems amenable to the idea.

Assessing the president's appointees is more complicated. Scientists have condemned some of Trump's choices at agencies involved in environmental regulation or climate science, citing their meager scientific credentials or views that are outside the mainstream. The appointees are clustered at the Environmental Protection Agency (EPA), the National Oceanic and Atmospheric Administration (NOAA), and the Department of the Interior. The list also includes three recently installed senior officials at the Census Bureau, which is embroiled in controversy over its plans for completing the 2020 census.

At the same time, most scientists give high marks to the officials who lead agencies that hand out the bulk of federal research dollars (and are generally not involved in hot-button regulatory issues). That list includes the heads of NIH—Obama-era hold-over Francis Collins—and NSF, where Sethuraman Panchanathan succeeded Obama appointee France Córdova after her 6-year term ended in March. Physical scientists also give good reviews to Paul Dabbar and Chris Fall, who manage the science portfolio at the Department of Energy (DOE).

A third group of Trump science appointees remains something of an enigma to the U.S. research community. They include the president's unofficial science adviser, Kelvin Droegemeier; Robert Redfield, head of the Centers for Disease Control and Prevention; and Stephen Hahn, head of the Food and Drug Administration.

The trio are considered able scientists and are generally respected by their peers. But Droegemeier, who leads the White House Office of Science and Technology Policy (OSTP), has disappointed many science policy insiders by failing to make good on promises to better coordinate federal policies that affect universities. "I give him an A for effort, and an F for performance," one observer says. And all three leaders have drawn complaints for their tepid responses when Trump has disputed settled science or attacked their agencies and the scientists who work for them.

But such broad strokes paint only a partial picture of how Trump has influenced the U.S. research enterprise. In the following pages, *Science* looks at how federal science agencies have fared under a president who has repeatedly boasted of "draining the swamp" in the nation's capital.

NIH grantees feel a chill

Trump's arrival brought fears of upheaval, but NIH watchers say the agency has managed to stay on course. Collins's warm relationship with congressional leaders has helped win generous budget increases. And Ned Sharpless, Trump's choice to lead its largest institute, the National Cancer Institute, has been "fantastic," says Jon Retzlaff, chief policy officer for the American Association for Cancer Research.

In contrast, researchers say White House pressure caused NIH to launch a damaging crackdown on scientists with foreign ties (p. 282). They also accuse Trump of political meddling in two important issues—fetal tissue research and pandemic research. In June 2019, the White House ended funding for NIH's in-house research using tissue from elective abortions and announced a new ethics review for extramural grants. This year, a 15-member ethics panel dominated by abortion opponents recommended approval of only one of 14 proposals that had passed review. And in April, NIH pulled a grant to the EcoHealth Alliance, a nonprofit organization working on bat viruses with the Chinese group that Trump accused—without evidence—of releasing the SARS-CoV-2 virus driving the pandemic.

Those actions "have sent a chilling message to scientists," says molecular biologist Keith Yamamoto of the University of California, San Francisco. "If problems that you have a real passion to dig into are deemed politically unsound, you could be out of luck. So watch out."

Smaller role for White House science office

Arriving 2 years into Trump's 4-year term to head OSTP, Droegemeier promised to streamline and improve how the federal government manages academic research. But an interagency panel he created to take on the task—the Joint Committee on the Research Environment (JCORE)—has yet to reach consensus on any of the four areas Droegemeier has targeted.

"He came in all fired up, promising to make things happen," one lobbyist says. "But so far nothing has come out of JCORE, and the research community is very disappointed."

Research advocates do praise OSTP for helping focus more attention on AI and quantum information science. But science lobbyists say the real driver of that initiative has been Michael Kratsios, a scientific neophyte who was nominally in charge of OSTP before Droegemeier joined the administration.

Kratsios "came into the job knowing less about science than any previous OSTP head," one university lobbyist says. "But he was eager to learn, and he listens. He's also figured out how to use his connections to advance the administration's agenda."

DOE stays strong

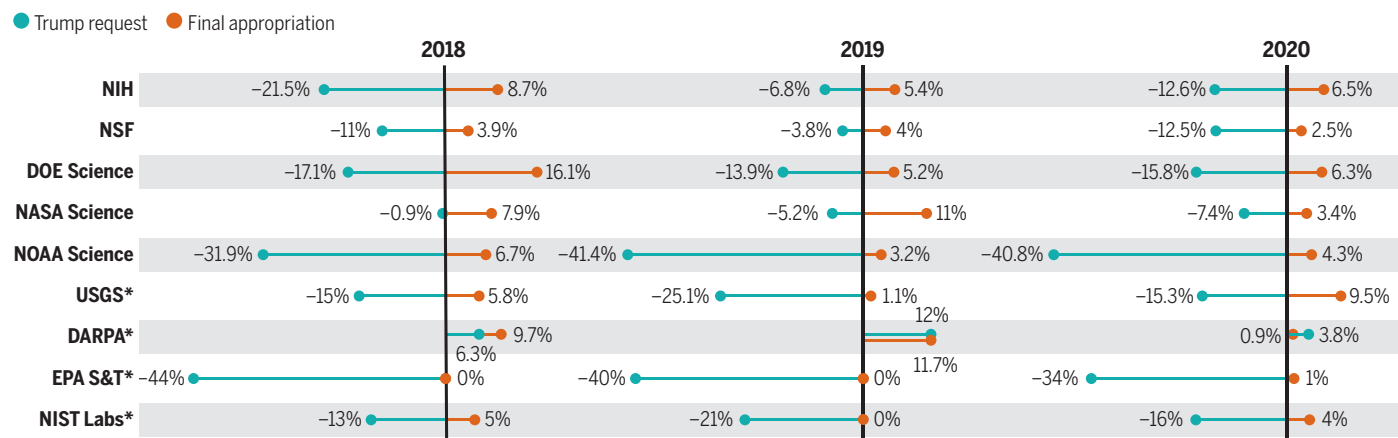
Trump's first energy secretary, Rick Perry, had vowed to eliminate DOE when he ran against Trump in 2016. But Perry surprised the community by becoming a champion of the department's science mission, and his successor, Dan Brouillette, has embraced that role since taking over in December 2019. Observers also credit undersecretary Dabbar for sustaining the political momentum behind several big projects at DOE's 17 national laboratories, including a new atom smasher to study nuclear physics at Brookhaven National Laboratory and a fast-neutron test reactor at Idaho National Laboratory.

Despite the Trump administration's distaste for clean energy research and its conviction that private industry is the real engine of innovation, DOE's \$7 billion Office of Science has fared well. It benefited handsomely from the administration's embrace of AI and quantum information science, where physicists and engineers try to leverage subtle quantum effects to develop more powerful supercomputers and secure communication systems. In July, for example, DOE announced it would build a prototype quantum network to connect Argonne National Laboratory, Fermi National Accelerator Laboratory, and the University of Chicago.

Fall, who was already working for the government when he became head of DOE's basic science shop in May 2019, thinks his office has thrived by avoiding ideological battles over the proper role of government in creating new technologies. "What we don't do is policy," he says. "I'm doing my level best to keep the Office of Science out of politics."

Trump's budget cuts dead on arrival

President Donald Trump has repeatedly asked Congress to approve deep spending cuts at most federal research agencies. But lawmakers have generally ignored his requests and have typically boosted science budgets—with some agencies getting hefty increases.



*U.S. Geological Survey (USGS), Defense Advanced Research Projects Agency (DARPA), Environmental Protection Agency Science & Technology (EPA S&T), National Institute of Standards and Technology (NIST Labs)

Expert advice under siege at EPA

Given candidate Trump's rhetoric opposing government regulation, his affection for fossil fuels, and his denial of climate change, it's no surprise that EPA has often disregarded science in devising environmental policy. Its approach to regulating particulate air pollution—often called PM_{2.5} (particulate matter smaller than 2.5 microns in diameter)—contains all the hallmarks of that approach, including appointing people tied to polluting industries to key posts, excluding experts from advisory roles, and using questionable methods to tip the scales when balancing benefits against costs.

Soon after his appointment in 2017, then-EPA Administrator Scott Pruitt launched several major changes that would likely help ease regulations of PM_{2.5}, which is linked to increased heart and lung diseases and premature deaths. He banned any EPA-funded scientist from serving on advisory boards that vet proposed regulations, but kept the door open to people associated with polluting industries. (A federal court overturned the ban earlier this year.) Pruitt also installed an industry consultant, Tony Cox, as chairman of the air pollution science committee and abolished an expert panel, led by Christopher Frey of North Carolina State University, that advised the committee on the science of particulate matter.

Although Pruitt was forced out of the agency in mid-2018, his replacement, Andrew Wheeler, has followed a similar path. He declined a recommendation from agency scientists to tighten PM_{2.5} limits, citing a study by the reconstituted committee that found the science behind such a reduction was uncertain. The agency's recent actions "just made the whole thing a charade," Frey says.

EPA officials have also proposed barring the agency from considering certain scientific studies as it develops regulations if the underlying data cannot be made public because of concerns about patient privacy or trade secrets. That's the case for some large studies on how air pollution affects public health, and for many industry-funded reviews of toxic chemicals. Researchers say the rule fails to recognize the legitimate need to protect the confidentiality of some data and will undermine the quality of EPA's rulemaking.

Hurricane forecast batters NOAA

Home to some of the country's premier climate scientists, NOAA managed to operate mostly under the radar until August 2019, when Trump announced erroneously that Hurricane Dorian posed a threat to the state of Alabama and apparently used a marker to alter a National Weather Service forecast showing its path. The White House and Commerce Department pushed NOAA's acting administrator, Neil Jacobs, to reprimand weather forecasters for their correction of the president's map and tweets. That political flap, dubbed Sharpiegate, ultimately led to the arrival last month of two new senior political appointees, David Legates and Ryan Maue, who have been dismissive of climate science.

"I have grave concerns around these appointments," says Jonathan White, a retired Navy admiral and CEO of the Consortium for Ocean Leadership. "NOAA has the best [climate] scientists in the government, and I'm very concerned these voices will be muzzled."



A hurricane forecast map altered with a marker touched off controversy in September 2019.

Interior questions climate impacts

As custodian for more than 1.8 billion square kilometers of federal land, the Department of the Interior has been a central player in the Trump administration's push for more oil and gas drilling. But critics say department officials have often overlooked, disregarded, or altered the relevant science, enabling them to dismiss the climate impacts of that drilling and discount potential harm to endangered species.

One early target was calculations of the economic toll from greenhouse gas emissions. Shortly after Trump took office, the department drastically reduced estimates by the Obama administration of such costs. It did so by considering only direct impacts in the United States and by reducing the dollar value of impacts on future generations.

The Trump administration has used the lower price tags to justify rolling back Obama-era limits on methane emissions from oil and gas wells, as well as carbon dioxide from cars and power plants, which fall under the authority of the Department of Transportation and EPA, respectively. But this year, a federal judge ruled the lower estimates were not defensible and that the Interior Department had tried "to erase the scientific and economic facts" used in the previous estimates.

The plight of endangered species has received little attention during the Trump administration, with the number of new species being listed for federal protection at an all-time low. The Fish and Wildlife Service, the branch of the Interior Department that decides whether a species is endangered, "just doesn't have the institutional support to really push back when politics gets in the way of science," says Brett Hartl of the Center for Biological Diversity, which frequently sues federal agencies over endangered species. "They're kind of a forgotten agency."

Relocation rattles USDA scientists

Agriculture Secretary Sonny Perdue upset scientists with his decision to move two of the agency's research centers—the National Institute of Food and Agriculture (NIFA) and the Economic Research Service (ERS)—from Washington, D.C., to Kansas City, Missouri. According to the Congressional Research Service, roughly 75% of the employees left the Department of Agriculture (USDA) rather than move, and many grants were delayed by several months.

Perdue said the new location would bring NIFA and ERS closer to their constituencies and save on rent. But many observers—including congressional Democrats—saw the move as an excuse to shrink ERS and diminish its ability to provide objective monitoring of myriad agricultural trends through its surveys and reports. And

they worried the departures of so many veteran staff would deprive USDA of institutional knowledge and expertise that would take years to replace.

On the plus side, USDA's decision this year to exempt certain gene-edited crops from its biotechnology regulations, potentially easing research, has been well received, says Karl Anderson, director of government relations for the American Society of Agronomy, the Crop Science Society of America, and the Soil Science Society of America. Anderson also applauds the agency's first ever set of long-range goals, which aim to increase agricultural production by 40% by 2050 while cutting the industry's environmental footprint in half. "I think it's a terrific effort," he says.

Scrutiny of foreign ties intensifies

The Trump administration's efforts to limit or prohibit scientific collaborations with China and other countries deemed to pose national security risks have set off alarms throughout the academic community. Although separate from the president's attempts to restrict immigration, both efforts run counter to the traditionally open environment that has propelled U.S. science since the end of World War II. Many researchers also regard them as exercises in racial and ethnic stereotyping.

The Obama administration pursued a handful of investigations, some later dropped, involving scientists with ties to China. But in the summer of 2018, NIH began to send letters to dozens of universities flagging nearly 200 faculty members believed to have hidden research support from Chinese entities. At the same time, university leaders heard themselves being accused of unwittingly handing over the fruits of federally funded research to China, the United States's chief rival as a scientific and economic superpower.

In November 2018, the Department of Justice announced its China Initiative, making it clear that NIH's investigations were part of a broader campaign. Several scientists have

been indicted and some have pleaded guilty, although the charges typically involve making false statements to federal officials or covering up their foreign ties rather than passing along sensitive technologies.

Several agencies have taken steps aimed at learning who else is funding research by their grantees and then deciding whether those other sources pose a threat to national

security. But NIH's actions are widely regarded as the most aggressive and, thus, potentially the most harmful. NSF, for example, insists on full disclosure but only occasionally initiates an investigation, and DOE has told its own scientists they cannot participate in foreign talent recruitment programs but has not altered its rules for grantees.

"Agencies are under tremendous pressure from the White House to find guilty people," says Stanford University physicist Steven Chu, a Nobel Prize winner and former energy secretary under Obama (and a past president of AAAS, *Science's* publisher). "NSF has tried to push back, but NIH has almost completely folded."

The country needs to defend itself against military and economic espionage, scientists say, but some worry the administration's actions to date have already damaged the U.S. research enterprise and that additional restrictions could be fatal.

"The potential loss is hard to estimate," Chu says. Noting the outside contribution of foreign-born scientists to U.S. technical innovation in the past 30 years, he adds, "It's scary to think [what would happen] if you shut that off."



Trump joined Middle Eastern leaders in 2017 at a new institute in Saudi Arabia studying terrorist threats.

A desire for new leadership

Looking ahead to such research-based challenges as the COVID-19 pandemic and climate change, many scientists crave leadership that respects science. On 2 September, for example, 81 Nobel laureates announced their support for Trump's opponent, Democrat Joe Biden. (So far, Trump has not received such an endorsement, although there was a "Scientists for Trump" group during the 2016 contest.)

In their letter, the laureates don't mention any specific policies that Biden has championed over nearly a half-century in public office, including his 8 years as vice president under Obama. But the statement makes clear that they think a Biden administration will do a better job of interacting with the scientific community.

"At no time in our nation's history has there been a greater need for our leaders to appreciate the value of science in formulating public policy," they write in a public letter. "Joe Biden has consistently demonstrated his willingness to listen to experts, his understanding of the value of international collaborations in research, and his respect for the contribution that immigrants make to the intellectual life of our country."

More than a political endorsement, the letter reflects a sense that the federal government has turned its back on science in the past 4 years and their hope that the next president will, in Obama's memorable phrase, "restore science to its rightful place." ■

Scientists and science are on the ballot

Nancy Goroff says she doesn't mind that her opponent calls her a "radical professor." In fact, Goroff, a New York Democrat running for a seat in the U.S. House of Representatives, says her scientific expertise is exactly what Congress needs to deal effectively with climate change, the COVID-19 pandemic, and a host of other issues.

A physical organic chemist and longtime faculty member at Stony Brook University, Goroff is one of several congressional candidates with scientific backgrounds on the ballot next month. (Voters in four states will also weigh in on science-related ballot items.) Nonpartisan polls give her a chance of defeating the Republican incumbent, lawyer Lee Zeldin, and becoming the first female Ph.D. scientist to serve in Congress.

Scientists running for Congress are no longer a novelty. But winning still is. A small army of people with scientific training—almost all Democrats—ran in 2018, vowing to counter what they viewed as the anti-science message coming from President Donald Trump and his administration. But only a handful were successful.

This year, all those rookie legislators are running for reelection to the House, and most are favored to win. The list includes two Illinois Democrats, Sean Casten and Lauren Underwood. Casten, an engineer, has been a vocal advocate for clean energy, while Underwood, a nurse and public health analyst, has been sharply critical of the administration's response to the pandemic. The cohort also features Representative Jim Baird (R-IN), who holds a Ph.D. in animal nutrition.

Goroff hopes her centrist positions will appeal to voters in a Long Island district that Trump carried easily in 2016. In contrast, Zeldin, who is one of Trump's most loyal supporters, is following the president's playbook of painting Democrats as "radicals" whose policies pose a threat to the country.

Goroff waves off the criticism. "They say that any Democrat is a communist or a socialist," she says. "And if they think that using facts and scientific evidence as the basis for making policy is radical, then that says more about them than about us."

Goroff earned her Ph.D. in organic chemistry from the University of California, Los



Voters lined up last month in Fairfax, Virginia, to cast their ballots in this year's elections.

Angeles, and came to Stony Brook in 1997. She studies the structure of semiconducting polymers with the goal of improving solar cells and other devices.

"Nancy isn't someone who publishes a lot of papers. But her work is always very solid," says Luis Echegoyen, a chemist at the University of Texas, El Paso, and current president of the American Chemical Society.

Goroff, who stepped down as department chair and went on leave when she launched her campaign in the spring of 2019, declines to place herself on the political spectrum. But her positions on most issues align with those of the Democratic presidential nominee, former Vice President Joe Biden. "She's no Bernie Sanders," says one longtime Stony Brook colleague, Stephen Koch, referring to the Vermont senator and democratic socialist who lost to Biden in the primaries.

That's true even on climate change, which Goroff has made a pillar of her campaign. Global warming is "the biggest threat to our way of life," she says. But she has not endorsed the Green New Deal, an ambitious plan to cut greenhouse gas emissions and create jobs being advocated by the party's progressive wing. "I have strong objections to some provisions, while others are appropriate," she explains.

In Montana, Democrat Kathleen Williams, a water resources scientist running for the state's only House seat, is also using climate change to differentiate herself from her opponent, Republican Matt Rosendale. Climate change "is real," she said in a recent debate in which she accused Rosendale of "hiding his head in the sand" after he ducked a question on the impact of human activity on the planet's climate.

Unlike Goroff, Williams is playing down any ties to the Democratic establishment. Instead, she vows to break with her party when necessary to broker a deal with Republicans. "Congress is broken" because of "hyperpartisanship," she asserted during the debate. Williams, a former state legislator, lost her 2018 bid to win the seat, but prodigious fundraising has put her in a stronger position this year.

In Wyoming, wildlife ecologist Merav Ben-David of the University of Wyoming is the Democratic candidate for a seat in the U.S. Senate. But she's a decided underdog against Republican Cynthia Lummis, a lawyer who has previously served four terms in the House.

In four states, residents will be voting on ballot initiatives with implications for U.S. researchers. California voters are being asked to approve an additional \$5.5 billion in bonds to fund the California Institute for Regenerative Medicine, the state's stem cell research programs, which voters created in 2004. Nevada could soon require the state's electric utility companies to double their use of renewable energy, to 50%. Voters approved the mandate in 2018, but the state constitution requires a second affirmative vote.

Colorado voters are being asked to support the reintroduction of gray wolves in portions of the state. The restoration effort would begin by the end of 2023. And Oregon could become the first state to allow the use of so-called magic mushrooms in clinical research settings. The active ingredient, psilocybin, has been shown to help those with depression, anxiety, and post-traumatic stress disorder. —J.M.

With reporting by Rasha Aridi, Eli Cahan, and Rebekah Tuchscherer.

WHAT IF BIDEN WINS?

A new president will have vast authority to rapidly shift science policy, but will confront obstacles beyond his control

By David Malakoff



If former Vice President Joe Biden wins the presidential election, he will face high expectations from the U.S. scientific community. Its members will be counting on him to bring science and leadership to the fight against COVID-19 while reversing a host of moves by President Donald Trump that many researchers regard as disastrous (see story, p. 278).

A President Biden will have vast authority to move quickly to undo many Trump policies. But he could be hampered by forces beyond his control, including which party controls the Senate, the ideological complexion of the courts, and—when it comes to fighting COVID-19—the progress of science itself.

Here's a look at some science-related actions Biden will likely pursue, and how quickly he might be able to accomplish them.

Tackle the COVID-19 pandemic.

Biden has made confronting the pandemic the centerpiece of his presidential campaign. The most dramatic immediate shift is likely to be in the tone and consistency of messaging coming from the Oval Office and federal health agencies. On his first day, Biden has

promised to “stop the political theater and willful misinformation that has heightened confusion and discrimination,” hold daily briefings that “put scientists and public health leaders front and center,” and ensure that government scientists “do not fear retribution or public disparagement for performing their jobs.” He's also pledged to rejoin the World Health Organization and boost funding for its pandemic efforts.

At home, Biden says he'll work with governors and local officials to encourage greater use of physical distancing and masks—possibly even mandating their use at federal facilities and on federal lands. And he's vowed to reverse the erosion of public trust in two key health agencies, the Centers for Disease Control and Prevention (CDC) and the Food and Drug Administration (FDA), by appointing new leadership and improving the transparency of decision-making.

Yet getting new agency leaders confirmed by the Senate could take months, observers say, and repairing the damage done to the credibility of those agencies could be slow. Efforts to mandate mask wearing or limit gatherings could face opposition, and how soon

a vaccine or effective new treatments arrive is largely out of a president's control. But a Biden administration could make headway against the pandemic by encouraging and coordinating a wide range of tactics including mask wearing, physical distancing, testing, contact tracing, and the development and distribution of treatments and vaccines.

Confront climate change.

Biden advisers say climate change is one of “the four crises” he will put a priority on addressing. (The others are the pandemic, the economy, and racial injustice.) Biden says the United States will rejoin the Paris climate accord on his first day in office—which he can do with the stroke of a pen—and he will issue executive orders to strengthen climate protections. Advocates want him to roll back Trump rules that weakened limits on power plant emissions set by former President Barack Obama, and to set even stiffer limits for cars than Obama did. Overall, Biden wants the United States to cease to be a net emitter of greenhouse gases by 2050, and the federal government to invest at least \$1.7 trillion over 10 years in clean energy technologies.

Achieving that ambitious agenda will likely require that Democrats control the U.S. Senate. Even with a Democrat-led Congress, however, Biden might only have a 2-year window, as the party in power often loses control of one chamber of Congress in midterm elections. Biden could also face pushback from conservative judges, especially on the Supreme Court, if he relies heavily on executive authority to push his agenda.

Change course on foreign policy.

A president has great leeway in deciding how the United States interacts with other nations, and research groups hope Biden will move aggressively on several fronts. Many want the country to re-engage with Iran to revive the nuclear deal—from which Trump withdrew in 2018—that limited its ability to produce nuclear weapons. Biden says he will “offer Tehran a credible path back to diplomacy” if Iran “returns to strict compliance with the nuclear deal.”

Another tough challenge will be establishing the rules for U.S. research collaborations with China. Under Trump, law enforcement agencies, the National Institutes of Health (NIH), and other agencies have stepped up investigations of scientists who failed to disclose funding ties to foreign institutions, leading to criminal, civil, and administrative punishments. Many of the known cases involve researchers who were born in China or had links to Chinese institutions. Critics say the effort has been racially tinged and has also hindered efforts to recruit foreign-born talent. They hope Biden will ease the scrutiny. But Biden has traditionally been a defense hawk, and China's harsh treatment of Uighurs and other religious minorities may limit moves to ease tensions.

On immigration, industry groups and universities hope Biden follows through on promises to ease restrictions on visas for students and high-skill workers. And some have applauded Biden's vow to protect the so-called Dreamers, undocumented immigrants who were brought to the United States as children, and end Trump's de facto ban on immigrants from many majority-Muslim nations.

Reverse Trump environmental policies.

Environmental scientists have a long wish list. They want Biden to undo changes in how agencies review the environmental impacts of major projects and evaluate the risks posed by toxic chemicals, which critics say downplay the risks and inflate economic benefits. The Environmental Protection Network, made up of former Environmental Protection Agency officials, wants Biden to kill a proposed rule that could bar the agency from using health and other data that can't

be made public because of concerns about patient privacy or trade secrets.

Conservation scientists, meanwhile, hope he will block federal permits for several high-profile energy and mining projects, including proposed pits in Alaska and Minnesota that threaten aquatic habitats. Paleontologists are looking to Biden to restore fossil-rich lands that Trump removed from several national monuments in western states, while ocean scientists want him to reimpose fishing limits that Trump lifted at a marine monument off the coast of New England.

But many of Trump's environmental policies could take years to unwind because of lawsuits and federal rules that require extensive comment periods. Democratic control of the Senate, however, could speed the process: Under a rarely used law, just a simple majority of both houses is needed to cancel rules finalized near the end of the Trump administration. (Republican lawmakers used the law to void many Obama-era rules at the start of Trump's term, when they controlled both chambers of Congress.)

Insulate health agencies from politics.

Biomedical researchers have been appalled by the Trump administration's baldly political moves to influence the work of NIH, CDC, and FDA. Those moves have included ordering NIH to cancel a grant that supported research into bat viruses in China, because Trump alleged—without evidence—that the pandemic virus escaped from a laboratory in Wuhan involved in the project. Trump also blocked or rewrote CDC and FDA policies and guidance that contradicted his views on the pandemic. And he instituted a de facto ban on using fetal tissue from elective abortions in research.

Biden promises to “let science lead,” raising hopes that he will reverse these moves and end political interference in the health agencies. Researchers are also optimistic that Biden will select a stellar replacement for NIH Director Francis Collins, whom many expect to depart after 11 years in the job.

Go big on spending.

Keeping the economy afloat through the pandemic will require massive federal spending, Biden says, and he will likely ask lawmakers to approve a host of spending initiatives early in his term. Universities and research groups want some of the money, saying federal science agencies need tens of billions of dollars to help them recover from the pandemic. And clean energy advocates are hoping the stimulus package would make combating climate change a clear priority at the Department of Energy (DOE). “We'll see much more pressure on [DOE to do work] that might lead to reductions in emissions,”

predicts Elgie Holstein, senior director for strategic planning at the Environmental Defense Fund and a former DOE chief of staff.

To pay for new spending, Biden is likely to propose restoring higher taxes on the wealthy and killing programs he sees as wasteful. One potential target is the Space Launch System (SLS), NASA's troubled heavy-lift rocket for the human space program. The SLS has cost \$20 billion so far and, after years of delays, isn't scheduled to launch until late 2021. Many NASA observers argue that commercial space firms, such as SpaceX, can do the job for less.

Still, with budget experts warning that the federal government's debt is soaring to record levels—it will soon exceed the size of the entire U.S. gross domestic product—the pressure to contain spending will grow. And tax revenues may fall if the economy continues to struggle, crippling Biden's ability to advance his agenda.

Reinvigorate the scientific workforce.

Under Trump, many researchers who work for the federal government have said they don't feel valued or respected. Employee surveys show job satisfaction at several science agencies has taken a nosedive, and there have been many anecdotal reports of researchers leaving their jobs. Biden says he wants to reverse that trend, starting by replacing Trump appointees who have suspect scientific credentials or hold views far out of the mainstream. “The house cleaning could be remarkable; in some cases you are going to see hacks who are flat-out science deniers replaced by appointees who not only understand the science, but have done it themselves,” says one lobbyist who requested anonymity because he still interacts with the Trump administration. Others speculate that Biden might raise the profile of science—and improve morale—by quickly filling the White House science adviser position. (Obama named John Holdren to do the job the month before he was sworn in.)

But it could take years to rebuild the expertise that some agencies have lost, a union that represents public employees warned earlier this year. And former government officials say a Biden administration will also need to strengthen current policies to protect researchers from political interference. Rick Spinrad of Oregon State University, Corvallis, a former chief scientist at the National Oceanic and Atmospheric Administration, says, “What we have seen [under Trump] is abuse and violation of scientific integrity policies—with no consequences.” ■

With reporting from Adrian Cho, Jon Cohen, Warren Cornwall, Jocelyn Kaiser, Jeffrey Mervis, Erik Stokstad, Paul Voosen, and Meredith Wadman.

INSIGHTS



PERSPECTIVES

VIEWPOINT: COVID-19

COVID-19 in children and young people

Children have a low risk of COVID-19 and are disproportionately harmed by precautions

By **Matthew D. Snape**^{1,2} and **Russell M. Viner**³

The severe acute respiratory syndrome coronavirus 2 (SARS-CoV-2) pandemic has brought distinct challenges to the care of children and adolescents globally. Unusually for a respiratory viral infection, children and adolescents are at much lower risk from symptomatic coronavirus disease 2019 (COVID-19) than any other age group. The near-global closure of schools in response

to the pandemic reflected the reasonable expectation from previous respiratory virus outbreaks that children would be a key component of the transmission chain. However, emerging evidence suggests that this is most likely not the case. A minority of children experience a postinfectious inflammatory syndrome, the pathology and long-term outcomes of which are poorly understood. However, relative to their risk of contracting disease, children and adolescents have been disproportionately affected

by lockdown measures, and advocates of child health need to ensure that children's rights to health and social care, mental health support, and education are protected throughout subsequent pandemic waves.

Evidence from contact-tracing studies suggest that children and teenagers are less susceptible to SARS-CoV-2 infection than adults; however, community swabbing and seroprevalence studies conducted outside of outbreak settings suggest that infection rates are similar to those in older

age groups (1–3). Only half of children and teenagers with antibodies against SARS-CoV-2 have experienced symptoms, and there is growing evidence that there is a broad range of presentations, emphasizing the limitations of community-based prevalence studies based on testing only children with respiratory symptoms. Hospitalization for severe acute COVID-19 in children is rare, but among these pediatric inpatients, respiratory symptoms are more apparent than in infected children in the community (4). Case fatality in hospitalized children is, fortunately, relatively low at 1% (compared with 27% across all ages) (4).

The reason for the lower burden of symptomatic disease in children is not yet clear. Upper airway expression of angiotensin-converting enzyme 2 (ACE2), a receptor for the SARS-CoV-2 spike protein, increases with age, and higher ACE2 expression correlates with being positive for SARS-CoV-2 genomic RNA in swabs of upper respiratory tracts from symptomatic children, but not with viral load (5). An alternative proposal is the absence in children of maladaptive immune responses that lead to acute respiratory distress syndrome (ARDS) in older age groups (6), but there are likely other unidentified mechanisms.

Understanding the nature of immune responses in children is important given the rare, but potentially severe, multisystem inflammatory syndrome observed in more than 1000 children and adolescents in multiple countries during the first wave of COVID-19 (7). Known variously as pediatric inflammatory multisystem syndrome temporally associated with SARS-CoV-2 (PIMS-TS), multisystem inflammatory syndrome in children (MIS-C), or Kawasaki-like disease, the illness presents with persistent fever accompanied, to a variable extent, by gastrointestinal symptoms, rash, and conjunctival inflammation. Laboratory markers of inflammation are very high, and myocarditis is a distinct, and potentially fatal, feature. Children and young people with PIMS-TS are more likely to have antibodies to SARS-CoV-2 than evidence of virus from nasal swabs, with presentations usually 4 to 6 weeks after infection. The cardiac involvement initially led to this condition being described as a variant of Kawasaki disease

(in which an unknown trigger leads to an inflammatory disease, resulting in coronary artery inflammation). However, a comprehensive case series clearly delineated PIMS-TS from Kawasaki disease, with children who experience PIMS-TS being substantially older and with increased circulating concentrations of ferritin (a marker of inflammation) and D-dimer and troponin (markers of cardiovascular damage), which are rarely seen in Kawasaki disease (8). A dominant feature of PIMS-TS is myocarditis, transient myocardial dysfunction, and shock, which are present in approximately half of UK and U.S. case series (8, 9).

“...school closures should be undertaken with trepidation given the indirect harms that they incur.”

In the UK, a Delphi national consensus statement has recently been proposed (10) to guide investigation and management of this condition, which focuses on supportive care and enrolling patients into a specific arm of the RECOVERY randomized controlled trial to evaluate the use of corticosteroids and intravenous immunoglobulin in patients with acute PIMS-TS. Fortunately, fatalities are rare [occurring in 10 of the 570 cases reported to the U.S. Centers for Disease Control and Prevention between March and July 2020, and none of 52 cases in a UK series (4, 9)]. However, the long-term consequences are unknown, and all children and teenagers who experience PIMS-TS require ongoing cardiac review. Proposed mechanisms for this illness have focused on a maladaptive acquired immune response to SARS-CoV-2 infection, and a dysregulated humoral immune response is suggested by increased antibodies against multiple, non-SARS-CoV-2, respiratory viruses in severe MIS-C but not mild MIS-C or acute COVID-19 (5).

Understanding this response is crucial when considering the risks and benefits of immunizing children against COVID-19, should a vaccine become available. Of the vaccines being tested in clinical trials, none have yet been administered to children, with priority instead being given, appropriately, to older age groups. The most advanced candidate, ChAdOX1-nCoV-19, is currently in phase 2 and 3 studies that include a pediatric arm for 5 to 12 year olds (NCT04400838), receiving half the full adult dose in this study. However, this study arm is not currently active and will commence enrolment only once the safety

profile in adults is more complete. Given the low rates of disease in children, they are likely to be a low priority to receive a vaccine unless it is definitively shown that (i) children have an important role in the transmission of the virus and (ii) the vaccine reduces viral shedding (and hence reduces transmission).

To what extent do children transmit SARS-CoV-2? Recent reports that young children acutely unwell with COVID-19 have concentrations of viral RNA in nasal aspirates that are similar to, or higher, than adults (5) raised concerns that their role in transmission may have been underestimated. However, one of these studies compared children within the first week of illness with adults with more than 7 days of symptoms, when viral load is expected to be reduced (5). Such studies need to be interpreted with consideration of the very low numbers of children with symptomatic COVID-19.

Of greater concern is the possibility that viral shedding could be occurring from asymptomatic children and that, given schools “bridge” households, this could create a pool of ongoing viral circulation responsible for introductions of virus to the pupils’ homes and beyond. Understanding this issue is fundamental to resolving what has been an unprecedented global disruption to primary (children of ~5 to 11 years) and secondary (children aged 11 to 18 years) education. Given the near universal closing of schools in conjunction with other lockdown measures, it has been difficult to determine what benefit, if any, closing schools has over other interventions. However, there is some reassurance: Multiple studies of contacts of primary and secondary school children with known SARS-CoV-2 infection showed minimal onward transmission in schools (3). Furthermore, after the reopening of primary schools in the UK, only 1 of 23,358 nasal swabs taken from children in June 2020 had detectable SARS-CoV-2, giving an estimate of 3.9 cases per 100,000 students (2). Looked at from another perspective, when household outbreaks of infection have occurred, it appears that children were responsible for only a small minority of household introductions of the virus. Also, recent surveys found that reopening of schools in a number of European countries in April and May had no clear impact on community transmission, with cases continuing to fall in most countries after reopening (11).

Nevertheless, recent experiences of substantial outbreaks of COVID-19 related to children and teenagers show that there is no room for complacency. In May, an Israeli secondary school was shut shortly after a postlockdown reopening after the identi-

¹Oxford Vaccine Group, Department of Paediatrics, University of Oxford, Oxford, UK. ²National Institute for Health Research (NIHR), Oxford Biomedical Research Centre, Oxford, UK. ³Great Ormond Street Institute for Child Health, University College London, London, UK. Email: matthew.snape@paediatrics.ox.ac.uk; r.viner@ucl.ac.uk

fication of two symptomatic students independently infected with SARS-CoV-2. A subsequent schoolwide testing campaign revealed that 153 (13.2%) students and 25 (16.6%) staff had detectable SARS-CoV-2 infection, and contact tracing revealed a further 87 cases in non-school attendees (12). Although formal studies were not conducted to definitively show school-based transmission, potential contributory factors included a heat wave that led to extensive use of air-conditioning and exemptions from face mask wearing, relatively crowded classrooms (with 35 to 38 per class with 1.1 to 1.3 m² between students), and shared schoolyard and outdoor spaces.

As schools in the Northern Hemisphere reopen after summer holidays, risk mitigation strategies adopted to variable degrees include creating separate cohorts (or “bubbles”) within schools that interact minimally with each other, use of face masks in crowded areas (if not the classroom itself), and regular screening of students and staff. The coming months will provide an invaluable opportunity to identify which of these measures are most effective at minimizing transmission, to generate a standard “best practice” that balances young peoples’ rights to an education with the need to protect the broader community from further transmission. However, it is inevitable that there will be students attending school while infected with SARS-CoV-2, and likely there will be some school outbreaks, with the frequency of these events reflecting levels of community transmission. Regardless, it is hard to support the opening of retail and hospital sectors while schools remain shut, as occurred in many countries earlier this year.

School closures and attendant loss of other protective systems for children (such as limited social care and health visiting) highlight the indirect, but very real, harms being disproportionately borne by children and teenagers as a result of measures to mitigate the COVID-19 pandemic. In the UK, it is estimated that the impact on education thus far may lead to a quarter of the national workforce having lower skills and attainment for a generation after the mid-2020s, leading to the loss of billions of dollars in national wealth (11). Additionally, there are a variety of other harms to children’s health, including the risk of reemergence of vaccine-preventable diseases such as measles because of disruptions to immunization programs.

There are many other areas of potential indirect harm to children, including an increase in home injuries (accidental and non-accidental) when children have been less visible to social protection systems because of lockdowns. In Italy, hospitalizations for

accidents at home increased markedly during the COVID-19 lockdown and potentially posed a higher threat to children’s health than COVID-19 (13). UK pediatricians report that delay in presentations to hospital or disrupted services contributed to the deaths of equal numbers of children that were reported to have died with SARS-CoV-2 infection (14). Many countries are seeing evidence that mental health in young people has been adversely affected by school closures and lockdowns. For example, preliminary evidence suggests that deaths by suicide of young people under 18 years old increased during lockdown in England (15).

The role of children in transmission of SARS-CoV-2 remains unclear; however, existing evidence points to educational settings playing only a limited role in transmission when mitigation measures are in place, in marked contrast to other respiratory viruses. In the event of seemingly inevitable future waves of COVID-19, there is likely to be further pressures to close schools. There is now an evidence base on which to make decisions, and school closures should be undertaken with trepidation given the indirect harms that they incur. Pandemic mitigation measures that affect children’s wellbeing should only happen if evidence exists that they help because there is plenty of evidence that they do harm. ■

REFERENCES AND NOTES

1. What’s the STORY, “Serum testing of representative youngsters” (2020); <https://bit.ly/2H30aGa>.
2. S. Ladhani, PHE publications gateway number: GW-1599 (Public Health England, 2020); <https://bit.ly/35G0mVV>.
3. R. M. Viner *et al.*, *medRxiv* 20108126 [Preprint] 21 August 2020; 10.1101/2020.05.20.20108126.
4. O. V. Swann *et al.*; ISARIC4C Investigators, *BMJ* **370**, m3249 (2020).
5. L. M. Yonker *et al.*, *J. Pediatr.* S0022-3476(20)31023-4 (2020); 10.1016/j.jpeds.2020.08.037.
6. A. Fialkowski *et al.*, *Pediatr. Pulmonol.* (2020); 10.1002/ppul.24981.
7. A. H. Rowley, *Nat. Rev. Immunol.* **20**, 453 (2020).
8. E. Whittaker *et al.*; PIMS-TS Study Group and EUCLIDS and PERFORM Consortia, *JAMA* **324**, 259 (2020); 10.1001/jama.2020.10369.
9. S. Godfred-Cato *et al.*; California MIS-C Response Team, *MMWR Morb. Mortal. Wkly. Rep.* **69**, 1074 (2020).
10. R. Horwood *et al.*, *medRxiv* 20156075 [Preprint] 23 July 2020; 10.1101/2020.07.17.20156075.
11. The DELVE Initiative, “Balancing the risks of pupils returning to schools” (Royal Society DELVE Initiative, 2020); <https://bit.ly/3iy8Q5l>.
12. C. Stein-Zamir *et al.*, *Euro Surveill.* **25**, (2020); 10.2807/1560-7917.ES.2020.25.29.2001352.
13. S. Bressan, E. Gallo, F. Tirelli, D. Gregori, L. Da Dalt, Arch. Dis. Child. *archdischild-2020-319547* (2020); 10.1136/archdischild-2020-319547.
14. R. M. Lynn, J. L. Avis, S. Lenton, Z. Amin-Chowdhury, S. N. Ladhani, *Arch. Dis. Child. archdischild-2020-319848* (2020); 10.1136/archdischild-2020-319848.
15. D. Odd *et al.*, “Child suicide rates during the COVID-19 pandemic in England: Real-time surveillance” (Healthcare Quality Improvement Partnership 2020); <https://bit.ly/3moxo2V>.

Published online 21 September 2020
10.1126/science.abd6165

HYDROGELS

Lubricating lipids in hydrogels

A self-renewing lipid layer substantially reduces friction and wear of a hydrogel surface

By Tannin A. Schmidt

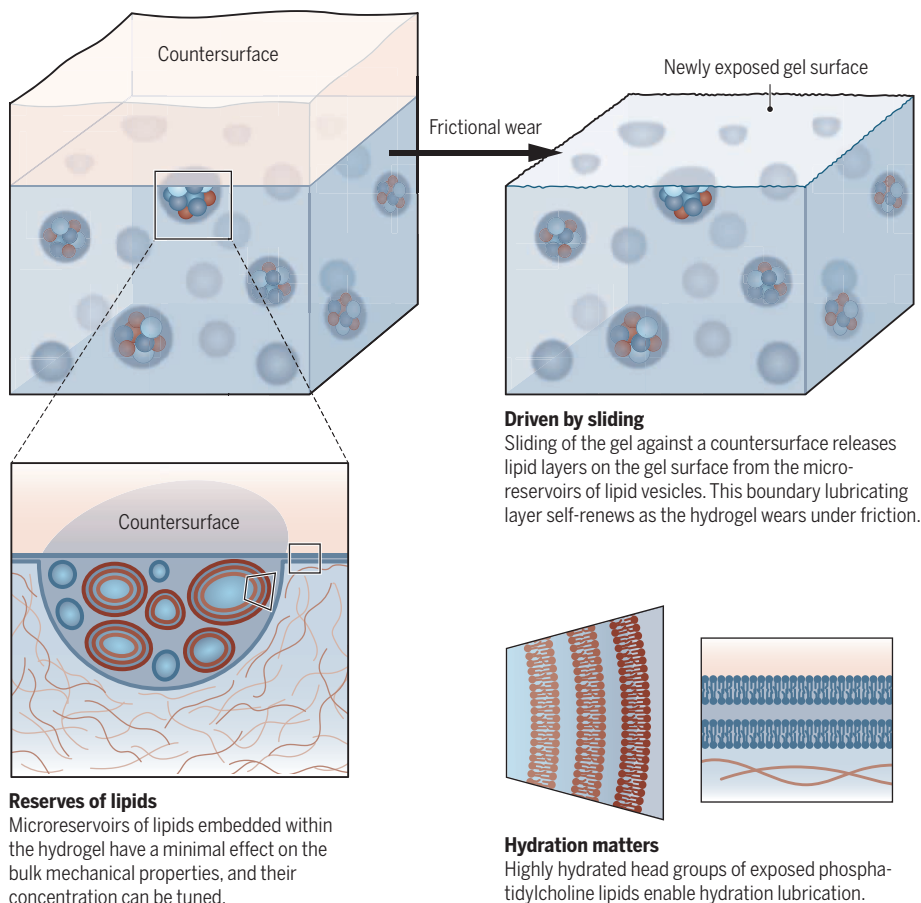
Hydrogels are hydrophilic polymer chain networks that can absorb large quantities of water or biological fluids. In many of their biomedical and other applications (1), hydrogels slide against another surface and must be well lubricated. Hydrogel lubrication is normally provided by fluid interfacial layers (2), but the long-lasting lubrication of articular cartilage in our joints (3–5) is partially the result of nonfluid, highly hydrated head groups of exposed phosphatidylcholine lipids (6). On page 335 of this issue, Lin *et al.* (7) mimic and modify this mechanism in various synthetic hydrogels by incorporating small concentrations of lipids to create a self-renewing, molecularly thin lipid-based boundary layer. The results are striking, with substantial reduction of friction (and wear) observed by as much as a factor of 100 relative to lipid-free hydrogels. Moreover, the effect remained even when gels were dried and rehydrated.

Articular cartilage is the lubricious, load-bearing tissue at the end of long bones in synovial joints that facilitates both low-friction and low-wear articulation. Although the low friction of cartilage is attributed in large part to fluid pressurization that can bear a substantial fraction of the load, lubricant molecules also play an important role in mediating friction, especially with surface-to-surface contact in the boundary mode of lubrication. Synovial fluid constituents, which include hyaluronan, lubricin, and surface-active phospholipids, all can and do contribute to the boundary lubrication of cartilage. Indeed, their independent and synergistic function has been an active area of research and discussion (3, 8–11).

Biomedical Engineering Department, School of Dental Medicine, University of Connecticut Health Center, Farmington, CT 06030, USA. Email: tschmidt@uchc.edu

Cartilage-inspired, lipid-based boundary-lubricated hydrogels

Liu *et al.* incorporated small concentrations of lipids to create a self-renewing, molecularly thin lipid-based boundary layer. This discovery has potential applications in numerous fields relevant to biology and medicine.



Although these molecules have been studied in the context of hydrogel lubrication in the past, Lin *et al.* found that embedding lipids in microreservoirs within hydrogels creates a material with self-renewing boundary lubrication.

Biotribology is the study of lubrication, friction, and wear when applied to biological systems or natural phenomena (12). Friction coefficients are systems variables that depend on test variables, surfaces, and geometries. With that dependence in mind, Lin *et al.* provide compelling data demonstrating the robust and effective lipid-based boundary lubrication in their hydrogels. They examined a number of different hydrogels, both biological and synthetic polymers [some quite different from the commonly used poly(hydroxyethylmethacrylate), pHEMA], and showed effective reduction of friction with the lipid incorporation. They also tested different test countersurfaces other than steel and again found effective friction reduction. Finally, they examined a wide range of sliding velocities (more than three

orders of magnitude). A near-constant friction coefficient provided evidence that boundary-mode lubrication is operative.

This last result highlights the importance of incorporating lipids into a hydrogel to provide self-renewing boundary lubrication. The authors further demonstrate that sliding is the driving mechanism for lipid-layer formation on the gel surface from the microreservoirs of lipid vesicles, and that the self-renewal of this boundary lubricating layer occurs as the hydrogel wears (ever so slightly) under friction (see the figure). Moreover, lubrication by external application of lipids, either through soaking and washing hydrogels or by their presence in solution, is far less effective than when the lipids are bulk-incorporated. Lipids from the surrounding solution had poorer access to the gel/countersurface interface relative to those incorporated into vesicles. Also, the incorporation of lipid vesicles did not alter the mechanical properties of the hydrogel, which may be relevant in various applications.

Additionally, the concentration of incorporated lipids could be altered, which al-

lowed tuning of the lubricating ability and duration of the hydrogels. A potential critical consideration regarding the utility of these hydrogels is that wear is required for these hydrogels to function in their self-renewing manner. Although the authors demonstrate that this wear is minimal and that the materials can sustain many cycles, this parameter could affect longevity and would need to be taken into consideration for different applications. Finally, one amazing feature of these hydrogels that could potentially open up many applications is that they retain their self-sustaining lubrication even after being fully dried in an oven to 60°C and rehydrated. Indeed, this robust property has implications for storage of hydrogels and potentially for their utility in harsh conditions that would not be possible for many other materials.

Lin *et al.* have demonstrated a simple yet effective way of creating self-lubricating hydrogels through incorporation of lipids, with minimal effect on the bulk mechanical properties. These materials may be useful in biomedical applications where sustained and extreme friction and wear would occur, as well as various applications of tissue engineering (13), biosensors, or even contact lenses. Given that hyaluronan and lubricin were initially studied as simple lubricants but were eventually examined more for their biological properties (14, 15), these hydrogels could serve in more complex biological functions beyond pure lubrication, such as drug delivery devices, anti-inflammatories, or immune-response modulators. Indeed, this discovery has potential application in numerous fields relevant to biology and medicine, and it will be of great interest to see where future research and applications lead. ■

REFERENCES AND NOTES

1. N. A. Peppas, J. Z. Hilt, A. Khademhosseini, R. Langer, *Adv. Mater.* **18**, 1345 (2006).
2. J. P. Gong, *Soft Matter* **2**, 544 (2006).
3. J. Seror, L. Zhu, R. Goldberg, A. J. Day, J. Klein, *Nat. Commun.* **6**, 6497 (2015).
4. G. D. Jay, K. A. Waller, *Matrix Biol.* **39**, 17 (2014).
5. A. Singhet *et al.*, *Nat. Mater.* **13**, 988 (2014).
6. W. H. Briscoe *et al.*, *Nature* **444**, 191 (2006).
7. W. Lin *et al.*, *Science* **370**, 335 (2020).
8. E. L. Radin, D. A. Swann, P. A. Weissner, *Nature* **228**, 377 (1970).
9. G. D. Jay, *Connect. Tissue Res.* **28**, 71 (1992).
10. T. A. Schmidt, N. S. Gastelum, Q. T. Nguyen, B. L. Schumacher, R. L. Sah, *Arthritis Rheum.* **56**, 882 (2007).
11. E. D. Bonnevill, D. Galesso, C. Secchieri, I. Cohen, L. J. Bonassar, *PLOS ONE* **10**, e0143415 (2015).
12. D. Dowson, *Proc. Inst. Mech. Eng.* **184**, 181 (1968).
13. A. Khademhosseini, R. Langer, *Biomaterials* **28**, 5087 (2007).
14. A. C. Petrey, C. A. de la Motte, *Front. Immunol.* **5**, 101 (2014).
15. N. Das, T. A. Schmidt, R. J. Krawetz, A. Dufour, *BioEssays* **41**, 1800166 (2019).

10.1126/science.abd3831

NEUROTECHNOLOGY

Advancing limb neural prostheses

Neurotechnology can overcome communication difficulties between prostheses and amputees

By **Stanisa Raspopovic**

Although sophisticated upper- and lower-limb prostheses have been developed, amputees cannot control them intuitively nor perceive sensations from them. These deficiencies result in serious issues, including risk of falls, decreased mobility, heart fatigue during walking, and lower functionality while grasping. Moreover, the prostheses are not perceived by the users as part of their own body (low embodiment), which increases cognitive burden during use or device abandonment. An ideal man-machine interface should enable effortless bidirectional communication between the user and the prosthesis. Neural prostheses that provide bidirectional interfacing with the residual nervous system exploit the persistence of the central and peripheral neural pathways devoted to motor control and sensing (1). A combination of neurotechnologies recently achieved previously unseen capabilities of prosthesis actuation and sensory restoration, but several hurdles need to be overcome before widespread use of these devices.

Upper-limb amputees actuate opening and closing of commercial hand prostheses through the contraction of residual muscles, with no possibility to control single digits. Above-knee amputees exploit their residual hip movements to initiate prostheses, which then execute predefined patterns of motion. Together with natural actuation, a physiologically plausible sensory feedback from prosthesis to amputee is missing, forcing users to continuously visually inspect their artificial limbs. A key limitation of prostheses actuation is that users must learn the nonintuitive control strategies (for example, contracting the biceps to close the hand).

In the case of amputations closer to the hand or foot, the control signals can be extracted from the residual muscles, but when amputations are at the thigh or shoulder level, muscles that control the hand or foot are lost. In these cases, a solution is surgical rerouting of nerves toward the other available muscles, called targeted muscular reinnervation (TMR). After this intervention, the

nerves grow into the new muscles and gain the capacity to excite the tissue. When users attempt movement, neural signals contract the chest muscles in the case of shoulder-level amputees (2) or residual thigh muscles in the case of the above-knee amputation (3) (see the figure). Sensors placed over the skin capture the electrical signal produced by muscle activity, which is then transformed into movement of the robotic arm or leg. Yet, control based on skin surface electrodes (2, 3) suffers from instability due to electrode movement or detachment.

Further development of the muscle reinnervation concept led to the regenerative peripheral nerve interface approach (4). The distal end of a transected peripheral nerve in the arm stump is sutured into a muscle graft, which is implanted with recording wires. These wires are in turn connected to prosthesis controls via cables passing through the skin (which have the potential to become broken or induce infections). This creates a natural amplifier of neural signals of volitional control by transducing them into high-gain myoelectric signals. A high signal-to-noise ratio of this biointerface enabled high-precision control, even for single finger movements in two amputees (4). To overcome the problems of skin electrodes and percutaneous wires, tiny implantable myoelectric sensors (IMESs), which capture the muscular signals directly, were developed. These sensors were injected into the reinnervated muscles of three above-elbow amputees and conferred long-term functional use (5). Whenever the movement intention of an amputee activates the implanted muscles, IMESs capture and amplify these electrical signals and send them wirelessly to the receiving coil embedded into the prosthesis socket to control the motors of the prostheses. This proof of concept needs to be demonstrated in a bigger cohort of patients and will hopefully increase controllable movements.

Alongside actuation, restoring sensory information from the artificial limb to the user is essential for functionality. Natural sensations from the missing extremity can be restored to the brain, inducing so-called phantom sensations, through electrical stimulation of the residual nerves proximal to the amputation. Peripheral nerves contain parallel tubular structures, called fascicles, that transmit different sensations (such as touch

and vibration) from specific areas of the limb. Several neural interfaces with different geometries and placement have been developed and preliminarily tested in upper-limb amputees. The stimulation of residual median and ulnar nerves (which innervate fingers and palm), through implanted transverse intrafascicular multichannel electrodes (TIMES) (6), restored tactile feedback from prostheses in four upper-limb amputees. Relying on the restored feedback, users controlled the amount of force exerted with the prosthesis and distinguished between objects with different compliances and shapes.

Other neurotechnologies that can restore sensory information include Utah slanted electrode arrays (USEAs). These consist of a grid of micrometric stimulating wires of different length that are implanted in peripheral nerve fibers (7) and deliver spatially focused (selective) feedback to hand amputees. In a complementary approach, remarkable stability of several years (in terms of functionality and biocompatibility) was achieved with flat interface nerve electrode (FINE) (8) implants. FINEs enable a gentle nerve flattening, placing the active contacts in proximity to the inner fascicles without penetrating the nerve like TIMES and USEAs do. Thus, FINEs are easier to implant and cause less nerve damage, but at the cost of higher stimulation current to elicit sensations.

Stimulation of leg nerves is a different challenge because they are bigger than nerves in the arm, and skin receptors have different density over the foot-sole skin compared with the palm. Through a meticulous surgery, multiple TIMES were implanted in the sciatic nerve (which innervates the foot and lower leg) and elicited selective foot and leg sensations in three above-knee amputees, augmenting their confidence during walking (9). This improved their mobility on stairs, avoidance of falls, and embodiment of the artificial leg while diminishing the cognitive load during use. Contrary to upper-limb amputation, leg amputation introduces additional health complications such as increased cardiovascular fatigue and decreased mobility. Two highly disabled, above-knee amputees equipped with intraneural feedback from prostheses experienced several health benefits, such as diminished cardiovascular fatigue and pain, increased mobility over uneven terrains, and brain load decrease (10).

In these studies, different sensations were restored in amputees, but there is limited evidence for perceptions of limb position, speed, and torque, namely proprioceptive sensations, which are essential for walking. To overcome this in below-knee amputees, a surgical approach connecting in series two opposing muscle-tendon ensembles (an agonist and an antagonist) was developed (11).

Neuroengineering Laboratory, Institute of Robotics and Intelligent Systems, Department of Health Sciences and Technology, ETH Zurich, Switzerland.
Email: stanisa.raspopovic@hest.ethz.ch

With this strategy, one muscle contracting and shortening (volitional or electrically activated) induces the stretching of the other in the opposing direction. This linked motion permits the natural body receptors embedded in the muscle-tendon to transmit information about muscle length, speed, and force, which is perceived by the brain as joint proprioception and used for precise stair walking. However, transfer of this elegant solution to more disabled above-knee amputees could represent a considerable challenge.

Sensations induced by these different approaches are close to natural but can be perceived as unpleasant electrical tin-

otic and beneficial use of such a bidirectional approach needs to be proven. It needs to be explored whether artificial motor and sensory signals together could be intuitively handled by the brain, without sensorimotor conflicts or cognitive overload, hopefully resulting in increased functionality.

Neural prostheses for sensory feedback restoration were connected to the stimulator, injecting electrical current into the nerves via percutaneous cables, which increases the probability of infections and has limited robustness. Thus, fully implantable wireless systems need to be developed. These systems should feature: long-term stability and safety

Bidirectional limb neural prostheses

Residual motor and sensory neurons in arms and legs of amputees can be used with implants and surgery techniques to confer different sensations and precise motor control of prostheses. Such bidirectional communication and possibly combinations of approaches should improve the quality of life for amputees.

● Residual nerve ● Muscle
■ Sensors on skin ■ Prosthetic device

1 Targeted muscle reinnervation

Nerves grow into new muscles, where they can excite the tissue. This is detected by sensors placed on the skin that then move the robotic prosthetic.

2 Regenerative interface

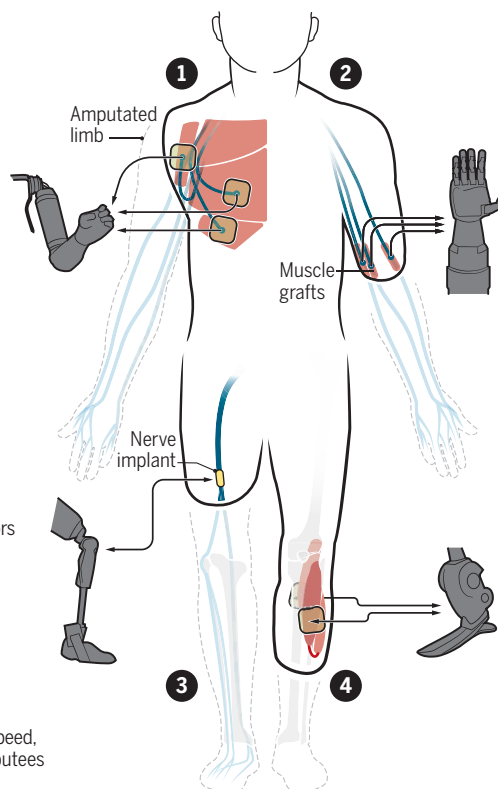
Transected peripheral nerves are sutured into a muscle graft and are implanted with myoelectric sensors that are connected to prosthesis motor controls.

3 Sensory interfacing

Sensory information, such as tactile feedback, can be restored by using various implants that stimulate electrically residual nerves.

4 Agonist-antagonist myoneural interface

Proprioceptive sensations, such as limb position and speed, are important for walking and can be restored in amputees through surgical connection of residual muscles.



gling. Time-variable electrical stimulation, precisely defined by using computational modeling (12), that simulates in silico the responses of tactile neurons innervating the glabrous (hairless) skin was preliminarily demonstrated to induce more natural sensations (7, 13) and could therefore potentially increase acceptance of these technologies. Computational modeling could optimize implant geometry and electrical parameters to personalize devices in the future.

Recently, muscular control implants and sensory stimulation were combined in four amputees, showing long-term stability and safety but with limited insights about sensory benefits or cognitive effects (14). The quantified long-term demonstration of the symbi-

of the implants, high battery capacity, stable leads (that currently are prone to breakage), and easy replacement of implants or their parts. Although typical implantable neurostimulators (such as pacemakers) have pre-programmed stimulation protocols, with no need for a continuous transcutaneous communication, for prostheses a high burden of information has to be wirelessly transmitted through the skin to enable bidirectional communication. This demands high battery capacity while maintaining a limited implant size for surgical placement, representing an important technological challenge. Presently, most implants require several hours-long surgeries, and therefore minimally invasive procedures should be developed.

Capturing information external to the limb is mandatory to trigger neurofeedback, but prostheses do not have sensors in robotic fingers or under the prosthetic foot. Thus, research efforts are devoted to the development of prosthetic electronic skin, which should be able to accommodate a high density of sensors over flexible polymeric structures (15). In the future, these could be imagined as gloves or socks, with robust and high-resolution sensors, placed over the prostheses to transmit different sensory signals such as pressure, movement, and temperature.

To date, these studies are mainly proof of concepts regarding an increase of quality of life or technological viability of neural prostheses, performed with their own metrics, making it difficult to objectively compare outcomes. They are not clinical studies of safety and efficacy, which are important to achieve the necessary medical certifications. Globally, the regulatory steps are demanding and costly, and when accounting for individualization of devices and smaller volume need, the economic cost is potentially high for end users. This could hinder the widespread use of these technologies. Public health care systems vary considerably, and each carries out its own assessment of health technology to support its decisions regarding reimbursement, mainly by demonstrated cost-effectiveness and benefits that increase “quality-adjusted life-years.” Therefore, it is of paramount importance to plan, from the first steps of bidirectional neural prosthesis testing, how to demonstrate safety and health gains because this would augment the likelihood of device approval. The future of neurotechnological intervention for amputees will be in the personalized and combined use of these technologies. Depending on the amputation level and patients’ characteristics, the customized combination of muscular and sensory interventions is likely to benefit amputees in the long term. ■

REFERENCES AND NOTES

1. G. S. Dhillon, K. W. Horch, *IEEE Trans. Neural Syst. Rehabil. Eng.* **13**, 468 (2005).
2. T. A. Kuiken et al., *JAMA* **301**, 619 (2009).
3. L. J. Hargrove et al., *N. Engl. J. Med.* **369**, 1237 (2013).
4. P. P. Vu et al., *Sci. Transl. Med.* **12**, eaay2857 (2020).
5. S. Salminger et al., *Sci. Robot.* **4**, eaaw6306 (2019).
6. S. Raspopovic et al., *Sci. Transl. Med.* **6**, 222ra19 (2014).
7. J. A. George et al., *Sci. Robot.* **4**, eaax2352 (2019).
8. D. W. Tan et al., *Sci. Transl. Med.* **6**, 257ra138 (2014).
9. F. M. Petrini et al., *Sci. Transl. Med.* **11**, eaav8939 (2019).
10. F. M. Petrini et al., *Nat. Med.* **25**, 1356 (2019).
11. T. R. Clites et al., *Sci. Transl. Med.* **10**, eaap8373 (2018).
12. H. Saal et al., *Proc. Natl. Acad. Sci. U.S.A.* **114**, 28 (2017).
13. G. Valle et al., *Neuron* **100**, 37 (2018).
14. M. Ortiz-Catalan et al., *N. Engl. J. Med.* **382**, 1732 (2020).
15. A. Chortos et al., *Nat. Mater.* **15**, 937 (2016).

ACKNOWLEDGMENTS

The author is supported by the European Research Council 2017-STG n.759998 (FeelAgain) and holds shares of SensArS Neuroprosthetics. I thank F. Petrini and M. Capogrosso for their thoughtful input.

10.1126/science.abb1073

SYNTHETIC BIOLOGY

Reconstituting tissue patterning

A synthetic morphogen reveals quantitative principles of tissue patterning

By Naama Barkai and Ben-Zion Shilo

Multicellular organisms develop through a sequence of patterning events, in which cells adopt distinct cell fates. In many instances, patterns are established by morphogen gradients that determine cell fates according to the position of cells within a uniform field. On pages 327 and 321 of this issue, Toda *et al.* (1) and Stapornwongkul *et al.* (2), respectively, use synthetic approaches to study morphogen gradients. Why are synthetic approaches helpful? Patterning systems operate in complex biological settings, and synthetic reconstitution isolates and defines the key players. Because the features of such systems depend directly on quantitative parameters, synthetic approaches allow reconstituting systems in which parameters can be precisely tuned and their effects measured with precision. Additionally, the regulation of patterning systems relies on different feedback loops, and synthetic rewiring highlights the logic of the critical circuits. Overall, the key parameters and players can be examined from different angles.

The concept of morphogen gradients as mediators of tissue patterning was proposed by Wolpert in 1969, coined as the “French-Flag” model (3). Morphogens are molecules that can trigger cells to adopt different fates, depending on the morphogen concentration the cells encounter. Localized production of a morphogen at a restricted source creates a concentration gradient that accordingly confers a complex, position-dependent patterning of the receiving cells (4). Experiments over the past three decades confirmed the involvement of morphogen gradients in a large number of patterning events, such as specification of distinct neural fates within the spinal cord or positioning of veins in the fly wing (5–7). Yet, these experiments also revealed that the actual establishment and utilization of morphogens are considerably more complex than initially envisioned.

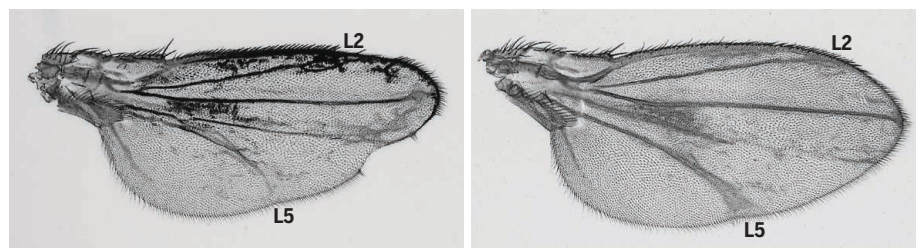
Questions arose as to whether the movement of morphogen across the field depends on passive diffusion in the extracellular milieu or if more active processes involving transport between cells through specialized mechanisms play a role (8).

Moreover, in all systems studied, morphogen distribution depends on a myriad of feedback loops regulating its movement, degradation, production, or downstream activity. Perhaps surprisingly, although systems utilizing patterning by morphogens are continuously discovered, the number of identified morphogens remains small: Systems representing different contexts or organisms repeatedly employ the same few morphogen molecules.

The potential of synthetic systems to disentangle the complexity of morphogen systems and reveal their design principles was demonstrated with the Hedgehog (HH) morphogen (9). The HH pathway is distinct

in heterologous settings, however, the synthetic approach is still limited by the properties and complexity of the selected pathway. This restricts the ability to fully test or construct artificial morphogen-based mechanisms. The studies by Toda *et al.* and Stapornwongkul *et al.* have overcome these hurdles by converting an inert molecule—green fluorescent protein (GFP)—into a morphogen. This allowed tight control of the morphogen parameters and a broad examination of morphogen-based mechanisms.

Toda *et al.* converted a secreted GFP into a morphogen by adapting a paradigm they previously established (10). In this system, a synthetic Notch receptor carrying a GFP-binding protein is activated to induce target genes of interest when presented with GFP that is anchored to a neighboring cell membrane. To follow the distribution of secreted GFP, the authors mixed receiving cells, carrying the synthetic Notch receptor, with cells carrying a transmembrane protein capable of binding GFP and anchoring



An engineered green fluorescent protein (GFP) response reconstitutes patterning in the *Drosophila melanogaster* wing pouch. Stapornwongkul *et al.* reconstituted wing patterning in a *dpp* (decapentaplegic) mutant background. Secreted GFP was expressed from a stripe of cells at the disc center. All cells in the wing pouch expressed chimeric receptors carrying the GFP nanobody on the extracellular domain (left panel). Additional expression of an anchoring protein displaying a GFP nanobody led to more accurate patterning (right panel). The nested expression of *sal* (homeotic spalt-major) and *omb* (optomotor-blind) target genes was restored, as reflected in proper localization of L2 and L5 longitudinal wing veins.

from most morphogen signaling pathways because it uses a “bifunctional-negative” strategy within the same molecule: The HH receptor Patched (PTCH) inhibits downstream HH signaling and also sequesters external HH. Binding of HH to PTCH relieves the PTCH inhibitory activity and induces the expression of PTCH as one of its downstream targets. What could be the consequence of such a design? Motivated by a mathematical model and using the ability to control parameters within a synthetic system, it was revealed that the double-negative design promotes reliability: It accelerates the approach to steady state and provides robustness to variation in ligand production rates

Synthetic systems therefore enable flexible control of parameters such as cell density or availability of different molecules. When using the normal signaling compo-

it. GFP is then made to act as a morphogen: Diffusible GFP is released from a localized source of secreting cells into a field composed of a mixture of receiving cells carrying the synthetic Notch receptor, and anchoring cells that capture the diffusible GFP and present it to the receiving cells.

This system provides easy control of different morphogen parameters. For example, changing the density of the anchor cells or the affinity by which they bind GFP modulated the range of GFP diffusion. Expression of a secreted inhibitory molecule from an opposite pole provided another means for reducing the range and level of the gradient. Additionally, a positive feedback loop can be generated by making secreted GFP

Department of Molecular Genetics, Weizmann Institute of Science, Rehovot 7610001, Israel. Email: naama.barkai@weizmann.ac.il; benzy.shilo@weizmann.ac.il

PHOTOS: STAPORNWONGKUL ET AL. (2)

a target gene for the synthetic receptor. Combining these manipulations, Toda *et al.* generated a propagating wave of patterning, akin to the movement of the morphogenetic furrow in the developing *Drosophila melanogaster* (fruit-fly) eye. Conversely, an engineered negative feedback response to the pathway dampened the response amplitude and accelerated the approach to steady state, which is the state at which most morphogen gradients function.

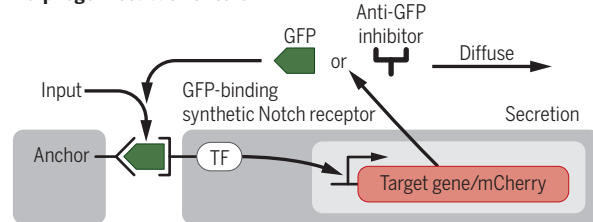
With this toolkit in hand, it was possible to generate elaborate patterns. In their final demonstration, the authors combined one pole that secreted the red fluorescent protein mCherry as the morphogen, and an opposite pole that secreted the inhibitor. The cells between the poles expressed synthetic receptors for either mCherry or GFP and carried the positive feedback to express secreted GFP. With this setting, three domains of gene expression could be identified, mimicking an expected morphogen response (see the figure).

Stapornwongkul *et al.* took on the additional challenge of examining whether a secreted GFP can act as a morphogen within the context of the whole organism. They focused on the well-characterized Dpp (decapentaplegic) gradient in the wing imaginal disc of *D. melanogaster* (5, 6), investigating whether a circuit can be engineered that will imitate Dpp function in disc patterning. They tested diffusion properties of secreted GFP by releasing it from the stripe of cells normally secreting Dpp in vivo. Having established the properties of GFP distribution, the authors investigated whether GFP distribution can replace the function of Dpp in patterning the wing disc. They engineered the normal Dpp receptors Thickveins (Tkv) and Punt (Put), to bind GFP. The assumption was that a GFP dimer would juxtapose the two receptors, leading to their activation. This was indeed the case, although, surprisingly, even a monomeric GFP was sufficient for pathway activation. A nested expression of the target genes *sal* (homeotic spalt-major) and *omb* (optomotor-blind) could be detected, but with a profile that differed from normal. However, when a nonsignaling membrane-tethered protein that facilitated GFP trapping was also expressed, the resulting gene expression pattern was markedly similar to the wild-type profile (see the images).

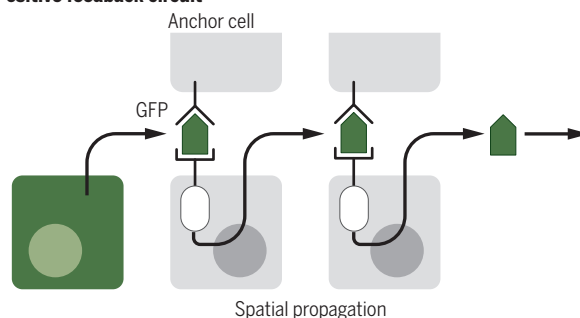
Generating a synthetic morphogen

Toda *et al.* created a source of secreted green fluorescent protein (GFP). The response was marked by transcription factor (TF)-mediated induction of mCherry expression. When the cells carried a positive feedback loop by induction of GFP expression, the response was propagated. When the cells harbored a negative feedback loop, the response was attenuated and steady state was reached faster.

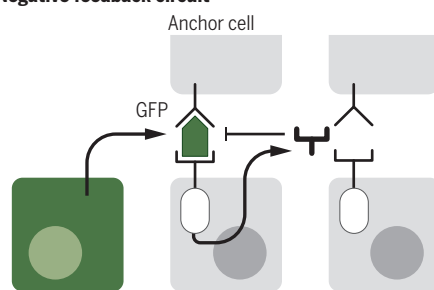
Morphogen feedback circuit



Positive feedback circuit



Negative feedback circuit



Nonsignaling receptors allow more stable trapping of the diffusible ligand, increasing the concentration of ligands presented to the signaling receptor. Such traps, however, also limit the diffusion of the morphogen. This explains the need for fine-tuning their expression, or alternatively, to allow nonsignaling receptors to dissociate from the membrane and traffic the associated morphogen further.

The generation of synthetic morphogen gradients with different regulatory modules represents an impressive technological feat. In addition to confirming previous ideas that were based on genetic manipulations, it allows detailed analysis of quantitative parameters that are not approachable with endogenous systems. Particularly informative is the ability to monitor, in time and space, the dynamics in which the system reaches steady state. The dynamics provides

essential clues regarding the generation and maintenance of a stable morphogen gradient. Such properties render these systems promising for addressing long-standing issues that are seminal to morphogen patterning. For example, an important question is how sharp borders of target-gene expression are created between adjacent groups of cells. Although morphogen gradients are continuous, sharp gene expression borders ensue, suggesting that cells can distinguish small differences in morphogen concentration and translate them to a “yes or no” decision regarding gene expression. The systems described by Toda *et al.* did not give rise to such sharp borders, suggesting that additional mechanisms are required.

Another intriguing topic involves the ability of developmental systems to buffer morphogen gradients against fluctuations (robustness) and adjust the gradient with tissue size (scaling). Several models have been proposed to explain robustness and scaling—for example, self-regulated production of a diffusible molecule that impinges on the global distribution of the morphogen. When expression of such a molecule depends on the morphogen, it allows measurement of the morphogen concentration at the edge of the gradient, and adjusts the entire profile accordingly (11). It will be exciting to investigate whether synthetic approaches could test such models rigorously in the future. In the long term, synthetic approaches may facilitate tissue engineering. With the

capacity to manipulate the production, diffusion, and response to engineered proteins and pathways, it may be easier to execute in culture developmental processes that will allow the formation of artificial tissues. ■

REFERENCES AND NOTES

1. S. Toda *et al.*, *Science* **370**, 327 (2020).
2. K. S. Stapornwongkul *et al.*, *Science* **370**, 321 (2020).
3. L. Wolpert, *J. Theor. Biol.* **25**, 1 (1969).
4. K. W. Rogers, A. F. Schier, *Annu. Rev. Cell Dev. Biol.* **27**, 377 (2011).
5. T. Lecuit *et al.*, *Nature* **381**, 387 (1996).
6. D. Nellen *et al.*, *Cell* **85**, 357 (1996).
7. A. Sagner, J. Briscoe, *Development* **146**, dev182154 (2019).
8. P. Müller *et al.*, *Development* **140**, 1621 (2013).
9. P. Li *et al.*, *Science* **360**, 543 (2018).
10. L. Morsut *et al.*, *Cell* **164**, 780 (2016).
11. B. Z. Shilo, N. Barkai, *Dev. Cell* **40**, 429 (2017).

ACKNOWLEDGMENTS

N.B. and B.-Z.S. are supported by grants from the US-Israel Binational Science Foundation.

10.1126/science.abe4217

IMMUNOLOGY

Immiscible immunity

Mammalian metabolism meets immunity at mitochondria-adjacent lipid droplets

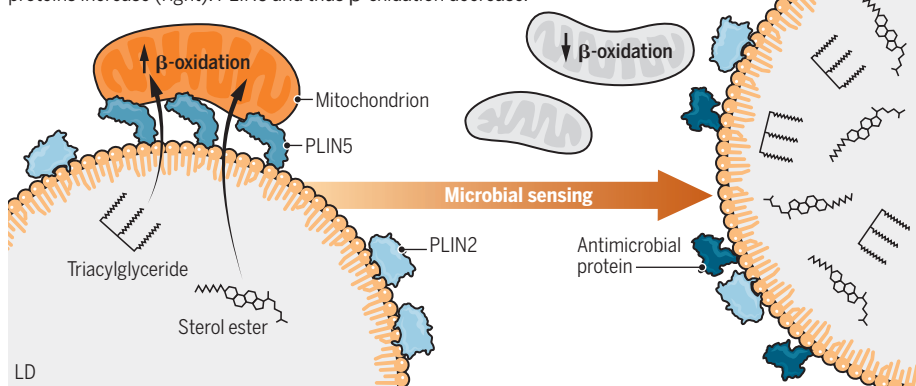
By Douglas R. Green

Oil and water do not mix. This simple fact drives the formation of the lipid-based boundaries of cells, nuclei, and most organelles that make life possible. But a simpler structure, the lipid droplet (LD), coalesces in the cell cytoplasm and comprises a core of neutral fatty acids [mostly triacylglycerides (TAGs) and sterol esters] surrounded by polar lipids (phospholipids and sterols) and associated proteins. An LD is, in essence, a drop of oil, but it has

A century later, they received interest (and perhaps organelle status) with the discovery of perilipins (PLINs), proteins that function in the assembly and stability of LDs (3). A link to infection came with the discovery, by several authors of Bosch *et al.*, that microbial stimulation of macrophages in *Drosophila* induces formation of LDs with antimicrobial activity (4). This activity was dependent on a protein, Jabba, that recruits histones to LDs, and flies lacking Jabba displayed increased sensitivity to bacterial infection. Extranuclear histones in flies and mammals are known to have

Double duty

Perilipin-5 (PLIN5) protein tethers lipid droplets (LDs) to mitochondria, and LDs provide fuel for β -oxidation (left). When the cells sense microbes, the LD proteome changes, and LDs grow in number and size. PLIN2 stabilizes LDs, and antimicrobial proteins increase (right). PLIN5 and thus β -oxidation decrease.



properties that many proponents suggest give it organelle status. As a rich energy reserve, LDs fuel β -oxidation in mitochondria and often physically associate with these organelles. It follows, however, that invading microorganisms similarly exploit LDs as an energy source and, therefore, that cells might “arm” LDs with innate host defense mechanisms. On page 309 of this issue, Bosch *et al.* (1) explore the relations between the antimicrobial activities of LDs and their function as a fuel depot for mitochondria.

LDs were identified more than 130 years ago and reside in all cells and cell types (2).

antimicrobial activity (5), but no Jabba homolog exists in mammals. Nevertheless, activation of cell-surface Toll-like receptors (TLRs), which are sensors of diverse microbial products, strongly stimulates TAG uptake, synthesis, and retention in human and mouse macrophages (6), suggesting a similar antimicrobial role for LDs in mammalian cells.

Bosch *et al.* examined hepatocytes in mice injected with the TLR4 ligand lipopolysaccharide (LPS; a bacterial toxin) and observed an increase in LDs with heightened antimicrobial activity. They also observed similar effects in human monocyte-derived macrophages treated with LPS. Using a proteomic approach, the authors found that 30% of the LD-associated proteome changed (for the most part, increased) in

response to LPS, including several PLIN proteins as well as proteins with known antiviral, antibacterial, and antiprotozoan activity (see the figure). Coexpression analysis revealed that expression of several of the latter proteins correlated with that of PLIN2, the major protein involved in the stabilization of LDs (7).

Among the antibacterial proteins in the PLIN2 cluster was cathelicidin (CAMP), a broadly active antimicrobial peptide with immune regulatory and chemotactic functions. Bosch *et al.* found that silencing CAMP expression in human macrophages prevented their antimicrobial response to intracellular *Escherichia coli*. CAMP is produced as a proprotein with an amino-terminal signal peptide that is cleaved before CAMP is secreted. However, the authors found that LD-associated CAMP retained the signal peptide, suggesting that the signal peptide of CAMP functions not only in secretion but also in targeting CAMP to LDs. By directly steering CAMP to LDs, the organelles acquired antimicrobial activity against *E. coli*, *Listeria monocytogenes*, and methicillin-resistant *Staphylococcus aureus*. LD-associated histones also increased in LPS-treated cells but appeared to play little to no role in antimicrobial effects of LDs.

Ligation of cell surface TLRs on mouse and human macrophages reduces mitochondrial β -oxidation, an effect attributed to down-regulation of adipose triglyceride lipase (ATGL) expression (6), and LPS-treated macrophages shift to a Warburg effect-like oxidative glycolysis (8). However, whereas Bosch *et al.* similarly found that LPS treatment decreased mitochondrial β -oxidation, they did not report substantial change in ATGL expression upon LPS treatment of hepatocytes. They did observe reduced expression of PLIN5, the major protein responsible for tethering mitochondria to LD (9). Another protein suspected of mediating such tethering, diacylglycerol *O*-acyltransferase 2 (10), was found by others to be up-regulated in LPS-treated macrophages (6), but again, Bosch *et al.* did not find this effect in hepatocytes. Nevertheless, they observed that LPS treatment reduced contact between LDs and mitochondria, and enforced expression of PLIN5 in cell lines increased the numbers and lengths of such contacts and prevented their reduction by LPS. These results suggest that regulation of PLIN5 expression controls the fueling of mitochondria by LD for β -oxidation.

Enforced expression of PLIN5 reduced the intracellular antimicrobial effects of LPS treatment in cell lines. This suggests that the uncoupling of mitochondria from

Department of Immunology, St. Jude Children's Research Hospital, Memphis, TN 38139, USA.
Email: douglas.green@stjude.org

LDs might be important for their antimicrobial effects. But why? Because LD-associated CAMP was the major factor mediating LPS-induced antibacterial activity, it might be that mitochondria compete with bacteria for LD binding or otherwise prevent the effects of CAMP on bacteria. Alternatively, the LPS-induced expression of CAMP (and perhaps other antimicrobial effectors) might depend on the LPS-induced metabolic shift to glycolysis. It would be useful to determine if enforced PLIN5 expression affects metabolism in LPS-treated cells and if this, in turn, affects expression of CAMP.

Although LPS ligation of TLR4 directly stimulates LD formation in macrophages (6), this effect in vivo depends in large part on the action of platelet-activating factor (PAF) (11). To what extent the LPS-induced changes noted by Bosch *et al.* in 30% of the LD proteome might result from PAF or other LPS-induced cytokines remains unknown. Nevertheless, the ability of LPs and presumably other TLR agonists to increase intracellular innate defenses against infection in mammals and how this relates to the functions of LDs and their interactions with mitochondria open new avenues for exploration.

“There is great and justifiable excitement regarding the functions of LDs [lipid droplets] and other membraneless organelles...”

There is great and justifiable excitement regarding the functions of LDs and other membraneless organelles and their associated phase transitions in many cellular processes. The studies by Bosch *et al.* suggest that we have much to learn about these drops of oil in cells. ■

REFERENCES AND NOTES

1. M. Bosch *et al.*, *Science* **370**, eaay8085 (2020).
2. R. V. Farese Jr., T. C. Walther, *Cell* **139**, 855 (2009).
3. A. S. Greenberg *et al.*, *J. Biol. Chem.* **266**, 11341 (1991).
4. P. Anand *et al.*, *eLife* **1**, e00003 (2012).
5. M. Hoeksema, M. van Eijk, H. P. Haagsman, K. L. Hartshorn, *Future Microbiol.* **11**, 441 (2016).
6. Y. L. Huang *et al.*, *J. Biol. Chem.* **289**, 3001 (2014).
7. M. Fukushima *et al.*, *In Vitro Cell. Dev. Biol. Anim.* **41**, 321 (2005).
8. L. A. O'Neill, E. J. Pearce, *J. Exp. Med.* **213**, 15 (2016).
9. H. Wang *et al.*, *J. Lipid Res.* **52**, 2159 (2011).
10. S. J. Stone *et al.*, *J. Biol. Chem.* **284**, 5352 (2009).
11. R. N. Gomes *et al.*, *Shock* **26**, 41 (2006).

ACKNOWLEDGMENTS

D.R.G. is supported by grants from the U.S. National Institutes of Health and by the ALSAC.

10.1126/science.abe7891

CELL BIOLOGY

A cellular sense of space and pressure

The nucleus measures cell confinement with a mechanosensitive phospholipase

By Zhouyang Shen^{1,2} and Philipp Niethammer¹

During health or disease, cells traverse great distances along complex landscapes of chemical and physical cues, for instance, to heal wounds or to seed cancer metastases in the body. They navigate through tight, fluid-filled tissue channels and squeeze through narrow blood vessel pores. To choose the best path while avoiding entrapment, cells must gauge the space around them and accommodate their movements to it. On pages 310 and 311 of this issue, Lomakin *et al.* (1) and Venturini *et al.* (2), respectively, find that embryonic, immune, and cancer cells sense confinement through deformation of their nucleus. Stretch in the nuclear membrane activates the enzyme cytosolic phospholipase A₂ (cPLA₂), which initiates cell blebbing and movements that may help cells to crawl within or out of narrow spaces. Both studies add to the emerging idea that the nucleus, besides its genetic functions, directly senses the cell's physical environment.

Previously, it was observed that different cell types start to wobble or pace around when confined (3, 4). This characteristic behavior is caused by contractions of their actin cortex, a meshwork of cytoskeletal filaments that underpins the plasma membrane. Once recruited to the actin meshwork, the molecular motor protein myosin II can slide actin filaments along each other to cause cortical contractions. These contractions pressurize the cellular fluid beneath, driving the formation of plasma membrane blebs (5). Within narrow spaces, this can produce cell movements (3, 4). Lomakin *et al.* and Venturini *et al.* provide an explanation for how cells detect their confinement.

Lomakin *et al.* use atomic force microscopy to systematically squeeze cultured human cancer cells with a flat cantilever. They observe that cells actively push back on the

cantilever when confined to heights of less than 10 μm, which indicates the onset of cortical contractility and blebbing. Confining embryonic zebrafish cells in chambers of similar heights, Venturini *et al.* observe rapid cell polarization and migration.

Cells can sense their physical environment through their plasma membrane, which harbors mechanosensitive ion channels and adhesion molecules that connect the actin cortex to the cell's exterior. The plasma membrane, with its underlying cortical meshwork, directly “touches” the walls of confined spaces. It is hence intuitive to think that it may sense the confinement. Lomakin *et al.* and Venturini *et al.* test this idea. Perturbing extracellular calcium (Ca²⁺), which is required for both cell adhesion and ion-channel mechanotransduction through the plasma membrane, hardly affects confinement sensing. Likewise, pharmacologic inhibition of mechanosensitive channels has little effect. Even barely adherent, rounded cells respond to confinement. Thus, some other mechanism must be involved.

Two earlier studies (6, 7) revealed that cPLA₂ senses nuclear swelling upon osmotic shock to initiate rapid immune cell chemotaxis to zebrafish tail fin wounds (6). Nuclear swelling activates cPLA₂, which then releases the unsaturated fatty acid arachidonic acid (AA) from nuclear membrane phospholipids. AA is converted into hormone-like lipids, called eicosanoids, which attract immune cells and control cell differentiation and survival, among other functions. In the presence of Ca²⁺, cPLA₂ was shown to sense nuclear swelling and compression through stretch in the nuclear membrane (7). These studies demonstrated that the nuclear membrane, much like the plasma membrane, rapidly perceives physical cues from the cell environment and converts them into chemical signals that drive inflammation in vivo.

The confinement behaviors investigated by Lomakin *et al.* and Venturini *et al.* are rapid and reversible. They do not depend on new protein synthesis but require an intact nucleus: Enucleated and mitotic cells do not show the response or do so

¹Cell Biology Program, Memorial Sloan Kettering Cancer Center, New York, NY 10065, USA. ²Louis V. Gerstner Jr. Graduate School of Biomedical Sciences, Memorial Sloan Kettering Cancer Center, New York, NY 10065, USA. Email: niethamp@mskcc.org

at much higher compression. Through pharmacologic and genetic perturbations, these studies identify intracellular Ca^{2+} and cPLA_2 as central regulators. cPLA_2 releases AA into the cytoplasm or supernatant of confined cells without causing neighboring cells to bleb. This points to second-messenger or autocrine functions of AA, or some other cPLA_2 product. After cPLA_2 has cleaved AA from its preferred lipid substrate, phosphatidylcholine, the remaining lysophosphatidylcholine can be converted to lysophosphatidic acid (LPA) by lysophospholipase D activity. LPA activates the small guanosine triphosphatase (GTPase) RhoA to cause cortical contractions and blebbing. Experiments carried out by Venturini *et al.* suggest that the RhoA pathway is activated downstream of cPLA_2 . Future work may further define the lipid(s) that mediate the confinement response.

Taking a careful look at the changes in nuclear structure upon confinement, Lomakin *et al.* and Venturini *et al.* observe that nuclear membrane folds disappear, nuclear pore distance increases, and cPLA_2 binds to the inner nuclear membrane, consistent with the onset of nuclear membrane stretch. From these and other quantitative approaches, the authors conclude that cortical actin-myosin contraction and blebbing-mediated motility result from critical (that is, membrane stretch-inducing) nuclear deformation, which is transduced by cPLA_2 into lipid second messengers. Lomakin *et al.* show that this mechanism allows immune and cancer cells to rapidly move under confinement or efficiently traverse dense extracellular matrix networks in vitro. cPLA_2 -deficient mice (8) and people (9) exhibit several postdevelopmental phenotypes. These have been mostly attributed to defects in eicosanoid signaling, but some of them—such as defective fertility, attenuated ischemic tissue damage, and reduced allergic responses of cPLA_2 -deficient mice—may be revisited for potential cell-autonomous contributions of nuclear membrane mechanotransduction by cPLA_2 . It should also be investigated whether or which other phospholipases can substitute for cPLA_2 in its mechanosensory role.

Cells tune the sensitivity of their “nuclear gauge” by altering the stability of their nuclear lamina, a dense filamentous meshwork beneath the nuclear membrane.

Lomakin *et al.* make nuclear membranes floppier by depleting two lamina-stabilizing components, lamin A and C. This reduces the ability of the cell to sense confinement. A floppier nuclear membrane may require more compression to fully unfold, stretch, and activate cPLA_2 . By contrast, it was previously shown that lamina destabilization promotes cPLA_2 activation upon nuclear swelling after hypotonic shock (6). Perhaps the regulation of nuclear membrane mechanotransduction is stimulus-dependent. Venturini *et al.* describe another instance of stimulus dependence: Although hypotonic cell swelling unfolds the nuclear membrane just like cell confinement, it produces less of an actin-myosin contraction

cleus. This would desensitize or inactivate the nuclear gauge mechanism. If ER membranes collapse into a stretched nucleus, the observations of Venturini *et al.* imply that it must happen slowly. Investigating whether and how membrane tension equilibrates between the ER and the nucleus is complicated by a lack of noninvasive methods to directly measure organelle stretch in intact cells in space and time. But cell-permeable membrane-tension dyes are under development (10), and a better understanding of how cPLA_2 and related proteins detect membrane stretch should inform the design of genetically encoded tension biosensors in the future.

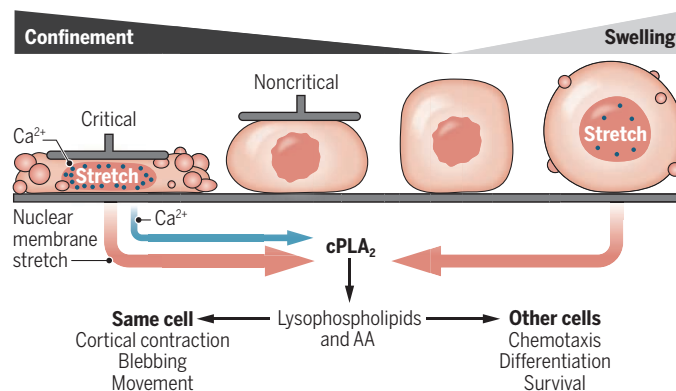
The studies by Lomakin *et al.* and

Venturini *et al.* provide evidence for a mechanotransduction paradigm in which the nuclear membrane takes the center stage (see the figure), as proposed previously (7, 11). Cells may use the nuclear “ruler” to detect their physical surroundings during confined migration or sense and adjust their “posture” in a three-dimensional tissue matrix. A similar mechanism mediates inflammatory lipid signaling during wound detection in zebrafish larvae (6). Recent research suggests that the nuclear membrane also becomes stretched during cell death (12). Cell and nuclear swelling are a hallmark of necrosis, but whether or how nuclear membrane mechanotransduction contributes to cell death signaling or tissue responses to

necrosis is unclear. Revealing which physiologies and pathologies are controlled by the nuclear gauge will be an important mission for future research. ■

Nuclear membrane mechanotransduction

Cells sense critical confinement and swelling through stretch in their nuclear membrane. Calcium (Ca^{2+}) concentration and nuclear membrane stretch together activate cytosolic phospholipase A_2 (cPLA_2), which cleaves nuclear membrane phospholipids into lysophospholipids and arachidonic acid (AA). These cleavage products are further metabolized to bioactive lipids that mediate cell-autonomous or paracrine effects.



response. The authors identify intracellular Ca^{2+} concentrations as a discriminating factor; these are higher during confinement than upon osmotic swelling. Venturini *et al.* propose that cells distinguish different mechanical stimuli by their differential effect on Ca^{2+} concentration and membrane stretch. It will be important to understand how these two cues collaborate at membranes to activate cPLA_2 .

Venturini *et al.* report that squeezed nuclei maintain their unfolded, stretched state for at least an hour, which could allow cells to persistently detect their confinement with little desensitization. Given the complex membrane topology of the nucleus, this observation is interesting and perhaps unexpected. The outer nuclear membrane connects to the endoplasmic reticulum (ER). Thus, perhaps the nuclear membrane stretch is quickly dissipated by membrane flow from the ER to the nu-

REFERENCES AND NOTES

1. A. J. Lomakin *et al.*, *Science* **370**, eaba2894 (2020).
2. V. Venturini *et al.*, *Science* **370**, eaba2644 (2020).
3. V. Rupprecht *et al.*, *Cell* **160**, 673 (2015).
4. Y.-J. Liu *et al.*, *Cell* **160**, 659 (2015).
5. G. T. Charras, *J. Microsc.* **231**, 466 (2008).
6. B. Enyedi, S. Kala, T. Nikolich-Zugich, P. Niethammer, *Nat. Cell Biol.* **15**, 1123 (2013).
7. B. Enyedi, M. Jelcic, P. Niethammer, *Cell* **165**, 1160 (2016).
8. A. Saphirstein *et al.*, *Biochim. Biophys. Acta* **1488**, 139 (2000).
9. D. H. Adler *et al.*, *J. Clin. Invest.* **118**, 2121 (2008).
10. A. Goujon *et al.*, *J. Am. Chem. Soc.* **141**, 3380 (2019).
11. B. Enyedi, P. Niethammer, *Cell. Mol. Bioeng.* **9**, 247 (2016).
12. M. Riegman *et al.*, *Nat. Cell Biol.* **22**, 1042 (2020).

ACKNOWLEDGMENTS

Z.S. and P.N. are supported by U.S. National Institutes of Health grant GM127356.

10.1126/science.abe3881

RETROSPECTIVE

Joe L. Martinez Jr. (1944–2020)

Neuroscientist and advocate of inclusion

By Keith A. Trujillo¹, Alfredo Quiñones-Hinojosa², Kenira J. Thompson³

Joe Louis Martinez Jr. died on 29 August at the age of 76. In addition to making extraordinary contributions to the fields of neurobiology and Chicano psychology, Joe was a tireless advocate of diversity, equity, and inclusion in the sciences. He established professional development programs for individuals from underrepresented groups and provided lifelong mentoring as they pursued careers in science and academia. Joe was passionately devoted to expanding opportunities in the sciences well before diversity became a visible goal for scientific organizations and academic institutions.

Born in Albuquerque, New Mexico, on 1 August 1944, Joe received his bachelor's degree in psychology from the University of San Diego in 1966; his master's in experimental psychology from New Mexico Highlands University in 1968; and his Ph.D. in physiological psychology from the University of Delaware in 1971. His faculty career began in 1972 at California State University, San Bernardino (CSUSB), shortly after the campus was established. He later completed postdocs in the laboratory of neurobiologist James McGaugh at the University of California, Irvine, and with neurobiologist Floyd Bloom at the Salk Institute for Biological Studies in San Diego, California.

The University of California, Berkeley, recruited Joe in 1982, and he served as a professor as well as the area head of biopsychology and faculty assistant to the vice chancellor for affirmative action. As the highest-ranking Hispanic faculty member in the University of California system, Joe used his voice to help others from underrepresented groups. However, he felt that he could have a greater impact on diversity in the sciences by helping to build a university with a high concentration of Hispanic students, so in 1995 he moved to the University of Texas, San Antonio (UTSA). He began as a professor of biology and went on to assume a range of leadership roles, including director

of the Cajal Neuroscience Institute. At UTSA, he worked with colleagues to obtain nearly \$18 million in funding for neuroscience research and education. In 2012, he moved to the University of Illinois at Chicago where he served as professor and psychology department head until his retirement in 2016. At each institution, he embraced the opportunity to provide guidance and mentoring to innumerable students, faculty, and staff.

In 1976, upon realizing that the psychological health and well-being of Hispanics was being overlooked at CSUSB, Joe organized the First Symposium on Chicano Psychology. The following year, he edited *Chicano Psychology*, a book highlighting pa-



pers from the conference, which established him as a founder of the field of Chicano psychology. The book, rereleased in 1984, remains essential reading for both researchers and health care providers. Joe's work in this area continues to influence thought on bilingual education and culturally sensitive mental health services.

Despite the success of his psychology work, Joe yearned to return to the lab. His preclinical research on the neurobiology of learning and memory had begun at the behavioral level, exploring the neurobiological substrates of learning and memory, and had moved into electrophysiological, neurochemical, and molecular mechanisms. He was at the forefront of demonstrating that drugs and neurotransmitters have the ability to modulate memory processes by acting on targets outside as well as inside the brain. He contributed to the finding that endogenous opioids are involved in learning and memory.

His work also showed that long-term potentiation (LTP) is associative in nature, thereby helping to establish LTP as a potential physiological basis for associative learning.

Joe's relentless dedication to diversity, equity, and inclusion by mentoring scientists around the country in career training programs made him stand out in the field. Committed to offering extraordinary professional development to students from underrepresented backgrounds, he was constantly seeking funding and developing programs in career awareness, lifelong mentorship, and professional networking. He cofounded the American Psychological Association's Diversity Program in Neuroscience and the Summer Program in Neuroscience, Excellence and Success (SPINES) at the Marine Biological Laboratory in Woods Hole, Massachusetts. Through these programs, for more than 20 years, he guided nearly 300 graduate students and postdoctoral fellows to careers in neuroscience and academia. He was also a founding member of the National Hispanic Science Network (NHSN), which is dedicated to improving the health equity of Hispanics by increasing interdisciplinary translational research and fostering the development of Hispanic scientists. Through the NHSN, Joe influenced the careers of hundreds more young scientists.

Students would often walk away from a pleasant conversation with Joe, only to realize later that he had shared a profound and inspiring message, as well as guidance that would serve them for years or decades to come. We all appreciated his low-key, understated approach to mentoring. K.A.T. met Joe in the 1980s, A.Q.-H. trained as an undergraduate researcher in Joe's laboratory in the early 1990s, and K.J.T. began as a postdoctoral fellow on Joe's research team in the late 1990s. Each of us remembers Joe fondly, not only for his mentorship and the opportunities he created for us, but also for his kind heart, extraordinary intellect, and his inspiring friendship. Joe made us all feel like family.

Joe was an elected fellow of multiple scientific societies, including the American Association for the Advancement of Science (AAAS, the publisher of *Science*). He was on the editorial board of 10 different psychology and neuroscience journals and held senior editorial positions for several others. Joe's accomplishments have been recognized with several prestigious awards, including the AAAS Lifetime Mentor Award in 1994. An extraordinary scientist, mentor, and activist, Joe was devoted to scientific excellence and to providing guidance and opportunities to others. His quiet yet strong presence will not be forgotten. ■

10.1126/science.abe7588

¹Department of Psychology and Office for Training, Research, and Education in the Sciences, California State University San Marcos, San Marcos, CA, USA. ²Department of Neurologic Surgery, Mayo Clinic, Jacksonville, FL, USA. ³Ponce Research Institute, Ponce Health Sciences University, Ponce, PR, USA. Email: keith@csusm.edu

POLICY FORUM

CLIMATE AND ENERGY

COVID-19 recovery funds dwarf clean energy investment needs

A modest fraction of current global stimulus funds can put the world on track to achieve Paris Agreement goals

By Marina Andrijevic^{1,2}, Carl-Friedrich Schleussner^{1,2}, Matthew J. Gidden^{1,3}, David L. McCollum^{4,5}, Joeri Rogelj^{3,6}

Governments around the globe are responding to the coronavirus disease 2019 (COVID-19)-related economic crisis with unprecedented economic recovery packages (1), which at the time of writing surpassed USD 12 trillion. Several influential voices, including the United Nations (UN) secretary-general, heads of state, companies, investors, and central banks, have called for post-COVID-19 economic recovery efforts to be used to catalyze the necessary longer-term transformation toward a more sustainable and resilient society. Here we shine a light on the opportunity for these investments to support a green recovery by inventorying and classifying the latest information on governments' fiscal stimulus plans (1) and comparing the size of these measures to estimates of low-carbon energy investment needs compatible with the 2015 UN Paris Agreement. We show that low-carbon investments to put the world on an ambitious track toward net zero carbon dioxide emissions by mid-century are dwarfed by currently announced COVID-19 stimulus funds. But marked differences across countries and regions at differing stages of development emphasize the role that international support and global partnership must play to create conditions that enable a global climate-positive recovery.

Current climate commitments by countries for the next decade remain woefully inadequate to meet the climate goals spelled out in the Paris Agreement (2). Decisive action in the coming decade would be needed to set the emissions of the most important greenhouse gas—carbon dioxide—on a path to net zero by mid-century (3) while ensuring that livelihoods of billions of people in developing countries continue to improve. The record decline in global greenhouse gas emissions in the first half of 2020 due to the COVID-19-related economic disruption will almost certainly rebound when economic

activity picks up again and could ultimately have a negligible impact on global warming over the longer term—unless COVID-19 recovery also induces a longer-term structural change in the economy (4).

STIMULUS PACKAGES TO DATE

Governments have announced a variety of policy responses aimed at alleviating the consequences of the COVID-19 crisis (1). We focus on economic stimulus tools deployed explicitly through countries' fiscal systems, taking stock of the packages for 149 countries [see table S1 in the supplementary materials (SM)]. As of end of August 2020, our tracking framework showed aggregate fiscal stimuli amounting to USD 12.2 trillion, 80% of which comes from countries in the Organization for Economic Cooperation and Development (see the figure and fig. S1). The U.S. stimulus is the largest single package to date, constituting a quarter of all global commitments, although the European Union (EU) as a bloc accounts for even more (combining measures by national governments and the European Commission).

Our disaggregation of the packages for this analysis follows the approach of the International Monetary Fund (IMF), whose COVID-19 Policy Tracker is the source for our stimulus data (1). Stimulus packages are divided into two categories: "above-the-line" measures and liquidity support. The former includes additional spending and forgone or deferred revenue, whereas the latter includes instruments such as loans, guarantees, and equity injections. About 70% of stimulus can be classified as "above-the-line" measures, with 7% targeted for the health sector and 63% for other sectors. The remaining 30% is for liquidity support.

The level of specification of countries' stimulus packages varies widely, limiting understanding of the explicit targets governments will aim to achieve with their plans. Although several governments have announced their intentions to earmark portions of their packages for a "green recovery," the exact details remain largely unclear, and

most governments have not yet signaled how they intend to spend their money. This uncertainty notwithstanding, the massive influx of support will be consequential in shaping the postpandemic global economy.

We demonstrate the potential impact that current stimulus could have for a low-carbon energy system transformation. Although such a transformation requires a wide array of policy measures to come to fruition, the spending and liquidity support being put forward can be a powerful catalyst for a climate-positive recovery.

INVESTMENT CONSISTENT WITH 1.5°C

Quantitative modeling studies of pathways compatible with the Paris Agreement agree that a low-carbon transformation is predicated on decarbonizing the production and use of energy (3, 5, 6), responsible for about two-thirds of economy-wide greenhouse gas emissions. To meet the Paris goals, energy supply would need to fully decarbonize by mid-century, if not before (3, 5, 6). Aggregate stimulus estimates (1), green recovery scenarios (7), or suggestions for green recovery policy packages (8) have been published, among a plethora of analyses related to the pandemic. We compare the magnitude of COVID-19 recovery stimulus to the levels of energy system investment required for putting the world on a path toward achieving the goals of the Paris Agreement (5), based on the average estimate across six energy-economy models that were included in the recent Special Report on Global Warming of 1.5°C by the Intergovernmental Panel on Climate Change (IPCC) (3). Although individual model estimates can differ by up to ±50%, the conclusions deriving from our analysis are nevertheless robust. Investments here refer to capital expenses for resource extraction, their conversion, power generation, transmission, and storage, together with efficiency improvements that reduce energy use in buildings, transport, and industry (see SM for details).

The crucial insight emerging from this comparison (see the figure) is the following: Low-carbon investments over the next several years to put the world on track toward net zero carbon dioxide emissions by mid-century are dwarfed by COVID-19 stimulus. Though impressive, a closer look at the numbers points to opportunities as well as challenges.

¹Climate Analytics, Berlin, Germany. ²Integrative Research Institute on Transformations of Human-Environment Systems, Humboldt University, Berlin, Germany. ³Energy Program, International Institute for Applied Systems Analysis, Laxenburg, Austria. ⁴Electric Power Research Institute, Palo Alto, CA, USA. ⁵Howard H. Baker Jr. Center for Public Policy, University of Tennessee, Knoxville, TN, USA. ⁶Grantham Institute for Climate Change and the Environment, Imperial College London, London, UK. Email: marina.andrijevic@hu-berlin.de; j.rogelj@imperial.ac.uk

Average annual low-carbon energy and end-use energy efficiency investment needs under a Paris-compatible pathway have been estimated at about USD 1.4 trillion per year globally over the near term between 2020 and 2024 (3, 5). This yearly estimate of low-carbon energy investments amounts to some 10% of the total pledged COVID-19 stimulus to date (see the figure and figs. S3 and S4), or about half of stimulus when investments are cumulated over the 5-year 2020–2024 period. Given that stimulus is expected to be spent over the course of a few fiscal years only and governments have traditionally

tilting toward a rather weak, pre-COVID climate policy environment worldwide (3, 5). The additional investment needed to shift low-carbon energy investment onto a Paris-compatible pathway thus amounts to about USD 300 billion per year globally over the coming 5 years (see the figure and figs. S5 to S7), less than 3% of total pledged stimulus to date or 12% when considered over the entire 2020–2024 period. Simply put, if even a fraction of current government stimulus would be directed in a responsible manner toward a green recovery, the marginal benefits for a low-carbon future could be considerable.

globally. This represents a mere 0.2% of the total announced stimulus to date (compare figs. S5 and S1), or 1% over the 2020–2024 period. These numbers highlight that a climate-positive COVID-19 recovery relies as much on supporting green investments as it does on avoiding lock-in in polluting ones.

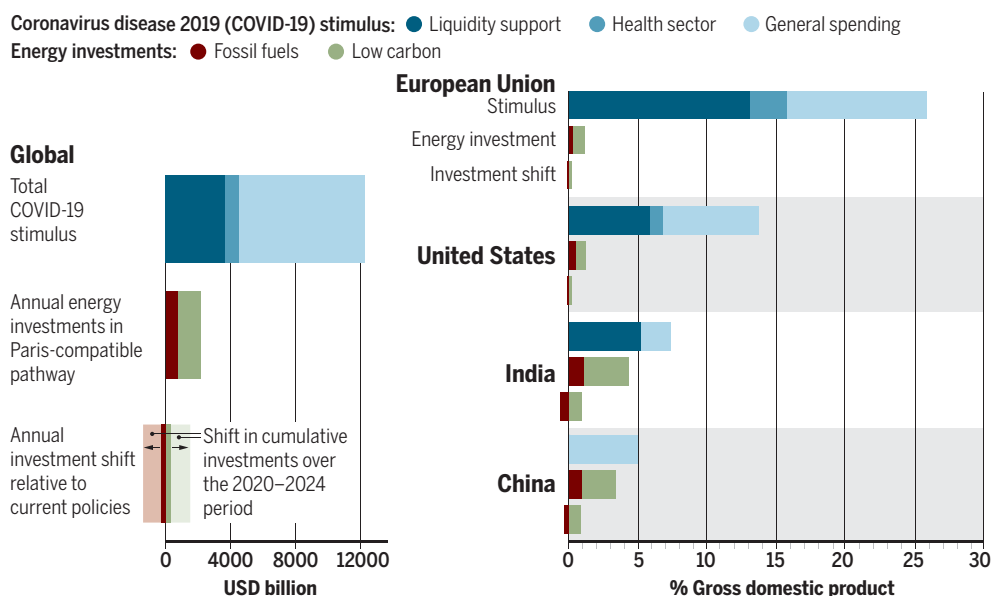
Of course, not all stimulus should be expected to go into the energy transition. Our analysis indicates that, understandably, a substantial number of shares of “above-the-line” measures are earmarked for other sectors, such as health and financial relief for individuals and households. Moreover, governments

are typically responsible for only a limited share of investment in low-carbon energy across the world (10). What governments can do, though, is mobilize private investment by channeling stimulus into dedicated public financing mechanisms. For example, liquidity measures for development banks can help them to proactively support low-carbon investments, particularly in developing countries, and through that reduce perceived risks faced by private investors (11).

Today's exceptional circumstances could also give rise to low-carbon energy and efficiency investment needs or opportunities that exceed those estimated by earlier studies. For example, today's historically low interest rates support the competitiveness of green technologies. Moreover, the investment estimates relied upon here derive from welfare-optimizing scenarios using neoclassical economic theory that assess substantial, yet sustained and gradual changes in investment patterns over the long term in an otherwise stable socioeconomic context (5). These assumptions are in stark contrast with today's reality. Nonequilibrium economic theory might be more adequate in a crisis context and may suggest that substantially increasing green investments beyond the estimates provided here could offer further benefits for growth (12).

Economic stimulus and energy investments

Liquidity support includes loans, guarantees, and quasi-fiscal operations. General spending reflects measures aimed at non-health sectors of the economy and which include supporting individuals, households, and businesses, as well as forgone and deferred revenue. Energy investments are representative of average annual energy system investments over the near term (2020–2024) in a low-carbon pathway consistent with achieving the UN Paris Agreement. Annual investment shifts represent the difference in fossil fuel and low-carbon investments between current policies and a low-carbon pathway consistent with the Paris Agreement. In the absence of specific sectoral allocations, announced stimulus is classified as General spending, e.g., for China. Data and additional figures are available in the supplementary materials.



played a minority role in energy investment globally, the potential for the current tranche of public funding to support a green recovery over the next years is thus enormous.

The comparison between stimulus funding and low-carbon energy investment needs becomes sharper when concentrating specifically on those investments above and beyond a non-Paris-compatible trajectory, like the one society has been on up to now. About USD 1.1 trillion per year of low-carbon energy investment has been estimated for such a non-Paris path, together with an accompanying USD 1.1 trillion in fossil fuels. These amounts would ensure sufficient infrastructure and technology deployment for global energy demand to be met, yet still

Despite the order-of-magnitude difference in these numbers, there is an important additional part to this story: Increases in low-carbon investments have to be accompanied by divestments from high-carbon fossil fuels in the range of USD 280 billion per year over the same near-term period. These divestments are distinct from the possible removal of fossil-fuel subsidies, which also range in the hundreds of billions of USD but mainly target consumption instead of production of fossil fuels (9). Subtracting divestments from investments indicates that the overall increase in net annual investments to achieve an ambitious low-carbon transformation in the energy sector are notably small (see fig. S3): about 20 additional billion USD per year

NATIONAL AND REGIONAL DIFFERENCES

Beyond the global situation, we find that when looking more regionally, total stimulus in all cases exceeds annual low-carbon energy investment needs for an ambitious Paris-compatible pathway (see figs. S8 and S9; here we look at macro regions as defined in table S2 and which are often used in energy-economy modeling). However, clear differences exist between regions and countries. The EU and United States have issued the largest stimulus packages globally, both in absolute terms and relative to

the size of their economies. Total stimulus exceeds average annual low-carbon energy investment needs by a factor of 20 in the United States and by over 30 in the EU (see the figure and fig. S2). Even when considering the entire 2020–2024 period, total stimulus remains several times larger than low-carbon energy investment needs.

Developing economies are in a different situation. So far, the combined stimulus available to low- and lower-middle income countries amounts to only a tiny fraction (less than 4%) of total global stimulus and even including upper-middle income economies raises this share to 14% only. These numbers exclude potential international support, which to date remains negligibly small compared to the pledged domestic COVID-19 stimulus. This discrepancy will not only affect developing countries' ability to recover from the COVID-19 crisis but also the world's collective ability to achieve the Paris Agreement climate goals.

Despite recovery packages in developing countries being smaller than in developed countries [both in absolute terms and as a share of gross domestic product (GDP)], annual low-carbon energy investment needs are generally larger in these rapidly growing economies in a relative sense (see the figure and fig. S8). For example, India's total annual low-carbon energy investment needs relative to its GDP are about four times higher than those of the EU, and the country's stimulus package relative to its GDP is about a quarter the size of the EU's.

Institutionalizing international support within intergovernmental systems such as the Green Climate Fund of the United Nations Framework Convention on Climate Change or multilateral development banks could help to solidify the partnerships needed to enable a global climate-positive recovery. Furthermore, targeted financial instruments, like blended finance, have also been suggested as a means to increase low-carbon investment flows to developing countries (11, 13). Blended finance uses government, multilateral, or philanthropic money to lower the risk for private investors and therewith mobilize additional private investments in developing countries. International support of only a small fraction of current COVID-19 stimulus could thus already provide a lever to catalyze a low-carbon transformation in this first half of the decade.

As developing countries are struggling with the economic fallout of the COVID-19 crisis, mobilizing additional domestic resources might seem challenging, both financially and politically. To this end, a range of measures with both near-term economic benefits and long-term climate-positive potential can prove effective (8).

ECONOMY-WIDE BENEFITS

In the context of a postcrisis recovery, governments will be looking for stimulus measures that can boost employment, scale rapidly, and increase societies' resilience to future shocks. Targeting a green transformation of the energy system as the proverbial engine of the economy can provide such ancillary benefits. Investment in clean energy has been identified as a driver of employment (7, 14); it can also spur innovation and diffusion of technologies across borders—an essential catalyst for low-carbon transformations of economies worldwide (15). Renewable energy investments have demonstrated a large potential for job creation and often offer a more desirable risk profile for investors (14). Technologies like solar photovoltaics and wind turbines are of a small, modular size that allows for a more rapid upscaling of production and much shorter project lead times.

At the same time, achieving a low-carbon transformation involves more than just investments in low-carbon energy. It requires a broad range of reinforcing policy

**“...a climate-positive
COVID-19 recovery relies as
much on supporting
green investments as it
does on avoiding lock-in in
polluting ones.”**

measures, including taxation and subsidy reform, research and innovation, professional training, and education. It will also require a variety of financial instruments, from direct infrastructural investments and capital spending to liquidity support and loan guarantees for private sector investments. In the post-COVID-19 context, this means that beyond the fiscal injections that governments can supply, recovery packages should encompass incentives, policies, taxes or rebates, mandates, and other supportive regulations that facilitate the achievement of long-term climate goals.

By serving as a clear signal to investors, green recovery packages also reduce the likelihood of stranded assets. By contrast, polluting recovery packages that include unconditional oil and gas company bailouts may serve to increase the number of assets that will someday be stranded. Unless governments embed their stimulus support in a coherent long-term vision—for example, by combining support to polluting sectors with a reorientation program for their workforce—the risk for additional

disruption and accompanying economic hardship in the medium term will remain high. All of these attributes make holistic green policies attractive in the context of a postcrisis recovery, and given the many ancillary society-wide benefits, governments may even choose to adopt green recovery targets beyond those presented here.

In sum, a small fraction of announced COVID-19 economic recovery packages could provide the necessary financial basis for a decided shift toward a Paris Agreement-compatible future. The dual crises of COVID-19 and climate change are global problems requiring bold government action, international cooperation, and sustainable and inclusive solutions. Though challenging politically, our findings show that these solutions are well within budget. ■

REFERENCES AND NOTES

1. IMF, *Policy Responses to COVID-19 - Policy Tracker*. International Monetary Fund (2020); www.imf.org/en/Topics/imf-and-covid19/Policy-Responses-to-COVID-19.
2. N. Höhne et al., *Nature* **579**, 25 (2020).
3. J. Rogelj et al., in *Global Warming of 1.5 °C. An IPCC special report on the impacts of global warming of 1.5 °C above preindustrial levels and related global greenhouse gas emission pathways, in the context of strengthening the global response to the threat of climate change, sustainable development, and efforts to eradicate poverty*, G. Flato et al., Eds. (IPCC/WMO, Geneva, Switzerland, 2018; www.ipcc.ch/report/sr15/), pp. 93–174.
4. P. Forster et al., *Nat. Clim. Chang.* **10**, 913 (2020).
5. D. L. McCollum et al., *Nat. Energy* **3**, 589 (2018).
6. L. Clarke et al., in *Climate Change 2014: Mitigation of Climate Change. Contribution of Working Group III to the Fifth Assessment Report of the Intergovernmental Panel on Climate Change*, O. Edenhofer et al., Eds. (Cambridge Univ. Press, 2014), pp. 413–510.
7. IEA, “Sustainable Recovery” (International Energy Agency, Paris, France, 2020); www.iea.org/reports/sustainable-recovery.
8. C. Hepburn, B. O’Callaghan, N. Stern, J. Stiglitz, D. Zenghelis, *Oxf. Rev. Econ. Policy* **36** (suppl. 1), S359 (2020).
9. J. Jewell et al., *Nature* **554**, 229 (2018).
10. IRENA, CPI, “Global Landscape of Renewable Energy Finance” (International Renewable Energy Agency, Abu Dhabi, 2018), p. 44.
11. B. Steffen, T. S. Schmidt, *Nat. Energy* **4**, 75 (2019).
12. H. Pollitt, J.-F. Mercure, *Clim. Policy* **18**, 184 (2018).
13. B. Tonkonogy, J. Brown, V. Micale, X. Wang, A. Clark, “Blended Finance in Clean Energy: Experiences and Opportunities” (Climate Policy Initiative, 2018), p. 38.
14. C. Wilson et al., *Science* **368**, 36 (2020).
15. D. Acemoglu et al., *Am. Econ. Rev.* **108**, 3450 (2018).
16. M. Andrijevic et al., *Climate-analytics/covid_recovery: Data and analysis scripts*, Zenodo (2020); <https://doi.org/10.5281/zenodo.4058546>.

ACKNOWLEDGMENTS

We thank E. Campiglio and J. Tanaka for their feedback on international financial support mechanisms, and acknowledge the contributions of J. Kim, B. Yesil, and K. Lee, who provided excellent research assistance for the curation of the data. M.A. and C.F.S. acknowledge support by the German Federal Ministry of Education and Research (01LS1905A). The views expressed in this paper are those of the authors and do not necessarily reflect those of their institutions. All data and codes are available at Zenodo (16).

SUPPLEMENTARY MATERIALS

science.sciencemag.org/content/370/6514/298/suppl/DC1

10.1126/science.abc9697



Frank Malina works on *Cosmos*, a piece meant to capture an astronaut's vision of the planets.

BOOKS *et al.*

HISTORY OF SCIENCE

Experiments in creativity

Artists and engineers joined forces in the 1960s, blurring the line between art and technology

By Ingrid Ockert

The acronym “STEAM,” which stands for science, technology, engineering, art, and math, came into popularity in 2011, as scientists and educators pondered the question of how to get more students interested in pursuing careers in science. Part of the answer, they reasoned, would be to make science courses more holistic by incorporating the arts—but how might this be done? For inspiration, they need only have looked to the 1960s, when a cadre of artists and engineers worked together to create media that would blur the lines between individuals, art, and technology.

That historic movement is the subject of W. Patrick McCray's excellent new book, *Making Art Work*, which provides a comprehensive history of postwar artistic and scientific collaborations in the United States. Over nine chapters, McCray's meticulous research challenges C. P. Snow's controversial “two-cultures” mode of thinking (*1*), which suggested that scientists and artists exist in different intellectual worlds. McCray's research reveals the ways in which experimental arts and sci-

ences collaborations of the past opened up opportunities for today's interdisciplinary relationships at universities and corporations.

McCray has built his career examining the intersections between scientists and non-scientists. Arguably the foremost scholar of interdisciplinary communities, his work illuminates the many contributions nonscientists have made to the creation of scientific culture. In *Making Art Work*, he carefully blends oral histories with insights derived from print archives.

McCray tells the story of three venues where the arts and sciences mix: an art collective known as Experiments in Art and Technology (E.A.T.), the intersectional academic journal *Leonardo*, and the Los Angeles County Museum of Art. But while these institutions form the book's main threads, the story transcends their specific endeavors, revealing much about the ways that scientists and artists create their identities.

The 1960s, we learn, was a period of existential identity crisis for engineers. Influenced by a barrage of popular articles and studies claiming that they led dull lives, engineers pushed back. Corporations such as

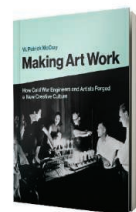
Bell Laboratories established creative spaces for their employees and served as patrons for artistic collaborations, while universities prioritized the provision of studio space where engineering students could dabble in the arts.

McCray introduces the reader to two central figures in the postwar movement that blurred the lines between artist and scientist: Frank Malina, an aeronautical engineer turned kinetic sculptor turned journal editor, and Billy Klüver, a Swedish engineer at Bell Laboratories. Individual artists and engineers had their own reasons for pursuing collaboration. Many of the engineers, including Malina and Klüver, had been drawn to careers in art before opting for more practical pursuits. The artists who sought out alliances, meanwhile, were often looking for engineers' expertise to help actualize their creative visions. But participants from both disciplines were often united by a shared interest in processes.

Many of the projects that resulted from this movement illuminated how art could be assembled and how technology could inspire audiences. In 1965, for example, Malina designed a stunning electrokinetic sculpture, called *Cosmos*, that captured an astronaut's vision of the planets from space. In *Grass Field*, artist Alex Hay and engineer Herb Schneider designed a bodysuit embedded with electronic sensors that would amplify the movements of Hay's heart, brain, and eye muscles and transmit them as sounds. Viewers watched as Hay sat motionless while the walls around them reverberated with noise.

McCray suggests that today's STEAM initiatives often have a clear economic underpinning, with many proponents believing that collaborations between the arts and sciences will lead to more innovative (and profitable) designs. This is a marked shift from the overall intention of the collaborations of the 1960s, which were driven by more philosophical concerns. The arts-and-technology community has also grown larger and more global over the past

50 years. Much like 50 years ago, however, this new renaissance of art and culture has prompted many unusual alliances. And, once these artistic and scientific collaborations are in place, they will take on a life of their own. “The experiment,” notes McCray, has “been switched on.” ■



Making Art Work
W. Patrick McCray
MIT Press, 2020. 384 pp.

REFERENCES AND NOTES

1. C. P. Snow, *The Two Cultures and the Scientific Revolution* (Oxford Univ. Press, 1959).

10.1126/science.abe4099

SCIENCE LIVES

Tales from times long past

Field adventures and human origin stories combine in a paleoanthropologist's compelling new memoir

By **Barbara J. King**

Why, unlike other primates, did our ancestors begin to walk upright? What factors enabled *Homo erectus* to develop new cultural practices and, later, to give rise to our own species? As paleoanthropologist Meave Leakey explains in *The Sediments of Time*, understanding climate change is key in answering such questions. Reflecting on 50 years of research, largely at field sites around Lake Turkana in Kenya's Great Rift Valley, the book—co-written with Leakey's daughter Samira Leakey—is an engaging memoir in which fieldwork adventures appear alongside dense details of Ice Age cycles, ice core technology, fossil anatomy, and geological research. It serves as an invitation to grasp how climate cycles have driven human evolution and how anthropogenic global warming now threatens our species (and a multitude of others).

A university student in the 1960s who wished to become a marine biologist, Meave Leakey encountered rampant sexism that kept women off research ships. "Eventually, I came to the realization that my chances of finding a job on a boat were terribly slim and that I would need to consider alternatives," she writes. When a friend alerted her to an advertisement for employment at a primate research center in Kenya, Meave rang the listed phone number and soon found herself working there for the paleoanthropologist Louis Leakey. Thus began her lifelong love affair with East Africa, one that eventually included Leakey's son Richard, whom she married in 1970.

Having joined a world-famous fossil-hunting family, Meave would go on to make spectacular finds that have reshaped how human evolution is understood and taught. In 1994, for instance, her team discovered an early hominin fossil at Kanapoi that was subsequently named *Australopithecus anamensis* and dated to between 3.9 and 4.2 million years ago. This find extended the time range for australopithecines—the same genus of hominin as the

famous Lucy—and, at the time, represented the earliest known hominin bipedality.

Meticulous cross-site research by paleoanthropologists, including Leakey herself, has revealed a shift in habitat and diet that occurred before the time of australopithecines, wherein many species moved from woodlands to grasslands and changed from browsers to grazers. We now know that an "inexorable drying trend" around 5 to 7 million years ago led to a reduction in forest cover and an increase in grasslands, which created new foraging opportunities.



Leakey, with husband Richard and daughter Louise, inspects fossil fragments in 1972.

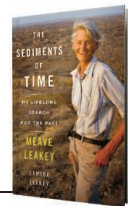
In turn, new selection pressures and bipedalism, a form of locomotion that was efficient and freed up hominin hands to take on fine manipulative tasks, emerged.

Again and again, Leakey's attention returns to climate. *Homo erectus*, she writes, evolved in a "glacial-interglacial icehouse world," where endurance hunting and increased social cooperation led to survival and migration out of Africa. Later, *Homo sapiens* had to cope with even greater extremes of cold and heat.

In the book's epilogue, Leakey draws a strange analogy between baboons destroy-

The Sediments of Time: My Lifelong Search for the Past

Meave Leakey with Samira Leakey
Houghton Mifflin Harcourt,
2020. 400 pp.



ing a vegetable garden and modern humans wrecking our planet, but she places blame for Earth's most recent climate disruption where it belongs. Our long evolutionary lineage is at a crisis point, she argues, and it is critical that we rein in consumerist greed and environmental destruction before it is too late.

The book shines in its descriptions of what it is like to set up base camp in remote, sometimes harsh conditions and to search the landscape relentlessly for small fragments of bone that are all but invisible to the untrained eye, and Leakey writes with a fine sense of humor. The image she creates of Louis and Richard Leakey stripping naked and carrying giraffe bones into the Serengeti plains to experiment with scavenging behavior is one not soon forgotten. Better yet, she writes with humility. Leakey frequently praises individual members of her team as well as other scientists, with evident admiration for their skills. There is a shadow biography of Richard in the book's pages, too, with tales ranging from the plane crash that necessitated a double leg amputation to his conservation work as the head of the Kenya Wildlife Service.

These considerable strengths offset the few places where the science takes a wrong turn. "At birth, a chimpanzee, like all other primates, is already grown enough to function independently of its mother," for example, is a misleading statement about an ape whose offspring depend on their mothers for years. Meanwhile, Leakey's openness to genomic analysis in paleoanthropology is welcome in a fossil hunter, but she credits much more to genes than most anthropologists would be comfortable with, from Richard Leakey's punctuality to his prominent ears. And her observation that "more and more people are abandoning their traditional lifestyles for the melting pot of the big city" comes off as insensitive to inequalities of global power, which I feel certain that, in reality, she is not.

Overall, however, *The Sediments of Time* is a marvelous account of what it is like for a celebrated scientist to take on some of the most vital and vexing questions regarding human origins and to come up with biocultural answers. ■

10.1126/science.abe4107

The reviewer is emerita professor of anthropology at William & Mary, Williamsburg, VA 23185, USA. Email: bjking@wm.edu



Ecosystems supported by Lake Balkhash in Kazakhstan are in jeopardy as desertification increases.

Edited by Jennifer Sills

Save Kazakhstan's shrinking Lake Balkhash

Kazakhstan is home to Lake Balkhash, one of the largest inland drainless lakes in the world. Estimated to be more than 35,000 years old (1), this lake has cultural, historical, and ecological value. However, since 1970, a substantial decrease in the Ili river runoff has led to a drawdown of water reaching the lake [(2), p. 18], leading to a decrease in water depth. Out of the original 16 lake systems around Lake Balkhash, only 5 remain (1). Preserving this lake ecosystem is crucial to halting the desertification process, which has already claimed a third of the lake and will have devastating effects on the diverse flora and fauna that depend on it.

Lake Balkhash's varying degrees of water mineralization support a wide variety of species; the western basin is freshwater, whereas the eastern basin is salty (3). The lake serves as a habitat for 20 species of fish, 6 of which live only in this lake (3), and 60 species of plants that don't grow anywhere else [(4), pp. 304–310]. More than 120 bird species rely on the lake [(2), pp. 24–26], 12 of which are listed in Kazakhstan's Red Book of endangered species [(4), p. 305]. Because the lake is located in a desert area, without runoff and with a dry continental climate and very little precipitation, these species

will have nowhere else to go if their water source disappears.

To protect Lake Balkhash, local legislation that regulates industrial exploitation of the lake water area should be updated and enforced. The media should actively promote environmental awareness among the population of Kazakhstan. Designating Lake Balkhash a national treasure would increase the social significance of the lake in Kazakhstan as well as abroad. Kazakhstan should monitor the lake and provide public access to up-to-date data on its parameters (especially the current volume of water). The country should also clearly define areas of responsibility among the states that are responsible for water resources management. Given rising water security risks in Kazakhstan, Lake Balkhash needs an international collaboration to provide urgent and effective protection. It is crucial that local and national policy-makers, law enforcement authorities, scientists, the public sector, socially responsible businesses, and the world community work together to protect this ancient lake.

Aizhan Ussenaliyeva

Save Lake Balkhash Project, Almaty, Kazakhstan.
Email: aizhanussenaliyeva@gmail.com

REFERENCES AND NOTES

1. D. K. Nourgaliev *et al.*, *Geophys. Res. Lett.* **30**, 1914 (2003).
2. V. N. Abrosov, *Lake Balkhash* (Nauka, 1973) [in Russian].
3. "Lake Balkhash," *Encyclopaedia Britannica* (2020); www.britannica.com/place/Lake-Balkhash#ref189927.
4. D. V. Sevastyanov, E. D. Mamedov, V. A. Rumyanzev, *The History of the Lakes Sevan, Issyk-Kul, Balkhash, Zai-san, and Aral* (Nauka, 1991) [in Russian].

10.1126/science.abe7828

Airborne transmission of SARS-CoV-2

There is overwhelming evidence that inhalation of severe acute respiratory syndrome coronavirus 2 (SARS-CoV-2) represents a major transmission route for coronavirus disease 2019 (COVID-19). There is an urgent need to harmonize discussions about modes of virus transmission across disciplines to ensure the most effective control strategies and provide clear and consistent guidance to the public. To do so, we must clarify the terminology to distinguish between aerosols and droplets using a size threshold of 100 μm , not the historical 5 μm (1). This size more effectively separates their aerodynamic behavior, ability to be inhaled, and efficacy of interventions.

Viruses in droplets (larger than 100 μm) typically fall to the ground in seconds within 2 m of the source and can be sprayed like tiny cannonballs onto nearby individuals. Because of their limited travel range, physical distancing reduces exposure to these droplets. Viruses in aerosols (smaller than 100 μm) can remain suspended in the air for many seconds to hours, like smoke, and be inhaled. They are highly concentrated near an infected person, so they can infect people most easily in close proximity. But aerosols containing infectious virus (2) can also travel more than 2 m and accumulate in poorly ventilated indoor air, leading to superspreading events (3).

Individuals with COVID-19, many of

whom have no symptoms, release thousands of virus-laden aerosols and far fewer droplets when breathing and talking (4–6). Thus, one is far more likely to inhale aerosols than be sprayed by a droplet (7), and so the balance of attention must be shifted to protecting against airborne transmission. In addition to existing mandates of mask-wearing, social distancing, and hygiene efforts, we urge public health officials to add clear guidance about the importance of moving activities outdoors, improving indoor air using ventilation and filtration, and improving protection for high-risk workers (8).

Kimberly A. Prather^{1*}, Linsey C. Marr^{2*}, Robert T. Schooley³, Melissa A. McDiarmid⁴, Mary E. Wilson^{5,6}, Donald K. Milton⁷

¹Scripps Institution of Oceanography, University of California San Diego, La Jolla, CA 92037, USA.

²Civil and Environmental Engineering, Virginia Tech, Blacksburg, VA 24061, USA. ³Department of Medicine, University of California San Diego, La Jolla, CA 92093, USA. ⁴Division of Occupational & Environmental Medicine, University of Maryland School of Medicine, Baltimore, MD 21201, USA.

⁵School of Medicine, University of California, San Francisco, CA 94143, USA. ⁶Harvard T.H. Chan School of Public Health, Boston, MA 02115, USA. ⁷Institute for Applied Environmental Health, University of Maryland, College Park, MD 20742, USA.

*Corresponding author. Email: kprather@ucsd.edu (K.A.P.); lmarr@vt.edu (L.C.M.)

REFERENCES AND NOTES

1. The National Academies of Sciences, Engineering, and Medicine, "Video 31—CQ1 reflection and syntheses: Identifying opportunities and gaps on the path ahead by Kim Prather" (Airborne Transmission of SARS-CoV-2: A Virtual Workshop, 26 to 27 August 2020); www.nationalacademies.org/event/08-26-2020/airborne-transmission-of-sars-cov-2-a-virtual-workshop.
2. J. A. Lednicky *et al.*, *Int. J. Infect. Dis.*, 10.1016/j.ijid.2020.09.025 (2020).
3. S. L. Miller *et al.*, *Indoor Air*, 10.1111/ina.12751 (2020).
4. K. A. Prather, C. C. Wang, R. T. Schooley, *Science* **368**, 1422 (2020).
5. V. Stadnytskyi, C. E. Bax, A. Bax, P. Anfinrud, *Proc. Natl. Acad. Sci. U.S.A.* **117**, 11875 (2020).
6. J. Ma *et al.*, *Clin. Infect. Dis.*, 10.1093/cid/ciaa1283 (2020).
7. W. Chen *et al.*, *Build. Environ.* **176**, 106859 (2020).
8. L. Morawska *et al.*, *Environ. Int.* **142**, 105832 (2020).

COMPETING INTERESTS

K.A.P. is Director of the National Science Foundation Center for Aerosol Impacts on Chemistry of the Environment. L.C.M.

is a member of the Science Advisory Board and holds stock options for Phylagen and is a paid reviewer for the Alfred P. Sloan Foundation. R.T.S. is a member of the Gilead Sciences Scientific Advisory Board and chairs Data Safety and Monitoring Boards for VIR, Gilead, and Merck. Honoraria for these activities are paid to the Regents of the University of California. R.T.S. has served as a scientific consultant to Pfizer and to AbbVie. M.A.M. is the unpaid Chair of the National Academy of Medicine Committee on Personal Protective Equipment for Workplace Safety and Health.

Published online 5 October 2020
10.1126/science.abf0521

Deliberate poisoning of Africa's vultures

Between September 2019 and March 2020, more than 2000 Critically Endangered (1) hooded vultures (*Necrosyrtes monachus*) were killed across eastern Guinea-Bissau. Investigations revealed that the vultures were intentionally poisoned to collect their heads for belief-based use. Locals sighted bait placed where vultures died and reported a demand for vulture heads in Senegal (2, 3). Toxicological analysis of carcasses confirmed poisoning with methiocarb (3), a carbamate pesticide banned in Europe (4) but still used in Guinea-Bissau. If unchecked, these poisonings are likely to continue, leading to further declines in the population of this imperiled species.

Old World vultures are among the most threatened groups of birds worldwide (5). In Africa, the illicit trade in vulture parts accounts for 29% of reported vulture deaths (6). In West Africa, up to 61 and 70% (inside and outside parks, respectively) of vultures disappeared in just 30 years (7). Hundreds of hooded vultures are traded yearly for belief-based use, and their heads are considered good luck charms (8). Prices are rising as they become more rare (8, 9). Guinea-Bissau is home to about 22% of the world's 197,000 hooded vultures (10, 11).

This blow to vulture conservation requires urgent action. Local stakeholders need to be made aware of the loss of critical ecosystem functions, such as waste removal and the likely control of disease (5, 12). African governments should raise awareness about existing anti-poisoning legislation among residents, authorities, and police and invest the human and financial resources required to effectively enforce these laws. In addition, the governments should curb cross-border and local trade. International partners must help West African countries develop and implement national action plans to conserve vultures and avoid their looming extinction.

Mohamed Henriques^{1*}, Ralph Buij^{2,3}, Hamilton Monteiro^{4,5}, Joãozinho Sá^{4,6}, Francisco Wambar⁴, José Pedro Tavares⁷, Andre Botha⁸, Geoffroy Citegetse⁹, Miguel Lecoq¹⁰, Paulo Catry¹¹, Darcy Ogada^{2,12}

¹Centro de Estudos do Ambiente e do Mar (CESAM),

Departamento de Biologia Animal, Faculdade de Ciências da Universidade de Lisboa, Lisboa, Portugal. ²The Peregrine Fund, Boise, ID 83709, USA. ³Wageningen University & Research, 6708 PB Wageningen, Netherlands. ⁴Organização para a Defesa e Desenvolvimento das Zonas Húmidas (ODZH), Bairro de Belém, Bissau, Guinea-Bissau.

⁵Instituto da Biodiversidade e Áreas Protegidas, Bissau, Guinea-Bissau. ⁶Gabinete de Planificação Costeira (GPC), Bairro de Belém, Bissau, Guinea-Bissau. ⁷Vulture Conservation Foundation, CH-8003 Zürich, Switzerland. ⁸Endangered Wildlife Trust, Modderfontein, 1645, South Africa. ⁹BirdLife International, Conservation of Migratory Birds Project, Dakar, Senegal. ¹⁰Lisbon, 1900-087, Portugal. ¹¹Marine and Environmental Sciences Centre, Instituto Universitário, Lisbon, Portugal. ¹²National Museums of Kenya, Nairobi, Kenya.

*Corresponding author. Email: mhenriquesbalde@gmail.com

10.1126/science.abd1862

10.1126/science.abd1862

10.1126/science.abd1862

10.1126/science.abd1862

10.1126/science.abd1862

10.1126/science.abd1862

10.1126/science.abd1862

10.1126/science.abd1862

10.1126/science.abd1862

10.1126/science.abd1862

10.1126/science.abd1862

10.1126/science.abd1862

10.1126/science.abd1862

10.1126/science.abd1862

10.1126/science.abd1862

10.1126/science.abd1862

10.1126/science.abd1862

10.1126/science.abd1862

10.1126/science.abd1862

10.1126/science.abd1862

10.1126/science.abd1862

10.1126/science.abd1862

10.1126/science.abd1862

10.1126/science.abd1862

10.1126/science.abd1862

10.1126/science.abd1862

10.1126/science.abd1862

10.1126/science.abd1862



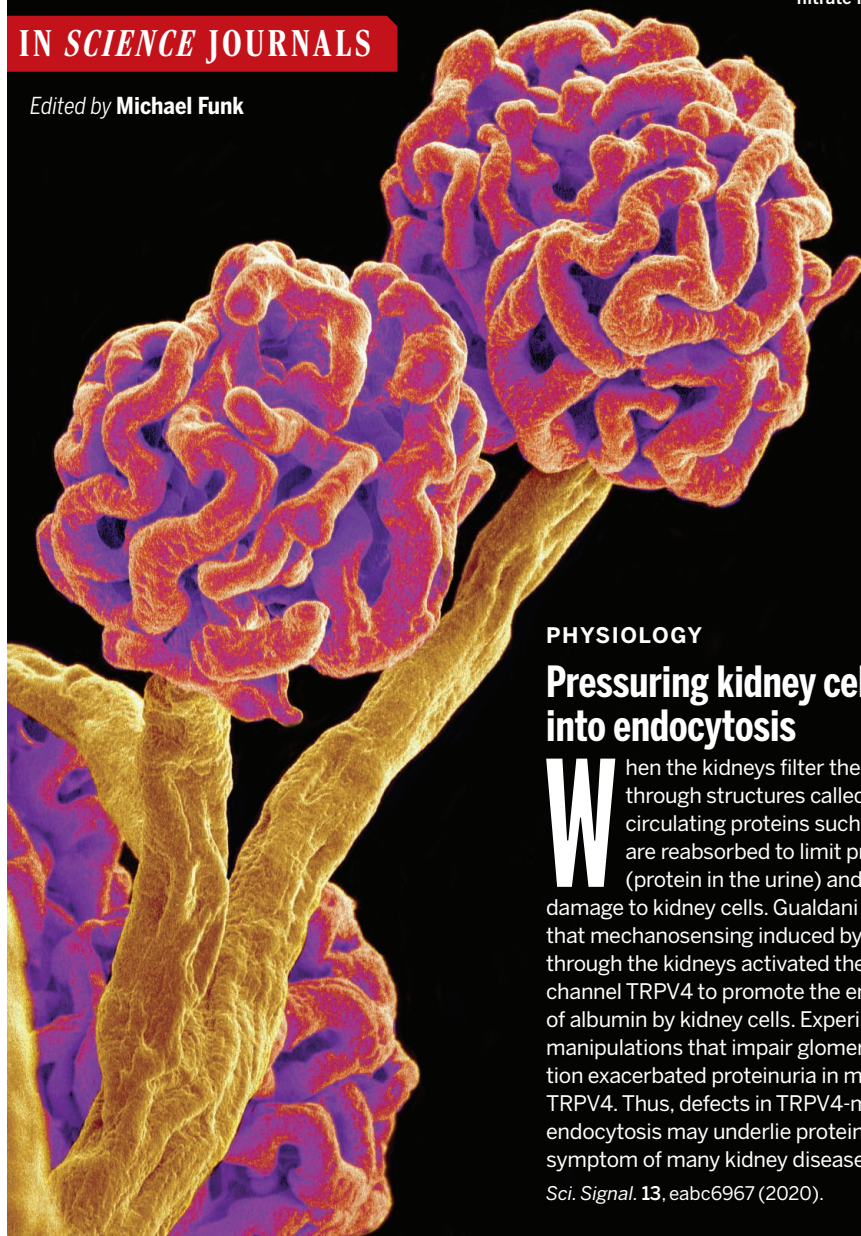
Hooded vultures (*Necrosyrtes monachus*) in Guinea-Bissau could be driven to extinction.

RESEARCH

IN SCIENCE JOURNALS

Edited by Michael Funk

Colored scanning electron microscope image of blood vessels in kidney glomeruli, which are structures that produce filtrate from the blood



PHYSIOLOGY

Pressuring kidney cells into endocytosis

When the kidneys filter the blood through structures called glomeruli, circulating proteins such as albumin are reabsorbed to limit proteinuria (protein in the urine) and prevent damage to kidney cells. Gualdani *et al.* found that mechanosensing induced by fluid flow through the kidneys activated the cation channel TRPV4 to promote the endocytosis of albumin by kidney cells. Experimental manipulations that impair glomerular filtration exacerbated proteinuria in mice lacking TRPV4. Thus, defects in TRPV4-mediated endocytosis may underlie proteinuria, a symptom of many kidney diseases. —WW
Sci. Signal. **13**, eabc6967 (2020).

THERMOGALVANICS

Recovering low-temperature heat

Low-temperature heat sources are both abundant and largely dissipated into the environment. Yu *et al.* discovered a way to boost the concentration gradient in a liquid thermogalvanic cell that allows low-temperature

heat to be recovered. The authors added a component that boosts the concentration gradient by forcing crystallization of the electrolyte at the cold end, and these crystals then melt at the hot end. This process boosts efficiency and is a potential method for recovering low-grade heat. —BG
Science, this issue p. 342

STRUCTURAL BIOLOGY

Attacking HIV by stabilizing its capsid

Current HIV treatments require drugs that must be taken daily, and care would be improved with an effective drug that is long-acting. GS-6207 (Lenacapavir) is a drug developed by Gilead Sciences that shows potential

for a 6-month dosing interval and is in phase 2/3 clinical trials. Bester *et al.* describe structural and biophysical studies that provide a basis for the potent antiviral activity of GS-6207. The HIV capsid is cone shaped, and GS-6207 binds two neighboring capsid subunits and stabilizes the curved capsid. GS-6207 also interferes with capsid binding of cofactors that play a role in viral infection. This insight into GS-6207 activity provides a platform for the rational development of improved long-acting therapies. —VV
Science, this issue p. 360

MUCOSAL IMMUNITY

A nose for inflammation

Nasal-associated lymphoid tissues (NALTs) are lymphoid organs in the nasal mucosa that are sites of inhaled antigen deposition. Bedford *et al.* studied the induction of immunity in NALTs and identified a role for conventional dendritic cells (cDCs) in suppressing T cell responses during the steady state. Similar cDCs are found in human NALTs in adenoids and tonsils and can also inhibit T cell responses and prevent immune activation. Inflammation in nasal mucosa caused by viral infection induces local recruitment of monocyte-derived DCs, which overrides the effects of cDCs and allows for T cell priming. These results provide mechanistic insight into steady-state and inflammatory responses in NALTs. —CNF
Sci. Immunol. **5**, eabb5439 (2020).

INORGANIC CHEMISTRY

Nitrogen lifts iron to hexavalence

The myriad ways that iron can interact with oxygen have been amply studied in biochemical and geochemical contexts. More recently, chemists have explored the extent to which nitrogen can likewise stabilize iron in high oxidation states. Martinez *et al.* now report that an iron center coordinated by carbene ligands can react

with an organic azide to form a pentavalent bis(imido) complex with two Fe=N bonds. One-electron oxidation then accessed the Fe(VI) oxidation state. Both compounds were sufficiently stable for crystallographic characterization. —JSY

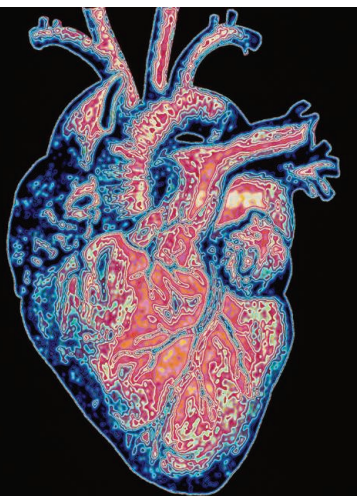
Science, this issue p. 356

PHYSIOLOGY

Metabolomics, at the heart

With heart failure a leading cause of death, a better understanding of metabolic function in the heart is a welcome advance. Murashige *et al.* measured more than 270 metabolites using liquid chromatography–mass spectrometry in human blood samples taken from an artery entering the heart and from a vein leaving it. Differences thus reflected the metabolic processes at work in the heart. Their results confirmed that hearts voraciously consume fatty acids. Hearts secrete, rather than consumed, amino acids, thus revealing active proteolysis. In patients with heart failure, ketone and lactate consumption increased, as did proteolysis. These findings could lead to strategies for fighting heart disease by altering metabolism. —LBR

Science, this issue p. 364



Artistic rendering of the human heart featuring exterior blood vessels, which deliver nutrients and oxygen to this energy-intensive organ

SPECTROSCOPY

The travel time of light in a molecule

There is currently considerable interest in experimental studies of various ultrafast processes. Of particular interest are the real-time dynamics of photoionization, one of the most fundamental processes caused by the light-matter interaction, in which the absorption of a photon leads to the ejection of an electron and the formation of anion. Using an electron interferometric technique, Grundmann *et al.* report a birth time delay on the order of a few hundred zeptoseconds between two electron emissions from the two sides of molecular hydrogen, which is interpreted as the travel time of the photon across the molecule. The proposed technique is generally applicable to more complex systems, and further studies are necessary to support this interpretation. —YS

Science, this issue p. 339

ECOLOGY

Species richness maintains mutualisms

Mutualistic communities of species that benefit each other are ubiquitous in ecosystems and are important for ecosystem functioning. However, the relationship between the persistence of mutualisms and species richness has remained unclear. Vidal *et al.* used a synthetic mutualism in brewer's yeast to experimentally test whether species richness buffers mutualistic communities against exploitation by species that do not provide benefits in return. They showed that richer mutualist communities survive exploitation more often than pairwise mutualisms and that higher species richness and functional redundancy allow mutualist communities to persist in the presence of exploiters. These results provide experimental support for the hypothesis that species richness is necessary for the function and maintenance of mutualistic communities. —AMS

Science, this issue p. 346

IN OTHER JOURNALS

Edited by **Caroline Ash**
and **Jesse Smith**



PHYSIOLOGY

Enduring muscular courtship

Several species of male amphibians and reptiles hold tight to their partners, possibly to prevent them mating with their rivals. The southern alligator lizard (*Elgaria multicarinata*) clamps its mate's head in its jaws for hours. This extreme muscular performance runs counter to expectations of reptilian muscle resilience. Nguyen *et al.* tested the sustained bite force of the adductor muscles of the lizard's jaw for fatigue. Muscle fibers can specialize, in terms of performance, into fast-acting twitch fibers and into slow-acting tonic fibers that are capable of fatigue-resistant contraction. Tonic fibers also exhibit slow calcium fluxes and relax slowly. The lizards' jaw muscle appears to have evolved to comprise fast-twitch fibers for eating and slow-tonic fibers that can sustain an extended courtship grip. —CA

Proc. R. Soc. London Ser. B **287**, 20201578 (2020).

The southern alligator lizard *Elgaria multicarinata* will grip the head of its mate for hours, thanks to specialized jaw muscle fibers.

SINGLE-CELL METHODS

Watching information flow inside cells

Each human cell has an information network like a subway system underpinning the

function of one of the world's major cities. Instead of human couriers, within our cells, messenger RNAs (mRNAs) carry information. Thousands of mRNAs emerge from the cell's nucleus with instructions

for cellular functions and disappear into the cytoplasm when their duties are fulfilled. Because of the development of single-cell sequencing techniques, we are now very good at counting these messengers, which are specific to each cell type in our body. Qiu *et al.* developed a new method to watch the movement of mRNAs. The technique can distinguish newly synthesized mRNAs from older ones and track each mRNA with a specific tag. This method provides a picture of the information flow inside cells and shows how they become disrupted by genetic perturbations that can cause cancer. —DJ

Nat. Methods **17**, 991 (2020).

IMMUNOLOGY Imaging antigen-specific T cells

Positron emission tomography (PET) has previously been exploited to trace immune responses in living animals. However, its use has been largely limited to cells expressing surrogate markers recognized by radiolabeled antibodies or cells genetically modified to take up radiolabeled substrates. Woodham *et al.* now report a noninvasive, in vivo method to track antigen-specific T cells that recognize known antigens presented by major histocompatibility complex (MHC) molecules. The authors made a class of radiolabeled peptide-bound MHC dimers linked to antibody Fc regions, which they called “synTacs.” In a mouse model of cancer, they were able to follow CD8⁺ T cells within tumors that recognized a particular oncoprotein. They could also detect influenza virus (IAV) nucleoprotein-specific CD8⁺ T cells in the lungs of IAV-infected mice. This work may help pave the way for future tools to noninvasively track human T cell responses during interventions such as vaccination and cancer immunotherapy. —STS

Nat. Methods **17**, 1025 (2020).

METALLURGY Nature's guide for alloy design

Metallic alloys composed of many different elements are often hard to identify and isolate because of the large number of potential combinations. Wei *et al.* started with a nine-element mixture and assessed the phase-separated zones that arose from natural mixing. They used the phase composition for designing a titanium-vanadium-niobium-hafnium refractory alloy with attractive ductility. This strategy provides a method for screening and isolating complex element compositions that may have outstanding properties. —BG

Nat. Mater. 10.1038/s41563-020-0750-4 (2020).

CONSERVATION Plastic trade-offs

In just over 100 years, plastics have become both a necessity and a scourge, replacing natural materials in a myriad of uses and becoming a ubiquitous contaminant both in ecosystems and within organisms. For human populations in and around tropical forests, natural materials are available to process and store food. Bitariho *et al.* looked at trade-offs between

using wild climbing plants to make baskets and winnowers and using plastic containers and devices. The authors accounted for food security, potential for plastic pollution, and the conservation status of 15 species of climbing plants around Bwindi Impenetrable National Park, Uganda. Families that had permission to collect wild climbing plants had more food storage and processing devices than those who did not. Although this study identified the risks of overharvesting one vulnerable climber species, it also showed that families with access to natural materials experienced greater food security and less plastic use and waste. —SNV

Conserv. Sci. Pract. **2**, e275 (2020).

OPTOELECTRONICS Directing the flow of photocurrent

The next generation of information-processing devices is expected to be more energy efficient if the spin or valley degrees of freedom of a material is used to encode and carry information. Rasmita *et al.* show that circularly polarized light can induce a directional photocurrent in heterostructures of the two-dimensional transition metal dichalcogenides MoS₂ and WSe₂.

The authors show that the direction of current flow is dependent on the polarization state of the light, and further control can be achieved with back-gating and an in-plane electric field. Combined with the possibility of engineering the heterostructures and the number of materials available with different properties, this work demonstrates that the monolayer transition metal dichalcogenides can serve as a versatile platform for future optoelectronic device technology. —ISO

Optica **7**, 1204 (2020).

ARCTIC OZONE The hole truth

Ozone loss in the Arctic stratosphere has never been as severe as that in the Antarctic ozone hole, but during the past year, it declined to a level a bit closer to that of its southern counterpart. Wohltmann *et al.* report that during the northern spring of 2020, Arctic stratospheric ozone levels fell to near zero in some places. This unprecedented depletion, caused by unusually cold and stable conditions in the Arctic stratosphere, could become more frequent or extensive if the recent trend toward colder Arctic winters continues. —HJS

Geophys. Res. Lett. 10.1029/2020GL089547 (2020).



The people who live around Bwindi Impenetrable Forest are skilled craftsfolk who select climbing plants for materials to make food-storage containers, thus avoiding the use of plastic alternatives that are not biodegradable.

ALSO IN SCIENCE JOURNALS

Edited by Michael Funk

CORONAVIRUS
COVID-19 risks
for children

There has been substantial discourse about how children are affected by severe acute respiratory syndrome coronavirus 2 (SARS-CoV-2) infection. A fraction of children develop a hyperinflammatory syndrome that is clearly a cause for concern. However, many children seem to develop mild or asymptomatic infections, yet they are harmed by the lockdown measures to prevent SARS-CoV-2 spread. In a Perspective, Snape and Viner discuss what is known about coronavirus disease 2019 (COVID-19) in children and young adults and whether they can spread the virus. They discuss the impacts of lockdowns on education, social care, and mental health, as well as deleterious effects on child health in terms of accidents at home and maintaining vaccination programs. Although more research is needed, such harms should be considered when evaluating control measures in the future. —GKA

Science, this issue p. 286**NEUROSCIENCE**
Improving prosthetics

People who use upper- and lower-limb prosthetics face numerous challenges caused by limitations in the interface between person and machine. Ideally, prosthetics should have bidirectional communication between the user and the device so that people can easily and intuitively use their devices. Key to bidirectional interfacing is motor control and sensing. In a Perspective, Raspopovic discusses approaches to providing improved motor control and sensing through various sensors and implants. Recent studies suggest that motor control and sensing can be combined to improve the experience for users of prosthetics, but there are

many challenges to overcome to ensure that such neurotechnologies improve quality of life and can be tolerated. —GKA

Science, this issue p. 290**NEURODEVELOPMENT**
A moment in time

As the brain develops, it does not simply get bigger. Like a building that depends on temporary scaffolds as its structures are assembled, the developing brain sets up the circuits that characterize the adult brain. Molnár *et al.* review the current state of knowledge about how brain connections are built and how autonomously established patterns are reshaped by activity from the sensory periphery. With the help of a transient population of neurons, the spontaneous activity of early circuits is molded by increasing inputs from the external world. When these normal developmental interactions are disrupted, consequent miswiring drives dysfunction in the adult brain. —PJH

Science, this issue p. 308**INNATE IMMUNITY**
Cells drop a bomb
on pathogens

Lipid droplets (LDs) accumulate in cells to serve as lipid storage organelles. They are also an attractive source of nutrients for many pathogens. Bosch *et al.* show that various proteins involved in innate immunity form complexes on LDs in response to bacterial lipopolysaccharide (see the Perspective by Green). Upon activation, LDs became physically uncoupled from mitochondria, driving a shift in cells from oxidative phosphorylation to aerobic glycolysis. This work highlights the ability of LDs both to kill pathogens directly and to establish a metabolic environment conducive to host defense. This may inform future antimicrobial strategies in the age of

antibiotic resistance. —STS

Science, this issue p. 309;

see also p. 294

CELL BIOLOGY
The nucleus makes
the rules

Single cells continuously experience and react to mechanical challenges in three-dimensional tissues. Spatial constraints in dense tissues, physical activity, and injury all impose changes in cell shape. How cells can measure shape deformations to ensure correct tissue development and homeostasis remains largely unknown (see the Perspective by Shen and Niethammer). Working independently, Venturini *et al.* and Lomakin *et al.* now show that the nucleus can act as an intracellular ruler to measure cellular shape variations. The nuclear envelope provides a gauge of cell deformation and activates a mechanotransduction pathway that controls actomyosin contractility and migration plasticity. The cell nucleus thereby allows cells to adapt their behavior to the local tissue microenvironment. —SMH

Science, this issue p. 311, p. 310;

see also p. 295

DEVELOPMENTAL BIOLOGY
Fiber tension enables
tissue scaling

Tissue development, homeostasis, and repair require cells to sense mechanical forces. Although many molecular actors implicated in cell mechanosensitivity have been extensively studied, the basis by which cells adapt their mechanical responses to their geometry remains poorly defined. López-Gay *et al.* now identify how two fundamental epithelial structures—stress fibers and tricellular junctions—endow *Drosophila* cells with an internal ruler to scale their mechanical

response with their area. This work explains how cells of different sizes within an epithelial tissue collectively adapt their mechanical response to control tissue shape and proliferation. Scaling of biological properties with size is a core property of other biological systems. —BAP

Science, this issue p. 312**NEUROSCIENCE**
How neuron types encode
behavioral states

What is the contribution of molecularly defined cell types to neural coding of stimuli and states? Xu *et al.* aimed to evaluate neural representation of multiple behavioral states in the mouse paraventricular hypothalamus. To achieve this goal, they combined deep-brain two-photon imaging with post hoc validation of gene expression in the imaged cells. The behavioral states could be well predicted by the neural response of multiple neuronal clusters. Some clusters were broadly tuned and contributed strongly to the decoding of multiple behavioral states, whereas others were more specifically tuned to certain behaviors or specific time windows of a behavioral state. —PRS

Science, this issue p. 313**MICROBIOTA**
Metabolic signals
from gut microbes

The gut is a stretchy, glandular, and highly innervated tube packed at its distal end with microorganisms. Disruption of the microbial community can lead to metabolic disorders such as obesity and diabetes. Muller *et al.* investigated how the microbiota interacts with the enteric nervous system to induce a metabolic outcome. A population of autonomous enteric neurons called CART⁺ neurons are enriched in the ileum and colon,

where most of the microbiota resides. Stimulation or ablation of the CART⁺ neurons alters blood glucose levels, insulin, and feeding behavior. Furthermore, by manipulating the microbiota, the density of enteric neurons responds plastically in an inducible and reversible manner. —CA

Science, this issue p. 314

MORPHOGENS

Engineering synthetic morphogens

Morphogens provide positional information during tissue development. For this behavior to occur, morphogens must spread out and form a concentration gradient; however, their mechanism of transport remains a matter of debate. Stapornwongkul *et al.* now show that in the presence of extracellular binding elements (binders), the inert green fluorescent protein (GFP) can form a detectable concentration gradient by diffusion in the developing fly wing (see the Perspective by Barkai and Shilo). When combining the expression of nonsignaling binders and receptors engineered to respond to GFP, a synthetic GFP gradient can substitute for a natural morphogen to organize growth and patterning. In related work, Toda *et al.* also show that GFP can be converted into a morphogen by providing anchoring interactions that tether the molecule, forming a gradient that can be recognized by synthetic receptors that activate gene expression. These synthetic morphogens can be used to program de novo multi-domain tissue patterns. These results highlight core mechanisms of morphogen signaling and patterning and provide ways to program spatial tissue organization independently from endogenous morphogen pathways. —BAP

Science, this issue p. 321, p. 327; see also p. 292

ULTRACOLD CHEMISTRY

Non-Feshbach ultracold molecules

The formation of ultracold molecules has already had a profound impact on many research areas of physics. However, conventional methods of producing such molecules are attainable only for a limited number of systems or they suffer for strong dephasing. He *et al.* sought to pair atoms, through coupling of their spins, to the two-body relative motion mediated by the inherent polarization gradients in a strongly focused trapping laser. They report a successful assembly of an ultracold ⁸⁷Rb-⁸⁵Rb molecule in an optical tweezer and observed coherent, long-lived atom-molecule Rabi oscillations. They further demonstrate the full control of the internal and external degrees of freedom in the atom-molecule system. —YS

Science, this issue p. 331

HYDROGELS

Slippery surfaces using lipids

In engineered systems, a reduction in friction can come from the use of lubricants or through surface coatings that are inherently slippery. For most hydrogels, which are cross-linked polymers heavily swelled with water, surface lubrication typically comes from trapped liquids that help to form a slippery surface. Drawing inspiration from articular cartilage that in part uses a lipid boundary layer, Lin *et al.* designed hydrogels with small concentrations of lipids that are continuously exuded toward the surface to make a slippery layer (see the Perspective by Schmidt). Friction and wear of the hydrogels was reduced by up to a factor of 100, and the effect was observed even after the hydrogels were dried and rehydrated. —MSL

Science, this issue p. 335; see also p. 288

SIGNAL TRANSDUCTION

Intricacies of amino acid sensing

The way in which cells sense amino acids derived from external proteins taken up by micropinocytosis and then degraded in the lysosome turns out to be different from the way in which they sense external amino acids taken up through transporters in the plasma membrane. Both sources of amino acids end up activating the mechanistic target of rapamycin complex 1 (mTORC1) protein kinase complex. However, Hesketh *et al.* found that cultured human cells sense amino acids derived from exogenous proteins in late endosomes by a mechanism independent of the Rag guanosine triphosphatases (GTPases) that control mTORC1 activation in response to external amino acids. Furthermore, the GATOR GTPase had an inhibitory effect on mTORC1 activation in response to proteins processed through the lysosome, opposite to its role in sensing amino acids taken up across the plasma membrane. —LBR

Science, this issue p. 351

MICROBIOTA

A parasite's bilious defense

The enteropathogenic parasite *Giardia lamblia* is a frequent cause of self-limited diarrhea in infected adult travelers. By contrast, parasitic infection of children in endemic areas is not associated with diarrheal disease but rather with reduced body weight gain and growth. Riba *et al.* established a *G. lamblia* infection model in neonatal mice. Infected neonatal animals displayed reduced weight gain and growth. Analysis of these animals showed that *G. lamblia* induced bile secretion and that an altered gut microbiota composition, bile acid modification by commensal bacteria, and subsequent alterations of lipid metabolism contributed to this phenotype. —OMS

Sci. Transl. Med. **12**, eaay7019 (2020).

PLANETARY SCIENCE

Protecting Earth's early atmosphere

When planetary bodies form with nascent atmospheres, those atmospheres are at risk of being stripped away by solar winds. However, a planet's magnetic field, if sufficiently strong, can provide a shield against solar winds and preserve the atmosphere. Previous studies have shown that the early Earth had a geomagnetic field, but its strength remains poorly understood and questions remain as to how Earth's early atmosphere survived. Green *et al.* hypothesized that one part of the answer may be the magnetic field of the nearby early Moon, for which there is evidence from paleomagnetic studies of returned lunar samples. Models of the coupled Earth and Moon magnetospheres suggest that they may have provided an effective barrier to strong solar winds, protecting Earth's atmosphere until at least 2.5 billion years ago. —KVH

Sci. Adv. **10**, 1126/sciadv.abc0865 (2020).

REVIEW SUMMARY

NEURODEVELOPMENT

Transient cortical circuits match spontaneous and sensory-driven activity during development

Zoltán Molnár*, Heiko J. Luhmann*, Patrick O. Kanold*

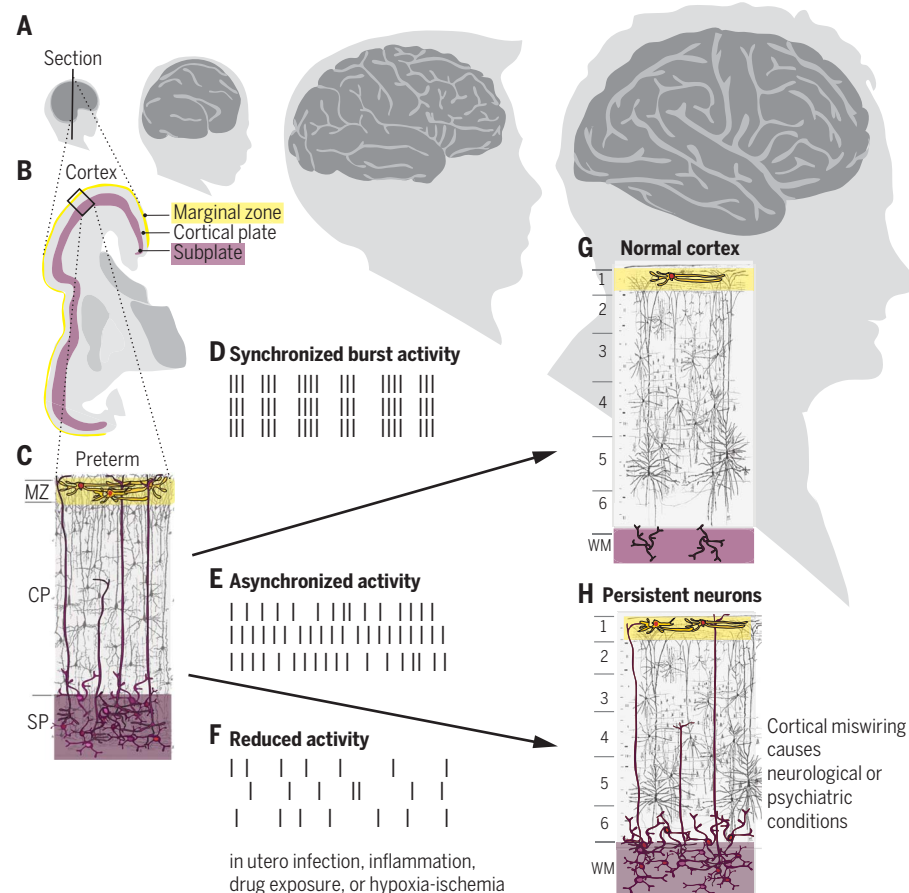
BACKGROUND: During early mammalian brain development, transient neurons and circuits form the scaffold for the development of neuronal networks. In the immature cerebral cortex, subplate neurons in the lower cortical layer and Cajal-Retzius cells in the marginal zone lay the foundations for cortical organization in horizontal layers and translaminar radial circuits (“cortical columns”). Patterns of spontaneous activity during early development synchronize local and large-scale cortical networks, which form the functional template for generation of cortical architecture and guide establishment of global thalamocortical and intracortical networks.

zontal layers and translaminar radial circuits (“cortical columns”). Patterns of spontaneous activity during early development synchronize local and large-scale cortical networks, which form the functional template for generation of cortical architecture and guide establishment of global thalamocortical and intracortical networks.

works. These networks become established in an autonomous fashion before the arrival of signals from the sensory periphery and before the maturation of cortical circuits. The subplate, which is a transient structure located below the developing cortical plate, orchestrates alignment of these autonomously established pathways by integrating spontaneous and sensory-driven activity patterns during critical stages of early development.

ADVANCES: The subplate contains heterogeneous neuronal populations with distinct characteristics, such as origin, birthdate, neurotransmitters, receptor expression, morphology, projections, firing properties, and their participation in specific intra- and extracortical connectivity. The transformation of this early subplate-driven circuit to the adult-like cortex requires patterned spontaneous activity and depends on the awakening of silent synapses in the cortical plate when thalamic inputs are progressively integrated. Moreover, a subpopulation of the glutamatergic and GABAergic (GABA, γ -aminobutyric acid) subplate neurons has widespread axonal projections that establish early large-scale networks. The early circuits are remodeled when Cajal-Retzius and subplate neurons largely disappear by programmed cell death. Both the programmed cell death and the remodeling of circuits may be also controlled by the transition from spontaneous synchronized burst to sensory-driven activity.

OUTLOOK: Functional impairments of these transient circuits (that include both transient and more permanent cell types) have great clinical relevance. Genetic abnormalities or early pathological conditions such as in utero infection, inflammation, exposure to pharmacological compounds, or hypoxia-ischemia induce functional disturbances in early microcircuits, which may lead to cortical miswiring at later stages and subsequent neurological and psychiatric conditions. A better understanding of the transition from early transient to permanent neuronal circuits will clarify mechanisms driving abnormal distribution and persistence of subplate neurons as interstitial white matter cells in pathological conditions. Exploring the transition from transient to permanent circuits helps us to understand causal foundations of certain pharmaco-resistant epilepsies and psychiatric conditions and to consider new therapeutic strategies to treat such disorders. ■



Early spontaneous synchronized neuronal activity sculpts cortical architecture. (A) Schematic outlines of brain development from the embryonic stage to adult. (B and C) Prenatal cortical circuits are dominated by early-generated, largely transient neurons in the subplate (SP) and marginal zone (MZ) before maturation of cortical plate (CP) neurons. (D to H) Transformation of early subplate-driven circuits to the adult-like six-layered cortex requires spontaneous synchronized burst activity (D) that also controls programmed cell death (apoptosis), arrangement of neurites and axons, and formation and awakening of synapses. Most subplate neurons disappear with development; a few survive in rodents as layer (L) 6b neurons or in primates as interstitial white matter (WM) cells (G). During prenatal and early postnatal stages, pathophysiological conditions such as hypoxia-ischemia, drugs, infection or inflammation may alter spontaneous activity [(E) and (F)]. These altered activity patterns may disturb subsequent developmental programs, including apoptosis (H). Surviving subplate neurons that persist in white matter or L6b may support altered circuits that could cause neurological or psychiatric disorders.

The list of author affiliations is available in the full article online.
*Corresponding author. Email: zoltan.molnar@dpag.ox.ac.uk (Z.M.); luhmann@uni-mainz.de (H.J.L.); pkanold@jhu.edu (P.O.K.)
Cite this article as Z. Molnár et al., *Science* 370, eabb2153 (2020). DOI: 10.1126/science.abb2153

READ THE FULL ARTICLE AT
<https://doi.org/10.1126/science.abb2153>

REVIEW

NEURODEVELOPMENT

Transient cortical circuits match spontaneous and sensory-driven activity during development

Zoltán Molnár^{1*}, Heiko J. Luhmann^{2*}, Patrick O. Kanold^{3,4*}

At the earliest developmental stages, spontaneous activity synchronizes local and large-scale cortical networks. These networks form the functional template for the establishment of global thalamocortical networks and cortical architecture. The earliest connections are established autonomously. However, activity from the sensory periphery reshapes these circuits as soon as afferents reach the cortex. The early-generated, largely transient neurons of the subplate play a key role in integrating spontaneous and sensory-driven activity. Early pathological conditions—such as hypoxia, inflammation, or exposure to pharmacological compounds—alter spontaneous activity patterns, which subsequently induce disturbances in cortical network activity. This cortical dysfunction may lead to local and global miswiring and, at later stages, can be associated with neurological and psychiatric conditions.

In the adult brain, neuronal communication is mediated primarily through chemical synapses, and neurons interact within a short time frame. The developing brain is not just a smaller version of the adult brain but rather has different types of interactions between immature cells. These interactions are slower, are not as well stereotyped and predicted, and rely more on spontaneous activity patterns than interactions in the adult brain. These early spontaneous activity patterns are mediated through transient neuronal networks that continue to exist during the gradual establishment of permanent networks. Transient alterations in activity during crucial developmental periods can lead to persistent changes in functional connectivity and therefore might underlie the manifestation of neurological and psychiatric conditions (1). Thus, fundamental knowledge on early steps of activity-dependent circuit formation has general biological, as well as practical clinical, implications.

The development of neural circuits starts early in embryogenesis. The preplate is the first postmitotic cortical neuronal layer (1) (Fig. 1) and is split into the marginal zone and subplate by later-arriving cortical plate neurons. Then, unfolding genetic programs of neurogenesis and neuronal migration interact with various forms of neuronal communication to establish the mature circuitry.

Before completion of neurogenesis and migration (Fig. 2, A and B), neocortical areas display distinct spontaneous and sensory-driven activity patterns, which can influence production and release of growth factors, influence maintenance of gap junctions, regulate transmitter release, and guide the precise topography of developing projections (2). Overall levels of activity can also contribute to cell survival, including of interneurons (3), Cajal-Retzius neurons (4), and thalamic neurons.

Developing neurons often show transient depolarizations, which can be transmitted to other neurons through gap junctions. Subsequently, neurons become capable of releasing various neurotransmitters, depending on the frequency and intensity of their firing. Subplate and Cajal-Retzius neurons can also release trophic factors and in this way directly influence cellular targets (5, 6).

Given the multitude of neuronal communication pathways, we review progress in understanding the role of neuronal electrical activity in the earliest neuronal networks of the cerebral cortex. We focus on a critical developmental stage, when cortical networks containing transient neurons begin to interact with the emerging inputs from the sensory periphery, and on reciprocal connectivity between the thalamus and cortex, as well as on connections within the cerebral cortex.

Spontaneous activity in early development

Spontaneous electrical activity, or electrical events occurring without apparent external generation, is a general feature of all developing networks, but the cellular mechanisms underlying the various activity patterns may differ and change profoundly during specific stages of development (Fig. 2, A to C) (7–9). Although the underlying mechanisms and functional role of the various activity patterns

have been mostly studied in animals, data from preterm and newborn human babies indicate a similar sequence. At distinct developmental periods, spontaneous activity influences or even controls neurogenesis and neuronal migration, synaptogenesis, apoptosis, and myelination (10, 11). In general, the sequence of spontaneous activity in developing neuronal networks shows four distinct phases (Fig. 2C).

1) At early embryonic stages (labeled 1 in Fig. 2C), spontaneous activity is sparse and asynchronous because neurons are not connected yet. Neurons in isolation reveal long calcium transients that appear stochastically and are influenced by ionotropic and metabotropic receptors activated by ambient or paracrine release of γ -aminobutyric acid (GABA) and glutamate. Subplate and Cajal-Retzius neurons already reveal relatively mature electrophysiological properties, for example, faster action potentials and higher discharge rates. Thalamic stimulation elicits long responses in rodent subplate, which likely represent action potentials followed by prolonged depolarizations (Fig. 3A) (12). Subplate neurons in postconception week (pcw) 17 to 23 fetal human cortex in vitro generate spontaneous depolarizations that depend on gap junctional coupling (13).

2) In the next stage (labeled 2 in Fig. 2C), bursts of correlated neuronal activity are generated by intrinsic mechanisms or synaptic interactions, including extrasynaptic receptors activated by ambient GABA or glutamate. Active neurons are coupled in small networks through electrical and/or chemical synapses and generate synchronized burst activity, which may be restricted to a local neuronal network, propagating as a “wave” to neighboring cortical areas or activating remote cortical and subcortical regions through axonal projections (14). Highly synchronized spontaneous activity in the form of calcium waves emerges as early as embryonic day 14.5 (E14.5) in mouse thalamus and propagates among sensory thalamic relay nuclei, thereby coordinating patterning of the cortical sensory area (15). At this age, the brainstem has not yet innervated the thalamus, indicating that this activity is generated within the thalamus. Thalamocortical systems are already assembled when the first peripheral inputs reach them. Therefore, initial thalamocortical loop formation occurs in an autonomous fashion, and periphery-related activity from sensory organs can subsequently modify these connections (16).

3) With maturation of intrinsic and synaptic electrophysiological properties, neurons fire in bursts and synchronize local networks (labeled 3 in Fig. 2C). Spindle burst or delta brush activity is a physiological hallmark of this distinct period in human and rodent development (Fig. 2B). Spindle bursts are triggered by signals from the sensory periphery (17), by endogenous thalamic activity (18), or

¹Department of Physiology, Anatomy and Genetics, Sherrington Building, University of Oxford, Parks Road, Oxford OX1 3PT, UK. ²Institute of Physiology, University Medical Center of the Johannes Gutenberg University Mainz, Duesbergweg 6, Mainz 55128, Germany. ³Department of Biomedical Engineering, Johns Hopkins University, School of Medicine, 720 Rutland Avenue, MRB 379, Baltimore, MD 21205, USA. ⁴Johns Hopkins University Kavli Neuroscience Discovery Institute, Baltimore, MD 21205, USA.

*Corresponding author. Email: zoltan.moltan@dpag.ox.ac.uk (Z.M.); luhmann@uni-mainz.de (H.J.L.); pkanold@jhu.edu (P.O.K.)

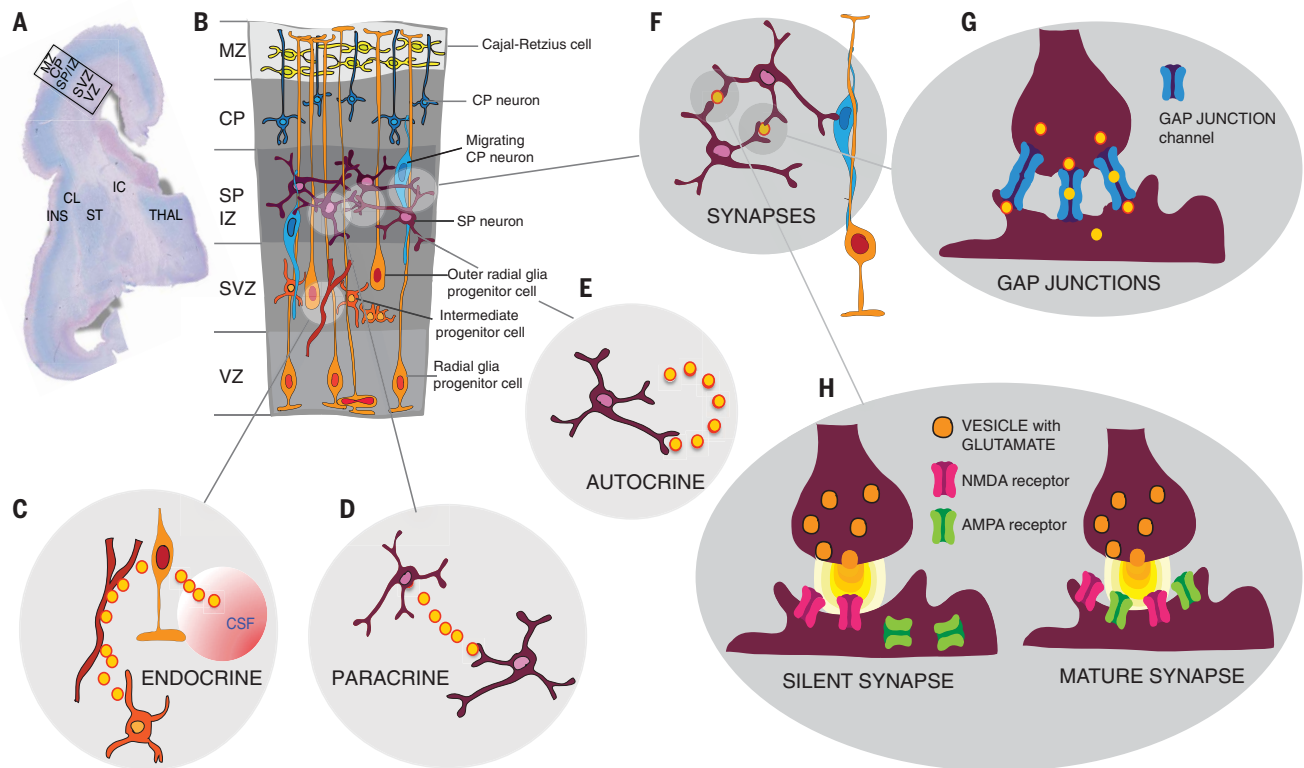


Fig. 1. Cellular interactions in developing brain. (A) Cross section of human brain at 18 gestational weeks (5). Subplate (SP) and intermediate zone (IZ) are blue; germinal zones are pink (marginal zone, MZ; cortical plate, CP; subventricular zone, SVZ; ventricular zone, VZ). CL, claustrum; INS, insula; ST, striatum; IC, internal capsula; THAL, thalamus. (B to H) Schematic illustration of cellular cortical components present

in developing cortex (B). Dividing radial glial progenitors in VZ are in contact with cerebrospinal fluid and receive endocrine signals, some through blood vessels (C). Immature neurons interact through paracrine (D) and autocrine (E) mechanisms or couple into local networks through electrical (G) and chemical (H) synapses (F). These various forms of communications coexist in the developing brain.

by activity from other neocortical areas. Short gamma bursts are present in rodent cortex during the same developmental period and also synchronize local radial neuronal networks, functional precolumns (9, 19, 20). Subplate neurons are required for this local burst activity, and subplate ablation causes disarrangement in the cortical architecture (21). At the embryonic and neonatal stages, this activity originates in the thalamus and controls the formation of the cortical map (18). The cholinergic system elicits some of these early activity patterns (7, 22, 23).

Cortical early network oscillations, developmentally followed by cortical giant depolarizing potentials represent the two activity patterns in newborn rodents during further development (9, 24). Endogenous activity in the somatosensory system often arises from central pattern generators in motor regions (8). However, because the somatosensory system is tightly linked with the motor system, it is often not possible to clearly separate “true” spontaneous activity from sensory activity evoked by motor action. Twitch-related activity is present in the somatosensory cortex (25) shortly after birth,

indicating that circuits from periphery to cortex are functional from early ages (26, 27).

Developing neurons do not oscillate at frequencies of spindle bursts, and oscillations are abolished by manipulating thalamocortical circuits and subplate neurons, suggesting that oscillations are generated by specific circuits, rather than individually oscillating neurons (21, 28–32). Death of neurons, changes in circuits or receptor composition, and changes in (intracellular) ion composition could all contribute to the developmental changes in oscillations. Moreover, because early activity patterns seem to be coordinated across the brain, the above considerations point to a key role of the thalamus in relaying, integrating, and sculpting early spontaneous and sensory-driven activity patterns.

In sensory systems, the periphery (7, 33) as well as central sources might initially independently generate spontaneous activity (14), but their interaction is unclear. Spontaneous peripheral activity is relayed via the thalamus to the developing cortex (34). Thus, it is not just a transient subplate, but rather a series of transient networks and structures that

all contribute to the changing spontaneous activity.

4) With further maturation of intrinsic membrane and synaptic properties, spontaneous activity becomes sparse and desynchronized (9) (labeled 4 in Fig. 2C). This gradual developmental shift from the dominant burst pattern to “adult-like” low-amplitude desynchronized activity is accompanied by a progressively stronger impact of the peripheral sensory input. However, sensory cortices can be activated by external stimuli (light, sound, touch, and muscle twitches) at surprisingly early stages—for example, in preterm human babies or early postnatal periods in altricial animals (35–39)—before the sensory organs are fully functional. In ferrets, primary auditory cortex (A1) responds to sounds as early as postnatal day 21 (P21) (38), whereas in mice, whisker stimulation elicits a cortical response at E18.5 (18). During the first postnatal week in rodents, L4 neurons exhibit spontaneous activity in a barrel map-like pattern, which is driven by the periphery but largely independent of self-generated whisker movements (26, 27, 40). This activity may be generated by gap junction-coupled dorsal root

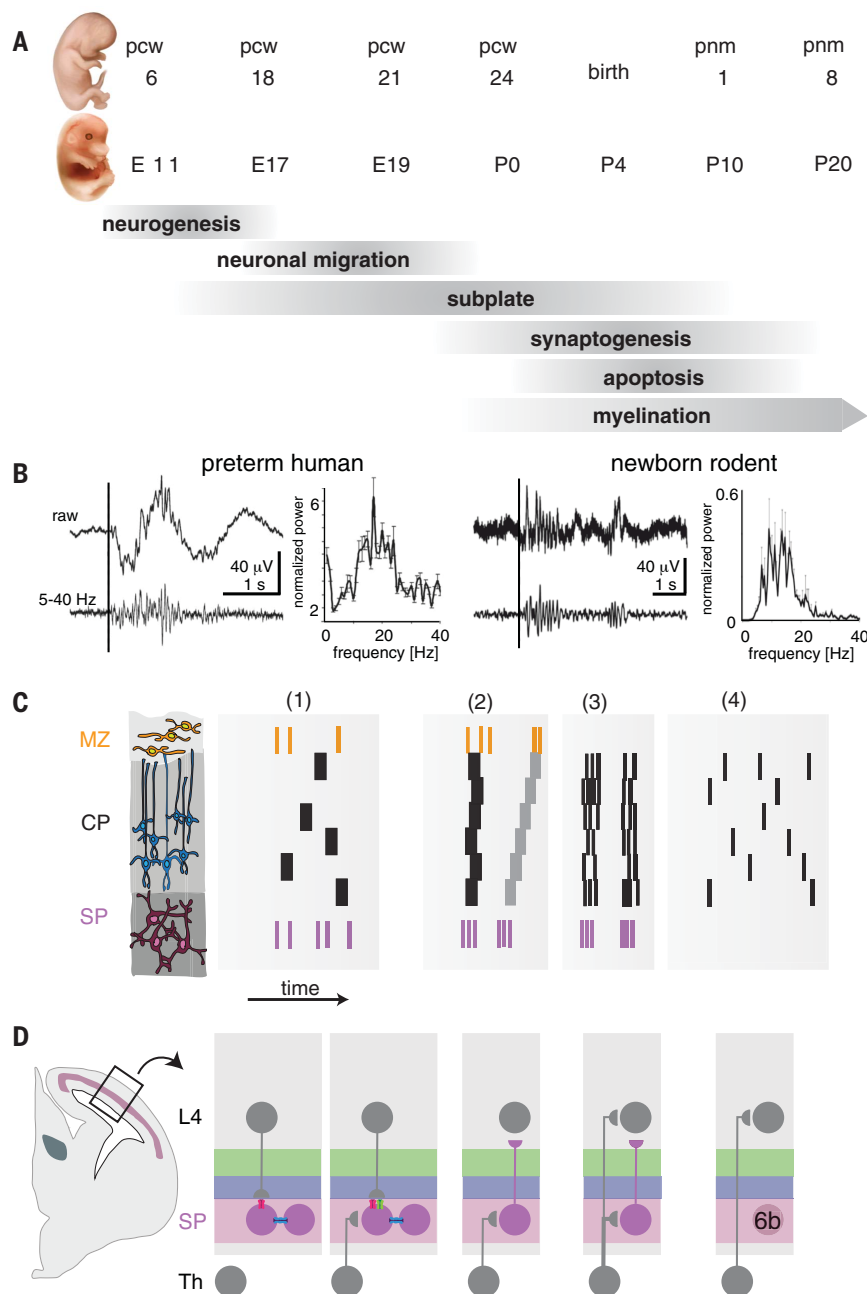


Fig. 2. Corticogenesis and relationship with spontaneous activity patterns. (A) Approximate time points of major developmental events in human neocortex at postconceptional weeks (pcw) and postnatal months (pnm) and in mouse cortex at embryonic (E) and postnatal (P) days (90). (B) Delta brush electroencephalogram activity and average fast-Fourier transformation spectrum evoked by hand movement (vertical bar) (35) in preterm human or after whisker stimulation in newborn rodent (vertical bar). Note the similarity in the spectrum. Images used with permission from (35). (C) Schematic illustration of developmental changes in spontaneous activity. (1) Cajal-Retzius and subplate neurons (yellow and purple bars, respectively) already discharge faster action potentials and at higher frequency than cortical plate neurons (black bars). (2) Neurons electrically coupled by gap junctions generate either local synchronized activity or propagating activity waves. (3) Discharges become faster and local networks discharge in synchronized bursts. Transient early-born neurons start to disappear during this phase. (4) Appearance of adult-like sparse desynchronized activity independent of transient neurons and circuits. (D) Subplate neurons are gap junction-coupled when thalamocortical projections arrive. Thalamic fibers (Th) first establish synapses with subplate neurons before innervating L4 neurons. Subplate and L4 connections transiently coexist to reinforce the more permanent thalamic projections that remain after subplate neurons lose their contact with thalamic projections and also lose their contact to L4 themselves. Few L6b neurons survive to adulthood (28).

ganglia or brainstem neurons. In the visual cortex of ferrets, long-range correlated spontaneous activity is generated through short-range interactions in the form of distributed coactive domains (41).

Instructive role of the subplate during development

In all three sensory systems, the thalamocortical projection is subserved by multiple subnuclei projecting to the respective cortical areas. Only primary thalamic nuclei receive direct input from the sensory periphery; higher-order thalamic nuclei receive their input from cortex and relay their output to other cortical areas, providing pathways for transthalamic cortico-cortical communications. During development, higher-order thalamic nuclei seem to provide most of the early projections to matched cortical areas (42), indicating that primary sensory areas are induced by sensory activity at later ages (43). The sensory systems differ with respect to timing, relative maturity, peripheral receptors, and brainstem circuits. Moreover, the early developmental period is characterized by a high degree of multisensory projections, especially to higher-order thalamic nuclei (42). Thus, early activity in each sensory system can influence the activity across sensory cortical areas, and deprivation can lead to cross-modal rewiring.

During development, the thalamocortical and corticothalamic systems undergo a dramatic transformation owing to the presence of transient circuits. Thalamic projections accumulate closer to the cortex, and corticothalamic projections accumulate outside the thalamus. Both assemble transient circuits with the subplate (28) (Fig. 2D) and the thalamic reticular nucleus (16). The period in which the thalamic connections are accumulating below the cortex (the so-called waiting period) is a crucial developmental period characterized by highly dynamic and essential interactions between thalamus and cortex (12, 38, 44, 45). Subplate neurons are among the first cortical neurons to mature and receive thalamic inputs before these innervate their eventual target (L4) (44–48) (Fig. 3A). In the auditory system in vivo, subplate neurons can respond to sensory stimuli before L4 neurons respond to sound (38) (Fig. 3A), and an early topography of sensory responses exists in subplate (Fig. 3B). Thus, given these developmental dynamics, this early stage should be more appropriately designated as the “proto-organizational” period.

Subplate neurons differ in their origin, birth-date, molecular profile, and morphology, as well as local and long-distance connectivity (31, 48–51), but the distinct roles of each subpopulation are unknown. Many subplate neurons provide excitatory input to L4 and other cortical layers, including L1 (45, 51, 52), and thus form a relay of thalamic information to

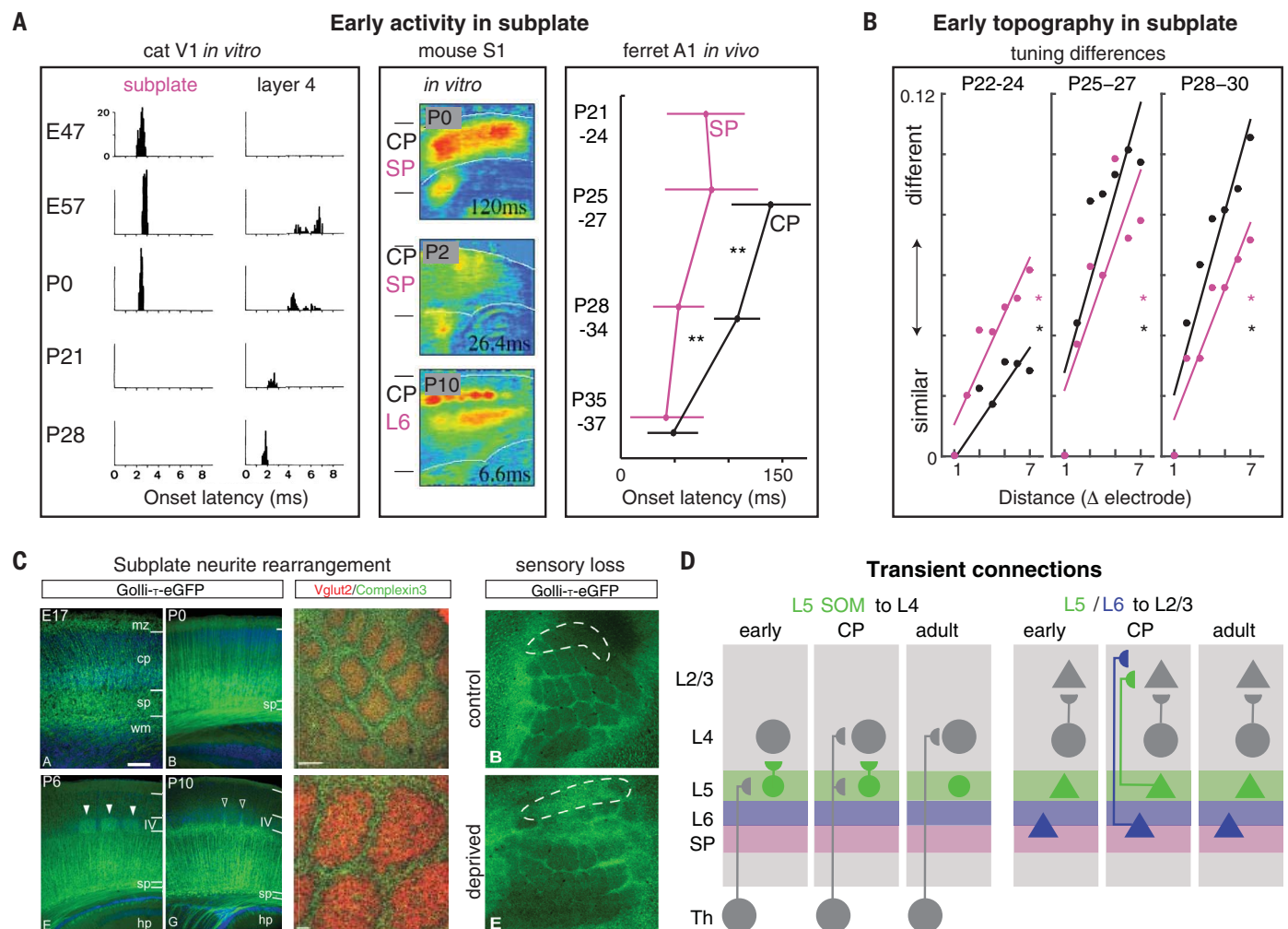


Fig. 3. Transient circuit topologies during thalamocortical development.

(A) Evoked responses in subplate and L4 after stimulation of the optic radiation in cat (44), of thalamus in mouse thalamocortical slices (12), and *in vivo* in ferret (38). Responses emerge and latencies are always shortest in SP. ** indicates statistical significance between the onset latencies in subplate and cortical plate. Image on the left used with permission from (44). (B) Topography is emerging in the subplate. Plotted is the difference in correlation of tuning curves between neighboring recording sites. Early evoked responses in subplate show larger tuning differences with increasing distances (38). (C) (Left) The integration of subplate neurites shows an age-

specific pattern (56). The filled arrowheads indicate clustering of neurites within the barrel; empty arrowheads indicate neurites clustering in the septa. Scale bars are 100 μ m for E17 and P0 and 200 μ m for P6 and P10. wm, white matter; hp, hippocampus. (Middle) Subplate axons target the septa in S1 barrel cortex (51). Scale bars are 200 μ m (top) and 50 μ m (bottom). (Right) Ablating a row of whiskers at birth changed the distribution of the corresponding neurites (56). The dashed white lines indicate the row of whiskers that was manipulated in the deprived condition and the same row in the control. (D) Various transient connections only present during specific stages of development and not in the adult (32, 39, 91). SOM, somatostatin-positive interneuron.

future thalamorecipient layers. Because of the excitatory nature of subplate neuron projections, these neurons have a possible instructive role in thalamocortical as well as intracortical connectivity (28, 53). Besides projecting into the developing cortical plate, subplate neurons also pioneer corticothalamic projections (28). Subsets of subplate neurons target higher-order thalamic nuclei (50, 51). Subplate neurons also receive inputs from the developing cortical plate, including L4 (31), as well as from both glutamatergic and GABAergic subplate neurons (31, 48). Although at young ages subplate neurons receive inputs from L4 through *N*-methyl-D-aspartate (NMDA) receptor-only connections (31, 53), intrasubplate and thala-

mocortical synapses on subplate neurons are not silent (54). Thus, at young ages, there is an NMDA receptor-mediated feedback from the eventual thalamorecipient L4 to the currently thalamorecipient subplate neurons. The emerging connectivity diagram points to an integrative role of subplate neurons at this key stage of development (53) (Fig. 2D).

Besides subplate neurons, Cajal-Retzius neurons in the marginal zone/LI represent another population of early-generated and transient neurons (55). Cajal-Retzius neurons receive mainly GABAergic synaptic inputs of mostly unknown origin, but some arise from subplate. The axonal targets of Cajal-Retzius cells and their role in spontaneous activity are unclear.

The early circuits that are dominated by transient neuronal cell types coexist with circuits that will prevail in the adult for a period of time. Subsequently, the increasing influence of the sensory periphery will trigger the dismantling of the transient networks. Arrangement of subplate neurites is regulated by sensory input, because sensory deprivation delays the remodeling of subplate neurites (56, 57) (Fig. 3C). Besides the largely transient subplate neurons, other transient connections exist within the cortical plate. For example, subsets of GABAergic L5A neurons receive thalamic inputs and transiently project to L4 (Fig. 3D); transient widespread connections exist from subgranular to supragranular layers

(39) (Fig. 3D); and GABAergic connections transition from early depolarizing to hyperpolarizing action (58, 59).

Instructive role of subplate in cortico-thalamo-cortical circuits

The corticothalamic projections start to extend toward the internal capsule immediately after the generation of the first preplate cells (Fig. 4A). Subplate projections cross the pallial-subpallial boundary simultaneously with the thalamic projections and they cofasciculate, providing vital scaffolds for thalamocortical ingrowth (60). Removal or repositioning of subplate neurons at this age prevents thalamic innervation of cortex (28). Subplate neurons pioneer the outgrowth of corticothalamic projections (28), and corticothalamic projections accumulate outside the thalamus before ingrowth (61).

At later ages, thalamocortical projections show anatomical rearrangements, for example, into

ocular dominance columns in V1 or barrels in rodent S1. Subplate neurites (56) and axons (51) also show patterned projections (Fig. 3C). Selective subplate lesions have shown that subplate neurons are required for the emergence of patterned thalamocortical projections and for functional maturation and plasticity of thalamocortical and potentially intracortical circuits (21, 62, 63). The role of subplate neurons outside primary sensory areas has been enigmatic.

Subplate projections to higher-order thalamic nuclei

Besides receiving ascending inputs from the sensory periphery, the thalamus is a target of cortical inputs. The thalamus comprises two functionally distinct components: the first and higher-order thalamic nuclei (64). Only the first-order nuclei (e.g., ventrobasal thalamus) receive direct input from the sensory periphery,

whereas higher-order nuclei (e.g., posterior thalamic nucleus) receive most inputs from cortex (Fig. 4, A to C). Thalamocortical circuits have been studied most extensively in sensory cortices, but higher-order thalamic nuclei have received increasing attention because of their presumed involvement in higher cognitive functions. First-order thalamic projections target L4 and provide inputs to L6a. By contrast, higher-order thalamic inputs target L5 and L1, potentially providing feedback modulation and integration with multisensory processing in L1.

First- and higher-order thalamic nuclei have very different relationships to thalamic reticular nucleus (TRN), because only first-order thalamic nuclei give collaterals to this thin sheet of GABAergic neurons (Fig. 4C). They also have different relationships to the corticothalamic projections from different origins. In adult, the corticothalamic inputs to first-order thalamic

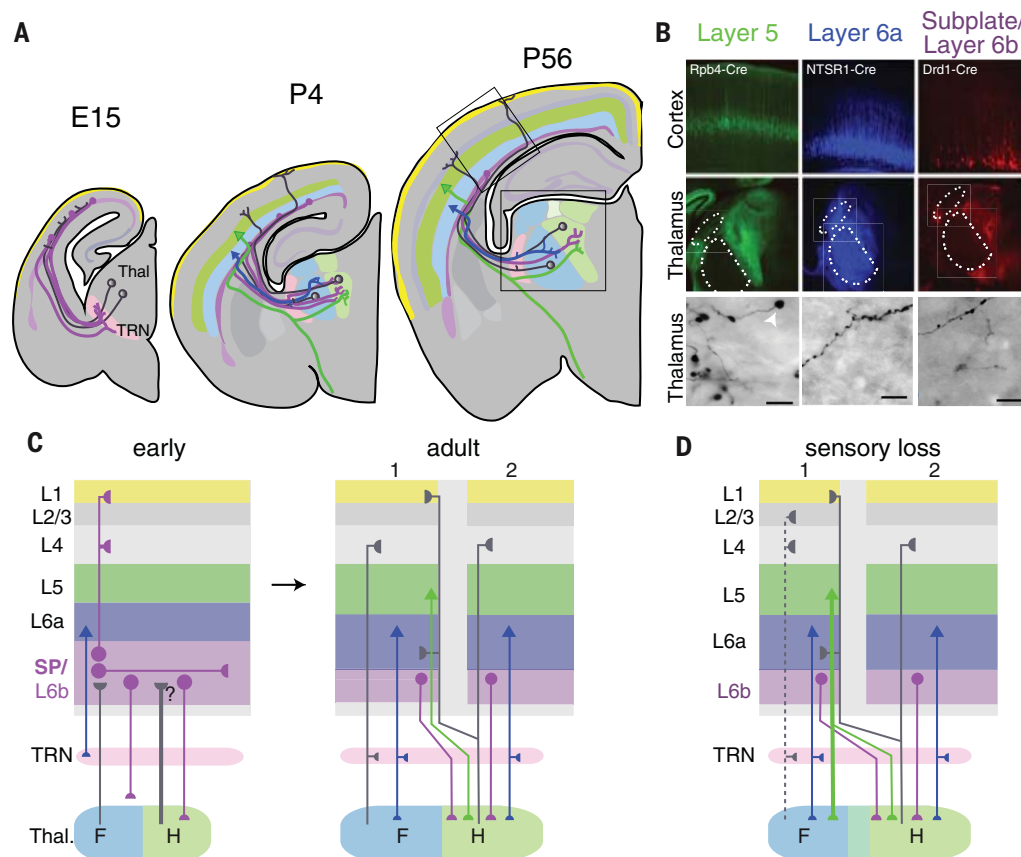


Fig. 4. Establishment and plasticity of thalamo-cortical-thalamic circuits.

(A) Development of thalamocortical connectivity in mouse (E15, P4, and P56). Thalamocortical projections cross the pallial-subpallial boundary simultaneously with corticothalamic projections; cofasciculate, providing mutual guidance; and accumulate in subplate or outside the thalamus, possibly in TRN. L5 projections give side branches selectively to higher-order thalamic nuclei. L6 projections innervate both nuclei. (B) Selective innervation of first- and higher-order thalamic nuclei. White circles illustrate dorsal lateral geniculate nucleus and ventrobasal thalamus (VB). L5 and L6b projections selectively innervate higher-order thalamic nuclei, whereas L6a lack such preference (50, 61, 92). L5 terminals from S1 to PO are larger than L6a

or L6b terminals from S1 to VB (92). Top and middle images are taken from coronal sections of the cortex and thalamus of three different reporter gene-expressing lines; bottom images are high-magnification photomicrographs from the biotinylated dextran amine-labeled corticothalamic projections in the thalamus. The dashed white lines indicate the outline of the lateral geniculate nucleus and ventrobasal thalamus. Scale bars are 10 μm. (C) Reciprocal thalamocortical connectivity during development and in adult. 1 and 2 indicate primary and secondary cortical areas, respectively. F, first-order thalamic nucleus; H, higher-order thalamic nucleus. (D) After sensory loss, cortical and thalamic connectivity in primary (1) and secondary (2) cortical areas is changed.

Box 1. Subplate and claustrum share similarities: Control of large-scale networks?

The claustrum has the strongest connectivity in the adult human brain, links all cortical areas, and is associated with higher cognitive functions (96, 97). Claustrum shares extensive similarities with the subplate. Their principal neurons are among the earliest born, and many markers expressed in the subplate/L6b are also expressed in the claustrum (98). Adult L6b neurons also link distant cortical areas (99). We hypothesize that subplate and claustrum perform similar functions as a key nexus between corticocortical, thalamocortical, and corticothalamic loops. Subplate neurons might function as developmental “operational” hub cells, similar to those of the developing hippocampus (100). Claustrum may perform comparable roles in the adult.

nuclei arise from L6 neurons that target both types of thalamic nuclei as well as the TRN (Fig. 4B). L5 neurons only send projections to higher-order thalamic nuclei and do not innervate TRN (50). The corticothalamic pathway is pioneered by subplate neurons (28), and specific populations of subplate neurons provide input to higher-order thalamic nuclei (50, 51). However, L5 projections enter the thalamus first (65) and provide strong input to higher-order nuclei. Retinal ablation at birth elicited L5 innervation of first-order dorsal lateral geniculate nucleus, suggesting that early peripheral activity can regulate corticothalamic innervation (61) (Fig. 4D).

Subplate neurons are on the nexus between thalamocortical and corticothalamic loops, thus their activity can change the function of these pathways and act like a gate (Fig. 4). Indeed, subplate neurons are targets of multiple neuromodulators (28), and subplate remnant L6b neurons are modulated by neurotensin and orexin, which is wake promoting, consistent with a gating role (66). Subplate neurons share many similarities with claustral neurons, suggesting a functional homology (see Box 1).

What does early activity do?

Neural activity regulates functional maturation of cells and circuits by driving the expression of ion channels and receptors or by changing morphology. Activity can also change cell identity by driving genetic programs, likely by adjusting final differentiation (67).

Higher-order thalamus enables cross-modal connections (42), that is, although manipulating peripheral spontaneous activity can alter ascending circuits in the matched system (7, 68, 69), effects can also be widespread. Cross-modal thalamocortical plasticity occurs when a sensory organ changes its input and another sensory modality takes over these pathways on the thalamic level (Fig. 4). In addition, cross-hierarchical corticothalamic plasticity exists, in which first-order thalamic nucleus adopts a “higher-order thalamic phenotype” by receiving input from L5 (61, 70). These two forms of plasticity might occur in parallel when sensory-driven activities are altered. Changes after peripheral manipulations are typically interpreted in the framework of thalamocortical competi-

tion, but developmental and cross-hierarchical changes have to be considered as well.

Without sensory input, thalamocortical circuits remain in a status resembling higher-order circuits (43). We thus hypothesize that higher-order thalamic nuclei are the early endogenous pattern generators in thalamocortical systems. Acquiring characteristics of higher-order thalamic nuclei might be the default developmental pathway when there is no sensory peripheral input. This default endogenous thalamocortical activity is suppressed together with the default differentiation path in first-order thalamic nuclei with normal spontaneous activity and normal sensory inputs (Fig. 4D). Thus, a specific pattern of spontaneous synchronized activity at a distinct time point may activate or inactivate a developmental program in a subset of immature neurons. We started to appreciate the variety and complexity of spontaneous activity patterns; however, the precise roles of each pattern in specific neurons at specific developmental stages are unknown.

Regulation of subplate neuronal death during development

Spontaneous activity also plays a role in controlling the number of surviving versus dying neurons. GABAergic neurons not only control the pattern of synchronized spontaneous activity and the emergence of functional network topography in developing cortex but also control apoptosis of interneurons (71, 72). Blockade of electrical activity for 6 hours *in vitro* doubles the number of apoptotic neurons (73). By contrast, synchronized network activity resembling physiological spindle bursts and gamma oscillations promotes neuronal survival and reduces apoptosis. This pro-survival effect is mediated by brain-derived neurotrophic factor (BDNF), which is released in response to synchronized burst discharges at 20 to 50 Hz (74). Thus, cell survival in the developing cortex is controlled by distinct patterns and not by the level of activity. Synchronized spindle bursts and gamma oscillations may be the adequate activity patterns to control the fate of cortical neurons at a developmental period, when apoptosis coincides with the expression of these patterns (Fig. 2, A to C). Besides showing pattern specificity,

activity-dependent apoptosis may be cell type-dependent. Cajal-Retzius and subplate neurons both highly express neurotrophin receptor p75 (p75NTR), which activates a pathway that induces death in Cajal-Retzius neurons (75) but survival in subplate neurons (76), suggesting that the same activity pattern may activate different intracellular pathways.

The normal integration, remodeling, and eventual death of subplate and marginal zone neurons are controlled by spontaneous activity and possibly early sensory activity (38, 56). Alterations in cortical activity patterns therefore could alter the distribution and number of surviving neurons. Understanding the dendritic maturation and programmed cell death of these transient neurons is key to understanding the subtle anatomical changes observed in the number and distribution of interstitial white matter and marginal zone cells in some neurological and psychiatric disorders (77). Damage of early-generated subplate neurons has been implicated in hypoxia-ischemia, autism, and epilepsy (78–80). The link between subplate gene expression patterns and cell numbers and distribution alterations in disorders is supported by several studies (49, 81).

Disturbances in spontaneous activity patterns during distinct stages of early development will interfere with apoptosis programs. Alcohol and general anesthetics modify spindle bursts and gamma oscillations in newborn rats and can induce widespread cortical cell death (82).

Clinical relevance

The spread of spontaneous activity in the thalamocortical network and cerebral cortex is broader in the human preterm as compared with the term infant (Fig. 5A). Widespread cortical activation in the preterm is also evident from resting-state electroencephalogram connectivity in the 8- to 15-Hz frequency band (spindle burst) (Fig. 5B). Premature babies show the full repertoire of resting-state dynamics that emerge during the period of rapid neural growth before term (~40 pcw) (83). Sensory, motor, default mode, frontoparietal, and executive control networks develop at different rates, suggesting that they are formed before the sensory periphery is fully functional and before acquisition of cognitive competencies takes place in later childhood. At the early stages, subplate is fully integrated into cortical circuits and may influence resting-state networks before term birth. Indeed, resting-state network activities in extremely immature human cerebral cortex are mostly restricted to lower cortical layers (83). We postulate that early transient circuits form the basis for activity patterns in the preterm and that the pathophysiological persistence of these circuits is involved in the manifestation of neurological and psychiatric disorders (Fig. 5C). All these changes could

occur according to a default timetable that is adjusted by sensory activity, general embryonic maturation, and various environmental factors, for example, nutrition, inflammation, maternal stress, and so on. We argue that spontaneous activity patterns are mediated through higher- and first-order thalamocortical systems and that the two pathways have to interact to produce the normal thalamo-cortico-thalamic circuits for the emergence of cognitive functions (Fig. 4). The two systems have different maturation timelines and process different aspects of sensory information and brain states. These spatiotemporal features have to be linked, and we speculate that unlinking or failure to link may cause cognitive disorders. Thus, a key developmental event is to keep the first-order and higher-order thalamic loops linked and aligned with the intracortical connections. Because subplate neurons connect to each other over long distances (31) and also project to the thalamus, they might form a network linking primary and higher-order areas, and, with the dissolution of subplate, this link is abolished.

The transient circuits are vulnerable, and the sensitive periods for disorders overlap with times when circuits process largely spon-

aneous activity patterns (Fig. 2). These circuits are vulnerable to hypoxia-ischemia (79, 84) and pharmacological manipulations—for example, prenatal valproate exposure (78)—and disrupting them will have implications on the development of the thalamo-cortico-thalamic networks. Large numbers of white matter and deep interstitial neurons without disturbances of the normal cortical layering are pathological characteristics seen in temporal lobe epilepsy (TLE). Neocortical surgical specimens of patients suffering from pharmacoresistant TLE demonstrated that these deep neurons expressed transcription factors that are highly expressed in subplate (85–87). Subplate-like neurons have also been identified in pediatric epilepsy patients (88), further supporting the hypothesis that subplate neurons may survive and may be causal to TLE.

A better understanding of the development of transient circuits, their roles in brain wiring, higher brain functions, and the consequences of retained white matter networks in cognitive conditions is needed to design new diagnostic and therapeutic approaches in neurodevelopmental disorders. However, investigations of changes in various disorders at adult stages can only give us limited clues on abnormal de-

velopmental processes. The interstitial white matter cells in these pathologies and miswiring are only the remnants of or consequence of malfunction of a transient neuronal population. Specific biomarkers are needed to detect and correct malfunction of transient populations at early ages.

Open questions and perspectives

1) Do all spontaneous activity patterns fulfill a particular functional role in development or are some of them just epiphenomena? The various forms of activity patterns change as the neuronal circuits get assembled, transformed, or disassembled. Linking these changing activity patterns to particular stages of circuit formation can give us diagnostic insights into normal and pathological circuit development.

2) What activity pattern is normal and what is abnormal? The presence or absence of synchrony and coordinated development between first- and higher-order circuits might not manifest clinically during development when temporal processing is imprecise and might lead to, on the surface, normal locally stable brain function. At later ages, if the brain is challenged by more rapid changes—for example, environmental insults, puberty, and so on—such deficits could be unmasked.

3) How do different spontaneous activity patterns interact (e.g., local burst activity versus propagating wave, periphery-driven versus cortical)? Many neural structures are capable of producing spontaneous activity. Nonlinear interactions might mediate the integration and transition between activity patterns owing to the presence of silent synapses in subplate.

4) Are higher-order thalamic nuclei the early endogenous pattern generators in the thalamo-cortical system? We speculate that first-order nuclei suppress the default endogenous thalamocortical activity based on emerging peripheral inputs and thereby induce a different transcriptional profile in targeted cortical neurons.

5) Enlarged subplate and higher-order thalamic circuits are a key feature of the primate brain. The human subplate can be five times larger than the cortical plate, indicating a primate specialization. Because key elements that determine projection neuron identity are shared between rodent and primates, are there subplate neurons that are only present in humans, and did subplate and higher-order nuclei coevolve?

6) Does a selective vulnerability of subgroups of subplate neurons contribute to distinct pathologies? We speculate that subtypes of subplate neurons mediate lemniscal, paralemniscal, and nonlemniscal development and that subplate circuits differ between primary and higher-order sensory cortical areas. Would alterations in different subplate circuits be the tipping point to enter distinct pathological

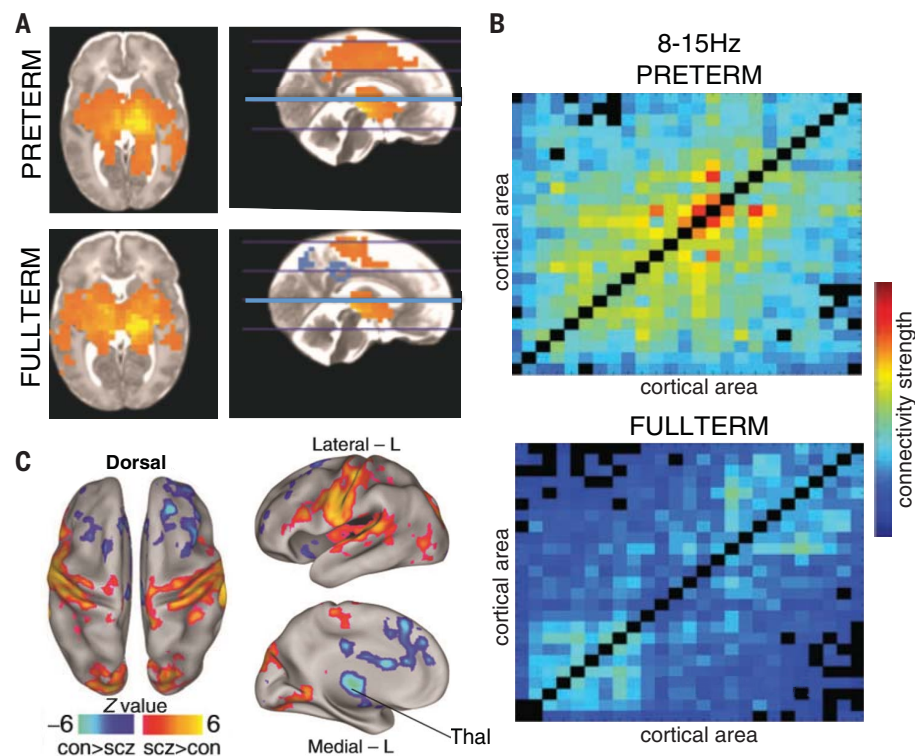


Fig. 5. Spontaneous activity in preterm and adult schizophrenics. (A) Resting-state functional magnetic resonance images (fMRIs) of pre- and fullterm infant brains showing widespread cortical activation in preterm (93). Image used with permission from (93). (B) Resting-state EEG connectivity matrix at 8 to 15 Hz, showing stronger connectivity (red and yellow) in preterm (94). Image used with permission from (94). (C) Resting-state fMRI data showing notable differences in thalamic connectivity between healthy (CON) individuals and individuals with schizophrenia (SCZ) (95). Image used with permission from (95).

developmental trajectories? Are some diseases higher-order thalamic diseases and others due to network asynchrony?

7) Persistent subplate and Cajal-Retzius neurons might play a role in cognitive disorders. Subplate neurons can synapse on migrating cortical plate neurons (89) and might alter neuronal differentiation. Therefore, early changes in subplate function could influence the delivery, positioning, and differentiation of cortical plate neurons, causing their accumulation in the subplate and contributing to abnormal connections.

REFERENCES AND NOTES

1. Z. Molnár *et al.*, New insights into the development of the human cerebral cortex. *J. Anat.* **235**, 432–451 (2019). doi: [10.1111/joa.13055](#); pmid: [31373394](#)
2. L. C. Katz, C. J. Shatz, Synaptic activity and the construction of cortical circuits. *Science* **274**, 1133–1138 (1996). doi: [10.1126/science.274.5290.1133](#); pmid: [8895456](#)
3. F. K. Wong *et al.*, Pyramidal cell regulation of interneuron survival sculpts cortical networks. *Nature* **557**, 668–673 (2018). doi: [10.1038/s41586-018-0139-6](#); pmid: [29849154](#)
4. M. Riva *et al.*, Activity-dependent death of transient Cajal-Retzius neurons is required for functional cortical wiring. *eLife* **8**, e50503 (2019). doi: [10.7554/eLife.50503](#); pmid: [31891351](#)
5. I. Adorjan *et al.*, Neuroserpin expression during human brain development and in adult brain revealed by immunohistochemistry and single cell RNA sequencing. *J. Anat.* **235**, 543–554 (2019). doi: [10.1111/joa.12931](#); pmid: [30644551](#)
6. H. Fukumitsu *et al.*, Simultaneous expression of brain-derived neurotrophic factor and neurotrophin-3 in Cajal-Retzius, subplate and ventricular progenitor cells during early development stages of the rat cerebral cortex. *Neuroscience* **84**, 115–127 (1998). doi: [10.1016/S0306-4522\(97\)00505-8](#); pmid: [9522367](#)
7. T. A. Seabrook, T. J. Burbridge, M. C. Crair, A. D. Huberman, Architecture, function, and assembly of the mouse visual system. *Annu. Rev. Neurosci.* **40**, 499–538 (2017). doi: [10.1146/annurev-neuro-071714-033842](#); pmid: [28772103](#)
8. H. J. Luhmann *et al.*, Spontaneous neuronal activity in developing neocortical networks: From single cells to large-scale interactions. *Front. Neural Circuits* **10**, 40 (2016). doi: [10.3389/fncir.2016.00040](#); pmid: [27252626](#)
9. H. J. Luhmann, R. Khazipov, Neuronal activity patterns in the developing barrel cortex. *Neuroscience* **368**, 256–267 (2018). doi: [10.1016/j.neuroscience.2017.05.025](#); pmid: [28528963](#)
10. A. H. Leighton, C. Lohmann, The wiring of developing sensory circuits-from patterned spontaneous activity to synaptic plasticity mechanisms. *Front. Neural Circuits* **10**, 71 (2016). doi: [10.3389/fncir.2016.00071](#); pmid: [27656131](#)
11. O. Blanquie *et al.*, Electrical activity controls area-specific expression of neuronal apoptosis in the mouse developing cerebral cortex. *eLife* **6**, e27696 (2017). doi: [10.7554/eLife.27696](#); pmid: [28826501](#)
12. S. Higashi, Z. Molnár, T. Kurotani, K. Toyama, Prenatal development of neural excitation in rat thalamocortical projections studied by optical recording. *Neuroscience* **115**, 1231–1246 (2002). doi: [10.1016/S0306-4522\(02\)00418-9](#); pmid: [12453494](#)
13. A. R. Moore *et al.*, Connexin hemichannels contribute to spontaneous electrical activity in the human fetal cortex. *Proc. Natl. Acad. Sci. U.S.A.* **111**, E3919–E3928 (2014). doi: [10.1073/pnas.1405253111](#); pmid: [25197082](#)
14. F. Siegel, J. A. Heimel, J. Peters, C. Lohmann, Peripheral and central inputs shape network dynamics in the developing visual cortex in vivo. *Curr. Biol.* **22**, 253–258 (2012). doi: [10.1016/j.cub.2011.12.026](#); pmid: [22264606](#)
15. V. Moreno-Juan *et al.*, Prenatal thalamic waves regulate cortical area size prior to sensory processing. *Nat. Commun.* **8**, 14172 (2017). doi: [10.1038/ncomms14172](#); pmid: [28155854](#)
16. Z. Molnár, S. Gareil, G. López-Bendito, P. Maness, D. J. Price, Mechanisms controlling the guidance of thalamocortical axons through the embryonic forebrain. *Eur. J. Neurosci.* **35**, 1573–1585 (2012). doi: [10.1111/j.1460-9568.2012.08119.x](#); pmid: [22607003](#)
17. I. L. Hanganu, Y. Ben-Ari, R. Khazipov, Retinal waves trigger spindle bursts in the neonatal rat visual cortex. *J. Neurosci.* **26**, 6728–6736 (2006). doi: [10.1523/JNEUROSCI.0752-06.2006](#); pmid: [16793880](#)
18. N. Antón-Bolaños *et al.*, Prenatal activity from thalamic neurons governs the emergence of functional cortical maps in mice. *Science* **364**, 987–990 (2019). doi: [10.1126/science.aav7617](#); pmid: [31048552](#)
19. M. Minlebaev, M. Colonnese, T. Tsintsadze, A. Sirota, R. Khazipov, Early γ oscillations synchronize developing thalamus and cortex. *Science* **334**, 226–229 (2011). doi: [10.1126/science.1210574](#); pmid: [21998388](#)
20. J. W. Yang *et al.*, Thalamic network oscillations synchronize ontogenetic columns in the newborn rat barrel cortex. *Cereb. Cortex* **23**, 1299–1316 (2013). doi: [10.1093/cercor/bhs103](#); pmid: [22593243](#)
21. E. A. Tolner, A. Sheikh, A. Y. Yukin, K. Kaila, P. O. Kanold, Subplate neurons promote spindle bursts and thalamocortical patterning in the neonatal rat somatosensory cortex. *J. Neurosci.* **32**, 692–702 (2012). doi: [10.1523/JNEUROSCI.1538-11.2012](#); pmid: [2238105](#)
22. I. L. Hanganu, A. Okabe, V. Lessmann, H. J. Luhmann, Cellular mechanisms of subplate-driven and cholinergic input-dependent network activity in the neonatal rat somatosensory cortex. *Cereb. Cortex* **19**, 89–105 (2009). doi: [10.1093/cercor/bhn061](#); pmid: [18440948](#)
23. E. Dupont, I. L. Hanganu, W. Kilb, S. Hirsch, H. J. Luhmann, Rapid developmental switch in the mechanisms driving early cortical columnar networks. *Nature* **439**, 79–83 (2006). doi: [10.1038/nature04264](#); pmid: [16327778](#)
24. C. Allene *et al.*, Sequential generation of two distinct synapse-driven network patterns in developing neocortex. *J. Neurosci.* **28**, 12851–12863 (2008). doi: [10.1523/JNEUROSCI.3733-08.2008](#); pmid: [19036979](#)
25. R. Khazipov *et al.*, Early motor activity drives spindle bursts in the developing somatosensory cortex. *Nature* **432**, 758–761 (2004). doi: [10.1038/nature03132](#); pmid: [15592414](#)
26. D. Akhmetshina, A. Nasretudinov, A. Zakharov, G. Valeeva, R. Khazipov, The nature of the sensory input to the neonatal rat barrel cortex. *J. Neurosci.* **36**, 9922–9932 (2016). doi: [10.1523/JNEUROSCI.1781-16.2016](#); pmid: [27656029](#)
27. J. C. Dooley, R. M. Glanz, G. Sokoloff, M. S. Blumberg, Self-generated whisker movements drive state-dependent sensory input to developing barrel cortex. *Curr. Biol.* **30**, 2404–2410.e4 (2020). doi: [10.1016/j.cub.2020.04.045](#); pmid: [32413304](#)
28. P. O. Kanold, H. J. Luhmann, The subplate and early cortical circuits. *Annu. Rev. Neurosci.* **33**, 23–48 (2010). doi: [10.1146/annurev-neuro-060909-153244](#); pmid: [20201645](#)
29. Y. Murata, M. T. Colonnese, Thalamus controls development and expression of arousal states in visual cortex. *J. Neurosci.* **38**, 8772–8786 (2018). doi: [10.1523/JNEUROSCI.1519-18.2018](#); pmid: [30150360](#)
30. H. Sun, H. J. Luhmann, W. Kilb, Resonance properties of different neuronal populations in the immature mouse neocortex. *Eur. J. Neurosci.* **36**, 2753–2762 (2012). doi: [10.1111/j.1460-9568.2012.08196.x](#); pmid: [22748148](#)
31. X. Meng, J. P. Kao, P. O. Kanold, Differential signaling to subplate neurons by spatially specific silent synapses in developing auditory cortex. *J. Neurosci.* **34**, 8855–8864 (2014). doi: [10.1523/JNEUROSCI.0233-14.2014](#); pmid: [24966385](#)
32. A. Marques-Smith *et al.*, A transient transaminergic GABAergic interneuron circuit connects thalamocortical recipient layers in neonatal somatosensory cortex. *Neuron* **89**, 536–549 (2016). doi: [10.1016/j.neuron.2016.01.015](#); pmid: [26844833](#)
33. H. C. Wang *et al.*, Spontaneous activity of cochlear hair cells triggered by fluid secretion mechanism in adjacent support cells. *Cell* **163**, 1348–1359 (2015). doi: [10.1016/j.cell.2015.10.070](#); pmid: [26627734](#)
34. T. A. Babola *et al.*, Homeostatic control of spontaneous activity in the developing auditory system. *Neuron* **99**, 511–524.e5 (2018). doi: [10.1016/j.neuron.2018.07.004](#); pmid: [30077356](#)
35. M. Milh *et al.*, Rapid cortical oscillations and early motor activity in premature human neonate. *Cereb. Cortex* **17**, 1582–1594 (2007). doi: [10.1093/cercor/bhl069](#); pmid: [16950867](#)
36. M. T. Colonnese *et al.*, A conserved switch in sensory processing prepares developing neocortex for vision. *Neuron* **67**, 480–498 (2010). doi: [10.1016/j.neuron.2010.07.015](#); pmid: [20696384](#)
37. A. Kaminska *et al.*, Cortical auditory-evoked responses in preterm neonates: Revisited by spectral and temporal analyses. *Cereb. Cortex* **28**, 3429–3444 (2018). doi: [10.1093/cercor/bhx206](#); pmid: [29194486](#)
38. J. M. Weiss, A. Isaiyah, P. V. Watkins, P. O. Kanold, Subplate neurons are the first cortical neurons to respond to sensory stimuli. *Proc. Natl. Acad. Sci. U.S.A.* **114**, 12602–12607 (2017). doi: [10.1073/pnas.1710793114](#); pmid: [29114043](#)
39. X. Meng *et al.*, Transient subgranular hyperconnectivity to L2/3 and enhanced pairwise correlations during the critical period in the mouse auditory cortex. *Cereb. Cortex* **30**, 1914–1930 (2020). doi: [10.1093/cercor/bhz213](#); pmid: [31667495](#)
40. H. Mizuno *et al.*, Patchwork-type spontaneous activity in neonatal barrel cortex layer 4 transmitted via thalamocortical projections. *Cell Rep.* **22**, 123–135 (2018). doi: [10.1016/j.celrep.2017.12.012](#); pmid: [29298415](#)
41. G. B. Smith, B. Hein, D. E. Whitney, D. Fitzpatrick, M. Kaschube, Distributed network interactions and their emergence in developing neocortex. *Nat. Neurosci.* **21**, 1600–1608 (2018). doi: [10.1038/s41593-018-0247-5](#); pmid: [30349107](#)
42. J. U. Henschke *et al.*, Early sensory experience influences the development of multisensory thalamocortical and intracortical connections of primary sensory cortices. *Brain Struct. Funct.* **223**, 1165–1190 (2018). pmid: [29094306](#)
43. G. Pouchelon *et al.*, Modality-specific thalamocortical inputs instruct the identity of postsynaptic L4 neurons. *Nature* **511**, 471–474 (2014). doi: [10.1038/nature13390](#); pmid: [24828045](#)
44. E. Friauf, C. J. Shatz, Changing patterns of synaptic input to subplate and cortical plate during development of visual cortex. *J. Neurophysiol.* **66**, 2059–2071 (1991). doi: [10.1152/jn.1991.66.6.2059](#); pmid: [1812236](#)
45. C. Zhao, J. P. Kao, P. O. Kanold, Functional excitatory microcircuits in neonatal cortex connect thalamus and layer 4. *J. Neurosci.* **29**, 15479–15488 (2009). doi: [10.1523/JNEUROSCI.4471-09.2009](#); pmid: [20007472](#)
46. I. Kostovic, P. Rakic, Developmental history of the transient subplate zone in the visual and somatosensory cortex of the macaque monkey and human brain. *J. Comp. Neurol.* **297**, 441–470 (1990). doi: [10.1002/cne.902970309](#); pmid: [2398142](#)
47. Z. Molnár, T. Kurotani, S. Higashi, N. Yamamoto, K. Toyama, Development of functional thalamocortical synapses studied with current source-density analysis in whole forebrain slices in the rat. *Brain Res. Bull.* **60**, 355–371 (2003). doi: [10.1016/S0306-9230\(03\)00061-3](#); pmid: [12781324](#)
48. I. L. Hanganu, W. Kilb, H. J. Luhmann, Functional synaptic projections onto subplate neurons in neonatal rat somatosensory cortex. *J. Neurosci.* **22**, 7165–7176 (2002). doi: [10.1523/JNEUROSCI.22-16-07165.2002](#); pmid: [12177212](#)
49. A. Hoerder-Suabedissen *et al.*, Expression profiling of mouse subplate reveals a dynamic gene network and disease association with autism and schizophrenia. *Proc. Natl. Acad. Sci. U.S.A.* **110**, 3555–3560 (2013). doi: [10.1073/pnas.1218510110](#); pmid: [23401504](#)
50. A. Hoerder-Suabedissen *et al.*, Subset of cortical layer 6b neurons selectively innervates higher order thalamic nuclei in mice. *Cereb. Cortex* **28**, 1882–1897 (2018). doi: [10.1093/cercor/bhy036](#); pmid: [29481606](#)
51. S. Viswanathan, A. Sheikh, L. L. Looger, P. O. Kanold, Molecularly defined subplate neurons project both to thalamocortical recipient layers and thalamus. *Cereb. Cortex* **27**, 4759–4768 (2017). doi: [10.1093/cercor/bhw271](#); pmid: [27655928](#)
52. R. Deng, J. P. Y. Kao, P. O. Kanold, Distinct transaminergic glutamatergic circuits to GABAergic interneurons in the neonatal auditory cortex. *Cell Rep.* **19**, 1141–1150 (2017). doi: [10.1016/j.celrep.2017.04.044](#); pmid: [28494864](#)
53. P. O. Kanold, R. Deng, X. Meng, The integrative function of silent synapses on subplate neurons in cortical development and dysfunction. *Front. Neuroanat.* **13**, 41 (2019). doi: [10.3389/fnana.2019.00041](#); pmid: [31040772](#)
54. S. Hirsch, H. J. Luhmann, Pathway-specificity in N-methyl-D-aspartate receptor-mediated synaptic inputs onto subplate neurons. *Neuroscience* **153**, 1092–1102 (2008). doi: [10.1016/j.neuroscience.2008.01.068](#); pmid: [18455878](#)
55. S. Kirischuk, H. J. Luhmann, W. Kilb, Cajal-Retzius cells: Update on structural and functional properties of these mystic neurons that bridged the 20th century. *Neuroscience* **275**, 33–46 (2014). doi: [10.1016/j.neuroscience.2014.06.009](#); pmid: [24931764](#)

56. M. C. Piñón, A. Jethwa, E. Jacobs, A. Campagnoni, Z. Molnár, Dynamic integration of subplate neurons into the cortical barrel field circuitry during postnatal development in the Golli-tau-eGFP (GTE) mouse. *J. Physiol.* **587**, 1903–1915 (2009). doi: [10.1113/jphysiol.2008.167767](https://doi.org/10.1113/jphysiol.2008.167767); pmid: [19289548](https://pubmed.ncbi.nlm.nih.gov/19289548/)
57. Z. Molnár, *Development of Thalamocortical Connections* (Springer, 1998).
58. C. Rivera et al., The K⁺/Cl⁻ co-transporter KCC2 renders GABA hyperpolarizing during neuronal maturation. *Nature* **397**, 251–255 (1999). doi: [10.1038/16697](https://doi.org/10.1038/16697); pmid: [9930699](https://pubmed.ncbi.nlm.nih.gov/9930699/)
59. K. Kirmse et al., GABA depolarizes immature neurons and inhibits network activity in the neonatal neocortex in vivo. *Nat. Commun.* **6**, 7750 (2015). doi: [10.1038/ncomms8750](https://doi.org/10.1038/ncomms8750); pmid: [26177896](https://pubmed.ncbi.nlm.nih.gov/26177896/)
60. Z. Molnár, R. Adams, C. Blakemore, Mechanisms underlying the early establishment of thalamocortical connections in the rat. *J. Neurosci.* **18**, 5723–5745 (1998). doi: [10.1523/JNEUROSCI.18-15-05723.1998](https://doi.org/10.1523/JNEUROSCI.18-15-05723.1998); pmid: [9671663](https://pubmed.ncbi.nlm.nih.gov/9671663/)
61. E. Grant, A. Hoerder-Suabedissen, Z. Molnár, The regulation of corticofugal fiber targeting by retinal inputs. *Cereb. Cortex* **26**, 1336–1348 (2016). doi: [10.1093/cercor/bhv315](https://doi.org/10.1093/cercor/bhv315); pmid: [26744542](https://pubmed.ncbi.nlm.nih.gov/26744542/)
62. P. O. Kanold, C. J. Shatz, Subplate neurons regulate maturation of cortical inhibition and outcome of ocular dominance plasticity. *Neuron* **51**, 627–638 (2006). doi: [10.1016/j.neuron.2006.07.008](https://doi.org/10.1016/j.neuron.2006.07.008); pmid: [16950160](https://pubmed.ncbi.nlm.nih.gov/16950160/)
63. P. O. Kanold, P. Kara, R. C. Reid, C. J. Shatz, Role of subplate neurons in functional maturation of visual cortical columns. *Science* **301**, 521–525 (2003). doi: [10.1126/science.1084152](https://doi.org/10.1126/science.1084152); pmid: [12881571](https://pubmed.ncbi.nlm.nih.gov/12881571/)
64. R. W. Guillery, S. M. Sherman, Thalamic relay functions and their role in corticocortical communication: Generalizations from the visual system. *Neuron* **33**, 163–175 (2002). doi: [10.1016/S0896-6273\(01\)00582-7](https://doi.org/10.1016/S0896-6273(01)00582-7); pmid: [11804565](https://pubmed.ncbi.nlm.nih.gov/11804565/)
65. F. Clascá, A. Angelucci, M. Sur, Layer-specific programs of development in neocortical projection neurons. *Proc. Natl. Acad. Sci. U.S.A.* **92**, 11145–11149 (1995). doi: [10.1073/pnas.92.24.11145](https://doi.org/10.1073/pnas.92.24.11145); pmid: [7479954](https://pubmed.ncbi.nlm.nih.gov/7479954/)
66. L. Bayer et al., Exclusive postsynaptic action of hypocretin-orexin on sublayer 6b cortical neurons. *J. Neurosci.* **24**, 6760–6764 (2004). doi: [10.1523/JNEUROSCI.1783-04.2004](https://doi.org/10.1523/JNEUROSCI.1783-04.2004); pmid: [15282280](https://pubmed.ncbi.nlm.nih.gov/15282280/)
67. I. Vitali et al., Progenitor hyperpolarization regulates the sequential generation of neuronal subtypes in the developing neocortex. *Cell* **174**, 1264–1276.e15 (2018). doi: [10.1016/j.cell.2018.06.036](https://doi.org/10.1016/j.cell.2018.06.036); pmid: [30057116](https://pubmed.ncbi.nlm.nih.gov/30057116/)
68. H. P. Xu et al., Spatial pattern of spontaneous retinal waves instructs retinotopic map refinement more than activity frequency. *Dev. Neurobiol.* **75**, 621–640 (2015). doi: [10.1002/dneu.22288](https://doi.org/10.1002/dneu.22288); pmid: [25787992](https://pubmed.ncbi.nlm.nih.gov/25787992/)
69. A. Clause et al., The precise temporal pattern of prehearing spontaneous activity is necessary for tonotopic map refinement. *Neuron* **82**, 822–835 (2014). doi: [10.1016/j.neuron.2014.04.001](https://doi.org/10.1016/j.neuron.2014.04.001); pmid: [24853941](https://pubmed.ncbi.nlm.nih.gov/24853941/)
70. L. Frangeul et al., A cross-modal genetic framework for the development and plasticity of sensory pathways. *Nature* **538**, 96–98 (2016). doi: [10.1038/nature19770](https://doi.org/10.1038/nature19770); pmid: [27669022](https://pubmed.ncbi.nlm.nih.gov/27669022/)
71. L. Modul et al., Assemblies of perisomatic GABAergic neurons in the developing barrel cortex. *Neuron* **105**, 93–105.e4 (2020). doi: [10.1016/j.neuron.2019.10.007](https://doi.org/10.1016/j.neuron.2019.10.007); pmid: [31780328](https://pubmed.ncbi.nlm.nih.gov/31780328/)
72. Z. R. S. Duan et al., GABAergic restriction of network dynamics regulates interneuron survival in the developing cortex. *Neuron* **105**, 75–92.e5 (2020). doi: [10.1016/j.neuron.2019.10.008](https://doi.org/10.1016/j.neuron.2019.10.008); pmid: [31780329](https://pubmed.ncbi.nlm.nih.gov/31780329/)
73. N. Heck et al., Activity-dependent regulation of neuronal apoptosis in neonatal mouse cerebral cortex. *Cereb. Cortex* **18**, 1335–1349 (2008). doi: [10.1093/cercor/bhm165](https://doi.org/10.1093/cercor/bhm165); pmid: [17965127](https://pubmed.ncbi.nlm.nih.gov/17965127/)
74. A. Golbs, B. Nimmervoll, J. J. Sun, I. E. Sava, H. J. Luhmann, Control of programmed cell death by distinct electrical activity patterns. *Cereb. Cortex* **21**, 1192–1202 (2011). doi: [10.1093/cercor/bhq200](https://doi.org/10.1093/cercor/bhq200); pmid: [20966045](https://pubmed.ncbi.nlm.nih.gov/20966045/)
75. O. Blanquie, L. Liebmann, C. A. Hübner, H. J. Luhmann, A. Sinning, NKCC1-mediated GABAergic signaling promotes postnatal cell death in neocortical Cajal-Retzius cells. *Cereb. Cortex* **27**, 1644–1659 (2017). pmid: [26819276](https://pubmed.ncbi.nlm.nih.gov/26819276/)
76. M. F. DeFreitas, P. S. McQuillen, C. J. Shatz, A novel p75NTR signaling pathway promotes survival, not death, of immunopurified neocortical subplate neurons. *J. Neurosci.* **21**, 5121–5129 (2001). doi: [10.1523/JNEUROSCI.21-14-05121.2001](https://doi.org/10.1523/JNEUROSCI.21-14-05121.2001); pmid: [11438587](https://pubmed.ncbi.nlm.nih.gov/11438587/)
77. S. Akbarian et al., Maldistribution of interstitial neurons in prefrontal white matter of the brains of schizophrenic patients. *Arch. Gen. Psychiatry* **53**, 425–436 (1996). doi: [10.1001/archpsyc.1996.01830050061010](https://doi.org/10.1001/archpsyc.1996.01830050061010); pmid: [8624186](https://pubmed.ncbi.nlm.nih.gov/8624186/)
78. D. A. Nagode et al., Abnormal development of the earliest cortical circuits in a mouse model of autism spectrum disorder. *Cell Rep.* **18**, 1100–1108 (2017). doi: [10.1016/j.celrep.2017.01.006](https://doi.org/10.1016/j.celrep.2017.01.006); pmid: [28147267](https://pubmed.ncbi.nlm.nih.gov/28147267/)
79. A. Sheikh et al., Neonatal hypoxia-ischemia causes functional circuit changes in subplate neurons. *Cereb. Cortex* **29**, 765–776 (2019). doi: [10.1093/cercor/bhx358](https://doi.org/10.1093/cercor/bhx358); pmid: [29365081](https://pubmed.ncbi.nlm.nih.gov/29365081/)
80. J. J. Volpe, Subplate neurons—Missing link in brain injury of the premature infant? *Pediatrics* **97**, 112–113 (1996). pmid: [8545202](https://pubmed.ncbi.nlm.nih.gov/8545202/)
81. D. Polioudakis et al., A single-cell transcriptomic atlas of human neocortical development during mid-gestation. *Neuron* **103**, 785–801.e8 (2019). doi: [10.1016/j.neuron.2019.06.011](https://doi.org/10.1016/j.neuron.2019.06.011); pmid: [31303374](https://pubmed.ncbi.nlm.nih.gov/31303374/)
82. J. Lebedeva et al., Inhibition of cortical activity and apoptosis caused by ethanol in neonatal rats in vivo. *Cereb. Cortex* **27**, 1068–1082 (2017). pmid: [26646511](https://pubmed.ncbi.nlm.nih.gov/26646511/)
83. V. Doria et al., Emergence of resting state networks in the preterm human brain. *Proc. Natl. Acad. Sci. U.S.A.* **107**, 20015–20020 (2010). doi: [10.1073/pnas.1007921107](https://doi.org/10.1073/pnas.1007921107); pmid: [21041625](https://pubmed.ncbi.nlm.nih.gov/21041625/)
84. P. S. McQuillen, R. A. Sheldon, C. J. Shatz, D. M. Ferriero, Selective vulnerability of subplate neurons after early neonatal hypoxia-ischemia. *J. Neurosci.* **23**, 3308–3315 (2003). doi: [10.1523/JNEUROSCI.23-08-03308.2003](https://doi.org/10.1523/JNEUROSCI.23-08-03308.2003); pmid: [12716938](https://pubmed.ncbi.nlm.nih.gov/12716938/)
85. L. Rossini et al., Altered layer-specific gene expression in cortical samples from patients with temporal lobe epilepsy. *Epilepsia* **52**, 1928–1937 (2011). doi: [10.1111/j.1528-1167.2011.03246.x](https://doi.org/10.1111/j.1528-1167.2011.03246.x); pmid: [21883179](https://pubmed.ncbi.nlm.nih.gov/21883179/)
86. Z. Richter et al., Characterization of neurons in the cortical white matter in human temporal lobe epilepsy. *Neuroscience* **333**, 140–150 (2016). doi: [10.1016/j.neuroscience.2016.07.011](https://doi.org/10.1016/j.neuroscience.2016.07.011); pmid: [27423628](https://pubmed.ncbi.nlm.nih.gov/27423628/)
87. W. Z. Wang et al., Subplate in the developing cortex of mouse and human. *J. Anat.* **217**, 368–380 (2010). doi: [10.1111/j.1469-7580.2010.01274.x](https://doi.org/10.1111/j.1469-7580.2010.01274.x); pmid: [20727056](https://pubmed.ncbi.nlm.nih.gov/20727056/)
88. C. Cepeda et al., Immature neurons and GABA networks may contribute to epileptogenesis in pediatric cortical dysplasia. *Epilepsia* **48**, 79–85 (2007). doi: [10.1111/j.1528-1167.2007.01293.x](https://doi.org/10.1111/j.1528-1167.2007.01293.x); pmid: [17910585](https://pubmed.ncbi.nlm.nih.gov/17910585/)
89. C. Ohtaka-Maruyama et al., Synaptic transmission from subplate neurons controls radial migration of neocortical neurons. *Science* **360**, 313–317 (2018). doi: [10.1126/science.aar2866](https://doi.org/10.1126/science.aar2866); pmid: [29674592](https://pubmed.ncbi.nlm.nih.gov/29674592/)
90. H. J. Luhmann, A. Fukuda, Can we understand human brain development from experimental studies in rodents? *Pediatr. Int.* **10.1111/ped.14339** (2020). doi: [10.1111/ped.14339](https://doi.org/10.1111/ped.14339); pmid: [32531857](https://pubmed.ncbi.nlm.nih.gov/32531857/)
91. S. N. Tuncdemir et al., Early somatostatin interneuron connectivity mediates the maturation of deep layer cortical circuits. *Neuron* **89**, 521–535 (2016). doi: [10.1016/j.neuron.2015.11.020](https://doi.org/10.1016/j.neuron.2015.11.020); pmid: [26844832](https://pubmed.ncbi.nlm.nih.gov/26844832/)
92. A. Hoerder-Suabedissen et al., Cell-specific loss of SNAP25 from cortical projection neurons allows normal development but causes subsequent neurodegeneration. *Cereb. Cortex* **29**, 2148–2159 (2019). doi: [10.1093/cercor/bhy127](https://doi.org/10.1093/cercor/bhy127); pmid: [29850799](https://pubmed.ncbi.nlm.nih.gov/29850799/)
93. M. Cao et al., Early development of functional network segregation revealed by connectomic analysis of the preterm human brain. *Cereb. Cortex* **27**, 1949–1963 (2017). doi: [10.1093/cercor/bhw038](https://doi.org/10.1093/cercor/bhw038); pmid: [26941380](https://pubmed.ncbi.nlm.nih.gov/26941380/)
94. A. Omidvarnia, P. Fransson, M. Metsäranta, S. Vanhatalo, Functional bimodality in the brain networks of preterm and term human newborns. *Cereb. Cortex* **24**, 2657–2668 (2014). doi: [10.1093/cercor/bht120](https://doi.org/10.1093/cercor/bht120); pmid: [23650289](https://pubmed.ncbi.nlm.nih.gov/23650289/)
95. A. Anticevic et al., Characterizing thalamo-cortical disturbances in schizophrenia and bipolar illness. *Cereb. Cortex* **24**, 3116–3130 (2014). doi: [10.1093/cercor/bht165](https://doi.org/10.1093/cercor/bht165); pmid: [23825317](https://pubmed.ncbi.nlm.nih.gov/23825317/)
96. N. T. Markov et al., A weighted and directed interareal connectivity matrix for macaque cerebral cortex. *Cereb. Cortex* **24**, 17–36 (2014). doi: [10.1093/cercor/bhs270](https://doi.org/10.1093/cercor/bhs270); pmid: [23010748](https://pubmed.ncbi.nlm.nih.gov/23010748/)
97. F. C. Crick, C. Koch, What is the function of the claustrum? *Philos. Trans. R. Soc. London Ser. B* **360**, 1271–1279 (2005). doi: [10.1098/rstb.2005.1661](https://doi.org/10.1098/rstb.2005.1661); pmid: [16147522](https://pubmed.ncbi.nlm.nih.gov/16147522/)
98. H. Bruguière et al., In search of common developmental and evolutionary origin of the claustrum and subplate. *J. Comp. Neurol.* **10002/cne.24922** (2020). doi: [10.1002/cne.24922](https://doi.org/10.1002/cne.24922); pmid: [32266722](https://pubmed.ncbi.nlm.nih.gov/32266722/)
99. T. A. Zolnik et al., Layer 6b is driven by intracortical long-range projection neurons. *Cell Rep.* **30**, 3492–3505.e5 (2020). doi: [10.1016/j.celrep.2020.02.044](https://doi.org/10.1016/j.celrep.2020.02.044); pmid: [32160552x](https://pubmed.ncbi.nlm.nih.gov/32160552x/)
100. R. Cossart, Operational hub cells: A morpho-physiologically diverse class of GABAergic neurons united by a common function. *Curr. Opin. Neurobiol.* **26**, 51–56 (2014). doi: [10.1016/j.conb.2013.12.002](https://doi.org/10.1016/j.conb.2013.12.002); pmid: [24650504](https://pubmed.ncbi.nlm.nih.gov/24650504/)

ACKNOWLEDGMENTS

We thank all previous and current members of our laboratories. We thank A. Hoerder-Suabedissen, E. Meijer, A. Sheikh, and S. Bandiera for comments on an earlier version of this manuscript and Z. Kanold-Tso for help with the illustrations in Fig. 2. **Funding:** P.O.K. is supported by NIH R01DC009607. H.J.L. is supported by Deutsche Forschungsgemeinschaft (SFB1080-A01). Work in Z.M.'s laboratory is supported by the MRC, Royal Society, and Oxford Martin School. Z.M. is an Einstein Visiting Fellow at Charité—Universitätsmedizin Berlin, Cluster of Excellence NeuroCure and Institute of Biochemistry. **Competing interests:** The authors declare no competing interests.

10.1126/science.abb2153

RESEARCH ARTICLE SUMMARY

INNATE IMMUNITY

Mammalian lipid droplets are innate immune hubs integrating cell metabolism and host defense

Marta Bosch^{*†}, Miguel Sánchez-Álvarez[†], Alba Fajardo, Ronan Kapetanovic, Bernhard Steiner, Filipe Dutra, Luciana Moreira, Juan Antonio López, Rocío Campo, Montserrat Marí, Frederic Morales-Paytuví, Olivia Tort, Albert Gubern, Rachel M. Templin, James E. B. Curson, Nick Martel, Cristina Català, Francisco Lozano, Francesc Tebar, Carlos Enrich, Jesús Vázquez, Miguel A. Del Pozo, Matthew J. Sweet, Patricia T. Bozza, Steven P. Gross, Robert G. Parton^{*}, Albert Pol^{*}

INTRODUCTION: In all eukaryotic cells, lipid droplets (LDs) store and supply essential lipids to produce signaling molecules, membrane building blocks, and metabolic energy. The LD monolayer also accommodates proteins not obviously related to lipids, such as transcription factors, chromatin components, and toxic proteins.

Common parasites (such as trypanosomes and *Plasmodium falciparum*), bacteria (such as mycobacteria and *Chlamydia*), and viruses (such as hepatitis C and dengue) induce and target LDs during their life cycles. The current view is that LDs support infection, providing microorganisms with substrates for effective growth.

RATIONALE: Successful innate defense is critical for survival, and host species have efficiently coevolved with pathogens to develop a plethora of immune responses. Multiple cues, including cellular stress and danger-associated molecular patterns such as lipopolysaccharide (LPS),

induce LD formation. Thus, LD localization and dynamics may potentially be advantageous for organizing an intracellular host defense. We have investigated the possibility that mammalian LDs have a direct and regulated role in innate immunity.

RESULTS: We show that mammalian LDs are endowed with a protein-mediated antimicrobial capacity, which is up-regulated during polymicrobial sepsis and by LPS. Light and electron microscopy demonstrated specific association of LDs and bacteria in human macrophages, suggesting the existence of docking mechanisms that facilitate the engagement of antibacterial LD proteins with bacteria.

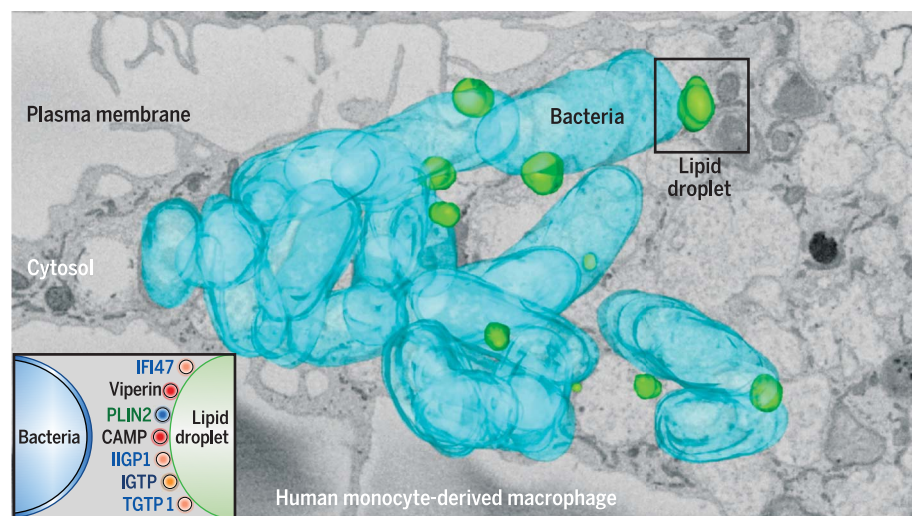
A comparative mass spectrometry profiling of proteins differentially associated with LDs in response to LPS (LPS-LDs) revealed the profound remodeling of the organelle proteome. A stringent evaluation identified 689 proteins differentially regulated on LPS-LDs (317 enriched and 372 reduced). Ingenuity Pathway

Analysis revealed an enrichment of innate immune system-related components and reduction of metabolism-related LD-resident proteins. Additional analyses suggested that LDs serve as innate immune hubs, integrating major intra- and extracellular immune responses.

Among the five members of the perilipin family of LD surface proteins (PLINs), PLIN5 was the only one down-regulated on LPS-LDs. PLIN5 reduction promoted physical and functional disconnection of LPS-LDs and mitochondria, with a concomitant reduction of oxidative metabolism and ketogenesis. Forced PLIN5 reexpression increased the number of LD-mitochondria contacts, reducing LD-bacteria interactions and compromising the antimicrobial capacity of cells.

By contrast, PLIN2 was the most up-regulated PLIN on LPS-LDs. Gene interaction analysis revealed that multiple immune proteins nucleated around PLIN2 in response to LPS. LPS-LDs accrued several interferon-inducible proteins such as viperin, IGTP, IIGP1, TGTP1, and IFI47. Furthermore, LPS-LDs also accumulated cathelicidin (CAMP), a broad-spectrum antimicrobial peptide with chemotactic properties. Cells overexpressing a LD-associated CAMP were more resistant to different bacterial species, including *Escherichia coli*, methicillin-resistant *Staphylococcus aureus*, and *Listeria monocytogenes*.

CONCLUSION: These results demonstrate that LDs form a first-line intracellular defense. They act as a molecular switch in innate immunity, responding to danger signals by both reprogramming cell metabolism and eliciting protein-mediated antimicrobial mechanisms. Mechanisms of LD trafficking and docking with phagocytic and parasitophorous membranes, observed here and described for several pathogens, may facilitate the delivery of immune proteins located on the LD surface. Intracellular LDs can provide infected cells with several biological benefits, serving as a location to attract pathogens as well as coordinating different immune systems that operate simultaneously against different classes of pathogens. LDs may also sequester cytotoxic compounds (such as antimicrobial peptides), reducing damage to other cellular organelles. In view of the widespread resistance to current antibiotics, this study helps decipher molecular mechanisms involved in antimicrobial defense that could be exploited for development of new anti-infective agents. ■



LDs mediate innate immune defense. Serial blockface scanning electron microscopy data reconstruction showing an infected macrophage. Bacteria (blue) and LDs (green) in the three-dimensional dataset have been colored and projected onto a single image. LDs associate with the bacteria surface (black square). This interaction is proposed to bring a specific set of antipathogenic proteins in contact with the membrane-enclosing bacteria (inset).

The list of author affiliations is available in the full article online.

^{*}Corresponding author. Email: martabosch@ub.edu (M.B.); r.parton@imb.uq.edu.au (R.G.P.); apols@ub.edu (A.P.)

[†]These authors contributed equally to this work.

Cite this article as M. Bosch et al., *Science* 370, eaay8085 (2020). DOI: 10.1126/science.aay8085

S READ THE FULL ARTICLE AT
<https://doi.org/10.1126/science.aay8085>

RESEARCH ARTICLE

INNATE IMMUNITY

Mammalian lipid droplets are innate immune hubs integrating cell metabolism and host defense

Marta Bosch^{1,2,*}†, Miguel Sánchez-Álvarez³†, Alba Fajardo¹, Ronan Kapetanovic^{4,5,6}, Bernhard Steiner⁴, Filipe Dutra⁷, Luciana Moreira⁷, Juan Antonio López^{8,9}, Rocío Campo⁸, Montserrat Mari^{10,11}, Frederic Morales-Paytuvi¹, Olivia Tort¹, Albert Gubern¹, Rachel M. Templin^{4,12}, James E. B. Curson^{4,5,6}, Nick Martel⁴, Cristina Català¹³, Francisco Lozano¹³, Francesc Tebar^{1,2}, Carlos Enrich^{1,2}, Jesús Vázquez^{8,9}, Miguel A. Del Pozo³, Matthew J. Sweet^{4,5,6}, Patricia T. Bozza⁷, Steven P. Gross¹⁴, Robert G. Parton^{4,12,*}, Albert Pol^{1,2,15,*}

Lipid droplets (LDs) are the major lipid storage organelles of eukaryotic cells and a source of nutrients for intracellular pathogens. We demonstrate that mammalian LDs are endowed with a protein-mediated antimicrobial capacity, which is up-regulated by danger signals. In response to lipopolysaccharide (LPS), multiple host defense proteins, including interferon-inducible guanosine triphosphatases and the antimicrobial cathelicidin, assemble into complex clusters on LDs. LPS additionally promotes the physical and functional uncoupling of LDs from mitochondria, reducing fatty acid metabolism while increasing LD-bacterial contacts. Thus, LDs actively participate in mammalian innate immunity at two levels: They are both cell-autonomous organelles that organize and use immune proteins to kill intracellular pathogens as well as central players in the local and systemic metabolic adaptation to infection.

Lipid droplets (LDs) are the major lipid storage organelles of eukaryotic cells (1). Common parasites (such as trypanosomes and *Plasmodium falciparum*), bacteria (such as mycobacteria and *Chlamydia*), and viruses [such as hepatitis C (HCV) and dengue (DENV)] induce and target LDs during their life cycles (2). The current view is that LDs support infection, providing invaders with substrates for survival and/or growth (3). However, successful innate defense is critical for survival, and host immune responses have coevolved with pathogens, developing a plethora of defense mechanisms. There is some limited evidence that LDs actively participate in innate defense (4, 5). For example, three innate immune system-related proteins localize to the LDs of infected cells: (i) viperin, which is active against two viruses assembled on LDs (HCV and DENV) (6); (ii) interferon- γ (IFN- γ)-inducible guanosine triphosphatase (GTPase) (IGTP), which is required for resistance to *Toxoplasma gondii* (7); and (iii) histones on LDs, which increase the survival of bacterially challenged *Drosophila* embryos (8). We analyzed whether mammalian LDs have a direct or regulated role in immune defense. Because

all eukaryotic cells accumulate LDs, this innate defense mechanism may be ubiquitous and therefore serve as a suitable target for therapeutic intervention.

Results

Mammalian LDs display regulated protein-mediated antibacterial activity

We selected hepatic LDs as a proof of concept that mammalian LDs participate in innate immunity. The liver modulates the systemic immune response, and hepatic LDs are targeted by LD-related pathogens (9). We tested the antibacterial capacity of hepatic LD proteins in a bacterial killing assay of *Escherichia coli*, an abundant component of the intestinal microbiota and cause of serious clinical infections. First, we injected mice with lipopolysaccharide (LPS), an activator of innate immunity (10). Because LPS-treated animals (LPS-mice) reduce food intake, LPS-mice were additionally fasted and compared with mice injected with saline buffer and identically fasted (CTL-mice). Both treatments promoted similar hepatic triglyceride levels (Fig. 1, A, B, and C), although morphological differences between LDs were evident from transmission electron microscopy

(TEM). The number of LDs in LPS-treated livers (LPS-LDs) was higher than in those of fasted animals (CTL-LDs), although LPS-LDs were smaller (Fig. 1, D and E). CTL- and LPS-LDs were purified (Fig. 1F and fig. S1A), and LD proteins were incubated with *E. coli*. Bacterial viability was estimated from the resulting colony-forming units (CFUs). LD proteins reduced bacterial growth, and LPS-LD proteins demonstrated enhanced antibacterial capacity (Fig. 1G). This enhancement was confirmed in suspension cultures (fig. S1C) and by use of LD proteins from fed mice (fig. S1, D and E). To determine LD antibacterial activity during an actual infection, mouse liver LDs were obtained after cecal ligation and puncture (CLP), a model of polymicrobial sepsis. CLP-LD proteins exhibited enhanced antibacterial capacity when compared with CTL-LDs (fig. S1, B and F). LPS- and CLP-LD proteins reduced bacterial growth even after a shorter incubation time (fig. S1, G and H). Bacterial growth was unaffected by oleic acid (OA), the major fatty acid component of hepatic LDs, or by cytosolic proteins from CTL- and LPS-livers (fig. S1, I and J). Thus, mammalian LDs have a protein-mediated antibacterial capacity, which is regulated by infection.

Next, we analyzed whether LDs reduce bacterial growth in human monocyte-derived macrophages (HMDMs) from healthy donors. In HMDMs, LD accumulation was promoted by incubation with OA, a fatty acid efficiently esterified into LDs (11). Untreated and LD-loaded HMDMs were infected with either nonpathogenic *E. coli* or the professional intramacrophage pathogen *Salmonella enterica* serovar Typhimurium (*Salm*). HMDMs responded to infection by increasing LD numbers (Fig. 1H). *E. coli* survival (Fig. 1I), but not phagocytic capacity (Fig. 1K), was reduced in LD-loaded HMDMs. By contrast, LDs did not reduce *Salm* survival (Fig. 1J), which is in keeping with this pathogen's ability to avoid antimicrobial responses (12). In *E. coli*-infected macrophages, LDs were often in the proximity of bacteria (Fig. 1, M to Q). Comparative analyses demonstrated that LDs were closer to and more frequently established longer contacts with *E. coli* than with *Salm* (Fig. 1L and fig. S2, A and B). These LD-*E. coli* contact sites increased in loaded HMDMs (fig. S2, C and D). TEM analysis revealed that in LD-*E. coli* contact sites, the LD monolayer (containing LD proteins) produced an apparent discontinuity in

¹Cell Compartments and Signaling Group, Institut d'Investigacions Biomèdiques August Pi i Sunyer (IDIBAPS), 08036, Barcelona, Spain. ²Department of Biomedical Sciences, Faculty of Medicine, Universitat de Barcelona, 08036, Barcelona, Spain. ³Mechanoadaptation and Caveolae Biology Laboratory, Cell and Developmental Biology Area, Centro Nacional de Investigaciones Cardiovasculares (CNIC), 28029, Madrid, Spain. ⁴Institute for Molecular Bioscience (IMB), University of Queensland, Brisbane, Queensland 4072, Australia. ⁵IMB Centre for Inflammation and Disease Research, University of Queensland, Brisbane, Queensland 4072, Australia. ⁶Australian Infectious Diseases Research Centre, University of Queensland, Brisbane, Queensland 4072, Australia. ⁷Laboratório de Imunofarmacologia, Instituto Oswaldo Cruz, FIOCRUZ, Rio de Janeiro, RJ, CEP 21.040-900, Brazil. ⁸Cardiovascular Proteomics Laboratory, Vascular Pathophysiology Area, CNIC, Instituto de Salud Carlos III 28029, Madrid, Spain. ⁹Centro de Investigación Biomédica en Red, Enfermedades Cardiovasculares (CIBER-CV), Instituto de Salud Carlos III 28029, Madrid, Spain. ¹⁰Department of Cell Death and Proliferation, Institut d'Investigacions Biomèdiques de Barcelona (IIBB)-CSIC, Barcelona, Spain. ¹¹Hepatocellular Signaling and Cancer Team, IDIBAPS, 08036, Barcelona, Spain. ¹²Centre for Microscopy and Microanalysis, University of Queensland, Brisbane, Queensland 4072, Australia. ¹³Immunoreceptors of the Innate and Adaptive System Team, IDIBAPS, 08036, Barcelona, Spain. ¹⁴Department of Developmental and Cell Biology, University of California, Irvine, Irvine, CA 92697, USA. ¹⁵Institució Catalana de Recerca i Estudis Avançats (ICREA), 08010, Barcelona.

*Corresponding author. Email: martabosch@ub.edu (M.B.); rparton@imb.uq.edu.au (R.G.P.); apols@ub.edu (A.P.) †These authors contributed equally to this work.

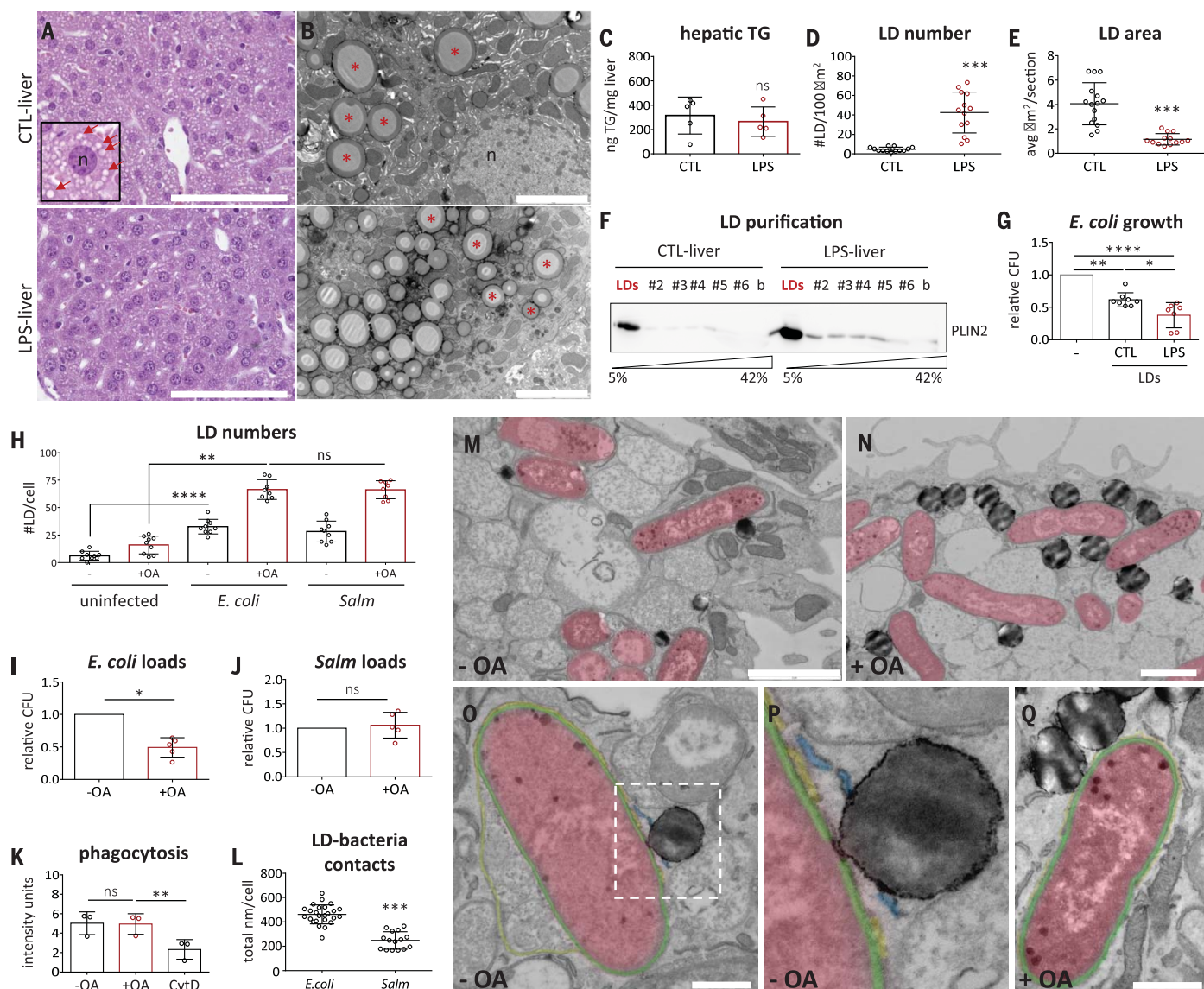


Fig. 1. Mammalian LDs display regulated protein-mediated antibacterial activity. (A) H&E-stained sections and (B) TEM images of (top) CTL- or (bottom) LPS-livers. Red arrows [(A), inset] and asterisks (B) indicate LDs, and “n” indicates the selected hepatocyte nucleus. Images are representative of (A) five or (B) two mice per condition. Scale bars, 100 μm (A) and 5 μm (B). (C) Hepatic triacylglycerol levels (TG) in CTL- and LPS-mice (five mice per condition). (D) Hepatic LD number and (E) mean LD area measured in TEM images of CTL- or LPS-livers. For each condition, at least 13 random liver sections, obtained from two mice per condition, were quantified (fig. S6). (F) CTL- and LPS-livers were fractionated in sucrose density gradients, and LDs floated onto the top fraction (“LDs”), as assessed with anti-PLIN2 immunoblotting (fig. S1A) (representative of five mice per condition). (G) *E. coli* were incubated for 16 hours in (gray) standard medium or medium supplemented with proteins from (black) CTL- or (red bar) LPS-LDs. CFU measurements were normalized to the standard medium condition ($n \geq 7$ independent experiments) (fig. S1). (H) Unloaded (black) and OA-loaded HMDMs (red bars) were infected with *E. coli* or *Salm* for 4 hours. LD number per cell was quantified in TEM images. At least

eight macrophages per group, obtained in three independent experiments, were analyzed. (I and J) Control (black) and OA-loaded HMDMs (red bars) were infected with (I) *E. coli* or (J) *Salm* and bacterial loads (CFU) determined 24 hours later ($n = 5$ independent experiments). (K) Control (black) and OA-loaded HMDMs (red bars) were incubated with pHrodo *E. coli* and bacterial loads measured (fluorescence units) ($n = 3$ independent experiments). Cyt D was used to inhibit phagocytosis. (L) Length of LD-bacteria contacts per cell was measured in TEM images of OA-loaded HMDMs infected with *E. coli* or *Salm* for 4 hours. At least 15 macrophages per group, obtained in three independent experiments, were analyzed (fig. S2, A to D). (M, O, and P) Control and (N and Q) OA-loaded HMDMs were infected with *E. coli* for 4 hours and analyzed in TEM images. Representative images have been pseudocolored blue (ER), red (*E. coli* interior), green (periplasm), and yellow (vacuolar membrane) (fig. S2, E and F) (representative of three independent experiments). Scale bars, 2 μm [(M) and (N)] and 0.5 μm [(O) and (Q)]. All graphs show means \pm SD; ns, not significant; * $P < 0.05$, ** $P < 0.01$, *** $P < 0.001$, **** $P < 0.0001$ in a paired t test [(C) to (E), (H) to (J), and (L)], and one-way ANOVA test [(G) and (K)].

the bacterial vacuolar membrane and probably interacted with the bacterial periplasm (Fig. 1, O to Q, and fig. S2, E and F). Thus, LD-loaded macrophages display enhanced antibacterial capacity, which suggests the existence of docking mechanisms that enable or facilitate the engagement of antibacterial LD proteins with bacteria.

Quantitative mass spectrometry analysis of LPS-LDs

To characterize the enhanced LPS-LD antibacterial capacity, we performed comparative mass spectrometry profiling of proteins differentially associated with LPS- or CTL-LDs (13). CTL- and LPS-livers were analyzed in parallel. Stringent analysis [false discovery rate (FDR) < 1] of LPS-livers identified 8563 proteins, of which 1136 (cut-off $|\Delta Zq| \geq 1.8$, where ΔZq reflects the differential Zq score for a protein in LPS-livers when compared with CTL-livers.) were differentially expressed (553 enriched and 583 reduced) (Fig. 2A and tables S1 and S2). In LPS-LDs, 3392 proteins were identified (table S3), of which 689 were differentially distributed (317 enriched and 372 reduced) (tables S4 and S5). Only 8% of the enriched and 0.8% of the down-regulated proteins in LPS-LDs followed an equivalent profile in LPS-livers (Fig. 2, A and B, and fig. S3A), indicating autonomous changes in LPS-LDs. Functional annotation enrichment analysis revealed the up-regulation of proteins related to the acute phase and inflammatory responses and reduction of mitochondrial proteins cofractionating with LDs (Fig. 2B and fig. S2A).

Published proteomic analyses show that ~7 to 10% of proteins in LD fractions are bona fide LD-resident proteins (14, 15), reflecting the tight interaction of LDs with other organelles. Of 3392 identified proteins in LPS-LDs, 238 (7%) were annotated as LD-resident proteins with the Ingenuity Pathway Analysis (IPA) platform or with at least one of the above proteomic analyses (Fig. 2C and table S6). Of these LD proteins, 72 were LPS-regulated (59 enriched and 13 reduced) (table S7). Thus, 30% of the identified LD proteome, including the five perilipins (PLINs), was LPS-sensitive. PLIN2 ($\Delta Zq = 6.47$) and RAB18 ($\Delta Zq = 7.10$) were highly enriched, and PLIN5 was the only down-regulated PLIN ($\Delta Zq = -4.13$) (table S7). Two immune proteins previously described on LDs, viperin (RSAD2, $\Delta Zq = 8.12$) and IGTP (IRGM3, $\Delta Zq = 6.7$), were identified on LPS-LDs, validating our proteomic strategy (table S4). IPA analysis of these LD-resident proteins demonstrated enrichment of innate immunity-related components and reduction of metabolism-related LD-resident proteins (fig. S3B).

To identify relevant candidates on LPS-LDs, we initially performed hierarchical clustering of proteins with similar variation profiles across each individual replicate, likely reflecting

coregulation (Fig. 2D). Gene interaction analysis of correlated proteins revealed the existence of several functionally connected protein networks, such as clusters of RAB GTPases, a cluster containing PLIN1 and histones, and a network of metabolism regulators, including PLIN3, PNPLA2 (ATGL), and ACSL4 (fig. S4A). The cluster containing proteins ranking highest for enrichment ($\Delta Zq > 3.14$) nucleated around PLIN2 and included viperin, IGTP, and several immune GTPases (GVIN, IFGGA1, IFGGB55, IFI47, and IFI35) (Fig. 2D). These functionally related proteins may also physically interact. We confirmed that PLIN2 interacts with IGTP (7) and detected a weak interaction with cathelicidin (fig. S4B). Last, we performed a gene interaction analysis across the whole LPS-sensitive LD proteome ($\Delta Zq > 1.8$). This analysis retrieved complex protein networks (Fig. 2E), suggesting that LDs are innate immune hubs integrating major intra- and extracellular responses.

We validated the proteomic data with immunoblotting and confirmed enrichment of PLIN2 and PLIN3 on LPS-LDs in contrast with the unregulated lipase HSL ($\Delta Zq = 0.04$) (Fig. 3A). PLIN2 expression was further confirmed in mouse liver sections (fig. S5A). PLIN2 in LPS- and CLP-livers was predominantly expressed in hepatocytes around periportal regions where cells receive blood and regulatory inflammatory mediators. Direct transcriptional regulation of LD proteins by inflammatory stimuli (fig. S5B) was assessed in human hepatic HuH7 cells treated with LPS, tumor necrosis factor (TNF), or IFN- γ . *PLIN2* and *PLIN5* expression was differentially regulated by individual cytokines (fig. S5C). Thus, LPS likely regulates LD protein composition directly and in conjunction with paracrine signaling networks.

Physical and functional uncoupling of LPS-LDs and mitochondria

Mitochondria are key organelles for innate immunity (16). During nutrient starvation, LDs contact mitochondria to supply fatty acids, fueling oxidative phosphorylation (OXPHOS) (17). By contrast, challenged innate immune cells increase aerobic glycolysis and reduce OXPHOS (16). Therefore, uncoupling LPS-LDs and mitochondria (Fig. 2B) may contribute to a reduction of OXPHOS in infected cells. Reduced interaction between LPS-LDs and mitochondria was confirmed through decreased cofractionation of ATP5D [a subunit of adenosine 5'-triphosphate (ATP) synthase, an OXPHOS enzyme] when compared with CTL-LDs (Fig. 3, A and B). Functional annotation of reduced mitochondrial proteins cofractionating with LPS-LDs matched with the whole mitochondrial proteome (MitoCarta 2.0) (Fig. 3C). This does not reflect a reduced mitochondrial content of LPS-livers as determined by hepatic citrate synthase activity and liver

cytochrome oxidase (*COI*) gene copy number (Fig. 3, D and E). The reduced number of contacts between LPS-LDs and mitochondria was then confirmed with TEM (Fig. 3F and fig. S6). In these images, endoplasmic reticulum (ER) membranes often separated LPS-LDs and mitochondria (fig. S6C). Last, we confirmed two functional consequences of uncoupling: (i) reduced mitochondrial β -oxidation of lipids supplied by LDs in LPS-primary hepatocytes (Fig. 3, G and H) and (ii) lower levels of circulating ketones in LPS-mice serum (Fig. 3I). These results extend and mechanistically explain early observations showing reduced β -oxidation and ketogenesis in rats infected with *Streptococcus pneumoniae*, *Francisella tularensis*, and *S. Typhimurium* (18).

PLIN5 tethers LDs and mitochondria (17). PLIN5 is the only PLIN down-regulated in LPS-LDs (fig. S3B and tables S5 and S7). During fasting, to facilitate LD-mitochondria contacts, PLIN5 levels increase on hepatic LDs (Fig. 3J). However, PLIN5 levels on LDs were reduced when fasted mice were treated with LPS (Fig. 3, A and J). Further, human *PLIN5* expression promoted coclustering of LDs and mitochondria in HuH7 cells (Fig. 3K). To explore the role of PLIN5 during infection, *PLIN5* was transfected in LPS-responsive human embryonic kidney (HEK) 293-TLR4⁺ cells (fig. S7, A to C), and the LD-mitochondria contacts were quantified. *PLIN5* expression increased the number and length of these contacts (Fig. 3L and fig. S7, D to F). In LPS-treated HEK293-TLR4⁺ cells, the overall length of the contacts was reduced in CTL- but not in *PLIN5*-expressing cells (Fig. 3L). In *PLIN5*-expressing cells, LPS only modestly reduced the total number of contacts (fig. S7E) and increased the average length of remaining contacts (fig. S7F). Thus, LPS directly regulates dynamics of LD-mitochondria contacts. Furthermore, PLIN5 down-regulation appears to be involved in the LPS-induced metabolic reprogramming.

We next evaluated the role of PLIN5 in other aspects of immune defense. *PLIN5*-overexpressing HEK293 cells exhibited a significantly reduced capacity to clear *E. coli* by comparison with that of *PLIN3*-overexpressing control cells (Fig. 3, M and N). Furthermore, THP-1 cells lentivirally transduced with *PLIN5* and subsequently infected with *E. coli* exhibited increased numbers of LD-mitochondria contacts (fig. S7, G to I), reduced LD-bacteria interactions (fig. S7J), and impaired antimicrobial capacity (Fig. 3, O and P). Thus, LPS-mediated PLIN5 down-regulation reduces LD-mitochondria tethering, enabling an effective antimicrobial response.

LDs accumulate and use innate immune proteins

Our proteomic analyses predicted complex immune protein networks on LDs (Fig. 2, D and E,

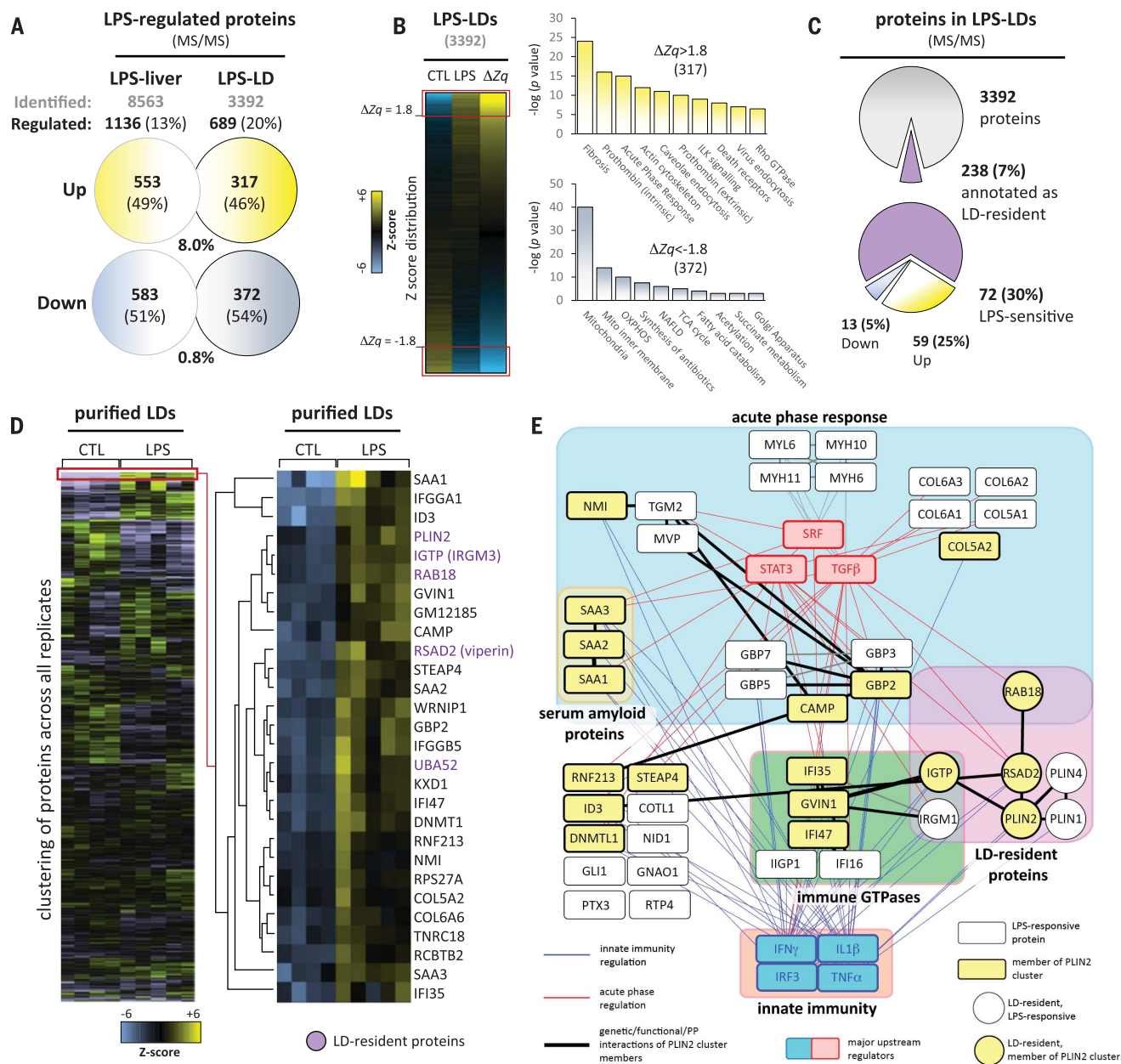


Fig. 2. Quantitative mass spectrometry analysis of LPS-LDs. (A) Summary of changes in the proteome of LPS-livers ($n = 3$ independent mice) and LPS-LDs ($n = 5$ independent LD fractions) when compared with those in CTL-livers ($n = 3$ independent mice) or CTL-LDs ($n = 4$ independent LD fractions), respectively. "Identified" (gray letters) indicates identified proteins, and "Regulated" (black letters) indicates proteins significantly cut-off [$|\Delta Zq| \geq 1.8$ modified by LPS. Among modified proteins, yellow and blue circles indicate up- and down-regulated proteins, respectively (tables S1 to S5). (B) Functional annotation enrichment analysis of proteins increasing ($|\Delta Zq| > 1.8$; yellow graphs) or decreasing ($|\Delta Zq| < -1.8$; blue graphs) on LPS-LDs when compared with CTL-LDs.

and fig. S4A). Given that many known anti-pathogenic proteins were associated with the PLIN2 cluster (Fig. 2D), we next assessed components of this cluster for LD association. The antiparasitic protein IGTP and the antiviral protein viperin as well as three GTPases (IIGP1, TGTPI, and IFI47) all associated with LDs (Fig. 4,

A to C, and figs. S8 and S9). Thus, multiple proteins associated with responses to different classes of pathogens localize to LDs.

The PLIN2 cluster also includes cathelicidin (CAMP; $\Delta Zq = 7.25$), a broad-spectrum antimicrobial peptide with chemotactic and immunomodulatory properties (19). Cathelicidins are

Enrichment as compared with the mouse genome for each category is expressed as $-\log(P)$ value). Analyses for CTL- and LPS-livers are shown in fig. S3A. (C) Pie charts summarizing LPS-induced changes in bona fide LD proteins. Protein details are in tables S6 and S7, and annotated interactions are provided in fig. S3B. (D) Hierarchical clustering of Zq values across replicates identifies functionally coherent protein subsets similarly regulated by LPS [threshold for cluster analysis, correlation coefficient (r) > 0.78]. The cluster nucleated around PLIN2 is included. Five additional clusters are detailed in fig. S4A. (E) Gene subnetwork from IPA analysis of all identified proteins up-regulated in LPS-LDs.

synthesized as proproteins which, after cleaving an N-terminal signal peptide, follow the exocytic pathway (fig. S10A). We confirmed the accumulation of CAMP on LPS-LDs (Fig. 4A) and the distribution of a human-tagged CAMP between the ER and LDs of HuH7 cells (Fig. 4B and fig. S10, B to E). CAMP on LDs had a

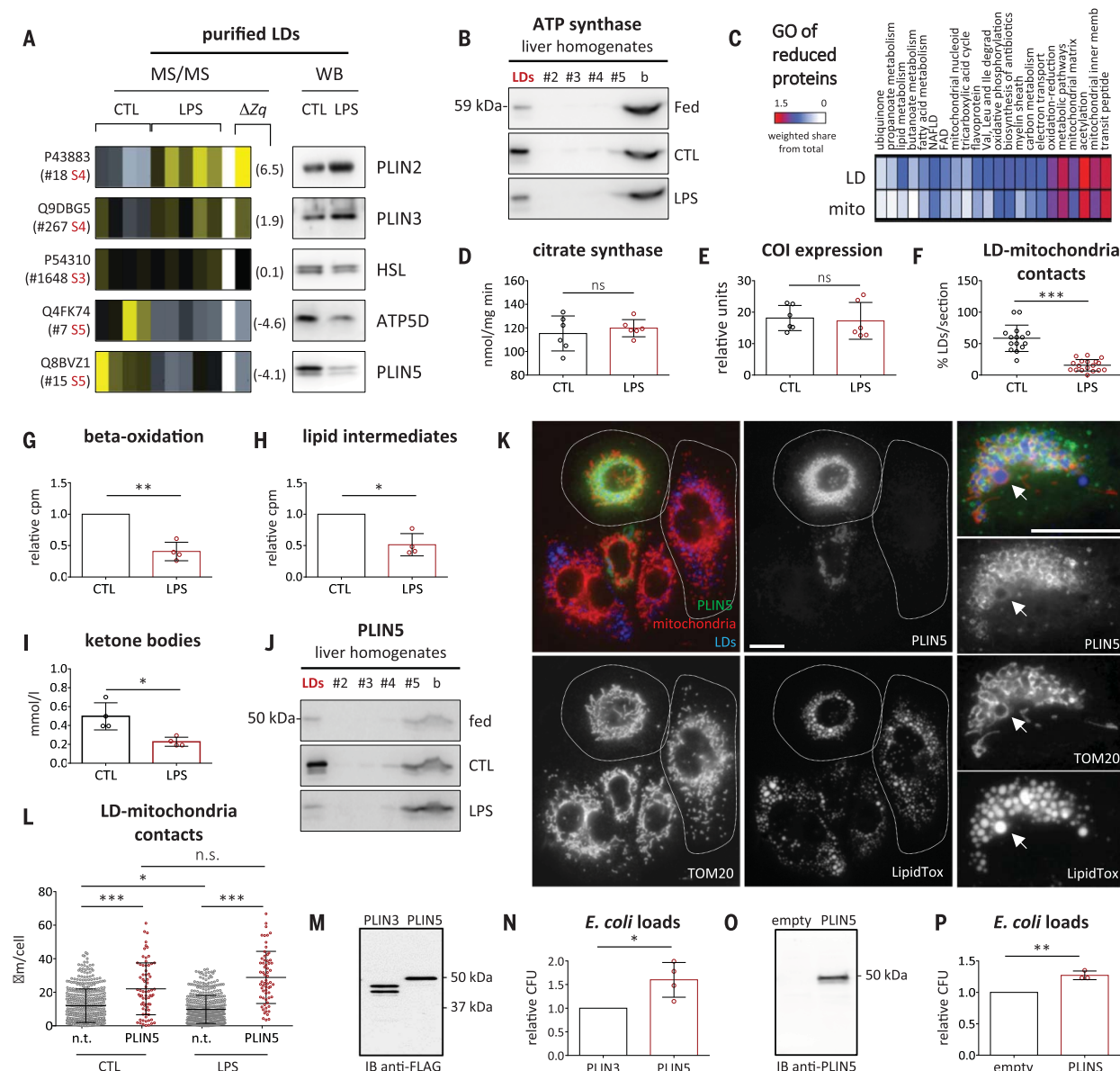


Fig. 3. Physical and functional uncoupling of LPS-LDs and mitochondria.

(A) Relative enrichment of selected proteins. Protein enrichment in LPS-LDs illustrated by a heatmap code (blue, depletion; yellow, enrichment). The ΔZq , UniProt ID, ranking (tables S3 to S5), and a representative immunoblot (representative of three mice per condition) are indicated. (B) Fed-, CTL-, and LPS-livers were fractionated in sucrose gradients, and LD-mitochondria cofractionation was determined through immunoblotting of ATP5D (a subunit of ATP synthase) (representative of three mice per condition). (C) Functional categories of down-regulated mitochondrial proteins cofractionating with LPS-LDs are compared with the whole mitochondrial proteome (MitoCarta 2.0). (D and E) The mitochondrial content of CTL- (black) and LPS-livers (red bars) was determined from (D) citrate synthase activity and (E) DNA copy number of COI (relative to GAPDH) ($n = 6$ independent livers). (F) Percentage of LDs interacting with mitochondria in CTL- (black) and LPS-livers (red bars) was quantified in TEM images. At least 15 random sections, obtained from two mice per condition, were analyzed (fig. S6). (G) Mitochondrial beta-oxidation and (H) formation of soluble intermediates (ketone bodies) of lipids stored in LDs were quantified for 16 hours in primary hepatocytes left untreated (black) or treated with LPS (red bars) (four mice per condition). (I) Ketones in sera of CTL- (black) and LPS-mice (red bars) (four mice per condition). (J) Fed-, CTL-, and LPS-livers were fractionated in density gradients and PLIN5 distribution analyzed by immunoblotting (represent-

ative of five mice per condition). (K) HuH7 cells were transfected with a tagged *PLIN5* and labeled with anti-FLAG antibodies (PLIN5), anti-TOM20 antibodies (mitochondria), and LipidTox (LDs). Contours of a representative transfected and nontransfected cell are indicated. (Right) An additional transfected cell. The arrows indicate a mitochondrion completely enwrapping a LD (representative of three independent experiments). Scale bar, 20 μm . (L) LPS-sensitive HEK293-TLR4⁺ cells transfected with a tagged *PLIN5* were loaded with OA (black) or with OA+LPS (red dots). The length of LD-mitochondria contacts per cell was measured in confocal microscopy images (an example is available in fig. S7, D to F). Sixty-six transfected cells and 470 nontransfected cells, obtained from three independent experiments, were analyzed. (M and N) HEK293 cells were transfected with FLAG-tagged *PLIN3* or *PLIN5* and loaded with OA, and (M) protein expression was determined by means of immunoblotting. (N) Cells were infected with *E. coli*, and bacterial loads quantified after 4 hours ($n = 4$ independent experiments). (O and P) THP-1 cells were transduced with *PLIN5*-encoding or empty lentiviral vectors. (O) *PLIN5* expression was confirmed through immunoblotting. (P) Transduced cells were infected with *E. coli*, and bacterial loads were evaluated after 8 hours ($n = 3$ independent experiments) (fig. S7, G to J). All graphs show means \pm SD; ns, not significant; $*P < 0.05$, $**P < 0.01$, $***P < 0.001$, in a paired *t* test [(D), (E), (G) to (I), (M), and (N)], one-way ANOVA test (L), and two-sided Student's *z* test on proportions (F).

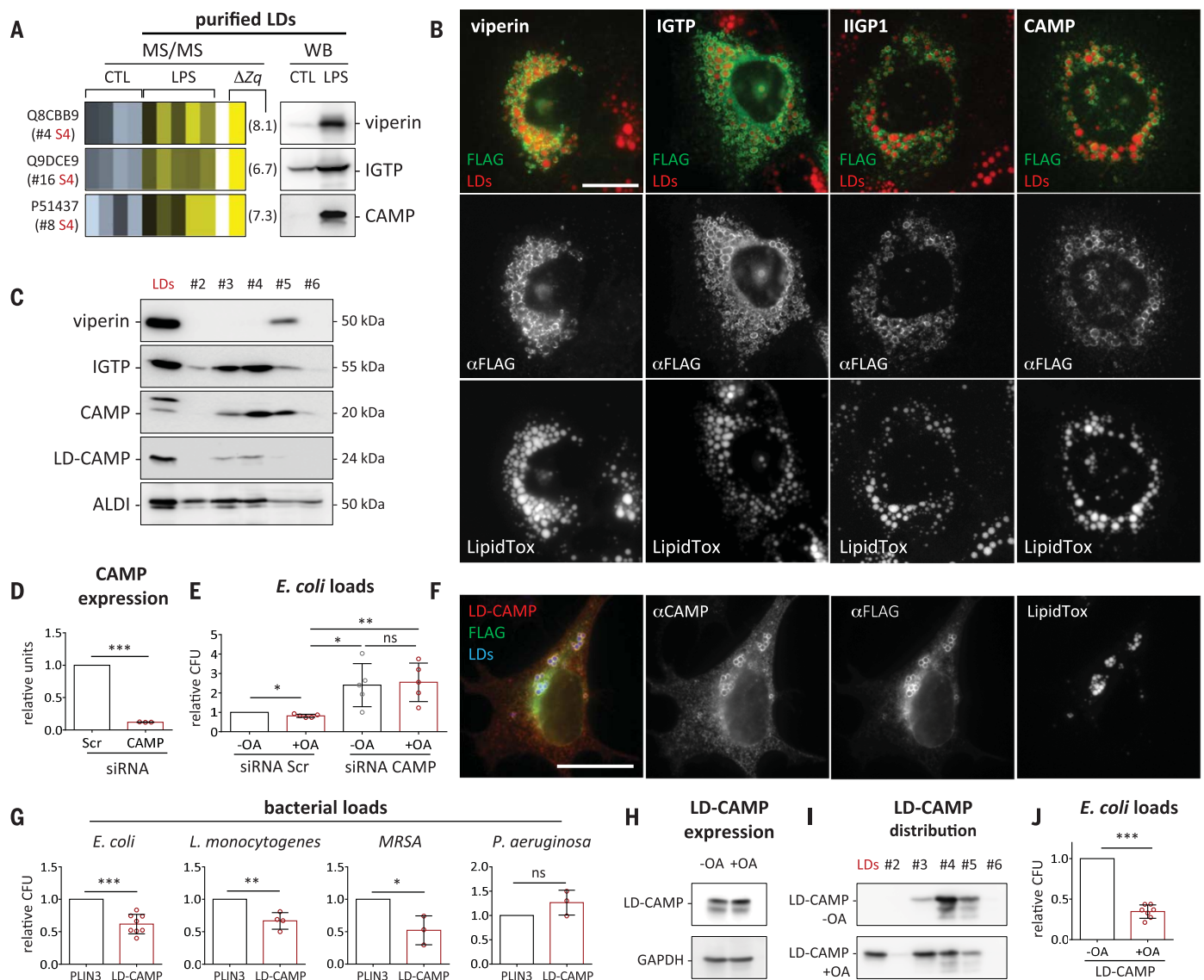


Fig. 4. LDs accumulate and use innate immune proteins. (A to C) Relative enrichment of selected proteins. Protein enrichment in LPS-LDs was evaluated as in Fig. 3. Accumulation of transfected proteins on LDs was confirmed in HuH7 cells by means of (B) immunofluorescence and (C) fractionation in density gradients (figs. S8 to S10 and S12). Scale bar, 20 μ m. (D and E) HMDMs were transfected with a scrambled (Scr) or with a CAMP siRNA, and (D) CAMP expression was determined by means of quantitative RT-PCR. Then, unloaded and OA-loaded HMDMs were infected with *E. coli* for 8 hours, and bacterial loads (CFU) were quantified ($n = 5$ independent experiments). (F) HEK293 cells were transfected with a tagged LD-CAMP (fig. S12) and loaded with OA. LD-CAMP was detected on

LDs (LipidTox) with antibodies to FLAG and to CAMP. The image is representative of three independent experiments. Scale bar, 20 μ m. (G) HEK293 cells were transfected with LD-CAMP (red) or *PLIN3* (black bars), loaded with OA, and infected with the indicated bacteria for 4 hours. Bacterial loads were quantified, and CFU values were normalized to *PLIN3*-cells ($n \geq 3$ independent experiments). (H to J) LD-CAMP-transfected HEK293 cells were incubated in control (black) or OA containing medium (red). (H) Cellular LD-CAMP levels and (I) LD accumulation were assessed through immunoblotting with anti-CAMP antibodies. (J) These cells were then infected with *E. coli* for 4 hours, and bacterial loads were quantified ($n = 7$). All graphs show means \pm SD; ns, not significant; * $P < 0.05$, ** $P < 0.01$, *** $P < 0.001$ in a paired *t* test.

higher molecular weight than that of CAMP in the ER (Fig. 4C and fig. S10E), suggesting that the CAMP hydrophobic domain functions as both a signal peptide cleaved for secretion via the ER as well as an uncleaved LD-targeting signal. An equivalent dual distribution occurs for other LD proteins that contain signal peptides, such as apolipoproteins (20). The low-molecular weight (20 kDa) CAMP species

corresponded to the protein with a cleaved signal peptide following the secretory pathway (fig. S10, F to H). Distribution of overexpressed CAMP, as well as other immune LD proteins, was not directly affected by LPS-TLR4 signaling (fig. S11). Thus, LPS does not directly regulate the intracellular trafficking of these proteins.

We next investigated the role of CAMP in HMDMs. Silencing of *CAMP* (Fig. 4D) impaired

the antibacterial response of the macrophages against *E. coli* (Fig. 4E). Furthermore, although LD loading significantly reduced bacterial survival, this treatment regime was unable to do so in CAMP-silenced HMDMs. Thus, the antibacterial activity of LDs in HMDMs appears to require CAMP. To further explore this possibility, a LD-resident CAMP was engineered through substitution of the CAMP signal peptide with

the ALDI LD-targeting motif (fig. S12, A and B) (21). Modified CAMP (LD-CAMP) accumulated on LDs of HuH7 cells (fig. S12, C to F) and showed a single electrophoretic mobility pattern, matching the higher-molecular weight CAMP that localized to LDs (Fig. 4C and fig. S12C). Next, HEK293 cells were transfected with LD-CAMP, and protein distribution on LDs was confirmed with antibodies to CAMP (Fig. 4F), demonstrating a native conformation. The antimicrobial capacity of LD-CAMP was then assessed. Bacterial loads of *E. coli*, *Listeria monocytogenes*, and methicillin-resistant *Staphylococcus aureus* (MRSA) were significantly reduced in LD-CAMP-expressing cells when compared with those expressing the *PLIN3* control (Fig. 4G). By contrast, *Pseudomonas aeruginosa* loads were not affected by LD-CAMP, suggesting that this pathogen subverts this innate defense response. The impact of LD-CAMP overexpression on bacterial survival was dependent on LD formation (Fig. 4, H to J). The tagged LD-CAMP demonstrated a similar antibacterial activity to that of wild-type CAMP and a slightly augmented stability when compared with an untagged LD-CAMP (fig. S12, G to J). Thus, LDs act as a molecular switch in innate immunity, responding to danger signals by both reprogramming cell metabolism and eliciting protein-mediated antimicrobial defense.

Discussion

Pathogens require host-derived lipids to support their life cycles, with LDs providing a source of these lipids (22). As a result, LDs also have the potential to deliver effective host defenses against intracellular pathogens. We show that at least 30% of the LD proteome is LPS-sensitive, suggesting that innate immunity has developed a host defense program that includes extensive LD remodeling. Our analyses demonstrate that complex clusters of immunity-related proteins organize on LDs of infected cells. In addition to previously described LD-resident immune proteins, such as viperin and IGTP, we have identified IIGP1, TGTP1, and IFI47. Our analysis also identified CAMP as a professional antibacterial protein efficiently functioning on LDs. These proteins may act individually, in a coordinated manner, and/or synergistically to kill pathogens.

Mechanisms of LD trafficking and docking with phagocytic and parasitophorous membranes, observed here and described for several pathogens (23–26), may facilitate the delivery of immune proteins located on the LD surface. Accumulation on LDs may provide stability to these proteins and may restrict these potentially cytotoxic peptides to LDs, preventing indiscriminate cellular damage (27). In this respect, we have shown that LPS triggers physical separation of LDs and mitochondria, at least partly because of reduced *PLIN5* levels on LPS-LDs (28). Uncoupling likely reflects both a self-

protection program (to avoid mitochondrial damage, in view of their prokaryotic evolutionary origin) and a means to maximize or increase the number of LDs available to interact with bacteria. Simultaneously, the reduced LD-mitochondria interaction may lead to distinctive immunometabolic features: (i) the accumulation of host LDs, resulting from reduced mitochondria-mediated LD consumption; (ii) reduced OXPHOS displayed by infected cells, owing to decreased fatty acid oxidation; and (iii) the low rates of ketogenesis displayed by infected animals.

These studies highlight that mammalian LDs constitute an intracellular first line of defense. LDs actively participate in at least two levels of the innate immune response, accumulating and using antibacterial proteins as well as regulating immune cell metabolism. Because widespread resistance to current antibiotics is common among pathogens, understanding the cellular mechanisms that elicit LD-mediated defense may inform future strategies for the development of anti-infective therapies (29, 30).

Materials and methods

Plasmids

pCMV6-IGTP-myc-FLAG (MR224617), pCMV6-CAMP-myc-FLAG (RC208872), pCMV6-IIGP1-myc-FLAG (MR206520), pCMV6-TGTP1-myc-FLAG (MR206553), and pCMV6-IFI47-myc-FLAG (MR206684) were purchased from OriGene Technologies (Rockville, Maryland). pcDNA3.1-VIPERIN-FLAG (OHu3432) was from Genscript (Piscataway, New Jersey). pcDNA3.1-*PLIN5*-FLAG (OHu04126) from GenScript was subcloned into pCMV6-myc-FLAG vector using primers containing EcoRI and XmaI sites. The LD-CAMP construct was derived from the plasmid pCMV6-CAMP-myc-FLAG: an equivalent EcoRI/BspEI sequence of pCMV6-CAMP-myc-FLAG was designed replacing the CAMP signal peptide (MKTQRDGHSLGRWSLVLLLGLVMPALAI) with the hydrophobic domain of ALDI (MDALVLFQLLVLLLTPLHLLALLGC) acquired from GeneScript, cloned in a PUC57 plasmid. Both fragments were swapped after an EcoRI/BspEI digestion. CAMP ΔN mutant, results from deletion of the amino acids 1–32. The cDNAs were acquired from GenScript and subcloned into pCMV6-myc-FLAG vector following the same strategy. pCMV6-CAMP-untagged was generated by polymerase chain reaction (PCR) using primers containing EcoRI and XmaI sites. The plasmid pCMV6-*PLIN2*-myc-FLAG tagged was derived from the plasmid pGFP-*PLIN2*, provided by Dr John McLauchlan (Institute of Virology, Glasgow) and subcloned into pCMV6 by PCR using primers containing EcoRI and XhoI sites. The plasmid pCMV6-*PLIN3*-myc-FLAG tagged was derived from the plasmid pcDNA 3×myc-tagged *PLIN3* provided by S. Pfeffer (Stanford University School of Med-

icine, Stanford, California), and subcloned into pCMV6 by PCR using primers containing EcoRI and XhoI sites. The lentiviral system utilizing pFTRE3G-PGK-puro (kindly provided by James Murphy, Walter and Elizabeth Hall Institute of Medical Research) for doxycycline-inducible gene expression has previously been described (31, 32). The plasmid pFTRE3G-*PLIN5* was obtained by subcloning *PLIN5* into pFTRE3G by PCR using primers containing BamHI sites.

Mouse studies

Animals and models of infection

C57BL/6J male mice (8 to 10 weeks old) were purchased from Charles River Laboratories (Wilmington, Massachusetts). Animals were kept under a controlled humidity and lighting schedule with a 12 hours dark period. Food and water were available ad libitum. All animals received humane care in compliance with institutional guidelines regulated by the European Community. The experimental protocols were approved by the Animal Care Committee of the University of Barcelona. The day before the experiment, animals were fasted overnight (16 hours) and in some cases intraperitoneally injected with 200 µl of saline buffer (CTL) or 6 mg/kg LPS (final dose) (L2639, Sigma-Aldrich, St Louis, Missouri). In some experiments (fed condition) food was available ad libitum. To induce sepsis by cecal ligation and puncture (CLP), mice were anesthetized with an intraperitoneal injection of 100 mg/kg ketamine (Richter Pharma AG, Wels) and 10 mg/kg xylazine (Rompun, Bayer, Leverkusen, Germany) and a 1-cm incision was made on the abdomen. The cecum was exposed and ligated below the ileocecal junction. A double puncture was made using a 22G needle, to induce severe sepsis. Sham-operated animals (CTL) underwent an identical laparotomy but without CLP. All mice received 1 ml of sterile saline subcutaneously as fluid resuscitation and antibiotic therapy by subcutaneous injection of 10 mg/kg meropenem (Merck Research Laboratory, Whitehouse Station, New Jersey) 6 hours after surgery.

Histological analysis

Liver sections were prepared and processed for hematoxylin and eosin (H&E) staining as previously described (33). For immunohistochemistry, liver sections were prepared and processed as described previously (34). The slides were blocked by incubation in 5% normal goat serum in PBS for 1 hour at room temperature followed by incubation with anti-*PLIN2* antibody (1:200; ab78920, Abcam, Cambridge, UK) overnight at 4°C. Sections were then washed three times in PBS and incubated with secondary goat anti-rabbit immunoglobulin G (IgG) Alexa Fluor 647 (1:250; A21244, ThermoFisher Scientific, Waltham, Massachusetts)

for 45 min at RT. After washing three times in PBS, slides were mounted with Dako Fluorescence Mounting Medium (Agilent Dako, #S3023).

Liver fractionation and hepatic LD purification

After liver perfusion with 0.9% NaCl and 0.1% EDTA solution, the liver was placed on a Petri dish, chopped with a scalpel for two min and transferred into a Dounce tissue grinder at a ratio of 1 g of tissue to 3 ml of homogenization buffer (25 mM Tris-HCl, pH 7.5, 100 mM KCl, 1 mM EDTA, and 5 mM EGTA). After three up-and-down strokes of each loose- and tight-pestle, the liver homogenate was centrifuged at 500g for 10 min at 4°C. 2.5 ml of the resulting post-nuclei supernatant (PNS) were mixed with an equal volume of 2.5 M sucrose and placed at the bottom of a sucrose step gradient of 25%, 15%, 10%, and 5% (w/v) sucrose in homogenization buffer, with an additional top layer of 25 mM Tris-HCl, pH 7.5, 1 mM EDTA and 5 mM EGTA, and centrifuged at 12,000g for 1 hour at 4°C (SW-41Ti rotor, Beckman Coulter, Pasadena, California). Six or seven fractions were collected from the top. Equal volumes of each fraction were used for immunoblotting. To purify LDs, the LD fraction on the top of the gradient was recovered and concentrated by re-floating LDs at 16,000g for 10 min at 4°C. The lower phase containing the excess buffer was removed by aspiration with a syringe and four volumes of ice-cold acetone were added to precipitate proteins and kept 48 hours at -20°C. The samples were centrifuged at 16,000g for 10 min at 4°C, the pellet washed with cold acetone 3 times, air-dried and reconstituted with 10 mM Tris-HCl, pH 7.5. After sonication, protein concentration was quantified by CBQCA protein quantitation kit (ThermoFisher Scientific). To purify cytosol extracts, 200 µl of PNS plus 600 µl of homogenization buffer were centrifuged at maximal speed for 1 hour (1×10^6 g in S140-AT Fixed Angle Rotor, ThermoFisher Scientific). A syringe (23G needle) was inserted below the floating LDs to remove 200 µl of cytoplasm and proteins were precipitated as described previously.

Bacterial killing assay (BKA)

E. coli (ATCC 25922) were grown to an O.D. at 600 nm of 1 and diluted 1:100 (1.5×10^5 colony-forming units (CFU/ml)). One hundred microliters of bacterial culture were mixed with 15 or 25 µg of LD-proteins. Incubation buffer (33 mM KH_2PO_4 , 60 mM K_2HPO_4 , 10 mM Na_2SO_4 , 1.7 mM sodium citrate, 10 mM MgSO_4) was then added up to 200 µl. Cultures were incubated for the indicated times at 37°C in a shaking incubator. Serial dilutions were plated in triplicate on LB-agar plates and surviving bacteria were quantitated as CFU/ml after overnight incubation at 37°C. Alternatively,

overnight incubations were centrifuged at 11,000g for 30 s and the bacterial pellet was resuspended in PBS and measured the absorbance by optical density at 600 nm with a Modulus Microplate Multimode Reader (Promega, Madison, Wisconsin). For monitoring bacterial growth in the presence or absence of OA (175 µg/ml) or gentamicin (200 µg/ml), *E. coli* cultures were diluted to an O.D. at 600 nm of 0.1 in 96-well flat-bottom plates and incubated at 37°C shaking. O.D. at 600 nm readings were taken every 20 min and monitored using a POLARstar Omega reader (BMG Labtech, Germany).

Serum parameters, hepatic triacylglycerol quantification, and mitochondrial content

Blood was extracted by cardiac puncture and sera obtained after centrifugation of blood samples at 6,000g for 15 min at 4°C in serum heparin separator tubes (Becton Dickinson, Franklin Lakes, New Jersey). Ketone bodies in serum were measured using a Ketone Body Assay Kit (MAK134; Sigma-Aldrich) according to the manufacturer's instructions. Triacylglycerol content of the liver was determined using the Triglyceride Detection Kit following manufacturer's instructions (BioSystems, Barcelona, Spain). Citrate synthase activity was measured as a reliable marker of mitochondrial content as previously described (35).

Fatty acid beta-oxidation

Primary hepatocytes were isolated as previously (36). To accumulate radiolabeled fatty acids in LDs, cells were treated for 4 hours with 1 µCi/ml of [^{14}C]-OA 175 µg/ml (NEC317050C, PerkinElmer, Waltham, Massachusetts). The media was then replaced with fresh media at 175 µg/ml of OA for an additional 4 hours followed by an overnight incubation with DMEM 0% FCS, low glucose (0.75 g per liter) with or without LPS (100 µg/ml) and sealed. Oxidation measurements were performed by trapping the released [^{14}C] carbon dioxide in a parafilm-sealed system on filter paper soaked in 1 M potassium hydroxide and measured using a Wallac 1409 Liquid Scintillation Counter. The rate of beta-oxidation was calculated as the amount of trapped [^{14}C] carbon dioxide in relative units produced per 0.5×10^6 cells. Results are expressed as the beta-oxidation rate relative to the untreated condition. Lipid soluble intermediates include those incompletely oxidized acid-soluble metabolites containing ^{14}C and were obtained after precipitation with perchloric acid and measured using a liquid scintillation counter.

Human macrophages studies

Cell culture

Human monocyte-derived macrophages (HMDMs) were obtained by differentiating CD14⁺ monocytes as previously described (37).

The human monocytic THP-1 cell line was obtained from the American Type Culture Collection (Rockville, Maryland). Cells were cultured in Roswell Park Memorial Institute 1640 Medium (RPMI, Gibco, ThermoFisher Scientific) containing 10% heat inactivated FBS (Bovogen Biologicals, Melbourne, VI, Australia), 5mM sodium pyruvate (Gibco), 10 mM HEPES (Gibco), 50 U/ml penicillin (Invitrogen, Carlsbad, California) and 50 µg/ml streptomycin (Invitrogen). Infection media are similar to complete media but without penicillin-streptomycin.

Bacterial strains and infection assays

For HMDMs infection, the following bacterial strains were used: *S. Typhimurium* SL1344 and *E. coli* K-12 MG1655. THP-1 cells were infected with *E. coli* K-12 MG1655. To induce LD formation, cells were treated with OA (178 µg/ml final) 18 hours prior infection. Bacterial infections were performed as previously described (37), with a multiplicity of infection (MOI) of 10 for *S. Typhimurium* and 100 for *E. coli*.

Flow cytometry

HMDMs were seeded at 0.5×10^6 cells/ml and treated with or without OA (178 ng/ml) for 16 hours. The next day, heat-killed pHrodoTM Green *E. coli* BioParticlesTM Conjugate (#P35366, ThermoFisher Scientific) were added to the well (50 µg/well) for 90 min. Cytochalasin D (10 µM, 30 min pre-treatment) was used as positive control to block phagocytosis (ThermoFisher Scientific). Cells were then harvested in ice-cold PBS containing 0.1% sodium azide and 25 mM EDTA. Flow cytometric analysis was performed using a GALLIOS Flow Cytometer (Beckman Coulter) and data were analyzed using Kaluza Analysis 1.3. software.

Fluorescence and quantitation of LD-bacteria proximity

HMDMs, plated on coverslips, were treated with OA (175 µg/ml) for 16 hours, then infected with *E. coli* strain MG1655 (MOI 10) or *Salmonella* SL1344 strain (MOI 10), both expressing mCherry constitutively. At 4 hours post-infection, cells were stained with BODIPY 647 (10 µg/ml; Molecular Probes Eugene, Oregon) for 30 min, before being washed with PBS and fixed with 4% paraformaldehyde (Electron Microscopy Science, Hatfield, Pennsylvania) for 10 min. Cells were then stained with 4',6-diamidino-2-phenylindole (DAPI) (20 ng/ml) and mounted on slides.

HMDM siRNA experiments

Day 6 HMDMs were harvested and resuspended in IMDM complete media containing 10 mM HEPES buffer (pH 7.2 to 7.5, Gibco). Combined sets of CAMP small interfering RNA (siRNA) (GGAAGCUGUGCUUCGUGCUAUA-GAU, AUCUAUAGCACGAAG CACAGCUUCC, GACAUCAGUUGUGAUAAAGGAUAACA,

UGUUAUCCUUAUCAC AACUGAUGUC, GCUUCACAGUGAAAGAGACAGUGUG, and CACACUGUCUCCUUC ACUGUGAAGC) or scramble siRNA were used as previously described (38). After 24 hours recovery, cells were treated with OA (37.5 µg/ml) for another 18 hours. HMDMs were then infected with *E. coli*.

Gene overexpression in THP-1 by lentiviral transduction

Lentiviral transduction was used for gene overexpression of *PLIN5* in THP-1 cells as previously described (38).

Cell culture studies

Cell culture and treatments

HuH7 and HEK293 cells were cultured in Dulbecco's modified Eagle's medium (DMEM, Biological Industries, Cromwell, Connecticut) 10% v/v fetal bovine serum (Biological Industries) supplemented with 4 mM L-glutamine, 1 mM pyruvate (Sigma-Aldrich), 50 U/ml penicillin, 50 µg/ml streptomycin, and non-essential amino acids (Biological Industries). HEK293 cells stably expressing human Toll-like receptor 4 (HEK293-TLR4⁺) have been characterized previously (39). OA treatments were performed using OA (O1008, Sigma-Aldrich) conjugated to fatty acid-free BSA (A8806, Sigma-Aldrich) at a molar ratio of 6:1. Cells were treated with recombinant human TNFα (20 ng/ml; 300-O1A, Preprotech, Rocky Hill, New Jersey), and IFNγ (10 ng/ml; 300-O2, Preprotech) and LPS (500 ng/ml) for 16 hours. Cells expressing CAMP-ΔN mutant were treated with MG132 (5 µM; 474790, Merck) for 24 hours.

Transfection

Six-well plates were seeded with 3×10^5 HuH7 cells or 4×10^5 HEK293 or HEK293-TLR4⁺ cells. Twenty-four hours after plating, cells were transfected using GENEJET PLUS (SignaGen, Rockville, Maryland), following the manufacturer's instructions. Six hours after transfection, cells were treated with OA (175 µg/ml) for 16 hours.

Bacterial strains and infection assays

The bacterial strains used were: *E. coli* (ATCC 25922), MRSA (strain 162057-900), *P. aeruginosa* (ATCC 27853), and *L. monocytogenes* (strain 10403S). HEK293 or HEK293-TLR4⁺ cells were seeded at 4×10^5 cells/plate in 6-well plates and transfected the next day. Six hours after transfection, culture media was replaced for antibiotic-free cell culture medium in presence of OA (175 µg/ml) and left overnight. Bacteria were grown overnight to stationary phase. The following day, bacteria were diluted 1:10 and grown to an O.D. at 600 nm of 0.54 to 0.56. They were then washed twice and resuspended in antibiotic-free cell culture medium and used at MOI of 0.5. Each infection was performed

in triplicate wells. After 1 hour, extracellular bacteria were removed by incubation with 200 µg/ml gentamycin-containing medium (G1914, Sigma-Aldrich) for 1 hour, followed by incubation with 20 µg/ml gentamycin-containing medium for 4 hours. To determine intracellular bacterial loads, cells were lysed with 0.1% Triton X-100 (T8787, Sigma-Aldrich) for 5 min and plated onto LB medium supplemented with 1.5% (w/v) agar.

Cell fractionation

HuH7 cells were seeded at 1.5×10^6 cells/plate, transfected the next day and loaded with 175 µg/ml OA overnight. Three 100-mm culture plates were used per each condition. A sucrose density gradient was performed as previously described (40).

Protein purification and coimmunoprecipitation

For purification of myc-tagged proteins, HuH7 cells were plated in 100-mm culture plates at 10×10^6 cells/plate, transfected the next day and loaded with 175 µg/ml OA overnight. Myc-tagged proteins from the cellular extract and secreted into the media were purified using a c-myc protein purification kit (MBL, Nagoya, Japan) according to the manufacturer's instructions. Samples were processed by SDS-PAGE and analyzed by immunoblotting. For immunoprecipitation, transfected HuH7 cells (five 100-mm culture plates per condition) were collected and lysed in buffer containing 50 mM Tris-HCl at pH 7.5, 150 mM NaCl, 5 mM EDTA, and 1% Triton X-100 supplemented with proteases and phosphatases inhibitors. Cell lysates were homogenized with a 23G needle syringe 10 times and centrifuged for 20 min at 16,000g at 4°C. The supernatant was then incubated with 1 µg of anti-FLAG antibody for 2 hours at 4°C, followed by addition of protein G Sepharose beads (P3296, Sigma-Aldrich) for 1 hour at 4°C. Immunoprecipitated proteins were washed three times with lysis buffer, suspended in 2X Laemmli buffer and analyzed by immunoblotting.

Gene expression by quantitative PCR (qPCR)

For quantitative RT-PCR, total RNA was isolated from liver homogenates, HuH7 or HEK293-TLR4⁺ cells using the RNeasy Lipid Tissue Mini Kit (QIAGEN, Hilden, Germany) according to the manufacturer's instructions. One microgram of total RNA was used for cDNA synthesis using the High Capacity cDNA Reverse Transcription Kit (Applied Bioscience, ThermoFisher Scientific) according to the manufacturer's instructions. qRT-PCR was performed using the Brilliant SYBR Green qPCR Master Mix (# 600548, Agilent Technologies, Santa Clara, California) and detected by the Mx3000P QPCR System (Agilent Technologies).

The following are the primers used for real-time PCR:

GAPDH: forward, 5'-CGACTTCAACAGCAAC-TCCCACTCTTCC-3' and reverse 5'-TGGGTGGT-CCAGGGTTTCTTACTCCTT-3'. Cytochrome C oxidase subunit I (*COI*): forward, 5'-GCCCCA-GATATAGCATTCCC-3' and reverse 5'-GT-TCATCCTGTTCCCTGCTCC-3'. *PLIN2*: forward 5'-ACACCCTCCTGTCCAACATC-3' and reverse 5'-AAGGGACCTACCAGCCAGTT-3'. *PLIN5*: forward 5'-GCGGTCTGCGATGTTTACAG-3' and reverse 5'-CTCCGAAGGTTGCTGGAGAA-3'. *RAB18*: forward 5'-GACGTGCTAACCCCTGAA-3' and reverse 5'-AACACCCTGTGCACCTCTAT-3'. *HSL*: forward 5'-CACCAGCCAACACTCAGCTA-3' and reverse 5'-GTGTGAGGAGGGTCATCGTT-3'. *HPRT*: forward 5'-GCAGTACAGCCCCAAA-TGG-3' and reverse 5'-AACAAAGTCTGGCC-TGTATCCA-3'. *CAMP*: forward 5'-CTGTCC-CCATACCCGCTTC-3' and reverse 5'-GACAC-AGTGTGCCCCAGGAC-3'. *TNFα*: forward 5'-CCATGTTGTAGCAAACCCCTCAA-3' and reverse 5'-GCTGGTATCTCTCAGCTCCA-3'. *IL8*: forward 5'-AGACAGCAGAGCACACAAGC-3' and reverse 5'-ATGGTTTCCTTCCGGTGGT-3'. *IL8 S*: forward 5'-CGGCTACCACATCCAAGGAA-3' and reverse 5'-GCTGGAATTACCGCGGCT-3'. The relative expression of each mRNA was normalized to the internal reference *GAPDH* (liver), *IL8S* (cultured cells), or hypoxanthine phosphoribosyl transferase (*HPRT*; macrophages).

TLR4-mediated IL-8 release assay

HEK293-TLR4⁺ cells were seeded at 4×10^5 cells/plate in 48-well plates in the presence or absence of LPS (250 ng/ml) for 18 hours. One hundred microliters of culture supernatant was used to measure interleukin-8 (IL-8) levels using the Human enzyme-linked immunosorbent assay (ELISA) IL-8 Set assay (555244; BD OptEIA, BD Biosciences) according to the manufacturer's protocol and detected by Epoch Multiplate Spectrophotometer (BioTek, Winooski, Vermont).

Immunofluorescence

HuH7 cells were grown in 10-mm glass coverslips. For HEK293 and HEK293-TLR4⁺ cells, glass coverslips were coated with 50 µg/ml of fibronectin (Sigma-Aldrich) for 30 min at room temperature and rinsed twice with PBS before seeding cells. Cells were fixed for 60 min in 4% paraformaldehyde, permeabilized in 0.15% Triton X-100 for 10 min, followed by blocking with 1% BSA (A7906, Sigma-Aldrich), 0.1% Tween in PBS for 15 min. Labeling was achieved by incubating cells for 1 hour at room temperature with primary antibodies diluted in blocking solution: rabbit polyclonal anti-PLIN2 (1:500; ab108323, Abcam), rabbit polyclonal anti-CAMP (1:200; ab180760, Abcam), rabbit polyclonal anti-TOM20 (1:500; ab186734, Abcam), mouse monoclonal anti-FLAG (1:500; F1804; Sigma). Primary antibodies were detected

with donkey anti-mouse IgG Alexa Fluor 488 (A21202), donkey anti-mouse IgG Alexa Fluor 555 (A31570), donkey anti-rabbit IgG Alexa Fluor 555 (A321094), and chicken anti-mouse IgG Alexa Fluor 647 (A21463) from ThermoFisher Scientific, diluted 1:250 in blocking solution. Finally, cells were labeled with DAPI (1:4000; ThermoFisher) and LDs were stained with BODIPY 493/503 (1:1000; Molecular Probes) for 10 min at room temperature, washed twice with PBS and coverslips were mounted with Mowiol (475904; Calbiochem, Merck). Alternatively, LDs were labeled with LipidTOX Deep Red (H34477; Molecular Probes) at 1:100 dilution in mounting media.

Microscopy

Optical and fluorescence microscopy

Imaging of H&E staining was performed with a Leica DMRB optical microscope (Leica, Wetzlar, Germany) equipped with a Leica DFC450 digital camera, using the 63X oil immersion objective lens. For immunohistochemistry and immunofluorescence, images were collected using a Leica AF600 motorized microscopy system (Leica Microsystems, Mannheim, Germany) equipped with a DMI6000 microscope, a Leica PL APO 63X numerical aperture 1.4 oil immersion, a high-resolution monochrome ORCA-spark CMOS Digital Camera, and a mercury metal halide bulb Leica EL6000 as light source. DAPI was acquired with a band pass excitation filter 340–380 nm, dichromatic mirror (400 nm) and a long pass emission filter (425 nm). A488 was acquired with a band excitation filter 480/40 nm, dichromatic mirror 505 nm and a band pass emission filter (527/30 nm). A555 was acquired with a band pass excitation filter 531/40 nm, dichromatic mirror reflection 499–555 and transmission 659–730 nm and a band pass emission filter (593/40 nm). A647 was acquired with excitation band pass filter 628/40 nm, dichromatic mirror reflection 549–651 nm and transmission 699–726 nm and a band pass emission filter (692/40 nm). Images were collected using the LAS X Navigator software. High-resolution images of liver areas were captured using the Tile Scan acquisition mode. For quantitation of LD-bacteria proximity, images were taken with 63X objective lens using a Zeiss Axiovert 200 Upright Microscope Stand with LSM 710 Meta Confocal Scanner, with spectral detection and Airyscan super resolution detector. Two-photon imaging with a fully tunable Mai Tai eHP DeepSee 760–1040 nm laser (Zeiss, Oberkochen, Germany). Images were analyzed using the Adobe Photoshop CS3 software (Adobe Systems Inc. San Jose, California) and ImageJ (NIH).

Electron microscopy and morphological measurements

Liver samples, HMDMs, or THP-1 cells in 3-cm dishes were processed for TEM as described

previously (41). For TEM, ultrathin sections (60 nm) were cut using an ultramicrotome (EM U26, Leica, Germany) and collected on copper mesh grids. Imaging was conducted on a Hitachi 7700 (Tokyo, Japan) at 80 kV. For serial block-face scanning electron microscopy (SBF-SEM), the stub was transferred to a Zeiss Sigma scanning electron microscope fitted with a Gatan 3view. Sectioning and imaging were conducted at 50-nm intervals with a voxel size of 11.5 by 11.5 nm, allowing for a field of view of 46 by 46 μ m. Data obtained from SBF-SEM were analyzed using Imod software (42). Image stacks were aligned manually using the Midas command. Structures of interest were then segmented using the manual drawing tool aided by an automated interpolator tool. A mesh was placed on the objects allowing then to be viewed in three dimensions.

Image analysis

Image analysis was performed using FLJI-Image J (Wayne Rasband, NIH) (43, 44). Custom-made macros were programmed with instructions for the automated image analysis pipelines.

LD-mitochondria contacts

Confocal images from fluorescently labeled HEK293 cells, Mitochondria (TOM20), LD (BODIPY), PLIN5 and nuclei (DAPI), were acquired to analyze contacts between mitochondria and LD under LPS and PLIN5 expression (fig. S7). Briefly, cells were segmented, individualized, and stored as Regions of Interest (ROI). LD segmentation was achieved through a Trainable Weka Segmentation classifier (45) on LD (BODIPY) channel image and mitochondria were segmented by intensity thresholding (autothreshold method “Otsu”). Contact regions between mitochondria and LD were first obtained by using the Colocalization Highlighter plugin (Pierre Bourdoncle, Institut Jacques Monod, Service Imagerie, Paris) and converted to a contour line section by skeletonization. Contact length and contact counts were quantified from each cell and stored in the results table. Mean PLIN5 intensity was quantified from each cell to differentiate expressing PLIN5 cells. The computer code is available at <https://zenodo.org/badge/latestdoi/280189667>.

Distribution of selected tagged human LD-proteins

To analyze distribution of selected tagged human LD-proteins in HuH7 cells, confocal z -sections from cells labeled with DAPI, anti-FLAG antibodies, anti-PLIN2 antibodies, and LipidTox were acquired. Briefly, cells were defined manually and LD-intensity thresholded. They were then converted to binary images stored in ROI Manager. The sum of intensities from anti-FLAG or anti-PLIN2 from LD ROIs was divided by the sum of intensities of anti-FLAG or anti-PLIN2 from each cell, multiplied

by 100 and expressed as percentage of anti-FLAG or anti-PLIN2 protein on LDs respectively. LDs that contained at least one pixel of anti-FLAG or anti-PLIN2 labeling were counted as positive LDs for that labeling. The total counts of positive LDs for anti-FLAG or anti-PLIN2 was divided by the total amount of LDs and expressed as a percentage. The computer code is available at <https://zenodo.org/badge/latestdoi/280200243>.

Immunoblotting

Cells were washed twice with cold PBS before being scraped into ice-cold 10 mM Tris, pH 7.5, 150 mM NaCl, 5 mM EDTA 0.1% Triton X-100 and a mixture of protease and phosphatase inhibitors. Cells were homogenized by sonication at 4°C. Protein was quantified with the Bio-Rad Protein Assay kit (Bio-Rad, Hercules, California). Immunoblotting of cells was performed as described previously (46). The blots were incubated with primary antibodies for 1 hour at room temperature. The primary antibodies used were: rabbit polyclonal anti-GFP (1:5000; ab290, Abcam), rabbit polyclonal anti-PLIN2 (1:5000; ab78920, Abcam), rabbit polyclonal anti-PLIN5 (1:1000; ab222811, Abcam), rabbit polyclonal anti-EEA1 (1:200; ab2900, Abcam), rabbit polyclonal anti-VAP-A (1:5000; ab181067, Abcam), mouse monoclonal anti-viperin (1:1000; ab107359, Abcam), rabbit polyclonal anti-CAMP (1:1000; ab180760, Abcam), guinea pig polyclonal anti-PLIN 3 (1:500; GP32, Progen, Heidelberg, Germany), guinea pig polyclonal PLIN5 (1:1000; GP31, Progen), guinea pig polyclonal PLIN2 (1:2000; GP41, Progen), mouse monoclonal anti-GM130 (1:2000; Labs 810822, BD-Biosciences San Jose, California), mouse monoclonal anti-Na/K ATPase (1:1000; 05-369 Upstate-Millipore, Darmstadt, Germany) rabbit polyclonal anti-HSL (1:1000; 4107, Cell Signaling, Leiden, the Netherlands), mouse monoclonal anti-IGTP (1:200; sc-136317, Santa Cruz Biotechnology, Dallas, Texas), rabbit polyclonal anti-CAMP (1:500; TA306515, OriGene), mouse monoclonal anti-FLAG (1:1000; F1804, Sigma-Aldrich), mouse monoclonal anti-ATP synthase (1:500; 7H10BD4F9, ThermoFisher Scientific), and goat polyclonal anti-GAPDH (1:5000; A00191, GenScript). After incubation with primary antibodies, membranes were washed and incubated with the following peroxidase-conjugated secondary antibodies (1:3000): goat anti-rabbit IgG (H+L)-HRP conjugate (1706515, BioRad), goat anti-mouse IgG (H+L)-HRP conjugate (1706516, BioRad), and peroxidase AffiniPure donkey anti-goat IgG (H+L) (705-035-147, Jackson ImmunoResearch, Ely, UK). HRP-conjugated secondary antibodies were detected with ECL (Biological Industries) and visualized using ImageQuant LAS4000 (GE Healthcare, Chicago, Illinois). Immunoblots were quantified using the Fiji-ImageJ software (NIH).

Quantitative proteomics and functional annotation analyses

Proteins were precipitated from either isolated lipid droplets (four and five independent replicates for CTL- and LPS-treated, respectively) or liver homogenates (three independent replicates per condition) with ice-cold acetone and solubilized in lysis buffer (50 mM Tris-HCl, pH 7.5, 2% SDS and 10 mM TCEP [Tris-(2-carboxyethyl)-phosphine hydrochloride]). Protein concentration in spun supernatants was determined by infrared spectrometry. Approximately 100 µg of total protein per sample were digested using standard FASP procedures. After alkylation, proteins were digested overnight at 37°C with modified trypsin (Promega) in 50 mM ammonium bicarbonate at a 30:1 protein:trypsin (w/w) ratio. Resulting peptides were eluted in 50 mM ammonium bicarbonate and 0.5 M sodium chloride. Trifluoroacetic acid (TFA) was added to a final concentration of 1%. Eluates were desalted through C18 Oasis-HLB cartridges (Waters corporation, Milford, Massachusetts), dried, and resuspended in 100 mM triethylammonium bicarbonate (TEAB) buffer. Equal amounts of each peptide sample were labeled using the 10-plex TMT Reagents (ThermoFisher Scientific) according to manufacturer's protocol. For increased proteome coverage, TMT-labeled samples were fractionated by high-pH reverse-phase chromatography (Pierce High pH Reversed-Phase Peptide Fractionation Kit, # 84868; ThermoFisher Scientific). Labeled peptides were chromatographed through a C-18 reversed phase nano-column (75 µm I.D. × 50 cm, 2-µm particle size, Acclaim PepMap RSLC, 100 C18; ThermoFisher Scientific) in a continuous acetonitrile gradient consisting of 0 to 30% B in 360 min, 50 to 90% B in 3 min (A = 0.1% formic acid; B = 90% acetonitrile, 0.1% formic acid; flow rate of 200 nL/min) for analysis in an Orbitrap Fusion mass spectrometer (ThermoFisher Scientific). Tandem mass spectrometry (MS/MS) spectra from the Nth-most intense parent ions were analyzed along the chromatographic run. For peptide identification, all spectra were analyzed with Proteome Discoverer (v. 2.10.81) using SEQUEST-HT (ThermoFisher Scientific) and queried onto the Uniprot database with the following search parameters: 2 maximum missed tryptic sites; precursor and fragment mass tolerances of 2 Da and 0.02 Da, respectively; carbamidomethyl cysteine and TMT modifications at N-terminal and Lys residues as fixed modifications, and methionine oxidation as dynamic modification. Peptide identification was performed using the probability ratio method (47), and FDR was calculated using inverted databases. The relative abundance of each protein was estimated from ion intensities of peptides with an FDR ≤ 1% and expressed in units of standard deviation according to their estimated variances (Z_q values), as previously described (13). Hierarchical

clustering was computed across all individual replicates (averaged distance) and a 0.78 correlation cut-off was established for subsequent analysis. Functional protein analysis was performed using the system biology triangle (SBT) algorithm and Ingenuity Pathway Analysis (IPA, QIAGEN) (48). Upstream pathway analysis and network modeling of interested protein clusters were run using the IPA platform (QIAGEN), and network representation was layered out using Cytoscape 2.0. Analysis shown in Fig. 3C shows the relative proportion of proteins identified for each indicated functional annotation term (retrieved from DAVID resource 6.7, including all KEGG and GO terms), from either mitochondrial protein identified among LPS-LD down-regulated proteins, or the MitoCarta 2.0 reference proteome. Mass spectrometry data have been deposited in Peptide Atlas (ID: PASS01610).

Statistical analysis

All data shown in graphs are the mean ± SD. Statistical significance was determined using paired *t* test, one-way analysis of variance (ANOVA) multiple comparisons test, or two-sided students *z* test on proportions, as specified in figure legends [not significant (ns), **P* < 0.05, ***P* < 0.01, ****P* < 0.001, and *****P* < 0.0001].

Figure preparation

Figures were created using Microsoft PowerPoint (Microsoft 365 MSO). Images were edited with Adobe Photoshop CS3 software (Adobe Systems). GraphPad Prism 7 (GraphPad Software) was used to create graphs and calculate statistical significances.

REFERENCES AND NOTES

1. A. Pol, S. P. Gross, R. G. Parton, Review: Biogenesis of the multifunctional lipid droplet: lipids, proteins, and sites. *J. Cell Biol.* **204**, 635–646 (2014). doi: [10.1083/jcb.201311051](https://doi.org/10.1083/jcb.201311051); pmid: 24590170
2. A. L. Vallochi, L. Teixeira, K. D. S. Oliveira, C. M. Maya-Monteiro, P. T. Bozza, Lipid Droplet, a key player in host-parasite interactions. *Front. Immunol.* **9**, 1022 (2018). doi: [10.3389/fimmu.2018.01022](https://doi.org/10.3389/fimmu.2018.01022); pmid: 29875768
3. P. Roingeard, R. C. Melo, *Cell. Microbiol.* **10.1111/cmi.12688** (2017).
4. M. Knight, J. Braverman, K. Asfaha, K. Gronert, S. Stanley, Lipid droplet formation in Mycobacterium tuberculosis infected macrophages requires IFN-γ/HIF-1α signaling and supports host defense. *PLOS Pathog.* **14**, e1006874 (2018). doi: [10.1371/journal.ppat.1006874](https://doi.org/10.1371/journal.ppat.1006874); pmid: 29370315
5. R. C. Melo, A. M. Dvorak, Lipid body-phagosome interaction in macrophages during infectious diseases: Host defense or pathogen survival strategy? *PLOS Pathog.* **8**, e1002729 (2012). doi: [10.1371/journal.ppat.1002729](https://doi.org/10.1371/journal.ppat.1002729); pmid: 22792061
6. E. R. Hinson, P. Cresswell, The antiviral protein, viperin, localizes to lipid droplets via its N-terminal amphipathic alpha-helix. *Proc. Natl. Acad. Sci. U.S.A.* **106**, 20452–20457 (2009). doi: [10.1073/pnas.0911679106](https://doi.org/10.1073/pnas.0911679106); pmid: 19920176
7. L. Bougnères et al., A role for lipid bodies in the cross-presentation of phagocytosed antigens by MHC class I in dendritic cells. *Immunity* **31**, 232–244 (2009). doi: [10.1016/j.immuni.2009.06.022](https://doi.org/10.1016/j.immuni.2009.06.022); pmid: 19699172
8. P. Anand et al., A novel role for lipid droplets in the organismal antibacterial response. *eLife* **1**, e00003 (2012). doi: [10.7554/eLife.00003](https://doi.org/10.7554/eLife.00003); pmid: 23150794
9. U. Protzer, M. K. Maini, P. A. Knolle, Living in the liver: Hepatic infections. *Nat. Rev. Immunol.* **12**, 201–213 (2012). doi: [10.1038/nri3169](https://doi.org/10.1038/nri3169); pmid: 22362353

10. J. C. Kagan, Lipopolysaccharide Detection across the Kingdoms of Life. *Trends Immunol.* **38**, 696–704 (2017). doi: [10.1016/j.it.2017.05.001](https://doi.org/10.1016/j.it.2017.05.001); pmid: 28551077
11. A. Herms et al., AMPK activation promotes lipid droplet dispersion on detyrosinated microtubules to increase mitochondrial fatty acid oxidation. *Nat. Commun.* **6**, 7176 (2015). doi: [10.1038/ncomms8176](https://doi.org/10.1038/ncomms8176); pmid: 26013497
12. J. Behnsen, A. Perez-Lopez, S. P. Nuccio, M. Raffatellu, Exploiting host immunity: The Salmonella paradigm. *Trends Immunol.* **36**, 112–120 (2015). doi: [10.1016/j.it.2014.12.003](https://doi.org/10.1016/j.it.2014.12.003); pmid: 25582038
13. P. Navarro et al., General statistical framework for quantitative proteomics by stable isotope labeling. *J. Proteome Res.* **13**, 1234–1247 (2014). doi: [10.1021/pr4006958](https://doi.org/10.1021/pr4006958); pmid: 24512137
14. N. Krahmer et al., Protein correlation profiles identify lipid droplet proteins with high confidence. *Mol. Cell. Proteomics* **12**, 1115–1126 (2013). doi: [10.1074/mcp.M112.020230](https://doi.org/10.1074/mcp.M112.020230); pmid: 23319140
15. K. Bersuker et al., A proximity labeling strategy provides insights into the composition and dynamics of lipid droplet proteomes. *Dev. Cell* **44**, 97–112.e7 (2018). doi: [10.1016/j.devcel.2017.11.020](https://doi.org/10.1016/j.devcel.2017.11.020); pmid: 29275994
16. E. L. Mills, B. Kelly, L. A. J. O'Neill, Mitochondria are the powerhouses of immunity. *Nat. Immunol.* **18**, 488–498 (2017). doi: [10.1038/ni.3704](https://doi.org/10.1038/ni.3704); pmid: 28418387
17. M. Bosch, R. G. Parton, A. Pol, *Semin. Cell Dev. Biol.* **10.1016/j.semcdb.2020.02.010** (2020).
18. H. A. Neufeld, J. A. Pace, F. E. White, The effect of bacterial infections on ketone concentrations in rat liver and blood and on free fatty acid concentrations in rat blood. *Metabolism* **25**, 877–884 (1976). doi: [10.1016/0026-0495\(76\)90120-7](https://doi.org/10.1016/0026-0495(76)90120-7); pmid: 181658
19. A. Fabisiak, N. Murawska, J. Fichna, LL-37: Cathelicidin-related antimicrobial peptide with pleiotropic activity. *Pharmacol. Rep.* **68**, 802–808 (2016). doi: [10.1016/j.pharep.2016.03.015](https://doi.org/10.1016/j.pharep.2016.03.015); pmid: 27117377
20. X. Shu, L. Nelbach, R. O. Ryan, T. M. Forte, Apolipoprotein A-V associates with intrahepatic lipid droplets and influences triglyceride accumulation. *Biochim. Biophys. Acta* **1801**, 605–608 (2010). doi: [10.1016/j.bbalip.2010.02.004](https://doi.org/10.1016/j.bbalip.2010.02.004); pmid: 20153840
21. S. Turro et al., Identification and characterization of associated with lipid droplet protein 1: A novel membrane-associated protein that resides on hepatic lipid droplets. *Traff. J.* **7**, 1254–1269 (2006). doi: [10.1111/j.1600-0854.2006.00465.x](https://doi.org/10.1111/j.1600-0854.2006.00465.x); pmid: 17004324
22. C. L. Libbing, A. R. McDevitt, R. P. Azcueta, A. Ahila, M. Mulye, Lipid droplets: A significant but understudied contributor of host bacterial interactions. *Cells* **8**, 354 (2019). doi: [10.3390/cells8040354](https://doi.org/10.3390/cells8040354); pmid: 30991653
23. J. L. Cocchiari, Y. Kumar, E. R. Fischer, T. Hackstadt, R. H. Valdivia, Cytoplasmic lipid droplets are translocated into the lumen of the *Chlamydia trachomatis* parasitophorous vacuole. *Proc. Natl. Acad. Sci. U.S.A.* **105**, 9379–9384 (2008). doi: [10.1073/pnas.0712241105](https://doi.org/10.1073/pnas.0712241105); pmid: 18591669
24. P. Peyron et al., Foamy macrophages from tuberculous patients' granulomas constitute a nutrient-rich reservoir for M. tuberculosis persistence. *PLOS Pathog.* **4**, e1000204 (2008). doi: [10.1371/journal.ppat.1000204](https://doi.org/10.1371/journal.ppat.1000204); pmid: 19002241
25. K. A. Mattos et al., Modulation of lipid droplets by Mycobacterium leprae in Schwann cells: A putative mechanism for host lipid acquisition and bacterial survival in phagosomes. *Cell. Microbiol.* **13**, 259–273 (2011). doi: [10.1111/j.1462-5822.2010.01533.x](https://doi.org/10.1111/j.1462-5822.2010.01533.x); pmid: 20955239
26. S. J. Nolan, J. D. Romano, I. Coppins, Host lipid droplets: An important source of lipids salvaged by the intracellular parasite *Toxoplasma gondii*. *PLOS Pathog.* **13**, e1006362 (2017). doi: [10.1371/journal.ppat.1006362](https://doi.org/10.1371/journal.ppat.1006362); pmid: 28570716
27. J. S. Mader, N. Mookherjee, R. E. Hancock, R. C. Bleackley, The human host defense peptide LL-37 induces apoptosis in a calpain- and apoptosis-inducing factor-dependent manner involving Bax activity. *Mol. Cancer Res.* **7**, 689–702 (2009). doi: [10.1158/1541-7786.MCR-08-0274](https://doi.org/10.1158/1541-7786.MCR-08-0274); pmid: 19435812
28. S. N. Keenan et al., Perilipin 5 deletion in hepatocytes remodels lipid metabolism and causes hepatic insulin resistance in mice. *Diabetes* **68**, 543–555 (2019). doi: [10.2337/db18-0670](https://doi.org/10.2337/db18-0670); pmid: 30617219
29. D. J. Greenwood et al., Subcellular antibiotic visualization reveals a dynamic drug reservoir in infected macrophages. *Science* **364**, 1279–1282 (2019). doi: [10.1126/science.aaf9689](https://doi.org/10.1126/science.aaf9689); pmid: 31249058
30. R. Dubey et al., Lipid droplets can promote drug accumulation and activation. *Nat. Chem. Biol.* **16**, 206–213 (2020). doi: [10.1038/s41589-019-0447-7](https://doi.org/10.1038/s41589-019-0447-7); pmid: 31932720

31. D. M. Moujalled *et al.*, TNF can activate RIPK3 and cause programmed necrosis in the absence of RIPK1. *Cell Death Dis.* **4**, e465 (2013). doi: [10.1038/cddis.2012.201](https://doi.org/10.1038/cddis.2012.201); pmid: [23328672](https://pubmed.ncbi.nlm.nih.gov/23328672/)
32. J. M. Murphy *et al.*, The pseudokinase MLKL mediates necroptosis via a molecular switch mechanism. *Immunity* **39**, 443–453 (2013). doi: [10.1016/j.immuni.2013.06.018](https://doi.org/10.1016/j.immuni.2013.06.018); pmid: [24012422](https://pubmed.ncbi.nlm.nih.gov/24012422/)
33. M. Bosch *et al.*, Hepatic primary and secondary cholesterol deposition and damage in niemann-pick disease. *Am. J. Pathol.* **186**, 517–523 (2016). doi: [10.1016/j.ajpath.2015.12.002](https://doi.org/10.1016/j.ajpath.2015.12.002); pmid: [26784526](https://pubmed.ncbi.nlm.nih.gov/26784526/)
34. A. Tutusaus *et al.*, A functional role of GAS6/TAM in nonalcoholic steatohepatitis progression implicates AXL as therapeutic target. *Cell. Mol. Gastroenterol. Hepatol.* **9**, 349–368 (2020). doi: [10.1016/j.jcmgh.2019.10.010](https://doi.org/10.1016/j.jcmgh.2019.10.010); pmid: [31689560](https://pubmed.ncbi.nlm.nih.gov/31689560/)
35. A. Barrientos, In vivo and in organello assessment of OXPHOS activities. *Methods* **26**, 307–316 (2002). doi: [10.1016/S1046-2023\(02\)00036-1](https://doi.org/10.1016/S1046-2023(02)00036-1); pmid: [12054921](https://pubmed.ncbi.nlm.nih.gov/12054921/)
36. M. Bosch *et al.*, Caveolin-1 deficiency causes cholesterol-dependent mitochondrial dysfunction and apoptotic susceptibility. *Curr. Biol.* **21**, 681–686 (2011). doi: [10.1016/j.cub.2011.03.030](https://doi.org/10.1016/j.cub.2011.03.030); pmid: [21497090](https://pubmed.ncbi.nlm.nih.gov/21497090/)
37. R. Kapetanovic *et al.*, *Salmonella* employs multiple mechanisms to subvert the TLR-inducible zinc-mediated antimicrobial response of human macrophages. *FASEB J.* **30**, 1901–1912 (2016). doi: [10.1096/fj.201500061](https://doi.org/10.1096/fj.201500061); pmid: [26839376](https://pubmed.ncbi.nlm.nih.gov/26839376/)
38. C. J. Stocks *et al.*, *J. Leukoc. Biol.* **2020**, 1–11 (2020).
39. S. Lauer, Y. A. Kunde, T. A. Apodaca, B. Goldstein, E. Hong-Geller, Soluble MD2 increases TLR4 levels on the epithelial cell surface. *Cell. Immunol.* **255**, 8–16 (2009). doi: [10.1016/j.cellimm.2008.08.009](https://doi.org/10.1016/j.cellimm.2008.08.009); pmid: [18845299](https://pubmed.ncbi.nlm.nih.gov/18845299/)
40. A. Kassar *et al.*, Acyl-CoA synthetase 3 promotes lipid droplet biogenesis in ER microdomains. *J. Cell Biol.* **203**, 985–1001 (2013). doi: [10.1083/jcb.201305142](https://doi.org/10.1083/jcb.201305142); pmid: [24368806](https://pubmed.ncbi.nlm.nih.gov/24368806/)
41. A. Herms *et al.*, Cell-to-cell heterogeneity in lipid droplets suggests a mechanism to reduce lipotoxicity. *Curr. Biol.* **23**, 1489–1496 (2013). doi: [10.1016/j.cub.2013.06.032](https://doi.org/10.1016/j.cub.2013.06.032); pmid: [23871243](https://pubmed.ncbi.nlm.nih.gov/23871243/)
42. J. R. Kremer, D. N. Mastronarde, J. R. McIntosh, Computer visualization of three-dimensional image data using IMOD. *J. Struct. Biol.* **116**, 71–76 (1996). doi: [10.1006/jsbi.1996.0013](https://doi.org/10.1006/jsbi.1996.0013); pmid: [8742726](https://pubmed.ncbi.nlm.nih.gov/8742726/)
43. J. Schindelin *et al.*, Fiji: An open-source platform for biological-image analysis. *Nat. Methods* **9**, 676–682 (2012). doi: [10.1038/nmeth.2019](https://doi.org/10.1038/nmeth.2019); pmid: [22743772](https://pubmed.ncbi.nlm.nih.gov/22743772/)
44. C. A. Schneider, W. S. Rasband, K. W. Eliceiri, NIH Image to ImageJ: 25 years of image analysis. *Nat. Methods* **9**, 671–675 (2012). doi: [10.1038/nmeth.2089](https://doi.org/10.1038/nmeth.2089); pmid: [22930834](https://pubmed.ncbi.nlm.nih.gov/22930834/)
45. I. Arganda-Carreras *et al.*, Trainable Weka Segmentation: A machine learning tool for microscopy pixel classification. *Bioinformatics* **33**, 2424–2426 (2017). doi: [10.1093/bioinformatics/btx180](https://doi.org/10.1093/bioinformatics/btx180); pmid: [28369169](https://pubmed.ncbi.nlm.nih.gov/28369169/)
46. A. Pol, D. Ortega, C. Enrich, Identification and distribution of proteins in isolated endosomal fractions of rat liver: Involvement in endocytosis, recycling and transcytosis. *Biochem. J.* **323**, 435–443 (1997). doi: [10.1042/bj3230435](https://doi.org/10.1042/bj3230435); pmid: [9163335](https://pubmed.ncbi.nlm.nih.gov/9163335/)
47. S. Martínez-Bartolomé *et al.*, Properties of average score distributions of SEQUEST: The probability ratio method. *Mol. Cell. Proteomics* **7**, 1135–1145 (2008). doi: [10.1074/mcp.M700239-MCP200](https://doi.org/10.1074/mcp.M700239-MCP200); pmid: [18303013](https://pubmed.ncbi.nlm.nih.gov/18303013/)
48. F. García-Marqués *et al.*, A novel systems-biology algorithm for the analysis of coordinated protein responses using quantitative proteomics. *Mol. Cell. Proteomics* **15**, 1740–1760 (2016). doi: [10.1074/mcp.M115.055905](https://doi.org/10.1074/mcp.M115.055905); pmid: [26893027](https://pubmed.ncbi.nlm.nih.gov/26893027/)

ACKNOWLEDGMENTS

We thank M. Calvo and G. Martín and acknowledge the use of the Advanced Optical Microscopy Facility of the University of Barcelona. We are indebted to C. Ferguson and J. Rae and acknowledge the use of the Australian Microscopy and Microanalysis Research Facility at the Center for Microscopy and Microanalysis at The University of Queensland. We thank J. Murphy (Walter and Elizabeth Hall Institute of Medical Research, Melbourne, Australia) for providing the pF_TRE3G_PGK_puro construct. We are indebted to the Protein Expression Facility (University of Queensland) for valuable assistance. We thank the Australian Red Cross Blood Service for providing buffy coats for the isolation of human monocytes. Last, we are indebted to the Citomics unit of IDIBAPS for their technical help. **Funding:** M.B. acknowledges support from 31/U/2016 from Fundació Marató de TV3. R.K. acknowledges support from an Australian Research Council Discovery Early Career Research Award (DE130100470). B.S. is supported by an Early Postdoc Mobility fellowship from the Swiss National Science Foundation (P2ZHP3_184024). M.J.S. is supported by a National Health and Medical Research Council (NHMRC) Senior Research Fellowship (APP1107914). M.S.-A. was recipient of a CNIC IPP fellowship (COFUND 2014). M.M. is supported by the Instituto de Salud Carlos III (FIS PI19/01410). O.T. is founded by Amgen 2018 Competitive Grant Program. A.P., R.G.P., S.P.G., and P.T.B. have been supported by RGPO020/2015 from the Human Frontier Science Program (HFSF). A.P. is supported by the Ministerio de Ciencia e Innovación (MICINN, RTI2018-098593-B-I00), Fundació

Marató de TV3 (31/U/2016), and the CERCA Programme/ Generalitat de Catalunya. R.G.P. was supported by the NHMRC of Australia (program grant APP1037320 and Senior Principal Research Fellowship 569452), and the Australian Research Council Centre of Excellence in Convergent Bio-Nanoscience and Technology (CE140100036). P.T.B. is supported by Conselho Nacional de Desenvolvimento Científico e Tecnológico (CNPq) of Brazil and Fundação de Amparo a Pesquisa do Estado do Rio de Janeiro (FAPERJ). M.A.D.P. was funded by MICINN (project grants SAF2014-51876-R and SAF2017-83130-R; and IGP-SO grant MINSEV1512-07-2016) and was a Worldwide Cancer Research Foundation grantee (#15-0404). J.V. is supported by MICINN (BIO2015-67580-P) and from the Carlos III Institute of Health-Fondo de Investigación Sanitaria (PRB2, IPT13/0001-ISCIII-SGEFI/FEDER, ProteoRed). The CNIC is supported by the MICINN and the Pro-CNIC Foundation and is a Severo Ochoa Center of Excellence (MICINN award SEV-2015-0505). **Author contributions:** M.B. and M.S.-A. contributed equally. Conceptualization: M.B., P.T.B., S.P.G., R.G.P., and A.P. Methodology: M.B., M.S.-A., and A.F. Formal analysis: M.B., R.G.P., and A.P. Investigation: M.B., M.S.-A., A.F., R.K., B.S., F.D., L.M., M.M., F.M.-P., O.T., A.G., R.M.T., J.E.B.C., C.C., N.M., J.A.L., R.C., and F.T. Resources and supervision: F.L., C.E., M.A.D.P., M.J.S., J.V., P.T.B., S.P.G., R.G.P., and A.P. Data curation: M.B., M.S.-A., F.T., R.G.P., and A.P. Writing (original draft): R.G.P. and A.P. Writing (review and editing): M.B., M.S.-A., M.S., P.T.B., S.P.G., R.G.P., and A.P. Visualization: R.G.P. and A.P. Project administration: P.T.B., S.P.G., R.G.P., and A.P. Funding acquisition: P.T.B., S.P.G., R.G.P., and A.P. **Competing interests:** None declared. **Data and materials availability:** Mass spectrometry data have been deposited in Peptide Atlas (ID: PASS01610). Computer code#1 to measure LD-mitochondria contacts can be found at <https://zenodo.org/badge/latestdoi/280189667>. Computer code#2 to quantify distribution of LD proteins can be found in: <https://zenodo.org/badge/latestdoi/280200243>. All other data are available in the main text or the supplementary materials.

SUPPLEMENTARY MATERIALS

science.sciencemag.org/content/370/6514/eaay8085/suppl/DC1
Materials and Methods
Figs. S1 to S12
Tables S1 to S7

[View/request a protocol for this paper from Bio-protocol.](#)

19 July 2019; resubmitted 29 April 2020
Accepted 21 August 2020
[10.1126/science.aay8085](https://doi.org/10.1126/science.aay8085)

RESEARCH ARTICLE SUMMARY

CELL BIOLOGY

The nucleus acts as a ruler tailoring cell responses to spatial constraints

A. J. Lomakin^{*†‡}, C. J. Cattin[†], D. Cuvelier[§], Z. Alraies[§], M. Molina, G. P. F. Nader, N. Srivastava, P. J. Saez, J. M. Garcia-Arcos, I. Y. Zhitnyak, A. Bhargava, M. K. Driscoll, E. S. Welf, R. Fiolka, R. J. Petrie, N. S. De Silva, J. M. González-Granado, N. Manel, A. M. Lennon-Duménil, D. J. Müller^{*}, M. Piel^{*†}

INTRODUCTION: The human body is a crowded place. This crowding is even more acute when the regulation of cell growth and proliferation fails during the formation of a tumor. Dealing with the lack of space in crowded environments presents cells with a challenge. This is especially true for immune cells, whose task is to patrol tissues, causing them to experience both acute and sustained deformation as they move. Although changes in tissue crowding and associated cell shape alterations have been known by pathologists to be key diagnostic traits of late-stage tumors since the 19th century, the impact of these changes on the biology of cancer and immune cells remains unclear. Moreover, it is not known whether cells can detect and adaptively respond to deformations in densely packed spaces.

RATIONALE: To test the hypothesis that cells possess an ability to detect and respond to environmentally induced changes in their shape, we fabricated artificial microenvironments that mimic the conditions experienced by tumor and immune cells in a crowded tissue. By combining dynamic confinement, force

measurements, and live cell imaging, we were able to quantify cell responses to precisely controlled physical perturbations of their shape.

RESULTS: Our results show that, although cells are surprisingly resistant to compressive forces, they monitor their own shape and develop an active contractile response when deformed below a specific height. Notably, we find that this is achieved by cells monitoring the deformation of their largest internal compartment: the nucleus. We establish that the nucleus provides cells with a precise measure of the extent of their deformation. Once cell compression exceeds the size of the nucleus, it causes the bounding nuclear envelope (NE) to unfold and stretch. The onset of the contractile response occurs when the NE reaches a fully unfolded state. This transition in the mechanical state of the NE and its membranes permits calcium release from internal membrane stores and activates the calcium-dependent phospholipase cPLA2, an enzyme known to operate as a molecular sensor of nuclear membrane tension and a critical regulator of signaling and metabolism. Activated cPLA2

catalyzes the formation of arachidonic acid, an omega-6 fatty acid that, among other processes, potentiates the adenosine triphosphatase activity of myosin II. This induces contractility of the actomyosin cortex, which produces pushing forces to resist physical compression and to rapidly squeeze the cell out of its compressive micro-environment in an “evasion reflex” mechanism.

CONCLUSION: Although the nucleus has traditionally been considered a passive storehouse for genetic material, our work identifies it as an active compartment that rapidly converts mechanical inputs into signaling outputs, with a critical role of its envelope in this sensing function. The nucleus is able to detect environmentally imposed compression and respond to it by generating a signal that is used to change cell behaviors. This phenomenon plays a critical role in ensuring that cells, such as the immune cells within a tumor, can adapt, survive, and efficiently move through a crowded and mechanically heterogeneous micro-environment. Characterizing the full spectrum of signals triggered by nuclear compression has the potential to elucidate mechanisms underlying signaling, epigenetic, and metabolic adaptations of cells to their mechanoenvironment and is thus an exciting avenue for future research. ■

The list of author affiliations is available in the full article online.

*Corresponding author. Email: alexis.lomakin@ccri.at, alexis.lomakin@meduniwien.ac.at (A.J.L.); daniel.mueller@bsse.ethz.ch (D.J.M.); matthieu.piel@curie.fr (M.P.)

†These authors contributed equally to this work.

‡These authors contributed equally to this work.

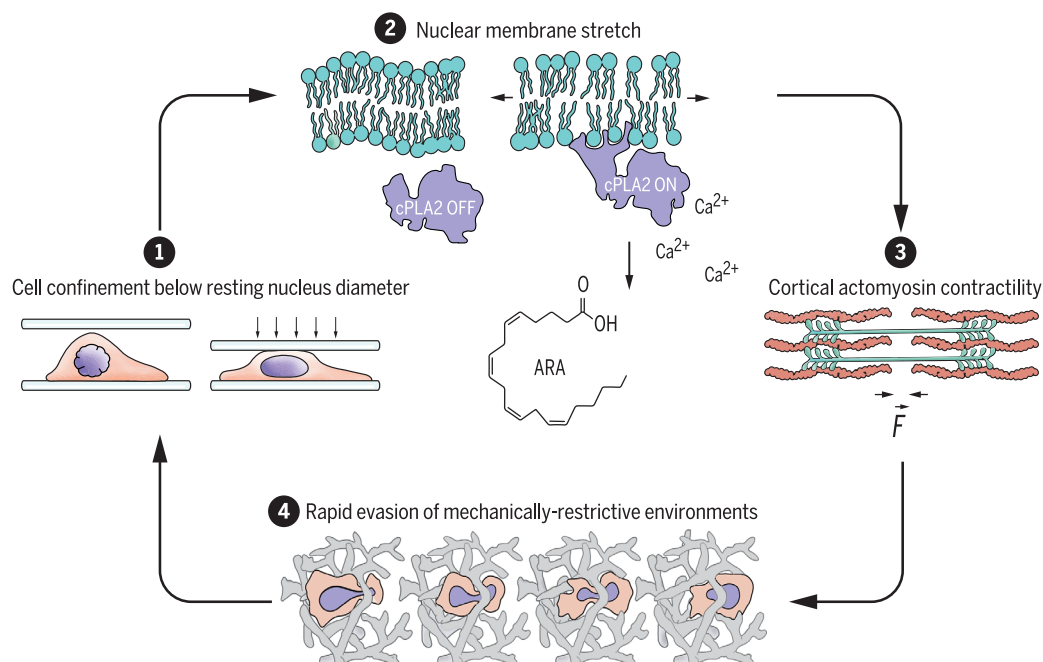
§These authors contributed equally to this work.

Cite this article as A. J. Lomakin et al., *Science* 370, eaba2894 (2020). DOI: 10.1126/science.aba2894

READ THE FULL ARTICLE AT
<https://doi.org/10.1126/science.aba2894>

The nuclear ruler and its contribution to the “life cycle” of a confined cell.

(1) Cell confinement below resting nucleus size, leading to nuclear deformation and to unfolding, and stretching of the nuclear envelope. (2) Nuclear membrane tension increase, which triggers calcium release, cPLA2 activation, and arachidonic acid (ARA) production. (3) Actomyosin force (F) generation. (4) Increased cell migratory capacity and escape from confinement.



RESEARCH ARTICLE

CELL BIOLOGY

The nucleus acts as a ruler tailoring cell responses to spatial constraints

A. J. Lomakin^{1,2,3,4,5,6,*†‡}, C. J. Cattin^{7‡§}, D. Cuvelier^{6,8¶}, Z. Alraies^{6,8,9¶}, M. Molina^{5##}, G. P. F. Nader^{6,8}, N. Srivastava^{6,8}, P. J. Saez^{6,8**}, J. M. Garcia-Arcos^{6,8}, I. Y. Zhitnyak^{6,8,10}, A. Bhargava⁹, M. K. Driscoll^{11,12}, E. S. Weir^{11,12}, R. Fiolka^{11,12}, R. J. Petrie¹³, N. S. De Silva⁹, J. M. González-Granado^{14,15}, N. Manel⁹, A. M. Lennon-Duménil⁹, D. J. Müller^{7*}, M. Piel^{6,8*†}

The microscopic environment inside a metazoan organism is highly crowded. Whether individual cells can tailor their behavior to the limited space remains unclear. In this study, we found that cells measure the degree of spatial confinement by using their largest and stiffest organelle, the nucleus. Cell confinement below a resting nucleus size deforms the nucleus, which expands and stretches its envelope. This activates signaling to the actomyosin cortex via nuclear envelope stretch-sensitive proteins, up-regulating cell contractility. We established that the tailored contractile response constitutes a nuclear ruler–based signaling pathway involved in migratory cell behaviors. Cells rely on the nuclear ruler to modulate the motive force that enables their passage through restrictive pores in complex three-dimensional environments, a process relevant to cancer cell invasion, immune responses, and embryonic development.

Much like modern-day engineered devices, cells in the human body are able to make measurements. For example, epithelial cells in the intestine monitor local cell densities and exit the tissue above a threshold density, preventing hyperplasia (1). Immune cells can estimate the pore size of surrounding tissues to choose the site of least mechanical resistance for migration (2). Epidermal stem cells use the amount of extracellular matrix (ECM) available for cell attachment and spreading as a guidance cue in their cell fate decision-making (3). These

examples illustrate the sensitivity of complex cell behaviors to environmental spatial and mechanical constraints, known in quantitative sciences as boundary conditions (BCs) (4). Although the importance of BCs in cell physiology is increasingly recognized, only a few mechanisms by which cells can measure specific BCs are precisely identified [e.g., the stiffness of the substrate on which cells grow (5) or the geometry of their adhesive environment (6)]. Among the known mechanisms, most are related to either strain (deformation) or stress (forces) and are collectively referred to as mechanotransduction pathways (7).

In this study, we investigated whether cells are also equipped with a mechanism to measure absolute dimensions, which could inform them about distances between neighboring cells or matrix pore size. In our previous study, we discovered that many histologically unrelated cell types change their migratory strategies in response to the specific confinement height (8). This almost universally leads to a long-lasting increase in actomyosin contractility and amoeboid cell propulsion in the absence of specific adhesion to the substrate. Together with similar findings in early zebrafish embryos (9), these observations illustrate the simplest case in which cells measure one of their dimensions to adapt their behavior to local BCs in vitro and in vivo. However, the mechanism underlying this phenomenon remained unknown.

Cells detect their height and trigger contractile responses below a threshold height

To elucidate the mechanism by which cells measure their dimensions, we applied a re-

ductionist approach in which the degree of cell confinement is precisely controlled and paralleled with quantitative microscopy. We confined single nonadherent, initially rounded, interphase cells by using an ion beam-sculpted flat silicon microcantilever (Fig. 1A) mounted on an atomic force microscopy (AFM) setup (10) and simultaneously monitored the actomyosin cytoskeleton dynamics and contractile force generation by employing confocal video-microscopy and AFM-based force spectroscopy.

Using the cell line HeLa-Kyoto (human cervical carcinoma) that expresses MYH9-GFP (myosin IIA), we performed confinement experiments in which the height of the same single cell is changed in a stepwise fashion, starting from 20 μm (average nonconfined cell diameter is $20 \pm 4 \mu\text{m}$, $n = 100$ cells). We found that upon reaching a specific confinement height, cells begin responding by steadily increasing the force with which they push against the confining cantilever (6- to 5- μm confinement in Fig. 1A). Each cell had its own trigger height at which it generated the force response (Fig. 1A, right graph). Most cells remained insensitive to 10- μm confinement (which corresponds to half of the initial cell height; Fig. 1B), whereas almost 100% of analyzed cells displayed the response upon reaching 5- μm confinement (Fig. 1A, right graph). We thus chose to systematically study the response of cells to 5- versus 10- μm confinement height.

Our analyses showed that cell confinement to 5 μm , but not 10 μm , stimulates rapid (2.05 ± 0.33 min, $n = 10$ cells) recruitment of myosin II (hereafter referred to as myosin) from the cytosol to the cortex (Fig. 1, C and D, fig. S1A, and movie S1), followed by cell cortex contraction and force production (Fig. 1E). Both phenomena required myosin activity (Fig. 1, D and E) and culminated in a sustained (up to several hours) and active nonapoptotic plasma membrane (PM) blebbing (movie S2), whose degree is directly proportional to cortical myosin concentration (fig. S1, B to D). Measuring cell blebbing index in several other primary and immortalized cell lines under different confinement heights confirmed the generality of our observations (fig. S1E). To test whether cells would also adapt their cortical actomyosin contractility to the degree of environmental confinement in a context that more closely recapitulates in vivo settings, we examined human fibrosarcoma cells HT1080 infiltrating three-dimensional (3D) cell-derived matrices (CDMs) (Fig. 1F). Cortical recruitment of myosin in these cells linearly scaled with the self-imposed smallest dimension of the cell (Fig. 1F), thus validating our AFM-based observations. Notably, switching cells back to the initial unconfined state in our AFM experiments induced a rapid (3.78 ± 0.94 min, $n = 7$ cells) relocation of myosin to the cytosol (fig. S1F), indicating that persistent contractility required a sustained

¹St. Anna Children's Cancer Research Institute (CCRI), Vienna, Austria. ²Ludwig Boltzmann Institute for Rare and Undiagnosed Diseases (LBI-RUD), Vienna, Austria. ³CeMM Research Center for Molecular Medicine, Austrian Academy of Sciences (ÖAW), Vienna, Austria. ⁴Medical University of Vienna (MUV), Vienna, Austria. ⁵Centre for Stem Cells and Regenerative Medicine, School of Basic and Medical Biosciences, King's College London, London, UK. ⁶Institut Curie, PSL Research University, CNRS, UMR 144, Paris, France. ⁷Department of Biosystems Science and Engineering, ETH Zurich, Basel, Switzerland. ⁸Institut Pierre Gilles de Gennes, PSL Research University, Paris, France. ⁹Institut Curie, PSL Research University, INSERM, U 932, Paris, France. ¹⁰N.N. Blokhin Medical Research Center of Oncology, Moscow, Russia. ¹¹Department of Cell Biology, University of Texas Southwestern Medical Center, Dallas, TX, USA. ¹²Lyda Hill Department of Bioinformatics, University of Texas Southwestern Medical Center, Dallas, TX, USA. ¹³Department of Biology, Drexel University, Philadelphia, PA, USA. ¹⁴LamimSys Lab, Departamento de Fisiología, Facultad de Medicina, Universidad Autónoma de Madrid (UAM), Madrid, Spain. ¹⁵Instituto de Investigación Hospital 12 de Octubre (imas12), Madrid, Spain.

*Corresponding author. Email: alexis.lomakin@ccri.at, alexis.lomakin@meduniwien.ac.at (A.J.L.); daniel.mueller@bse.ethz.ch (D.J.M.); matthieu.piel@curie.fr (M.P.)

†These authors contributed equally to this work.

‡These authors contributed equally to this work.

§Present address: F. Hoffmann-La Roche Ltd., Basel, Switzerland.

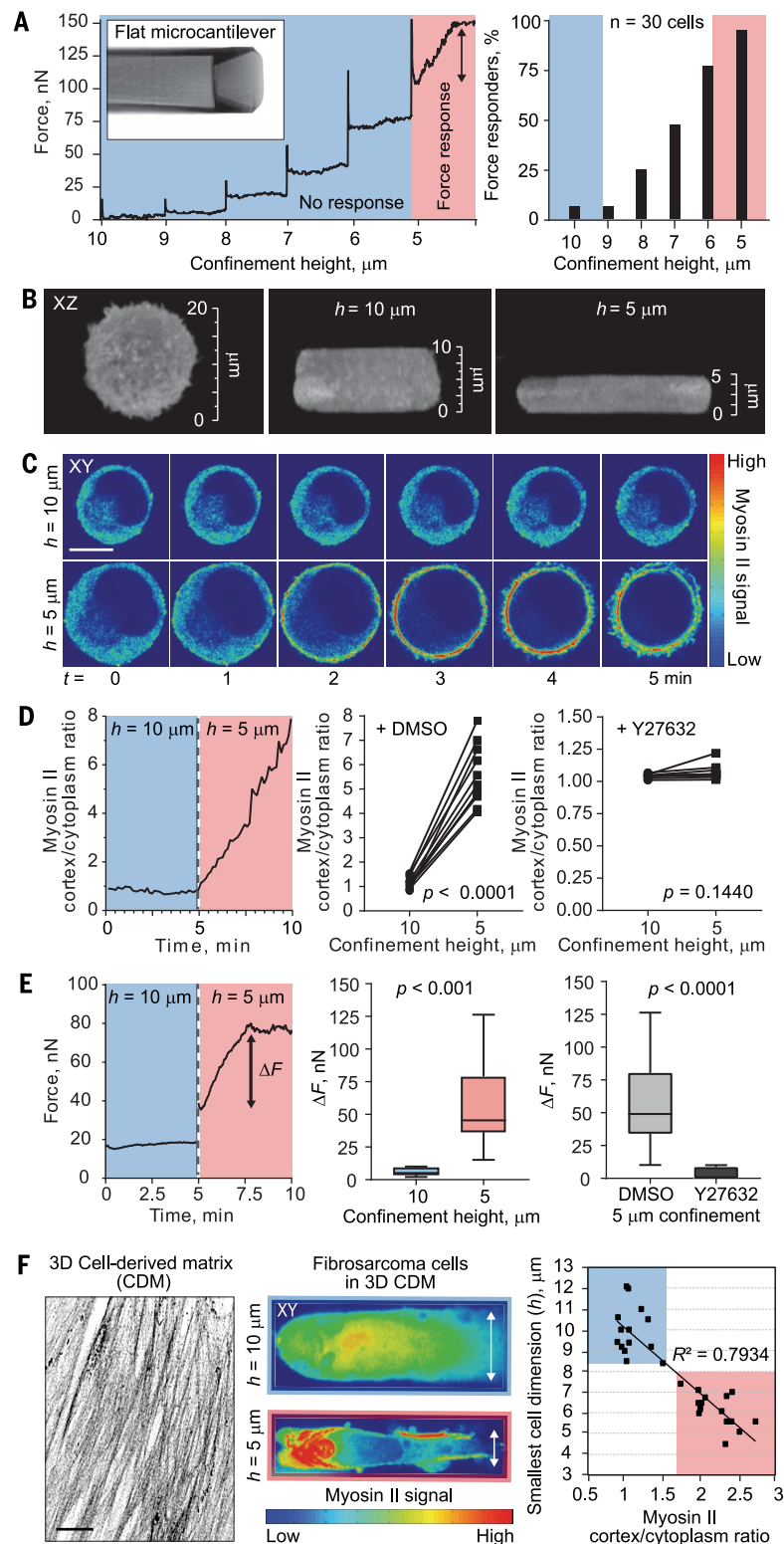
¶These authors contributed equally to this work.

#Present address: Institute for Bioengineering of Catalonia (IBEC), Barcelona Institute of Science and Technology (BIST) and University of Barcelona, Barcelona, Spain.

**Present address: Department of Biochemistry and Molecular Cell Biology, University Medical Center Hamburg-Eppendorf, Hamburg, Germany.

Fig. 1. Cells sense their own height and up-regulate actomyosin contractility at a specific height. (A) (Left)

Representative force curve in response to stepwise (1- μ m increment, 5-min interval) confinement of a cell by the flat microcantilever. (Right) Percentage of cells displaying a sustained force increase (>15 nN) as a function of height. (B) 3D images (xz views) of the same live HeLa-Kyoto cell expressing MYH9-GFP at indicated heights (h). (C) Time-lapse image sequence of the same live cell (xy views; single, midplane, confocal slices) at 10 μ m (top), followed by a height change to 5 μ m (bottom). Scale bar, 10 μ m. (D) (Left) Representative graph of myosin cortex-to-cytoplasm ratio as a function of time in the same live cell upon 10- μ m and subsequently 5- μ m confinement. (Middle and right) The same ratio measured in single live cells at 10- μ m and subsequently 5- μ m confinement in the presence of DMSO or the ROCK inhibitor Y27632 (n = 10 cells per condition; P value, paired t test). Measurements were taken 5 min after application of each confinement height. (E) (Left) Representative force response curve (ΔF , force increase) as a function of time in the same live cell upon 10- μ m and subsequently 5- μ m confinement. (Middle) Statistical analysis of force response (ΔF) in cells at 10 versus 5 μ m. (Right) Statistical analysis of force response (ΔF) to 5- μ m confinement in cells treated with DMSO or Y27632. Measurements were taken 5 min after application of the confinement. Data are from ≥ 2 experiments (mean \pm SD; n = 10 cells per condition; P value, unpaired t test). (F) (Left) Representative image of 3D dermal fibroblast CDM stained with a collagen I antibody. (Middle and right) The same ratio measured in single live cells at 10- μ m and subsequently 5- μ m confinement in the presence of DMSO or the ROCK inhibitor Y27632 (n = 10 cells per condition; P value, paired t test). Measurements were taken 5 min after application of each confinement height. (E) (Left) Representative force response curve (ΔF , force increase) as a function of time in the same live cell upon 10- μ m and subsequently 5- μ m confinement. (Middle) Statistical analysis of force response (ΔF) in cells at 10 versus 5 μ m. (Right) Statistical analysis of force response (ΔF) to 5- μ m confinement in cells treated with DMSO or Y27632. Measurements were taken 5 min after application of the confinement. Data are from ≥ 2 experiments (mean \pm SD; n = 10 cells per condition; P value, unpaired t test). (F) (Left) Representative image of 3D dermal fibroblast CDM stained with a collagen I antibody. (Middle and right) The same ratio measured in single live cells at 10- μ m and subsequently 5- μ m confinement in the presence of DMSO or the ROCK inhibitor Y27632 (n = 10 cells per condition; P value, paired t test). Measurements were taken 5 min after application of each confinement height.



confinement below the threshold height. Collectively, these experiments showed that single cells can sense the difference between 10 and 5 μ m and can trigger a sustained, yet reversible, active contractile response at a specific height.

Cell height-specific contractile responses depend on nuclear envelope- and/or endoplasmic reticulum-mediated signals

We next performed experiments to narrow the range of potential mechanisms involved in this height-dependent contractile response.

Confinement experiments on adherent, well-spread cells showed qualitatively the same threshold-like response as we established for rounded nonadherent cells (fig. S2, A to C). Moreover, experimental manipulations of extracellular $[Ca^{2+}]$ or $[Mn^{2+}]$ to modulate

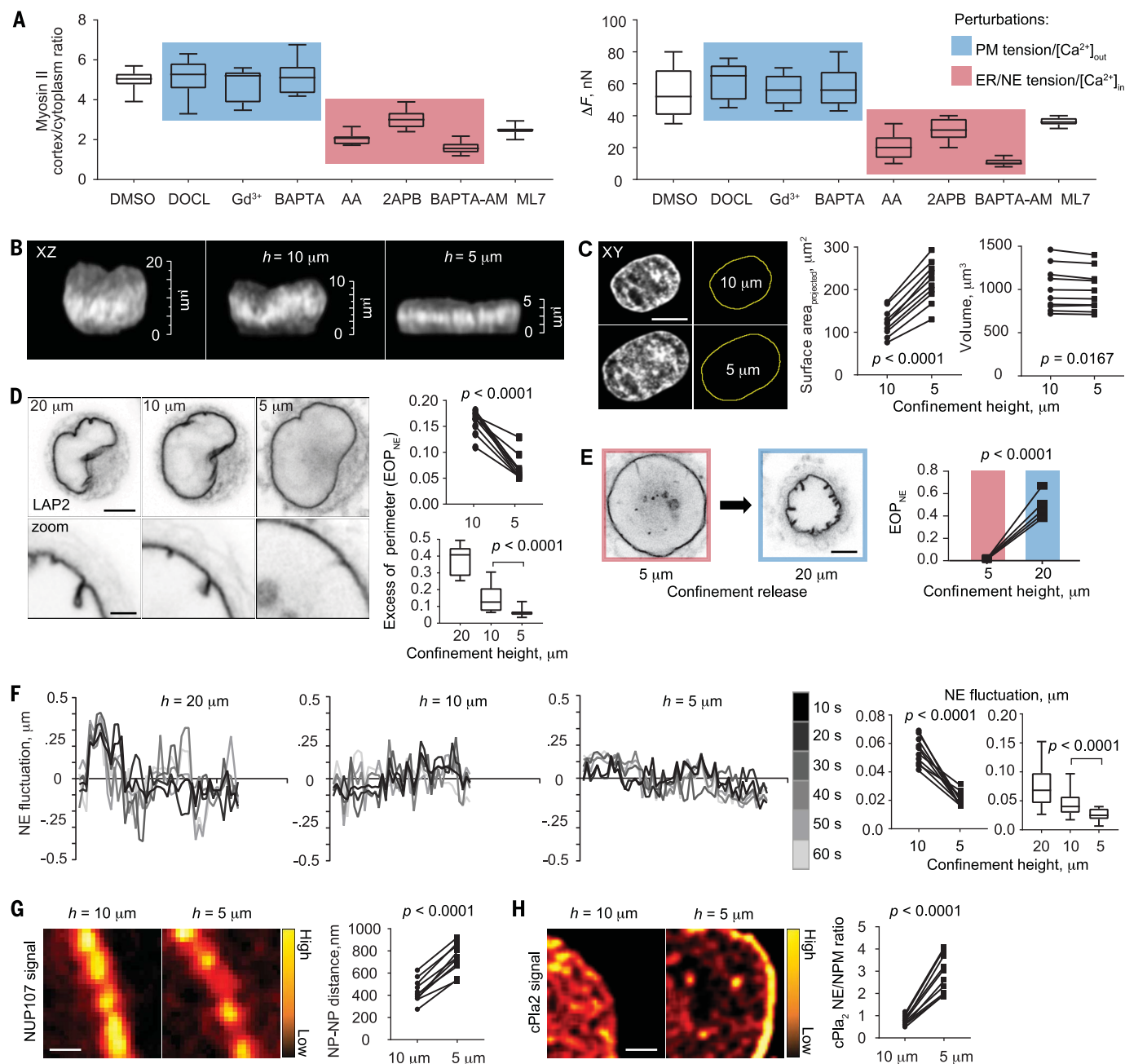


Fig. 2. The height-specific contractile response is controlled by mechanisms associated with nuclear-ER membrane stretch. (A) Cortical myosin levels (left) and force response (ΔF ; right) to 5- μm confinement of HeLa-Kyoto cells treated with drugs affecting PM tension and extracellular $[\text{Ca}^{2+}]_{\text{out}}$ (blue) or ER-NE tension and intracellular $[\text{Ca}^{2+}]_{\text{in}}$ (red). See table S1 for drug target description and materials and methods for drug concentrations. Data are from ≥ 2 experiments (mean \pm SD; $n = 10$ cells per perturbation; see table S2 for statistics). (B) 3D xz views of the DAPI-stained nucleus at 20, 10, and 5 μm . (C) (Left) xy views of the nucleus at 10 and 5 μm . (Middle and right) Measurements of nuclear area and volume at 10 and subsequently 5 μm ($n = 10$ cells; P value, paired t test). Scale bar, 10 μm . (D) (Left top) Images of the LAP2-GFP-labeled NE confined to 20, 10, and 5 μm . Scale bar, 5 μm . (Left bottom) Zoomed-in view of a gradually opening nuclear fold. Scale bar, 2.5 μm . (Right) EOP_{NE} at 10 μm and subsequently 5 μm (upper

graph, $n = 10$ different cells; P value, paired t test) and statistics of EOP_{NE} in cell populations at 20, 10, and 5 μm (lower graph, data are from ≥ 2 experiments; mean \pm SD; $n = 30$ cells per height; P value, unpaired t test). (E) Images of the LAP2-GFP-labeled NE and EOP_{NE} quantifications in live cells confined to 5 μm and unconfined to 20 μm ($n = 10$ cells; P value, paired t test). Scale bar, 5 μm . (F) NE fluctuation curves at various confinement heights (h) and quantifications of NE fluctuations at 10 and subsequently 5 μm ($n = 10$ cells; P value, paired t test) or in cell populations at 20, 10, and 5 μm (mean \pm SD; $n = 30$ cells per height; P value, unpaired t test). (G) Images of NUP107-GFP-labeled nuclear pores (NPs) and quantification of inter-NP (NP-NP) distance at 10 and subsequently 5 μm ($n = 10$ cells; P value, paired t test). Scale bar, 0.5 μm . (H) Images of nuclear cPlax2-mKate2 signal and quantification of its NE-to-nucleoplasm (NE/NPM) ratio at 10 and subsequently 5 μm ($n = 10$ cells; P value, paired t test). Scale bar, 1.5 μm .

engagement of integrins during cell contact with the surface of the confining cantilever (11) did not affect the response in nonadherent suspended cells (fig. S2D). This suggested that the sensing mechanism does not depend on classical integrin-based mechanotransduction pathways. The sustained increase in contractility (fig. S1D), and the fact that the response was dependent on the confinement height per se rather than the speed of confinement (fig. S3), renders unlikely a signal originating from strain in the actin cortex or the PM, because these structures dissipate stress in minutes as a result of fast turnover (12). A natural candidate that matches the range of relevant confinement heights at which the response is triggered and that can display long-term stress due to slow turnover of its stiff elastic shell is

the cell nucleus (13). Indeed, the nucleus, and more specifically its envelope, has been shown in the recent years to trigger diverse cell responses when the nuclear compartment is deformed: entry of the transcription factors YAP/TAZ (14), activation of the ATR kinase (15), release of calcium (16), activation of the calcium-dependent phospholipase cPLA2 (17), and nuclear envelope (NE) rupture accompanied by DNA damage (18). Considering that the response to confinement was reversible and required only a few minutes for its manifestation, potential changes at the level of cell transcription and translation are not likely, and we confirmed this experimentally by acutely inhibiting the processes of transcription and translation (fig. S4A). Blocking the ATR kinase activity did not yield a pheno-

type either (fig. S4B). Moreover, ruptures of neither the NE nor the PM were observed at 5- μm confinement (fig. S4, C and D), excluding a mechanism based on an extracellular signal influx through transient holes in the PM or mixing of cytoplasmic and nuclear contents.

We thus performed a small pharmacological inhibitors screen, targeting mechanotransductive pathways compatible with a cellular confinement response on a time scale of minutes (table S1). The screen (Fig. 2A and table S2) showed that extracellular calcium, PM-associated stretch-sensitive channels, and PM tension are not involved in the response to confinement. However, intracellular calcium, intracellular stretch-sensitive calcium channels associated with the perinuclear endoplasmic reticulum (ER), the calcium-dependent myosin light chain

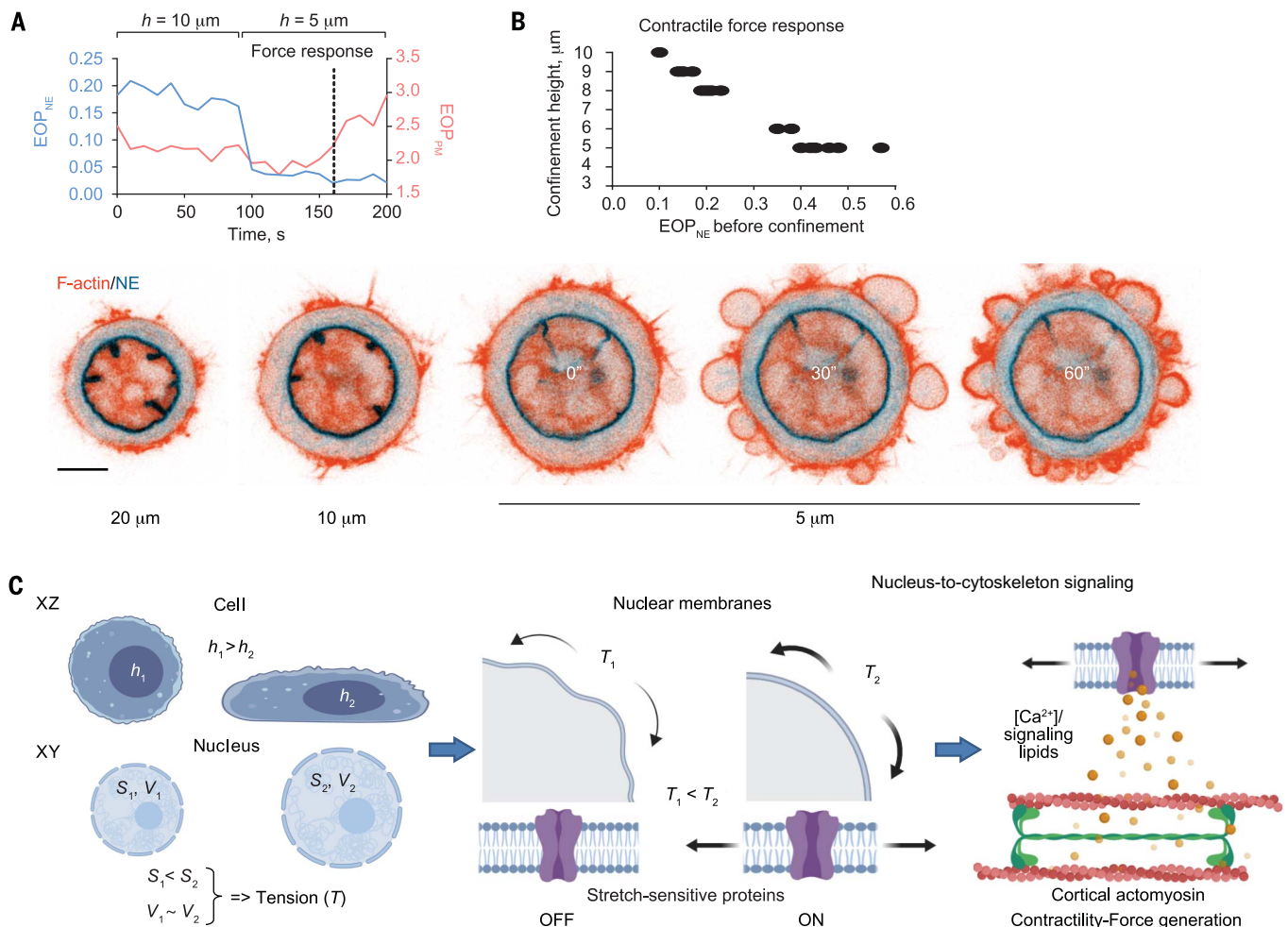


Fig. 3. The nuclear ruler working model. (A) (Top) Representative graph of temporal evolution of NE unfolding (EOP_{NE}, blue) and PM blebbing (EOP_{PM}, red). (Bottom) Time-lapse image sequence of the LAP2-GFP-labeled NE (blue) and Lifeact-mCherry-labeled F-actin (red) in the same live cell responding to the sequential confinement to 20, 10, and 5 μm . Scale bar, 5 μm . (B) Height for the onset of contractile force response as a function of the degree of NE folding (EOP_{NE}) before confinement ($n = 20$ cells).

(C) Sketch of the working model: Cells use the nucleus as an internal ruler for their height. When a cell deforms below the resting height (h_1) of its nucleus, the nuclear surface area (S) increases while the nuclear volume (V) remains constant. At a critical height (h_2), the NE fully expands and gets stretched increasing its tension (T). The increase in NE tension stimulates stretch-sensitive proteins whose activity promotes and/or reinforces cortical actomyosin contractility.

kinase MLCK, and the NE tension sensor cPLA2 were required for the contractile response, pointing to a signal emanating from the perinuclear ER and/or the NE to activate actomyosin contraction at a specific confinement height. Consistently, imaging of intracellular calcium with the GCaMP6 calcium biosensor revealed a strong increase in cytosolic calcium upon 5- μm confinement (fig. S5A), which was inhibited by blocking intracellular stretch-sensitive calcium channels InsP3Rs with 2APB (fig. S5B), but not via chelation of extracellular calcium with BAPTA (fig. S5A). Conversely, adding ionomycin (to artificially increase cytosolic calcium concentration) or the signaling lipid arachidonic acid (ARA) [an omega-6 fatty acid that can be produced in a NE stretch-sensitive manner via enzymatic activity of cPLA2 on nuclear membranes (17)] to cells confined to 10 μm induced persistent blebbing without further confinement (fig. S5C). Finally, analysis of the supernatant of a population of confined cells (using a microfabricated confinement device; see materials and methods) showed an increase in ARA production upon 5- μm confinement, which is lost upon cPLA2 inhibition with AACOCF3/AA (fig. S5D). Notably, unlike Y27632, which globally perturbed basal cell contractility at both 10 and 5 μm , the drugs yielding a phenotype in our mini-screen exerted their effect only at 5 μm , as follows from our measurements of cortical cell tension, cell pressure, and myosin cortex-to-cytosol ratio at 10 μm (fig. S5E). This indicated that the targets of the drugs become functionally engaged in a trigger-like fashion when the cell is confined below 10 μm . These results, together with the controls for drugs activity (fig. S5F), suggested that the nuclear membrane compartment, continuous with the perinuclear ER, might be involved in measuring the cell dimensions and triggering the contractile response below a specific confinement height.

The trigger height for contractile cell responses is determined by NE tension

To understand how the NE-perinuclear ER and associated signaling pathways could be engaged in triggering the sustained contractile response of cells to a specific confinement height, we decided to characterize nuclear shape and deformation state at 20-, 10-, and 5- μm confinement (Fig. 2B). We observed that the nuclear volume undergoes only very minor changes, whereas projected surface area of the nucleus increases substantially between 10- and 5- μm confinement (Fig. 2C), suggesting a potential expansion of the NE. Indeed, we found that the NE in rounded nonadherent cells displays large folds and wrinkles, which become less prominent at 10 μm and completely disappear at 5 μm (Fig. 2D). To characterize this phenomenon quantitatively, we estimated the NE folding index by measuring

the excess of the perimeter of the NE (EOP_{NE}) in the same single cell at various heights or by statistically comparing this parameter across populations of cells confined to a specific height. We found that EOP_{NE} decreases as cells get more confined [Fig. 2D; we also confirmed this result with an additional metric: standard deviation of the local curvature along the NE perimeter (fig. S5G)]. Unconfining cells led to a rapid refolding of the envelope, concomitant with the loss of the contractile response (Fig. 2E). These measurements suggested that within the range of confinement heights applied in our experiments, the nucleus maintains a constant volume by progressively unfolding its envelope until it reaches a fully unfolded state at 5 μm . A higher degree of confinement and more severe nuclear compression result in a substantial loss of nuclear volume [reported previously on the basis of micropipette aspiration experiments (19)] and, eventually, NE

rupture events that become predominant below 3- μm confinement height (20).

As the NE fully unfolds, it is likely to reach a state in which it stretches and becomes tensed. To estimate this parameter, we first measured the thermally and actively driven fluctuations of the NE on the time scale of seconds [see materials and methods and (21)]. We found that the amplitude of the fluctuations systematically decreases as cells get more confined (Fig. 2F), consistent with an increase in the NE tension. Imaging nuclear pores in the NE of the same cell at various heights showed that confinement from 10 to 5 μm causes neighboring nuclear pores to become more distant from each other, consistent with a stretching of the NE (Fig. 2G). Finally, we observed that the mKate2-tagged phospholipase cPla2, sensing lipid crowding in the NE (17), remains in the nucleoplasm at 10 μm but relocalizes to the NE at 5 μm

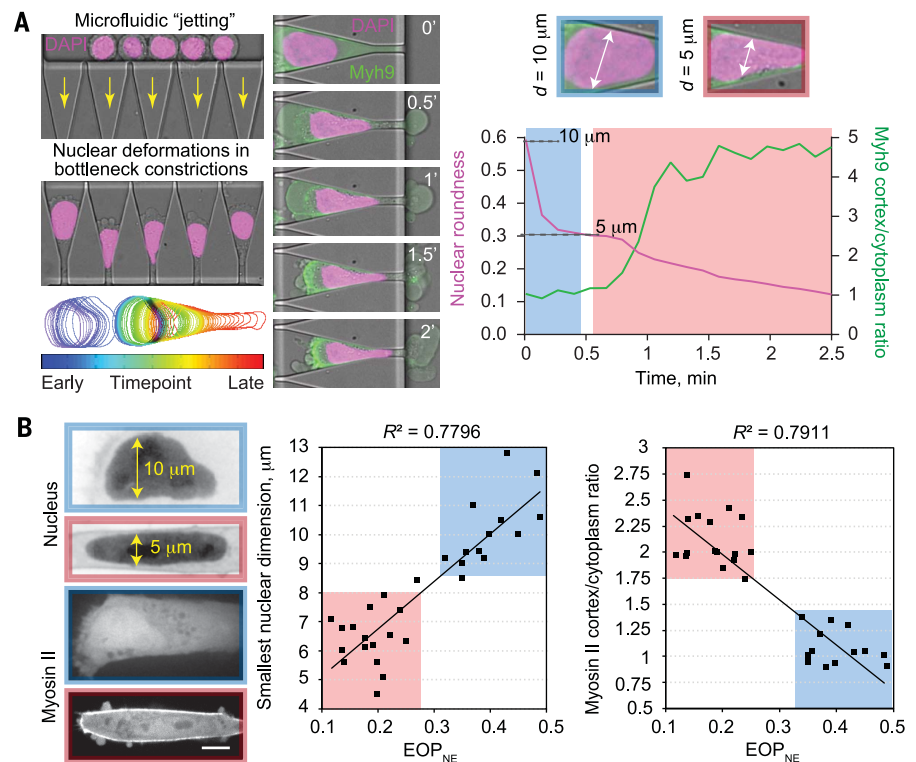


Fig. 4. Correlation between nuclear stretching and cortical recruitment of myosin in experimentally deformed and spontaneously moving cells. (A) (Left) Representative images of DAPI-stained (magenta) HeLa-Kyoto cells microfluidically pushed into bottleneck PDMS constrictions. Color-coded nuclear outlines at different time points for a cell pushed into the constriction are shown at the bottom. (Middle) Representative image sequence of the nucleus (magenta) and MYH9-GFP-labeled myosin (green) in a live cell pushed into the constriction. (Right top and bottom) Images of the nucleus inside the bottleneck constriction reaching roundness equivalent to 10- and 5- μm confinement heights, and graph of the nuclear roundness index (magenta) and myosin cortical recruitment (green) in time representative of $n = 30$ cells. **(B)** (Left) Representative images (xy views, single confocal slices) of RFP-NLS-labeled nuclei (top) and GFP-MLC2-labeled myosin in HT1080 cells within 3D CDM. (Middle) Smallest nuclear dimension plotted against corresponding values of EOP_{NE} . (Right) Myosin cortex-to-cytoplasm ratio plotted against corresponding values of EOP_{NE} ($n = 30$ cells). Scale bar, 5 μm .

(Fig. 2H), a transition previously shown to be triggered by nuclear membrane tension increase and to correspond with cPLA2 enzyme activation (17). Overall, these observations suggested that confinement to 5 μm stretches the NE.

To assess whether the height threshold at which cells display the active contractile response coincides with the induction of NE stretching, we took advantage of the variety of nuclear shapes and folding states in the cell population and systematically investigated these parameters along with contractile force and cell morphology readouts. First, correlative recording of F-actin and the NE (Fig. 3A, bottom images) enabled us to observe that NE unfolding temporally precedes the onset of the contractile response (Fig. 3A, top graph, and movie S3), with a delay of 38 ± 17 s ($n = 20$ cells). This is compatible with a causal link between the NE unfolding-stretching and the onset of a sustained contractile response. Second, we found that cells with more folded nuclei before confinement (larger EOP_{NE}) start to contract at a lower confinement height (Fig. 3B), indicating that the degree of NE folding sets the sensitivity threshold for the ability of cells to discriminate between different confinement heights.

Because we used cultured proliferating cells in our experiments, a source of cell-to-cell variability in responses to confinement could come from the cell cycle stage, which introduces a natural range of NE states in a cell population (27). Therefore, we decided to test a FUCCI HeLa cell line expressing

fluorescent cell cycle stage markers in our confinement experiments. We determined that unconfined G_1 cells have significantly higher values of EOP_{NE} than G_2 cells (fig. S5H). Whereas the unconfined cell height and mechanical state (basal cortical tension and cell pressure) at 10- μm confinement were similar for rounded, nonadherent G_1 and G_2 cells (fig. S5H), G_2 cells required less confinement than G_1 cells to trigger the contractile response (fig. S5H, bottom right graph). This result further confirmed that the state and size of the nucleus defines a ruler to trigger the active contractile cell response. It also suggested that the nuclear ruler might render proliferating cells more or less sensitive to deformations, depending on their cell cycle stage.

The nuclear ruler working model

Collectively, our results suggested the following working model (Fig. 3C): Each single cell in the rounded state has a certain nuclear volume and an excess of NE surface area stored in NE folds. When one of the dimensions of the cell is reduced below the resting nuclear diameter, the nucleus deforms and its envelope unfolds. Once the NE reaches full unfolding, it stretches, potentially together with the perinuclear ER, leading to calcium release from internal stores and cPLA2 relocalization onto the stretched NE, followed by cPLA2 enzyme activation and production of ARA. Both calcium ions and ARA are classical second messenger molecules with a well-known stimulatory effect on actomyosin contractility (22–24), thus

mechanistically linking cell height to cell contractility. Consistent with this model, the correlative live recording of cPLA2-mKate2, calcium (GCaMP6-EGFP), and forces during cell height change from 10 to 5 μm and show relocalization of cPLA2 within 20 s and intracellular calcium increase within less than 1 min, both phenomena preceding the contractile response of the cell (fig. S5I).

A first direct prediction of the nuclear ruler model is that as cells start squeezing through a tissue opening with a size smaller than a resting nuclear diameter, they should deform, unfold, and stretch their nuclei. This activity would lead to an increase in cortical myosin concentration. To test this prediction in a controlled and quantitative manner, we microfluidically flowed HeLa cells through microchannels with bottleneck constrictions. We found that nuclear deformations reflected in changes of the nuclear roundness index precede myosin accumulation at the cortex and that this takes place when the nuclear diameter is changed to ~ 5 μm , but not 10 μm (Fig. 4A). To examine whether these dependencies can be observed in spontaneously migrating cells in a more physiological context, we looked at invasive HT1080 cells maneuvering through a 3D CDM. By plotting myosin cortical accumulation against the PM excess of perimeter (i.e., cell blebbing and thus contractility measure), we verified that our measure of myosin recruitment at the cell cortex is a good predictor of the degree of cell contractility in 3D (fig. S6). This parameter scaled with the extent of

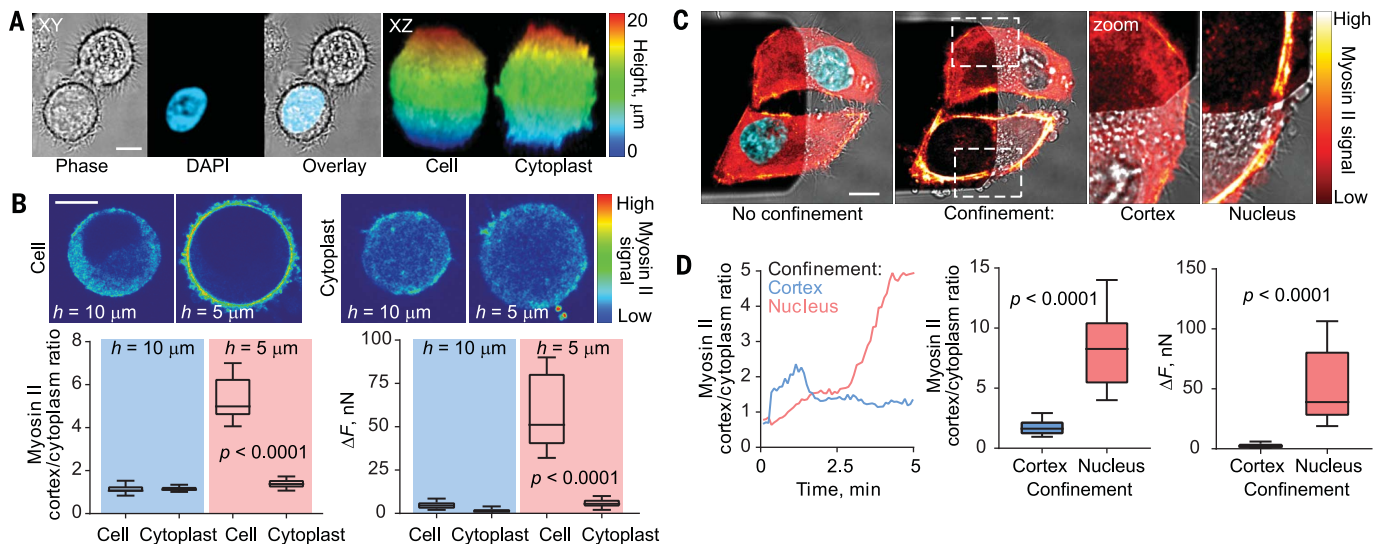


Fig. 5. Enucleated cells and cells regiospecifically confined to avoid the nucleus do not trigger contractile responses at relevant heights. (A) (Left) Representative images (xy views) of a nucleated [DAPI (blue)-positive] cell and an enucleated (DAPI-negative) cytoplasm. (Right) xz views of a cell and a cytoplasm of similar height representative of those selected for analyses. Scale bar, 5 μm . (B) Images (top) and quantifications (bottom) of myosin cortical accumulation (left) and force response (ΔF , right) in cells ($n = 10$) and cytoplasts ($n = 10$) confined to

10 versus 5 μm . Data are from ≥ 2 experiments; mean \pm SD; P value, unpaired t test. Scale bar, 10 μm . (C) Regiospecific confinement of the nuclear region (lower cell) versus the nucleus-free lamella (upper cell). Cyan, DAPI nuclear stain; Red hot, myosin signal; Dashed squares, zoomed regions (right images). Scale bar, 10 μm . (D) Quantifications of myosin cortical accumulation and force response (ΔF) upon nuclear ($n = 10$) and lamellar cortex ($n = 10$) confinement. Data are from ≥ 2 experiments; mean \pm SD; P value, unpaired t test.

nuclear surface folding, which in turn was dependent on the smallest nuclear dimension (Fig. 4B). These data showed that both imposed and spontaneous nuclear deformations observed in migrating cells correlate with the contractile response, suggesting that the nuclear ruler could be relevant in physiological contexts such as cells circulating in blood capillaries or migrating through dense tissues.

Cells without the nucleus show defective contractile responses to spatial confinement

A second prediction of our working model is that removing the cell nucleus should affect the contractile response to confinement. We thus produced cytoplasts by cell enucleation using centrifugation (25). This resulted in a mixed population of enucleated cytoplasts and nucleated cells (Fig. 5A). Cytoplasts, on average, had a smaller volume than nucleated cells (fig. S7A) but a rather similar height (cell volume scales to the cubic root of cell diameter). Thus, we were able to compare nucleated cells and enucleated cytoplasts of similar initial heights confined to 10 and 5 μm . Whereas nucleated cells showed the expected contractile response at 5 μm , this was not the case for enucleated cytoplasts (Fig. 5B and movie S4). Cytoplasts were not deficient in the contractile response pathway, because confining them further to 1 μm triggered both a force response and myosin recruitment at the cortex (fig. S7B), although to a significantly lesser extent than nucleated cells at 5 μm . Moreover, although the response of cytoplasts was reduced upon treatment with 2APB inhibiting

calcium release from internal stores, it was not affected by treatment with the cPLA2 inhibitor AACOCF3 (fig. S7B). This suggested that the pathway triggered at 1 μm in cytoplasts could be different from that activated in nucleated cells at 5 μm . Such pathway might involve direct compression of other endomembranes [e.g., the ER that remained present in enucleated cytoplasts (fig. S7C)].

To further demonstrate the difference in responsiveness to confinement provided by the nucleus versus the rest of the cell, we used spread nucleated cells and took advantage of the small size of the wedged cantilever tip to apply a local deformation on the cell (Fig. 5C). This experiment showed that locally compressing the cell cortex in the lamellar region, even down to <1 μm (fig. S8 and movie S5), produces only a very transient response, whereas confining the part of the cell that contains the nucleus results in a sustained contractile response (Fig. 5D and movie S6). Upon nuclear deformation, myosin cortical recruitment occurred even in the region that was not directly confined (Fig. 5D). This showed that the contractile response is not due to the cell deformation per se, but rather to a signal that could get released locally and propagate away from the nucleus (indeed, the increase in contractility in the nonconfined part manifested with a slight delay compared with that in the nuclear region; movie S6). In conclusion, consistent with our working model, the nucleus is required to set the size at which the contractile response is triggered, and the

deformation of nuclear or nucleus-associated compartments is necessary to trigger the sustained response.

Cells with altered NE properties have a defective nuclear ruler

We further tested the nuclear ruler model by affecting the stiffness and the folded state of the NE. Lamin A/C-depleted cells (fig. S9A) displayed nuclear dysmorphia and a floppier (Fig. 6A) but did not undergo excessive cell death, even upon confinement to 5- μm height (fig. S9B), at which the depleted cells also show a high rate of NE ruptures (Fig. 6A, bottom left graph). This mechanical instability of the NE, together with the modifications of NE viscoelastic properties upon lamin A/C depletion, could contribute to the relaxation of tension in the envelope. Although volume, projected area (fig. S9C), and surface folding (fig. S9D) of lamin A/C-depleted nuclei were not significantly affected, we found that NE fluctuations in the depleted cells did not decrease in response to 20-, 10-, and 5- μm confinement (Fig. 6A, top right graph), in contrast to control cells (Fig. 2F). This suggested that the envelope of depleted nuclei remained floppy at all confinement heights. Confinement of depleted cells to 5 μm did not trigger intracellular calcium release, nor did it increase levels of ARA production (fig. S9E, “5 μm confinement” subpanel). Consistently, although their basal mechanics were unaltered at 10 μm (fig. S9E, “10 μm confinement” subpanel), the depleted cells displayed an attenuated contractile response at 5- μm confinement (Fig. 6A, bottom right graph, and fig. S9F). This finding is consistent with the nuclear ruler model and further suggests that the level of lamin A/C, which varies considerably in different cell types and environmental conditions, can modulate the response of cells to spatial confinement by affecting the mechanical properties of the NE.

The inner nuclear membrane and ER membrane protein lamin B receptor (LBR) is known to control NE folding in a dose-dependent manner (26). Its overexpression leads to perinuclear ER expansion and overproduction of NE membranes, which in turn provides additional NE surface area to accommodate excess membrane protein (27, 28). Indeed, our measurements of nuclear surface folding showed that LBR-GFP overexpressing (OE) cells have a highly folded nucleus and fail to unfold it in response to 5- μm confinement, in contrast to LAP2/LAP2b-expressing (control) cells (Fig. 6B, images and top graph, and fig. S9G). Consistently, LBR overexpression abrogated both cytoplasmic calcium increase and levels of ARA production at 5 μm (fig. S9H, “5 μm confinement” subpanel). Although their basal cortical mechanics were unaltered at 10 μm (fig. S9H, “10 μm confinement” subpanel), LBR-GFP OE cells significantly impaired contractile responses

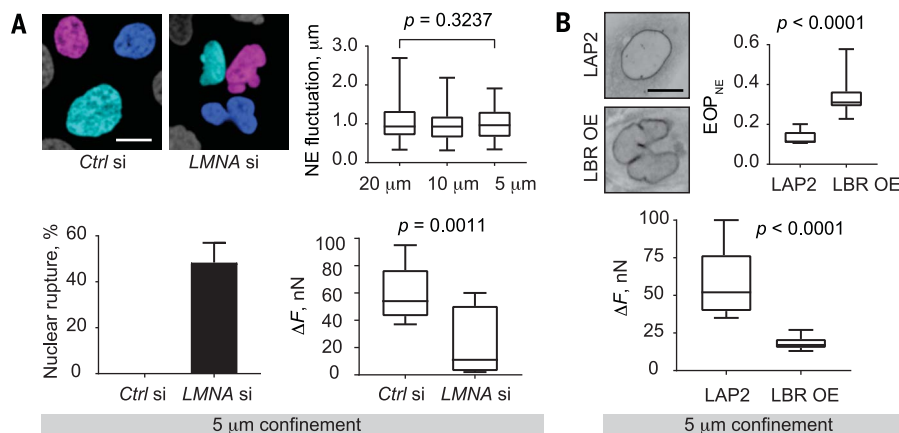


Fig. 6. The nuclear ruler is defective in cells with altered NE properties. (A) (Top left) Representative images of DAPI-stained nuclei in HeLa-Kyoto cells treated with control or *LMNA* siRNA. (Top right) Quantifications of NE fluctuations in *LMNA* siRNA-treated cells under 20-, 10-, and 5- μm confinement (data are from ≥ 2 experiments; mean \pm SD; $n = 20$ cells per height; P value, unpaired t test). (Bottom left) Percentage of cells displaying nuclear rupture at 5 μm . Data are from ≥ 2 experiments; $n = 15$ cells per condition. (Bottom right) Force response (ΔF) to 5- μm confinement. Data are from ≥ 2 experiments; mean \pm SD; $n = 10$ (Ctrl si) and 15 (*LMNA* si) cells; P value, unpaired t test. Scale bar, 10 μm . (B) (Top) Representative images of NE in HeLa-Kyoto cells stably expressing LAP2-GFP or ectopically overexpressing (OE) LBR-GFP and corresponding EOP_{NE} quantifications. Data are from ≥ 2 experiments; mean \pm SD; $n = 10$ cells per condition; P value, unpaired t test). (Bottom) Force response (ΔF) to 5- μm confinement. Data are from ≥ 2 experiments; mean \pm SD; $n = 10$ (LAP2) and 15 (LBR OE) cells; P value, unpaired t test. Scale bar, 10 μm .

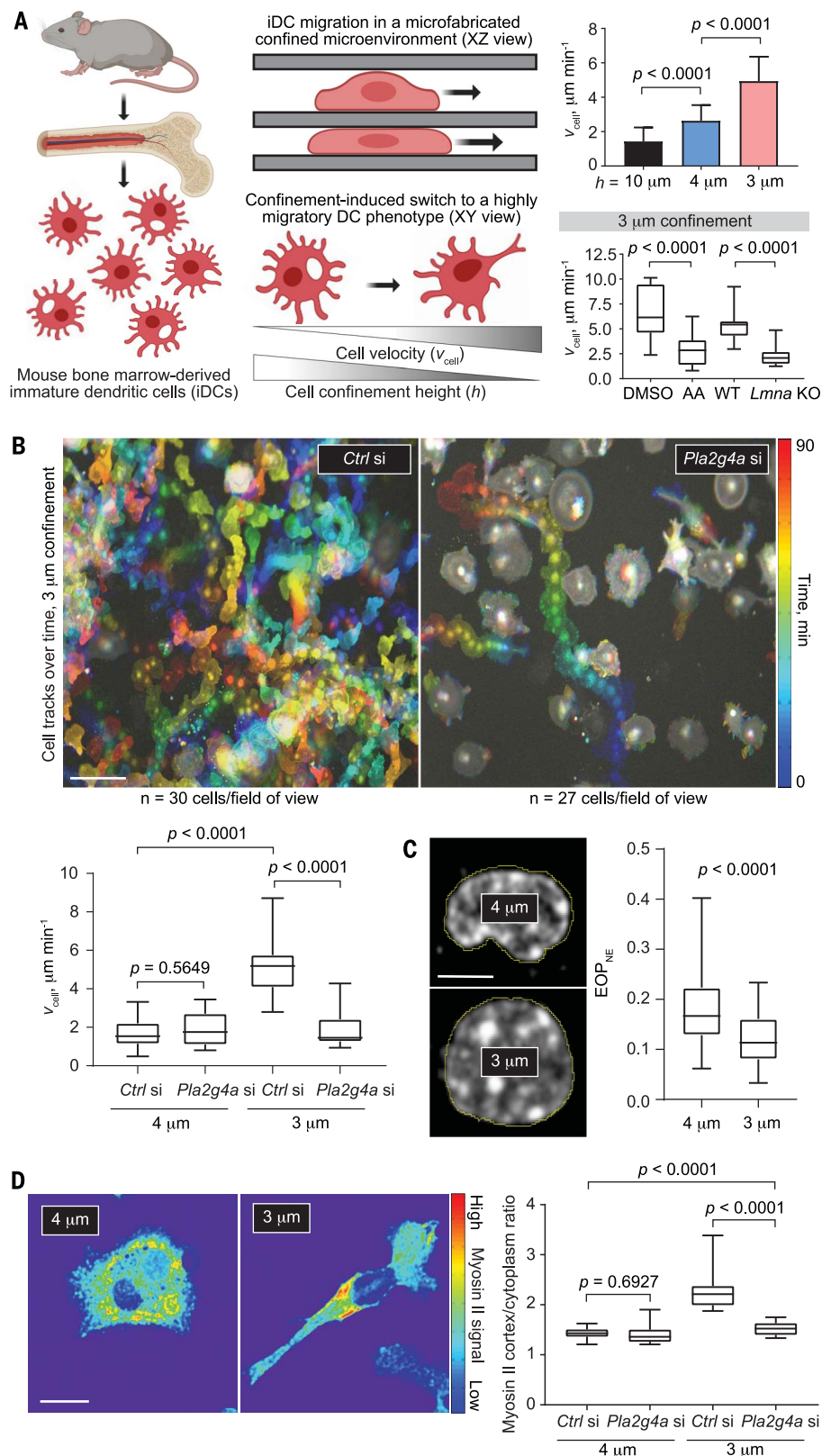
Fig. 7. The nuclear ruler function in immune

cell migration. (A) (Left and middle) Cartoons illustrating primary culture of iDCs and their confinement between two parallel surfaces inducing a highly migratory DC phenotype.

(Right top) iDC velocity measured at 10- μ m ($n = 20$ cells), 4- μ m ($n = 35$ cells), and 3- μ m ($n = 35$ cells) confinement height (h). (Right bottom) Cell velocity (v_{cell}) measured at 3- μ m confinement in control [DMSO and wild-type (WT)] versus cPLA2-inhibited (AACOCF3/AA treatment) or *Lmna* knockout (KO) cells ($n = 20$ cells per condition). Data are from ≥ 2 experiments; mean \pm SD; P value, unpaired t test. **(B)** (Top) Temporal color-coded cell tracks from a representative time-lapse movie of control (*Ctrl* si) and cPLA2a-depleted (*Pla2g4a* si) LifeAct-GFP-expressing iDCs under 3- μ m confinement.

(Bottom) Statistical analysis of cell velocity (v_{cell}) for control and depleted cells at 4- versus 3- μm confinement. Data are from ≥ 2 experiments; mean \pm SD; $n = 20$ cells per condition; P value, unpaired t test. Scale bar, 50 μm . **(C)** Representative images of DAPI-stained nuclei (xy view, single confocal slices) and EOP_{NE} quantifications in iDCs at 4- versus 3- μm confinement. Data are from ≥ 2 experiments; mean \pm SD; $n = 35$ cells per condition; P value, unpaired t test.

Scale bar, 5 μm . **(D)** Representative images and quantifications of myosin cortical accumulation in control (*Ctrl* si) and cPLA2a-depleted (*Pla2g4a* si) MYH9-GFP-expressing iDCs at 4- and 3- μm confinement. Data are from ≥ 2 experiments; mean \pm SD; $n = 20$ cells per condition; P value, unpaired t test. Scale bar, 15 μm .



to 5- μm confinement (Fig. 6B, bottom graph, and fig. S9I). Therefore, we concluded that NE folding and unfolding constitutes a key element of the nuclear ruler mechanism. These findings further suggested that modulation of NE com-

ponents that affect the extent of NE folding [e.g., LBR and SUN2 (29)] could allow different cell types to trigger responses to various levels of confinement or to measure different ranges of sizes, depending on their function.

The nuclear ruler participates in adaptive modulation of cell propulsion during confined migration

We hypothesized that the nuclear ruler mechanism can be used by migrating cells to increase

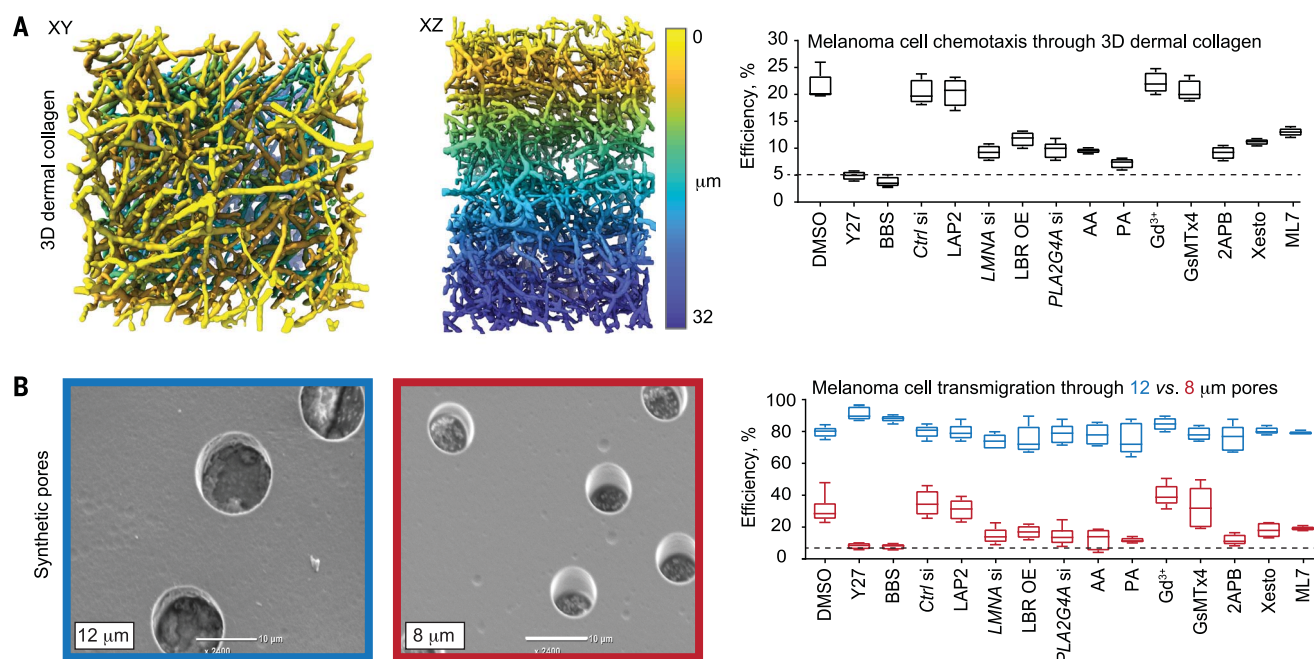


Fig. 8. The nuclear ruler function in cancer cell migration. (A) (Left) 3D light-sheet microscopy images of atelopeptide fibrillar bovine dermal collagen (1.7 mg ml^{-1}) lattices. (Right) Quantifications of the percentage of human MCs A375P able to chemotactically transmigrate through the lattice (1 mm thick) in the presence of the broad-spectrum matrix metalloproteinase inhibitor GM6001 in conditions affecting cell contractility (Y27, BBS, and ML7), NE properties (LMNA si and LBR OE), cPLA2 expression and activity (PLA2G4A si, AA, and PA), and stretch-sensitive calcium release (Gd³⁺, GsMTx4, 2APB, and Xesto). Data are from ≥ 2 experiments; mean \pm SD; $n \geq 300$ cells per condition. See table S3 for

drug target description and pairwise statistical comparisons; see materials and methods for drug concentrations. **(B)** Scanning electron microscopy images of polycarbonate membranes with 12- μm (blue) and 8- μm (red) pores (scale bar, 10 μm), and quantifications of the percentage of A375P cells able to chemotactically transmigrate through the pores in the conditions specified in (A). Data are from ≥ 2 experiments; mean \pm SD; $n \geq 300$ cells per condition. See table S3 for drug target description and pairwise statistical comparisons; see materials and methods for drug concentrations. The dotted line in (A) and (B) represents the cell transmigration rate upon global perturbation of actomyosin contractility.

their propulsion when surrounding space becomes limited, explaining the switch to fast amoeboid migration upon confinement of slow mesenchymal cells, which we reported previously (8). In support of this hypothesis, we found that single HeLa-Kyoto cells, remaining under the confining AFM cantilever for prolonged periods of time, can spontaneously initiate movement, enabling the cells to evade the cantilever (fig. S10A). We also observed the predicted increase in migration speed upon confinement of immature mouse bone marrow-derived dendritic cell (iDC) populations using our microfabricated confiner device (Fig. 7A) (30). This speed increase was lost upon functional ablation of cPLA2 (Fig. 7A, bottom graph; fig. S10B, upper right graph; and Fig. 7B, right graph) or lamin A (Fig. 7A, bottom graph) (31) and corresponded specifically to the confinement height (3 μm) at which iDC nuclei get fully unfolded (Fig. 7C). Consistently, myosin accumulated at the iDC cortex in a cPLA2-dependent manner specifically at 3 μm (Fig. 7D). A large fraction of iDCs at 3 μm switched to a migratory polarized cell shape phenotype, characteristic of fast-moving cells, that was almost entirely lost upon cPLA2 depletion (Fig. 7B, fig. S10B, and movie S7). Overall, the data obtained from both HeLa-Kyoto

cells and primary iDCs suggested that the nuclear ruler pathway could be involved in triggering a contractile “evasion reflex,” helping invasive cells to either rapidly escape or penetrate the most confined regions of dense tissues.

To further test the function of the nuclear ruler in invasive cell migration, we assessed the protease-independent ability of human metastatic skin melanoma cells (MCs), a well-established cellular model employing contractility-driven, amoeboid invasive motion in vivo (32), to chemotactically transmigrate (fig. S10C) through 3D dermal collagen gels or synthetic polycarbonate membranes with different porosity. 3D collagen lattices (Fig. 8A, left images) displayed pore sizes ranging from 1 to 12 μm (fig. S10D), thus representing a heterogeneous, mechanically restrictive environment in which cells are expected to deform their nuclei. Indeed, perturbations targeting the nuclear ruler pathway affected the efficiency of MC transmigration through 3D collagen (Fig. 8A, right graph, and table S3). Consistent with the diameter of their nuclei ($11 \pm 2 \mu\text{m}$, $n = 100$ cells), MCs were dependent on basal actomyosin contractility or pathways associated with the nuclear ruler only when transmigrating through 8- but not 12- μm pores of polycarbonate membranes (Fig. 8B, left images; fig. S10E; and table S3). These results suggested

that, owing to the nuclear ruler, migratory cells can use the energetically costly actomyosin contractility motor on demand, when the local cell environment becomes restrictive to migration.

Discussion

Collectively, our data establish a nongenetic function for the nucleus as an internal ruler. Relying on this ruler, cells can measure the degree of their environmental confinement and rapidly tailor specific behaviors to adapt to the confinement at time scales shorter than those associated with changes in gene expression. In the context of cell migration, such tailored cellular behaviors might help cells avoid environmental entrapment, which is relevant to cancer cell invasion, immune cell patrolling of peripheral tissues, and progenitor cell motility within a highly crowded cell mass of a developing embryo (33). The nuclear ruler mechanism defines an active function for the nucleus in cell migration, potentially explaining why enucleated cells show a poor motile capacity in dense collagen gels (34). Engaging the nuclear ruler and generating propulsive forces, cells can push their large nucleus through small openings, thus overcoming the rate-limiting effect of the bulky and stiff nucleus on confined migration. However, some highly specialized

and short-lived cells, such as neutrophils, trade nuclear size and stiffness for uncompromised migration through dense tissue regions. To achieve this, maturing neutrophils transcriptionally up-regulate LBR and down-regulate LMNA expression that makes the nucleus highly pliable (35) and might cancel its rate-limiting effect and ruler function in the context of confined migration.

The nuclear ruler mechanism relies on NE tension sensing by the phospholipid-hydrolyzing enzyme cPLA2 (13, 17). The enzymatic activity of cPLA2 is fundamental to the eicosanoid biosynthetic pathway known for its function as an essential mediator of paracrine inflammatory signaling in the immune system, with effects on immune cell contractility and migration (36, 37). The function we propose here relies on direct mechanical activation of cPLA2 and subsequent release of ARA, but it does not exclude the induction of the downstream signaling associated with ARA metabolism. When we confined the nucleus in only one cell of a pair of closely juxtaposed cells, we did not observe any signs of contractility activation in the neighboring cell (fig. S11), which suggests that paracrine signaling might not be sufficient to activate contractility in this case. Fully characterizing the signaling cascade triggered by mechanical activation of the cPLA2 pathway and subsequent changes in lipid metabolism in the context of confined cell migration is an important perspective for future studies. We also showed that the nuclear ruler pathway depends on stretch-activated intracellular calcium release. Here, we pinpointed a role for InsP3Rs, but there are many other stretch-sensitive calcium channels on the ER and nuclear membranes (38) that could contribute to the pathway in a cell type- or context-specific fashion.

Establishing the nucleus as an internal ruler of the extracellular environment opens avenues of research in the field of single-cell migration as well as in tissue homeostasis and developmental biology. Indeed, morphological changes associated with cell spreading on the ECM are known to affect nuclear morphology and cell cycle progression (39). Therefore, the nuclear ruler might contribute to cell fate choices during tissue growth. Given that cell crowding in tissues such as epithelia alters the cell shape and aspect ratio, tissue cells [in addition to the known mechanisms (1)] may use the nucleus as a sensor of local cell density.

Materials and methods

Cell culture

Human cervical adenocarcinoma cells HeLa-Kyoto stably expressing myosin IIA (MYH9)-GFP and LifeAct-mCherry or MYH9-GFP and the PM-targeting CAAX box fused to mCherry, or LAP2/LAP2b-GFP, NUP107-GFP, HeLa (CCL-2) cells stably expressing cPla2-mKate2, human fibrosarcoma cells HT1080 expressing GFP-

myosin light chain 2 and RFP-NLS, primary human foreskin fibroblasts (HFFs), human MCs A375P, *N-rasV12* oncogene-transformed rat liver epithelial cells IAR-2, and canine kidney epithelial cells MDCK-2 were maintained in DMEM/F12 supplemented with 10% FBS (Invitrogen) at 37°C and 5% CO₂. Human epidermal stem cells were cultured as previously described (40). All cell lines were tested for mycoplasma contamination using MycoScope PCR Mycoplasma Detection Kit (Genlantis). Mouse bone-marrow-derived immature dendritic cells (iDCs) were obtained by culturing bone marrow cells (from both male and female 8- to 10-week-old LifeAct-GFP mice (41), MYH9-GFP mice (42), and control (JAX mice stock number: 000664) or *Lmna* KO mice (31) for 10 to 11 days in complete DC medium (IMDM medium supplemented with fetal calf serum (FCS, 10%), glutamine (20 mM), penicillin-streptomycin (100 U/ml), β -mercaptoethanol (50 μ M), and granulocyte-macrophage colony-stimulating factor/GM-CSF (50 ng/ml)-containing supernatant obtained from transfected J558 cells.

Transfection procedure, expression vectors, and siRNA oligonucleotides

Cells were transfected with plasmid DNA using Lipofectamine LTX reagent (Invitrogen) transiently or stably, according to manufacturer's protocol. For RNA interference experiments, cells were transfected with small interfering RNA (siRNA) oligonucleotides using Lipofectamine RNAiMAX reagent (Invitrogen), according to manufacturer's protocol. In experiments on cPLA2a knockdown in bone marrow-derived mouse immature dendritic cells (iDCs), the cells were transfected using the Amaxa mouse Dendritic Cell Nucleofector Kit (Lonza).

The following expression vectors were used for plasmid DNA transfections: empty vector pEGFP-C1 (Clontech); Addgene plasmids: 61996 LBR pEGFP-N2 (646) (43), 40753 pGP-MV-GCaMP6s (44), 86849 pBOB-EF1-FastFucci-Puro (45). To knock down LMNA or cPLA2a, cells were transfected with nontargeting siRNA (control) or validated ON-TARGETplus SMARTpool siRNA reagents (Dharmacon) targeting human-specific *LMNA* mRNA (cat. no. L-004978-00-0005), human-specific *PLA2G4A* mRNA (cat. no. L-009886-00-0005), or mouse-specific *Pla2g4a* mRNA (cat. no. L-063167-01-0010). Unless stated otherwise, cells were analyzed 72 hours post-transfection using standard Western blot or immunofluorescent analysis protocols. Based on quantitative densitometry of proteins, the knockdown efficiency was estimated as $84.7 \pm 2.5\%$ (3 repeats). Additionally, lentiviral transductions were performed to achieve lamin A knockdown in HeLa cells. Viral particles were produced by transfection of 0.8 million 293FT cells with 3 μ g DNA and 8 μ l TransIT-293 (Mirus Bio) per well. For shRNA mediated knockdown

of lamin A, 0.4 μ g CMV-VSVG, 1 μ g psPAX2 and 1.6 μ g of either pLKO.1-puro-LMNAsh4 (TRCN0000061837, target sequence GCCGTG-CTTCCTCTCACTCAT) or pLKO1-puro-shLACZ (target sequence GCGATCGTAATCACCCGAGTG) as negative control were combined. Viral supernatants were harvested 48 hours post-transfection, filtered at 0.45 μ m, and added on to HeLa cells that had been seeded 1 day before transduction at a 2:1 ratio of viral supernatant:medium containing protamine at a final concentration of 1 μ g/ml. Cells were washed once in PBS and passaged at 48 hours post-transduction with 2 μ g/ml of puromycin for selection of stably transduced cells.

Drug treatments

The following pharmacological inhibitors and chemical compounds were used: 10 μ M ROCK-mediated contractility inhibitor Y27632 (Y27) (EMD), 10 μ M myosin II ATPase inhibitor blebbistatin (BBS) (Toronto Research Chemicals), 20 μ M Ca²⁺-sensitive myosin light chain kinase/MLCK inhibitor ML-7 (Sigma-Aldrich), 1 mM apoptosis inducer hydrogen peroxide (H₂O₂), 1 μ M transcription inhibitor triptolide (TRP) (Tocris Bioscience), 50 μ g ml⁻¹ translation inhibitor cycloheximide (CHX) (Sigma-Aldrich), 1 μ M AZD6738 inhibiting the Serine/Threonine protein kinase Ataxia Telangiectasia and Rad3 related (ATR) capable of sensing NE tension (Tocris Bioscience), 10 μ M nonspecific PM permeability marker propidium iodide (PI) (Sigma-Aldrich), 0.4 mM PM tension reducer sodium deoxycholate (DOCL) (Sigma-Aldrich), 10 μ M gadolinium (III) chloride (Gd³⁺) or 5 μ M peptide GsMTx4 from the tarantula venom affecting mechanosensitive ion channels on the PM (Tocris Bioscience), 2 mM extracellular Ca²⁺ chelator BAPTA (Sigma-Aldrich), 10 μ M intracellular Ca²⁺ chelator BAPTA-AM (Sigma-Aldrich), 10 μ M ionomycin (IOM) directly facilitating the transport of Ca²⁺ across the PM (Sigma-Aldrich), 70 μ M signaling lipid arachidonic acid (ARA) (a product of enzymatic activity of the NE stretch-sensitive enzyme cPLA2) activating actomyosin contractility (Cayman Chemical), 20 μ M AACOCF3 (AA) or 10 μ M PACOCF3 (PA) inhibiting the NE stretch-sensitive enzyme cPLA2 (Tocris Bioscience), 100 μ M 2APB or 10 μ M Xestospongin C (Xesto) blocking stretch-activated inositol triphosphate receptors (InsP3Rs) on the ER/nuclear membranes (Tocris Bioscience), and 20 μ M broad-spectrum matrix metalloproteinase inhibitor GM6001 (Merck Millipore). Growth medium was supplemented with 1% DMSO (vol/vol) (Sigma-Aldrich) in control experiments.

Western blotting

Cells were collected and resuspended in Laemmli buffer. Proteins were separated using sodium dodecyl sulfate polyacrylamide gel electrophoresis

(SDS-PAGE) and transferred onto PVDF membranes. After incubation with primary [Lamin A/C antibody no. 2032 (Cell Signaling Technology), cPLA2a antibody no. PA5-29100 (Invitrogen), and GAPDH antibody no. #ab9483 (Abcam)] and secondary [IRDye and VRDye (LI-COR)] antibodies, the membranes were visualized using Odyssey CLx Infrared Imaging System (LI-COR).

Quantitative PCR (qPCR)

To assess the efficacy of the siRNA treatment, qPCR was carried out on iDCs after 48 hours of the siRNA treatment. RNA extraction was performed using RNeasy Micro RNA kit (Qiagen), according to the manufacturer's protocol. cDNA was produced using the high capacity cDNA synthesis kit (Thermo Fisher), according to the manufacturer's protocol, starting from 1 µg of RNA. Quantitative PCR experiments were performed using Taqman Gene Expression Assay (Applied Biosystems) and carried out on a Lightcycler 480 (Roche) using the settings recommended by the manufacturer. The following primers were used: Mm01284324.m1 for PLA2g4 and Mm99999915 for GAPDH as a control. cPLA2a expression was assessed in si-control and si-cPLA2a iDCs. Samples were run in triplicate for each condition. Data were subsequently normalized to GAPDH values, and to the values obtained in control iDCs. The fold change was calculated using the formula $2^{-\Delta\Delta CT}$.

Single-cell flat AFM-based confinement coupled to live cell imaging

Trypsinized cells were resuspended in CO₂-independent, phenol red-free DMEM/F-12 medium supplemented with 10% FBS (Invitrogen) and plated on glass-bottomed 35-mm dishes (FluoroDish, WPI). Experiments with non-adherent cells were initiated 30 min after cell plating to allow for cell sedimentation. Spread cells were obtained 6 hours post cell plating. Dishes with cells were mounted in a dish heater (JPK Instruments) and kept at 37°C under an inverted light microscope (Axio Observer.Z1; Zeiss) equipped with a confocal microscope unit (LSM 700; Zeiss) and AFM head (CellHesion 200; JPK Instruments).

Focused ion beam (FIB)-sculpted, flat silicon microcantilevers were processed and calibrated as described in (46). The microcantilevers were fixed on a standard JPK glass block and mounted in the AFM head. The cantilever was lowered on the cell to a preset height with a constant speed of 0.5 µm·s⁻¹, and the resulting varying force and cantilever height were recorded over time. At the same time, differential interference contrast and fluorescence images at the midplane of the confined cell (the imaging settings were readjusted to the medial plane of the cell each time the cell was confined to a specific height) were recorded every 5 s using a 63× water immersion objective. All microscopy

equipment was placed, and experiments were carried out in a custom-made isolation box.

Determination of cell pressure and cortical tension

Cell geometry, pressure, and cortical tension were measured on the basis of AFM and imaging data, as described in (46) and (47).

Production of cytoplasts

Enucleated cells were generated as described in (25) and (48).

Microfabrication-based confinement of cell populations

To obtain large quantities of confined cells for cell population or biochemical studies, cell confinement was performed using a homemade device (8) consisting of a suction cup made in polydimethylsiloxane (PDMS, RTV615, GE) used to press a confining coverslip bearing PDMS microspacers (micropillars) on top of the culture substrate populated with cells. The height of the micropillars (10 µm versus 5 µm) determines the height for spatial confinement of cells between the coverslip and the substrate. A version of the cell confiner adapted to multi-well plates was used to perform multiple experiments in parallel (20). The molds for the PDMS microspacers were fabricated following standard photolithography procedures. The surface of the confining side was always treated with nonadhesive PLL-PEG (SuSoS).

Assaying activation of apoptosis in live cells

To detect levels of active apoptotic caspases, the Image-iT LIVE Red Poly Caspases detection kit based on a fluorescent inhibitor of caspases (FLICA) methodology (I35101, Molecular probes) was used according to the manufacturer's protocol.

Biochemical measurements of ARA release

Cells were confined using microfabricated devices as described in the subsection "Microfabrication-based confinement of cell populations." Confinement was released, and the cells were immediately extracted with Dole's solution (heptane, isopropyl alcohol, 1 N sulfuric acid; 10:40:1). Pentafluorobenzyl esters of the fatty acids were prepared and quantified by gas chromatography-mass spectrometry with reference to an internal standard of d8-AA as described in (49).

Epithelial monolayer stretching

A custom-made stretching device was used to perform epithelial monolayer stretching experiments, as described in (1).

Chemotactic transmigration assays

Serum-starved A375P cells were harvested and transferred in serum-free medium to the upper compartment of 5-µm-pore, 8-µm-pore (cat. No. 3421 and 3428, Corning), or 12-µm-pore

(cat. no. CBA-107, Cell Biolabs Inc.) polycarbonate membrane inserts (transwells). Cell density was adjusted according to the specific area of each transwell with 5×10^4 , 1.5×10^5 , and 7.5×10^5 cells added to 5-, 12-, and 8-µm transwells, respectively. Cells were allowed to transmigrate toward the lower compartment containing 10% FBS for 12 hours. Transmigration efficiency was calculated as number of cells at the lower compartment divided by the number of cells added to the upper compartment of a transwell.

To examine the ability of A375P cells to chemotax through 3D collagen gels, atelopeptide fibrillar bovine dermal collagen (cat. no. 5005-B; PureCol, Advanced BioMatrix) was prepared at 1.7 mg ml⁻¹ in DMEM and allowed to polymerize in the upper compartment of the 12-µm-pore polycarbonate membrane insert (cat. no. CBA-107, Cell Biolabs Inc.). Serum-starved cells were seeded on top of the collagen pad in serum-free medium, allowed to adhere and transmigrate through the collagen layer and the membrane toward the lower compartment containing 10% FBS for 24 hours. Transmigration efficiency was calculated as number of cells at the lower compartment divided by the number of cells added to the upper compartment of the transwell.

Generation of 3D CDMs

HFFs were plated at high density on gelatin-coated and glutaraldehyde-treated 35-mm (4 × 10⁵ cells, MatTek) or 50-mm (5.7 × 10⁵ cells, Warner Instruments) glass-bottom dishes. Cultures were maintained for 10 days, adding new media with 50 µg/ml ascorbic acid every other day. The matrices were denuded of cells by adding extraction buffer (20 mM NH₄OH and 0.5% Triton X100 in PBS) for 10 min at room temperature and washed with PBS.

Quantitative image analysis

Fluorescence intensity levels (mean gray values, arbitrary units) were obtained from background subtracted images using the ImageJ/Fiji software (NIH; <http://rsb.info.nih.gov/ij/index.html>).

The Imaris (version 8.3) image analysis software (Bitplane) was used to measure nuclear volume reconstructed from 3D confocal microscopy images.

The dimensionless parameter excess of perimeter (EOP) was calculated to estimate the amount of NE or PM area stored in macro- and microfolds. To calculate EOP, we first obtained values for perimeter (P) and surface area (A) from 2D images taken at the maximum radius of the nucleus (NE marker LAP2-GFP labeling) or cell (PM marker CAAX box-mCherry labeling). Next, we introduced R_0 as the radius of the circle defined by the area A , which allowed us to compute EOP as the ratio between $(P - 2\pi R_0)$ and $(2\pi R_0)$. EOP values of a

highly folded object tend to be close to 1, whereas EOP of an object with a smooth surface tend to be close to 0. Additional theoretical calculations were performed to account for experimentally observed changes in nuclear aspect ratio (AR); no significant contribution of AR changes to the measured values of EOP was observed.

Nuclear roundness index was obtained using the shape descriptors tool in ImageJ/Fiji.

The MIPAR v.3.2.3. image analysis software (MIPAR Software) and the Kappa plugin for ImageJ/Fiji (<https://github.com/brouhardlab/Kappa/tree/master/docs/fit-the-curve-to-the-data>) were used to estimate NE surface curvature.

To measure NE fluctuations, nuclei of live cells expressing LAP2-GFP were recorded using a high frame rate acquisition mode (250 msec per frame) for 5 min. The position of each nucleus was corrected for linear and rotational drift using the Stackreg plugin of the ImageJ/Fiji software. Upon drift correction, the edge of the nucleus was registered at a given angle. NE fluctuations were calculated by measuring the standard deviation of the NE from its mean position. To precisely position the NE, linescans across the NE (intensities along a line of 1 pixel in width perpendicular to the NE) were made at different positions along the NE. For each point along the NE and for each time point in the movie, the point of maximum intensity was calculated on the linescan and a parabola was fitted on points before and after the maxima to determine the localization of the NE with a subpixel resolution. For each position along the NE, the mean position was taken as the mean of all time points. The standard deviation of the position of the NE around this mean position was taken as one measure for the fluctuation of the NE. Each point along the NE contributes one measure. Obtained mean NE fluctuation values were expressed in micrometers. The same approach can be applied to measure PM fluctuations. A floppy, and thus less tensed, membrane is expected to fluctuate more, whereas a membrane under tension exhibits no or diminished fluctuations.

The distance between neighboring nuclear pores (NP-NP distance) was estimated for the same living cell expressing a NP marker NUP107-GFP at different degrees of spatial confinement. To this end, a medial confocal slice of the nucleus was obtained to then trace individual NPs along the NE using the Linescan function of the MetaMorph (version 7.7) software (Molecular Devices). Each individual NP was resolved as a local maximum of fluorescence intensity on the Linescan diagram. The distance between nearest local maxima was represented as NP-NP distance.

Cell speed was analyzed using the manual tracking plugin of ImageJ/Fiji.

To measure collagen pore sizes, collagen fibers were imaged via axially swept light-sheet microscopy (50). The fibers were then detected from the deconvolved images by applying a steerable filter (51) followed by non-maximum suppression. We then calculated pore sizes using a custom-written Matlab code implementing the algorithm described in (2).

Statistics and reproducibility of experiments

Unless stated otherwise, statistical significance was determined by two-tailed unpaired or paired Student's *t* test after confirming that the data met appropriate assumptions (normality, homogenous variance, and independent sampling). Statistical data are presented as average \pm either SEM or SD. Sample size (*n*) and *P* value are specified in the text of the paper or figure legends. Samples in most cases were defined as the number of cells counted or examined within multiple different fields of view on the same dish or slide, and thus represent data from a single sample within a single experiment. When data from a single sample are shown, they are representative of at least three additional samples from independent experiments.

REFERENCES AND NOTES

- G. T. Eisenhoffer *et al.*, Crowding induces live cell extrusion to maintain homeostatic cell numbers in epithelia. *Nature* **484**, 546–549 (2012). doi: [10.1038/nature10999](https://doi.org/10.1038/nature10999); pmid: [22504183](https://pubmed.ncbi.nlm.nih.gov/22504183/)
- J. Renkawitz *et al.*, Nuclear positioning facilitates amoeboid migration along the path of least resistance. *Nature* **568**, 546–550 (2019). doi: [10.1038/s41586-019-1087-5](https://doi.org/10.1038/s41586-019-1087-5); pmid: [30944468](https://pubmed.ncbi.nlm.nih.gov/30944468/)
- B. Trappmann *et al.*, Extracellular-matrix tethering regulates stem-cell fate. *Nat. Mater.* **11**, 642–649 (2012). doi: [10.1038/nmat3339](https://doi.org/10.1038/nmat3339); pmid: [22635042](https://pubmed.ncbi.nlm.nih.gov/22635042/)
- M. D. Vahey, D. A. Fletcher, The biology of boundary conditions: Cellular reconstitution in one, two, and three dimensions. *Curr. Opin. Cell Biol.* **26**, 60–68 (2014). doi: [10.1016/j.cub.2013.10.001](https://doi.org/10.1016/j.cub.2013.10.001); pmid: [24529247](https://pubmed.ncbi.nlm.nih.gov/24529247/)
- R. Oria *et al.*, Force loading explains spatial sensing of ligands by cells. *Nature* **552**, 219–224 (2017). doi: [10.1038/nature24662](https://doi.org/10.1038/nature24662); pmid: [29211717](https://pubmed.ncbi.nlm.nih.gov/29211717/)
- M. Théry, A. Jiménez-Dalmaroni, V. Racine, M. Bornens, F. Jülicher, Experimental and theoretical study of mitotic spindle orientation. *Nature* **447**, 493–496 (2007). doi: [10.1038/nature05786](https://doi.org/10.1038/nature05786); pmid: [17495931](https://pubmed.ncbi.nlm.nih.gov/17495931/)
- J. Z. Kechagia, J. Ivaska, P. Roca-Cusachs, Integrins as biomechanical sensors of the microenvironment. *Nat. Rev. Mol. Cell Biol.* **20**, 457–473 (2019). doi: [10.1038/s41580-019-0134-2](https://doi.org/10.1038/s41580-019-0134-2); pmid: [31182865](https://pubmed.ncbi.nlm.nih.gov/31182865/)
- Y.-J. Liu *et al.*, Confinement and low adhesion induce fast amoeboid migration of slow mesenchymal cells. *Cell* **160**, 659–672 (2015). doi: [10.1016/j.cell.2015.01.007](https://doi.org/10.1016/j.cell.2015.01.007); pmid: [25679760](https://pubmed.ncbi.nlm.nih.gov/25679760/)
- V. Ruprecht *et al.*, Cortical contractility triggers a stochastic switch to fast amoeboid cell motility. *Cell* **160**, 673–685 (2015). doi: [10.1016/j.cell.2015.01.008](https://doi.org/10.1016/j.cell.2015.01.008); pmid: [25679761](https://pubmed.ncbi.nlm.nih.gov/25679761/)
- M. P. Stewart, Y. Toyoda, A. A. Hyman, D. J. Müller, Tracking mechanics and volume of globular cells with atomic force microscopy using a constant-height clamp. *Nat. Protoc.* **7**, 143–154 (2012). doi: [10.1038/nprot.2011.434](https://doi.org/10.1038/nprot.2011.434); pmid: [22222789](https://pubmed.ncbi.nlm.nih.gov/22222789/)
- F. Kong, A. J. García, A. P. Mould, M. J. Humphries, C. Zhu, Demonstration of catch bonds between an integrin and its ligand. *J. Cell Biol.* **185**, 1275–1284 (2009). doi: [10.1083/jcb.200810002](https://doi.org/10.1083/jcb.200810002); pmid: [19564406](https://pubmed.ncbi.nlm.nih.gov/19564406/)
- A. G. Clark, O. Wartlick, G. Salbreux, E. K. Paluch, Stresses at the cell surface during animal cell morphogenesis. *Curr. Biol.* **24**, R484–R494 (2014). doi: [10.1016/j.cub.2014.03.059](https://doi.org/10.1016/j.cub.2014.03.059); pmid: [24845681](https://pubmed.ncbi.nlm.nih.gov/24845681/)

- B. Enyedi, P. Niethammer, A Case for the Nuclear Membrane as a Mechanotransducer. *Cell. Mol. Bioeng.* **9**, 247–251 (2016). doi: [10.1007/s12195-016-0430-2](https://doi.org/10.1007/s12195-016-0430-2); pmid: [27453760](https://pubmed.ncbi.nlm.nih.gov/27453760/)
- A. Elosegui-Artola *et al.*, Force Triggers YAP Nuclear Entry by Regulating Transport across Nuclear Pores. *Cell* **171**, 1397–1410.e14 (2017). doi: [10.1016/j.cell.2017.10.008](https://doi.org/10.1016/j.cell.2017.10.008); pmid: [29107331](https://pubmed.ncbi.nlm.nih.gov/29107331/)
- A. Kumar *et al.*, ATR mediates a checkpoint at the nuclear envelope in response to mechanical stress. *Cell* **158**, 633–646 (2014). doi: [10.1016/j.cell.2014.05.046](https://doi.org/10.1016/j.cell.2014.05.046); pmid: [25083873](https://pubmed.ncbi.nlm.nih.gov/25083873/)
- N. Itano, S. Okamoto, D. Zhang, S. A. Lipton, E. Ruoslahti, Cell spreading controls endoplasmic and nuclear calcium: A physical gene regulation pathway from the cell surface to the nucleus. *Proc. Natl. Acad. Sci. U.S.A.* **100**, 5181–5186 (2003). doi: [10.1073/pnas.0531397100](https://doi.org/10.1073/pnas.0531397100); pmid: [12702768](https://pubmed.ncbi.nlm.nih.gov/12702768/)
- B. Enyedi, M. Jelcic, P. Niethammer, The Cell Nucleus Serves as a Mechanotransducer of Tissue Damage-Induced Inflammation. *Cell* **165**, 1160–1170 (2016). doi: [10.1016/j.cell.2016.04.016](https://doi.org/10.1016/j.cell.2016.04.016); pmid: [27203112](https://pubmed.ncbi.nlm.nih.gov/27203112/)
- M. Raab *et al.*, ESCRT III repairs nuclear envelope ruptures during cell migration to limit DNA damage and cell death. *Science* **352**, 359–362 (2016). doi: [10.1126/science.1247611](https://doi.org/10.1126/science.1247611); pmid: [27013426](https://pubmed.ncbi.nlm.nih.gov/27013426/)
- A. C. Rowat, J. Lammerding, J. H. Ipsen, Mechanical properties of the cell nucleus and the effect of emerin deficiency. *Biophys. J.* **91**, 4649–4664 (2006). doi: [10.1529/biophysj.106.086454](https://doi.org/10.1529/biophysj.106.086454); pmid: [16997877](https://pubmed.ncbi.nlm.nih.gov/16997877/)
- M. Le Berre, J. Aubertin, M. Piel, Fine control of nuclear confinement identifies a threshold deformation leading to lamina rupture and induction of specific genes. *Integr. Biol.* **4**, 1406–1414 (2012). doi: [10.1039/c2ib20056b](https://doi.org/10.1039/c2ib20056b); pmid: [23038068](https://pubmed.ncbi.nlm.nih.gov/23038068/)
- F.-Y. Chu, S. C. Haley, A. Zidovska, On the origin of shape fluctuations of the cell nucleus. *Proc. Natl. Acad. Sci. U.S.A.* **114**, 10338–10343 (2017). doi: [10.1073/pnas.1702226114](https://doi.org/10.1073/pnas.1702226114); pmid: [28900009](https://pubmed.ncbi.nlm.nih.gov/28900009/)
- F.-C. Tsai, T. Meyer, Ca²⁺ pulses control local cycles of lamellipodia retraction and adhesion along the front of migrating cells. *Curr. Biol.* **22**, 837–842 (2012). doi: [10.1016/j.cub.2012.03.037](https://doi.org/10.1016/j.cub.2012.03.037); pmid: [22521790](https://pubmed.ncbi.nlm.nih.gov/22521790/)
- P. Solanes *et al.*, Space exploration by dendritic cells requires maintenance of myosin II activity by IP3 receptor 1. *EMBO J.* **34**, 798–810 (2015). doi: [10.1525/embj.201489056](https://doi.org/10.1525/embj.201489056); pmid: [25637353](https://pubmed.ncbi.nlm.nih.gov/25637353/)
- M. C. Gong *et al.*, Arachidonic acid inhibits myosin light chain phosphatase and sensitizes smooth muscle to calcium. *J. Biol. Chem.* **267**, 21492–21498 (1992). pmid: [1328235](https://pubmed.ncbi.nlm.nih.gov/1328235)
- V. Rodionov, E. Nadezhzhina, J. Pelloquin, G. Borisov, Digital fluorescence microscopy of cell cytoplasm with and without the centrosome. *Methods Cell Biol.* **67**, 43–51 (2001). doi: [10.1016/S0091-679X\(01\)67004-3](https://doi.org/10.1016/S0091-679X(01)67004-3); pmid: [11550480](https://pubmed.ncbi.nlm.nih.gov/11550480/)
- S. Gravenmann *et al.*, Dosage effect of zero to three functional LBR-genes in vivo and in vitro. *Nucleus* **1**, 179–189 (2010). doi: [10.4161/nucl.11113](https://doi.org/10.4161/nucl.11113); pmid: [21326950](https://pubmed.ncbi.nlm.nih.gov/21326950/)
- Y. Ma *et al.*, Lamin B receptor plays a role in stimulating nuclear envelope production and targeting membrane vesicles to chromatin during nuclear envelope assembly through direct interaction with importin beta. *J. Cell Sci.* **120**, 520–530 (2007). doi: [10.1242/jcs.03355](https://doi.org/10.1242/jcs.03355); pmid: [17251381](https://pubmed.ncbi.nlm.nih.gov/17251381/)
- J. Ellenberg *et al.*, Nuclear membrane dynamics and reassembly in living cells: Targeting of an inner nuclear membrane protein in interphase and mitosis. *J. Cell Biol.* **138**, 1193–1206 (1997). doi: [10.1083/jcb.138.6.1193](https://doi.org/10.1083/jcb.138.6.1193); pmid: [9298976](https://pubmed.ncbi.nlm.nih.gov/9298976/)
- D. A. Donahue *et al.*, SUN2 Overexpression Deforms Nuclear Shape and Inhibits HIV. *J. Virol.* **90**, 4199–4214 (2016). doi: [10.1128/JVI.03202-15](https://doi.org/10.1128/JVI.03202-15); pmid: [26865710](https://pubmed.ncbi.nlm.nih.gov/26865710/)
- M. Le Berre, E. Zlotek-Zlotkiewicz, D. Bonazzi, F. Lautenschlaeger, M. Piel, in *Methods in Cell Biology* (Elsevier, 2014), pp. 213–229.
- Y. Kim, Y. Zheng, Generation and characterization of a conditional deletion allele for Lmna in mice. *Biochem. Biophys. Res. Commun.* **440**, 8–13 (2013). doi: [10.1016/j.bbrc.2013.08.082](https://doi.org/10.1016/j.bbrc.2013.08.082); pmid: [23998933](https://pubmed.ncbi.nlm.nih.gov/23998933/)
- V. Sanz-Moreno *et al.*, Rac activation and inactivation control plasticity of tumor cell movement. *Cell* **135**, 510–523 (2008). doi: [10.1016/j.cell.2008.09.043](https://doi.org/10.1016/j.cell.2008.09.043); pmid: [18984162](https://pubmed.ncbi.nlm.nih.gov/18984162/)
- V. Venturini, F. Pezzano, F. C. Castro, H.-M. Häkkinen, S. Jiménez-Delgado, M. Colomer-Rosell, M. M. Sánchez, Q. Tolosa-Ramon, S. Paz-López, M. A. Valverde, P. Loza-Alvarez, M. Krieg, S. Wieser, V. Ruprecht, The nucleus measures shape deformation for cellular proprioception and regulates adaptive morphodynamics. *bioRxiv* 865949 [Preprint]. 5 December 2019. <https://doi.org/10.1101/865949>
- D. M. Graham *et al.*, Enucleated cells reveal differential roles of the nucleus in cell migration, polarity, and mechanotransduction.

- J. Cell Biol.* **217**, 895–914 (2018). doi: [10.1083/jcb.201706097](https://doi.org/10.1083/jcb.201706097); pmid: 29351995
35. H. R. Manley, M. C. Keightley, G. J. Lieschke, The Neutrophil Nucleus: An Important Influence on Neutrophil Migration and Function. *Front. Immunol.* **9**, 2867 (2018). doi: [10.3389/fimmu.2018.02867](https://doi.org/10.3389/fimmu.2018.02867); pmid: 30564248
 36. P. V. Afonso *et al.*, LTB4 is a signal-relay molecule during neutrophil chemotaxis. *Dev. Cell* **22**, 1079–1091 (2012). doi: [10.1016/j.devcel.2012.02.003](https://doi.org/10.1016/j.devcel.2012.02.003); pmid: 22542839
 37. R. Majumdar, A. Tavakoli Tameh, C. A. Parent, Exosomes Mediate LTB4 Release during Neutrophil Chemotaxis. *PLoS Biol.* **14**, e1002336 (2016). doi: [10.1371/journal.pbio.1002336](https://doi.org/10.1371/journal.pbio.1002336); pmid: 26741884
 38. M. T. Alonso, J. García-Sancho, Nuclear Ca(2+) signalling. *Cell Calcium* **49**, 280–289 (2011). doi: [10.1016/j.ceca.2010.11.004](https://doi.org/10.1016/j.ceca.2010.11.004); pmid: 21146212
 39. J. Aureille *et al.*, Nuclear envelope deformation controls cell cycle progression in response to mechanical force. *EMBO Rep.* **20**, e48084 (2019). doi: [10.15252/embr.201948084](https://doi.org/10.15252/embr.201948084); pmid: 31368207
 40. F. Watt, B. Simon, D. Prowse, in *Cell Biology* (Elsevier, 2006), pp. 133–138.
 41. J. Riedl *et al.*, Lifeact mice for studying F-actin dynamics. *Nat. Methods* **7**, 168–169 (2010). doi: [10.1038/nmeth0310-168](https://doi.org/10.1038/nmeth0310-168); pmid: 20195247
 42. Y. Zhang *et al.*, Mouse models of MYH9-related disease: Mutations in nonmuscle myosin II-A. *Blood* **119**, 238–250 (2012). doi: [10.1182/blood-2011-06-358853](https://doi.org/10.1182/blood-2011-06-358853); pmid: 21908426
 43. N. Zuleger *et al.*, System analysis shows distinct mechanisms and common principles of nuclear envelope protein dynamics. *J. Cell Biol.* **193**, 109–123 (2011). doi: [10.1083/jcb.201009068](https://doi.org/10.1083/jcb.201009068); pmid: 21444689
 44. T.-W. Chen *et al.*, Ultrasensitive fluorescent proteins for imaging neuronal activity. *Nature* **499**, 295–300 (2013). doi: [10.1038/nature12354](https://doi.org/10.1038/nature12354); pmid: 23868258
 45. S.-B. Koh *et al.*, A quantitative FastFucci assay defines cell cycle dynamics at a single-cell level. *J. Cell Sci.* **130**, 512–520 (2017). doi: [10.1242/jcs.195164](https://doi.org/10.1242/jcs.195164); pmid: 27888217
 46. C. J. Cattin *et al.*, Mechanical control of mitotic progression in single animal cells. *Proc. Natl. Acad. Sci. U.S.A.* **112**, 11258–11263 (2015). doi: [10.1073/pnas.1502091112](https://doi.org/10.1073/pnas.1502091112); pmid: 26305930
 47. E. Fischer-Friedrich, A. A. Hyman, F. Jülicher, D. J. Müller, J. Helenius, Quantification of surface tension and internal pressure generated by single mitotic cells. *Sci. Rep.* **4**, 6213 (2014). doi: [10.1038/srep06213](https://doi.org/10.1038/srep06213); pmid: 25169063
 48. V. Rodionov, E. Nadezhkina, G. Borisy, Centrosomal control of microtubule dynamics. *Proc. Natl. Acad. Sci. U.S.A.* **96**, 115–120 (1999). doi: [10.1073/pnas.96.1.115](https://doi.org/10.1073/pnas.96.1.115); pmid: 9874781
 49. D. Riendeau *et al.*, Arachidonyl trifluoromethyl ketone, a potent inhibitor of 85-kDa phospholipase A2, blocks production of arachidonate and 12-hydroxyeicosatetraenoic acid by calcium ionophore-challenged platelets. *J. Biol. Chem.* **269**, 15619–15624 (1994). pmid: 8195210
 50. K. M. Dean, P. Roudot, E. S. Welf, G. Danuser, R. Fiolka, Deconvolution-free Subcellular Imaging with Axially Swept Light Sheet Microscopy. *Biophys. J.* **108**, 2807–2815 (2015). doi: [10.1016/j.bpj.2015.05.013](https://doi.org/10.1016/j.bpj.2015.05.013); pmid: 26083920
 51. M. Jacob, M. Unser, *IEEE Trans. Pattern Anal. Machine Intell.* **26**, 1007–1019 (2004).

ACKNOWLEDGMENTS

The authors wish to acknowledge I. Poser and A. Hyman (Max Planck Institute of Molecular Cell Biology and Genetics, Dresden, Germany) for providing stable BAC transgenic HeLa cell lines expressing various fluorescent protein markers, P. Niethammer (Sloan Kettering Institute, New York, NY, USA) for sharing the HeLa cell line that stably expresses cPlax2-mKate2, and V. Sanz-Moreno (Queen Mary University of London, London, UK) for providing A375P cells. LBR pEGFP-N2 (646) was a gift from E. Schirmer (Addgene plasmid no. 61996; <http://n2t.net/addgene:61996>; RRID: Addgene_61996). pGP-CMV-GCaMP6s was a gift from D. Kim and the GENIE Project (Addgene plasmid no. 40753; <http://n2t.net/addgene:40753>; RRID: Addgene_40753). pBOB-EF1-FastFucci-Puro was a gift from K. Brindle and D. Jodrell (Addgene plasmid no. 86849; <http://n2t.net/addgene:86849>; RRID: Addgene_86849). We thank L. Allison and R. Fleck (Centre for Ultrastructural Imaging at King's College London, London, UK) and D. Mathys (Swiss Nanoscience Institute at University of Basel, Basel, Switzerland) for performing scanning electron microscopy of polycarbonate membranes and focused ion beam-based flat AFM cantilever nanofabrication, respectively. We are grateful to B. Baum (University College London, London, UK), D. Gerlich (Institute of Molecular Biotechnology of the Austrian Academy of Sciences, Vienna, Austria), and M. Kraakman (Children's Cancer Research Institute, Vienna, Austria) for comments on the manuscript. We also thank G. Charras (University College London, London, UK) for the advice about estimating internuclear pore distance in nuclei at various degrees of spatial confinement, and N. Carpi (Institut Curie, Paris, France) for technical assistance with experiments. We also thank A. Willart, L. Barbier, and P. Vargas (Institut Curie, Paris, France) for performing additional experiments during the revision of the article, which were finally not included in the article but helped our reasoning. Some illustrations accompanying figures of the present manuscript were partially generated using the BioRender.com online tool. **Funding:** The research leading to these results has received funding from the People Programme (Marie Skłodowska-Curie Actions) of the European Union's Seventh Framework Programme (FP7/2007-2013) under REA grant agreement PCOFUND-GA-2013-609102, through the PRESTIGE programme coordinated by Campus France. A.J.L. was supported by the Marie Curie & PRESTIGE Fellowship (grant 609102), London Law Trust Medal Fellowship (grant MGS9403), and a Career Grant for Incoming International Talent (grant 875764) from the Austrian Research Promotion Agency (FFG). D.J.M. was supported by the National Center of Competence in Research (NCCR) Molecular Systems Engineering. This work was also supported by the Institut Pierre-Gilles de Gennes-IPGG (Equipement d'Excellence, "Investissements d'avenir," program ANR-10-EQPX-34 and Laboratoire d'Excellence, "Investissements d'avenir" program ANR-

10-IDEX-0001-02 PSL and ANR-10-LABX-31. This work was additionally supported by the Institut National du Cancer (INCa grant 2018-PL Bio-02) to M.P. and INCa (grant 2019-PL BIO-07) and INSERM Plan Cancer Single Cell (grant 19CS007-00) to N.M. and M.P. R.J.P. was supported by the National Institute of General Medical Sciences of the National Institutes of Health under Award Number R01GM126054. R.F. received funding from the National Institutes of Health (grants R35GM133522-01 and R33CA235254-02). J.M.G.G. was financed by Instituto de Salud Carlos III (ISCIII) (PI17/01395; PI20/00306) and I3 SNS program. M.D. was supported by the National Institute of General Medical Sciences (grant K99GM123221). N.S.D.S. received a Marie Skłodowska-Curie Individual Fellowship (DCBIO 751735) and an EMBO Long-Term Fellowship (ALTF 1298-2016). I.Z. was supported by a Metchnikov Fellowship from the Franco-Russian Scientific Cooperation Program and the Russian Science Foundation (grant 16-15-10288). **Author contributions:** A.J.L., C.J.C., D.J.M., and M.P. designed the project. A.J.L. and M.P. jointly supervised the project. A.J.L. and C.J.C. performed all key experiments and analyzed the data. D.C. analyzed most of force spectroscopy data and developed analytical approaches to estimate the degree of nuclear membrane folding. Z.A.G.P.F.N., P.J.S., and A.M.L.D. performed experiments with primary mouse immature dendritic cells. M.M. performed experiments with A375P cells. G.P.F.N. performed experiments with HeLa-cPlax2 cells and with Lamin A/C-depleted HeLa cells. N.S. performed experiments with HeLa-LAP2 cells and developed analytical approaches to estimate the degree of nuclear membrane fluctuation. J.M.G.A. and I.Z. performed Western blot analysis of LMNA knockdown efficiency as well as experiments on the effect of transcription and translation inhibition in HeLa cells. J.M.G.A. additionally assisted with manuscript preparation for submission. A.B. performed shRNA-mediated LMNA knockdown in HeLa cells. N.D.S. and J.M.G.G. provided *Lmna* KO DCs and mice. N.M. supervised A.B. and N.S.D.S. M.K.D., E.S.W., and R.F. analyzed 3D collagen data. R.J.P. performed experiments with HT1080 cells in 3D CDMs. A.J.L., C.J.C., D.J.M., and M.P. wrote the manuscript. All authors discussed the results and implications, and commented on the manuscript at all stages; **Competing interests:** The authors declare no competing interests. **Data and materials availability:** All data are available in the main text or the supplementary materials.

SUPPLEMENTARY MATERIALS

science.sciencemag.org/content/370/6514/eaba2894/suppl/DC1
Figs. S1 to S11
Tables S1 to S3
MDAR Reproducibility Checklist
Movies S1 to S7

[View/request a protocol for this paper from Bio-protocol.](#)

20 November 2019; resubmitted 29 June 2020
Accepted 28 August 2020
10.1126/science.aba2894

RESEARCH ARTICLE SUMMARY

CELL BIOLOGY

The nucleus measures shape changes for cellular proprioception to control dynamic cell behavior

Valeria Venturini, Fabio Pezzano, Frederic Català Castro, Hanna-Maria Häkkinen, Senda Jiménez-Delgado, Mariona Colomer-Rosell, Monica Marro, Queralt Tolosa-Ramon, Sonia Paz-López, Miguel A. Valverde, Julian Weghuber, Pablo Loza-Alvarez, Michael Krieg, Stefan Wieser*, Verena Ruprecht*

INTRODUCTION: Human beings are equipped with multiple senses (sight, hearing, smell, taste, touch, and proprioception) to help them to react properly to their environment. The human body is composed of trillions of cells that similarly require multiple sensations to fulfill their task in specific tissues. From a cellular perspective, the three-dimensional (3D) tissue microenvironment is a crowded place in which cells experience a multitude of physical constraints and mechanical forces. These conditions can lead to cell shape changes—for example, as observed when motile cells squeeze through tight spaces or when cells deform in densely packed tissue regions. To guarantee tissue integrity and homeostasis, cells need to be able to respond to these mechanical challenges in their tissue microenvironment, both in the adult organism and during embryonic development. How cells can measure their own shape and adapt their dynamic behavior to the physical surroundings remains an open question.

RATIONALE: The actomyosin cytoskeleton is a structural scaffold within cells that controls mechanical cell properties and dynamic cellular processes such as cell migration. Cytoskeletal

networks can contract and thereby generate force by using the activity of myosin II motor proteins. Cell contractility influences the mode and speed of cell migration. Various cell types have been observed to switch to a highly contractile and fast amoeboid cell migration type in constrained environments. This suggests the presence of a conserved mechanosensitive pathway capable of translating mechanical cell deformations into adaptive cytoskeletal arrangements that allow cells to react dynamically to changes in their tissue microenvironment.

RESULTS: Here, we show that the nucleus, the biggest organelle in the cell, translates cell shape changes into a deformation signal regulating cell behavior. We found that variable cell squeezing defines the specific set point of cell contractility, with increased cell deformation leading to higher cortical myosin II levels and promoting fast amoeboid cell migration. This adaptive cellular response to deformation was rapid (<1 min), stable over time (>60 min), and reversible upon confinement release. We found that changes in cell behavior were associated with nucleus stretch and unfolding of the inner nuclear membrane (INM), supporting

the idea that the nucleus functions as a fast mechanical responder for sensing cell shape variations. We show that INM unfolding triggered a calcium-dependent mechanotransduction pathway via the activation of cytosolic phospholipase A2 (cPLA₂) and metabolite production of arachidonic acid (AA) that regulates myosin II activity. This establishes the nucleus as an intracellular mechano-gauge that measures shape deformations and directly controls morphodynamic cell behavior. Furthermore, we found that the combination of nuclear deformation and intracellular calcium levels, regulated by nuclear positioning, allows cells to distinguish distinct shape deformations and adapt their behavior to changing tissue microenvironments.

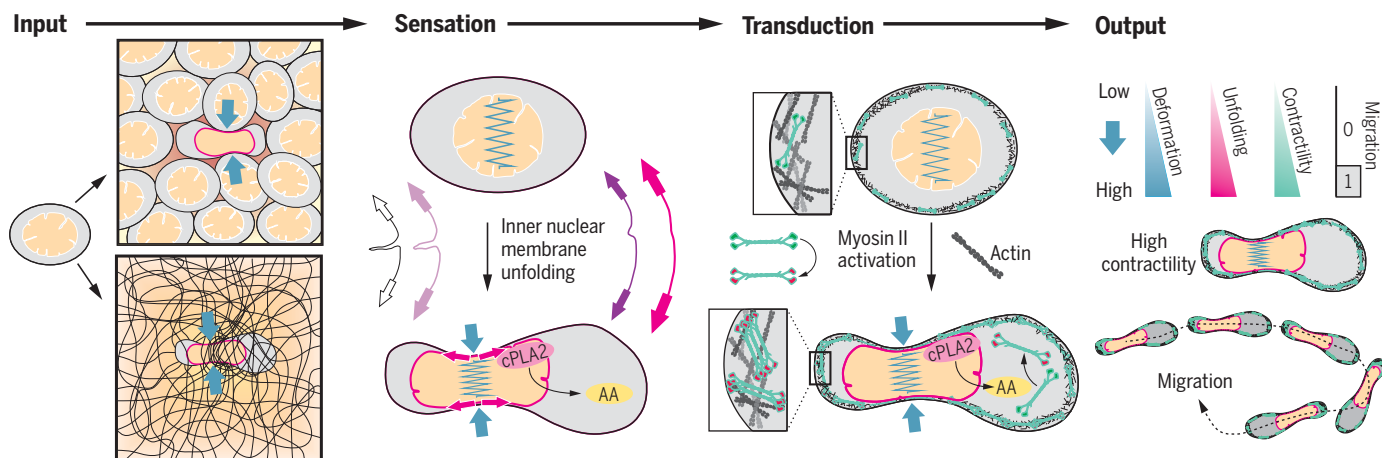
CONCLUSION: Here, we show that the nucleus acts as a central hub for cellular proprioception, which, in a manner similar to how we sense our body posture and movement, enables single cells to precisely interpret and respond to changes in their 3D shape. The rapid increase in cell contractility and migration competence upon cell squeezing equips cells with a rapid “evasion reflex”: In constrained environments, cells polarize and acquire a rapid migratory phenotype that enables cells to move away and squeeze out from tight spaces or crowded tissue regions. The nucleus thus allows cells to decode changes in their shape and to adjust their behavior to variable tissue niches, relevant for healthy and pathological conditions. ■

The list of author affiliations is available in the full article online.

*Corresponding author. Email: stefan.wieser@icfo.eu (S.W.); verena.ruprecht@crg.eu (V.R.)

Cite this article as V. Venturini et al., *Science* **370**, eaba2644 (2020). DOI: 10.1126/science.aba2644

S READ THE FULL ARTICLE AT
<https://doi.org/10.1126/science.aba2644>



The nucleus acts as an elastic mechanotransducer of cellular shape deformation and controls dynamic behavior. Cell shape changes induce inner nuclear membrane unfolding and activation of the cPLA₂-AA pathway. This transduces mechanical nucleus stretch into myosin II recruitment to the cell cortex regulating actin cytoskeleton contractility and cellular behavior. High contractility levels further lead to motile cell transformation and initiate amoeboid cell migration.

RESEARCH ARTICLE

CELL BIOLOGY

The nucleus measures shape changes for cellular proprioception to control dynamic cell behavior

Valeria Venturini^{1,2}, Fabio Pezzano², Frederic Català Castro¹, Hanna-Maria Häkkinen², Senda Jiménez-Delgado², Mariona Colomer-Rosell¹, Monica Marro¹, Queralto Tolosa-Ramon², Sonia Paz-López³, Miguel A. Valverde³, Julian Weghuber⁴, Pablo Loza-Alvarez², Michael Krieg¹, Stefan Wieser^{1,*}, Verena Ruprecht^{2,5,*}

The physical microenvironment regulates cell behavior during tissue development and homeostasis. How single cells decode information about their geometrical shape under mechanical stress and physical space constraints within tissues remains largely unknown. Here, using a zebrafish model, we show that the nucleus, the biggest cellular organelle, functions as an elastic deformation gauge that enables cells to measure cell shape deformations. Inner nuclear membrane unfolding upon nucleus stretching provides physical information on cellular shape changes and adaptively activates a calcium-dependent mechanotransduction pathway, controlling actomyosin contractility and migration plasticity. Our data support that the nucleus establishes a functional module for cellular proprioception that enables cells to sense shape variations for adapting cellular behavior to their microenvironment.

The three-dimensional (3D) shape of an organism is built by active force-generating processes at the cellular level and the spatiotemporal coordination of morphodynamic cell behavior. Contractility of the actomyosin cell cortex represents a major cellular force production mechanism underlying cellular shape change (1), cell polarization (2), and active cell migration dynamics (3). Contractility levels are regulated by the activity of nonmuscle myosin II motor proteins (4) and are precisely controlled to tune single-cell and tissue morphodynamics during development (5, 6) and tissue homeostasis and disease in the adult organism (7, 8). Still, mechanisms that regulate the set-point level of cortical contractility on the single-cell level remain poorly understood.

To adjust cortical contractility levels, cells need to make quantitative measures of their mechanochemical 3D tissue microenvironment and translate this information into a defined morphodynamic output response. Morphogens that act as chemical information carriers during embryogenesis have attracted major attention (9), modulating cytoskeletal and cellular dynamics via receptor signaling pathways that tune protein activities (such as phosphorylation states) and/or protein expres-

sion levels. In contrast, physical parameters of the 3D tissue niche and mechanical forces gain importance as regulators of cellular morphodynamics and myosin II-dependent cortical contractility levels (10, 11). In vivo, mechanical cell deformation and cellular packing density in crowded tissue regions has been shown to influence major morphodynamic processes such as cortical actomyosin contractility (12, 13), cell division (14–17), and cell extrusion and invasion (18). Ex vivo studies have provided further evidence on the single-cell level that physical cell deformation is sufficient to modulate cortical myosin II localization and motor protein activity (19, 20) and influence morphodynamic cell behavior (21, 22).

A recent example is the identification of a fast amoeboid migration mode, called stable-bleb migration, that is triggered by an increase in cortical contractility via genetic or physical cell perturbation (23). This morphodynamic migration switch was shown to be present in both undifferentiated and lineage-committed embryonic progenitor cells and was also identified in various other cell types (24–29). This finding suggests that a conserved, albeit unknown, mechanosensitive cellular signaling module regulates myosin II-based cortical contractility and motile cell transformation depending on cellular shape deformations in constrained tissue microenvironments.

Cell contractility levels increase upon cell confinement and regulate migration plasticity

To approach the question of how cells can measure and adaptively respond to physical cell shape changes within their 3D tissue microenvironments, we established a synthetic approach that enables the mimicking of me-

chanical cell deformations in controlled 3D microconfinement assays (30). Primary progenitor stem cells were isolated from blastula stage zebrafish embryos and cultured in planar confinement assays of defined height to mimic various cell deformation amplitudes (fig. S1A). Lowering confinement height in discrete steps increased cell deformation, which scaled nonlinearly with a pronounced enrichment of myosin II at the cell cortex relative to cortical actin accumulation (Fig. 1, A and B; fig. S1, B to D; and movie S1). Cortical accumulation of myosin II was accompanied by an increase in cellular bleb size (fig. S1E and movie S1), indicative of an active increase in cortical contractility levels depending on confinement height. Myosin II relocalization to the cell cortex in confined cells was rapid [half-time ($t_{1/2}$) < 1 min] (Fig. 1, C and D) and temporally stable under confinement. Distinct plateaus of cortical myosin II enrichment were evident, with myosin II relocalization increasing for larger cell deformations (Fig. 1C). A cell confinement height smaller than 7 μm caused a pronounced increase in cell lysis during compression, defining a maximal threshold deformation of ~30% of the initial cell diameter (d), given a blastula cell size of $d \sim 25 \mu\text{m}$ (fig. S3H). Overall, these data support that the physical microenvironment defines a specific set-point level of cortical contractility as a function of cell deformation.

We have previously shown that an increase in myosin II-mediated cortical contractility induced a stochastic motility switch into a highly motile amoeboid migration phenotype called stable-bleb mode (23). In accordance with these results, rapid cortical myosin II enrichment in confinement resulted in spontaneous cell polarization which initiated amoeboid cell migration (Fig. 1, E and F; fig. S1, F and G; and movies S2 and S3). Polarized cells revealed characteristic actomyosin density gradients from the cell front toward the rear, accompanied by fast retrograde cortical flows (fig. S1H and movies S2 and S3); these cortical flows have been shown to power fast amoeboid migration in polarized cells (23, 31). Meanwhile, unpolarized cells showed random tumbling with minimal net translocation (figs. S1, F and G, and S2A). These data support that physical cell deformation in confinement is sufficient to increase actomyosin network contractility and trigger rapid amoeboid cell migration.

Release of cell compression induced a rapid relocalization of cortical myosin to the cytoplasm (Fig. 1G and fig. S1I), followed by a rapid loss of cell polarization and related migratory capacity (fig. S1G and movie S4). Interfering with myosin II activity via blebbistatin inhibited cell polarization and associated cell motility in confinement (Fig. 1E and fig. S1J), in accordance with a necessary role of myosin II-based contractility in cell polarization and

¹ICFO – Institut de Ciències Fotòniques, The Barcelona Institute of Science and Technology, 08860 Castelldefels, Spain. ²Centre for Genomic Regulation (CRG), The Barcelona Institute of Science and Technology, 08003 Barcelona, Spain. ³Laboratory of Molecular Physiology, Department of Experimental and Health Sciences, Universitat Pompeu Fabra (UPF), Barcelona, Spain. ⁴School of Engineering, University of Applied Sciences Upper Austria, Stelzhamerstraße 23, Wels 4600, Austria. ⁵Department of Experimental and Health Sciences, Universitat Pompeu Fabra (UPF), Barcelona, Spain

*Corresponding author. Email: stefan.wieser@icfo.eu (S.W.); verena.ruprecht@crgeu (V.R.)

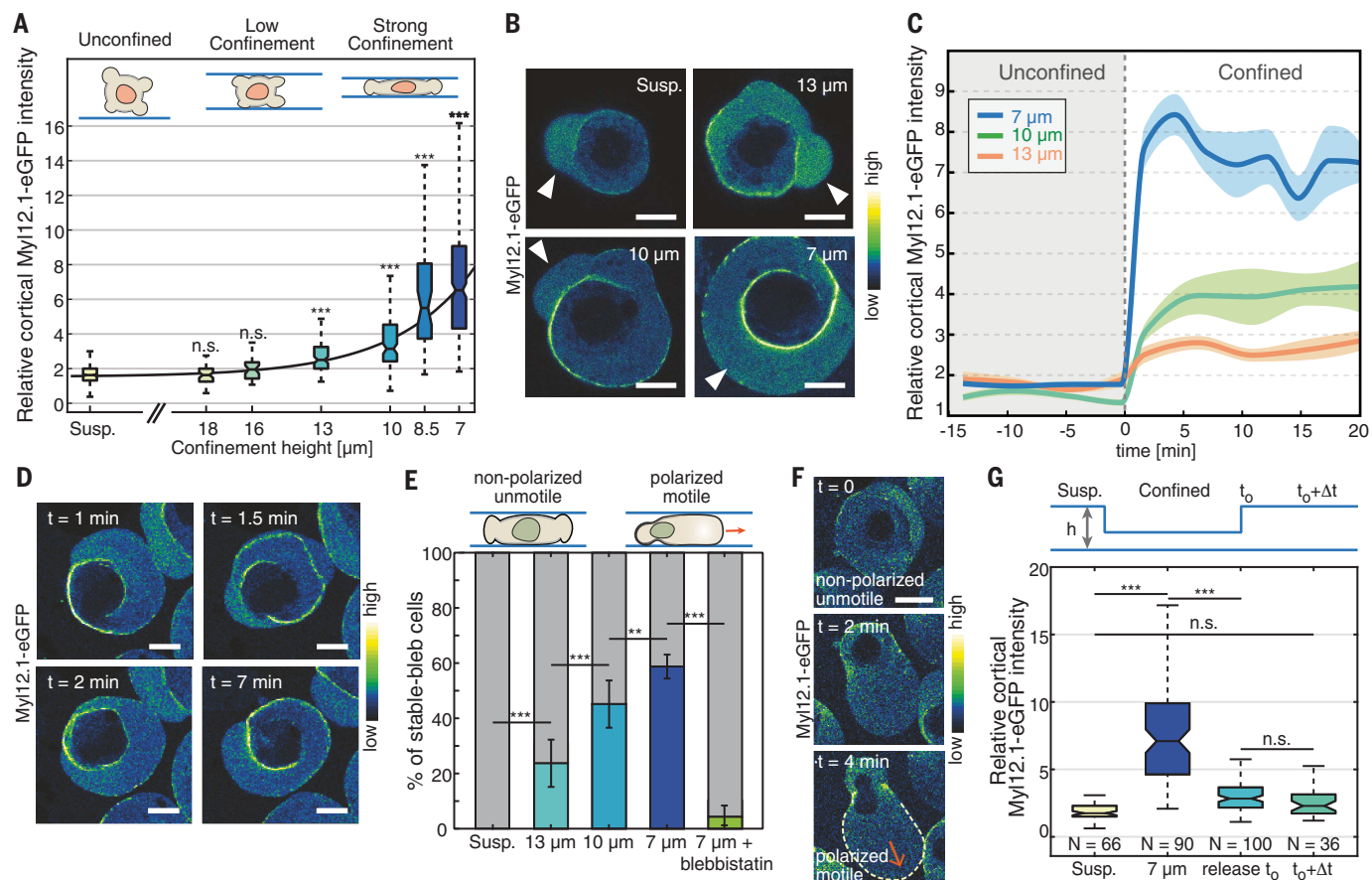


Fig. 1. Cell deformation in confined environments defines cell contractility, polarization, and fast amoeboid cell migration. (A) Relative cortical myosin II enrichment for decreasing confinement height in unpolarized progenitor cells [$N = 477$ cells (suspension, unconfined); $N = 56$ (18 μm); $N = 35$ (16 μm); $N = 103$ (13 μm); $N = 131$ (10 μm); $N = 49$ (8.5 μm); $N = 348$ (7 μm)]. Significance values are with respect to the suspension condition. Black line shows a monoexponential fit with offset to the data. (B) Exemplary confocal fluorescence images of control progenitor stem cells in suspension (Susp.) and indicated confinement heights expressing Myl12.1-eGFP (myosin II). White arrows point to cellular blebs. (C) Temporal dynamics of cortical myosin II recruitment upon mechanical confinement at time (t) = 0 at the indicated heights. Thick lines correspond to the mean, and areas correspond to the standard error of the

mean (SEM). $N > 50$ cells for all conditions. (D) Exemplary cross-sectional time-lapse images of myosin II-eGFP-expressing cells under 7 μm confinement. (E) Percentage of polarized motile stable-bleb cells in suspension at indicated confinement heights and myosin II inhibition (blebbistatin) at 7 μm (each $N > 500$). (F) Representative time-lapse images of a myosin II-eGFP-expressing cell undergoing spontaneous stable-bleb cell polarization and migration initiation. Dashed line shows the stable-bleb cell front and red arrow points in the direction of movement. (G) Relative cortical myosin II enrichment during reversible cell confinement. Cells were confined for 15 min before confinement was released, and cortical myosin II levels were measured at t_0 (0 to 5 min) and at $t_0 + \Delta t$ (30 to 60 min) after release. h, height. *** $P < 0.0001$, ** $P < 0.001$; n.s., not significant. All scale bars, 10 μm .

migration induced by mechanical cell shape deformation. Cortical myosin II enrichment and cell polarization occurred independently of caspase activation (fig. S1K), supporting that morphodynamic changes are not caused by the activation of proapoptotic signaling programs. Furthermore, transcriptional inhibition did not block cortical myosin II relocalization and cell polarization (fig. S1L), indicating that a nongenetic program is regulating cellular morphodynamics under cell compression.

During gastrulation, blastoderm embryonic progenitor stem cells specify into different lineages (ectoderm, mesoderm, endoderm) and acquire distinct biomechanical and morphodynamic characteristics, driving germ layer positioning and shape formation of the em-

bryo (32, 33) (Fig. 2, A and B). To test the mechanosensitive response to cell deformation at later developmental stages, we obtained different progenitor cell types from embryos via genetic induction or using endogenous reporter lines. Under confinement, nonmotile ectodermal cells rapidly polarized and started to migrate in an amoeboid stable-bleb mode. Similarly, mesendodermal cells underwent a fast mesenchymal-to-amoeboid transition in confinement (Fig. 2, B to D; fig. S2A; and movies S3 and S5). The fraction of polarized stable-bleb cells and their cell speed were comparable for different progenitor cell types in confinement (fig. S2, B and C). Together, these results support that physical cell shape deformation in confined tissue microenvironments activates a mechanosensitive signaling

pathway regulating adaptive cortical contractility levels and morphodynamic migration plasticity in pluripotent and lineage-committed embryonic stem cells.

The cell nucleus is a mechanosensor of large cell shape deformation

We next sought to identify potential mechanisms that control cellular shape deformation sensing and adaptive morphodynamic behavior. Cortical myosin II relocalization and amoeboid cell transformation occurred on passivated confinement surfaces independently of adhesive substrate coating (figs. S2, A and C, and S3A) and cell-cell contact formation (fig. S3B). These observations support that the activation of cortical contractility in confinement occurs independently of adhesion-dependent

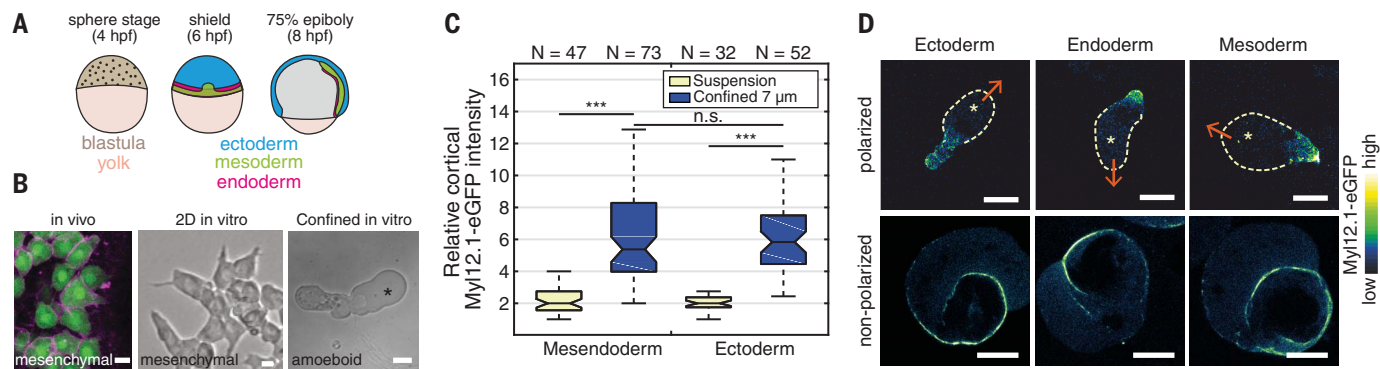


Fig. 2. Physical confinement triggers amoeboid migration in different cell lineages. (A) Sketch of the developing zebrafish embryo at sphere [4 hours post-fertilization (hpf)], shield (6 hpf), and 75% epiboly (8 hpf) stage. (B) Exemplary confocal and bright-field images of mesodermal cells in vivo expressing Lyn-Tomato (magenta, membrane) and GFP (green) under the mezzo promoter (left), induced mesendodermal cells in vitro plated on a 2D fibronectin-coated surface (middle), and under 7 μ m confinement (right). Asterisk indicates stable-bleb cell

front. (C) Relative cortical myosin II intensity for mesendodermal and ectodermal progenitor cells in control suspension and confinement conditions. (D) Exemplary confocal images of stable-bleb polarized (top) and nonpolarized (bottom) progenitor cell types expressing myosin II-eGFP under 7 μ m confinement. From left to right: ectoderm, endoderm, and mesoderm cells. Dashed line and yellow asterisks indicate the stable-bleb cell front, and red arrows indicate the direction of cell migration. *** $P < 0.0001$. All scale bars, 10 μ m.

mechanotransduction pathways (34). The temporal characteristics of myosin II relocalization dynamics in confined cells showing a fast, stable, and reversible accumulation of cortical myosin II (Fig. 1, C and D) suggested that shape deformation is sensed by a non-dissipative cellular element that can rapidly measure and convert gradual cellular shape changes into stable contractility response levels.

The actomyosin cytoskeleton itself has been implicated to act as a mechanosensitive network (20), but it generally limits deformation sensing due to rapid turnover of the cell cortex (35). To test for the activation of mechanosensitive ion channels, we used gadolinium and GsMTx4, inhibitors of stretch-activated channels, with GsMTx4 having been shown to block the tension-dependent Piezo1 channel, which is activated after confinement of human cancer cells (36). Treatment with both inhibitors did not result in a significant reduction in cortical myosin II accumulation under cell deformation (fig. S3C), despite the presence of functional Piezo1 channels in these cells, as validated with the Piezo1-specific agonist Yoda (fig. S3D).

Notably, we observed that cortical myosin II enrichment only started to occur below a threshold confinement height ($\sim 13 \mu$ m) that correlated with the spatial dimension of the nucleus (Fig. 3A and fig. S3H). Analyzing nuclear shape change versus cortical myosin accumulation revealed a biphasic behavior, with a first phase in which the nucleus diameter remained nearly constant and no myosin II accumulation was observed, and a second phase in which the relative myosin accumulation linearly increased with the relative change in nucleus diameter (Fig. 3, A and B, and fig. S3E). In accordance with this observation, we expected a propor-

tional change of nuclear surface ruffling upon deformation of an initially spherical nucleus. Measuring of nuclear surface folding by the expression of the inner nuclear membrane (INM) protein Lap2b-eGFP (enhanced green fluorescent protein-tagged lamina-associated polypeptide 2) revealed that membrane ruffling was continuously reduced when nucleus deformation started to occur at a threshold deformation of $\sim 13 \mu$ m (Fig. 3, C to E; fig. S3F; and movie S6). In addition, analysis of nucleus membrane curvature for confined versus control cells in suspension indicated INM surface unfolding (Fig. 3, F and G, and movie S6), with no significant difference in total nuclear volume and surface (fig. S3G). Nucleus deformation further correlated with cortical myosin II accumulation in the endogenous in vivo context during the blastula-to-gastrula transition, when a gradient of cellular packing density appears from the animal pole toward the lateral margin (37) (fig. S2, D and E).

To further probe the dependence of cortical myosin II accumulation on nucleus size, we dissociated primary embryonic stem cells from early and late blastula stages, as cells reduce their size in consecutive rounds of early cleavage divisions (fig. S3H). Deforming cells of different sizes under similar confinement heights revealed that myosin II accumulation is correlated with relative changes in nucleus deformation but not cell deformation (Fig. 4, A and B). To test a functional role of the nucleus in regulating cortical contractility levels during cellular shape deformation, we analyzed cortical myosin II accumulation in mitotic cells that present a disassembled nuclear envelope. To arrest cells in mitosis and further increase the percentage of mitotic cells, we used nocodazole, a microtubule-disrupting drug.

Confinement of mitotic cells (either spontaneous or nocodazole-induced) did not trigger a cortical myosin II accumulation at a 7 μ m confinement height as it did in interphase blastula cells (Fig. 4C) or cell polarization (fig. S3I). However, mitotic cells did accumulate myosin II (Fig. 4D) and polarize (fig. S3I) in response to lysophosphatidic acid (LPA), a potent activator of Rho/Rho-associated coiled-coil containing protein kinase (ROCK) signaling, which has previously been shown to induce rapid cortical myosin II enrichment and amoeboid migration in zebrafish embryonic progenitor stem cells (23). During entry into mitosis, cells gradually lost cortical myosin II accumulations, which temporally correlated with the start of nuclear envelope breakdown (Fig. 4E). Altogether, these data show that myosin II enrichment is associated with nuclear shape deformation and stable INM membrane unfolding. This suggests that the nucleus functions as a continuous nondissipative sensor element of cell deformation involved in the mechanosensitive regulation of cortical contractility levels and cellular morphodynamics.

To directly test biophysical characteristics of the nucleus, we developed an assay to probe intracellular nucleus mechanics by optical tweezer measurements. For this purpose, latex beads of 1 μ m size were injected into one-cell-stage embryos that dispersed across embryonic cells during early cleavage cycles and acted as intracellular force probes to measure rheological properties of the nucleus (fig. S4A). Trapezoidal loads were measured for cells in suspension and under 10- μ m confinement (fig. S4, B to E). The recorded force followed the fast initial indentation to reach a peak force before it relaxed to a nonzero constant force-plateau. The relaxation time remained

unchanged between suspension ($\tau = 6.08 \pm 1.1$ s) and confined cells ($\tau = 4.00 \pm 0.6$ s) (fig. S4, D to H), suggesting a passive but rapid (second-scale) relaxation of a viscous component. The force-plateau on a long time scale corresponds to an elastic component of the nucleus (fig. S4I), in line with previous measurements that identified an elastic behavior of the nucleus (38) that can act as a cellular strain gauge. In addition, we observed that INM unfolding was stable over a measurement period of 60 min (fig. S4J) under mechanical cell deformation, supporting that INM stretch does not relax over extended time periods.

Nuclear deformation activates a calcium-dependent mechanotransduction pathway regulating myosin II activity

We next aimed to identify nucleus deformation-dependent signaling pathways that link the spatiotemporal correlation of nuclear shape changes with fast myosin II activation and

changes in morphodynamic cell behavior. Our previous observations suggested that nucleus deformation and associated mechanosensitive processes at the INM interface are involved in the regulation of myosin II activity and cortical contractility. Among a set of molecules tested under confinement conditions (table S1), we identified cytosolic phospholipase A2 (cPLA₂) as a key molecular target mediating the activation of cortical myosin II enrichment (Fig. 5, A and B) and amoeboid cell transformation under cell compression (Fig. 5C). Inhibition of cPLA₂ by pharmacological interference using pyrrophenone robustly blocked cortical myosin II relocation under varying confinement heights (fig. S5A). Furthermore, we observed a significant reduction of cortical myosin II levels in confined cells by morpholino (MO) interference with cPLA₂, while overexpression of cPLA₂ mRNA rescued the morphant phenotype and led to a myosin II accumulation comparable to that in control cells (Fig. 5, A and B). Residual

myosin II activation in cells obtained from morphant embryos suggests a maternal contribution of cPLA₂ protein in the early embryo that cannot be targeted by MO interference. To exclude that other mechanisms, such as structural changes in the actin network, prevent cortical myosin II relocation under cPLA₂ inhibition, we added LPA as an exogenous myosin II activator to cPLA₂ inhibited cells. Under this condition, myosin II was strongly accumulated at the cell cortex (fig. S5, B and C) and induced cell polarization associated with amoeboid motility (Fig. 5C). These data support that myosin II can be activated by extrinsic pathways when cPLA₂ signaling is inhibited and remains competent to bind to the cell cortex.

Recent work identified that the activation of proinflammatory signaling during leukocyte recruitment to wounding sites is regulated by tension-sensitive binding of cPLA₂ to the INM (39). We thus tested a role of cPLA₂ in the nucleus by generating a modified cPLA₂

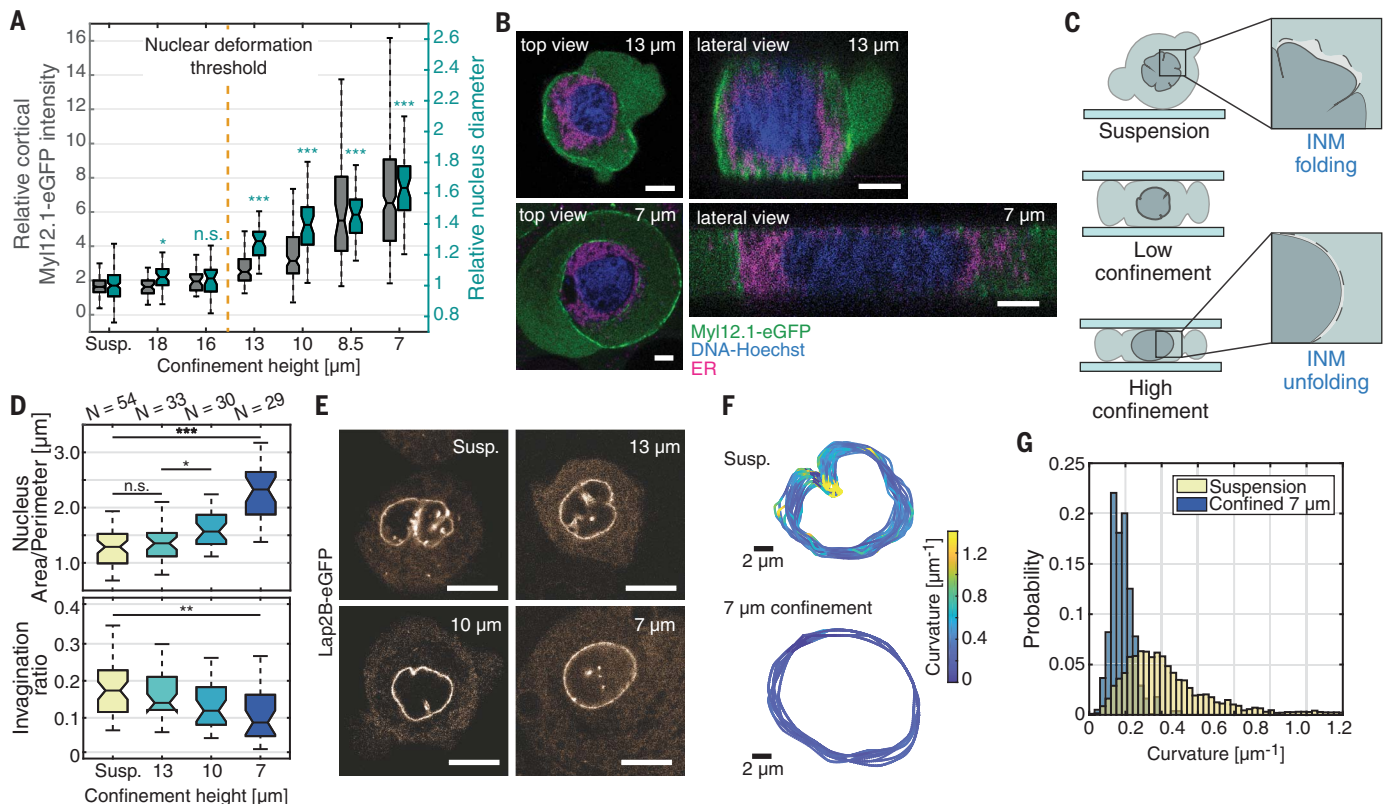


Fig. 3. Nuclear envelope unfolding is associated with increasing cortical contractility. (A) Double boxplot of relative cortical myosin II enrichment (left axis, gray) and relative nuclear diameter (right axis, teal) for decreasing confinement height. Statistical test for relative nuclear diameter performed with respect to suspension [$N = 144$ cells (suspension); $N = 44$ (18 μm); $N = 32$ (16 μm); $N = 37$ (13 μm); $N = 45$ (10 μm); $N = 37$ (8.5 μm); $N = 50$ (7 μm)]. Statistical tests for cortical myosin II levels and experimental N related to Fig. 1A. (B) Exemplary confocal top views (x-y) and lateral views (y-z) of progenitor stem cells expressing myosin II-eGFP stained with DNA-Hoechst and ER-TrackerRed in 13 and 7 μm confinement. (C) Illustration

showing the unfolding of the inner nuclear membrane (INM) with increasing cell confinement. (D) Nuclear area-to-perimeter ratio (top) and nuclear invagination ratio (bottom) for increasing confinement. (E) Exemplary confocal images of cells expressing Lap2B-eGFP under varying cell deformation. (F) Curvature analysis of nuclear shape for 20 consecutive frames ($t_{\text{lag}} = 10$ s) for unconfined (suspension, top) and 7 μm confined nuclei (bottom). (G) Histogram of nuclear curvature for unconfined and 7 μm confined nuclei related to (F) with $N = 10$ cells for each condition ($P < 10^{-12}$). *** $P < 0.0001$, ** $P < 0.001$, * $P < 0.01$. Scale bar in (B), 5 μm ; all other scale bars, 10 μm .

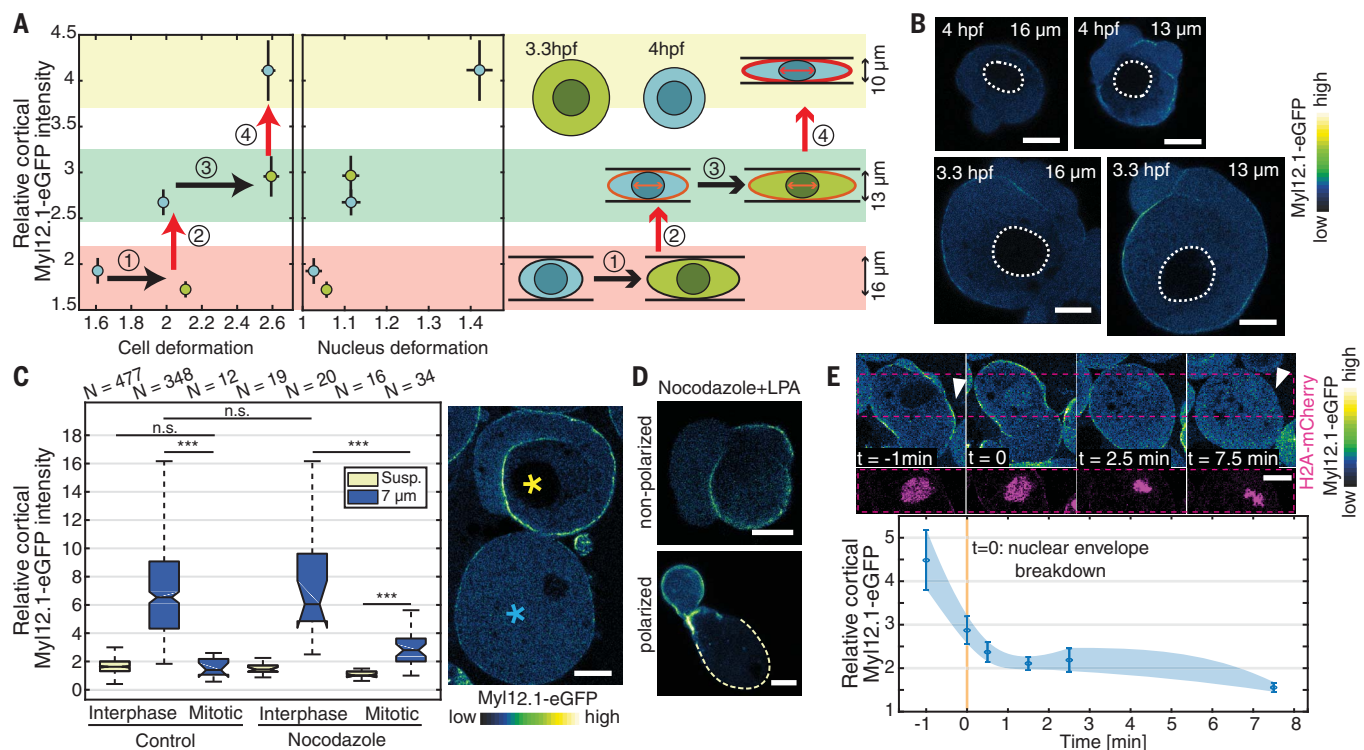


Fig. 4. Nucleus size and integrity determine the morphodynamic cell response to confinement. (A) Relative cortical myosin II intensity with respect to cell deformation as defined by the ratio of cell size to confinement height (left) and nucleus deformation (right) measured via relative nucleus diameter increase (right) for cells dissociated from embryos at high-oblong (3.3 hpf) and sphere (4 hpf) stage and cultured under similar confinement heights, as indicated. Data points and error bars indicate mean and SEM; 3.3 hpf: $N = 58$ (16 μm), $N = 61$ (13 μm); 4 hpf: $N = 44$ (16 μm), $N = 60$ (13 μm), $N = 45$ (10 μm). The Pearson correlation coefficient between myosin II intensity and nuclear deformation is 0.48. (B) Exemplary confocal images of progenitor cells expressing myosin II-eGFP under 16 and 13 μm confinement dissociated from 4 hpf (top) and 3.3 hpf (bottom) embryos. Dashed lines outline cell nuclei. (C) Relative cortical myosin II enrichment for interphase and mitotic cells under

7 μm confinement cultured in suspension (control) in the presence of 1 μM nocodazole. Exemplary confocal images of progenitor cells expressing myosin II-eGFP in interphase (yellow asterisk) or during mitosis (cyan asterisk) under 7 μm confinement. (D) Exemplary confocal images of progenitor unpolarized (top) and polarized (bottom) cells expressing myosin II-eGFP during mitosis treated with 1 μM nocodazole and 50 μM LPA. Dashed line shows the stable-bleb cell front. (E) Cortical myosin II intensity of $N = 7$ cells undergoing mitosis, and representative confocal time-lapse images of cells expressing myosin II-eGFP and H2A-mCherry at indicated time points ($t = 0$, time of nuclear envelope breakdown). The arrows point to the cell cortex with cortical myosin II enrichment ($t = -1$ min) or loss of cortical myosin II levels ($t = 7.5$ min). Data points and error bars indicate mean and SEM. *** $P < 0.0001$. All scale bars, 10 μm .

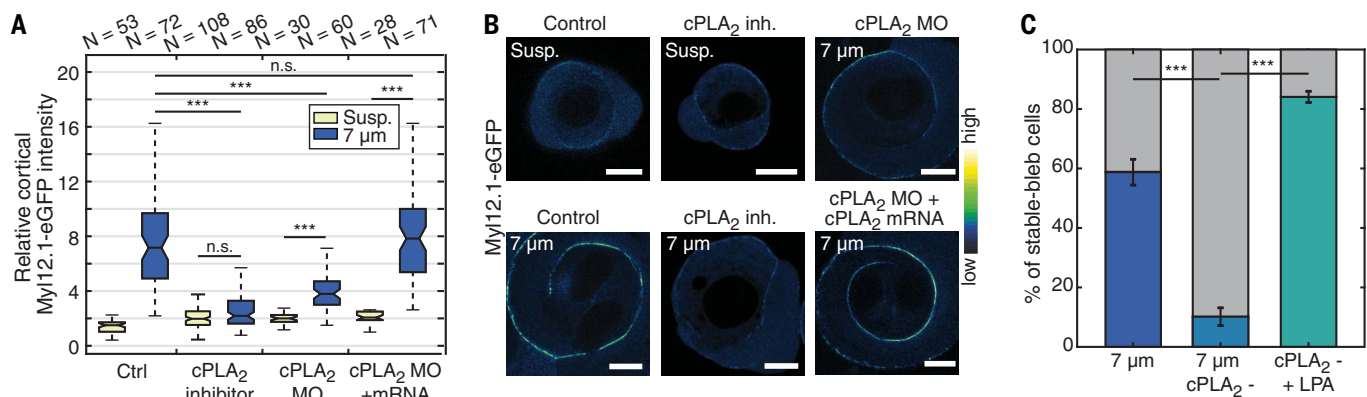


Fig. 5. Nucleus deformation activates a mechanosensitive lipase signaling pathway regulating myosin II activity. (A) Relative cortical myosin II intensity for progenitor cells cultured in suspension versus 7 μm confinement conditions for control cells (DMEM), with cPLA₂ inhibitor, or injected with cPLA₂ MO and cPLA₂ MO + cPLA₂ mRNA. (B) Exemplary confocal images of progenitor cells expressing myosin II-eGFP related to (A) for indicated conditions. (C) Percentage of stable-bleb polarized cells for control cells under 7 μm confinement and in the presence of cPLA₂ inhibitor or unconfined (suspension) cells stimulated with 50 μM LPA. For all conditions, $N > 200$ cells. *** $P < 0.0001$. All scale bars, 10 μm .

construct containing a nuclear export sequence (NES). Using leptomycin B as a blocker of nuclear export, we observed an accumulation of cPLA₂-NES-GFP within the nucleus, showing a concomitant increase of cortical myosin II levels in confined cells (Fig. 6, A and B). These data support that cPLA₂ localization in the nucleus is required for myosin II enrichment at the cortex.

We further validated that cortical myosin II enrichment in cells of different sizes (early versus late blastula cells) and different embryonic cell lineages (mesendoderm or ectoderm cells) depends on the activation of cPLA₂ signaling. Pharmacological inhibition of cPLA₂ activity blocked cortical myosin II relocalization in confined cells (Fig. 6C) and strongly reduced cell polarization and associated migration competence (fig. S2B), supporting a consistent role of cPLA₂ activation under physical cell deformation across early to late developmental stages. These data support that activation of cPLA₂ signaling in the nucleus mediates adaptive cytoskeletal and morphodynamic behavior under cell deformation.

Arachidonic acid (AA) is the primary cleavage product generated by cPLA₂ activity (40).

To directly validate whether nucleus deformation in confinement triggers cPLA₂ activity, we measured the release of AA by Raman spectroscopy. The analysis of Raman spectra confirmed the specific production of AA in confined cells (Fig. 6D and fig. S5E), with the increase in AA production in confined versus control cells being specifically blocked in the presence of cPLA₂ inhibitor (Fig. 6E). We further observed that AA was exclusively detected in the cytoplasm of confined cells, which suggests that AA is directly released from nuclear membranes into the cytoplasm. These data support that cell confinement leads to enhanced cPLA₂ activity and production of AA associated with INM unfolding and stretching of the nucleus surface.

AA has been implicated in both the direct (41) and indirect regulation of myosin II activity via protein phosphorylation (42). We tested the involvement of the Rho/ROCK and myosin light chain kinase (MLCK) as key regulators of myosin II activity (4). MLCK inhibition showed no significant effect on myosin II enrichment in confined cells, whereas a pronounced reduction of cortical myosin II recruitment was observed when using staurosporine,

a general kinase inhibitor, and under specific inhibition of Rho activity (Fig. 6F). Using a RhoA–Förster resonance energy transfer (FRET) sensor further indicated an increased RhoA activity in confined cells versus control cells in suspension, which was significantly reduced in the presence of cPLA₂ inhibitor in confined cells (fig. S5F). These data support that AA production by cPLA₂ activity initiates upon nuclear envelope unfolding, regulating phosphorylation-dependent myosin II activity at the cell cortex. AA and its metabolic products have been widely implicated in para- and autocrine signaling functions involving G protein-coupled receptors (43). We assessed the role of AA product release by compressing cells directly under micropillars at a height of ~7 μm, leading to confined and nonconfined cells in close proximity (fig. S5G). Whereas confined cells showed high levels of cortical myosin II and amoeboid cell transformation, nonconfined cells in direct contact revealed no alterations in cortical myosin II and cellular morphodynamics (fig. S5H). These results support that cPLA₂-dependent myosin II activation does not depend on the release of diffusible signals and regulates cellular

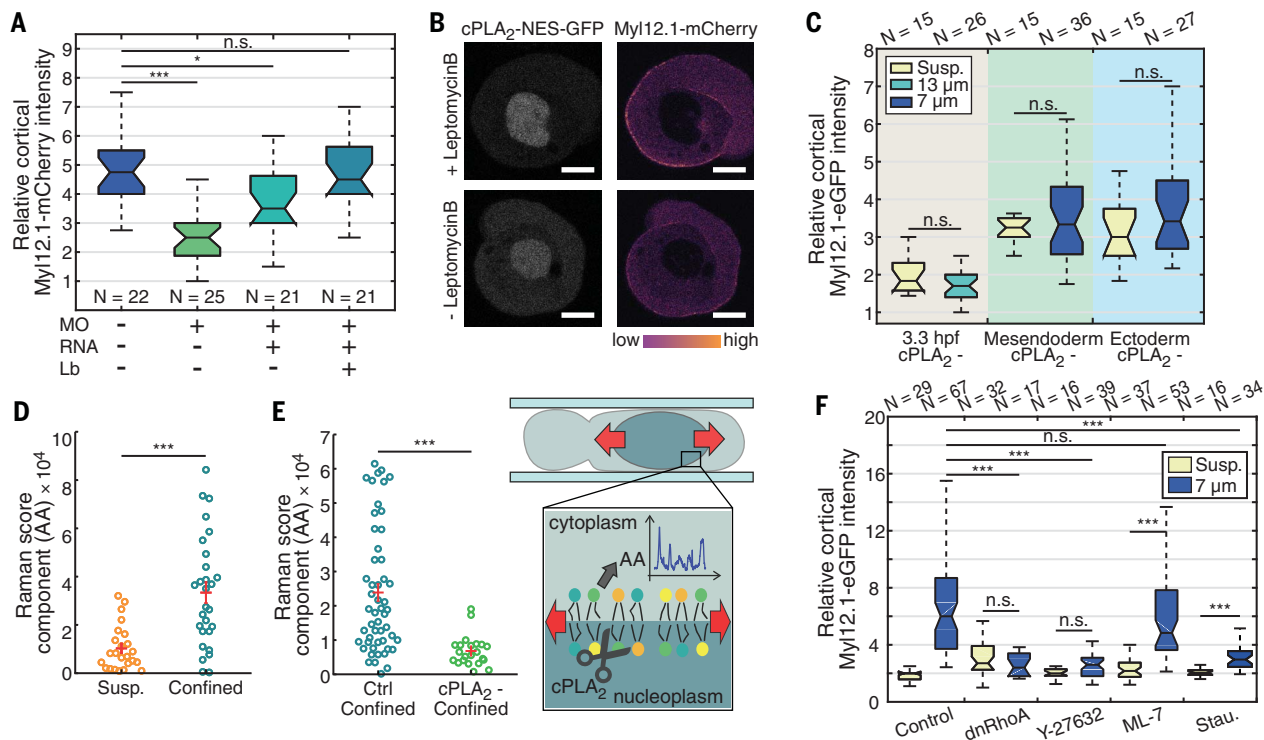


Fig. 6. cPLA₂ activity at the inner nuclear membrane generates AA as a metabolite regulating cortical contractility in confinement. (A) Relative cortical myosin II fluorescence intensity for cells dissociated from controls (uninjected) embryos or embryos injected with cPLA₂ MO, cPLA₂ MO + cPLA₂-NES-GFP mRNA (RNA) and with or without addition of leptomycin B (Lb). (B) Exemplary confocal fluorescence images of cell expressing myosin II–mCherry (right) and cPLA₂-NES-GFP (left) under 7 μm confinement with (top) or without (bottom) the addition of Lb. (C) Relative cortical myosin II fluorescence intensity upon

cPLA₂ inhibition for cells dissociated at 3.3 hpf, induced mesoderm, or ectoderm cells in suspension and upon confinement at indicated height. (D and E) Scores of Raman component associated to AA in (D) suspension (unconfined, N = 24) and confined cells (10 μm, N = 28) and (E) in control confinement condition (Ctrl, N = 52) or treated with cPLA₂ inhibitor (N = 22). Red lines indicate mean and SEM. (F) Relative cortical myosin II intensity for control cells and different chemical (Y-27637, ML-7, staurosporine) or genetic interference [dominant negative RhoA (dnRhoA)] with myosin II regulators. ***P < 0.0001, *P < 0.01. All scale bars, 10 μm.

morphodynamics via a cell-autonomous increase of cortical contractility under cell deformation in confinement.

Interference with intracellular calcium levels by addition of BAPTA-AM [1,2-bis(2-aminophenoxy)ethane-*N,N,N',N'*-tetraacetic acid acetoxymethyl ester] or in combination with cPLA₂ inhibitor blocked myosin II enrichment in confined cells without altering cortical myosin II levels in unconfined control cells (fig. S5I). LPA stimulation of BAPTA-AM-treated cells confirmed that myosin II can be activated by the Rho-ROCK signaling pathway in the absence of intracellular calcium and remains competent to bind the cell cortex (fig. S5C). Similarly, chelating extracellular calcium reduced cortical myosin II relocation, while depletion of internal calcium stores using thapsigargin led to a slight increase in myosin II enrichment in confinement (fig. S5I). The addition of ionomycin showed that high intracellular calcium levels, in the absence of cellular shape deformation, were not sufficient to evoke AA production (fig. S5J) and cortical myosin II enrichment (fig. S5, B and D). This suggests that intracellular calcium has a permissive function for cPLA₂ association with the INM and increasing

cortical contractility under cell confinement. Our findings are in line with the observation that cPLA₂ contains a calcium-dependent C2 domain that modulates protein binding to the INM (44–46), which has been shown to be further enhanced and stabilized by mechanical stretching of the nucleus (39). Consistently, cPLA₂ showed a transient localization to the INM in the presence of ionomycin, while additional mechanical stretch due to hypotonic swelling or cell confinement induced a stable association with the INM (fig. S3, J and K).

INM unfolding and nucleus positioning enable the decoding of different types of cell shape deformations

To study whether INM unfolding under cell confinement was sufficient to trigger cPLA₂ activity, we measured cortical myosin II levels and amoeboid migration competence under hypotonic swelling of cells. Quantification of nuclear shape parameters (size, volume, and surface) revealed that hypotonic swelling induced comparable nuclear surface expansion and INM unfolding as nucleus deformation under a confinement height of 7 μ m (fig. S6, A to C). Cortical myosin II levels in hypotonic conditions (Fig. 7A and movie S7) and

associated changes in bleb size (fig. S6D) and cell polarization rate (Fig. 7C) were significantly lower than those of cells deformed at a 7 μ m confinement height. These observations suggest that nuclear envelope unfolding alone is not sufficient to trigger high levels of cortical myosin II enrichment under isotropic cell stretching in hypotonic conditions versus anisotropic cell deformation in confinement.

Comparing intracellular calcium levels between deformed cells in confinement and under hypotonic conditions showed a pronounced increase in intracellular calcium concentrations in confined cells, with a specific calcium increase in the cell nucleus (Fig. 7B and fig. S6E). Ectopically increasing intracellular calcium levels under hypotonic conditions via the addition of ionomycin led to a pronounced and rapid increase in cortical myosin II enrichment in a cPLA₂-dependent manner (fig. S6F and movie S7) that triggered spontaneous cell polarization (Fig. 7, C and D, and fig. S6G). As in confined cells, cell polarization under this condition was associated with a rapid transformation of nonmotile cells into a highly motile stable-bleb amoeboid mode with fast migration speed under confinement *ex vivo*

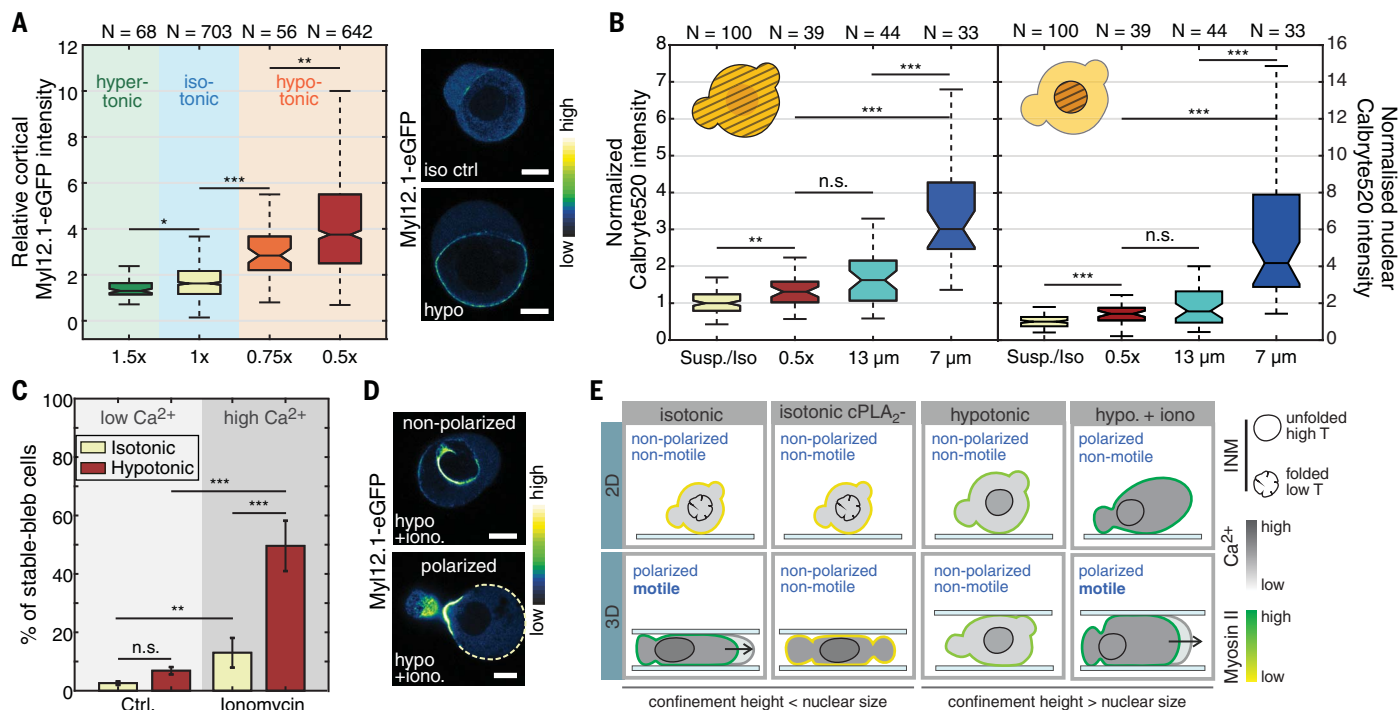


Fig. 7. Nucleus stretch and intracellular positioning enable an adaptive cellular response to different types of physical cell deformation. (A) Relative cortical myosin II enrichment for progenitor cells cultured under different osmolality conditions. (B) Normalized cortical (left) and nuclear (right) Ca²⁺ levels (Calbryte520) for control (Ctrl) and hypotonic (0.5x) conditions and mechanical confinement (13 and 7 μ m). (C) Percentage of stable-bleb polarized cells in isotonic and hypotonic (0.5x) conditions for cells cultured in DMEM (Ctrl) or supplemented with 1 μ M ionomycin. *N* > 1000 cells for all conditions. (D) Exemplary

confocal images of cells expressing myosin II-eGFP in isotonic (ctrl, top left), hypotonic (bottom left) and hypotonic conditions supplemented with ionomycin treatment (right): nonpolarized cell (top) and stable-bleb polarized cell (bottom). (E) Sketch of cell polarization and motile cell behavior in 2D (top) versus 3D confined environments (bottom) and for control conditions (isotonic media; first column) versus cPLA₂ interference (second column) and hypotonic condition alone (third column) or in the presence of ionomycin (fourth column). high T, high tension; low T, low tension. ****P* < 0.0001, ***P* < 0.001, **P* < 0.01. All scale bars, 10 μ m.

and in vivo (Fig. 7E; fig. S6, H, I, and M; and movies S7 and S8). Raman spectroscopy to directly measure cPLA₂ activity confirmed that hypotonic stress increased AA levels (fig. S5K) in a cPLA₂-dependent manner (fig. S5L), with addition of ionomycin in hypotonic conditions further increasing AA production (fig. S5M). Furthermore, relative measured AA levels directly correlated with cortical myosin II levels (fig. S5N). Together, these data reveal that different mechanical shape deformations regulate intracellular calcium levels and modulate cPLA₂ activity under similar INM stretch; uniaxial compression in confinement induces high intracellular calcium levels specifically in the nucleus, while isotropic radial stretch in hypotonic stress conditions leads to a lower intracellular calcium levels. Independently modulating nucleus deformation and calcium levels under different shape deformations confirmed that both parameters engage synergistically to regulate cortical contractility (Fig. 8A) and cellular dynamics under anisotropic stress (Fig. 7E), thereby enabling a cell to distinguish between different types of shape deformation and to acquire a specific morphodynamic response.

Intracellular nucleus positioning appeared as a promising candidate to differentially modulate calcium levels. Endoplasmic reticulum-plasma membrane (ER-PM) proximity has been implicated as an important regulator of cellular calcium signaling (47). Visualization of membrane-proximal ER structures showed that the ER was highly dynamic under con-

ditions of low confinement but was increasingly immobilized between the nucleus-PM interface for larger cell deformations in confinement (movie S9). In addition, the expanding nucleus contact area close to the plasma membrane closely correlated with an intracellular calcium increase (fig. S6J). We speculated that stromal interaction molecule-Orai (STIM-Orai), with STIM proteins located at the ER and Orai proteins representing calcium-selective PM calcium channels, could be involved in cellular calcium regulation in confined cells. STIM-Orai proteins have an established function in store-operated calcium entry upon depletion of calcium from the ER, which is mediated via ER-PM proximity (48, 49). Analysis of STIM-Orai protein localization revealed that both proteins accumulate at the interface between the nucleus and plasma membrane in confined cells at 7 μm (fig. S6, K and L). In contrast, we observed a homogeneous distribution of both channels in cells under 13 μm confinement height when the ER was not spatially confined between the nucleus and PM. These data support that ER immobilization is associated with the specific enrichment of STIM-Orai in the ER-PM contact region where mechanical ER confinement occurs. Inhibition of the STIM-Orai complex using 2-aminoethoxydiphenyl borate (2APB) further blocked myosin II enrichment under cell deformation in confinement (fig. S5I). Our observations support that mechanical compression of the cell nucleus induces a tight connectivity between ER-PM structures and STIM-Orai

localization at the ER-PM contact interface involved in the up-regulation of intracellular calcium levels in confined cells.

Discussion

Our data support that the nucleus establishes a core element to measure cellular shape deformation via two key physical parameters: (i) nuclear shape deformation leading to INM unfolding and (ii) intracellular spatial positioning of the nucleus. In this model, INM unfolding under nuclear shape change allows for the deformation-dependent activation of cPLA₂ signaling, whereby cPLA₂ activity is modulated by intracellular calcium levels set by nucleus-PM proximity (Fig. 8B and fig. S7A). The parameter space of these two variables (INM unfolding and calcium levels) provides a dual-input identifier for a cell to decode distinct shape deformations as exemplified on anisotropic cell deformation in confinement versus isotropic hypotonic cell stretching, allowing cells to acquire a specific adaptive response depending on the type of physical shape deformation (fig. S7B).

Biochemical, physical, and mechanical cues in the surrounding of a cell create manifold information for cells, which is continuously sensed, integrated, and transduced to allow for complex cellular functioning. Here, we show that the cell nucleus functions as a cellular mechano-gauge for precisely decoding cellular shape changes, allowing cells to adaptively and rapidly tune cytoskeletal network properties and morphodynamic behavior within their 3D tissue microenvironment during development. This mechanism lays a foundation for functional principles underlying cellular proprioception that, comparable to the sensing of spatiotemporal changes in body posture and movement (50), enable a precise interpretation of shape changes on the single-cell level.

The nucleus, being the largest organelle in the cell, represents a prominent structure for transmission and modulation of mechano-sensitive processes (51–55), and nucleus deformation has been shown to influence nuclear transport and cell differentiation (56–58), chromatin organization (59–61), migration (62–66), and pathfinding in constrained environments (67). Our findings support that nucleus deformation and its intracellular positioning establish a cellular sensing module that equips cells to rapidly and reversibly adapt their dynamic response to shape fluctuations. This “nuclear ruler pathway” was also identified in an accompanying study (68), supporting its conservation between embryonic and differentiated cells in the adult organism. The observation of a rapid contractile cell response upon cell squeezing in confinement which is followed by fast amoeboid motility is reminiscent of a “cellular escape reflex” that enables cells to cope with physical constraints and acute

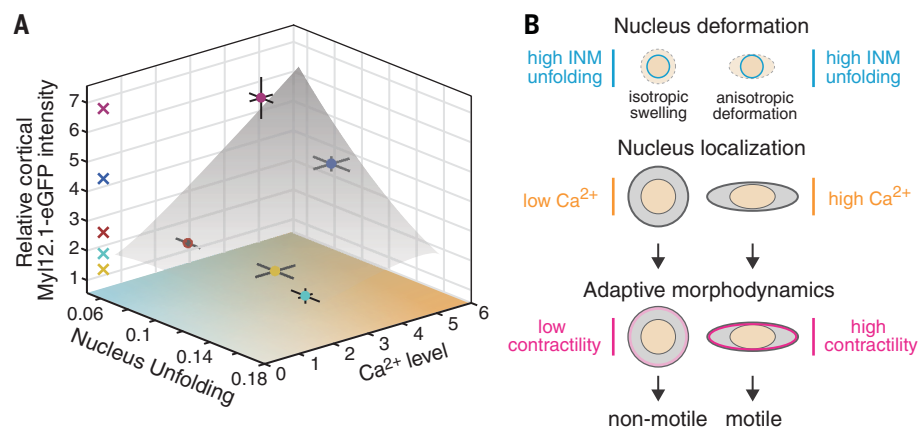


Fig. 8. INM unfolding and intracellular calcium levels enable cells to decode isotropic stretch versus cell squeezing in confinement. (A) Normalized relative cortical myosin II fluorescence intensity as a function of nucleus unfolding and normalized Ca²⁺ (Calbryte520) intensity for different physical cell deformations [dark blue, 7 μm confinement; light blue, 13 μm confinement; yellow, 7 μm confinement + BAPTA-AM; red, hypotonic (0.5 \times) condition; magenta, hypotonic condition (0.5 \times) + ionomycin]. Data indicate mean and SEM. The gray area sketches the relation between cortical myosin II and nuclear deformation versus intracellular calcium levels. [Calcium data related to Fig. 4B, except for hypo + ionomycin ($N = 41$) and BAPTA-AM + 7 μm ($N = 9$); for nuclear unfolding related to Fig. 2D and fig. S6B, and for cortical myosin II levels related to Figs. 1A and 4A and figs. S5I and S6F]. (B) Sketch depicting how nucleus deformation and intracellular nucleus positioning correlate with INM unfolding and intracellular calcium levels, which differentially regulate cortical contractility and cellular morphodynamics.

deformations of their shape. Such a mechanism might be relevant for various biological processes associated with migration plasticity of cancer and immune cells in constrained 3D tissue niches (69–72), mechanochemical feedback processes during morphogenesis (73), and homeostatic tissue functions such as cell density regulation (74), which require accurate mechanisms to detect variations in cellular size and shape and multicellular packing density in crowded 3D tissues.

Materials and methods

Zebrafish maintenance

Zebrafish (*Danio rerio*) were maintained as previously described (75). Embryos were kept in E3 medium at between 25° and 31°C before experiments and staged according to morphological criteria (76) and hours post-fertilization (hpf). Wild-type embryos were obtained from the AB strain background. All protocols used have been approved by the Institutional Animal Care and Use Ethic Committee (PRBB-IACUEC) and implemented according to national and European regulations. All experiments were carried out in accordance with the principles of the 3Rs (replacement, reduction, and refinement).

Transgenic fish lines

The following transgenic lines were used: Tg(actb2:Lifect-GFP) (77), Tg(actb2:Myl12.1-eGFP) (78), Tg(actb2:Myl12.1-mcherry) (4), Tg(mezzo:eGFP) (23), and Tg(actb2:Lyn-TdTomato) (79). All progenitor cells expressing Myl12.1-eGFP (myosin II) and Lifect-GFP (actin) were obtained from Tg(actb2:Myl12.1-eGFP) and Tg(actb2:Lifect-GFP).

Cell culture

To culture progenitor cells, embryos were manually dechorionated in E3 buffer at sphere stage (4 hpf) or different stages, if indicated. Five to twenty embryos were transferred to Dulbecco's minimum essential medium–nutrient mixture F-12 (DMEM-F12; with l-glutamine and 15 mM HEPES, without sodium bicarbonate and phenol red) culture medium (Sigma) and mechanically dissociated by manual tapping followed by centrifugation at 200g for 3 min.

Sample preparation and surface coatings

The following products for surface coatings at the indicated concentration have been used: 0.5 mg/ml PLL(20)-g[3,5]-PEG(2) (Susos) and 0.2 mg/ml fibronectin (Sigma-Aldrich). Before PLL-PEG coating, both coverslips and dishes were plasma cleaned. Uncoated or PLL-coated glass dishes #1.5 were purchased from MatTek (MatTek Corporation).

Cell confiner

Cells were confined using a dynamic confiner (4DCell) similar to previously established pla-

nar microconfinement methods (30). To confine cells at different heights, multiple Si molds were produced by photolithography in a clean room (Nanofabrication Laboratory, ICFO) by depositing a SU-8 resin on a silicon wafer. In brief, a photomask with the desired geometry was created. Confinement coverslips were prepared with polydimethylsiloxane (PDMS) with the following heights: 18, 16, 13, 10, 8.5, and 7 μ m. Coverslips were always plasma cleaned, coated with PLL-PEG (if not indicated otherwise), and equilibrated in DMEM before each experiment. A pressure pump (AF1 microfluidic pressure pump, Elveflow) together with the ESI software was used to change the pressure for tuning the confinement heights. For Raman measurements and optical tweezers, two coverslips separated with microbeads or with a PDMS membrane were used (height = 10 μ m).

Reagents and inhibitor treatments

Pharmacological inhibitors were used at the following concentrations: 1 μ M cPLA₂ inhibitor (pyrrophenone, Merck-Millipore), 10 μ M Bapta-AM (Cayman), 10 μ M blebbistatin(+) (Tocris Bioscience), 10 μ M Y-27632 (Tocris Bioscience), 10 μ M ML-7 hydrochloride (Tocris Bioscience), 1 μ M nocodazole (Sigma), 50 nM leptomycinB (Sigma-Aldrich), 1 μ M ionomycin (Sigma-Aldrich), 1 μ M thapsigargin (Thermo Fisher), 10 μ M GsMTx4 (Tocris), 50 μ M 2-APB (Biogen-Santa Cruz), 10 μ M gadolinium chloride (Tocris), 2 μ M actinomycin D (PanReac), 100 μ M Z-VAD(OMe)-FMK (Abcam), 1 μ M staurosporine (Abcam), and 1-oleoyl lysophosphatidic acid (LPA, Tocris Bioscience). Measurements were done directly after exposure to MLCK inhibitor, GsMTx4, ionomycin, and LPA; all other inhibitors were preincubated for 30 and 60 min for Y-27632 prior to experiments.

Fluorescence staining

Calbryte520 (AAT Bioquest) was used to study calcium dynamics. The staining kit–Red Fluorescence–Cytopainter (ER Tracker, Abcam) or ER-Tracker Green (BODIPY FL Glibenclamide) was used to visualize the endoplasmic reticulum respectively for confocal 3D colors imaging and for TIRF microscopy experiment. DNA-Hoechst (Thermo Fisher) was used to stain the cell nucleus. Cells were incubated with 5 μ M Calbryte520 for 20 min, with 1 μ M ER-tracker for 30 min and 1 μ g/ml DNA-Hoechst for 7 to 10 min, as reported in the corresponding protocols. After incubation, cells were washed, centrifuged at 200g for 3 min and resuspended in DMEM media.

Variable osmotic culture conditions

D-Mannitol (Sigma) was diluted in DMEM to obtain a culture medium with an osmolarity of ~450 milliosmoles per liter (corresponding to a 1.5 \times media). Milli-Q water was added to DMEM for hypotonic conditions.

REFERENCES AND NOTES

- G. Salbreux, G. Charras, E. Paluch, Actin cortex mechanics and cellular morphogenesis. *Trends Cell Biol.* **22**, 536–545 (2012). doi: [10.1016/j.tcb.2012.07.001](https://doi.org/10.1016/j.tcb.2012.07.001); pmid: [22871642](https://pubmed.ncbi.nlm.nih.gov/22871642/)
- N. W. Goehring, S. W. Grill, Cell polarity: Mechanochemical patterning. *Trends Cell Biol.* **23**, 72–80 (2013). doi: [10.1016/j.tcb.2012.10.009](https://doi.org/10.1016/j.tcb.2012.10.009); pmid: [23182746](https://pubmed.ncbi.nlm.nih.gov/23182746/)
- A. C. Callan-Jones, R. Voituriez, Actin flows in cell migration: From locomotion and polarity to trajectories. *Curr. Opin. Cell Biol.* **38**, 12–17 (2016). doi: [10.1016/j.ceb.2016.01.003](https://doi.org/10.1016/j.ceb.2016.01.003); pmid: [26627283](https://pubmed.ncbi.nlm.nih.gov/26627283/)
- M. Vicente-Manzanares, X. Ma, R. S. Adelstein, A. R. Horwitz, Non-muscle myosin II takes centre stage in cell adhesion and migration. *Nat. Rev. Mol. Cell Biol.* **10**, 778–790 (2009). doi: [10.1038/nrm2786](https://doi.org/10.1038/nrm2786); pmid: [19851336](https://pubmed.ncbi.nlm.nih.gov/19851336/)
- M. A. Wozniak, C. S. Chen, Mechanotransduction in development: A growing role for contractility. *Nat. Rev. Mol. Cell Biol.* **10**, 34–43 (2009). doi: [10.1038/nrm2592](https://doi.org/10.1038/nrm2592); pmid: [19197330](https://pubmed.ncbi.nlm.nih.gov/19197330/)
- T. Lecuit, P. F. Lenne, E. Munro, Force generation, transmission, and integration during cell and tissue morphogenesis. *Annu. Rev. Cell Dev. Biol.* **27**, 157–184 (2011). doi: [10.1146/annurev-cellbio-100109-104027](https://doi.org/10.1146/annurev-cellbio-100109-104027); pmid: [21740231](https://pubmed.ncbi.nlm.nih.gov/21740231/)
- E. M. Balzer et al., Physical confinement alters tumor cell adhesion and migration phenotypes. *FASEB J.* **26**, 4045–4056 (2012). doi: [10.1096/fj.12-211441](https://doi.org/10.1096/fj.12-211441); pmid: [22707566](https://pubmed.ncbi.nlm.nih.gov/22707566/)
- K. J. Sonnenmann, W. M. Bement, Wound repair: Toward understanding and integration of single-cell and multicellular wound responses. *Annu. Rev. Cell Dev. Biol.* **27**, 237–263 (2011). doi: [10.1146/annurev-cellbio-092910-154251](https://doi.org/10.1146/annurev-cellbio-092910-154251); pmid: [21721944](https://pubmed.ncbi.nlm.nih.gov/21721944/)
- J. Briscoe, S. Small, Morphogen rules: Design principles of gradient-mediated embryo patterning. *Development* **142**, 3996–4009 (2015). doi: [10.1242/dev.129452](https://doi.org/10.1242/dev.129452); pmid: [26628090](https://pubmed.ncbi.nlm.nih.gov/26628090/)
- G. Charras, E. Sahai, Physical influences of the extracellular environment on cell migration. *Nat. Rev. Mol. Cell Biol.* **15**, 813–824 (2014). doi: [10.1038/nrm3897](https://doi.org/10.1038/nrm3897); pmid: [25355506](https://pubmed.ncbi.nlm.nih.gov/25355506/)
- P. Roca-Cusachs, R. Sunyer, X. Trepat, Mechanical guidance of cell migration: Lessons from chemotaxis. *Curr. Opin. Cell Biol.* **25**, 543–549 (2013). doi: [10.1016/j.ceb.2013.04.010](https://doi.org/10.1016/j.ceb.2013.04.010); pmid: [23726023](https://pubmed.ncbi.nlm.nih.gov/23726023/)
- M. Duda et al., Polarization of myosin II refines tissue material properties to buffer mechanical stress. *Dev. Cell* **48**, 245–260.e7 (2019). doi: [10.1016/j.devcel.2018.12.020](https://doi.org/10.1016/j.devcel.2018.12.020); pmid: [30695698](https://pubmed.ncbi.nlm.nih.gov/30695698/)
- A. Sumi et al., Adherens junction length during tissue contraction is controlled by the mechanosensitive activity of actomyosin and junctional recycling. *Dev. Cell* **47**, 453–463.e3 (2018). doi: [10.1016/j.devcel.2018.10.025](https://doi.org/10.1016/j.devcel.2018.10.025); pmid: [30458138](https://pubmed.ncbi.nlm.nih.gov/30458138/)
- J. Aureille et al., Nuclear envelope deformation controls cell cycle progression in response to mechanical force. *EMBO Rep.* **20**, e48084 (2019). doi: [10.15252/embr.201948084](https://doi.org/10.15252/embr.201948084); pmid: [31368207](https://pubmed.ncbi.nlm.nih.gov/31368207/)
- S. A. Gudipaty et al., Mechanical stretch triggers rapid epithelial cell division through Piezo1. *Nature* **543**, 118–121 (2017). doi: [10.1038/nature21407](https://doi.org/10.1038/nature21407); pmid: [28199303](https://pubmed.ncbi.nlm.nih.gov/28199303/)
- E. Mariani et al., Live-cell delamination counterbalances epithelial growth to limit tissue overcrowding. *Nature* **484**, 542–545 (2012). doi: [10.1038/nature10984](https://doi.org/10.1038/nature10984); pmid: [22504180](https://pubmed.ncbi.nlm.nih.gov/22504180/)
- G. T. Eisenhoffer et al., Crowding induces live cell extrusion to maintain homeostatic cell numbers in epithelia. *Nature* **484**, 546–549 (2012). doi: [10.1038/nature10999](https://doi.org/10.1038/nature10999); pmid: [22504183](https://pubmed.ncbi.nlm.nih.gov/22504183/)
- M. Georgouli et al., Regional activation of myosin II in cancer cells drives tumor progression via a secretory cross-talk with the immune microenvironment. *Cell* **176**, 757–774.e23 (2019). doi: [10.1016/j.cell.2018.12.038](https://doi.org/10.1016/j.cell.2018.12.038); pmid: [30712866](https://pubmed.ncbi.nlm.nih.gov/30712866/)
- J. H. Kim et al., Mechanical tension drives cell membrane fusion. *Dev. Cell* **32**, 561–573 (2015). doi: [10.1016/j.devcel.2015.01.005](https://doi.org/10.1016/j.devcel.2015.01.005); pmid: [25684354](https://pubmed.ncbi.nlm.nih.gov/25684354/)
- T. Luo, K. Mohan, P. A. Iglesias, D. N. Robinson, Molecular mechanisms of cellular mechanosensing. *Nat. Mater.* **12**, 1064–1071 (2013). doi: [10.1038/nmat3772](https://doi.org/10.1038/nmat3772); pmid: [24141449](https://pubmed.ncbi.nlm.nih.gov/24141449/)
- C. J. Cattin et al., Mechanical control of mitotic progression in single animal cells. *Proc. Natl. Acad. Sci. U.S.A.* **112**, 11258–11263 (2015). doi: [10.1073/pnas.1502029112](https://doi.org/10.1073/pnas.1502029112); pmid: [26305930](https://pubmed.ncbi.nlm.nih.gov/26305930/)
- T. Lämmermann, M. Sixt, Mechanical modes of 'amoeboid' cell migration. *Curr. Opin. Cell Biol.* **21**, 636–644 (2009). doi: [10.1016/j.ceb.2009.05.003](https://doi.org/10.1016/j.ceb.2009.05.003); pmid: [19523798](https://pubmed.ncbi.nlm.nih.gov/19523798/)

23. V. Ruprecht *et al.*, Cortical contractility triggers a stochastic switch to fast amoeboid cell motility. *Cell* **160**, 673–685 (2015). doi: [10.1016/j.cell.2015.01.008](https://doi.org/10.1016/j.cell.2015.01.008); pmid: [25679761](https://pubmed.ncbi.nlm.nih.gov/25679761/)
24. J. S. Logue *et al.*, Erk regulation of actin capping and bundling by Eps8 promotes cortex tension and leader bleb-based migration. *eLife* **4**, e08314 (2015). doi: [10.7554/eLife.08314](https://doi.org/10.7554/eLife.08314); pmid: [26163656](https://pubmed.ncbi.nlm.nih.gov/26163656/)
25. A. W. Holle *et al.*, Cancer cells invade confined microchannels via a self-directed mesenchymal-to-amoeboid transition. *Nano Lett.* **19**, 2280–2290 (2019). doi: [10.1021/acs.nanolett.8b04720](https://doi.org/10.1021/acs.nanolett.8b04720); pmid: [30775927](https://pubmed.ncbi.nlm.nih.gov/30775927/)
26. T. Brunet, M. Albert, W. Roman, D. C. Spitzer, N. King, A flagellate-to-amoeboid switch in the closest living relatives of animals. *bioRxiv* 2020.06.26.171736 (28 June 2020); <https://doi.org/10.1101/2020.06.26.171736>
27. M. Ibo, V. Srivastava, D. N. Robinson, Z. R. Gagnon, Cell blebbing in confined microfluidic environments. *PLOS ONE* **11**, e0163866 (2016). doi: [10.1371/journal.pone.0163866](https://doi.org/10.1371/journal.pone.0163866); pmid: [27706201](https://pubmed.ncbi.nlm.nih.gov/27706201/)
28. Y. J. Liu *et al.*, Confinement and low adhesion induce fast amoeboid migration of slow mesenchymal cells. *Cell* **160**, 659–672 (2015). doi: [10.1016/j.cell.2015.01.007](https://doi.org/10.1016/j.cell.2015.01.007); pmid: [25679760](https://pubmed.ncbi.nlm.nih.gov/25679760/)
29. R. Zhao *et al.*, Cell sensing and decision-making in confinement: The role of TRPM7 in a tug of war between hydraulic pressure and cross-sectional area. *Sci. Adv.* **5**, eaaw7243 (2019). doi: [10.1126/sciadv.aaw7243](https://doi.org/10.1126/sciadv.aaw7243); pmid: [31355337](https://pubmed.ncbi.nlm.nih.gov/31355337/)
30. M. Le Berre, E. Zlotek-Zlotkiewicz, D. Bonazzi, F. Lautenschlaeger, M. Piel, Methods for two-dimensional cell confinement. *Methods Cell Biol.* **121**, 213–229 (2014). doi: [10.1016/B978-0-12-800281-0.00014-2](https://doi.org/10.1016/B978-0-12-800281-0.00014-2); pmid: [24560512](https://pubmed.ncbi.nlm.nih.gov/24560512/)
31. M. Bergert *et al.*, Force transmission during adhesion-independent migration. *Nat. Cell Biol.* **17**, 524–529 (2015). doi: [10.1038/ncb3134](https://doi.org/10.1038/ncb3134); pmid: [25774834](https://pubmed.ncbi.nlm.nih.gov/25774834/)
32. M. Krieg *et al.*, Tensile forces govern germ-layer organization in zebrafish. *Nat. Cell Biol.* **10**, 429–436 (2008). doi: [10.1038/ncb1705](https://doi.org/10.1038/ncb1705); pmid: [18364700](https://pubmed.ncbi.nlm.nih.gov/18364700/)
33. L. Solnica-Krezel, D. S. Sepich, Gastrulation: Making and shaping germ layers. *Annu. Rev. Cell Dev. Biol.* **28**, 687–717 (2012). doi: [10.1146/annurev-cellbio.092910-154043](https://doi.org/10.1146/annurev-cellbio.092910-154043); pmid: [22804578](https://pubmed.ncbi.nlm.nih.gov/22804578/)
34. A. D. Bershadsky, N. Q. Balaban, B. Geiger, Adhesion-dependent cell mechanosensitivity. *Annu. Rev. Cell Dev. Biol.* **19**, 677–695 (2003). doi: [10.1146/annurev.cellbio.19.111301.153011](https://doi.org/10.1146/annurev.cellbio.19.111301.153011); pmid: [14570586](https://pubmed.ncbi.nlm.nih.gov/14570586/)
35. A. Saha *et al.*, Determining physical properties of the cell cortex. *Biophys. J.* **110**, 1421–1429 (2016). doi: [10.1016/j.bpj.2016.02.013](https://doi.org/10.1016/j.bpj.2016.02.013); pmid: [27028651](https://pubmed.ncbi.nlm.nih.gov/27028651/)
36. W. C. Hung *et al.*, Confinement sensing and signal optimization via Piezo1/PKA and myosin II pathways. *Cell Rep.* **15**, 1430–1441 (2016). doi: [10.1016/j.celrep.2016.04.035](https://doi.org/10.1016/j.celrep.2016.04.035); pmid: [27160899](https://pubmed.ncbi.nlm.nih.gov/27160899/)
37. N. I. Petridou, S. Grigolon, G. Salbreux, E. Hannezo, C. P. Heisenberg, Fluidization-mediated tissue spreading by mitotic cell rounding and non-canonical Wnt signalling. *Nat. Cell Biol.* **21**, 169–178 (2019). doi: [10.1038/s41556-018-0247-4](https://doi.org/10.1038/s41556-018-0247-4); pmid: [30559456](https://pubmed.ncbi.nlm.nih.gov/30559456/)
38. K. N. Dahl, S. M. Kahn, K. L. Wilson, D. E. Discher, The nuclear envelope lamina network has elasticity and a compressibility limit suggestive of a molecular shock absorber. *J. Cell Sci.* **117**, 4779–4786 (2004). doi: [10.1242/jcs.10357](https://doi.org/10.1242/jcs.10357); pmid: [15331638](https://pubmed.ncbi.nlm.nih.gov/15331638/)
39. B. Enyedi, M. Jelcic, P. Niethammer, The cell nucleus serves as a mechanotransducer of tissue damage-induced inflammation. *Cell* **165**, 1160–1170 (2016). doi: [10.1016/j.cell.2016.04.016](https://doi.org/10.1016/j.cell.2016.04.016); pmid: [27203112](https://pubmed.ncbi.nlm.nih.gov/27203112/)
40. E. A. Dennis, J. Cao, Y. H. Hsu, V. Magrioti, G. Kokotos, Phospholipase A2 enzymes: Physical structure, biological function, disease implication, chemical inhibition, and therapeutic intervention. *Chem. Rev.* **111**, 6130–6185 (2011). doi: [10.1021/cr200085w](https://doi.org/10.1021/cr200085w); pmid: [21910409](https://pubmed.ncbi.nlm.nih.gov/21910409/)
41. T. Katayama *et al.*, Stimulatory effects of arachidonic acid on myosin ATPase activity and contraction of smooth muscle via myosin motor domain. *Am. J. Physiol. Heart Circ. Physiol.* **298**, H505–H514 (2010). doi: [10.1152/ajpheart.00577.2009](https://doi.org/10.1152/ajpheart.00577.2009); pmid: [19933418](https://pubmed.ncbi.nlm.nih.gov/19933418/)
42. M. Brown, J. A. Roulson, C. A. Hart, T. Tawadros, N. W. Clarke, Arachidonic acid induction of Rho-mediated transendothelial migration in prostate cancer. *Br. J. Cancer* **110**, 2099–2108 (2014). doi: [10.1038/bjc.2014.99](https://doi.org/10.1038/bjc.2014.99); pmid: [24595005](https://pubmed.ncbi.nlm.nih.gov/24595005/)
43. L. Sun, R. D. Ye, Role of G protein-coupled receptors in inflammation. *Acta Pharmacol. Sin.* **33**, 342–350 (2012). doi: [10.1038/aps.2011.200](https://doi.org/10.1038/aps.2011.200); pmid: [22367283](https://pubmed.ncbi.nlm.nih.gov/22367283/)
44. M. Peters-Golden, K. Song, T. Marshall, T. Brock, Translocation of cytosolic phospholipase A2 to the nuclear envelope elicits topographically localized phospholipid hydrolysis. *Biochem. J.* **318**, 797–803 (1996). doi: [10.1042/bj3180797](https://doi.org/10.1042/bj3180797); pmid: [8836122](https://pubmed.ncbi.nlm.nih.gov/8836122/)
45. A. Dessen *et al.*, Crystal structure of human cytosolic phospholipase A2 reveals a novel topology and catalytic mechanism. *Cell* **97**, 349–360 (1999). doi: [10.1016/S0092-8674\(00\)80744-8](https://doi.org/10.1016/S0092-8674(00)80744-8); pmid: [10319815](https://pubmed.ncbi.nlm.nih.gov/10319815/)
46. J. E. Burke, E. A. Dennis, Phospholipase A₂ biochemistry. *Cardiovasc. Drugs Ther.* **23**, 49–59 (2009). doi: [10.1007/s10557-008-6132-9](https://doi.org/10.1007/s10557-008-6132-9); pmid: [18931897](https://pubmed.ncbi.nlm.nih.gov/18931897/)
47. A. Gallo, C. Vannier, T. Galli, Endoplasmic reticulum-plasma membrane associations: Structures and functions. *Annu. Rev. Cell Dev. Biol.* **32**, 279–301 (2016). doi: [10.1146/annurev-cellbio.111315-125024](https://doi.org/10.1146/annurev-cellbio.111315-125024); pmid: [27298092](https://pubmed.ncbi.nlm.nih.gov/27298092/)
48. S. Carrasco, T. Meyer, STIM proteins and the endoplasmic reticulum-plasma membrane junctions. *Annu. Rev. Biochem.* **80**, 973–1000 (2011). doi: [10.1146/annurev-biochem-061609-165311](https://doi.org/10.1146/annurev-biochem-061609-165311); pmid: [21548779](https://pubmed.ncbi.nlm.nih.gov/21548779/)
49. X. Qin *et al.*, Increased confinement and polydispersity of STIM1 and Orai1 after Ca²⁺ store depletion. *Biophys. J.* **118**, 70–84 (2020). doi: [10.1016/j.bpj.2019.11.019](https://doi.org/10.1016/j.bpj.2019.11.019); pmid: [31818466](https://pubmed.ncbi.nlm.nih.gov/31818466/)
50. R. Das, S. Wieser, M. Krieg, Neuronal stretch reception – Making sense of the mechanosense. *Exp. Cell Res.* **378**, 104–112 (2019). doi: [10.1016/j.yexcr.2019.01.028](https://doi.org/10.1016/j.yexcr.2019.01.028); pmid: [30817929](https://pubmed.ncbi.nlm.nih.gov/30817929/)
51. T. J. Kirby, J. Lammerding, Emerging views of the nucleus as a cellular mechanosensor. *Nat. Cell Biol.* **20**, 373–381 (2018). doi: [10.1038/s41556-018-0038-y](https://doi.org/10.1038/s41556-018-0038-y); pmid: [29467443](https://pubmed.ncbi.nlm.nih.gov/29467443/)
52. Z. Jahed, M. R. Mofrad, The nucleus feels the force, LINCed in or not? *Curr. Opin. Cell Biol.* **58**, 114–119 (2019). doi: [10.1016/j.celbio.2019.02.012](https://doi.org/10.1016/j.celbio.2019.02.012); pmid: [31002996](https://pubmed.ncbi.nlm.nih.gov/31002996/)
53. C. S. Janota, F. J. Calero-Cuenca, E. R. Gomes, The role of the cell nucleus in mechanotransduction. *Curr. Opin. Cell Biol.* **63**, 204–211 (2020). doi: [10.1016/j.celbio.2020.03.001](https://doi.org/10.1016/j.celbio.2020.03.001); pmid: [32361559](https://pubmed.ncbi.nlm.nih.gov/32361559/)
54. R. P. Martins, J. D. Finan, G. Farshid, D. A. Lee, Mechanical regulation of nuclear structure and function. *Annu. Rev. Biomed. Eng.* **14**, 431–455 (2012). doi: [10.1146/annurev-bioeng-071910-124638](https://doi.org/10.1146/annurev-bioeng-071910-124638); pmid: [22655599](https://pubmed.ncbi.nlm.nih.gov/22655599/)
55. Y. Xia, C. R. Pfeiffer, S. Cho, D. E. Discher, J. Irianto, Nuclear mechanosensing. *Emerg Top Life Sci* **2**, 713–725 (2018). doi: [10.1042/ETLS20180051](https://doi.org/10.1042/ETLS20180051); pmid: [31693005](https://pubmed.ncbi.nlm.nih.gov/31693005/)
56. A. Elosegui-Artola *et al.*, Force triggers YAP nuclear entry by regulating transport across nuclear pores. *Cell* **171**, 1397–1410.e14 (2017). doi: [10.1016/j.cell.2017.10.008](https://doi.org/10.1016/j.cell.2017.10.008); pmid: [29107331](https://pubmed.ncbi.nlm.nih.gov/29107331/)
57. J. Swift *et al.*, Nuclear lamin-A scales with tissue stiffness and enhances matrix-directed differentiation. *Science* **341**, 1240104 (2013). doi: [10.1126/science.1240104](https://doi.org/10.1126/science.1240104); pmid: [23990565](https://pubmed.ncbi.nlm.nih.gov/23990565/)
58. M. Almonacid, M. E. Terret, M. H. Verlhac, Nuclear positioning as an integrator of cell fate. *Curr. Opin. Cell Biol.* **56**, 122–129 (2019). doi: [10.1016/j.celbio.2018.12.002](https://doi.org/10.1016/j.celbio.2018.12.002); pmid: [30594054](https://pubmed.ncbi.nlm.nih.gov/30594054/)
59. K. Damodaran *et al.*, Compressive force induces reversible chromatin condensation and cell geometry-dependent transcriptional response. *Mol. Cell Biol.* **29**, 3039–3051 (2018). doi: [10.1091/mbc.E18-04-0256](https://doi.org/10.1091/mbc.E18-04-0256); pmid: [30256731](https://pubmed.ncbi.nlm.nih.gov/30256731/)
60. A. Kumar *et al.*, ATR mediates a checkpoint at the nuclear envelope in response to mechanical stress. *Cell* **158**, 633–646 (2014). doi: [10.1016/j.cell.2014.05.046](https://doi.org/10.1016/j.cell.2014.05.046); pmid: [25083873](https://pubmed.ncbi.nlm.nih.gov/25083873/)
61. M. M. Nava *et al.*, Heterochromatin-driven nuclear softening protects the genome against mechanical stress-induced damage. *Cell* **181**, 800–817.e22 (2020). doi: [10.1016/j.cell.2020.03.052](https://doi.org/10.1016/j.cell.2020.03.052); pmid: [32302590](https://pubmed.ncbi.nlm.nih.gov/32302590/)
62. A. L. McGregor, C.-R. Hsia, J. Lammerding, Squish and squeeze – the nucleus as a physical barrier during migration in confined environments. *Curr. Opin. Cell Biol.* **40**, 32–40 (2016). doi: [10.1016/j.celbio.2016.01.011](https://doi.org/10.1016/j.celbio.2016.01.011); pmid: [26895141](https://pubmed.ncbi.nlm.nih.gov/26895141/)
63. R. Majumdar, K. Steen, P. A. Coulombe, C. A. Parent, Non-canonical processes that shape the cell migration landscape. *Curr. Opin. Cell Biol.* **57**, 123–134 (2019). doi: [10.1016/j.celbio.2018.12.013](https://doi.org/10.1016/j.celbio.2018.12.013); pmid: [30852463](https://pubmed.ncbi.nlm.nih.gov/30852463/)
64. R. J. Petrie, H. Koo, K. M. Yamada, Generation of compartmentalized pressure by a nuclear piston governs cell motility in a 3D matrix. *Science* **345**, 1062–1065 (2014). doi: [10.1126/science.1256965](https://doi.org/10.1126/science.1256965); pmid: [25170155](https://pubmed.ncbi.nlm.nih.gov/25170155/)
65. C. M. Denais *et al.*, Nuclear envelope rupture and repair during cancer cell migration. *Science* **352**, 353–358 (2016). doi: [10.1126/science.aad7297](https://doi.org/10.1126/science.aad7297); pmid: [27013428](https://pubmed.ncbi.nlm.nih.gov/27013428/)
66. M. Raab *et al.*, ESCRT III repairs nuclear envelope ruptures during cell migration to limit DNA damage and cell death. *Science* **352**, 359–362 (2016). doi: [10.1126/science.aad7611](https://doi.org/10.1126/science.aad7611); pmid: [27013426](https://pubmed.ncbi.nlm.nih.gov/27013426/)
67. J. Renkawitz *et al.*, Nuclear positioning facilitates amoeboid migration along the path of least resistance. *Nature* **568**, 546–550 (2019). doi: [10.1038/s41586-019-1087-5](https://doi.org/10.1038/s41586-019-1087-5); pmid: [30944468](https://pubmed.ncbi.nlm.nih.gov/30944468/)
68. A. J. Lomakin *et al.*, The nucleus acts as a ruler tailoring cell responses to spatial constraints. *Science* **370**, eaab2894 (2020).
69. S. van Helvert, C. Storm, P. Friedl, Mechanoreciprocity in cell migration. *Nat. Cell Biol.* **20**, 8–20 (2018). doi: [10.1038/s41556-017-0012-0](https://doi.org/10.1038/s41556-017-0012-0); pmid: [29269951](https://pubmed.ncbi.nlm.nih.gov/29269951/)
70. H. D. Moreau, M. Piel, R. Voituriez, A. M. Lennon-Duménil, Integrating physical and molecular insights on immune cell migration. *Trends Immunol.* **39**, 632–643 (2018). doi: [10.1016/j.it.2018.04.007](https://doi.org/10.1016/j.it.2018.04.007); pmid: [29779848](https://pubmed.ncbi.nlm.nih.gov/29779848/)
71. V. te Boekhorst, L. Preziosi, P. Friedl, Plasticity of cell migration in vivo and in silico. *Annu. Rev. Cell Dev. Biol.* **32**, 491–526 (2016). doi: [10.1146/annurev-cellbio.111315-125201](https://doi.org/10.1146/annurev-cellbio.111315-125201); pmid: [275676118](https://pubmed.ncbi.nlm.nih.gov/275676118/)
72. D. Wirtz, K. Konstantopoulos, P. C. Searson, The physics of cancer: The role of physical interactions and mechanical forces in metastasis. *Nat. Rev. Cancer* **11**, 512–522 (2011). doi: [10.1038/nrc3080](https://doi.org/10.1038/nrc3080); pmid: [21701513](https://pubmed.ncbi.nlm.nih.gov/21701513/)
73. E. Hannezo, C.-P. Heisenberg, mechanochemical feedback loops in development and disease. *Cell* **178**, 12–25 (2019). doi: [10.1016/j.cell.2019.05.052](https://doi.org/10.1016/j.cell.2019.05.052); pmid: [31251912](https://pubmed.ncbi.nlm.nih.gov/31251912/)
74. S. A. Gudipaty, J. Rosenblatt, Epithelial cell extrusion: Pathways and pathologies. *Semin. Cell Dev. Biol.* **67**, 132–140 (2017). doi: [10.1016/j.semcdb.2016.05.010](https://doi.org/10.1016/j.semcdb.2016.05.010); pmid: [27212253](https://pubmed.ncbi.nlm.nih.gov/27212253/)
75. W. Westerfield, *The Zebrafish Book: A Guide for the Laboratory Use of Zebrafish (Brachydanio rerio)* (Univ. of Oregon Press, 1995).
76. C. B. Kimmel, W. W. Ballard, S. R. Kimmel, B. Ullmann, T. F. Schilling, Stages of embryonic development of the zebrafish. *Dev. Dyn.* **203**, 253–310 (1995). doi: [10.1002/ajpa.1002030302](https://doi.org/10.1002/ajpa.1002030302); pmid: [8589427](https://pubmed.ncbi.nlm.nih.gov/8589427/)
77. M. Behrndt *et al.*, Forces driving epithelial spreading in zebrafish gastrulation. *Science* **338**, 257–260 (2012). doi: [10.1126/science.1224143](https://doi.org/10.1126/science.1224143); pmid: [23066079](https://pubmed.ncbi.nlm.nih.gov/23066079/)
78. J. L. Maître *et al.*, Adhesion functions in cell sorting by mechanically coupling the cortices of adhering cells. *Science* **338**, 253–256 (2012). doi: [10.1126/science.1225399](https://doi.org/10.1126/science.1225399); pmid: [22923438](https://pubmed.ncbi.nlm.nih.gov/22923438/)
79. J. Compagnon *et al.*, The notochord breaks bilateral symmetry by controlling cell shapes in the zebrafish laterality organ. *Dev. Cell* **31**, 774–783 (2014). doi: [10.1016/j.devcel.2014.11.003](https://doi.org/10.1016/j.devcel.2014.11.003); pmid: [25535919](https://pubmed.ncbi.nlm.nih.gov/25535919/)

ACKNOWLEDGMENTS

We acknowledge the Super-resolution Light Microscopy and Nanoscopy (SLN) Facility of ICFO for their support with imaging experiments and J. Osmond (Nanofabrication Laboratory, ICFO) for the design and production of molds for generating confinement coverslips, and further support from the CRG Core Facilities for Genomics and Advanced Light Microscopy. We thank the following labs that kindly provided plasmids: pCS2+ lefty/casanova (courtesy C.-P. Heisenberg); pCS2+ lynr-TdTomato (courtesy B. Alsina); pTriEx-RhoA FLARE-sc Biosensor WT was a gift from K. Hahn (Addgene plasmid #12150; RRID:Addgene_12150). We thank C.-P. Heisenberg, M. Piel, and A. J. Lomakin for discussions on this work and B. Lehner, V. Malhotra, S. P. Maurer, and the Ruprecht and Wieser lab members for critical reading of the manuscript. **Funding:** V.V. acknowledges support from the ICFOSTepestone PhD Programme funded by the European Union's Horizon 2020 research and innovation program under Marie Skłodowska-Curie grant agreement 665884. F.P. and Q.T.-R. acknowledge grants funded by Ministerio de Ciencia, Innovación y Universidades and Fondo Social Europeo (FSE) (BES2017-080523-SO, PRE2018-084393). M.A.V. acknowledges support from the Spanish Ministry of Science, Education and Universities through grant RTI2018-099718-B-I00 and an institutional "Maria de Maeztu Programme" for Units of Excellence in R&D (CEX2018-000792-M) and FEDER funds. J.W. was supported by the Christian Doppler Forschungsgesellschaft (Josef Ressel Center for Phytogetic Drug Research). S.W. and M.K. acknowledge support from the Spanish Ministry of Economy and Competitiveness through the Severo Ochoa program for Centres of Excellence in R&D (CEX2019-000910-S), from Fundació Privada Cellex, Fundació Mig-Puig, and from Generalitat de Catalunya through the CERCA program and LaserLab

(654148). M.K. acknowledges support through Spanish Ministry of Economy and Competitiveness (RYC-2015-17935, EQC2018-005048-P, AEI-010500-2018-228, and PGC2018-097882-A-I00), Generalitat de Catalunya (2017 SGR 1012), the ERC (715243), and the HFSP (CDA00023/2018). S.W. acknowledges support through the Spanish Ministry of Economy and Competitiveness via MINECO's Plan Nacional (PGC2018-098532-A-I00). V.R. acknowledges support from the Spanish Ministry of Science and Innovation to the EMBL partnership, the Centro de Excelencia Severo Ochoa, the CERCA Programme/Generalitat de Catalunya, and the MINECO's Plan Nacional (BFU2017-86296-P). **Author contributions:** V.R. and S.W. designed the research. V.V. performed key experiments and data analysis. F.P. contributed to hypotonic and interference experiments and RNA preparations. F.C.C. and V.V. performed optical tweezer experiments, and F.C.C. analyzed the data. M.M. and V.V.

performed Raman experiments, and M.M. analyzed the data. M.C.-R. analyzed the Lap2B-GFP data. H.-M.H. and Q.T.-R. performed in vivo experiments and H.-M.H. performed injections and helped with mesendoderm-ectoderm experiments. S.J.-D. cloned plasmids, synthesized mRNA, and performed mRNA and bead injections. S.P.-L. performed calcium imaging related to the role of Piezo channels. M.A.V. supervised S.P.-L. and contributed with discussions and support to calcium imaging experiments. J.W. provided biological reagents and supported molecular cloning. M.K. supervised F.C.C. and designed tweezer experiments. S.W. and V.R. supervised the project, contributed to data analysis, and wrote the manuscript. P.L.-A. supervised M.M. **Competing interests:** The authors declare no competing interests. **Data and materials availability:** All data relevant for the conclusions of this work are available in the main text or the supplementary materials.

SUPPLEMENTARY MATERIALS

science.sciencemag.org/content/370/6514/eaba2644/suppl/DC1

Supplementary Methods

Figs. S1 to S7

Table S1

References (80–86)

MDAR Reproducibility Checklist

Movies S1 to S9

[View/request a protocol for this paper from Bio-protocol.](#)

20 November 2019; resubmitted 29 June 2020

Accepted 28 August 2020

10.1126/science.aba2644

RESEARCH ARTICLE SUMMARY

DEVELOPMENTAL BIOLOGY

Apical stress fibers enable a scaling between cell mechanical response and area in epithelial tissue

Jesús M. López-Gay, Hayden Nunley, Meryl Spencer, Florencia di Pietro, Boris Guirao, Floris Bosveld, Olga Markova, Isabelle Gague, Stéphane Pelletier, David K. Lubensky*, Yohanns Bellaïche*

INTRODUCTION: How biological properties scale with organ or body size is a question fundamental to development and physiology; however, at the cellular level, the scaling between size and properties such as mechanosensitivity remains poorly explored. Mechanosensitivity, the property by which cells sense mechanical forces, plays a fundamental role in proliferation and self-organization. In epithelial tissues, forces sensed at adherens junctions modulate cell

behavior via the Hippo/YAP pathway. Although cell geometry, including apical cell area, can vary considerably among cells within a tissue, little attention has been given to whether or how epithelial cells scale their mechanical response to their size or whether such scaling is important for development.

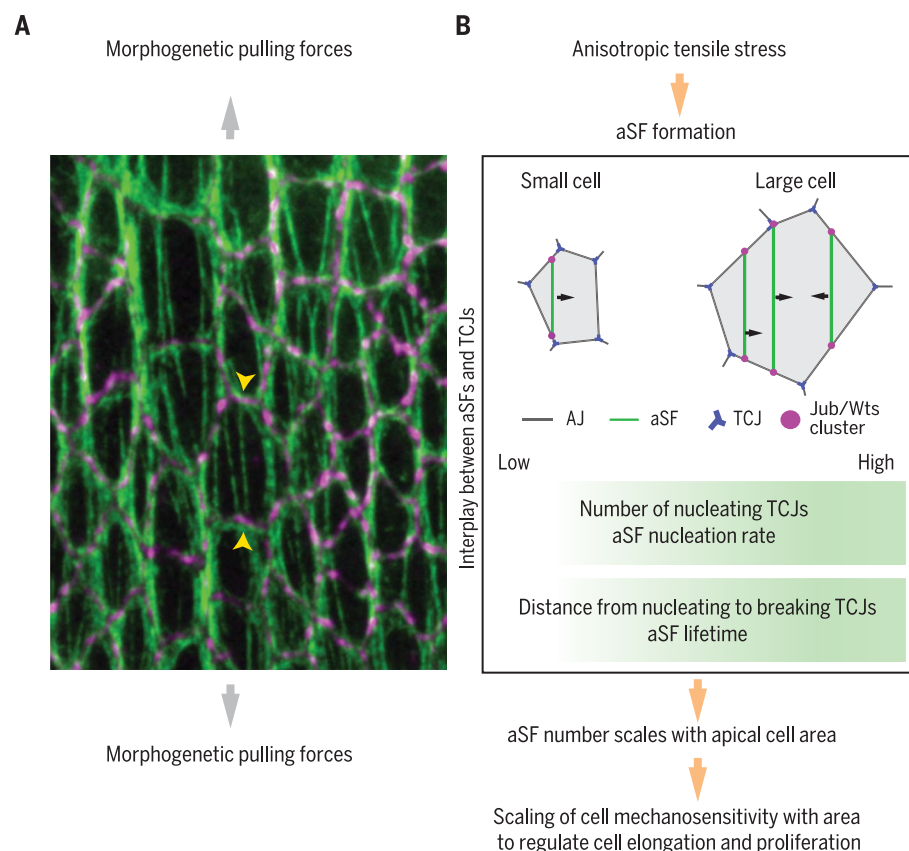
RATIONALE: To probe the interplay between cell size and mechanical response, we first need

to better understand how epithelial tissues respond to endogenous forces during morphogenesis. To characterize such tissue response via genetics, imaging, and mechanical perturbations, we used the *Drosophila* pupal dorsal thorax epithelium as a model system. Because, as in most tissues, cell size varies substantially within this epithelium, it is amenable to the investigation of the possible scaling of mechanosensitivity with cell size.

RESULTS: We observed that in response to morphogenetic forces, cells form apical stress fibers (aSFs), contractile actomyosin bundles that span the cell at the level of the adherens junctions. Through physical modeling and experiments, we found that the number of aSFs per cell scales with cell apical area. This scaling is critical to limit the elongation of larger cells relative to smaller cells under morphogenetic stress, and thus controls the final tissue shape. Moreover, because of the clustering of Hippo components at the tips of aSFs, the scaling of aSF number with cell apical area translates into a scaling between Hippo/YAP activation and cell area; the latter scaling favors the proliferation of larger cells and controls the final number of cells within the tissue.

To identify the “ruler” that enables the scaling of mechanosensitivity with cell area, we explored aSF dynamics. aSFs nucleate at tricellular junctions (TCJs), the position where three cells meet; aSFs then peel from the cortex and often break as they encounter another TCJ. Because both the number of TCJs and the separation between TCJs change as a function of cell area, we hypothesized that TCJs might provide an internal cell “ruler.” Predictions of computer simulations, experimentally tested via the modulation of TCJ number and positions, indicate that the scaling is mainly driven by the number of TCJs and their spatial distribution, which mediate an increase in aSF nucleation rate and lifetime in larger cells.

CONCLUSION: Our work uncovers a scaling between the number of aSFs per cell and cell apical area in response to morphogenetic stress. The number of TCJs and their spatial distribution largely account for this scaling. Thus, our work defines a functional link between TCJs and aSFs. Because TCJs and stress fibers are prevalent biological structures, the molecular characterization of their interplay might shed light on numerous aspects of tissue mechanics, proliferation, and morphogenesis. ■



An interplay between apical stress fibers (aSFs) and tricellular junctions (TCJs) drives area-dependent cell mechanical response to morphogenetic stresses. (A) aSFs labeled by Myosin II (green) in the *Drosophila* pupal dorsal thorax epithelium under extensile morphogenetic stress (large gray arrows); the tips of one aSF are indicated by yellow arrowheads. Adherens junctions are labeled in purple by E-cadherin. (B) Schematic of the scaling of cell mechanosensitivity with cell area and the resulting control of tissue elongation and proliferation under anisotropic morphogenetic stress.

The list of author affiliations is available in the full article online.

*Corresponding author. Email: dkluben@umich.edu (D.K.L.); yohanns.bellaiche@curie.fr (Y.B.)

Cite this article as J. M. López-Gay et al., *Science* 370, eaabb2169 (2020). DOI: 10.1126/science.abb2169

S READ THE FULL ARTICLE AT
https://doi.org/10.1126/science.abb2169

RESEARCH ARTICLE

DEVELOPMENTAL BIOLOGY

Apical stress fibers enable a scaling between cell mechanical response and area in epithelial tissue

Jesús M. López-Gay^{1,2}, Hayden Nunley³, Meryl Spencer⁴, Florencia di Pietro^{1,2}, Boris Guirao^{1,2}, Floris Bosveld^{1,2}, Olga Markova^{1,2}, Isabelle Gague^{1,2}, Stéphane Pelletier^{1,2}, David K. Lubensky^{3,4*}, Yohanns Bellaïche^{1,2*}

Biological systems tailor their properties and behavior to their size throughout development and in numerous aspects of physiology. However, such size scaling remains poorly understood as it applies to cell mechanics and mechanosensing. By examining how the *Drosophila* pupal dorsal thorax epithelium responds to morphogenetic forces, we found that the number of apical stress fibers (aSFs) anchored to adherens junctions scales with cell apical area to limit larger cell elongation under mechanical stress. aSFs cluster Hippo pathway components, thereby scaling Hippo signaling and proliferation with area. This scaling is promoted by tricellular junctions mediating an increase in aSF nucleation rate and lifetime in larger cells. Development, homeostasis, and repair entail epithelial cell size changes driven by mechanical forces; our work highlights how, in turn, mechanosensitivity scales with cell size.

Mechanical forces play an essential role in sculpting tissue shapes as tissues develop into their adult forms during morphogenesis (1). Within epithelial tissues, cells generate forces that are sensed by neighboring cells, and numerous studies have defined the critical roles of cell mechanosensitivity in epithelial morphogenesis, proliferation, and self-organization (1). In epithelia, mechanosensing occurs in particular at the level of the adherens junctions (AJs) through the Hippo/YAP pathway (1–3). Cell geometry, including apical cell area, varies considerably among cells within a tissue. Yet little attention has been given to whether and how epithelial cells adapt their mechanical response to their geometry or whether such adaptation is important for tissue dynamics and morphogenesis.

Apical stress fibers form in response to morphogenetic forces

To investigate the possible interplay between cell geometry and cell mechanical response, we first aimed to better understand how epithelial tissues respond to endogenous morphogenetic forces. To this end, we used the *Drosophila* pupal dorsal thorax's monolayered epithelium (notum), a well-established model to study cytoskeleton dynamics, mitosis, morphogenesis, and mechanics (4–9).

In its posterior and central region (black dashed box in Fig. 1A and fig. S1, A to A"), this tissue proliferates and elongates as tensile

mechanical stress increases along the medial-lateral (m-l) axis and becomes anisotropic between 18 and 26 hours after pupa formation (hAPF) (Fig. 1B, fig. S1, B and C, and movie S1) (4, 10). In this region and prior to 18 hAPF, Myosin II (MyoII) is localized at the junctional cortex and in an apical medial pool (Fig. 1C, left). Between 18 and 26 hAPF, the MyoII apical-medial pool reorganizes into MyoII fibers that form at the cell apex (Fig. 1, B and C, and movie S2). These fibers are oriented along the m-l axis and are under tensile stress (Fig. 1, D to F, fig. S1D, and movie S3). The fiber tips are positioned at the level of the AJs (Fig. 1C and fig. S1, E to F"). Known components of stress fibers, including Zyxin (Zyx), Enabled (Ena), and α -Actinin (Actn), are distributed along or at the tips of the fibers (Fig. 1G, fig. S1, G to Q, and table S1). Because we found that MyoII fibers are apical, connected to apical AJs, and tensile, we refer to them as apical stress fibers (aSFs). aSFs oriented along the main axis of tensile stress are present in other tissue regions (green dashed box in fig. S1, A', R, and S), and myosin-rich fibers anchored at the level of AJs have been observed in several tissues and cell types (11–14). To test whether aSF formation is a response to mechanical stress, we reduced mechanical stress in the central tissue domain by complementary approaches: by expressing a dominant negative form of MyoII heavy chain (*zip*^{DN}) in the lateral tissue region (fig. S2, A and A') or by applying a 20% compressive mechanical strain in the tissue plane on the living animal (fig. S2, B to C'). Both approaches led to a reduced number of aSFs and a disturbance of their m-l orientation (Fig. 1, H to N). Conversely, locally increasing contractility by reducing MyoII phosphatase activity leads to an increase of the number of aSFs in the surrounding cells (fig. S2, D to F). We conclude

that an increase in mechanical stress promotes the formation of tensile aSFs along the tissue's main stress axis.

Apical stress fiber number scales with cell area to limit cell elongation

The role of stress fibers is far from understood in vivo, and the relative contributions of cell-cell junctions and stress fibers in epithelial tissue mechanics are unexplored. We therefore investigated the roles of aSFs in morphogenesis by both experimental and modeling approaches. Because aSFs are under tension (Fig. 1F, fig. S3K, and movies S3 and S4), we tested whether aSFs regulate cell and tissue elongation. Toward this goal, we screened for loss-of-function mutants affecting aSF number at 26 hAPF (table S1). Abrogating Actn function [using either RNA interference (RNAi) or a CRISPR/Cas9-generated null allele] in the central posterior region of the tissue leads to a drastic decrease in aSF number per cell as well as to an increase in cell and tissue elongation along the main axis of mechanical stress (Fig. 2, A to D, and fig. S3, A to H"). This increase in elongation occurred without a major change in the tissue's global mechanical stress (fig. S3I), indicating that aSFs prevent cell and tissue elongation in response to mechanical stress generated during morphogenesis. To explore the respective mechanical roles of aSFs and AJs, we then used laser ablation to estimate the tensions of aSFs and AJs (fig. S1D and fig. S3, J and K). The recoil velocity upon aSF ablation was around one-third of that observed for ablation of AJs aligned with the m-l axis; this suggests that aSFs have lower tension than similarly oriented AJs (Fig. 2E, fig. S3K, and movies S3 and S4). By sequentially ablating an aSF and then an AJ from the same cell, we found that aSFs diminish the tension exerted on the AJ (Fig. 2E and movies S5 and S6). Consistently, AJ recoil velocity upon laser ablation was increased in *actn*^{RNAi} cells relative to control cells at 26 hAPF, but not at 18 hAPF when aSFs are absent (Fig. 2F). To further understand aSFs' contribution to cell and tissue morphogenesis, we considered a simple vertex model of a regular cell packing in mechanical equilibrium with or without aSFs (Fig. 2, G and H, supplementary text, and fig. S4). As observed experimentally, the model shows that aSFs oriented along the main stress axis limit cell and tissue elongation (Fig. 2H and fig. S4). Furthermore, mirroring our observation in *actn*^{RNAi} cells, the model establishes that at high stress anisotropies, aSFs are more efficient at limiting cell elongation than simply up-regulating tension along AJs (Fig. 2H and fig. S4). The model also predicts that cells with a larger apical area require more aSFs (or more tension per aSF) to limit cell elongation to maintain the same aspect ratio under anisotropic mechanical stress (Fig. 2I, supplementary text, and fig. S4).

¹Institut Curie, PSL Research University, CNRS UMR 3215, INSERM U934, F-75248 Paris Cedex 05, France. ²Sorbonne Universités, UPMC Univ Paris 06, CNRS, CNRS UMR 3215, INSERM U934, F-75005 Paris, France. ³Biophysics Program, University of Michigan, Ann Arbor, MI 48109, USA. ⁴Department of Physics, University of Michigan, Ann Arbor, MI 48109, USA. *Corresponding author. Email: dkubens@umich.edu (D.K.L.); yohanns.bellaiche@curie.fr (Y.B.)

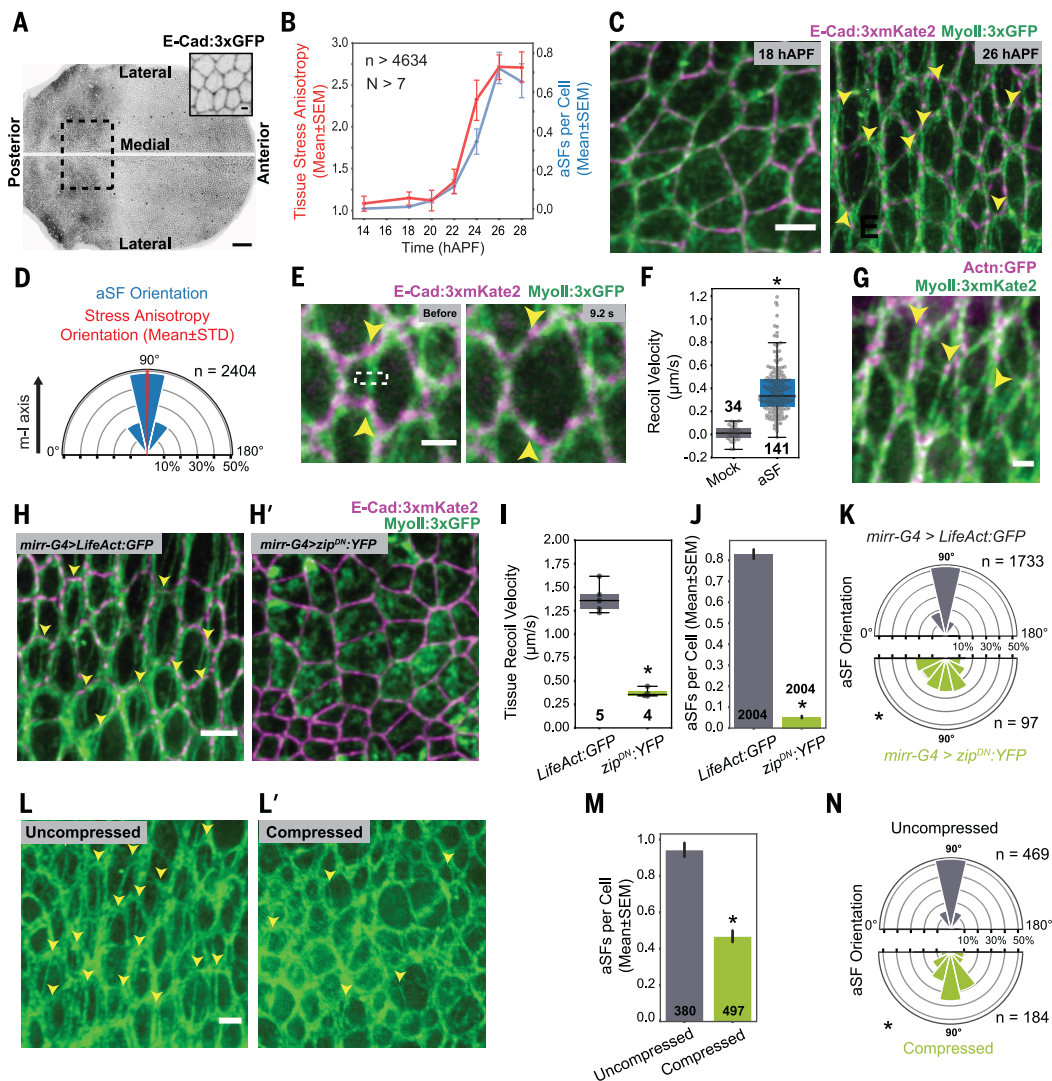


Fig. 1. aSF formation in response to tissue mechanical stress. (A) Pupal dorsal thorax labeled by E-cadherin:3xGFP (E-Cad:3xGFP) at 26 hAPF; inset shows close-up view. White line, midline; dashed box, posterior and central region where aSFs form and where protein distributions and quantifications are reported at 26 hAPF in all figures, unless otherwise stated. (B) Tissue stress anisotropy estimated by laser ablation (red) and number of aSFs per cell over all cell sizes (blue) as a function of developmental time; n and N , numbers of cells and tissue ablations at each time point, respectively. (C) E-Cad:3xKate2 and MyoII:3xGFP distributions at 18 hAPF and 26 hAPF. Arrowheads denote aSFs. (D) Orientation of aSFs (blue) at 26 hAPF and of the tissue's main stress axis (mean \pm STD in red and light red, respectively; note that the STD is barely wider than the line thickness); n , aSF number. (E) E-Cad:3xKate2 and MyoII:3xGFP distributions before ablation and 9.2 s after aSF ablation. Dashed box, ablated region; arrowheads, positions of the AJs prior to and after aSF ablation. (F) Recoil velocity

upon mock and aSF ablation; n , number of ablations. $P < 10^{-5}$. (G) Actin:GFP and MyoII:3xKate2 distributions at 26 hAPF. Arrowheads indicate some aSFs. (H and H') E-Cad:3xKate2 and MyoII:3xGFP distributions in the posterior central region in the *mirr-G4>LifeAct:GFP* [control, (H)] and *mirr-G4>zip^{DN}:YFP* (H') animals. Arrowheads, aSFs. (I to K) Medial-lateral (m-l) tissue recoil velocity upon anterior-to-posterior (a-p) ablation [(I); n , number of ablations; $P < 10^{-2}$] as well as number of aSFs per cell and aSF orientation [(J) and (K); n , number of aSFs; $P < 10^{-5}$] in control *mirr-G4>LifeAct:GFP* versus *mirr-G4>zip^{DN}:YFP* tissues. (L and L') MyoII:3xGFP distributions at 26 hAPF in an uncompressed tissue (L) and in a tissue compressed along the m-l axis (L'). Arrowheads, aSFs. (M and N) aSF number per cell (M) and orientation (N) in uncompressed tissue versus compressed tissue at 26 hAPF; n , number of aSFs per cell. $P < 10^{-5}$. Scale bars, 50 μ m (A), 5 μ m [(C), (H), and (L)], 2 μ m [(E), (G), and inset in (A)]. * $P < 0.05$ [Kruskal-Wallis test in (F), (I), (J), and (M); Levene test for equality of variances in (K) and (N)].

On the basis of these predictions, we investigated the relationship among individual aSF tension, aSF number per cell, and cell apical area at 26 hAPF. First, laser ablation suggests that the tension supported by one aSF is independent of cell apical area (fig. S3L). Second, the number of aSFs per cell scales with the cell's apical area (Fig. 2J and fig. S3, M and N). Finally, when we ablated more than one

aSF within a given cell, the cell elongated more with each additional aSF ablation (Fig. 2K and movie S7). We then investigated whether a change in cell apical area leads to a change in the number of aSFs. By comparing the cell area and aSF number per cell in interphase cells 1 hour before and 1 hour after cytokinesis, we found that a reduced cell apical area is associated with a reduced number of aSFs per

cell (fig. S3O). Conversely, preventing cell division or cytokinesis leads to an increase in cell area and an increase in aSF number per cell (Fig. 2L and fig. S3O).

We then tested whether the scaling between cell area and aSF number is important for limiting cell elongation. Fractional cell elongation is independent of cell area in control cells (fig. S3P), and aSF ablation leads to a

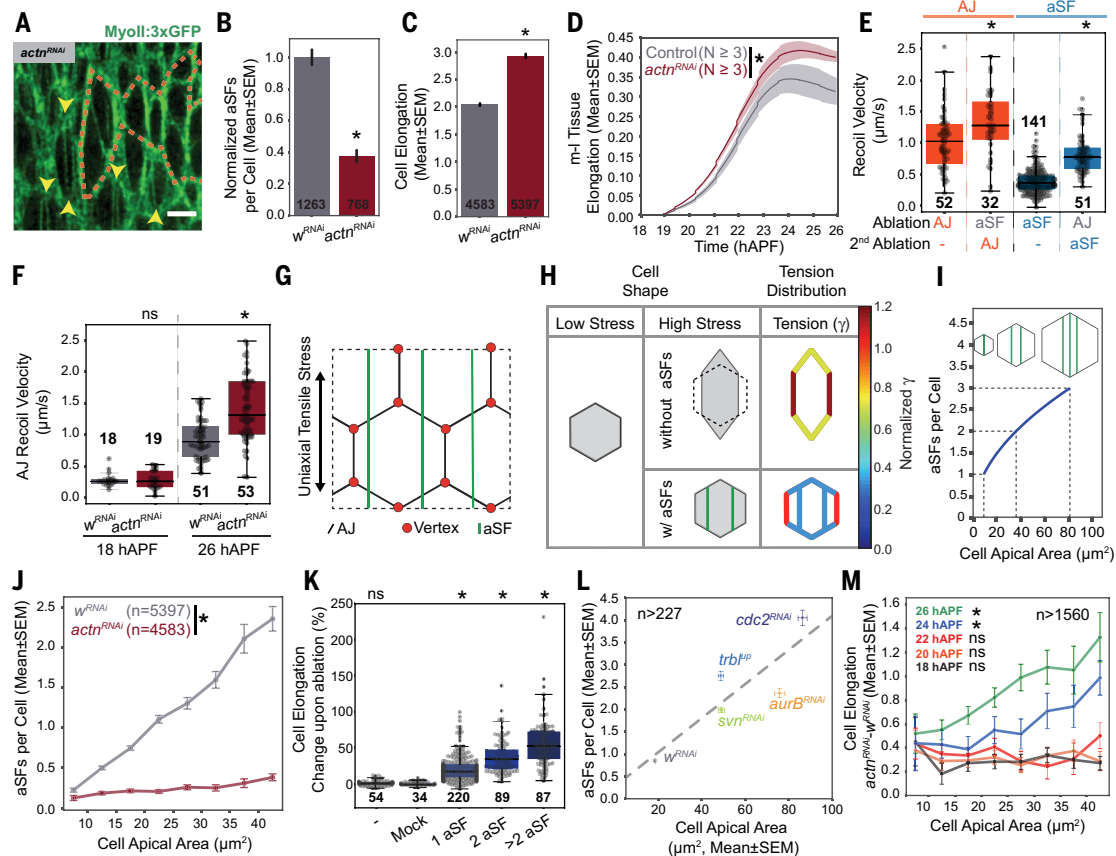


Fig. 2. Scaling between cell apical area and aSF number per cell.

(A) MyoII:3xGFP distribution in *actr^{RNAi}* cells (outlined by an orange dashed line) marked by Cxa::tBFP accumulation (not shown) and in control cells. Arrowheads, aSFs. (B) aSF number per cell in *w^{RNAi}* control and *actr^{RNAi}* clones at 26 hAPF; *n*, number of cells. $P < 10^{-5}$. (C) m-I cell elongation of *w^{RNAi}* control and *actr^{RNAi}* clone at 26 hAPF. *n*, number of cells. $P < 10^{-5}$. (D) m-I tissue elongation in control versus *actr^{RNAi}* clones in the tissue's central posterior region between 19 and 26 hAPF. *N*, number of clones. $P < 10^{-5}$. (E) Recoil velocity (orange) of ablated AJ without prior aSF ablation and after aSF ablation was performed (*n*, number of ablations; $P < 0.05$); graph of recoil velocity (blue) upon aSF ablation without prior AJ ablation and after ablation of a neighboring AJ (*n*, number of ablations; $P < 10^{-5}$). (F) AJ recoil velocity upon ablation in *w^{RNAi}* control and *actr^{RNAi}* clones at 18 hAPF [not significant (ns)] and 26 hAPF ($P < 10^{-4}$); *n*, number of ablations. (G) Schematic of the vertex model of a regular cell packing with aSFs under uniaxial stress. (H) Cell elongation and tension distribution (γ , color scale) in the model without or with aSFs at fixed cell size and orientation and at fixed uniaxial tissue stress. Gray cells, differential cell elongation; colored cells, tension

magnitude at AJ and individual aSFs (at fixed tension per aSF). See fig. S4I for parameter values. (I) Number of aSFs per cell (at fixed tension per aSF) required for cells to remain regular under uniaxial stress versus cell apical area. See fig. S4I for parameter values. (J) aSF number per cell versus apical cell size in *w^{RNAi}* control and *actr^{RNAi}* clones at 26 hAPF; *n*, number of cells. $P < 10^{-5}$. (K) Changes in cell elongation (percentage) without ablation, upon mock aSF ablation (i.e., ablation next to an aSF), and upon ablation of an increasing number of aSFs in a cell; *n*, number of cells without ablation, with mock ablations, or with ablations of aSFs. $P < 10^{-3}$. (L) Cell apical area versus aSF number per cell in control *w^{RNAi}*, *survivor^{RNAi}* (*svr^{RNAi}*), *aurB^{RNAi}*, *tribbles* overexpression (*trbl^{UP}*), and *cdc2^{RNAi}* clones. Numbers of cells: *w^{RNAi}*, *n* = 2903; *svr^{RNAi}*, *n* = 872; *aurB^{RNAi}*, *n* = 402; *trbl^{UP}*, *n* = 356; *cdc2^{RNAi}*, *n* = 227. (M) Difference in m-I cell elongation between *actr^{RNAi}* cells and *w^{RNAi}* control clones as a function of apical cell size at different hAPF; *n*, minimum number of cells at each hAPF and condition. $P < 10^{-4}$. Scale bar, 5 μ m. * $P < 0.05$ [Kruskal-Wallis test without Conover post hoc test in (B), (C), (E), and (F) or with Conover post hoc test in (K); analysis of covariance (ANCOVA) in (J) and (M); mixed analysis of variance (ANOVA) in (D)].

cell elongation that increases with cell area (fig. S3, P and Q). Moreover, the elongation of *actr^{RNAi}* cells increases with their apical area as the stress anisotropy increases (Fig. 2M and fig. S3P). We conclude that a scaling between aSF number and cell area reduces tissue elongation under anisotropic stress by ensuring that cell elongation is independent of cell area.

Scaling between cell area and Hippo/Yki signaling via aSF number scaling

We next explored whether the scaling between cell area and aSF number translates into bio-

chemical regulation in conditions of mechanical stress. aSFs are located away from the nucleus (fig. S1E'); this suggests that aSFs do not regulate YAP/TAZ (Yorkie, Yki in *Drosophila*) activity by direct nuclear deformation, as found in individual cultured cells (2, 15). We therefore investigated alternative mechanisms through which aSFs might modulate Hippo/Yki activity in epithelial tissues. The LIM domain protein Ajuba (Jub) is a component of the Hippo/Yki pathway that binds to the Warts (Wts) kinase. Jub binding results in Wts inhibition and thus Yki activity up-regulation (16, 17). Previous findings indicate that an in-

crease of MyoII contractility leads to the increased recruitment of Jub to the AJs and that this recruitment promotes Hippo/Yki signaling (18–21). In the dorsal thorax, we observed that at high mechanical stress (26 hAPF), Jub and Wts form clusters at the tips of the aSFs (Fig. 3, A and B, and fig. S5, A to D). Furthermore, quantitative analyses of the Jub and Wts distributions showed that the number of Jub and Wts clusters as well as the ratio of Jub and Wts intensity in clusters to that elsewhere along the AJ (ratio^{in/out} of cluster) increases between low stress (18 hAPF) and high stress (26 hAPF) (Fig. 3C and fig. S5, E and F). Accordingly, Jub

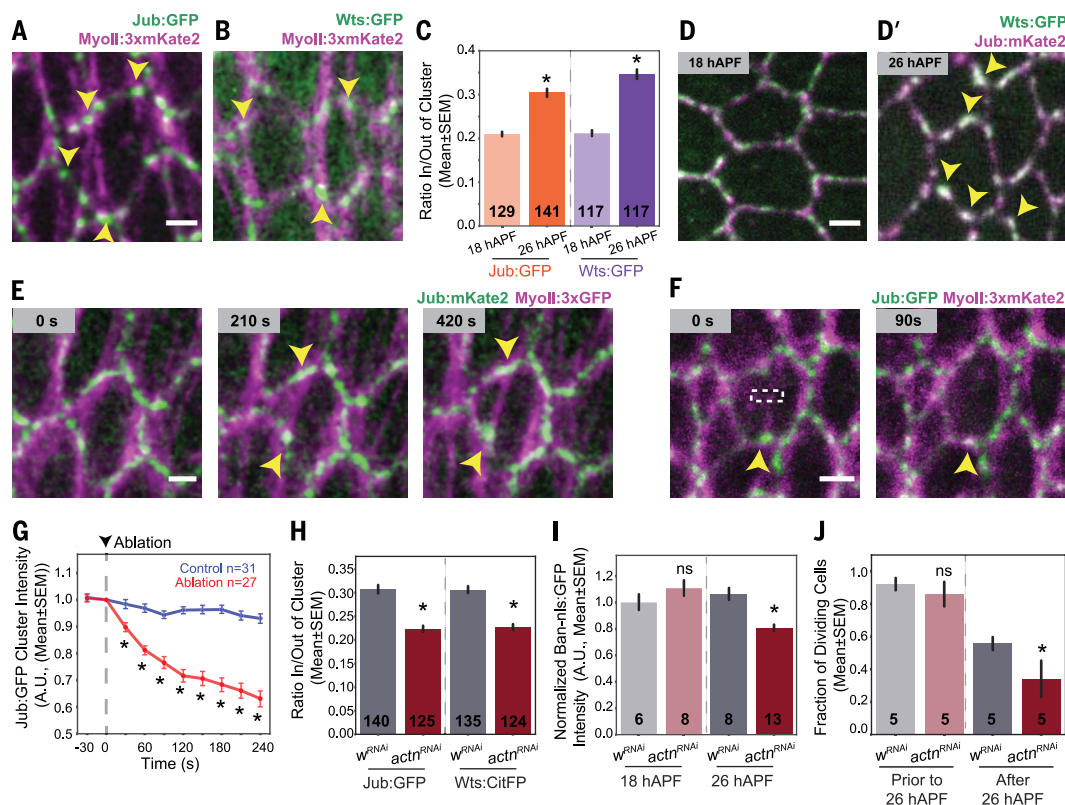


Fig. 3. Hippo component clustering and aSF formation. (A and B) Jub:GFP (A), Wts:GFP (B), and MyoII:3xmKate2 [(A) and (B)] distributions at 26 hAPF. Arrowheads, aSF tips. (C) Jub:GFP and Wts:GFP ratio^{in/out} of clusters at 18 hAPF (low stress) and 26 hAPF (high stress); n , number of cells. $P < 10^{-5}$ for the comparison between 18 hAPF and 26 hAPF for both Jub:GFP and Wts:GFP. (D and D') Jub:mKate2 and Wts:GFP distributions at 18 hAPF [low stress, (D)] and 26 hAPF [high stress, (D')]. Arrowheads, Jub:mKate2 and Wts:GFP co-clusters. (E) Jub:mKate2 and MyoII:3xGFP distributions during aSF formation. $t = 0$ corresponds to aSF nucleation; arrowheads, aSFs. (F) Jub:GFP distribution before and after ($t = 90$ s) ablation (dashed box) of the MyoII:3xmKate2-labeled aSF; arrowhead, cluster prior to and after ablation. (G) Jub:GFP cluster

intensities in mock ablated aSF (control, blue) and upon aSF ablation (red); n , number of clusters; A.U., arbitrary units. $P < 10^{-3}$ after time point 30 s. (H) Jub:GFP and Wts:GFP ratio^{in/out} of clusters in *w^{RNAi}* control and *actn^{RNAi}* clones at 26 hAPF; n , number of cells. $P < 10^{-5}$ for Jub:GFP and Wts:GFP. (I) *Ban-nls:GFP* normalized intensity in *w^{RNAi}* control and *actn^{RNAi}* clones at 18 and 26 hAPF; N , number of animals. 18 hAPF, ns; 26 hAPF, $P < 10^{-3}$. (J) Fraction of cells that divide between 18 and 26 hAPF and between 26 and 34 hAPF in *pnr-G4>w^{dsRNA}* control and *pnr-G4>actn^{dsRNA}* tissues; N , number of animals. Prior to 26 hAPF, ns; after 26 hAPF, $P < 0.05$. Scale bars, 2 μ m. * $P < 0.05$ [Kruskal-Wallis without Conover post hoc test in (C), (H), and (I) or with Conover post hoc test in (G); one-tailed Wilcoxon signed-rank test in (J)].

and Wts colocalization increases under high mechanical stress (Fig. 3, D to D', and fig. S5G). Thus, an increase in mechanical stress correlates with the formation of Jub and Wts co-clusters at the tips of the aSFs along the AJs. To determine whether Jub clustering modulates Hippo signaling, we used the Cry2Olig optogenetic clustering system (22) to induce Jub clustering independent of aSF formation. We found that light-induced clustering of Jub is sufficient to cocluster Wts and to up-regulate Yki activity (fig. S5, H to J, and movie S8). Next, we explored whether the formation of aSFs and their associated tension modulate Jub and Wts clustering, Hippo/Yki activity, and cell proliferation. High-resolution time-lapse imaging showed that as an aSF forms or is displaced along the AJ, cortical Jub:mKate2 and Wts: CitFP flow and accumulate at the aSF tip (Fig. 3E, fig. S5, K and K', and movie S9). Conversely, upon ablation of a previously formed aSF, the Jub:GFP or Wts:GFP clusters initially present

at that aSF's tip are strongly reduced (Fig. 3, F and G, fig. S5, L and M, and movie S10). Although the loss of Actn function does not affect the total amount of Jub and Wts at the junction (fig. S5, P and Q), it decreases the number of Jub and Wts clusters and their colocalization as well as the ratios^{in/out} of Jub and Wts clusters (Fig. 3H and fig. S5, R and S). Last, we found that the loss of Actn function leads to a decrease of *Ban-nls:GFP* Yki transcriptional reporter expression (23) and cell proliferation, specifically under high stress (Fig. 3, I and J, and fig. S5, T to V). We conclude that aSFs promote the coclustering of Jub and Wts at their tips, accounting for the down-regulation of Wts activity and the up-regulation of Yki transcriptional activity.

Having characterized the link between aSF formation and Yki transcriptional activation at 26 hAPF, we explored whether the scaling between aSF number and cell apical area might result in the scaling of Yki activity with

cell apical area. We quantified the intensity of *Ban-nls:GFP* as a function of cell apical area. *Ban-nls:GFP* levels increase as cell apical area increases from 10 to 32 μ m² and then reach a plateau for cells between 32 and 40 μ m² (Fig. 4A and fig. S6A). In contrast, the level of *nls:GFP* under the control of a ubiquitin promoter (*Ubi-nls:GFP*) is independent of cell apical area (Fig. 4A). In agreement with the proposed role of Jub clustering in Yki activity regulation, we found that the *Ban-nls:GFP* signal increases with the Jub ratio^{in/out} (Fig. 4B). Furthermore, we observed that under stress both the Jub and Wts ratios^{in/out} of clusters increase with cell apical area, consistent with the notion that a larger fraction of Wts is inhibited in larger cells under stress (Fig. 4C and fig. S6, B and C). If aSFs contribute to the scaling between cell size and Hippo/Yki pathway activation, the impact of Actn loss of function on Wts and Jub clustering should be more pronounced in larger cells. Accordingly,

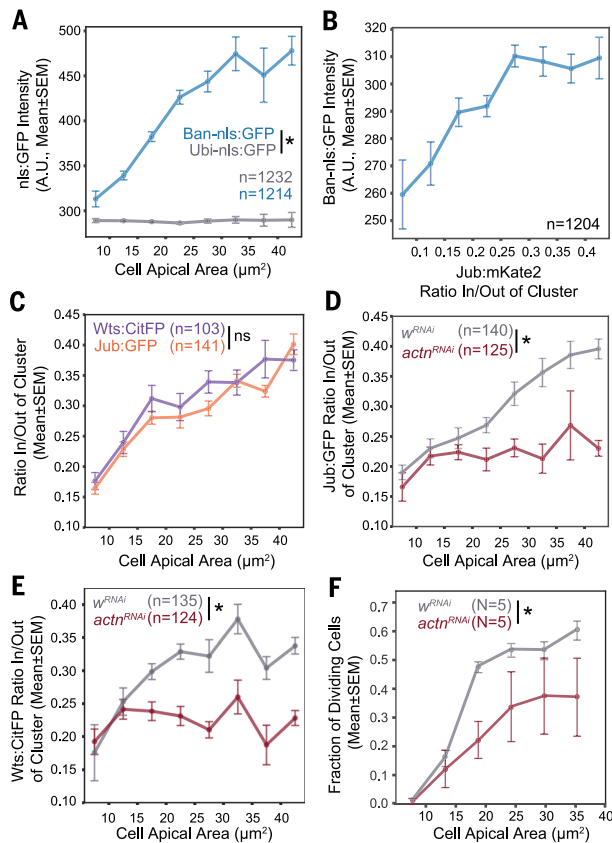


Fig. 4. Hippo scaling as a function of cell apical area. (A) *Ban-nls:GFP* and *Ubi-nls:GFP* intensity versus apical cell area; *n*, number of cells. $P < 10^{-5}$. (B) *Ban-nls:GFP* intensity versus *Jub:mKate2* ratio^{in/out} of cluster; *n*, number of cells. (C) *Wts:CitFP* and *Jub:GFP* ratio^{in/out} of cluster versus apical cell area; *n*, number of cells. (D and E) *Jub:GFP* (D) and *Wts:CitFP* (E) ratio^{in/out} of cluster versus apical cell size in *wRNAi* control and *actnRNAi* clones; *n*, number of cells. $P < 10^{-4}$. (F) Fraction of cells that divide between 22 hAPF and 34 hAPF as a function of apical cell size in *pnr-G4>wdsRNA* control and *pnr-G4>actnRNAi* tissues; *N*, number of animals. $P < 0.05$. * $P < 0.05$ [ANCOVA for difference in regression slopes in (A), (C), (D), and (E); mixed ANOVA in (F)].

Jub and *Wts* clustering is not affected in small *actnRNAi* cells, whereas clear differences exist between large *actnRNAi* cells and large control cells (Fig. 4, D and E, and fig. S6D). Furthermore, we observed that the effect of *Actn* loss of function on cell proliferation mirrors the defects observed in *Jub* and *Wts* clustering in *actnRNAi* cells (Fig. 4F). Finally, we increased cell apical area by preventing cytokinesis and observed a corresponding increase in both *Jub* ratio^{in/out} of clusters and *Ban-nls:GFP* level (fig. S6, E and F). Together, these findings indicate that the scaling between cell area and aSF number leads to a scaling between cell area and the clustering of *Jub* and *Wts*, and thus to the scaling of Hippo/Yki signaling activity with apical cell size in epithelial tissues.

Tricellular junctions promote scaling between aSF number and apical area

Having established the role of aSFs in scaling cells' mechanical and biochemical responses under mechanical stress, we next explored the

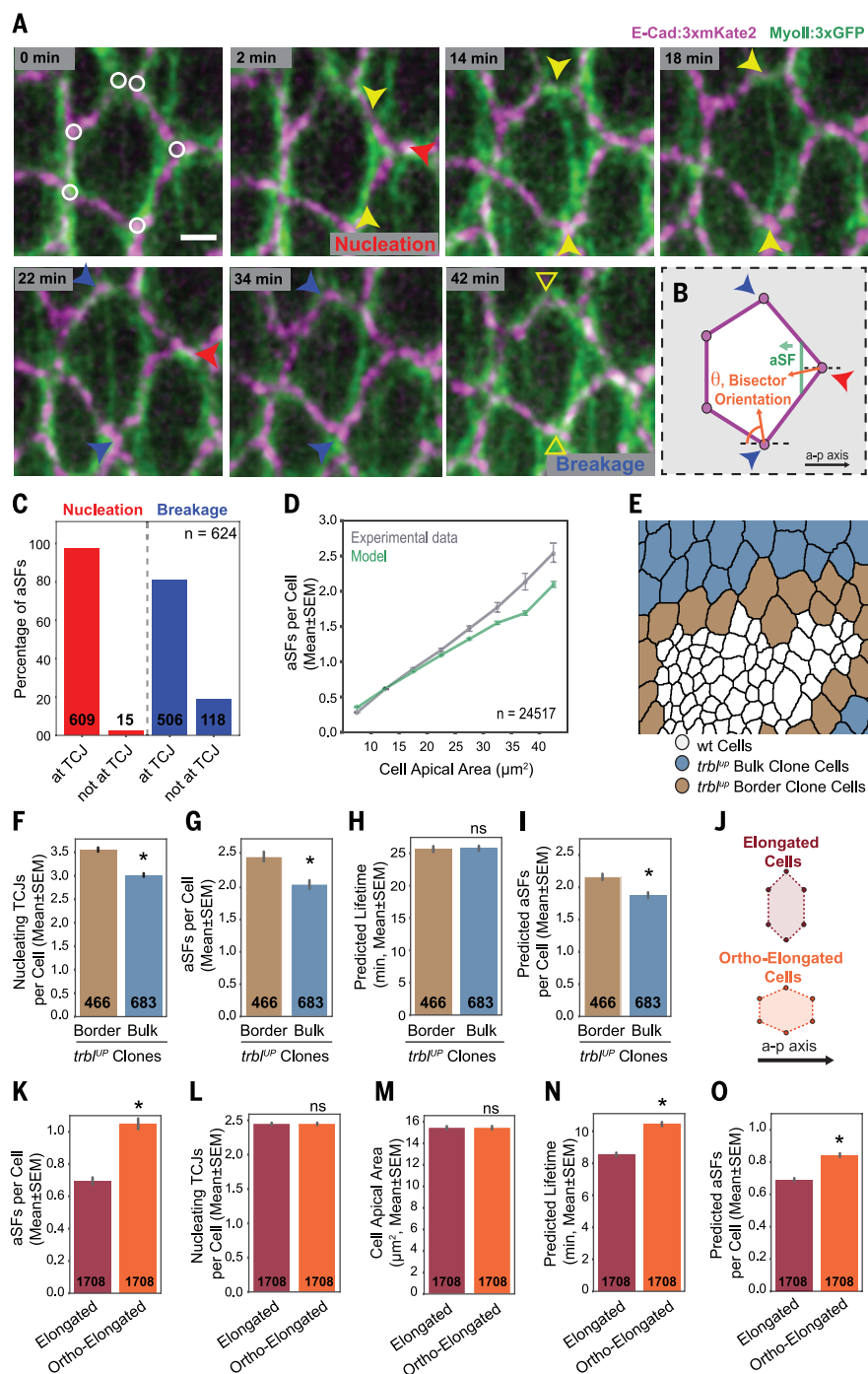
origins of the scaling of aSF number with cell apical area. Stress fiber formation is best studied in individual cells where the fibers' spatial organization depends on cell shape (24, 25). Yet even in this context, the mechanisms controlling stress fiber number and dynamics are not fully understood (24, 25). To investigate how the scaling between cell size and aSF number is achieved in epithelial tissues under anisotropic stress, we analyzed aSF dynamics at 26 hAPF. Through live imaging of aSFs, we found that aSFs form at curved regions of cell-cell junctions aligned with the main axis of tensile stress (Fig. 5, A and B, and movie S11). In epithelial tissues, tricellular junctions (TCJs), points where three cells meet, are often the most curved regions of the cell apical contour (26). Accordingly, aSFs mainly nucleate at TCJs (Fig. 5, A to C). After nucleation, aSFs sweep across the cell as they peel from the cortex, most often breaking as they encounter another TCJ (Fig. 5, A to C). A TCJ's propensity to nucleate or to break aSFs varies simply as a function of the orientation of the

TCJ's bisector with respect to the main stress axis (fig. S7, A to F, fig. S8, L, M, and T, and supplementary text). Thus, we could classify a TCJ as a "nucleating TCJ" or a "breaking TCJ" based on this orientation. Although the exact mechanical and molecular mechanisms driving aSF nucleation and breakage at TCJs remain to be understood, the TCJs' role in both processes suggests a geometric mechanism for the scaling of aSF number with cell apical area based on the following trends: The larger cells in a tissue have more TCJs (27) and thus might have higher rates of aSF nucleation. A typical nucleating TCJ is also farther from a typical breaking TCJ in larger cells, so that aSFs in larger cells could be expected to take longer to travel from one to the other. Together, these two effects would lead to larger cells' having more aSFs as the result of an increase in both aSF nucleation rate and aSF lifetime.

To test this hypothesis, we analyzed how aSF nucleation rates and lifetimes differ between small and large cells. Large cells on average have higher aSF nucleation rates and longer lifetimes than small cells, in agreement with our proposed geometric mechanism (fig. S8, N to R). Next, we performed computer simulations to quantify how much of the observed scaling of aSF number with cell apical area could be explained by differences in the number of TCJs and their positions. In these simulations, we considered a simple model where only the geometric effects are present; we did not include any explicit dependence on cell size (see supplementary text). We applied this model to cell shapes and orientations taken directly from experimental images at 26 hAPF. We found that our geometric TCJ model explains ~75% of the observed variation of aSF number with cell apical area with only one free parameter. This parameter can be interpreted as essentially equivalent to the junctional cortex thickness, and the fitted value agrees well with direct thickness measurements ($0.50 \pm 0.12 \mu\text{m}$ versus $0.51 \pm 0.12 \mu\text{m}$; Fig. 5D, supplementary text, and fig. S8S).

To further show that the number of aSFs within a cell depends on the properties of its TCJs, we sought to vary TCJ number and position independently of cell apical area and in a population of genetically identical cells. To accomplish this, we performed two distinct analyses. First, we took advantage of the fact that a large cell in contact with smaller cells typically has more TCJs than a large cell surrounded by other large cells (28). To generate large cells with different local environments, we induced clones of large cells by blocking the G_2/M transition through overexpression of *trbl* (*trbl*^{UP} clones) and compared *trbl*^{UP} cells at the boundary of the clone (border cells) to cells within the clone (bulk cells, Fig. 5E). As anticipated, *trbl*^{UP} cells at the boundary of the clone have more nucleating TCJs (Fig. 5F) and

Fig. 5. TCJs contribute to a scaling between cell area and aSF number. (A) E-Cad:3xmKate2 and MyoII:3xGFP distributions as an aSF nucleates ($t = 0$ min; circles denote TCJs), peels from the cortex ($t = 2$ to 14 min), moves toward TCJs ($t = 18$ to 22 min), briefly stalls at TCJs ($t = 34$ min), and breaks ($t = 42$ min). Red arrowhead, nucleating TCJ; yellow arrowheads, aSF tips; blue arrowheads, breaking TCJs; open yellow arrowheads, aSF tip positions at the time of breakage. (B) Illustration of an aSF nucleating at a nucleating TCJ (red arrowhead) and peeling from the cortex until the aSF tips reach breaking TCJs (blue arrowheads) and of the TCJ opening angle α and TCJ bisector orientation θ with respect to the a-p axis. Orange arrows indicate the TCJ bisector, which makes an angle θ with the a-p axis ($\theta \approx 5^\circ$ for the nucleating TCJ at right; $\theta \approx 80^\circ$ for the breaking TCJ at bottom). (C) aSF nucleation (red) and breakage (blue) events at TCJs; n , total number of aSFs. (D) Experimental (gray) and model-predicted (green) aSF number per cell versus apical area. The model explains $\sim 75\%$ of the variance of aSF number with cell apical area; n , number of cells. (E) Schematic based on a Jub:GFP image illustrating the positions of the control (white), border (brown), and bulk (blue) *trbl*^{UP} cells. (F to I) Nucleating TCJs per cell [(F), $P < 10^{-5}$], aSF number per cell [(G), $P < 10^{-2}$ controlling for cell apical area differences], predicted aSF lifetime (H), and predicted aSF number per cell [(I), $P < 10^{-2}$ controlling for cell apical area differences] in *trbl*^{UP} border and bulk cells; n , number of cells. (J) Schematic of elongated (top) and ortho-elongated (bottom) cells. (K to O) aSF number per cell [(K), $P < 10^{-5}$], nucleating TCJs per cell (L), cell apical area (M), predicted aSF lifetime [(N), $P < 10^{-5}$], and predicted aSF number per cell [(O), $P < 10^{-5}$] in elongated and ortho-elongated cells; n , number of cells. Scale bar, 2 μm . * $P < 0.05$ [Kruskal-Wallis tests in (F) to (I) and (K) to (O)].



thus might be expected to have more aSFs. To verify that no other differences in cell shape or TCJ distribution lead to a counter-vailing difference in predicted aSF lifetime between border and bulk cells, we simulated our geometric model of aSF nucleation and breakage on cell sizes and shapes taken from our images of *trbl*^{UP} clones; the model indeed predicts that *trbl*^{UP} cells at the boundary of the clone should have more aSFs per cell than *trbl*^{UP} bulk cells (Fig. 5I and fig. S9, A to G). Further, we found experimentally that, controlling for any small difference in

cell size between these two populations, cells at the boundary have on average more aSFs than cells within the clone (Fig. 5, G and H, and fig. S9, A to G). Thus, these results substantiate our hypothesis that an increase in the number of TCJs correlates with an increase in the number of aSFs.

We then analyzed whether the spatial distribution of TCJs modulates aSF number. If the distance between the nucleating TCJ and the breaking TCJ(s) is critical to control aSF number, we predict that cells that are elongated orthogonal to the uniaxial mechanical stress

(hereafter referred to as ortho-elongated) should have more aSFs than cells of a similar size elongated parallel to the main stress axis (Fig. 5J). By restricting our analysis to such ortho-elongated cells, we showed that at constant nucleating TCJ number and cell size, the number of aSFs is higher in ortho-elongated cells, as predicted (Fig. 5, K to O, and fig. S9, H to J). On the basis of quantitative analyses of aSF nucleation and lifetime, modeling, and experiments, we propose that the number and positions of TCJs are major contributors to the scaling of aSF number with cell apical area in

tissues under uniaxial tension (fig. S10). TCJs thus play an unexpected role in the regulation of cells' mechanical properties and signaling under mechanical stress.

Discussion

Scaling between body size and metabolic or biomechanical properties has been the subject of intense study for decades (29, 30). More recently, investigations of the scaling of morphogen gradients with tissue area or length have unveiled novel mechanisms of cell fate specification during development (31, 32). Here, we have uncovered a scaling between the number of aSFs per cell and cell apical area in an epithelial tissue. We have furthermore provided evidence that this scaling is critical to control cell and tissue elongation as well as proliferation in response to epithelial morphogenetic forces. Existing work has emphasized the roles of stress fibers as anchors to extracellular matrix (ECM) via focal adhesions and the stress fibers' roles in cell locomotion, cell mechanics and Hippo/YAP regulation (24, 33). Our work highlights the contributions of aSFs anchored to AJs as regulators of both tissue morphogenesis and proliferation under physiological morphogenetic mechanical stress. We have also found that aSFs promote the coclustering of Jub and Wts in the control of Hippo/YAP signaling. The full characterization of the molecular interactions between aSF components and Hippo/YAP regulators at the tips of the aSFs will be critical to decipher how aSFs promote the recruitment of Jub to the aSF tips in response to tissue stress. Interestingly, mammalian Jub localizes at ECM-integrin focal adhesions (34); this recruitment of Jub to focal adhesions might provide a complementary mechanism of Hippo/YAP mechanical regulation in individual cells (2, 15, 33, 35–37). Cell cycle regulation is well predicted by a combination of cell area and tension in multicellular assemblies in culture (38). Therefore, it will be useful to analyze whether the mechanisms we uncovered might generally explain the interplay between cell area and mechanical forces in cell proliferation control. Earlier studies have shown that oriented cell divisions relax uniaxial tissue stress in a manner that depends on cell elongation (39); it will be of interest to explore how aSFs, by limiting elongation while promoting the division of larger-area cells, might modulate tissue stress or mechanical properties.

Our characterization of the aSF dynamics illustrates that the number and distribution of TCJs largely account for the scaling between cell apical area and aSF number. Thus, our work defines a functional link between TCJs and aSFs. Because TCJs and stress fibers are prevalent biological structures (24, 26), the molecular characterization of their interplay might shed light on numerous aspects

of tissue mechanics, proliferation, and morphogenesis.

Materials and methods

Drosophila stocks used in this study are given in table S2. Methods for genetics, molecular biology, live imaging, laser ablations, and quantifications as well as statistics are described in the supplementary materials. The MatLab codes, the Python Jupyter Notebook for plotting and statistical analyses, and the Fiji macros used are available upon request. Physical modeling, computer simulations, and associated quantifications are described in the supplementary text.

REFERENCES AND NOTES

- E. Hannezo, C.-P. Heisenberg, Mechanochemical Feedback Loops in Development and Disease. *Cell* **178**, 12–25 (2019). doi: [10.1016/j.cell.2019.05.052](#); pmid: [31251912](#)
- J. R. Davis, N. Tapon, Hippo signalling during development. *Development* **146**, dev167106 (2019). doi: [10.1242/dev.167106](#); pmid: [31527062](#)
- D. Pinheiro, Y. Bellaiche, Mechanical Force-Driven Adherens Junction Remodeling and Epithelial Dynamics. *Dev. Cell* **47**, 3–19 (2018). doi: [10.1016/j.devcel.2018.09.014](#); pmid: [30300588](#)
- F. Bosveld et al., Mechanical control of morphogenesis by Fat/Dachsous/Four-jointed planar cell polarity pathway. *Science* **336**, 724–727 (2012). doi: [10.1126/science.1221071](#); pmid: [22499807](#)
- R. Levayer, C. Dupont, E. Moreno, Tissue Crowding Induces Caspase-Dependent Competition for Space. *Curr. Biol.* **26**, 670–677 (2016). doi: [10.1016/j.cub.2015.12.072](#); pmid: [26898471](#)
- S. Curran et al., Myosin II Controls Junction Fluctuations to Guide Epithelial Tissue Ordering. *Dev. Cell* **43**, 480–492.e6 (2017). doi: [10.1016/j.devcel.2017.09.018](#); pmid: [29107560](#)
- N. Founounou, N. Loyer, R. Le Borgne, Septins regulate the contractility of the actomyosin ring to enable adherens junction remodeling during cytokinesis of epithelial cells. *Dev. Cell* **24**, 242–255 (2013). doi: [10.1016/j.devcel.2013.01.008](#); pmid: [23410939](#)
- F. Bosveld et al., Epithelial tricellular junctions act as intraplane cell shape sensors to orient mitosis. *Nature* **530**, 495–498 (2016). doi: [10.1038/nature16970](#); pmid: [26886796](#)
- D. Pinheiro et al., Transmission of cytokinesis forces via E-cadherin dilution and actomyosin flows. *Nature* **545**, 103–107 (2017). doi: [10.1038/nature22041](#); pmid: [28296858](#)
- B. Guirao et al., Unified quantitative characterization of epithelial tissue development. *eLife* **4**, e08519 (2015). doi: [10.7554/eLife.08519](#); pmid: [26653285](#)
- V. Vasioukhin, C. Bauer, M. Yin, E. Fuchs, Directed actin polymerization is the driving force for epithelial cell-cell adhesion. *Cell* **100**, 209–219 (2000). doi: [10.1016/S0092-8674\(00\)81559-7](#); pmid: [10660044](#)
- J. Millán et al., Adherens junctions connect stress fibres between adjacent endothelial cells. *BMC Biol.* **8**, 11 (2010). doi: [10.1186/1741-7007-8-11](#); pmid: [20122254](#)
- M. K. L. Han, J. de Rooij, Converging and Unique Mechanisms of Mechanotransduction at Adhesion Sites. *Trends Cell Biol.* **26**, 612–623 (2016). doi: [10.1016/j.tcb.2016.03.005](#); pmid: [27036655](#)
- S. Huveners et al., Vinculin associates with endothelial VE-cadherin junctions to control force-dependent remodeling. *J. Cell Biol.* **196**, 641–652 (2012). doi: [10.1083/jcb.201108120](#); pmid: [22391038](#)
- A. Elosegui-Artola et al., Force Triggers YAP Nuclear Entry by Regulating Transport across Nuclear Pores. *Cell* **171**, 1397–1410.e14 (2017). doi: [10.1016/j.cell.2017.10.008](#); pmid: [29107331](#)
- M. Das Thakur et al., Ajuba LIM proteins are negative regulators of the Hippo signaling pathway. *Curr. Biol.* **20**, 657–662 (2010). doi: [10.1016/j.cub.2010.02.035](#); pmid: [20303269](#)
- Y. Abe, M. Ohsugi, K. Haraguchi, J. Fujimoto, T. Yamamoto, LAT52-Ajuba complex regulates γ -tubulin recruitment to centrosomes and spindle organization during mitosis. *FEBS Lett.* **580**, 782–788 (2006). doi: [10.1016/j.febslet.2005.12.096](#); pmid: [16413547](#)
- C. Rauskolb, S. Sun, G. Sun, Y. Pan, K. D. Irvine, Cytoskeletal tension inhibits Hippo signaling through an Ajuba-Warts complex. *Cell* **158**, 143–156 (2014). doi: [10.1016/j.cell.2014.05.035](#); pmid: [24995985](#)
- H. Alégot et al., Recruitment of Jub by α -catenin promotes Yki activity and *Drosophila* wing growth. *J. Cell Sci.* **132**, jcs222018 (2019). doi: [10.1242/jcs.222018](#); pmid: [30659113](#)
- C. Ibar et al., Tension-dependent regulation of mammalian Hippo signaling through LIMD1. *J. Cell Sci.* **131**, jcs214700 (2018). doi: [10.1242/jcs.214700](#); pmid: [29440237](#)
- R. Sarpal et al., Role of α -Catenin and its mechanosensing properties in regulating Hippo/YAP-dependent tissue growth. *PLOS Genet.* **15**, e1008454 (2019). doi: [10.1371/journal.pgen.1008454](#); pmid: [31697683](#)
- A. Taslimi et al., An optimized optogenetic clustering tool for probing protein interaction and function. *Nat. Commun.* **5**, 4925 (2014). doi: [10.1038/ncomms5925](#); pmid: [25233328](#)
- H. Matakatsu, S. S. Blair, Separating planar cell polarity and Hippo pathway activities of the protocadherins Fat and Dachsous. *Development* **139**, 1498–1508 (2012). doi: [10.1242/dev.070367](#); pmid: [22399682](#)
- L. Blanchoin, R. Boujemaa-Paterski, C. Sykes, J. Plastino, Actin dynamics, architecture, and mechanics in cell motility. *Physiol. Rev.* **94**, 235–263 (2014). doi: [10.1152/physrev.00018.2013](#); pmid: [24382887](#)
- E. Kassianidou et al., Extracellular Matrix Geometry and Initial Adhesive Position Determine Stress Fiber Network Organization during Cell Spreading. *Cell Rep.* **27**, 1897–1909.e4 (2019). doi: [10.1016/j.celrep.2019.04.035](#); pmid: [31067472](#)
- T. Higashi, A. L. Miller, Tricellular junctions: How to build junctions at the TRIckiest points of epithelial cells. *Mol. Biol. Cell* **28**, 2023–2034 (2017). doi: [10.1091/mbc.e16-10-0697](#); pmid: [28705832](#)
- M. C. Gibson, A. B. Patel, R. Nagpal, N. Perrimon, The emergence of geometric order in proliferating metazoan epithelia. *Nature* **442**, 1038–1041 (2006). doi: [10.1038/nature05014](#); pmid: [16900102](#)
- W. T. Gibson et al., Control of the mitotic cleavage plane by local epithelial topology. *Cell* **144**, 427–438 (2011). doi: [10.1016/j.cell.2010.12.035](#); pmid: [21295702](#)
- T. A. McMahon, J. T. Bonner, *On Size and Life* (Scientific American Library, 1983).
- A. J. Spence, Scaling in biology. *Curr. Biol.* **19**, R57–R61 (2009). doi: [10.1016/j.cub.2008.10.042](#); pmid: [19174137](#)
- B.-Z. Shilo, N. Barkai, Buffering Global Variability of Morphogen Gradients. *Dev. Cell* **40**, 429–438 (2017). doi: [10.1016/j.devcel.2016.12.012](#); pmid: [28292422](#)
- D. Čapek, P. Müller, Positional information and tissue scaling during development and regeneration. *Development* **146**, dev177709 (2019). doi: [10.1242/dev.177709](#); pmid: [31862792](#)
- K. D. Irvine, B. I. Shraiman, Mechanical control of growth: Ideas, facts and challenges. *Development* **144**, 4238–4248 (2017). doi: [10.1242/dev.151902](#); pmid: [29183937](#)
- S. J. Pratt et al., The LIM protein Ajuba influences p130Cas localization and Rac1 activity during cell migration. *J. Cell Biol.* **168**, 813–824 (2005). doi: [10.1083/jcb.200406083](#); pmid: [15728191](#)
- M. Aragona et al., A mechanical checkpoint controls multicellular growth through YAP/TAZ regulation by actin-processing factors. *Cell* **154**, 1047–1059 (2013). doi: [10.1016/j.cell.2013.07.042](#); pmid: [23954413](#)
- K. Wada, K. Itoga, T. Okano, S. Yonemura, H. Sasaki, Hippo pathway regulation by cell morphology and stress fibers. *Development* **138**, 3907–3914 (2011). doi: [10.1242/dev.070987](#); pmid: [21831922](#)
- Z. Meng et al., RAP2 mediates mechanoresponses of the Hippo pathway. *Nature* **560**, 655–660 (2018). doi: [10.1038/s41586-018-0444-0](#); pmid: [30135582](#)
- M. Uroz et al., Regulation of cell cycle progression by cell-cell and cell-matrix forces. *Nat. Cell Biol.* **20**, 646–654 (2018). doi: [10.1038/s41556-018-0107-2](#); pmid: [29802405](#)
- B. G. Godard, C. P. Heisenberg, Cell division and tissue mechanics. *Curr. Opin. Cell Biol.* **60**, 114–120 (2019). doi: [10.1016/j.cob.2019.05.007](#); pmid: [31288206](#)

ACKNOWLEDGMENTS

We thank S. Blair, N. Brown, J. Jiang, G. Struhl, and the Bloomington, Vienna, Harvard Medical School, and Kyoto Stock Centres for reagents; the PICT-HiSA@BDD imaging facility (ANR-10-INBS-04); and A. Bardin, F. Graner, E. Hannezo, M. O'Connor, P. Leopold, J.-L. Maitre, N. Minc, A. Maugarny-Cales, L. Alpar, and E. van Leeuwen for comments. **Funding:** ANR-MaxForce, ERC Advanced (340784), ARC (SL220130607097), ANR Labex

DEEP (11-LBX-0044, ANR-10-IDEX-0001-02), NSF IOS1353914 and DMR1056456. J.M.L.-G. and F.d.P. acknowledge ARC and FRM fellowships, respectively. H.N. and M.S. were supported by NSF Graduate Research Fellowships under grant DGE1256260. D.K.L. was supported by Curie Mayent-Rothschild and ICAM senior fellowships. **Author contributions:** J.M.L.-G., D.K.L., H.N., and Y.B. designed the project; I.G. and S.P. produced reagents; J.M.L.-G., F.d.P., F.B., and O.M. performed experiments; J.M.L.-G., H.N., M.S., and B.G. developed methods and data analysis scripts; J.M.L.-G., H.N., M.S., B.G., F.d.P., and F.B. analyzed the data; D.K.L., H.N., and

M.S. developed theoretical models and performed simulations; and J.M.L.-G., D.K.L., H.N., and Y.B. wrote the manuscript. **Competing interests:** The authors declare no competing financial interests. **Data and materials availability:** All data are available in the main text or the supplementary materials.

SUPPLEMENTARY MATERIALS

science.sciencemag.org/content/370/6514/eabb2169/suppl/DC1
Materials and Methods
Supplementary Text

Figs. S1 to S10
Tables S1 and S2
References (40–130)
Movies S1 to S11
MDAR Reproducibility Checklist

[View/request a protocol for this paper from Bio-protocol.](#)

18 February 2020; accepted 13 August 2020
10.1126/science.abb2169

RESEARCH ARTICLE SUMMARY

NEUROSCIENCE

Behavioral state coding by molecularly defined paraventricular hypothalamic cell type ensembles

Shengjin Xu*, Hui Yang, Vilas Menon, Andrew L. Lemire, Lihua Wang, Fredrick E. Henry, Srinivas C. Turaga, Scott M. Sternson*

INTRODUCTION: Brain function is often compared to an orchestral ensemble, where subgroups of neurons that have similar activity are analogous to different types of instruments playing a musical score. Brains are composed of specialized neuronal subtypes that can be efficiently classified by gene expression profiles measured by single-cell RNA sequencing (scRNA-seq). Are these molecularly defined cell types the “instruments” in the neural ensemble? To address this question, we examined the neural ensemble dynamics of the hypothalamic paraventricular nucleus (PVH), a small

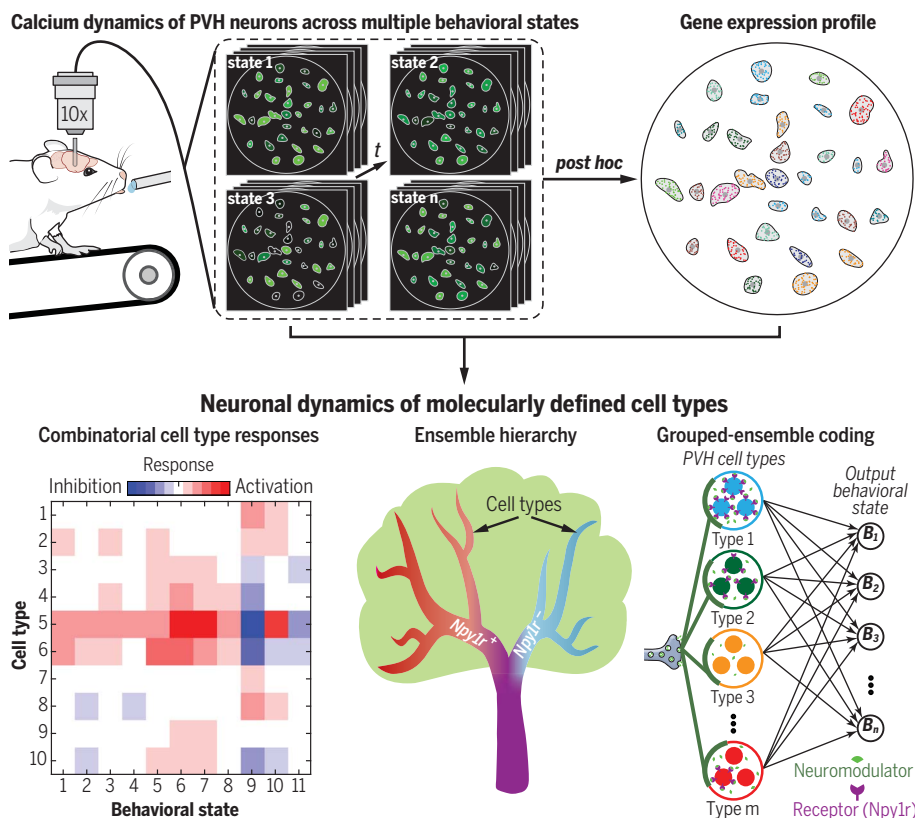
brain region that is important for behavior states such as hunger, thirst, and stress. Past work has emphasized specialized behavioral state-setting roles for different PVH cell types, but it is not clear whether the dynamics of the PVH ensemble support this view.

RATIONALE: We considered three possibilities for how PVH neurons could be involved in encoding behavioral states: (i) PVH neurons of a molecularly defined cell type may respond similarly and be specialized for a behavioral state as a “labeled-line,” (ii) molecularly defined

cell types may show unrelated activity patterns and be irrelevant to behavioral state coding, and (iii) molecularly defined neurons may respond similarly within a type, but behavioral state may be encoded by combinations of cell types. To evaluate the role of molecularly defined cell types in the neural ensemble, it is important to monitor activity in many individual neurons with sub-second temporal resolution along with quantitative gene expression information about each cell. For this, we developed the CaMA (calcium and RNA multiplexed activity) imaging platform in which deep-brain two-photon calcium imaging of neuron activity is performed in mice during multiple behavioral tasks. This is followed by ex vivo multiplexed RNA fluorescent in situ hybridization to measure gene expression information in the in vivo-imaged neurons.

RESULTS: We simultaneously imaged calcium activity in hundreds of PVH neurons from 10 cell types across 11 behavioral states. Within a molecularly defined cell type, neurons often showed similar activity patterns such that we could predict functional responses of individual neurons solely from their quantitative gene expression information. Behavioral states could be decoded with high accuracy based on combinatorial assemblies of PVH cell types, which we called “grouped-ensemble coding.” Labeled-line coding was not observed. The neuromodulatory receptor gene *neuropeptide receptor neuropeptide Y receptor type 1* (*Npy1r*) was usually the most predictive gene for neuron functional response and was expressed in multiple cell types, analogous to the “conductor” of the PVH neural ensemble.

CONCLUSION: Our results validated molecularly defined neurons as important information processing units in the PVH. We found correspondence between the gene expression hierarchies used for molecularly defined cell type classification and functional activity hierarchies involving coordination by neuromodulation. CaMA imaging offers a solution to the problem of how to rapidly evaluate the function of the panoply of cell types being uncovered with scRNA-seq. CaMA imaging bridges a gap between the abstract digital elements typically described in systems neuroscience with the “wetware” associated with traditional molecular neuroscience. Merging these two areas is essential to understanding the relationships of gene expression, brain function, behavior, and ultimately neurological diseases. ■



CaMA imaging reveals combinatorial cell type coding of behavior states. CaMA imaging records calcium dynamics of PVH neurons across multiple behavioral states followed by gene expression profiling. Combinatorial assemblies of PVH cell types encoded behavioral states. The PVH neural activity ensemble was split by *Npy1r* expression into two main cell classes that were subdivided into cell types. Thus, neuromodulation coordinates cell types for grouped-ensemble coding to represent different survival behaviors such as eating, drinking, and stress.

The list of author affiliations is available in the full article online.

*Corresponding author. Email: xus@janelia.hhmi.org (S.X.); sternsons@janelia.hhmi.org (S.M.S.)

Cite this article as S. Xu et al., *Science* 370, eabb2494 (2020). DOI: 10.1126/science.abb2494



READ THE FULL ARTICLE AT

<https://doi.org/10.1126/science.abb2494>

RESEARCH ARTICLE

NEUROSCIENCE

Behavioral state coding by molecularly defined paraventricular hypothalamic cell type ensembles

Shengjin Xu^{1*}, Hui Yang^{1,2}, Vilas Menon^{1†}, Andrew L. Lemire¹, Lihua Wang¹, Fredrick E. Henry^{1‡}, Srinivas C. Turaga¹, Scott M. Sternson^{1*}

Brains encode behaviors using neurons amenable to systematic classification by gene expression. The contribution of molecular identity to neural coding is not understood because of the challenges involved with measuring neural dynamics and molecular information from the same cells. We developed CaRNA (calcium and RNA multiplexed activity) imaging based on recording in vivo single-neuron calcium dynamics followed by gene expression analysis. We simultaneously monitored activity in hundreds of neurons in mouse paraventricular hypothalamus (PVH). Combinations of cell-type marker genes had predictive power for neuronal responses across 11 behavioral states. The PVH uses combinatorial assemblies of molecularly defined neuron populations for grouped-ensemble coding of survival behaviors. The neuropeptide receptor neuropeptide Y receptor type 1 (Npy1r) amalgamated multiple cell types with similar responses. Our results show that molecularly defined neurons are important processing units for brain function.

Neuron activity and neuronal gene expression are considered distinct facets of brain function. Large-scale neuron activity recordings reveal discrete groups of neurons that respond similarly (1–4), and gene expression brain atlases show differential expression patterns across the brain (5). Single-cell transcriptomic studies reveal that the brain is composed of hundreds of molecularly defined neuronal subtypes (6–8). Molecular markers facilitate repeatedly returning to the same type of neurons and also serve as genetic elements that can be used for targeting functionally similar neurons for causality testing (9, 10) or potentially therapeutics (11). These applications can only be justified if molecular markers categorize neurons into groups with similar neuronal dynamics (12) that together encode distinct behavioral states. However, there is limited knowledge about the relationship between activity patterns of cells in the neural ensemble and their underlying gene expression profiles. Therefore, the merit of using neuronal gene expression as a proxy for neurons with similar activity patterns is controversial (12–17).

We set out to determine (i) the role of molecularly defined cell types for encoding different behavioral states and (ii) the association of neuronal marker genes with distinct func-

tional response types of the neuronal ensemble from the mouse paraventricular hypothalamus (PVH). The PVH mediates appetite, stress, thirst, and autonomic functions. This brain region is well known for its diverse peptide-expressing cell types (18, 19), and there are distinct behavioral and physiological consequences of PVH neuropeptide pharmacology (20) as well as cell type-selective optogenetic and chemogenetic perturbations (21–23). Molecular and cellular perturbation studies have indicated that the PVH acts as a behavioral state “switchboard” in which each molecularly defined population influences a distinct behavioral state as a labeled-line (24). However, it is not known if this is consistent with the natural dynamics of PVH neurons during these behaviors.

We considered three models for the role of molecularly defined cell types to encode behavioral states. The labeled-line model encodes different behavioral states based on the activity pattern of distinct, molecularly defined cell types (Fig. 1A). Labeled-line coding is frequently assumed for information processing in hard-wired neural functions involving essential survival behaviors (25–27). At the other end of the spectrum, the full neural ensemble encodes behavioral state irrespective of cell type identity and is primarily a product of neural plasticity (Fig. 1B) (28). In this case, molecular identity is a poor predictor of behavioral state, and functional ensembles are formed using rules that are independent of cell type. An intermediate model is grouped-ensemble coding, in which the members of some molecularly defined cell types show coordinated responses and encode behavioral states based on specific combinations of cell types (Fig. 1C).

It has been extremely difficult to distinguish these models because there has not been a suitable approach to simultaneously examine the functional dynamics of individual neurons having distinct molecular identities across many behavioral states within a single animal. Several methods have been developed to map gene expression onto neuronal function (29–33). However, these methods have limitations of temporal sensitivity, dynamic range, molecular diversity, or restrictions to transparent organisms that have prevented evaluation of this type of problem. Thus, an unbiased and systematic method to relate multigene expression of individual neurons to their activity patterns in vivo on a subsecond time scale is needed to combine molecular and systems neuroscience.

To address this problem, we developed the CaRNA (calcium and RNA multiplexed activity) imaging platform, a comprehensive, three-part strategy compatible with recording neuron dynamics deep in the mouse brain (Fig. 1D). In the first step, we used single-cell RNA sequencing (scRNA-seq) to classify PVH cells into molecular types (Fig. 1D, a and b). In the second step, we performed volumetric, deep-brain, pan-neuronal, two-photon calcium imaging in awake, behaving animals without regard to PVH neuronal subtypes to measure the response dynamics of hundreds of neurons during multiple behavioral states (Fig. 1D, c). Subsequently, the brain was removed, sectioned, and the neurons in the ex vivo tissue sections were registered to those from the in vivo imaging volume (Fig. 1D, d and e). In the final step, molecular identity of the neurons imaged in vivo was determined post hoc by performing multiple rounds of three-plex RNA-fluorescent in situ hybridization (FISH) on the ex vivo tissue sections, guided by marker genes from scRNA-seq in step 1 (Fig. 1D, f to i). This approach enables monitoring the dynamics of many molecularly defined neurons in parallel, within a deep-brain region, and across multiple behaviors.

RESULTS

Molecularly defined cell types within PVH scRNA-seq of PVH neurons

We used scRNA-seq to transcriptionally profile 706 manually picked PVH cells from 10 animals. We applied iterative unsupervised clustering (8) to group cells into 12 molecularly defined cell types within the PVH (fig. S1A). Differentially expressed marker genes for these clusters included canonical PVH neuropeptides: oxytocin (*Oxt*), vasopressin (*Avp*), corticotropin-releasing hormone (*Crh*), thyrotropin-releasing hormone (*Trh*), somatostatin (*Sst*), proenkephalin (*Penk*), and prodynorphin (*Pdyn*). Within these broad classes, clusters were further divided into subgroups based on the expression of additional marker genes: glutamic acid decarboxylase 2 (*Gad2*), reelin (*Reln*),

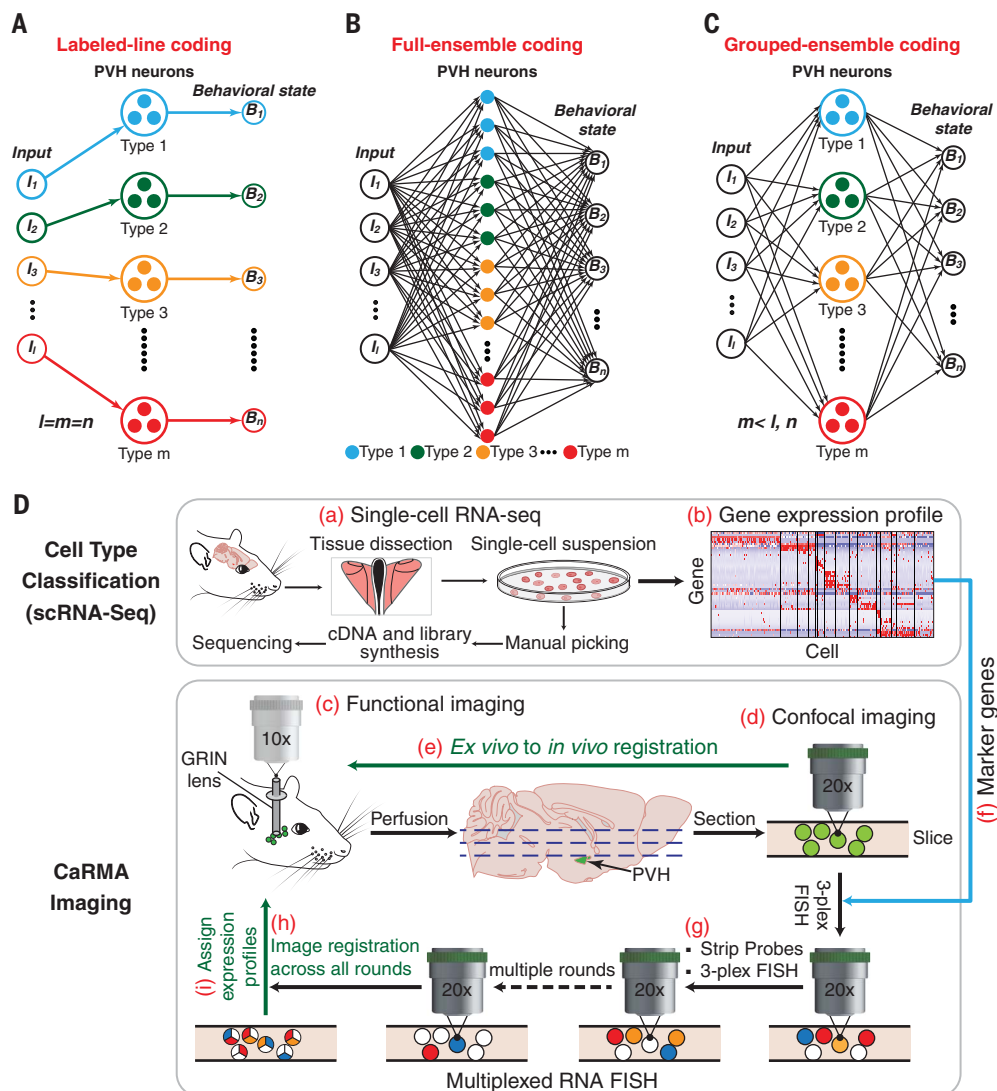
¹Janelia Research Campus, Howard Hughes Medical Institute, Ashburn, VA 20147, USA. ²Dominick P. Purpura Department of Neuroscience, Albert Einstein College of Medicine, Bronx, NY 10461, USA.

*Corresponding author. Email: xus@janelia.hhmi.org (S.X.); sternsons@janelia.hhmi.org (S.M.S.)

†Present address: Center for Translational and Computational Neuroimmunology, Department of Neurology, Columbia University Medical Center, New York, NY 10032, USA.

‡Present address: Innate Pharma, Rockville, MD 20850, USA.

Fig. 1. CaMA imaging for investigating models of behavioral state coding by molecularly defined cell types. (A to C) Models of multiple molecularly defined cell types encoding multiple behavioral states after processing diverse internal and external inputs (*I*). (A) Labeled-line coding uses a specialized cell type for a behavioral state in which individual members respond similarly, where the number of encoding cell types (*m*) is equal to the number of distinctly encoded behavioral states (*n*). (B) In a full-ensemble-coding model, molecularly defined cell types do not respond similarly, and behavioral state coding is independent of cell type. (C) Grouped-ensemble coding uses combinations of molecularly defined cell types in which individual molecularly defined cell types act as a coherent functional unit. (D) Schematic of the CaMA imaging platform.



netrin G1 (*Ntng1*), and neuropeptide Y receptor type 1 (*Npy1r*) (fig. S1B). All PVH clusters expressed *Sim1*, contained the excitatory neuron marker *Vglut2* (*Slc17a6*), and lacked the inhibitory neuron marker *Vgat* (*Slc32a1*). This targeted, deep-sequencing approach provides a combinatorial set of marker genes for molecularly defined cell type assignment.

12-plex FISH in PVH

We mapped the spatial and coexpression pattern of these 11 differentially expressed genes plus *Vglut2* by performing four rounds of three-plex FISH from two mice in PVH subregions separated by 280 μm : the anterior PVH (aPVH, 1394 cells), middle PVH (mPVH, 1855 cells), and posterior PVH (pPVH, 1263 cells) (Fig. 2A). This was achieved by developing new methods for stripping fluorescently labeled probes, aligning individual cells in three dimensions across multiple rounds of FISH using 4',6-diamidino-2-phenylindole (DAPI) fluorescence, as well as generalizable methods for three-dimensional

(3D) segmentation of cell boundaries (figs. S2 to S4; see the materials and methods).

We observed marker gene enrichment in different PVH subregions (Fig. 2B): Two genes (*Gad2* and *Ntng1*) were significantly enriched in aPVH, three genes (*Vglut2*, *Crh*, and *Avp*) were significantly enriched in mPVH, and nine genes (*Vglut2*, *Gad2*, *Npy1r*, *Crh*, *Reln*, *Ntng1*, *Pdyn*, *Oxt*, and *Avp*) were significantly enriched in pPVH. Pairwise gene coexpression also differed based on anterior-posterior position (fig. S5). For example, a majority of *Crh* cells coexpressed *Npy1r* in pPVH (75%) but considerably less in mPVH (30%) and aPVH (35%).

We determined the proportions of PVH cells in situ that expressed 0 to 12 of the marker genes (Fig. 2C). Coexpression (more than two genes) was common (81% of cells), and the mode was three genes. Unsupervised hierarchical clustering of gene expression profiles from these 4512 PVH cells resulted in 13 transcriptional clusters (Fig. 2, D to F). The spatial distribution of these molecularly defined cell

types was largely intermingled but some well-organized patterns were apparent (Fig. 2G; fig. S6, A and B; and table S1). Expression levels of the marker genes were distributed continuously, with strong rightward skew and high variance (Fig. 2H). Clustering implicitly thresholded gene coexpression relationships, and most FISH clusters (12/13) were dominated by high expression of one gene (Fig. 2E). FISH clusters were correlated with the scRNA-seq dataset (fig. S6, C and D). Likewise, scRNA-seq clusters were represented in the FISH dataset (fig. S6, E to G) and mapped to different regions of the PVH (fig. S6G).

CaMA imaging

To record PVH neuronal dynamics, we expressed GCaMP6m in PVH neurons without regard to neuronal subtypes. A thin gradient refractive index (GRIN) lens was implanted into the PVH (Fig. 3A). Volumetric two-photon calcium imaging was acquired from PVH neurons under the GRIN lens (range: 80 to 240 μm)

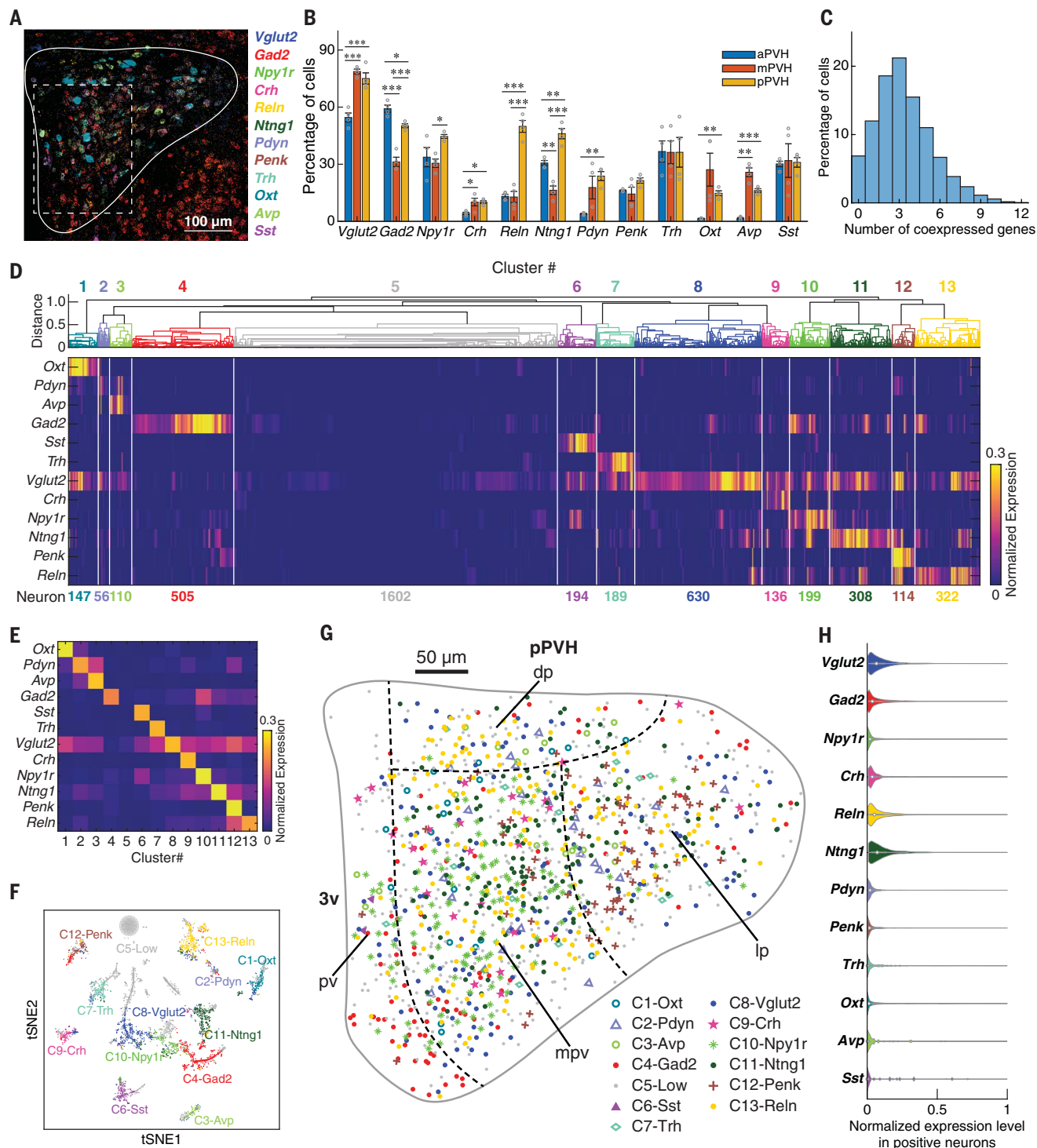


Fig. 2. Molecular and spatial characterization of PVH neurons by multiplexed FISH with 12 marker genes. (A) Maximum intensity projection image of multiplexed FISH with 12 marker genes in pPVH. Right, mRNA puncta pseudocolor legend. Solid white line is the contour of pPVH; dashed white line is the region in fig. S4B. (B) Percentages of cells expressing each marker gene in aPVH, mPVH, and pPVH. Error bars indicate mean \pm SEM. Gray circles are sample data. * $P < 0.05$, ** $P < 0.01$, *** $P < 0.001$. Statistics are provided in table S2. (C) Histogram of PVH cells coexpressing various number of marker genes. (D) Gene expression profiles of 13 molecularly defined PVH cell types from hierarchical clustering of normalized expression of 12 marker

genes. (E) Mean expression pattern of marker genes in 13 cell types. (F) Cell types in (D) plotted by t -distributed stochastic neighbor embedding (tSNE). "Cell types" are transcriptional clusters denoted as Ci -xxx, where i is the cluster number in (D) and xxx is a highly expressed gene or "Low" (low expression for all probed genes). (G) Spatial organization of 13 molecularly defined cell types in PVH (data are from four samples). Each symbol represents one neuron. PVH subregion boundaries are from reference (55). pv, periventricular; dp, dorsal parvicellular; lp, lateral parvicellular; mpv, medial parvicellular ventral zone; 3v, 3rd ventricle. (H) Normalized expression levels of marker genes from PVH neurons.

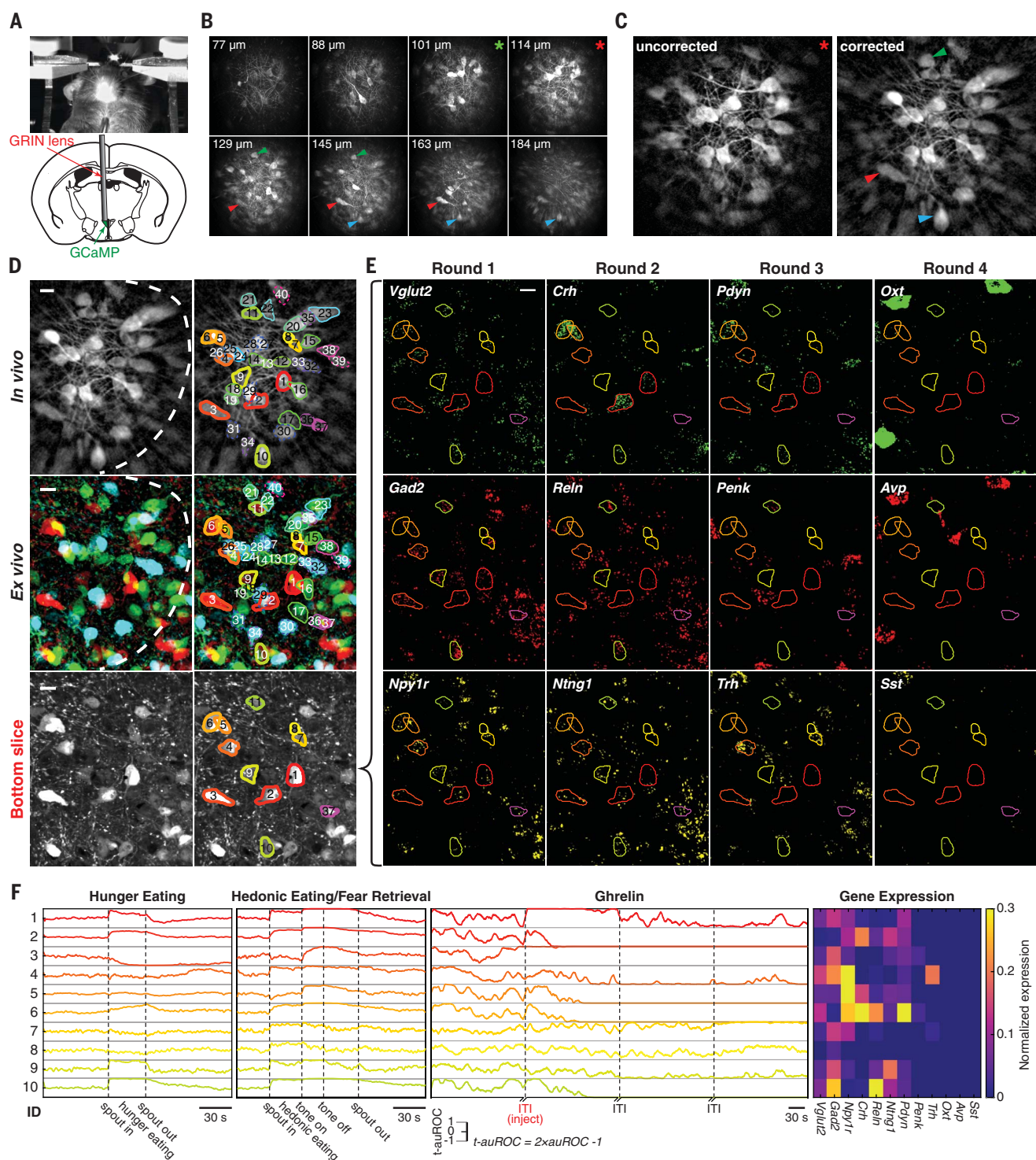


Fig. 3. Ex vivo ↔ in vivo registration for CaMA imaging. (A) Top, head-fixed mouse during two-photon calcium imaging of PVH neurons through a GRIN lens. Bottom, schematic of GRIN lens targeting GCaMP-expressing PVH neurons. (B) Eight planes from a two-photon imaging volume during behavior. Upper left, distances between imaging planes and GRIN lens. Arrowheads mark the corresponding neurons in (C). Red or green asterisks indicate the imaging plane in Fig. 3C or fig. S9A, respectively. (C) Computational correction of optical aberrations from in vivo imaging. Arrowheads indicate neurons from deeper imaging planes in (B) because of field-of-view (FOV) curvature correction. (D) Example neurons showing the ex vivo registration to

a substack of the in vivo image volume. Ex vivo image is overlay of z-projected confocal stacks from three consecutive 14-μm brain slices (pseudocolors: cyan, green, and red indicate top, middle, and bottom slices). White dashed line is the resolvable in vivo FOV. Dashed, thin, and thick contours are neurons from the top, middle, and bottom slices, respectively. (E) Four rounds of three-plex FISH from neurons in the bottom slice in (D). (F) Calcium dynamics of neurons in (E) across multiple behavioral states and their 12-plex gene expression profiles. t-auROC, transformed auROC (see the materials and methods); ID, neuron number from (D); ITI, intertrial interval (2 min). Scale bars in (D) and (E), 15 μm.

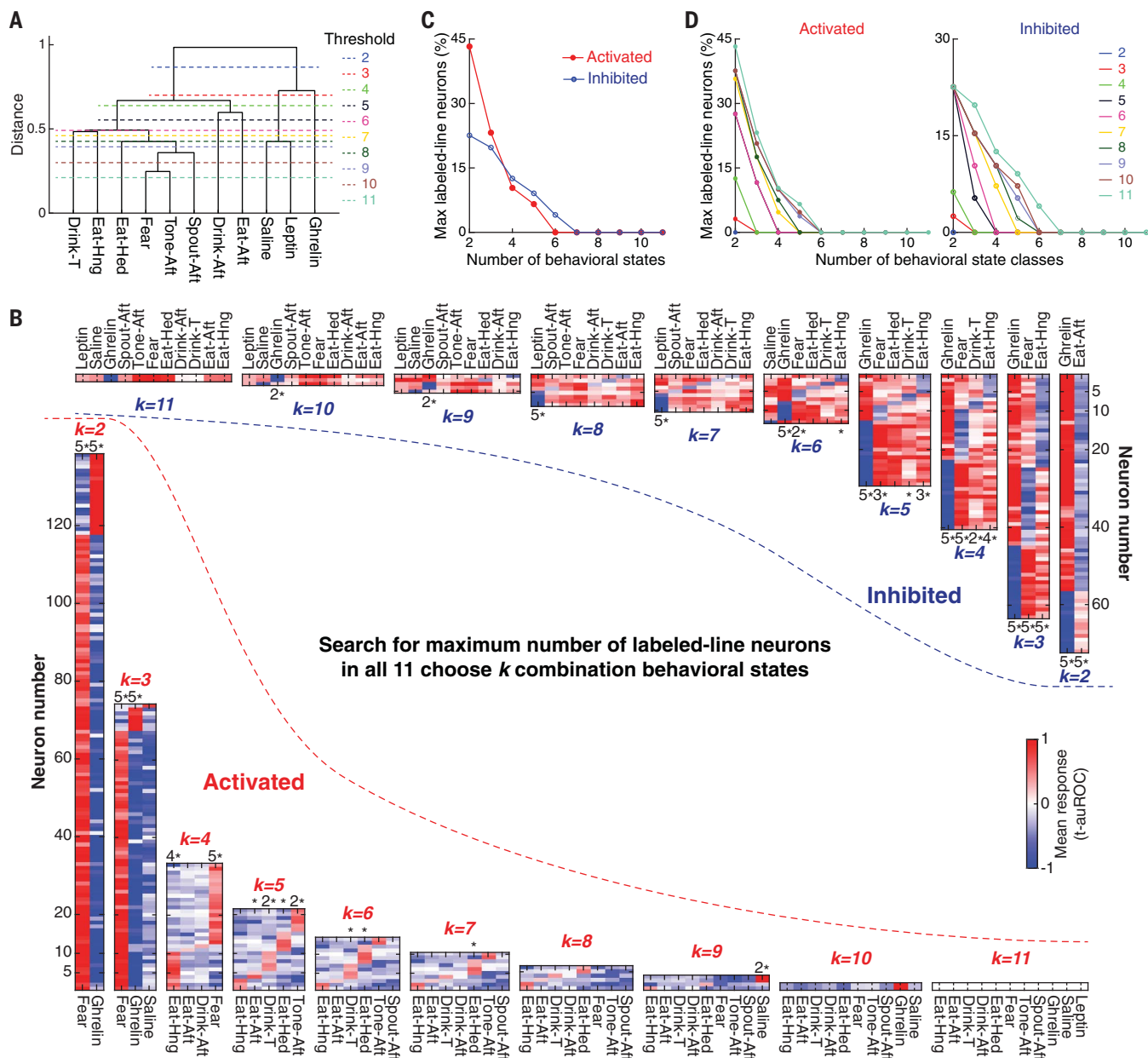


Fig. 4. Screening for labeled-line neurons encoding multiple behavioral states. (A) Dendrogram of neuron ensemble response similarities across 11 behavioral states. Dashed lines are thresholds for grouping state classes. (B) Mean response maps of the maximum number of labeled-line neurons in all 11-choose- k combinations of behavioral states. Bottom left, Activated labeled-line neuron sets. Top right, inhibited labeled-line neuron sets. Fisher's exact test was used to evaluate whether neurons are significantly specialized for a behavioral state. (C) Number of labeled-line neurons depends on the number of behavioral states. (D) Number of labeled-line neurons depends on the number of behavioral state-classes [see (A)]. *, $P < 0.05$; 2*, $P < 0.01$; 3*, $P < 0.001$; 4*, $P < 0.0001$; 5*, $P < 0.00001$.

in a head-fixed behaving mouse (Fig. 3B). We performed a set of calcium-imaging experiments involving eating during hunger, drinking water during thirst, hedonic eating (ad libitum fed, palatable food), fear retrieval (movie S1), and hormone-induced hunger (ghrelin) or energy surfeit (leptin) sequentially over 10 days (fig. S7). Subsequently, the brain was removed and sectioned.

To register the GCaMP-expressing neurons in the ex vivo-sectioned brain to the in vivo image volume, the sections below the GRIN

lens were imaged by confocal microscopy. Because the GRIN lens introduced multiple optical distortions, we characterized these aberrations and transformed the in vivo image volume coordinates to the view obtained by confocal imaging in ex vivo tissue sections (fig. S8). For a successful in vivo \leftrightarrow ex vivo alignment, it was crucial to correct field curvature introduced by the GRIN lens (fig. S8, C, D, F, and J), as well as the nonlinear relationship between sample position and objective lens position (fig. S8, H and J) and

depth-dependent magnification changes (fig. S8, C, D and I). After correcting for these aberrations (Fig. 3C and fig. S9A), we found neurons with distinctive shapes in the two-photon-imaging volume (neurons 1 to 3 in Fig. 3D; neurons 1, 2, 4, and 35 in fig. S9B) that could be recognized in the ex vivo confocal images. We used these neurons as starting points to match the surrounding neurons imaged in vivo and ex vivo with 96% correspondence between two independent observers. Most of the neurons (89.3%, 334/374) imaged



Fig. 5. Calcium dynamics and gene expression profile of PVH neurons

across 11 behavioral states. (A) Calcium response dynamics of the same PVH neurons (319 cells) during multiple behaviors from three mice. Neurons are clustered by gene expression profiles in (B). Temporal scale bars, 1 min. (B) Gene expression profile (12-plex RNA-FISH) of neurons in (A). Molecularly defined cell types are clustered based on the expression of the first nine genes. Cluster 11 has two neurons with high *Sst* expression even though *Sst* was not used for clustering (excluded for later analysis because of low neuron count; see the materials and methods). (C) Cell types in (B) plotted by tSNE. “Molecular clusters” are denoted as MC*i*-xxx, where *i* is the cluster number in (B) and xxx is a highly expressed gene or “Low” (low expression for all probed genes). (D) Spatial distribution of these cell types in the three imaging FOVs (dashed circles).

Colored arrowheads indicate the corresponding neurons in (E). (E) Fluorescence image of GCaMP-expressing example neurons within a FOV (dashed circle). Blue is DAPI and green is GCaMP. (F) Responses of MC5-Crh and MC8-Penk neurons during fear retrieval. Left, response traces of individual neurons. Middle, red shaded lines are the mean responses \pm SEM across neurons; gray lines are purities. Right, instantaneous consistent-responses. (G) Different response temporal profiles of MC5-Crh and MC6-Pdyn neurons. Top, Mean responses aligned with food or water presentation. Bottom, Cumulative distribution of instantaneous response slopes of individual neurons from these cell types during the light-blue-shaded periods from the top panel (two-sample Kolmogorov-Smirnov test). (H) Temporal maximum for consistent-response and corresponding response and purity of PVH cell types defined by combinatorial gene expression profiles across 11 behavioral states.

in vivo could be found in the brain slices, and 95.5% (319/334) of the aligned neurons could be tracked across the entire sequence of experiments (Fig. 3D and fig. S9B).

After matching neurons between the in vivo and ex vivo image spaces, we quenched GCaMP6m with acidic buffer (34) and performed four rounds of three-plex RNA-FISH (Fig. 3E and fig. S9C). We developed a non-rigid 3D registration pipeline for the GCaMP-expressing brain slices across multiple rounds of processing (fig. S10). Calcium dynamics of individual neurons during multiple behaviors were extracted from the in vivo image volumes (fig. S11), along with the corresponding molecular profiles for each neuron acquired from ex vivo tissue sections (Fig. 3F and fig. S9D). These computational and image analysis tools are available online (see “Data and materials availability” in the Acknowledgments).

PVH ensemble activity across 11 behavioral states

We recorded calcium dynamics of 319 neurons from three mice in the same portion of the pPVH (fig. S12) during all behaviors. We segmented the behavioral tasks into 11 behavioral states (fig. S7). These behavioral states could be well separated by unsupervised clustering of the recorded PVH neural activity patterns (Fig. 4A).

Labeled-line coding

First, we investigated whether this PVH ensemble showed evidence for labeled-line coding of behavioral states irrespective of any gene expression information. A labeled-line neuron was defined as specifically activated or inhibited in one state but not in other states. We searched for the maximum number of labeled-line neurons among all k combinations of 11 behavioral states (Fig. 4B). Although selectively tuned neurons were evident with comparison of a small number of behavioral states, the number of neurons showing apparent labeled-line coding was dependent on the number of behavioral states examined (Fig. 4C). Beyond six behavioral states, there were no selective neurons for each state. Moreover, the proportions of neurons selective for each behavioral state

were statistically greater than chance for not more than four states (Fig. 4B). We also considered the possibility that grouping similar states might make labeled-line coding more apparent. States were grouped into “state classes” either subjectively based on ideas about behavioral similarity (fig. S13A) or systematically based on PVH neuronal response similarity metrics for unsupervised clustering (Fig. 4A). However, grouping further reduced performance of the labeled-line model (Fig. 4D and figs. S13 and S14). Examining a small number of behavioral states might thus lead to the erroneous conclusion that a set of neurons is involved in highly selective labeled-line coding. Although the labeled-line configuration cannot be excluded for some brain functions, labeled-line coding is poorly scalable.

Molecularly defined neural ensemble responses

Next, we used unsupervised clustering of gene expression profiles to group the PVH neurons into 11 molecularly defined clusters (MCs) (Fig. 5, A to C; see the materials and methods) so that we could evaluate the activity patterns in molecularly defined cell types across 11 behavioral states. Although GCaMP expression was not observed in *Oat-* or *Avp*-expressing neurons because of adeno-associated virus tropism (fig. S15), these 11 MCs were consistent with cell types clustered from FISH-only pPVH tissue (fig. S16). Spatially, these molecularly defined cell types were intermingled, primarily in the medial parvicellular and lateral parvicellular subdivisions of the pPVH (Fig. 5, D and E).

Response purity within molecular clusters

If cell type information is important to encode a behavioral state, then we expected that neurons within a molecularly defined type, grouped solely using gene expression information, should respond similarly in that state. When we looked at MC5-Crh neurons in response to hedonic eating and fear retrieval, we found that neurons within this cluster responded similarly. By contrast, MC8-Penk neurons showed highly heterogeneous responses in these states (Fig. 5F). Thus, molecularly defined

neurons do not necessarily respond similarly in all behaviors and may be tuned to only some behavioral states.

We quantified the similarity of neuronal responses within each cell type cluster using linear purity (fig. S17; see the materials and methods). During fear cue presentation, MC5-Crh had high purity (approaching 1), whereas MC8-Penk had low purity (close to zero; Fig. 5F). Cell types with purity >0.5 can be considered to respond similarly (fig. S17). Next, we defined a metric called “consistent-response”, which weights cell type activity by the response purity (Fig. 5F and fig. S17). A high consistent-response molecularly defined cell type is composed of neurons that respond strongly to a stimulus with similar temporal dynamics. Low consistent-response cell types have either low purity (a diversity of responses) or low response magnitude in a behavioral state (fig. S17).

Combinatorial molecularly defined cell type tuning to behavioral states

We computed the temporal maximum of consistent-responses and purities of each cell type in 11 behavioral states (Fig. 5H and fig. S18, B and C). In the consistent-response map, some cell types responded differently to individual behavioral states, whereas others were similarly tuned across multiple states. MC8-Penk neurons, which had relatively low response and low purity during fear, showed higher purity activation after injection of the hormone ghrelin. This demonstrates that molecularly defined neurons are tuned to respond similarly in some behaviors but not others. The purity of the molecularly defined cell types resulting from unsupervised clustering of multiple genes produces significantly higher response purities than when cells are grouped by expression of a single gene (fig. S19, A to C). The high purity activation response to food consumption of MC5-Crh neurons that highly express *Crh* and coexpress *Vglut2* and *Npy1r* in the pPVH is opposite to the inhibitory response reported by low-resolution, multineuron fiber photometry measurements of all CRH neurons in the PVH, although both methods give the same response to fear-inducing

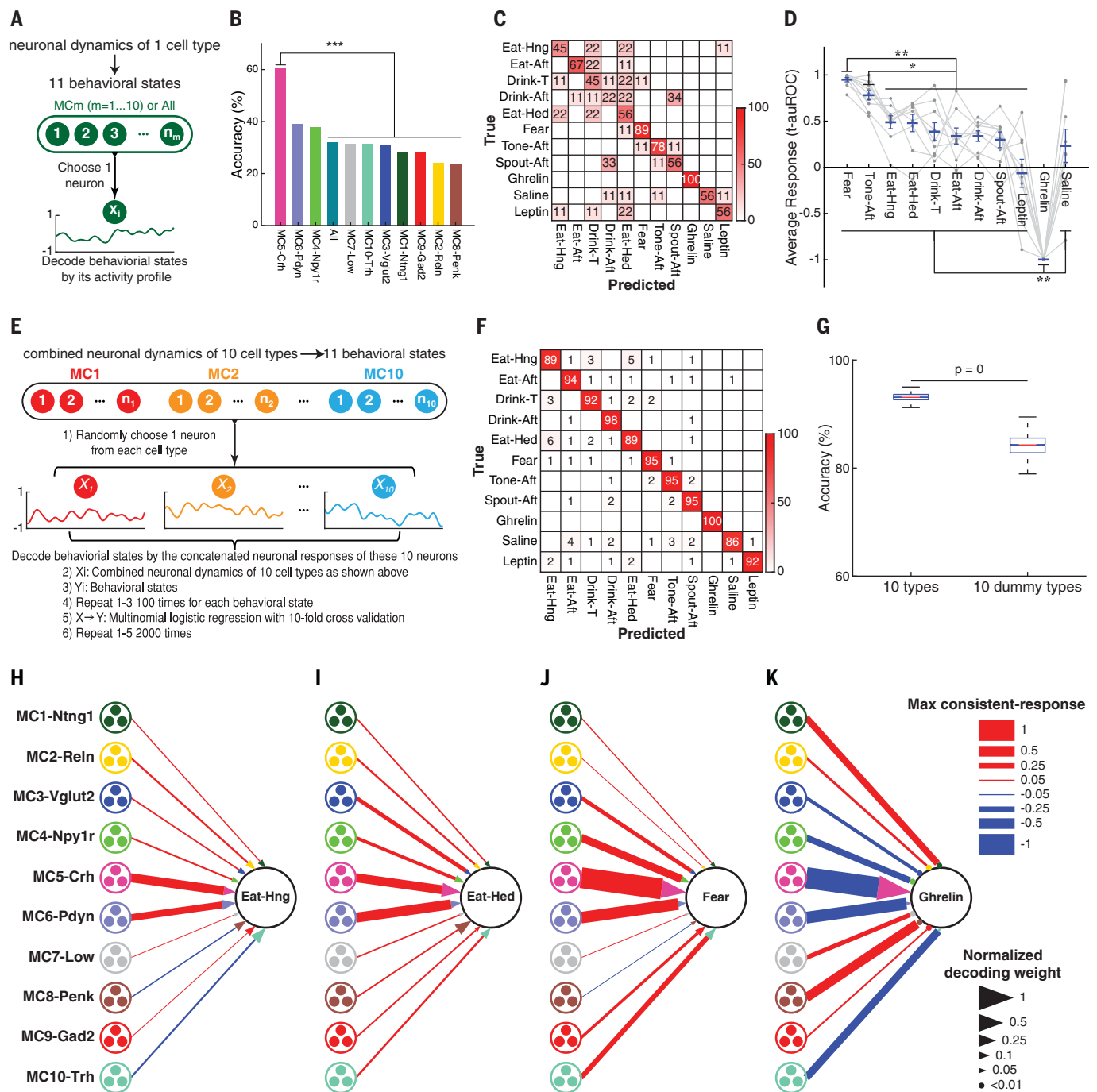


Fig. 6. Decoding behavioral states with neuron dynamics of molecularly defined PVH cell types. (A) Schematic procedure for decoding behavioral states with the temporal dynamics from individual cell types or all neurons (All, disregards cell type). (B) Decoding accuracies for all behavioral states using the temporal dynamics of one cell type or All neurons (Chi-squared test followed by the Marascuillo procedure was used). (C) Normalized confusion matrix for behavioral state decoding using MC5-Crh neurons. (D) Response amplitude differences of MC5-Crh neurons across behavioral states. Blue lines are mean responses; error bars are SEM; gray connected circles are individual MC5-Crh neuron responses (one-way repeated-measures ANOVA followed by Tukey-Kramer test). (E) Schematic of procedure for decoding behavioral states with the combined temporal response profiles of the PVH cell types using one neuron from each cell type. (F) Average confusion

matrix with the combined neuronal dynamics of 10 neurons using the procedure in (E). (G) Decoding accuracies with the combined neuronal dynamics of 10 neurons from 10 PVH cell types or from 10 dummy cell types that scramble cell type information (fig. S21B). Box plots show the median, interquartile range, and minimum to maximum values of the distributions of decoding accuracies (Wilcoxon rank-sum test). (H to K) Cell type ensemble response-decoding diagrams for homeostatic and hedonic eating, fear, and ghrelin injection. Diagrams with temporal maximum of consistent-response (proportional to line width) for each cell type and their decoding weights (proportional to arrowhead area) for hunger eating (H), hedonic eating (I), fear retrieval (J), and ghrelin injection (K). Behavioral state decoding is for all 11 behavioral states (also see fig. S24). * $P < 0.05$, ** $P < 0.01$, *** $P < 0.001$. Statistics are provided in table S2.

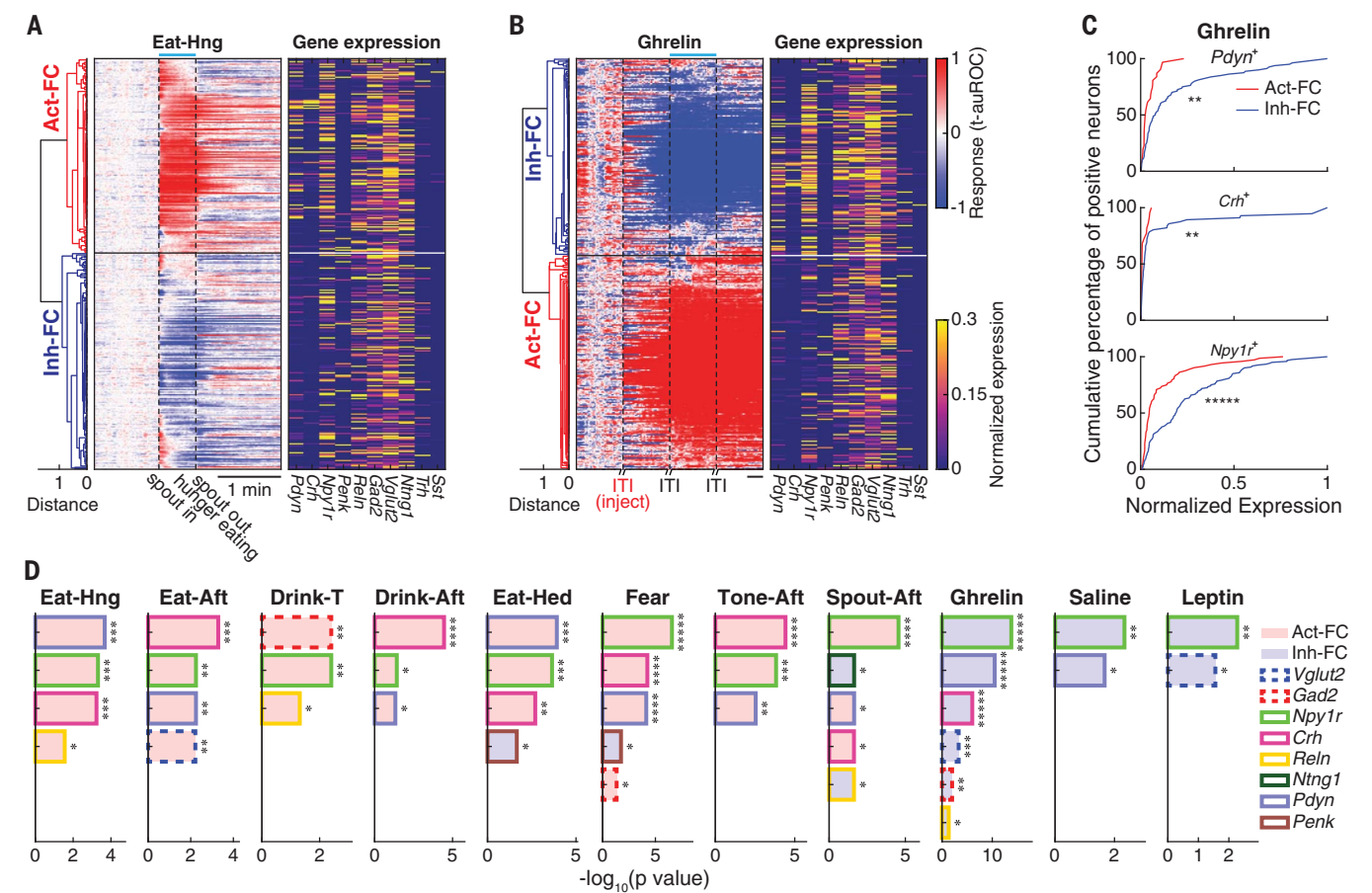


Fig. 7. Functional clustering of PVH neurons and differential enrichment of marker genes in 11 behavioral states. (A and B) Hierarchical clustering of PVH neurons based on their responses while eating in a hunger state (A) and after ghrelin injection (B). Right, gene expression profiles of individual neurons. Blue bar marks the behavioral state. Temporal scale bar, 1 min. (C) Comparisons of expression-level distributions of *Pdyn* in *Pdyn*⁺ neurons (top), *Crh* in *Crh*⁺

neurons (middle), and *Npy1r* in *Npy1r*⁺ neurons (bottom) between FCs in (B) after ghrelin injection. (D) Enrichment of marker genes in the FCs across 11 behavioral states. Gene enrichments were ranked by $-\log_{10}(P \text{ value})$. Gene identity is indicated by bar outline, and the bar fill color indicates the enriched FC. * $P < 0.05$, ** $P < 0.01$, *** $P < 0.001$, **** $P < 10^{-4}$, ***** $P < 10^{-5}$. Statistics are provided in table S2.

stimuli (35, 36). However, low-expressing *Crh*⁺/*Vglut2*⁺/*Npy1r*⁺ neurons in the pPVH were inhibited in response to food ingestion (fig. S20), and this cell type is more prevalent in the mPVH (fig. S20, F and G), which is the major target region in the reported photometry experiments (35, 36). Thus, CaMA imaging is a powerful platform for systematically discovering the relationship between cell types defined by multiple gene markers and their response consistency in different behavioral states.

The consistent-response map shows the relationships between molecularly defined cell type activity patterns for behavioral state coding (Fig. 5H). From these data, it is apparent that behavioral state is not represented by a single molecularly defined cell type (fig. S19D). Instead, the consistent-response pattern indicates combinatorial coding. What is different from previous views of hypothalamic circuits is that behavioral state is encoded by the different combinations, magnitudes, and temporal dy-

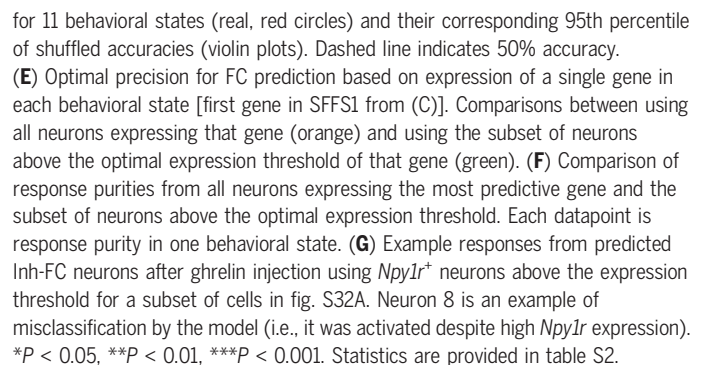
namics of cell type activity patterns. For example, MC5-Crh and MC6-Pdyn showed similar consistent-responses during hunger eating, drinking, and hedonic eating (absolute differences ≤ 0.18 ; Fig. 5H), but their temporal response profiles were significantly different (Fig. 5G). MC5-Crh neurons ramped to maximum magnitude, whereas MC6-Pdyn neurons responded more quickly to the ingested stimuli (Fig. 5G). Similarly, the return to baseline after withdrawing food, water, or the offset of the fear retrieval cue was slower for MC5-Crh (fig. S18A). Although these cell types have similar consistent-response measures, their different temporal dynamics indicate distinct functions for encoding behavioral states, as is also the case for other cell types (fig. S18A).

Decoding behavioral states with molecularly defined cell types
Individual cell type coding

CaMA imaging enabled us to investigate whether behavioral states can be quantitatively

decoded from the PVH ensemble dynamics of molecularly defined cell types. Because cell type encoding of behavioral states has been traditionally examined either one cell type at a time (37–39) or was used without regard to cell type (2, 3, 40), we first examined the decoding performance of individual molecularly defined cell types to distinguish 11 behavioral states.

We used multinomial logistic regression classification to determine the overall performance of predicting behavioral states from the temporal dynamics of single neurons without regard to cell type (All) as well as from single neurons of known cell types (Fig. 6A; see the materials and methods). Single neurons from several cell types showed decoding performance superior to a classifier trained using all neurons without regard to cell type (Fig. 6B and fig. S21A). The decoding accuracy from the dynamics of MC5-Crh neurons was the highest (Fig. 6B), and the confusion matrix for behavioral state decoded by MC5-Crh neurons showed perfect decoding of the



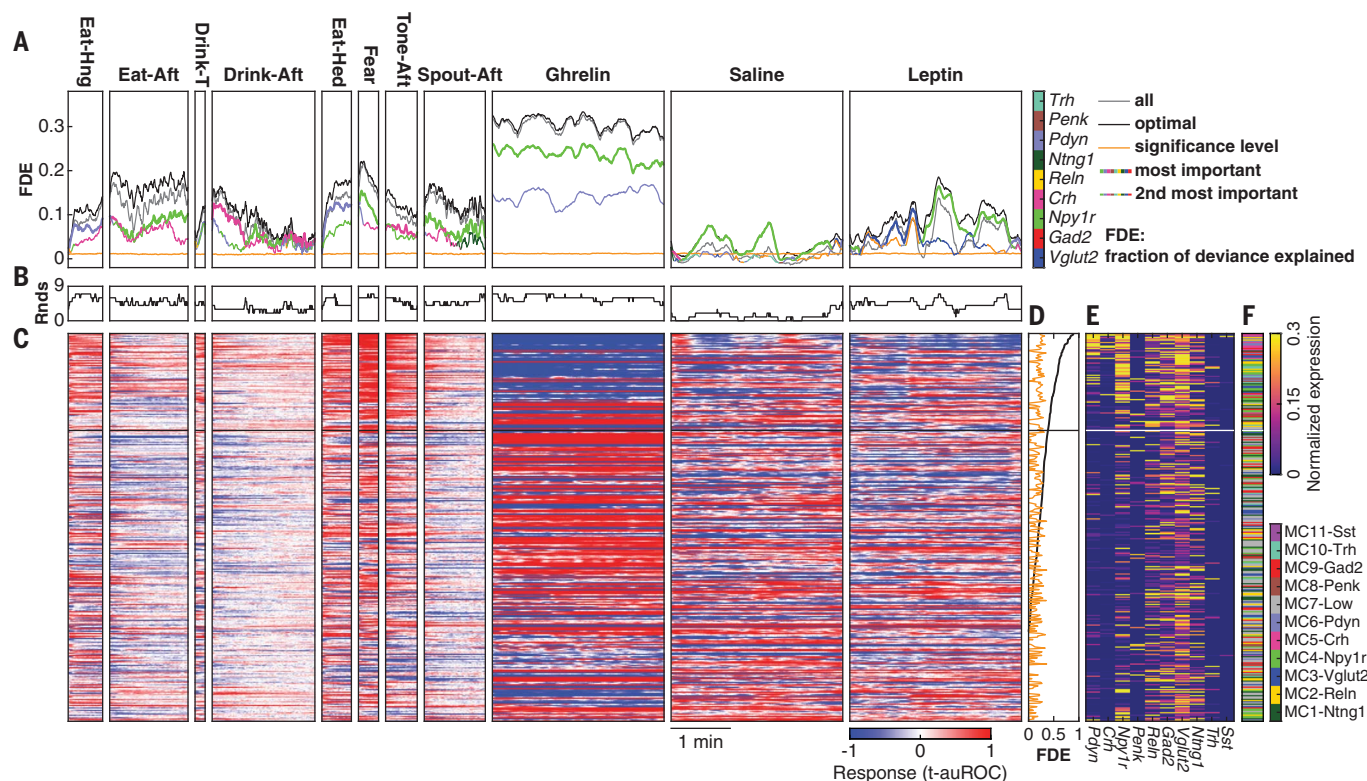


Fig. 9. Gene expression profiles of individual PVH neurons predict their temporal responses in multiple behavioral states. (A) Prediction performance (fraction of deviance explained, FDE) of neuronal response at each timestamp using expression levels of all marker genes, the optimal gene set, and the two most important genes measured by mSFFS. The optimal gene set was composed of the genes that provided the highest FDE from mSFFS at each timestamp. Significance level is the 95th percentile FDE after shuffling

gene expression profiles. (B) Number of SFFS rounds with FDE above significance level in each timestamp. (C) Responses of PVH neurons ranked by FDE across behavioral states. (D) FDE ordered high to low of individual neurons for the entire time series across all behavioral states. (E and F) Gene expression profiles (E) and molecularly defined cell types (F) of the corresponding neurons in (D). Black or white lines in (C) to (F) indicate the boundary of the most highly predictive quartile.

ghrelin-induced hunger state and high decoding performance for fear retrieval (Fig. 6C). MC5-Crh neurons showed significantly different response amplitude and sign across several behavioral states (Fig. 6D), which explained the high decoding performance. However, our analysis also showed that individual cell types in the PVH are insufficient to decode many behavioral states.

Grouped-ensemble cell type ensemble coding

CaRMA imaging enables the activity of many cell types to be imaged simultaneously in the same animal. This permitted us to test models of behavioral state coding using an ensemble of molecularly defined cell types (Fig. 1C) or, alternatively, an ensemble of neurons in which molecularly defined cell type information was ignored (Fig. 1B). We trained a classifier on an ensemble of molecularly defined cell types model by randomly choosing one cell's activity trace from each of 10 molecularly defined cell types and concatenating them into 10-cell ensembles for each behavioral state (repeated 100 times with replacement), followed by multinomial logistic regression for 11 behavioral

states using 10-fold cross-validation (accuracy: $93.13 \pm 0.02\%$, Fig. 6, E and F; see the materials and methods). With molecularly defined cell type information, 11 different behavioral states could be accurately decoded with the combinatorial responses of only 10 PVH neurons, one from each of the 10 cell types. This was significantly higher decoding accuracy ($P = 0$; Fig. 6G) than a neural ensemble that ignores molecularly defined cell type information by randomly assigning neurons into dummy cell types (fig. S21B).

We also examined the effect of adjusting the hierarchical molecularly defined cell type clustering threshold on behavioral state decoding. Purity and decoding accuracy generally increased with the number of molecular clusters (figs. S22 and S23). Although grouped-ensemble coding was supported with a range of clustering thresholds, this approach involves “peeking” at the functional responses to supervise molecular clustering. Because our objective was to evaluate the predictive value of molecular information on functional and behavioral responses, we proceeded using the unbiased determination of 11 MCs in the pPVH ensemble (to avoid circular logic). Taken to-

gether, our findings support a grouped-ensemble coding strategy used by molecularly defined PVH neurons (Fig. 1C).

Cell type ensemble response-decoding diagrams

To reveal the relative contributions of different molecularly defined cell types to grouped-ensemble coding (Fig. 1C) for different behavioral states in the PVH, we used the multinomial regression coefficients and the consistent-response measurements to generate cell type response-decoding diagrams for each behavioral state (Fig. 6, H to K, and fig. S24). In these diagrams, cell type consistent-responses are weighted by each cell type's contribution to decoding accuracy and quantitatively summarized across multiple behavioral states. MC5-Crh and MC6-Pdyn neurons had large consistent-responses in several behavioral states (23, 35, 36). These neurons were activated by negative and positive stimuli, indicating an unexpected general role for encoding salience of diverse stimuli in a variety of different states. Other molecularly defined cell types, such as MC8-Penk and MC10-Trh neurons, contributed substantial weights for distinguishing behavioral

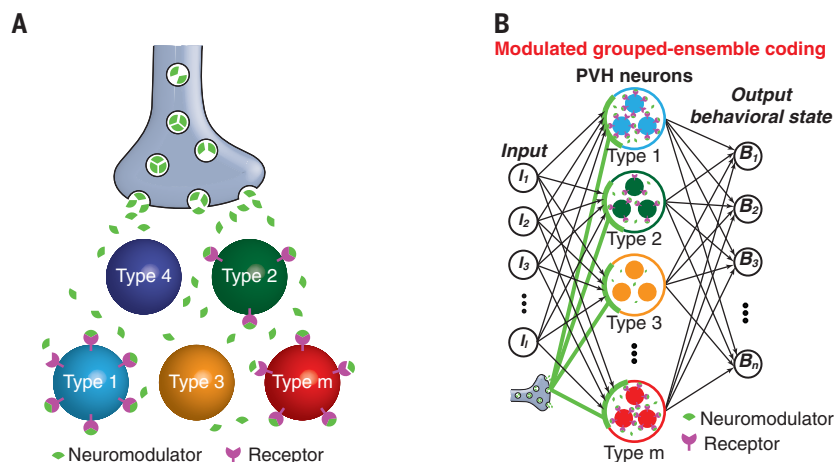


Fig. 10. Cooperative regulation of multiple cell types by neuromodulation. (A) Diagram illustrating volume diffusion of a neuromodulator to selectively regulate subgroups of cell types expressing its receptor. (B) Schematic of modulated grouped-ensemble coding model for multiple behavioral states that includes the role of neuromodulation. Neuromodulator release cooperatively regulates multiple PVH cell types expressing its receptor. This coding configuration highlights the relationship between the hierarchical functional organization of PVH neurons and their molecular hierarchy.

states (Fig. 6, H to K, and fig. S24C). For example, food withdrawal (Eat-Aft) in hunger elicited a transient inhibitory response in MC10-Trh after spout retraction that transitions to a prolonged activated response, which was not observed after removing water in thirst (Drink-Aft) (fig. S25A). This contributes to behavioral state coding (fig. S25B) and is also consistent with past work indicating that TRH neurons project to the arcuate nucleus and activate hunger-associated Agouti-related peptide (AGRP) neurons (22). By contrast, most MC8-Penk neurons showed prolonged inhibition after food withdrawal in hunger but only transient inhibition after drinking in thirst (fig. S25, C and D). More generally, these response-decoding diagrams show a functional organization in the pPVH, with major branches associated with the sign and amplitude of broadly tuned MC5-Crh and MC6-Pdyn neurons and individual twigs associated with a more selective combinatorial code of cell types that distinguish behavioral states.

Gene expression prediction of ensemble functional responses

Grouped-ensemble coding relies on similar responses from the neurons that make up a cell type, thereby simplifying the neural ensemble to component cell types instead of the much larger total number of cells. Consistent-response maps also indicate higher-level organization based on similar responses between groups of cell types. For example, MC5-Crh and MC6-Pdyn show similar response tuning to multiple behavioral states. By contrast, MC8-Penk typically responds oppositely to these cell types (Figs. 5H and 6, H to K, and fig. S24C). Thus, different molecularly defined cell types may

have coordinated activity patterns that comprise hierarchical functional groupings in the neural ensemble. This raises the second major question: Do differentially expressed genes map to functional response types in the neural ensemble?

We aimed to identify optimal combinations of genes that best predict the functional response classes within the neuronal ensemble. Moreover, neurons have complex dynamics during behaviors, so we assessed the temporal window over which molecular markers offer useful predictive information about functional responses.

Differential gene expression in functional clusters

For each behavioral state, we grouped all neurons on the basis of their neuronal response dynamics into functional clusters (FCs) by unsupervised hierarchical clustering (Fig. 7, A and B, and fig. S26). Two FCs emerged for each behavioral state associated with primarily activated (Act-FC) or inhibited (Inh-FC) neurons. We first examined how functional clustering segregates neuron gene expression profiles.

A subset of gene expression profiles specifically segregated with functional response clusters (Fig. 7, A to C, and fig. S26). We performed differential gene expression analyses between the two FCs in each behavioral state (fig. S27A), which was measured by either the *P* value of the expression-level difference or by the ratio of expression level between FCs (Fig. 7D and fig. S27B). *Npy1r* was significantly enriched across 11 behavioral states and was ranked as the first or second enriched gene by *P* value. *Crh* and *Pdyn* were significantly enriched in eight and nine behavioral states, respectively. Moreover,

if *Npy1r*, *Pdyn*, and *Crh* were enriched for a behavioral state, then they were found in the same FC because of partial coexpression in the same cells. For example, *Npy1r*, *Pdyn*, and *Crh* were enriched in the Act-FC for Eat-Hed (hedonic) and Fear states. By contrast, the Inh-FC was enriched with neurons expressing *Penk*. We also examined combinations of molecularly defined cell types within FCs in each behavioral state. For most behavioral states (eight of 11 states), activated or inhibited FCs also showed significant enrichment of cell types (fig. S28). The cell types with the highest FC selectivity were MC5-Crh and MC6-Pdyn, which also showed high consistent-responses in most behavioral states (Fig. 5H). These gene and cell type enrichment analyses demonstrated a strong association between neuron function during behavior and the molecular profile of individual neurons. However, this analysis lacks useful metrics for ranking the predictive power of gene expression for functional response class, and it does not define the optimal set of marker genes for predicting responses across the neural ensemble.

Gene expression prediction of FCs

We therefore determined the best gene combinations for predicting neuron functional response classes in each behavioral state (Fig. 8A). We used supervised machine learning to predict the FCs of individual PVH neurons solely by their gene expression profiles with a logistic regression classifier (Fig. 8B; see the materials and methods). Three normalized features represented the expression level of each gene (figs. S29 and S30A). This approach does not binarize gene expression by thresholding. Instead, it explicitly incorporates the broad continuous distribution of gene expression levels that we found (Fig. 2H) as the independent variables in the predictive model. Sequential forward feature selection (SFFS) determines the most predictive individual gene for FC classification and sequentially adds the next most predictive gene until predictive accuracy no longer increases. This approach identified optimal gene sets that best predicted the functional response class while minimizing the contribution of redundant gene coexpression information (Fig. 8C and fig. S30, B to D). We compared the predictive power of the molecular profiles for functional response class with the 95th percentile of predictive accuracies after shuffling the relationship between gene expression of individual neurons and their FCs (Fig. 8, C and D, and fig. S30B). The two behavioral states during which neuronal ensemble response could be best predicted by gene expression profiles were during ghrelin-induced hunger [accuracy: 73%, area under the receiver-operating characteristic (auROC): 0.784, *P* = 0] and fear retrieval (accuracy: 69.9%, auROC: 0.745, *P* = 0) states. The lowest

predictive accuracy was for saline injection (accuracy: 62.1%, auROC: 0.570, $P = 0.0005$) (Fig. 8D and fig. S30D).

Predictive contribution of individual genes

Combinations of genes always had higher predictive power for functional response class than single genes (fig. S30B). In addition, for all behavioral states, the optimal accuracies from the first round of SFFS (SFFS1) with just two to six genes were higher than the accuracies predicted with all genes (Fig. 8C). This showed that a subset of genes provided higher prediction performance than the whole set of genes (41). Next, we quantitatively assessed and ranked the predictive accuracy of single genes for FCs across 11 behavioral states. *Pdyn*, *Npy1r*, or *Crh* showed the highest predictive power in the first round for all behavioral states. *Npy1r* was always in the optimal gene set from SFFS1 in all behavioral states. Moreover, *Npy1r* expression strongly predicted fear-activated neurons. We determined the roles of individual genes within the optimal gene set to improve prediction performance by measuring the average coefficients of those genes from logistic regression (Fig. 8C). For ghrelin-induced hunger, SFFS1 showed an additive relationship for *Npy1r* and *Pdyn* prediction of the inhibited functional response class (Fig. 8C). Both genes have been previously associated with appetite control by the PVH (42). For food consumption during hunger (Eat-Hng), *Pdyn* and *Npy1r* predicted the activated response type, whereas the inhibited response class was predicted by *Trh* and *Penk* (Fig. 8C). For fear retrieval, *Npy1r* and *Crh* best predicted activated neurons and *Penk* predicted fear-inhibited neurons (Fig. 8C).

Multiple rounds of SFFS (mSFFS; see the materials and methods) revealed genes that could compensate for the removal of the most predictive gene from the previous rounds (fig. S30B). This indicated that the most predictive genes could be largely compensated by combinations of additional genes in subsequent rounds. For example, *Pdyn* was most predictive during Eat-Hng, but this predictive accuracy was largely replaced by *Crh* in round 2 and *Npy1r* in round 3 of mSFFS, and we found that *Npy1r* neurons coexpressed *Pdyn* and *Crh* in a hierarchical relationship in pPVH (fig. S30, E and F). Consistent with this, *Npy1r* showed statistically significant predictive power for every behavioral state, but if *Npy1r* was removed from the analysis, its predictive power could be largely replaced by other genes (fig. S30B). Thus, the hierarchical gene expression relationship of these three genes in the pPVH was associated with similar neuron functional responses. Neurons with low or no *Npy1r* expression typically responded oppositely. We also found similar results for the predictive power of marker genes for neuron FCs

concatenated across all 11 behavioral states (fig. S31).

Gene expression levels for improved FC prediction

Using the quantitative gene expression level to predict functional responses also offers a systematic method for defining the gene expression threshold that targets a functional response class with the best precision for each behavioral state. We identified optimal cut points for the gene expression threshold using Youden's J statistic with the ROC curve (fig. S32). Prediction precision with a single gene was up to 40% higher, and response purity was significantly improved when the optimal expression threshold was used instead of a lower threshold based on expression over background (Fig. 8, E to G). Thus, neuronal functional identity is not a binary quality of gene expression.

Temporal profile of gene → functional response prediction

Next, we investigated how the predictive power of gene expression profiles was related to neuron temporal dynamics. For example, does a gene have similar predictive value throughout a state? For each timestamp (0.4-s interval), we modeled the relationship of gene expression level to neuronal response (Fig. 9, A to C, and fig. S33A). Our results complemented those obtained from prediction of FCs, including (i) higher predictive power of combinatorial expression profile (Fig. 9A), (ii) improvement in prediction performance by mSFFS (Fig. 9A), (iii) redundant information in molecular profiles for predicting temporal response (Fig. 9B), and (iv) that *Npy1r* predictive power was high and statistically significant across all behavioral states (Fig. 9A). However, predictive power depended on cell type-specific neuronal dynamics. During eating and drinking, the predictive power of marker genes increased as consumption progressed. For example, *Pdyn* neuron activity rose more quickly than *Pdyn* predictive accuracy for Eat-Hed and Eat-Hng. In this case, the transient activation at onset of food presentation was not specific within *Pdyn*-expressing neurons but was also widespread in *Pdyn*-negative neurons (fig. S33B). This shows that cell type-specific responses develop progressively in some behaviors. By contrast, fear retrieval showed an immediate cell type-specific response that was best predicted by *Npy1r* and gradually became less well predicted by gene expression (fig. S33B).

In five of 11 behavioral states (Eat-Hng, Drink-Thirst, Eat-Hed, Fear, and Ghrelin), a single gene had the greatest predictive accuracy throughout a behavioral state. However, for six other states, the most predictive gene for the ensemble functional response switched with time. Moreover, using the optimal pre-

dictions of neural activity, we ranked neurons by the fraction of deviance explained with our linear regression models along the entire time series across behavioral states (Fig. 9, C and D, fig. S33A). A majority of neurons (65%) showed statistically significant predictive power. Neurons within the top quartile of predictive powers showed significantly higher expression levels of *Vglut2*, *Gad2*, *Npy1r*, *Crh*, *Reln*, *Pdyn*, and *Trh* (fig. S33D). Next, we remapped the corresponding gene expression profiles onto molecularly defined cell types (Fig. 9, E and F). MC4-Npy1r, MC5-Crh (exclusively), and MC6-Pdyn neurons were enriched in the most highly predictive quartile (fig. S33E), consistent with the high predictive accuracy associated with *Npy1r* coexpression.

DISCUSSION

Neural coding by an ensemble-of-cell-types indicates that many molecularly defined neurons also form functional groupings that work in concert to encode behavioral state. It is unlikely that coding in the pPVH follows the labeled-line model because we could not find such neurons in the ensemble irrespective of molecular identity. Our results validate the use of molecularly defined cell types to reduce the dimensionality of the PVH neuronal ensemble to understand behavioral state coding. Ensemble-of-cell-types coding of behavioral states provides superior efficiency, scalability, and flexibility than labeled-line coding and offers superior robustness (due to redundancy) than cell type-independent, full-ensemble coding. Operationally, grouping by molecularly defined cell types is justified by high consistent-responses and is analogous to the pooling operation in artificial neural networks, which is used to extract invariant information (43–45). This may also be a key function when molecularly defined circuits are used for coding behavioral states, which should be invariant to irrelevant external conditions. Taken together, these cell types and the patterns of activity reported here provide a parts list for systematically examining the neural coding of behavioral state by the PVH. CaRNA imaging offers a quantitative method to evaluate the extent to which other brain regions rely on molecularly defined cell type ensemble coding.

Using CaRNA imaging, we demonstrate an important role for gene expression information to predict both neuron functional response class as well as temporal dynamics within the PVH neural ensemble. High predictive power of *Npy1r* for neuron activity was observed with all analysis methods. However, combinations of other cell type marker genes also showed significant prediction for functional responses. The highest consistent-response cell types, MC5-Crh and MC6-Pdyn, coexpressed *Npy1r*, and cell types that responded

oppositely typically lacked *Npy1r*. scRNA-seq analysis revealed hierarchical relationships of gene expression within neuron populations, where the smallest subpopulations are designated as “types” and the largest subdivisions as “classes” that encompass many types (46). We found evidence that this molecular hierarchy extends to functional responses in the neuronal ensemble, in which similarly tuned neuron types form classes that can be well described by a neuromodulator receptor gene that is expressed across multiple molecularly defined cell types (fig. S30, E and F). This is interesting in the context of the neuromodulatory function of *Npy1r* and its endogenous agonist NPY (47). Because *Npy1r* is expressed across multiple cell types and NPY signals through volume transmission (48), this receptor can cooperatively regulate diverse cell types (Fig. 10A). This may enhance the generality of neural output in the presence of noisy neural inputs, which is important to facilitate behavioral state coding but is also a computational role akin to regularization in machine learning. Nevertheless, despite the response similarity between neurons that express *Npy1r*, there are reliable temporal differences that map onto cells with specific gene expression profiles. These temporal responses are important for distinguishing behavioral states and functional response types in the neuronal ensemble. In the analogy of an orchestral ensemble, *Npy1r* is a conductor selectively coordinating the responses of multiple cell types (Fig. 10B) that are like instruments that play together but maintain distinctive contributions to a score.

Marker-gene expression in the PVH can be dynamic (49, 50), but to the extent that this affects our results, it may degrade the predictive accuracy of gene expression level to a functional or behavioral response. Additional genetic markers (51, 52) may improve these predictions by offering increased coverage of all neurons in the ensemble. However, predictive accuracies solely from gene expression information are not expected to be perfect because functional responsiveness is also influenced by plasticity and connectivity mechanisms that are independent of cell type (13, 16, 28). Moreover, our findings also highlight potential limitations of site-specific recombinase (e.g., Cre) mouse lines that use low gene expression thresholds to specify cell type identity (53, 54).

Although we focused here on decoding behavioral states and predicting functional responses solely from molecular information about the underlying cells, we found that if functional information is used to supervise clustering, then molecularly defined cell types can be defined with higher purity (17). This may be useful in the future for better defining combinations of molecular markers and their

expression levels that are optimal for targeting specific functional perturbations.

CaMA imaging provides a solution to the general problem of assessing functional roles for the large number of new molecularly defined cell types that are being discovered routinely using single-cell transcriptomics. Because CaMA imaging does not rely on genetic modifications, only viral targeting, it is applicable to any organism suitable for in vivo functional imaging. By producing unbiased and systematic datasets that integrate genes, neuron dynamics, and behavior, CaMA imaging offers a path to discoveries about the organization of brain function at both the molecular level and the systems level.

REFERENCES AND NOTES

- C. Stringer et al., Spontaneous behaviors drive multidimensional, brainwide activity. *Science* **364**, 255 (2019). doi: [10.1126/science.aav7893](https://doi.org/10.1126/science.aav7893); pmid: [31000656](https://pubmed.ncbi.nlm.nih.gov/31000656/)
- J. E. Allen, T. E. Sutherland, Crystal-clear treatment for allergic disease. *Science* **364**, 738–739 (2019). doi: [10.1126/science.aax6175](https://doi.org/10.1126/science.aax6175); pmid: [31123126](https://pubmed.ncbi.nlm.nih.gov/31123126/)
- J. Gründemann et al., Amygdala ensembles encode behavioral states. *Science* **364**, eaav8736 (2019). doi: [10.1126/science.aav8736](https://doi.org/10.1126/science.aav8736); pmid: [31000636](https://pubmed.ncbi.nlm.nih.gov/31000636/)
- X. Chen et al., Brain-wide organization of neuronal activity and convergent sensorimotor transformations in larval zebrafish. *Neuron* **100**, 876–890.e5 (2018). doi: [10.1016/j.neuron.2018.09.042](https://doi.org/10.1016/j.neuron.2018.09.042); pmid: [30473013](https://pubmed.ncbi.nlm.nih.gov/30473013/)
- E. S. Lein et al., Genome-wide atlas of gene expression in the adult mouse brain. *Nature* **445**, 168–176 (2007). doi: [10.1038/nature05453](https://doi.org/10.1038/nature05453); pmid: [17151600](https://pubmed.ncbi.nlm.nih.gov/17151600/)
- A. Saunders et al., Molecular diversity and specializations among the cells of the adult mouse brain. *Cell* **174**, 1015–1030.e16 (2018). doi: [10.1016/j.cell.2018.07.028](https://doi.org/10.1016/j.cell.2018.07.028); pmid: [30096299](https://pubmed.ncbi.nlm.nih.gov/30096299/)
- A. Zeisel et al., Molecular architecture of the mouse nervous system. *Cell* **174**, 999–1014.e22 (2018). doi: [10.1016/j.cell.2018.06.021](https://doi.org/10.1016/j.cell.2018.06.021); pmid: [30096314](https://pubmed.ncbi.nlm.nih.gov/30096314/)
- B. Tasic et al., Shared and distinct transcriptomic cell types across neocortical areas. *Nature* **563**, 72–78 (2018). doi: [10.1038/s41586-018-0654-5](https://doi.org/10.1038/s41586-018-0654-5); pmid: [30382198](https://pubmed.ncbi.nlm.nih.gov/30382198/)
- A. R. Adamantidis, F. Zhang, A. M. Aravanis, K. Deisseroth, L. de Lecea, Neural substrates of awakening probed with optogenetic control of hypocretin neurons. *Nature* **450**, 420–424 (2007). doi: [10.1038/nature06310](https://doi.org/10.1038/nature06310); pmid: [17943086](https://pubmed.ncbi.nlm.nih.gov/17943086/)
- D. Atasoy, S. M. Sternson, Chemogenetic tools for causal cellular and neuronal biology. *Physiol. Rev.* **98**, 391–418 (2018). doi: [10.1152/physrev.00009.2017](https://doi.org/10.1152/physrev.00009.2017); pmid: [29351511](https://pubmed.ncbi.nlm.nih.gov/29351511/)
- C. J. Magnus et al., Ultrapotent chemogenetics for research and potential clinical applications. *Science* **364**, eaav5282 (2019). pmid: [30872534](https://pubmed.ncbi.nlm.nih.gov/30872534/)
- M. Jazayeri, A. Afraz, Navigating the neural space in search of the neural code. *Neuron* **93**, 1003–1014 (2017). doi: [10.1016/j.neuron.2017.02.019](https://doi.org/10.1016/j.neuron.2017.02.019); pmid: [28279349](https://pubmed.ncbi.nlm.nih.gov/28279349/)
- K. Hardcastle, S. Ganguli, L. M. Giocomo, Cell types for our sense of location: Where we are and where we are going. *Nat. Neurosci.* **20**, 1474–1482 (2017). doi: [10.1038/nn.4654](https://doi.org/10.1038/nn.4654); pmid: [29073649](https://pubmed.ncbi.nlm.nih.gov/29073649/)
- C. F. Stevens, Neuronal diversity: Too many cell types for comfort? *Curr. Biol.* **8**, R708–R710 (1998). doi: [10.1016/S0960-9822\(98\)70454-3](https://doi.org/10.1016/S0960-9822(98)70454-3); pmid: [9778523](https://pubmed.ncbi.nlm.nih.gov/9778523/)
- T. E. Holy, “Yes! We’re all individuals!”: Redundancy in neuronal circuits. *Nat. Neurosci.* **13**, 1306–1307 (2010). doi: [10.1038/nrn110-1306](https://doi.org/10.1038/nrn110-1306); pmid: [20975750](https://pubmed.ncbi.nlm.nih.gov/20975750/)
- S. Fusi, E. K. Miller, M. Rigotti, Why neurons mix: High dimensionality for higher cognition. *Curr. Opin. Neurobiol.* **37**, 66–74 (2016). doi: [10.1016/j.conb.2016.01.010](https://doi.org/10.1016/j.conb.2016.01.010); pmid: [26851755](https://pubmed.ncbi.nlm.nih.gov/26851755/)
- A. J. Northcutt et al., Molecular profiling of single neurons of known identity in two ganglia from the crab *Cancer borealis*. *Proc. Natl. Acad. Sci. U.S.A.* **116**, 26980–26990 (2019). doi: [10.1073/pnas.1911413116](https://doi.org/10.1073/pnas.1911413116); pmid: [31806754](https://pubmed.ncbi.nlm.nih.gov/31806754/)
- W. E. Armstrong, “Hypothalamic supraoptic and paraventricular nuclei,” in *The Rat Nervous System*, G. Paxinos, Ed. (Elsevier, 2004), pp. 369–388.
- R. A. Romanov et al., Molecular interrogation of hypothalamic organization reveals distinct dopamine neuronal subtypes. *Nat. Neurosci.* **20**, 176–188 (2017). doi: [10.1038/nn.4462](https://doi.org/10.1038/nn.4462); pmid: [27991900](https://pubmed.ncbi.nlm.nih.gov/27991900/)
- L. W. Swanson, P. E. Sawchenko, Hypothalamic integration: Organization of the paraventricular and supraoptic nuclei. *Annu. Rev. Neurosci.* **6**, 269–324 (1983). doi: [10.1146/annurev.ne.06.030183.001413](https://doi.org/10.1146/annurev.ne.06.030183.001413); pmid: [6132586](https://pubmed.ncbi.nlm.nih.gov/6132586/)
- M. M. Li et al., The paraventricular hypothalamus regulates satiety and prevents obesity via two genetically distinct circuits. *Neuron* **102**, 653–667.e6 (2019). doi: [10.1016/j.neuron.2019.02.028](https://doi.org/10.1016/j.neuron.2019.02.028); pmid: [30879785](https://pubmed.ncbi.nlm.nih.gov/30879785/)
- M. J. Krashes et al., An excitatory paraventricular nucleus to AgRP neuron circuit that drives hunger. *Nature* **507**, 238–242 (2014). doi: [10.1038/nature12956](https://doi.org/10.1038/nature12956); pmid: [24487620](https://pubmed.ncbi.nlm.nih.gov/24487620/)
- T. Füzési, N. Daviu, J. I. Wamsteeker Cusulin, R. P. Bonin, J. S. Bains, Hypothalamic CRH neurons orchestrate complex behaviours after stress. *Nat. Commun.* **7**, 11937 (2016). doi: [10.1038/ncomms11937](https://doi.org/10.1038/ncomms11937); pmid: [27306314](https://pubmed.ncbi.nlm.nih.gov/27306314/)
- C. B. Saper, B. B. Lowell, The hypothalamus. *Curr. Biol.* **24**, R1111–R1116 (2014). doi: [10.1016/j.cub.2014.10.023](https://doi.org/10.1016/j.cub.2014.10.023); pmid: [25465326](https://pubmed.ncbi.nlm.nih.gov/25465326/)
- K. K. Ishii et al., A labeled-line neural circuit for pheromone-mediated sexual behaviors in mice. *Neuron* **95**, 123–137.e8 (2017). doi: [10.1016/j.neuron.2017.05.038](https://doi.org/10.1016/j.neuron.2017.05.038); pmid: [28648498](https://pubmed.ncbi.nlm.nih.gov/28648498/)
- A. K. Graebner, M. Iyer, M. E. Carter, Understanding how discrete populations of hypothalamic neurons orchestrate complicated behavioral states. *Front. Syst. Neurosci.* **9**, 111 (2015). doi: [10.3389/fnsys.2015.00111](https://doi.org/10.3389/fnsys.2015.00111); pmid: [26300745](https://pubmed.ncbi.nlm.nih.gov/26300745/)
- S. M. Sternson, Hypothalamic survival circuits: Blueprints for purposive behaviors. *Neuron* **77**, 810–824 (2013). doi: [10.1016/j.neuron.2013.02.018](https://doi.org/10.1016/j.neuron.2013.02.018); pmid: [23473313](https://pubmed.ncbi.nlm.nih.gov/23473313/)
- D. O. Hebb, *The Organization of Behavior* (Erlbaum, 1949/2002).
- J. R. Moffitt et al., Molecular, spatial, and functional single-cell profiling of the hypothalamic preoptic region. *Science* **362**, eaav5324 (2018). doi: [10.1126/science.aav5324](https://doi.org/10.1126/science.aav5324); pmid: [30385464](https://pubmed.ncbi.nlm.nih.gov/30385464/)
- D. Lee, M. Kume, T. E. Holy, Sensory coding mechanisms revealed by optical tagging of physiologically defined neuronal types. *Science* **366**, 1384–1389 (2019). doi: [10.1126/science.aax8055](https://doi.org/10.1126/science.aax8055); pmid: [31831669](https://pubmed.ncbi.nlm.nih.gov/31831669/)
- M. Lovett-Barron et al., Multiple convergent hypothalamus-brainstem circuits drive defensive behavior. *Nat. Neurosci.* **23**, 959–967 (2020). doi: [10.1038/s41593-020-0655-1](https://doi.org/10.1038/s41593-020-0655-1); pmid: [32572237](https://pubmed.ncbi.nlm.nih.gov/32572237/)
- M. Lovett-Barron et al., Ancestral circuits for the coordinated modulation of brain state. *Cell* **171**, 1411–1423.e17 (2017). doi: [10.1016/j.cell.2017.10.021](https://doi.org/10.1016/j.cell.2017.10.021); pmid: [29103613](https://pubmed.ncbi.nlm.nih.gov/29103613/)
- A. M. Kerlin, M. L. Andermann, V. K. Berezovskii, R. C. Reid, Broadly tuned response properties of diverse inhibitory neuron subtypes in mouse visual cortex. *Neuron* **67**, 858–871 (2010). doi: [10.1016/j.neuron.2010.08.002](https://doi.org/10.1016/j.neuron.2010.08.002); pmid: [20826316](https://pubmed.ncbi.nlm.nih.gov/20826316/)
- L. M. Barnett, T. E. Hughes, M. Drobizhev, Deciphering the molecular mechanism responsible for CaMPP6m's Ca²⁺-dependent change in fluorescence. *PLOS ONE* **12**, e0170934 (2017). doi: [10.1371/journal.pone.0170934](https://doi.org/10.1371/journal.pone.0170934); pmid: [28182677](https://pubmed.ncbi.nlm.nih.gov/28182677/)
- C. Li et al., Defined paraventricular hypothalamic populations exhibit differential responses to food contingent on caloric state. *Cell Metab.* **29**, 681–694.e5 (2019). doi: [10.1016/j.cmet.2018.10.016](https://doi.org/10.1016/j.cmet.2018.10.016); pmid: [30472090](https://pubmed.ncbi.nlm.nih.gov/30472090/)
- J. Kim et al., Rapid, biphasic CRF neuronal responses encode positive and negative valence. *Nat. Neurosci.* **22**, 576–585 (2019). doi: [10.1038/s41593-019-0342-2](https://doi.org/10.1038/s41593-019-0342-2); pmid: [30833699](https://pubmed.ncbi.nlm.nih.gov/30833699/)
- Y. Mandelblat-Cerf et al., Bidirectional anticipation of future osmotic challenges by vasopressin neurons. *Neuron* **93**, 57–65 (2017). doi: [10.1016/j.neuron.2016.11.021](https://doi.org/10.1016/j.neuron.2016.11.021); pmid: [27989461](https://pubmed.ncbi.nlm.nih.gov/27989461/)
- J. Y. Cohen, S. Haesler, L. Vong, B. B. Lowell, N. Uchida, Neuron-type-specific signals for reward and punishment in the ventral tegmental area. *Nature* **482**, 85–88 (2012). doi: [10.1038/nature10754](https://doi.org/10.1038/nature10754); pmid: [22258508](https://pubmed.ncbi.nlm.nih.gov/22258508/)
- J. N. Betley et al., Neurons for hunger and thirst transmit a negative-valence teaching signal. *Nature* **521**, 180–185 (2015). doi: [10.1038/nature14416](https://doi.org/10.1038/nature14416); pmid: [25915020](https://pubmed.ncbi.nlm.nih.gov/25915020/)
- Y. Li et al., Neuronal representation of social information in the medial amygdala of awake behaving mice. *Cell* **171**, 1176–1190.e17 (2017). doi: [10.1016/j.cell.2017.10.015](https://doi.org/10.1016/j.cell.2017.10.015); pmid: [29107332](https://pubmed.ncbi.nlm.nih.gov/29107332/)
- G. V. Trunk, A problem of dimensionality: A simple example. *IEEE Trans. Pattern Anal. Mach. Intell.* **1**, 306–307 (1979). doi: [10.1109/TPAMI.1979.4766926](https://doi.org/10.1109/TPAMI.1979.4766926); pmid: [21868861](https://pubmed.ncbi.nlm.nih.gov/21868861/)
- A. Kask, L. Rågo, J. Harro, Evidence for involvement of neuropeptide Y receptors in the regulation of food intake: Studies with Y₁-selective antagonist BIBP3226. *Br. J.*

- Pharmacol.* **124**, 1507–1515 (1998). doi: [10.1038/sj.bjp.0701969](https://doi.org/10.1038/sj.bjp.0701969); pmid: [9723965](https://pubmed.ncbi.nlm.nih.gov/9723965/)
43. M. Ranzato, F. J. Huang, Y. Boureau, Y. LeCun, “Unsupervised learning of invariant feature hierarchies with applications to object recognition,” in *IEEE Conference on Computer Vision and Pattern Recognition* (IEEE, 2007), pp. 1–8; <https://doi.org/10.1109/CVPR.2007.383157>.
 44. D. H. Hubel, T. N. Wiesel, Receptive fields, binocular interaction and functional architecture in the cat’s visual cortex. *J. Physiol.* **160**, 106–154 (1962). doi: [10.1113/jphysiol.1962.sp006837](https://doi.org/10.1113/jphysiol.1962.sp006837); pmid: [14449617](https://pubmed.ncbi.nlm.nih.gov/14449617/)
 45. Y. LeCun, I. Kanter, S. A. Solla, “Second order properties of error surfaces: Learning time and generalization,” in *Advances in Neural Information Processing Systems* 3, R. P. Lippmann, J. E. Moody, D. S. Touretzky, Eds. (NIPS, 1990), pp. 396–404.
 46. H. Zeng, J. R. Sanes, Neuronal cell-type classification: Challenges, opportunities and the path forward. *Nat. Rev. Neurosci.* **18**, 530–546 (2017). doi: [10.1038/nrn.2017.85](https://doi.org/10.1038/nrn.2017.85); pmid: [28775344](https://pubmed.ncbi.nlm.nih.gov/28775344/)
 47. H. Herzog, 30 Years of NPY research. *Neuropeptides* **46**, 251 (2012). doi: [10.1016/j.nepe.2012.10.002](https://doi.org/10.1016/j.nepe.2012.10.002); pmid: [23141043](https://pubmed.ncbi.nlm.nih.gov/23141043/)
 48. S. O. Fetissov, J. Kopp, T. Hökfelt, Distribution of NPY receptors in the hypothalamus. *Neuropeptides* **38**, 175–188 (2004). doi: [10.1016/j.nepe.2004.05.009](https://doi.org/10.1016/j.nepe.2004.05.009); pmid: [15337370](https://pubmed.ncbi.nlm.nih.gov/15337370/)
 49. R. A. Romanov, A. Alpar, T. Hökfelt, T. Harkany, Molecular diversity of corticotropin-releasing hormone mRNA-containing neurons in the hypothalamus. *J. Endocrinol.* **232**, R161–R172 (2017). doi: [10.1530/JOE-16-0256](https://doi.org/10.1530/JOE-16-0256); pmid: [28057867](https://pubmed.ncbi.nlm.nih.gov/28057867/)
 50. A. G. Watts, L. W. Swanson, Diurnal variations in the content of prepro corticotropin-releasing hormone messenger ribonucleic acids in the hypothalamic paraventricular nucleus of rats of both sexes as measured by in situ hybridization. *Endocrinology* **125**, 1734–1738 (1989). doi: [10.1210/endo-125-3-1734](https://doi.org/10.1210/endo-125-3-1734); pmid: [2788078](https://pubmed.ncbi.nlm.nih.gov/2788078/)
 51. K. H. Chen, A. N. Boettiger, J. R. Moffitt, S. Wang, X. Zhuang, RNA imaging. Spatially resolved, highly multiplexed RNA profiling in single cells. *Science* **348**, aaa6090 (2015). doi: [10.1126/science.aaa6090](https://doi.org/10.1126/science.aaa6090); pmid: [25858977](https://pubmed.ncbi.nlm.nih.gov/25858977/)
 52. S. Shah, E. Lubeck, W. Zhou, L. Cai, In situ transcription profiling of single cells reveals spatial organization of cells in the mouse hippocampus. *Neuron* **92**, 342–357 (2016). doi: [10.1016/j.neuron.2016.10.001](https://doi.org/10.1016/j.neuron.2016.10.001); pmid: [27764670](https://pubmed.ncbi.nlm.nih.gov/27764670/)
 53. J. A. Harris *et al.*, Anatomical characterization of Cre driver mice for neural circuit mapping and manipulation. *Front. Neural Circuits* **8**, 76 (2014). doi: [10.3389/fncir.2014.00076](https://doi.org/10.3389/fncir.2014.00076); pmid: [25071457](https://pubmed.ncbi.nlm.nih.gov/25071457/)
 54. K. Y. Lee *et al.*, Lessons on conditional gene targeting in mouse adipose tissue. *Diabetes* **62**, 864–874 (2013). doi: [10.2337/db12-1089](https://doi.org/10.2337/db12-1089); pmid: [23321074](https://pubmed.ncbi.nlm.nih.gov/23321074/)
 55. J. Biag *et al.*, Cyto- and chemoarchitecture of the hypothalamic paraventricular nucleus in the C57BL/6J male mouse: A study of immunostaining and multiple fluorescent tract tracing. *J. Comp. Neurol.* **520**, 6–33 (2012). doi: [10.1002/cne.22698](https://doi.org/10.1002/cne.22698); pmid: [21674499](https://pubmed.ncbi.nlm.nih.gov/21674499/)
 56. S. Xu, H. Yang, V. Menon, A. L. Lemire, L. Wang, F. E. Henry, S. C. Turaga, S. M. Sternson, Code for CaRMA imaging analysis pipelines, example data, preprocessed multiplex FISH data, and preprocessed CaRMA imaging data for: Behavioral state coding by molecularly defined paraventricular hypothalamic cell type ensembles, GitHub (2020); <https://github.com/sternson-lab/CaRMA-imaging>.
- ACKNOWLEDGMENTS**
- We thank V. Goncharov and C. McRaven for assistance with two-photon microscope construction; M. Barbic and T. Harris for the one-photon and two-photon excitable grid target; Z. Guo for GRIN lens testing; A. Hu for brain sectioning; J. Arnold for the low-friction treadmill; and N. Spruston, A. Lee, M. Ahrens, and V. Jayaraman for comments on the manuscript. **Funding:** Research was funded by HHMI (S.M.S.). **Author contributions:** S.M.S. and S.X. conceived the project and designed the experiments and analyses. S.X. built the two-photon microscope, designed the behavior control and log system, performed two-photon-GRIN-lens calcium-imaging experiments, and analyzed the data. H.Y., S.X., S.M.S., and F.E.H. developed the multiplex FISH method. H.Y. and S.X. performed the multiplex FISH experiments. A.L.L., L.W., and F.E.H. performed scRNA-seq. V.M. analyzed the scRNA-seq data and assisted in the gene and cell type enrichment analysis. S.C.T. supervised the machine-learning analyses. S.M.S. and S.X. wrote the manuscript with input from other authors. **Competing interests:** S.M.S., F.E.H., H.Y., and S.X. have filed a patent application on multiplexed FISH methods. **Data and materials availability:** The GEO submission ID for the single-cell PVH data is GSE148568. Code for CaRMA imaging analysis pipelines, example data, preprocessed multiplex FISH data, and preprocessed CaRMA imaging data are available at GitHub (56).
- SUPPLEMENTARY MATERIALS**
- science.sciencemag.org/content/370/6514/eabb2494/suppl/DC1
Materials and Methods
Figs. S1 to S33
Tables S1 and S2
References (57–68)
Movie S1
MDAR Reproducibility Checklist
- [View/request a protocol for this paper from Bio-protocol.](#)
- 19 February 2020; accepted 18 August 2020
[10.1126/science.abb2494](https://doi.org/10.1126/science.abb2494)

RESEARCH ARTICLE

MICROBIOTA

Microbiota-modulated CART⁺ enteric neurons autonomously regulate blood glucosePaul A. Muller^{1*†‡}, Fanny Matheis^{1*}, Marc Schneeberger^{2*}, Zachary Kerner¹, Veronica Jové³, Daniel Mucida^{1‡}

The gut microbiota affects tissue physiology, metabolism, and function of both the immune and nervous systems. We found that intrinsic enteric-associated neurons (iEANs) in mice are functionally adapted to the intestinal segment they occupy; ileal and colonic neurons are more responsive to microbial colonization than duodenal neurons. Specifically, a microbially responsive subset of viscerofugal CART⁺ neurons, enriched in the ileum and colon, modulated feeding and glucose metabolism. These CART⁺ neurons send axons to the prevertebral ganglia and are polysynaptically connected to the liver and pancreas. Microbiota depletion led to NLRP6- and caspase 11-dependent loss of CART⁺ neurons and impaired glucose regulation. Hence, iEAN subsets appear to be capable of regulating blood glucose levels independently from the central nervous system.

Enteric-associated neurons (EANs) comprise a numerous and heterogeneous population of neurons innervating the gastrointestinal (GI) tract that monitor and respond to various environmental cues such as mechanical stretch and luminal content (1, 2). The vast majority of luminal stimuli are derived from the diet and commensal microbes, which may be sensed directly by EAN fibers positioned along the intestinal epithelium or indirectly through signals derived from non-neuronal cells inhabiting the same compartment (1, 3). Intrinsic EANs (iEANs) are neural crest-derived and organized in two distinct layers: the myenteric or Auerbach's plexus and submucosal or Meissner's plexus (2). iEANs can operate autonomously and are primarily tasked with modulation of intestinal motility and secretory function (2). Recent studies have demonstrated that the gut microbiota influences the basal activity of intestine-associated cells, including EANs and immune cells (2, 3), as well as host metabolism (4). These studies highlight the impact of the gut microbiota on EANs and key mammalian physiological processes; however, the cellular circuits and molecular components that mediate gut-EAN communication remain poorly understood. We sought to determine how the microbiota affects iEANs to better characterize their role in host physiology.

Microbiota-dependent transcriptional changes in enteric neurons are region-specific

To profile iEANs in an untargeted and region-specific manner, we performed translating ribosomal affinity purification (TRAP), a cell type-specific actively translated mRNA profiling approach. We interbred pan-neuronal *Snap25*^{Cre} mice with *Rpl22*^{lsl-HA} (RiboTag) mice, allowing hemagglutinin (HA) immunoprecipitation of actively translated mRNA. Expression of HA-tagged ribosomes was observed in neurons in the myenteric plexus of *Snap25*^{RiboTag} mice (Fig. 1A). RNA sequencing (RNA-seq) of bound transcripts revealed significant enrichment of neuron-specific genes and pathways in Cre⁺ animals compared with Cre⁻ animals (fig. S1, A to C). Given their deep integration into the intestinal tissue, we sought to understand how iEANs might differ from extrinsic EANs (eEANs) (5) innervating the gut. TRAP RNA-seq (TRAP-seq) analysis of iEANs and eEANs (nodose, NG; celiac-superior mesenteric, CG-SMG; and dorsal root ganglion, DRG) (5) suggested that iEANs possess a distinct translational profile (Fig. 1B and fig. S2A). We found that iEANs were primarily defined by enriched transcripts related to neuropeptide signaling as compared with either NG and DRG or CG-SMG, which had increased expression of transcripts involved in sensory processes and catecholamine production, respectively (Fig. 1C and fig. S2, B to D).

Comparison between translational profiles of myenteric iEANs isolated from the duodenum, ileum, and colon indicated that iEANs segregate based on their anatomical location (6) (Fig. 1D and fig. S3, A to C). The proximal small intestine is highly absorptive and enriched with enteroendocrine cell (EEC) subsets associated with lipid and nutrient detection (7). Consistently, we found that duodenal iEANs,

in comparison to ileal and colonic iEANs, express significantly higher levels of transcripts encoding receptors involved in the response to proximal EEC- or iEAN-derived signals, such as cholecystokinin receptor A (*Cckar*), glucagon receptor (*Gcgr*), and tachykinin receptor 3 (*Tacr3*) (Fig. 1E and fig. S3, A to C). There are also regional differences in neuropeptide transcripts, including neuropeptide Y (*Npy*) enrichment in duodenum iEANs. Terminal ileum and colon iEANs are enriched in neuropeptide transcripts, including somatostatin (*Sst*), cocaine- and amphetamine-regulated transcript (CART, encoded by *Cartpt*), proenkephalin (*Penk*), gastrin releasing peptide (*Grp*), agouti-related peptide (*AgRP*), and tachykinin 1 (*Tac1*), all of which, besides *AgRP*, are thought to be involved in controlling intestine motility through the myenteric plexus (8–12) (Fig. 1E and fig. S3, A to C). Immunofluorescence analysis confirmed a region-specific compartmentalization of neuropeptides at the protein level and identified regional differences in neuronal numbers along the intestine (Fig. 1F and fig. S3D). For instance, NPY, which is typically involved in intestinal inflammation or inhibition of neurotransmission (13, 14), was enriched in duodenum iEANs (Fig. 1G and fig. S3E). By contrast, the neuropeptide SST, which is involved in EEC regulation of several GI hormones (15) and inhibition of smooth muscle contraction (8, 13), is highly expressed in the ileum and colon but scarcely expressed in the duodenum (Fig. 1H and fig. S3F). We also observed increased numbers of CART⁺ neurons, which are thought to play a role in intestinal nitrous oxide neurotransmission and neuroprotection (9, 16), in the ileum and colon (Fig. 1I and fig. S3, G to I). Finally, we found that duodenum iEANs are particularly enriched in pleiotropic growth factors previously shown to be expressed in intestinal epithelium, such as follistatin 1 (*Fstl1*) (17) and WNT inhibitory factor 1 (*Wif1*) (18). Immunofluorescence analysis confirmed prominent FST1⁺ neurons and nerve fibers in the duodenum that were absent in the ileum and sparse within the colon (Fig. 1J and fig. S3J). These data reveal the region-specific translational profiles of iEANs that likely reflect the function of distinct intestinal regions.

Because the density and diversity of the gut microbiota increase from the proximal to distal intestine, we examined whether regionally distinct iEAN translational programs are partially influenced by the microbiota. To determine if microbial stimuli influence iEAN morphology, we first performed AdipoClear on whole-mount intestinal tissue followed by light-sheet microscopy of iEANs in the ileum and colon of germ-free (GF) or specific pathogen-free (SPF) mice. In both GF and SPF mice, iEANs were organized into distinct plexuses, and we observed vast mucosal innervation

¹Laboratory of Mucosal Immunology, The Rockefeller University, New York, NY, USA. ²Laboratory of Molecular Genetics, Howard Hughes Medical Institute, The Rockefeller University, New York, NY, USA. ³Laboratory of Neurogenetics and Behavior, Howard Hughes Medical Institute, The Rockefeller University, New York, NY, USA.

*These authors contributed equally to this work.

†Present address: Kallyope, New York, NY, USA.

‡Corresponding author. Email: pmuller@rockefeller.edu (P.A.M.); mucida@rockefeller.edu (D.M.)

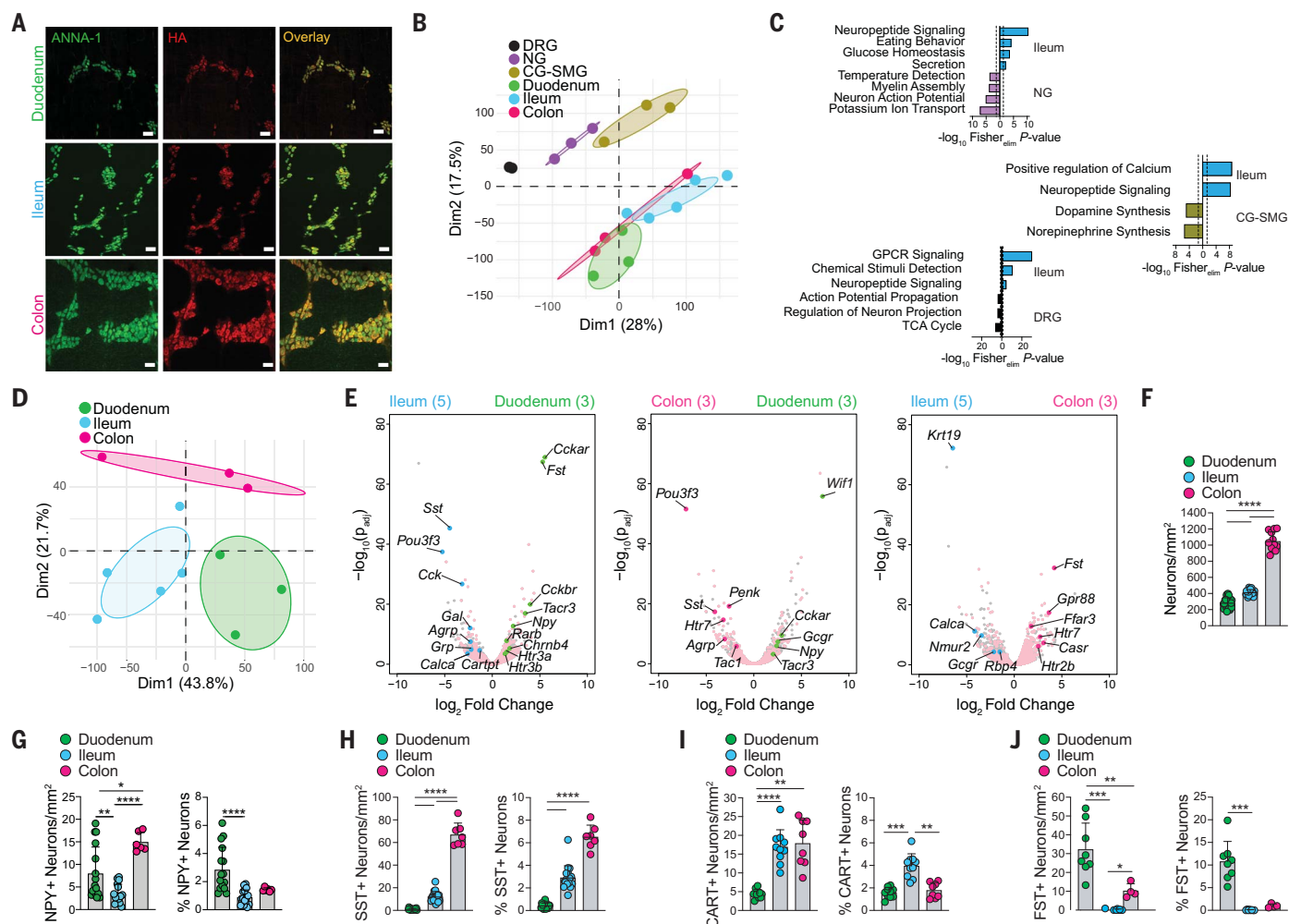


Fig. 1. TRAP-seq profiling of iEANS reveals anatomical region-specific differences. *Snapt25*^{RiboTag} SPF mice were analyzed in (A) to (E). (A) Whole-mount immunofluorescence (IF) of duodenum, ileum, and colon myenteric plexus using anti-neuronal nuclear (ANNA-1, green) and anti-HA (red) antibodies. Scale bars are 50 μ m. (B) Principal components analysis (PCA) of neuronal transcriptomes from DRG, NG, CG-SMG, duodenum, ileum, and colon. (C) Gene ontology (GO) pathways of differentially expressed genes (DEGs) [\log_2 fold change (FC) > 1, and adjusted P value (P_{adj}) < 0.05] enriched in ileum versus indicated ganglia. GPCR, G protein-coupled receptor; TCA cycle, tricarboxylic acid cycle. (D) PCA of neuronal transcriptomes from duodenum, ileum, and colon. (E) Volcano plots of

DEGs between myenteric iEANS. Pink dots represent all intestine neuronal immunoprecipitation (IP)-enriched transcripts; colored dots represent DEGs of interest between each pair of intestine segments. Sample numbers are indicated in parentheses. (F) Number of total iEANS in different gut regions. (G to J) Numbers and percentages of (G) NPY⁺, (H) SST⁺, (I) CART⁺, and (J) FST⁺ myenteric iEANS in different gut regions. * P < 0.05, ** P < 0.01, *** P < 0.001, and **** P < 0.0001; for numbers of iEANS in (F) to (J). Brown-Forsythe and Welch analysis of variance (ANOVA) with Dunnett's T3 multiple comparisons test was performed; for percentages of iEANS in (G) to (J), Kruskal-Wallis test with Dunn's multiple comparisons test was performed. Error bars indicate SD.

in the small and large intestines that extended into individual villi with fibers adjacent to the epithelium (Fig. 2A and movies S1 to S4). We noted that ileum villi are thin and blunted in GF animals, inherently leading to different nerve fiber structure (Fig. 2A and movies S1 to S4).

To determine whether the microbiota affects iEAN gene expression profiles along the intestine, we rederived *Snapt25*^{RiboTag} mice under GF conditions (fig. S4A). Analysis of TRAP-seq from duodenum, ileum, and colon myenteric iEANS of GF *Snapt25*^{RiboTag} mice revealed microbiota-dependent transcriptional changes in each region (Fig. 2, B and C). Al-

though no transcripts were significantly up-regulated in the duodenum in SPF mice compared with GF mice, 750 and 117 transcripts were significantly up-regulated in the ileum and colon, respectively (Fig. 2C). The absence of significant microbiota-dependent changes in the duodenum could be related to the decreased microbial density and diversity in this region. Furthermore, principal components analysis showed that duodenum, ileum, and colon samples from GF mice all clustered together with duodenum samples of SPF mice (Fig. 2B). To determine whether these distal regions gain a "duodenum-like" gene expres-

sion profile, we generated a list of transcripts enriched in SPF duodenum as compared with SPF ileum and colon (table S1). A subset of duodenum-enriched transcripts was up-regulated in the ileum, but not colon, of GF animals as compared with SPF animals (Fig. 2D). The third principal component also showed segregation of colon samples from the small intestine, which may reflect the presence of iEANS derived from sacral progenitors in the large intestine, or functional differences between colon and ileum (fig. S4B). Direct comparison between regions in GF mice also indicated segregation, suggesting that certain features of region-specific

iEAN programming are microbiota-independent (fig. S4C).

In the ileum and colon, we found microbiota-dependent transcripts encoding neuropeptides associated with neuro-immune cross-talk, such as *Nmu* (19); EAN physiological function, such as *Sst* or *Cartpt*; and functions outside of the intestine, like *Agrp* (colon only) (Fig. 2, C and E). SST and CART protein expression changes were confirmed by quantification of immunofluorescence images from GF and SPF mice (Fig. 2, F and G, and fig. S4, D to G). Quantification of iEANs in the myenteric plexus of GF and SPF mice also revealed a significant reduction in iEAN numbers in the duodenum and ileum, but not colon, of GF mice (Fig. 2H and fig. S4H). Finally, analysis of GF and SPF datasets using PASTAA (predicting associated transcription factors from annotated affinities) identified cAMP response element-binding protein (CREB) among the most enriched

transcription factors for the ileum and colon in SPF mice (fig. S4I). Because the level of phosphorylated CREB (pCREB) in neurons is often used as an indirect measure of activation and it is a mediator of neuropeptide transcription (20), we used immunofluorescence analysis of pCREB at serine-133, which is a key modification to induce gene transcription. We found a significant reduction of pCREB in the ileum myenteric plexus of GF mice compared with SPF mice (fig. S4, J and K), demonstrating that iEANs may be hypoexcitable under gnotobiotic conditions, as previously proposed (21), and providing a possible explanation for the reduction in neuropeptide transcripts observed.

To address whether altered neuropeptide levels and iEAN numbers in GF mice are the result of a developmental defect, we provided adult C57BL/6 GF mice with age- and sex-matched feces from SPF mice on a matched

GF diet (exGF). Colonization of 8-week-old GF animals with SPF feces was sufficient to increase the number of SST⁺ and CART⁺ neurons in the colon and ileum to levels similar to SPF animals after 2 weeks, as well as a notable increase in the density of SST⁺ and CART⁺ nerve fibers (Fig. 2, F and G, and fig. S4, L to O). We also noted that recolonization restored iEAN numbers in the ileum, whereas the colon remained unaffected by colonization (Fig. 2H). These results establish both regional differences and the microbial influence on iEAN numbers and gene expression profiles, particularly on neuropeptidergic coding.

Microbiota modulate iEAN numbers through NLRP6 and caspase 11

We next asked if microbiota-dependent changes in iEANs can be observed in SPF mice after administration of broad-spectrum antibiotics or if a microbiome must be absent from birth.

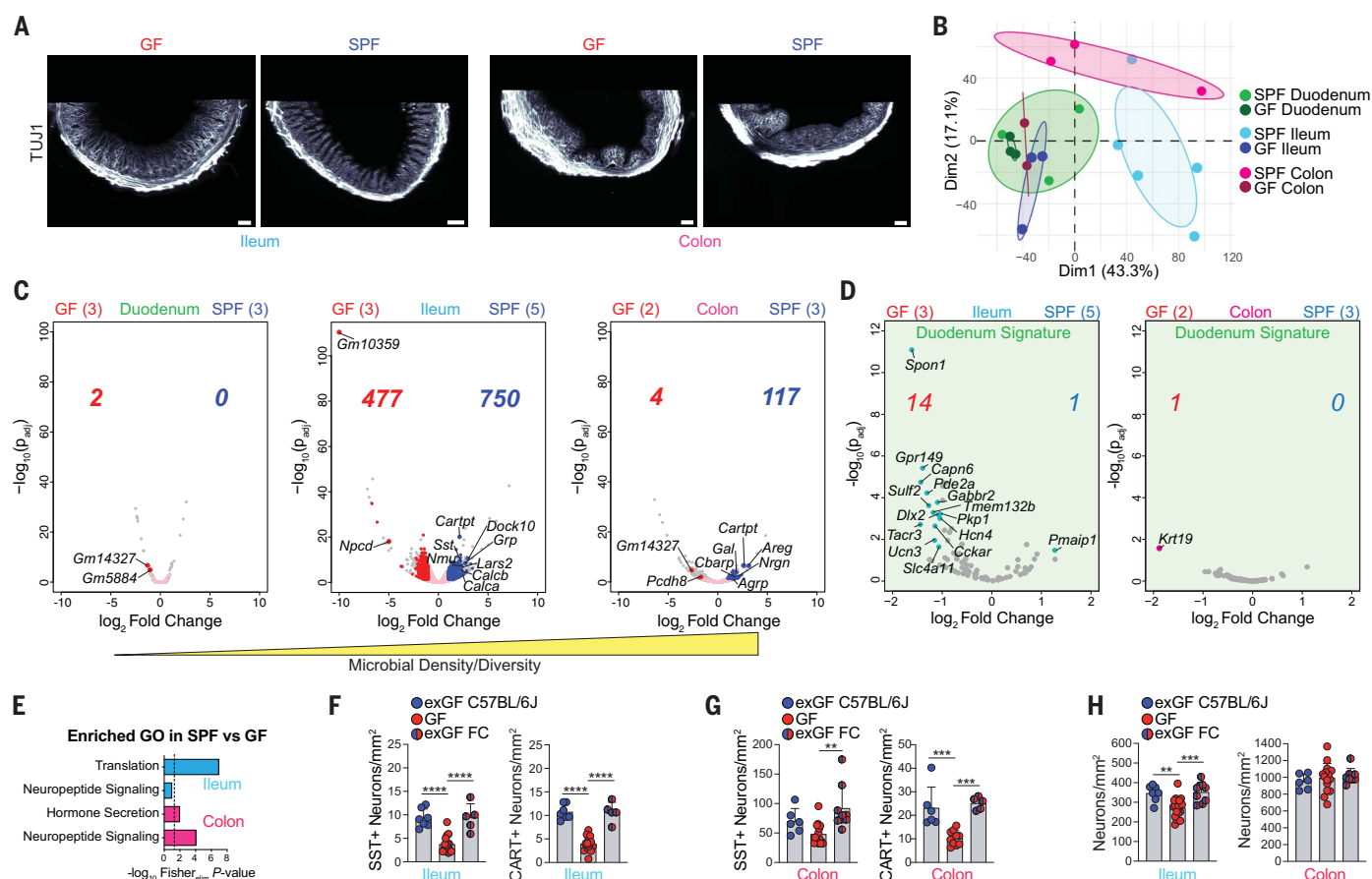


Fig. 2. Microbiota affect iEAN translomes in a compartmentalized manner.

(A) AdipoClear light-sheet images of ileum and colon of GF or SPF C57BL/6J mice using anti-TUJ1 antibody. Scale bars for ileum and GF colon are 200 μ m; scale bar for SPF colon is 100 μ m. (B) PCA of GF and SPF iEANs from duodenum, ileum, and colon. (C and D) Volcano plots of (C) duodenum, ileum, and colon iEAN DEGs between GF and SPF mice and (D) differentially expressed "duodenum signature" transcripts in ileum and colon iEANs of GF and SPF mice. Pink dots represent all intestine neuronal IP-enriched transcripts; colored dots and numbers represent significantly differentially expressed transcripts (\log_2 FC > 1, and P_{adj} < 0.05). Sample

numbers are indicated in parentheses. (E) GO pathways of DEGs enriched in SPF versus GF samples. In (B) to (E), *Snap25^{FluoTag}* mice were analyzed. (F and G) Numbers of SST⁺ and CART⁺ iEANs in (F) ileum and (G) colon of GF mice, exGF mice, and GF mice colonized with exGF feces (exGF FC). (H) Total iEANs in ileum (left) and colon (right) of GF, exGF, and exGF FC mice. ** P < 0.01, *** P < 0.001, and **** P < 0.0001; for numbers of SST⁺ iEANs in (F) and (G), CART⁺ iEANs in (F), and total iEANs in (H), one-way ANOVA with Tukey's multiple comparisons test was performed; for numbers of CART⁺ iEANs in (G), Brown-Forsythe and Welch ANOVA with Dunnett's T3 multiple comparisons test was performed. Error bars indicate SD.

We administered antibiotics (vancomycin, ampicillin, metronidazole, and neomycin) through drinking water to SPF mice for 2 weeks and detected a significant decrease in the number of iEANs in the ileum and colon but not in the duodenum (Fig. 3A and fig. S5A). We recently described an inflammasome-dependent pathway whereby caspase 11 (caspase 4 in humans) and NOD-like receptor family pyrin domain containing 6 (NLRP6) are key mediators of neuronal death after infection (22). To evaluate whether the iEAN reduction observed after microbiota depletion was also dependent on this pathway, *Casp11^{-/-}* *Casp11^{-/-}* (ICE^{-/-}) or *Casp11^{-/-}* mice were exposed to Splenda or antibiotics in the drinking water. Quantification of iEANs in the ileum of antibiotic-treated mice did not reveal iEAN loss in ICE^{-/-} or *Casp11^{-/-}* mice, suggesting an additional role for caspase 11 in the reduction of iEANs during dysbiosis (Fig. 3A and fig. S5, A to D). We confirmed that these changes in neuronal numbers were not the effect of morphological differences in the intestine induced by antibiotics or genotype (fig. S5, E to G). Furthermore, neuronal- and neuroendocrine-specific deletion (*Snap25*) of *Nlrp6* and *Casp11* may prevent loss of enteric neurons after antibiotic administration (Fig. 3, B and C). Importantly, this neuronal reduction was not permanent, because antibiotic withdrawal for 2 weeks resulted in the recovery of neuronal numbers to SPF levels (Fig. 3D). Treatment with vancomycin, ampicillin, or metronidazole alone, but not neomycin or a single dose of streptomycin,

also induced a reduction in total neuronal numbers, suggesting a possible role for specific bacteria in the physiological iEAN maintenance (Fig. 3E and fig. S5, H and I). Quantification of microbiota load after oral or intraperitoneal antibiotic administration, and subsequent neuronal quantification, further suggested that neuronal loss was induced by microbial depletion and not by direct antibiotic neurotoxicity or dysbiosis per se (fig. S5, J to M). We next examined the microbiota-modulated neuropeptide pathways that we identified in GF mice and analogously observed a significant decrease in number and percentage of SST⁺ and CART⁺ neurons in the ileum and colon, but not duodenum, after antibiotic treatment (Fig. 3F). Consistently, short-term microbial depletion by single-dose streptomycin administered to wild-type (WT) mice or continuous broad-spectrum antibiotic treatment of *Casp11^{-/-}*, *Casp11^{-/-}*, *Snap25^{Nlrp6}*, and *Snap25^{ΔCasp11}* mice did not affect neuropeptide-specific iEAN numbers in the ileum and colon (Fig. 3, F to H, and fig. S6, A to O). Given that neuropeptide expression can vary with drastic changes in nutrient availability during fasting (fig. S7, A to C), we confirmed that antibiotic treatment did not result in body weight change at the time of analysis, indicating that food intake was comparable between groups (fig. S7D). The above data establish that iEANs, including SST⁺ and CART⁺ neuropeptide subsets, can be tuned by the microbiota. Additionally, these analyses define a role for caspase 11 and the noncanonical inflamma-

some sensor NLRP6 in microbiota-mediated iEAN regulation.

Microbiota-modulated CART⁺ iEANs are viscerofugal and glucoregulatory

To test possible functional roles for microbiota-modulated iEANs in intestinal physiology, we focused on CART⁺, NPY⁺, and AGRP⁺ neuronal populations because of their distinct features. CART⁺ neurons are enriched in the ileum and colon and are bidirectionally modulated by the microbiota, and unlike SST, CART is not expressed by EECs in these gut regions (23). Meanwhile, AGRP⁺ neurons are particularly enriched in the colon and reduced in GF mice, and NPY⁺ neurons are enriched in the duodenum and not affected by the microbiota. These three neuropeptides are also expressed by neuronal populations in the hypothalamus that work in concert to regulate energy balance (24) and, as such, could potentially play a similar role in gut-specific circuits to influence feeding behavior. Whole-mount analysis of intestinal muscularis externa using RNA in situ hybridization confirmed the expression of *Npy* and *Cartpt* in the ileum and colon and *AgRP* in the midcolon (fig. S8, A to C). We obtained Cre lines corresponding to the three neuropeptides and validated *Cre*, *Cartpt*, *Npy*, and *AgRP* expression in the periphery using in situ hybridization (fig. S8, D to G). Because these neuropeptides are known to be expressed in both the periphery and central nervous system (CNS) (13, 24–26), we used a local retrograde viral delivery approach into the duodenum,

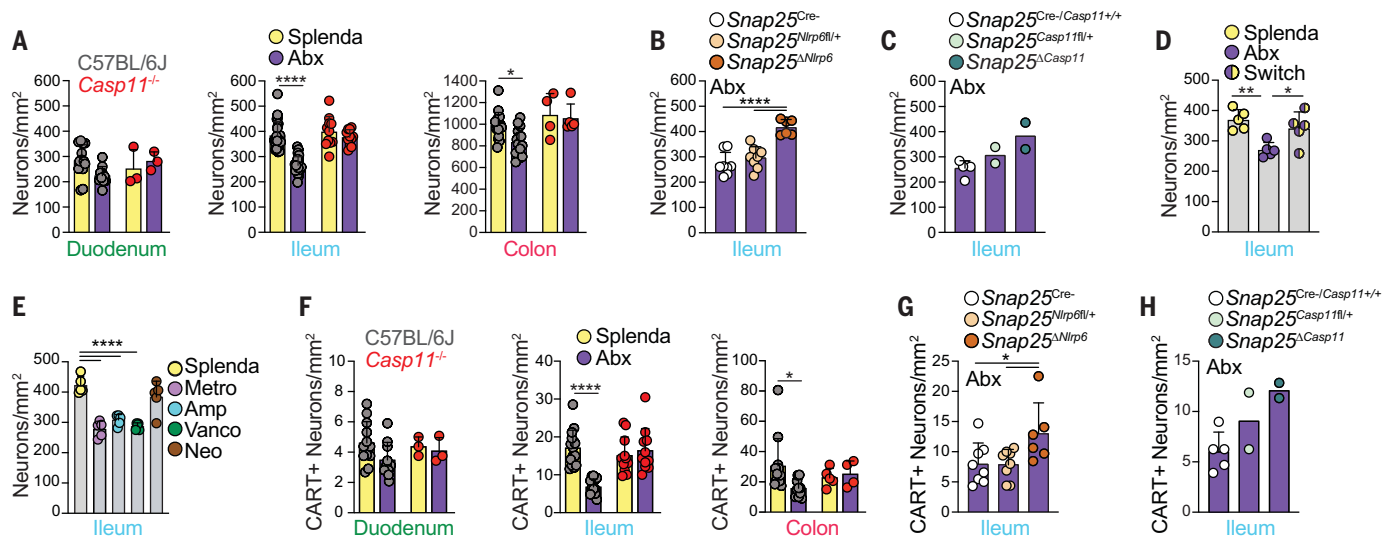


Fig. 3. iEAN loss after antibiotic treatment is mediated by NLRP6 and caspase 11. (A) Myenteric iEAN numbers in duodenum, ileum, and colon of C57BL/6J and *Casp11^{-/-}* mice treated with antibiotics (vancomycin, ampicillin, metronidazole, and neomycin, referred to collectively as Abx) or Splenda. (B and C) Ileal myenteric iEAN numbers for (B) *Snap25^{Nlrp6}* or (C) *Snap25^{ΔCasp11}* mice on Abx. (D) Ileal myenteric iEAN numbers for C57BL/6J SPF mice after 4 weeks on Abx or Splenda, or Abx followed by Splenda for 2 weeks each (Switch). (E) Ileal myenteric iEAN numbers for C57BL/6J SPF mice on

metronidazole (Metro), ampicillin (Amp), vancomycin (Vanco), neomycin (Neo), or Splenda. (F) CART⁺ myenteric iEAN numbers in duodenum, ileum, and colon of C57BL/6J and *Casp11^{-/-}* mice on Abx or Splenda. (G and H) CART⁺ ileal myenteric iEAN numbers for (G) *Snap25^{Nlrp6}* and control or (H) *Snap25^{ΔCasp11}* and control mice on Abx. *P < 0.05, **P < 0.01, and ****P < 0.0001; for (A) and (F), two-way ANOVA with Tukey's multiple comparisons test was performed; for (B), (D), (E), and (G), one-way ANOVA with Tukey's multiple comparisons test was performed. Error bars indicate SD.

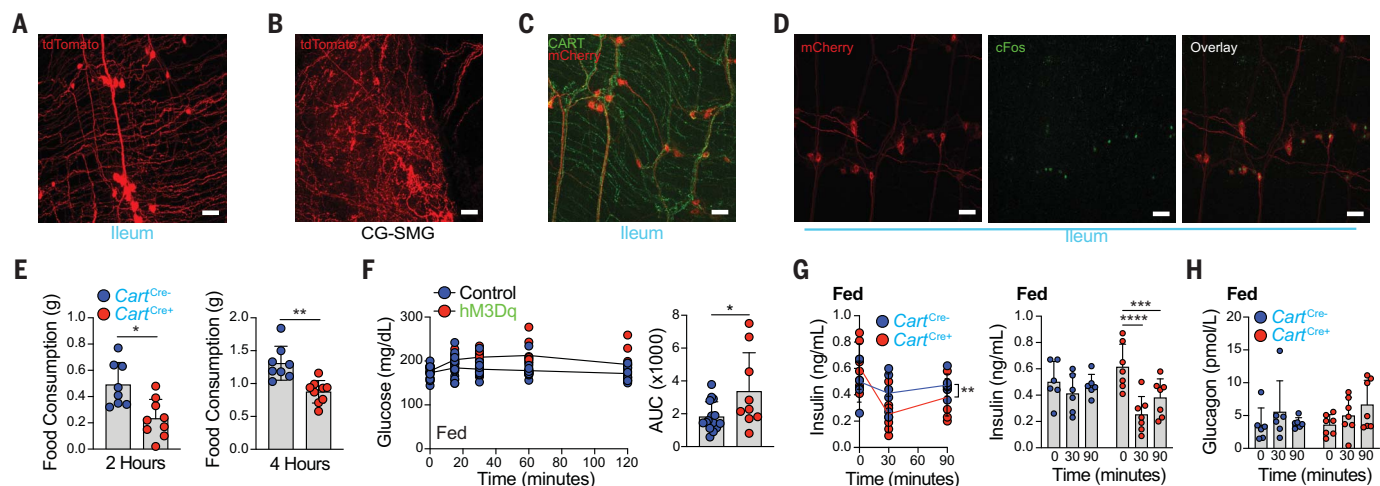


Fig. 4. CART⁺ iEANs in the distal intestine are viscerofugal and glucoregulatory. (A and B) Whole-mount IF image of the (A) ileum myenteric plexus (MP) and (B) CG-SMG of *Cart^{Cre+}* injected with AAVrg-FLEX-tdTomato into (A) ileum and (B) duodenum, ileum, and colon. (C and D) Whole-mount IF image of the ileum MP of *Cart^{Cre+}* mice injected with AAV9-hSyn-DIO-hM3Dq-mCherry into the ileum. (C) stained for CART (green) and mCherry (red) and (D) 3 hours after C21 administration, stained for mCherry (red) and cFos (green). (E) Food consumption at night 2 hours (left) and 4 hours (right) after C21 administration in *Cart^{Cre+}* and *Cart^{Cre-}* mice injected with AAV9 as in (C). (F) Blood glucose

levels after C21 administration (left) and area under curve (AUC) analysis (right) in fed *Cart^{Cre+}* and *Cart^{Cre-}* (control) mice injected with AAV9-hSyn-DIO-hM3Dq-mCherry or control AAV9-hSyn-DIO-mCherry into ileum and colon. (G and H) Plasma (G) insulin and (H) glucagon levels after C21 administration in *Cart^{Cre+}* and *Cart^{Cre-}* mice injected with AAV9-hSyn-DIO-hM3Dq-mCherry into ileum and colon. Scale bars in (A) to (D) are 50 μ m. **P* < 0.05, ***P* < 0.01, ****P* < 0.001, and *****P* < 0.0001; for (E) and (F), two-tailed unpaired Student's *t* test was performed; for (G), two-way (left) or one-way ANOVA (right) with Tukey's multiple comparisons test was performed. Error bars indicate SD.

ileum, and colon to guide us on subsequent gut-restricted adeno-associated virus (AAV) approaches. Injection of retrograde AAV (AAVrg)-FLEX-tdTomato into the intestine of *Cart^{Cre}*, *Npy^{Cre}*, and *Agrp^{Cre}* mice (generating *Cart^{Cre}*^{EAN-tdTomato}, *Npy^{Cre}*^{EAN-tdTomato}, and *Agrp^{Cre}*^{EAN-tdTomato}, respectively) revealed a prominent population of tdTomato⁺ neurons in the myenteric plexus of *Cart^{Cre}*^{EAN-tdTomato} and *Npy^{Cre}*^{EAN-tdTomato} mice (Fig. 4A and fig. S8, H and I). *Npy^{Cre}*^{EAN-tdTomato} and *Cart^{Cre}*^{EAN-tdTomato} neurons displayed considerable innervation of the circular and longitudinal smooth muscle within these segments of the intestine, with *Cart^{Cre}*^{EAN-tdTomato} also exhibiting dense interganglionic patterning (Fig. 4A and fig. S8, H and I). We found a sparse population of tdTomato⁺ neurons in the midcolon of *Agrp^{Cre}*^{EAN-tdTomato}, which exhibited muscular and interganglionic innervation (fig. S8J). We confirmed a lack of tdTomato expression in the submucosal plexus, NG, DRG, and CG-SMG in *Cart^{Cre}*^{EAN-tdTomato} and *Agrp^{Cre}*^{EAN-tdTomato} mice. We also observed a population of tdTomato⁺ neurons in the submucosal plexus and gut-projecting CG-SMG neurons in *Npy^{Cre}*^{EAN-tdTomato} mice (fig. S8K). Additionally, a significant number of tdTomato⁺ fibers were detected in the CG-SMG of *Cart^{Cre}*^{EAN-tdTomato} mice (Fig. 4B and fig. S8L), suggesting that some CART⁺ neurons are viscerofugal (iEAN projecting axons outside of the intestine and previously described as mechanosensitive) (27).

To directly modulate neuronal activity and assess the function of these intestine neuropeptide populations, we used a gut-restricted

chemogenetic approach by injecting excitatory DREADD (designer receptor exclusively activated by designer drugs) virus (AAV9-FLEX-Syn-hM3Dq-mCherry) into the distal ileum and proximal colon of *Cart^{Cre}* and *Npy^{Cre}* mice or into the midcolon of *Agrp^{Cre}* mice (Fig. 4, C and D, and fig. S9A). We found no change in total intestinal transit time for any of the three neuropeptide lines tested after administration of the DREADD ligand, compound 21 (C21), although changes in either small or large intestine motility separately cannot be ruled out (fig. S9, B to D). However, we observed a significant decrease in food consumption during day feeding at 1 and 2 hours, as well as during night feeding at 2 and 4 hours, after C21 injection in *Cart^{Cre}*^{EAN-hM3Dq} but not *Npy^{Cre}*^{EAN-hM3Dq} or *Agrp^{Cre}*^{EAN-hM3Dq} mice (Fig. 4E and fig. S9, E to G). We found no clear evidence for hM3Dq (mCherry) expression outside of the distal ileum and proximal colon, indicating that the observed changes in feeding behavior are dependent on iEAN-specific neuronal stimulation. We next evaluated whether the reduction in feeding was accompanied by acute changes in blood glucose or by glucoregulatory hormone levels that can regulate the activity of CNS nuclei that control feeding behavior (28). We assessed the effects of either excitatory (hM3Dq) or inhibitory (hM4Di) DREADD viruses in *Cart^{Cre}* mice, again injected into their distal ileum and proximal colon. Administration of C21 led to significantly higher blood glucose levels in *Cart^{Cre}*^{EAN-hM3Dq} mice than in control mice, whereas inhibition of these neurons in *Cart^{Cre}*^{EAN-hM4Di} mice did

not change blood glucose levels (Fig. 4F and fig. S9, H and I). On measurement of canonical glucoregulatory hormones, we found a significant decrease in insulin levels at 30 and 90 min after C21 administration to *Cart^{Cre}*^{EAN-hM3Dq} mice, whereas glucagon levels were not significantly altered (Fig. 4, G and H). These data indicate that stimulation of ileum and colon CART⁺ iEANs results in increased blood glucose and decreased insulin levels, with a subsequent reduction in food consumption.

We next asked how CART⁺ iEANs can exert their glucoregulatory function. One possible route could be through direct detection of signals coming from the epithelium. However, imaging analyses confirmed that CART⁺ neurons are not present in the submucosal plexus nor do they project to the epithelium (fig. S10, A and B, and movie S5). We confirmed their viscerofugal nature with viral anatomical and cholera toxin subunit B (CTB) tracing (Fig. 5, A and B, and movie S5). We also noted that some CART⁺ neurons appear to directly interact with other CART⁺ viscerofugal neurons (fig. S10C). These CART⁺ viscerofugal neurons send axonal projections to the CG-SMG, which in turn provides sympathetic innervation to several visceral organs, including the pancreas and liver (29, 30). Sympathetic innervation of the pancreatic islets can stimulate glucagon release and inhibit insulin secretion through adrenergic receptor engagement on alpha and beta cells, respectively (29). Sympathetic stimulation of the liver can drive gluconeogenesis and glycogenolysis through hepatocyte adrenergic receptor activation

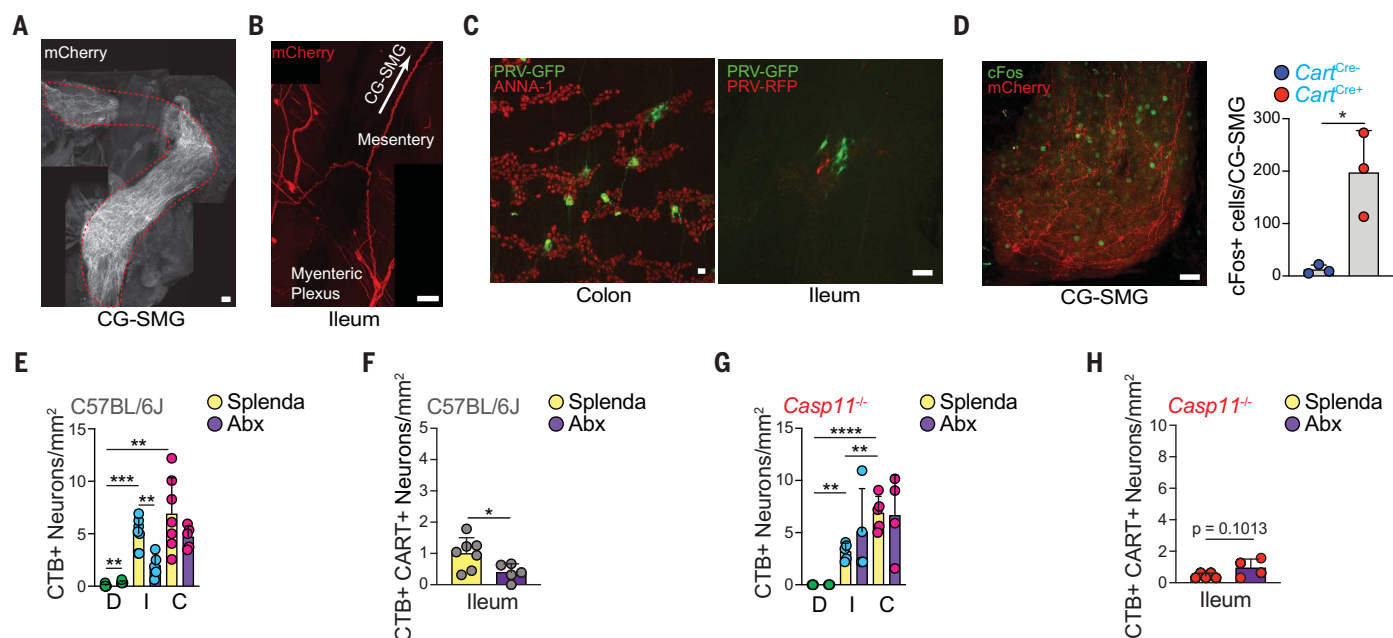


Fig. 5. CART⁺ viscerofugal neurons are polysynaptically connected to the liver and pancreas through the CG-SMG. (A and B) Whole-mount IF image of (A) CG-SMG and (B) ileum MP of *Cart^{Cre}* mice injected with AAV9-hSyn-DIO-hM3Dq-mCherry into ileum and colon. Scale bars are 100 μ m. (C) Whole-mount IF image of colon (left) and ileum MP (right) of SPF mice injected with PRV-GFP (pancreas) and PRV-RFP (liver). Scale bars are 50 μ m. (D) (Left) cFos (green) and mCherry (red) expression and (right) number of cFos⁺ neurons in the CG-SMG of *Cart^{Cre}* mice injected with AAV as in (A), 3 hours after C21 injection. Scale bar is 50 μ m. (E and G) CTB-AF647⁺ neuron numbers in duodenum, ileum,

and colon (labeled D, I, and C, respectively) of (E) C57BL/6J or (G) *Caspi11^{-/-}* mice treated with Splenda or antibiotics for 2 weeks after CTB injection into the CG-SMG. (F and H) CTB-AF647⁺ CART⁺ neuron numbers in the ileum of (F) C57BL/6J or (H) *Caspi11^{-/-}* mice treated with Splenda or antibiotics for 2 weeks after CTB injection into the CG-SMG. * $P < 0.05$, ** $P < 0.01$, *** $P < 0.001$, and **** $P < 0.0001$; for (D) and comparisons between Splenda and Abx [(E) to (H)], two-tailed Student's unpaired t test was performed; for Splenda group comparisons between gut segments [(E) and (G)], one-way ANOVA with Tukey's multiple comparisons test was performed. Error bars indicate SD.

(30). To determine if a synaptically connected circuit exists between the gut, sympathetic ganglia, and the pancreas or liver, we performed polysynaptic retrograde tracing using pseudo-rabies virus (PRV). We injected enhanced green fluorescent protein (EGFP)-expressing PRV into the pancreas and monomeric red fluorescent protein (mRFP)-expressing PRV into the parenchyma of the liver and assessed their synaptic connections to the CG-SMG and the intestine (fig. S10D). We detected viral spread or CTB labeling from both organs to the CG-SMG as early as 1 day after injection (fig. S10E). We observed GFP⁺ neurons in the myenteric plexuses of the duodenum, ileum, and colon 4 days after injection, with the highest concentration of neurons occurring in the colon and ileum, whereas RFP⁺ neurons were only observed in the ileum (Fig. 5C). We did not observe dual RFP and GFP labeling of ileal viscerofugal neurons, suggesting that the pancreas and liver are connected by two separate circuits. Together, we found that glucoregulatory organs are polysynaptically connected to the gut through viscerofugal neurons.

To investigate whether CART⁺ viscerofugal neuron activation could directly modulate sympathetic neuronal activity, we dissected the CG-SMG after C21 administration and measured cFos expression as an indicator of sympathetic

activation (5). As expected, we observed a significant increase in cFos expression in C21-injected *Cartpt^{EAN-hM3Dq}* mice as compared with control mice (Fig. 5D). Inhibition of catecholamine release by guanethidine prevented the increase in glucose levels in C21-treated *Cartpt^{EAN-hM3Dq}* mice, further suggesting the involvement of sympathetic activation (fig. S11A). However, guanethidine administration did not prevent the reduction in blood glucose induced by antibiotics (fig. S11B). To determine whether neuropeptide release affects glucose regulation, we exogenously administered CART peptide in antibiotic- or control-treated mice but observed no change in blood glucose (fig. S11C). However, we cannot definitively rule out a direct effect of CART peptide owing to incomplete knowledge of its role in the periphery and lack of identified receptor(s). Next, we investigated whether viscerofugal populations would be affected after microbial depletion. Indeed, retrograde fluorescent CTB tracing from the CG-SMG revealed a loss of CTB⁺ neurons, including CTB⁺ CART⁺ neurons, specifically in the ileum of antibiotic-treated mice, whereas only a minor reduction was observed in the colon and no changes were found in the sparsely retrograde-labeled duodenum (Fig. 5, E and F, and fig. S11, D to J). As expected, administration of antibiotics to

Caspi11^{-/-} mice did not result in loss of viscerofugal neurons (Fig. 5, G and H, and fig. S11, K to Q), demonstrating that their loss is also dependent on this noncanonical inflammasome effector. We conclude that intestinal CART⁺ neurons that can modulate blood glucose are viscerofugal and microbiota-dependent.

Modulation of glucose by the microbiota is dependent on CART⁺ iEANS

To confirm whether microbiota depletion affects glucose regulation, we analyzed antibiotic-treated SPF and GF mice and found a significant reduction in blood glucose, irrespective of diet or feeding state (Fig. 6, A and B, and fig. S12, A, B, and H), corroborating previous studies (31–33). Consistent with neuronal loss, ampicillin treatment alone specifically led to a reduction in blood glucose levels (Fig. 6C). Fasting blood glucose levels could be rescued after colonization with the microbiota from SPF animals, irrespective of genetic background (Fig. 6D and fig. S12, C to G). To determine whether microbiota-mediated changes in glucose levels are associated with loss of iEANS, we measured blood glucose levels in global or conditional knockout mice targeting NLRP6 and its downstream effector caspase 11, because these genotypes did not lose iEANS or CART⁺ iEANS after antibiotic treatment.

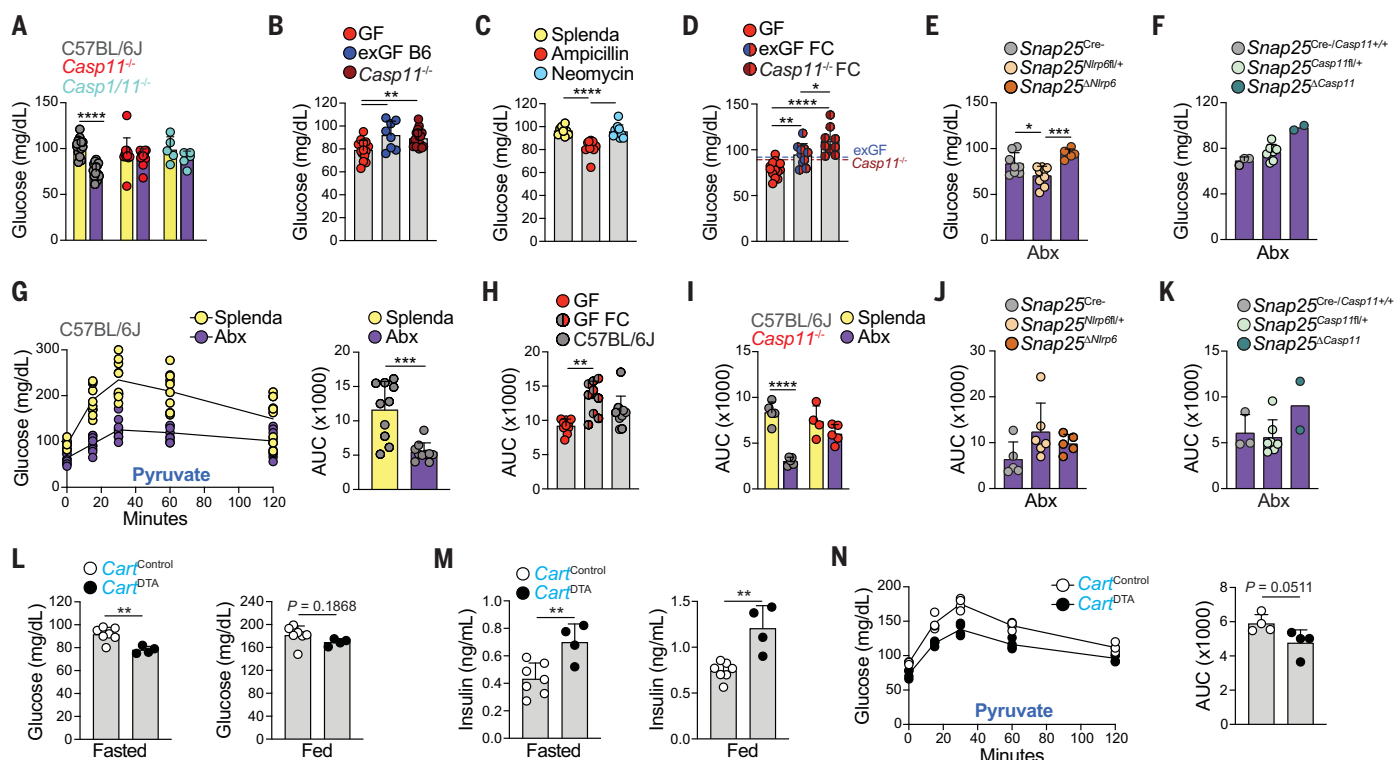


Fig. 6. Control of blood glucose is microbiota- and CART⁺ iEAN-dependent. (A to G) Blood glucose levels of fasted (A) C57BL/6J, *Casp11^{-/-}*, and *Casp11^{+/+}* mice treated with Abx or Splenda; (B) GF, exGF B6, and *Casp11^{-/-}* mice; (C) C57BL/6J mice on ampicillin, neomycin, or Splenda; (D) GF, exGF FC, and *Casp11^{-/-}* FC mice; (E) *Snap25^{Nlrp6}* mice on Abx; and (F) *Snap25^{ΔCasp11}* mice on Abx. (G) In (G), an intraperitoneal pyruvate tolerance test (IP-PTT) of fasted C57BL/6J mice on Abx or Splenda is presented, with blood glucose curves shown on the left and AUC analysis shown on the right. (H and I) IP-PTT AUC analysis of fasted (H) GF, GF FC, and C57BL/6J mice housed in bioexclusion isolator cages, and (I) C57BL/6J and *Casp11^{-/-}*

mice on Abx or Splenda. (J and K) IP-PTT AUC analysis of fasted (J) *Snap25^{Nlrp6}* and control or (K) *Snap25^{ΔCasp11}* and control mice on Abx. (L to N) *Cart^{Cre}* mice injected with AAV5-DTA into ileum and colon. Shown are (L) fasted (left) or fed (right) blood glucose levels, (M) fasted (left) or fed (right) plasma insulin levels, and (N) fasted IP-PTT blood glucose curves (left) and AUC analysis (right). * $P < 0.05$, ** $P < 0.01$, *** $P < 0.001$, **** $P < 0.0001$; for (G) and (L) to (N), two-tailed unpaired Student's *t* test was performed; for (B) to (E), (H), and (I), one-way ANOVA with Tukey's multiple comparisons test was performed; for (A) and (J), two-way ANOVA with Tukey's multiple comparisons test was performed. Error bars indicate SD.

We found that blood glucose levels in *Casp11^{-/-}*, *Casp11^{+/+}*, *Snap25^{Nlrp6}*, and *Snap25^{ΔCasp11}* mice were higher after antibiotic treatment as compared with that of WT and heterozygous controls (Fig. 6, A, E, and F, and fig. S12H).

We sought to determine which glucose-modulating pathways may be regulated by changes in the microbiota and, more specifically, whether the NLRP6–caspase 11 inflammasome pathway was involved. We first confirmed that glucagon-like peptide 1 (GLP-1) is increased in antibiotic-treated mice (31) but found that this increase was independent of caspase 11 (fig. S12I). Furthermore, administration of the GLP-1 receptor (GLP-1R)–blocking peptide Exendin-9-39 did not change fasting blood glucose levels of antibiotic-treated WT mice (fig. S12J). Additionally, insulin levels did not change after antibiotic treatment in WT, *Casp11^{-/-}*, and *Casp11^{+/+}* mice (fig. S12K). We next investigated whether pyruvate-induced gluconeogenesis (33) was affected by microbial manipulation. We observed significantly blunted temporal changes in blood glucose levels in GF and antibiotic-treated SPF mice

compared with control SPF mice after pyruvate administration (Fig. 6, G to I, and fig. S12, L and M). This effect was rescued by microbiota reconstitution in GF mice (Fig. 6H and fig. S12L) or global loss of caspase 11 in SPF mice (Fig. 6I and fig. S12N); additionally, it was partially rescued in SPF mice with neuronal-specific deletion of NLRP6 and caspase 11 (Fig. 6, J and K, and fig. S12, O and P). Of note, because we noticed antibiotic-resistant bacteria in global *Casp11^{-/-}* mice, these experiments were performed after antibiotic depletion followed by microbiota reconstitution from “antibiotic-resistant” feces from *Casp11^{-/-}* mice (fig. S12Q). These data suggest that iEANs can regulate liver gluconeogenesis independently of pancreatic insulin production or intestinal GLP-1 release in a microbiota- and inflammasome-dependent manner.

To directly test the necessity of gut CART⁺ neurons in glucose regulation, we injected AAV5-mCherry-FLEX-DTA into the ileum and colon of *Cartpt^{Cre}* mice to selectively delete intestinal CART⁺ neurons. Two weeks after CART⁺ neuron ablation, we observed a significant reduction

in blood glucose levels in fasted animals and a significant increase in insulin levels in fasted and fed animals compared with control AAV5 mice injected with control AAV5 (Fig. 6, L and M, and fig. S13, A and B). Similar to what was observed in GF and antibiotic-treated mice, we found a trend toward decreased gluconeogenic capacity (Fig. 6N). Thus, loss of CART⁺ viscerofugal iEANs decreases blood glucose levels, presumably owing to the lack of pancreas- and liver-specific sympathetic regulation. Gut CART⁺ neurons are therefore both sufficient and necessary to modulate blood glucose through glucoregulatory organs. Together, these experiments establish a microbiota-sensitive, polysynaptic glucoregulatory circuit connecting the gut, sympathetic ganglia, and the liver and pancreas (fig. S14).

Discussion

The gut microbiota influences several physiological and pathological processes, including local nutrient absorption and lipid metabolism (4, 31, 32, 34), as well as activation of the gut-associated and systemic immune systems (35). Dysbiosis or depletion of commensal

bacteria has also been shown to affect iEAN excitability and neurochemical code (21, 36), behavioral, or cognitive disorders (37). Our data revealed microbial- and region-dependent iEAN functional specialization with the potential to perform metabolic control independent of the CNS. Adding to our recent findings (22), here we describe a distinct role for the non-canonical inflammasome components NLRP6 and caspase 11 in controlling iEAN numbers and subsequent glucose regulation in response to microbiota levels. Although we do not know the ligand(s) that activate the noncanonical inflammasome pathway, bile acids may represent an interesting mediator (38) because we did not observe significant iEAN expression of direct pathogen recognition receptors, such as Toll-like receptors. It remains to be determined whether CART⁺ viscerofugal neurons respond to the presence of glucose in the intestinal lumen, release of neuropeptides, or the movement of fecal matter. It will also be important to determine how CART⁺ viscerofugal neurons are functionally connected to potential sensors such as intrinsic primary afferents, EECs, or mechanosensitive populations and the downstream neuronal populations required to perform glucoregulatory functions (39, 40). Finally, the ability of viscerofugal neurons in the distal ileum and proximal colon to increase blood glucose through a peripheral circuit warrants additional investigations into CNS-independent iEAN circuits. Because we focused on the functional characterization of selected neuropeptides in this study, it will be important to further explore if additional microbiota-modulated and/or microbiota-independent iEAN neuropeptide pathways play complementary or redundant roles in GI physiology, including feeding behavior (3, 32, 36, 39, 40). Targeting peripheral-restricted circuits, such as the one uncovered here, could bypass undesirable CNS effects for the treatment of metabolic disorders, such as type 2 diabetes.

Note added in proof: Our final mouse experiments were substantially affected by Rockefeller

coronavirus disease 2019 (COVID-19) lab closures, and thus we acknowledge that our initial sample sizes for *Snapt25^{ΔCasp11}* were below the standard for an animal experiment, despite two independent experiments having been run. In the time between the First Release and print publication, we were able to complete a final antibiotic treatment experiment in *Snapt25^{ΔCasp11}* mice. We present these findings with increased *n* in fig. S15.

REFERENCES AND NOTES

1. E. A. Mayer, *Nat. Rev. Neurosci.* **12**, 453–466 (2011).
2. J. B. Furness, L. R. Rivera, H. J. Cho, D. M. Bravo, B. Callaghan, *Nat. Rev. Gastroenterol. Hepatol.* **10**, 729–740 (2013).
3. H. Veiga-Fernandes, D. Mucida, *Cell* **165**, 801–811 (2016).
4. V. K. Ridaura et al., *Science* **341**, 1241214 (2013).
5. P. A. Muller et al., *Nature* **583**, 441–446 (2020).
6. Q. Sang, H. M. Young, *Cell Tissue Res.* **284**, 39–53 (1996).
7. F. M. Gribble, F. Reimann, *Annu. Rev. Physiol.* **78**, 277–299 (2016).
8. D. H. Teitelbaum, T. M. O'Dorisio, W. E. Perkins, T. S. Gaginella, *Am. J. Physiol.* **246**, G509–G514 (1984).
9. E. Ekblad, M. Kuhar, N. Wierup, F. Sundler, *Neurogastroenterol. Motil.* **15**, 545–557 (2003).
10. A. Lecci, M. Altamura, A. Capriati, C. A. Maggi, *Eur. Rev. Med. Pharmacol. Sci.* **12** (suppl. 1), 69–80 (2008).
11. P. Holzer, *Regul. Pept.* **155**, 11–17 (2009).
12. L. P. Degen et al., *Gastroenterology* **120**, 361–368 (2001).
13. J. R. Grider, *J. Pharmacol. Exp. Ther.* **307**, 460–467 (2003).
14. K. N. Browning, G. M. Lees, *Neurogastroenterol. Motil.* **12**, 33–41 (2000).
15. O. J. Mace, B. Tehan, F. Marshall, *Pharmacol. Res. Perspect.* **3**, e00155 (2015).
16. K. Makowska et al., *C. R. Biol.* **341**, 325–333 (2018).
17. K. Sonoyama, S. Rutatip, T. Kasai, *Am. J. Physiol. Gastrointest. Liver Physiol.* **278**, G89–G97 (2000).
18. T. Byun et al., *J. Clin. Pathol.* **58**, 515–519 (2005).
19. V. Cardoso et al., *Nature* **549**, 277–281 (2017).
20. V. Lakhina et al., *Neuron* **85**, 330–345 (2015).
21. K. A. McVey Neufeld, A. Perez-Burgos, Y. K. Mao, J. Bienenstock, W. A. Kunze, *Neurogastroenterol. Motil.* **27**, 627–636 (2015).
22. F. Matheis et al., *Cell* **180**, 64–78.e16 (2020).
23. A. R. Gunawardene, B. M. Corfe, C. A. Staton, *Int. J. Exp. Pathol.* **92**, 219–231 (2011).
24. M. J. Waterson, T. L. Horvath, *Cell Metab.* **22**, 962–970 (2015).
25. R. Gupta, Y. Ma, M. Wang, M. D. Whim, *Endocrinology* **158**, 2572–2584 (2017).
26. X. Yuan, Y. Huang, S. Shah, H. Wu, L. Gautron, *eNeuro* **3**, ENEURO.0174-16.2016 (2016).
27. T. J. Hibberd, V. P. Zagorodnyuk, N. J. Spencer, S. J. Brookes, *Neuroscience* **225**, 118–129 (2012).

28. J. Havrankova, J. Roth, M. Brownstein, *Nature* **272**, 827–829 (1978).
29. J. A. Love, E. Yi, T. G. Smith, *Auton. Neurosci.* **133**, 19–34 (2007).
30. K. Mizuno, Y. Ueno, *Hepatol. Res.* **47**, 160–165 (2017).
31. A. Zarrinpar et al., *Nat. Commun.* **9**, 2872 (2018).
32. A. M. Martin et al., *Proc. Natl. Acad. Sci. U.S.A.* **116**, 19802–19804 (2019).
33. T. I. Krisko et al., *Cell Metab.* **31**, 592–604.e9 (2020).
34. T. Korem et al., *Cell Metab.* **25**, 1243–1253.e5 (2017).
35. K. Honda, D. R. Littman, *Nature* **535**, 75–84 (2016).
36. J. M. Yano et al., *Cell* **161**, 264–276 (2015).
37. S. Kim et al., *Nature* **549**, 528–532 (2017).
38. M. Levy et al., *Cell* **163**, 1428–1443 (2015).
39. M. M. Kaelberer et al., *Science* **361**, eaat5236 (2018).
40. W. Han et al., *Cell* **175**, 665–678.e23 (2018).

ACKNOWLEDGMENTS

We thank all Mucida Lab members, the Bio-imaging and Genomics Centers, and Rockefeller University employees for their continuous assistance; and A. Rogoz and S. Gonzalez for the maintenance of mice. We thank J. Friedman for the generous use of lab equipment and resources. We also thank A. Lockhart, G. Donaldson, and the Nussenzweig, Victoria, and Lafaille labs for fruitful discussions. **Funding:** This work was supported by NIH P40 OD010996 (Core), Gilliam HHMI (V.J.), NIH UL1TR001866 (P.A.M. and D.M.), and NIH F31 DK112601; Philip M. Levine (P.A.M.), Anderson Graduate (F.M.), and Kavli fellowships (P.A.M. and M.S.); NIDDK grant K99 DK120869; the Robertson Therapeutic Development Fund (M.S.); the Burroughs Wellcome Fund; the Kenneth Rainin Foundation; the Food Allergy FARE/FASI Consortium; and NIH R01DK126407 and Transformative R01DK116646 (D.M.). **Author contributions:** P.A.M. initiated, designed, performed, and helped supervise the research and wrote the manuscript. F.M. and M.S. designed and performed experiments. Z.K. performed experiments. V.J. performed part of the RNA-seq analysis. D.M. initiated, designed, and supervised the research and wrote the manuscript. All authors revised and edited the manuscript and figures. **Competing interests:** The authors declare no competing financial interests. **Data and materials availability:** TRAP-seq data for extrinsic ganglia and intestine segments were previously deposited in the Gene Expression Omnibus under accession numbers GSE145986 and GSE156142, respectively.

SUPPLEMENTARY MATERIALS

science.sciencemag.org/content/370/6514/314/suppl/DC1
Materials and Methods
Figs. S1 to S15
Table S1
References (41–51)
MDAR Reproducibility Checklist
Movies S1 to S5

[View/request a protocol for this paper from Bio-protocol.](#)

14 July 2020; accepted 18 August 2020
Published online 27 August 2020
10.1126/science.abd6176

MORPHOGENS

Patterning and growth control in vivo by an engineered GFP gradient

Kristina S. Stapornwongkul¹, Marc de Gennes¹, Luca Cocconi^{1,2},
Guillaume Salbreux^{1*†}, Jean-Paul Vincent^{1*}

Morphogen gradients provide positional information during development. To uncover the minimal requirements for morphogen gradient formation, we have engineered a synthetic morphogen in *Drosophila* wing primordia. We show that an inert protein, green fluorescent protein (GFP), can form a detectable diffusion-based gradient in the presence of surface-associated anti-GFP nanobodies, which modulate the gradient by trapping the ligand and limiting leakage from the tissue. We next fused anti-GFP nanobodies to the receptors of Dpp, a natural morphogen, to render them responsive to extracellular GFP. In the presence of these engineered receptors, GFP could replace Dpp to organize patterning and growth in vivo. Concomitant expression of glycosylphosphatidylinositol (GPI)-anchored nonsignaling receptors further improved patterning, to near-wild-type quality. Theoretical arguments suggest that GPI anchorage could be important for these receptors to expand the gradient length scale while at the same time reducing leakage.

During development, morphogens provide positional information by forming long-range concentration gradients. Despite the importance of morphogens, there is still no consensus on how they spread within tissues (1). The most parsimonious view is that morphogens travel by diffusion (1–3). However, epithelia, monolayered sheets of cells, present a particular challenge for diffusion-based mechanisms, as ligand leakage is expected to occur, thus compromising planar gradient formation (4) and possibly affecting the development of other tissues and organs (5).

Much of our knowledge about the formation and interpretation of morphogen gradients in epithelia comes from studies of the bone morphogenetic protein (BMP) homolog Decapentaplegic (Dpp) in wing imaginal discs of *Drosophila*. In these epithelial pouches, Dpp is produced by a stripe of cells and spreads to form a gradient that organizes growth and patterning along the anterior–posterior (A/P) axis (6). It has been suggested that Dpp spreads by planar transcytosis or on specialized filopodia called cytonemes (7, 8). Both mechanisms would ensure planar transport; however, so far, direct functional evidence remains scant. By contrast, there is extensive genetic evidence for the requirement of glypicans in morphogen transport (9–11). It has been suggested that morphogens can piggyback on laterally diffusing glypicans and pass from cell to cell through cycles of dissociation and reassociation, thus remaining within the plane of the epithelium. Here, we have taken a forward engineering

approach to investigate whether an inert protein can form a diffusion-based gradient in the basolateral space of a developing pseudostratified epithelium and specify positional information.

Extracellular binders reveal a diffusion-based gradient

Synthetic approaches have become a powerful tool to uncover the key features of natural processes (12, 13). To assess the ability of an inert protein to form a gradient in wing imaginal discs of *Drosophila*, we engineered flies to express, from a localized source, green fluorescent protein (GFP) appended with a secretion targeting signal (SecGFP). This was achieved by integrating SecGFP coding DNA into the *patched* (*ptc*) locus (fig. S1), a gene which, like *dpp*, is expressed along the A/P boundary (Fig. 1A). GFP was detectable, albeit weakly, in the expression domain (Fig. 1, B and C, no binders). GFP fluorescence was also present uniformly in the peripodial space, an enclosed lumen on the epithelium's apical side. By contrast, the basolateral space was devoid of detectable GFP, most likely because it is exposed to the larval circulation, which could provide an escape route (fig. S2A). Indeed, GFP can cross the basal lamina to and from the hemolymph (fig. S2), and leakage could therefore prevent locally expressed GFP from forming a detectable gradient in the basolateral space. Natural morphogens, which form gradients, are known to bind various receptors and extracellular components (11). We therefore asked whether adding GFP-binding species in the extracellular space would reduce leakage and enable the formation of a detectable gradient in SecGFP-expressing wing imaginal discs.

Extracellular GFP-binding proteins are readily engineered by fusing a transmembrane protein (e.g., human CD8) to one of the many charac-

terized anti-GFP nanobodies (14), such as GBP1 (also known as vhhGFP4), which binds GFP with a dissociation constant (K_d) of 0.23 nM (15, 16); we refer to this antibody as Nb1^{high}. DNA encoding this fusion protein (Nb1^{high}CD8) was knocked into the *hedgehog* (*hh*) locus so that it could be expressed at a physiological level in a domain that abuts the *ptc* expression domain (Fig. 1A, gray shading), where SecGFP is produced. In the presence of both genetic modifications, a gradient of GFP fluorescence was readily detectable (Fig. 1, B and C, *hh-Nb1^{high}CD8*) in both the basolateral and apical regions. Here, we focused on the basolateral gradient; a discussion of the apical gradient can be found in fig. S3. The basolateral GFP profile (Fig. 1D, green curve) differed somewhat from a classic exponential, with a shoulder near the source and a nonzero tail far from the source (length scales and nonzero tail values are listed in table S1). Because GFP can diffuse in and out of imaginal discs, we considered the possibility that the nonzero tail could arise from GFP that escaped into the hemolymph (GFP^{hemo}). This was tested by trapping GFP in the hemolymph with Nb1^{high}CD8 expressed at the surface of the fat body, a sprawling organ that lines the body cavity (fig. S2A). In the resulting imaginal discs, the GFP profile decayed all the way to background level, showing that the tail indeed originated from the hemolymph (Fig. 1, C and D, purple curve). In conclusion, a single extracellular binding species reveals the gradient of an inert protein in vivo, but leakage in the hemolymph occurs and interferes with the gradient's shape, most obviously far from the source, at the tail end of the gradient.

Key parameters of gradient formation

Having established that an inert protein can form a gradient in a developing epithelium, we set out to investigate the importance of the surface binders' affinity for GFP. To ask if the high affinity of Nb1 for GFP (0.23 nM) is needed for a detectable gradient to form, this parameter was changed by using, as an extracellular binder, LaG3, which binds GFP with a K_d of 25 nM (17); we refer to this protein as Nb^{low}. In imaginal discs carrying *ptc-SecGFP* and *hh-Nb^{low}CD8*, GFP fluorescence was above background but not detectably graded (Fig. 1, C and D, compare blue and black curves; fig. S4 informs a discussion of Nb-mediated GFP fluorescence boosting). This indicated that a low-affinity binder can trap extracellular GFP, but also that sufficiently high affinity is needed for a meaningful gradient of surface-associated GFP to form.

To formalize the role of extracellular binders and leakage in GFP gradient formation, we devised a diffusion–degradation–leakage mathematical model (Fig. 2A and supplementary text), building on previous work (18, 19). Free

¹The Francis Crick Institute, 1 Midland Road, London NW1 1AT, UK. ²Imperial College, Department of Mathematics, London, UK. *Corresponding author. Email: jp.vincent@crick.ac.uk (J.-P.V.); guillaume.salbreux@crick.ac.uk (G.S.)

[†]Present address: Department of Genetics and Evolution, University of Geneva, Quai Ernest-Ansermet 30, 1205 Geneva, Switzerland.

GFP was assumed to diffuse in the intercellular space with a diffusion constant D and to bind and unbind at rates k_{on} and k_{off} to receptors internalized and degraded at rate k . The flux between hemolymph and the epithelium was assumed to be driven by the concentration difference between them, with a proportionality coefficient κ . At steady state, in the posterior compartment (where the receptors are expressed), the concentrations of free (c) and receptor-bound (n_b) GFP follow these equations:

$$0 = D\partial_x^2 c - \frac{k}{h} n_b - \kappa(c - c_H) \quad (1)$$

$$n_b = n_T \frac{k_{\text{on}} c}{k_{\text{off}} + k_{\text{on}} c + k} \quad (2)$$

where n_T refers to the density of receptors at the cell surface, h is the intercellular distance, and c_H is the free GFP concentration in the hemolymph. Analytical exploration of the model showed that it recapitulated the essential features of the bound GFP gradient profile (Fig. 2B and fig. S5): (i) close to the source, receptor saturation leads to a shoulder; (ii) further away from the source, the profile decays on a length scale determined by the diffusion constant, the degradation of receptors, and leakage to the hemolymph; (iii) far from the source, the concentration of GFP remains at a constant nonzero value that depends on the hemolymph GFP concentration.

We then tested whether the model, and its consideration of leakage in particular, could quantitatively account for observed experimental profiles. To derive the concentration c_H of GFP in the hemolymph, we surmised that it is set by the balance between input from tissue leakage and loss by degradation in the hemolymph (k_H) (supplementary text, where we also discuss the contribution of other larval tissues that produce and degrade the ligand). Parameters were chosen from reasonable estimates or published data, with the remaining unknown parameters obtained from a fit to experimental curves, as described in table S2. Our fitting procedure indicated a substantial leakage rate, κ , of $\sim 1/(13 \text{ s})$. Comparison of Figs. 2C and 1D shows that the model provides a suitable framework to rationalize experimental observations. The effect of reducing affinity was recapitulated by setting this parameter to that measured for Nb^{low} (Fig. 2C, blue curve). Being a poor binder, $\text{Nb}^{\text{low}}\text{CD8}$ is unable to trap much GFP at the cell surface, reducing the amplitude of the gradient near the source. Consequently, $\text{Nb}^{\text{low}}\text{CD8}$ takes up and degrades GFP at a relatively low rate, leading to increased leakage (supplementary text, section 1.5). Thus, lowering ligand–binder affinity adversely affects the gradient both by reducing gradient amplitude and by increasing

the concentration of GFP in the hemolymph. The model also replicated the effect of the fat body trap by increasing the hemolymph degradation rate ~ 20 -fold (Fig. 2C, purple curve).

The model could also be used for de novo predictions. With the parameters determined above, it predicted that increasing ligand production at the source should lead to gradient extension as well as flattening near the source because of saturation (fig. S6A). This was indeed found experimentally in imaginal discs overexpressing SecGFP under the control of *ptc-Gal4* (fig. S6, B to D). Also confirmed experimentally was the prediction that increasing receptor expression (achieved by boosting the

level of $\text{Nb}^{\text{high}}\text{CD8}$ ~ 20 -fold, with *hh-Gal4* and *UAS-Nb1^{high}CD8*) (fig. S7A illustrates the quantification) would lead to a steepening of the gradient and an increase in GFP level near the source, although the latter was not as marked in the experiment as in the model (Fig. 3, compare A and C). Both model and experiment showed a reduced nonzero tail in this condition, confirming that receptor-mediated internalization contributes to limiting leakage into the hemolymph. Therefore, increasing ligand–receptor avidity could contribute to reducing the amount of GFP^{hemo} flowing back in the tissue, although this could be at the cost of a reduced range.

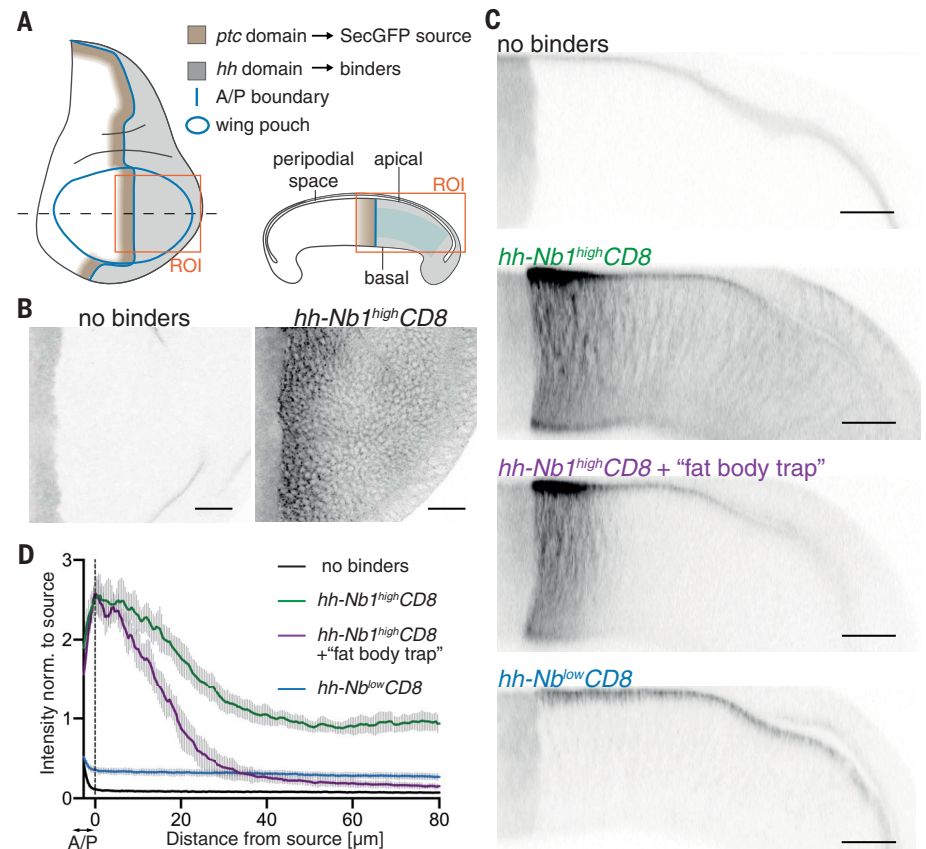


Fig. 1. Establishment of a GFP gradient in a developing epithelium. (A) Schematic representation of a wing imaginal disc of *Drosophila*. SecGFP is expressed under the control of the *ptc* promoter (brown), and a membrane-tethered anti-GFP nanobody is expressed under the control of the *hh* promoter (gray). The region of interest (ROI) indicates the areas depicted in (B) and (C). Blue shading indicates the region used to generate the profiles shown in (D). (B) In the absence of binders, SecGFP can be seen at the source but is not detectable in basolateral focal planes. Upon expression of high-affinity binders in the posterior compartment (*hh-Nb1^{high}CD8*), a gradient is readily seen. (C) Cross sections of imaginal discs expressing SecGFP in the *ptc* domain show that, in the absence of binders, GFP is detectable in the peripodial space but not in the basolateral space. In the presence of binders (*hh-Nb1^{high}CD8*), a gradient can be seen in the basolateral space but with a nonzero tail, which is largely abrogated by concomitant activation of *UAS-Nb1^{high}CD8* in the fat body (+ fat body trap). Only a shallow basolateral gradient is detected when a low-affinity binder is expressed (*hh-Nb1^{low}CD8*). (D) Fluorescence intensity profiles derived from preparations like those shown in (C). The vertical dotted line marks the estimated posterior edge of the source. The numbers of discs analyzed are as follows: no binders, $n = 10$; *hh-Nb1^{high}CD8*, $n = 11$; *hh-Nb1^{high}CD8* + fat body trap, $n = 7$; *hh-Nb1^{low}CD8*, $n = 10$. Scale bars, 20 μm .

Engineering a GFP-dependent signaling gradient in vivo

In the previous section, we identified minimal conditions for an inert protein to form a gradient along the plane of a developing epithelium. We

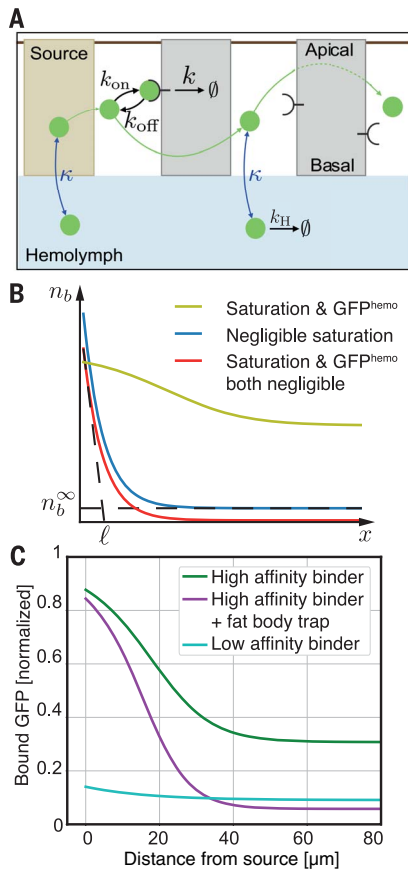


Fig. 2. A diffusion-degradation-leakage model for GFP gradient formation. (A) Schematic representation of the model for gradient formation. Parameters are described in the main text and supplementary text. (B) Main features of bound GFP profiles predicted by the model using parameters listed in table S2 (unless specified otherwise). The yellow-green curve shows the profile exhibiting receptor saturation near the source and a nonzero tail due to GFP^{hemo} (ligand production rate $j = 0.5 \text{ nM/s}$, $n_T = 100 \text{ nM}$). The blue curve shows that without saturation, the gradient is an exponential with a nonzero tail, $n_b^0 \leq n_T c_H k_{on}/k_{off}$, and a decay length $l = \sqrt{D/(k_r + \kappa)}$ that depends on diffusion, effective degradation with rate k_r , and leakage with rate κ ($j = 3 \cdot 10^{-4} \text{ nM/s}$, $n_T = 3 \cdot 10^4 \text{ nM}$). The red curve shows that the ligand concentration set to zero in the hemolymph abolishes the nonzero tail (blue curve with $c_H = 0$). The supplementary text, section 1.3, provides full parameter definitions. (C) Bound GFP profiles normalized to the total concentration of receptors. The blue and green curves were obtained with the known on- and off-rates for the low- and high-affinity receptors, respectively. The purple curve was obtained by increasing degradation in the hemolymph. Compare to corresponding experimental curves in Fig. 1D.

next asked if this gradient could provide positional information. The best-characterized morphogen in wing imaginal discs is Dpp, which promotes growth and specifies the position of veins along the A/P axis. As a first step toward asking if GFP could substitute for Dpp in vivo, we engineered the Dpp receptors Thickveins (Tkv) and Punt (Put) to render them responsive to GFP. Normally, Dpp dimers bind to two pairs of Tkv and Put, leading to phosphorylation of Mad (20) and transcriptional repression of the *brinker* gene (*brk*) (21). The resulting inverse Brk gradient in turn controls the nested expression of target genes such as *spalt* (*sal*) and *optomotor-blind* (*omb*) (22, 23) (Fig. 4A). We reasoned that GFP dimers might initiate the same signaling cascade if Tkv and Put were fused to anti-GFP nanobodies [GBP1 (referred to here as Nb1^{high}) and GBP6 (here called Nb2^{high})] that recognize nonoverlapping epitopes (16, 24) (fig. S8A). We created plasmids to express Nb2^{high}Tkv and Nb1^{high}Put and co-transfected them in S2 cells. Addition of GFP dimers (or monomers) to the culture medium led to accumulation of phospho-Mad (pMad), suggesting that the chimeric receptors can be activated by GFP (fig. S8B), although we cannot be sure that the signaling kinetics normally achieved by the natural ligand were entirely recapitulated.

On the basis of these encouraging results with cultured cells, we created a transgene that expresses, in a Flippase (Flp)-dependent manner, both engineered receptors under the control of the *ubiquitin* (*ubi*) promoter (Fig. 4B). This transgene, *ubi-[-STOP>Nb2^{high}Tkv 2A Nb1^{high}Put]*, where > indicates Flp recombination targets, is referred to here as SR (for signaling receptors). We also developed a *dpp* allele that can be inactivated but at the same time be made to express secreted GFP dimers upon Flp expression (*dpp-[-Dpp>SecGFP:GFP]*) (Fig. 4C; validated in fig. S9). First, we used the previously described *dpp-[-Dpp>]* allele (25) to confirm that inactivation of *Dpp* throughout the wing primordium with *rotund-Gal4* (*rn-Gal4*) and *UAS-Flp* abrogated growth and patterning, even in the presence of GFP-responsive receptors (Fig. 4D, column 2). Crucially, with *dpp-[-Dpp>SecGFP:GFP]*, which produces GFP upon *Dpp* inactivation, recognizably patterned wings developed (Fig. 4D, column 3). Note that no GFP gradient was detectable in this genetic background, perhaps because of rapid internalization and degradation of GFP by the signaling receptors. The rescuing activity of secreted GFP dimers was further assessed in imaginal discs by staining for various markers of Dpp signaling. pMad immunoreactivity was unexpectedly low in the GFP-producing cells (fig. S10). Most relevant to this study, however, signaling activity was graded on either side of the source, including in the posterior compartment, which relies entirely on ligand diffusion

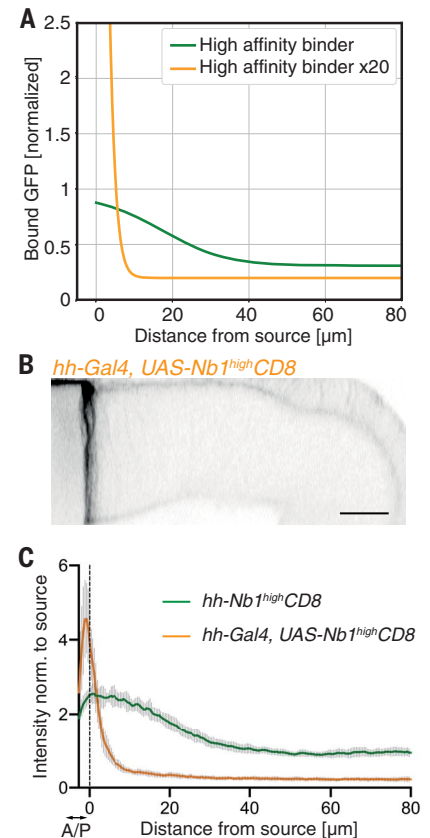
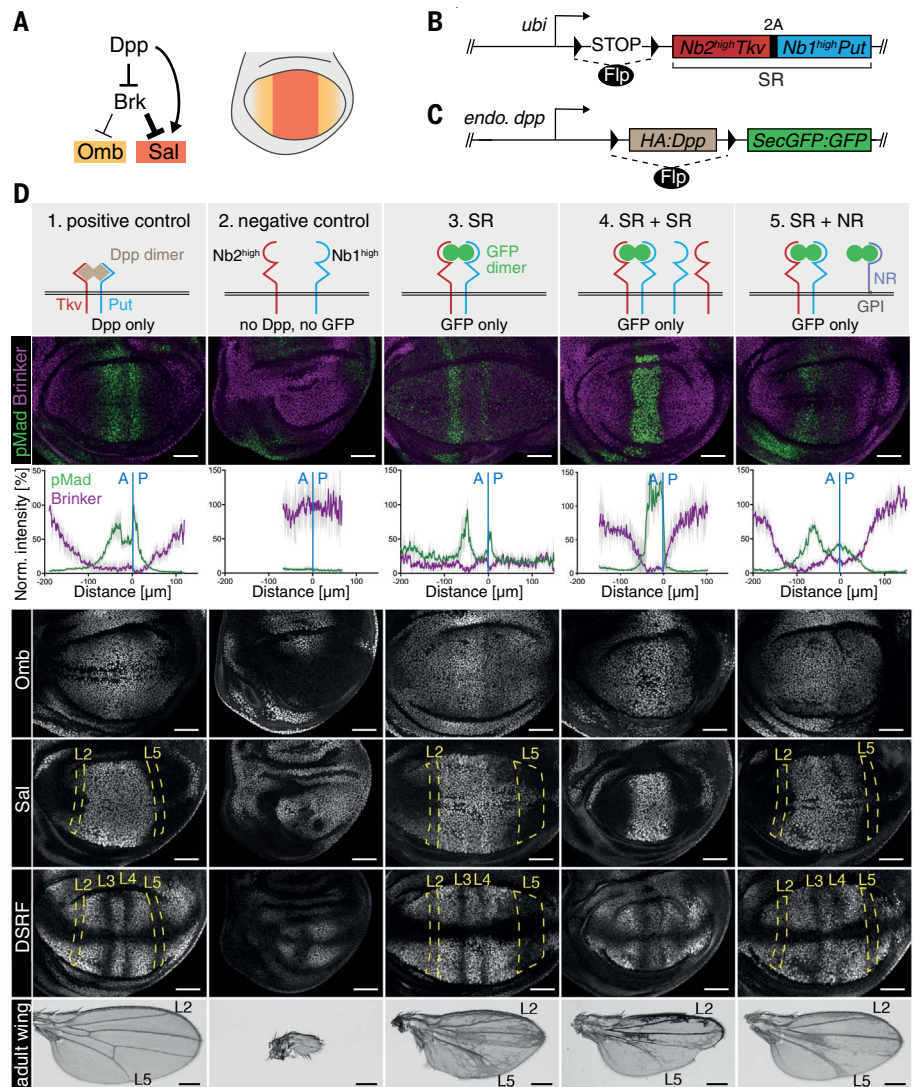


Fig. 3. Predicted and experimental effects of increasing binder expression. (A) Predicted GFP profile after a 20-fold increase in binder expression (orange; compare to the green curve, which is reproduced from Fig. 2C). Note the steep gradient and the lower nonzero tail. Bound GFP concentrations are normalized to the lower value of total receptor concentration. (B) Cross section of a *ptc-SecGFP* imaginal disc overexpressing the high-affinity binder (*hh-Gal4, UAS-Nb1^{high}CD8*). (C) GFP profiles in *hh-Gal4, UAS-Nb1^{high}CD8* (orange curve, $n = 8$), and *hh-Nb1^{high}CD8* discs (green curve from Fig. 1D). Scale bars, 20 μm.

(26). In addition, pMad immunoreactivity was also present in a salt-and-pepper manner throughout the whole pouch, as if residual signaling activity persisted far from the source. In agreement, *brk* was repressed over a wider range than in control discs. Both *sal* and *omb* were expressed in GFP-rescued discs, although in a range that did not recapitulate the wild-type situation; in the posterior compartment, the Sal domain boundary was fuzzy, whereas the domain of Omb was too broad. Normally, Sal and Omb ensure the patterned down-regulation of the *Drosophila* serum response factor (DSRF), which is required for vein fate specification (27). However, in the “rescue” condition, an oversized domain of DSRF down-regulation could be seen in the posterior compartment, along with a corresponding

Fig. 4. Rescue of growth and patterning by GFP.

(A) Target genes of Dpp signaling in the pouch, which give rise to the wing. (B) Schematic representation of SR, the transgene for conditional expression of engineered receptors. (C) The *dpp* locus engineered to allow Flp-mediated replacement of an essential region by sequences encoding secreted GFP dimers. Throughout the study, *rn-Gal4* and *UAS-Flp* were used to inactivate *Dpp* and/or trigger SR expression specifically in the pouch. (D) Phenotypes of wing imaginal discs and adult wings of various genotypes (columns). The positive control (column 1) shows imaginal discs and wings from a *dpp*-[>*Dpp*>*SecGFP:GFP*] homozygous larva. Flp is absent and *Dpp* is therefore expressed as in wild-type discs. For the negative control (column 2), we used larvae homozygous for a different conditional allele (*dpp*-[>*Dpp*>J] (25) and carrying the SR transgene. Here, Flp expression inactivates *Dpp* in the pouch without triggering GFP:GFP production while at the same time activating expression of the engineered receptors. The resulting phenotypes recapitulated those of classical *dpp* mutants (e.g., *brk* derepression and growth impairment). Abrogation of Dpp activity shows that the engineered receptors do not trigger signaling in the absence of GFP. If, in combination with the SR transgene, the *dpp*-[>*Dpp*>*SecGFP:GFP*] allele is used (column 3, SR), signaling activity (e.g., pMad immunoreactivity near the source) and growth are restored, albeit imperfectly. Note the occasional spots of pMad throughout the pouch, the expanded zone of *brk* repression, the fuzzy boundary of *sal* expression in the posterior compartment, and the disrupted vein pattern. Adding a second SR transgene (column 4, same genotype as in column 3 with one additional SR transgene, SR+SR) led to enhanced pMad at the source and a narrowing of the signaling gradient (relative to SR alone). Addition of non-signaling receptors (column 5, same genotype as in column 3 with addition of *dally-Nb^{low}GPI*, SR+NR) extended the signaling gradient (relative to SR alone). Note the absence of background pMad far from the source and the wild-type-like expression of target genes. Note, however, that vein L4 was often disrupted and vein L5 was slightly broadened in the distal part. Scale bars, 50 μ m (for wing discs) or 0.25 mm (for adult wings).



spawling vein L5 in surviving adult wings. Ectopic vein material was also seen throughout the wings, which was probably a result of global ectopic Dpp signaling. Despite these limitations, the above results suggest that a GFP gradient can stimulate growth and provide substantial patterning information through engineered receptors.

Signaling activity far from the GFP source, e.g., in the form of ectopic pMad, suggests the presence of GFP dimers throughout the disc, perhaps as a result of re-entry from the hemolymph. During our initial analysis of the GFP gradient, we found that leakage could be reduced by increasing the level of extracellular binders (Fig. 3, B and C). We therefore asked if a similar strategy could be used to reduce nonzero tail signaling in rescued discs. Indeed, with two copies of the transgene expressing engineered GFP-responsive receptors (SR +

SR), background pMad immunoreactivity was largely abrogated (Fig. 4D, column 4). The target genes *omb* and *sal* were still expressed in a nested fashion; however, the width of these domains, as well as that of the zone of *brk* repression, were narrower than in the wild type (Fig. 4D, compare column 1 with column 4). This suggests that a twofold increase in receptor expression had the beneficial effect of reducing the adverse effect of leakage on signaling activity far from the source, but at the expense of a reduced range. These results can be understood qualitatively in the context of our gradient model (supplementary text section 1.3.2): at low receptor density, receptor activation is too low to trigger target gene activation; at intermediate receptor density, leakage can lead to a high ligand concentration in the hemolymph, triggering signaling and target gene activation far from the source

(fig. S5, F and G); at higher receptor density, hemolymph concentration drops but the gradient scale shortens because of increased degradation in the tissue. It appears, therefore, that long-range GFP gradients with low residual signaling far from the source may only be achievable within a narrow range of parameters (fig. S5, F and G).

Beneficial effects of GPI-anchored nonsignaling receptors

The above analysis suggests that, by solely modulating the expression of signaling receptors, it is difficult to reduce leakage without shortening the gradient. Natural morphogens bind not only to signaling receptors but also to nonsignaling extracellular proteins such as glypicans, glycosylphosphatidylinositol (GPI)-anchored heparan sulfate proteoglycans (II). We therefore set out to investigate whether low-affinity,

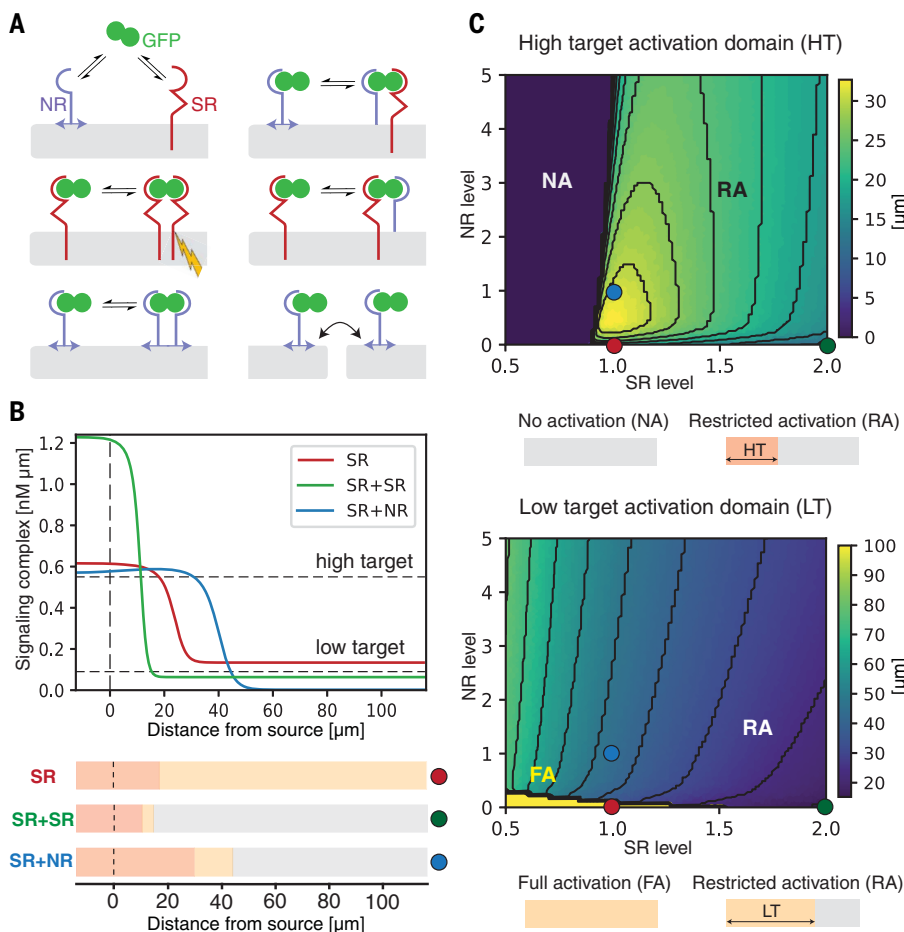


Fig. 5. Modeling the effect of GPI-anchored non-signaling receptors on a gradient length scale.

(A) Schematic representation of the molecular interactions considered by our model, including GFP dimer handover and NR hopping. Signal transduction (yellow lightning bolt) is activated by GFP-bound signaling receptor dimers (SR). See supplementary text for details. (B) Predicted profiles of signaling complexes in three conditions: a reference case with signaling receptors only (SR; red), doubling SR levels (SR + SR; green), and adding non-signaling receptors (SR + NR; blue). As observed experimentally, doubling SR leads to a steeper gradient, whereas adding NR reduces GFP^{hemo} signaling and extends the gradient, due to non-signaling receptor effective diffusion. For illustration, arbitrary thresholds were chosen to indicate the position where high- and low-level target genes would be activated (tables S2 and S3 report the parameter values). (C) Width of the high (top) and low (bottom) target activation domains [arbitrary threshold shown in (B)], as a function of normalized levels of SR and NR. Warmer colors indicate a wider target activation domain. Colored dots show parameter combinations used in (B). (Top) For the normalized SR value of 1, increasing NR initially lengthens the high target domain, while a further increase shortens it by preventing access of GFP to SR [as observed experimentally (fig. S11)]. (Bottom) For the normalized SR value of 1 and in the absence of NR, GFP^{hemo} signaling dominates and low target gene is activated throughout (bright yellow region). Increasing SR or NR production both lead to a reduction in the low target domain size.

GPI-anchored, extracellular binders (non-signaling receptors, NR) would improve the performance of the signaling gradient. As a first step, we created a DNA fragment encoding Nb^{low} [K_d of 25 nM, chosen to mimic the affinity of BMP for heparin (28)] tethered to the extracellular face of the plasma membrane by a GPI anchor, Nb^{low}GPI. This fragment was expressed with *rn-Gal4*, which concomitantly triggered expression of Flp to inactivate *Dpp* and initiated expression of SecGFP and the engineered receptors. In the resulting imaginal discs, the signaling activity of SR was suppressed (fig. S11), perhaps because excess Nb^{low}GPI prevented SecGFP from accessing the signaling receptors. To achieve a more reasonable expression level, we inserted the Nb^{low}GPI-encoding fragment in the *dally* locus, one of the two glypican-encoding genes of *Drosophila*. This allele (*dally-Nb^{low}GPI*) was then combined with all the previously described genetic elements needed for a GFP signaling gradient to form. Addition of this non-signaling receptor extended the pMad gradient and narrowed the domain of *brk* repression, an indication of reduced GFP^{hemo} signaling far from the source (Fig. 4D, compare columns 3 and 5). Indeed, with this combination of

signaling and non-signaling receptors, target gene expression (controlled entirely by GFP dimers) was comparable to that in wild-type imaginal discs, and the resulting wings were notably well patterned, proportioned, and consistently sized (fig. S12).

To rationalize how non-signaling receptors could improve the signaling gradient's characteristics, we devised a formal description of the relevant molecular interactions (Fig. 5A, fig. S13C, supplementary text and table S3). In this framework, GFP dimers bind signaling and non-signaling receptors and transit from one configuration to another. Signaling receptors typically undergo rapid endocytosis upon binding to their ligands. By contrast, GPI-anchored binders could have a longer lifetime (29), allowing them to hand over ligands to signaling receptors (30). Simulations showed, however, that addition of membrane-tethered nonreceptors does not extend the signaling gradient, although they can alter its shape near the source (supplementary text and fig. S13D). We next considered the relevance of the labile nature of GPI anchors (31). Locally expressed GFP-GPI spreads within wing imaginal discs (32, 33), suggesting that GPI-anchored proteins can detach from cells and possibly reinsert them-

selves nearby, a process we call hopping (Fig. 5A). Simulations introducing a tissue-scale effective diffusion constant, $D_r = 0.1 \mu\text{m}^2/\text{s}$, for GFP-Nb^{low}GPI (representing lateral diffusion in the cell membrane and intercellular hopping) can explain the extension of the signaling gradient by Nb^{low}-GPI (Fig. 5B). In fact, we find that, in the absence of NR diffusion (or with a low diffusion constant), NRs can only shorten the gradient, as nondiffusing NRs provide an additional route for ligand degradation without contributing to ligand spread (fig. S13, D and E, and supplementary text). At a high NR concentration, competition for the ligand with SR inhibits signaling (Fig. 5C), as observed experimentally (fig. S11). For intermediate concentrations of the NR, however, NR diffusion enables the gradient range to increase while preventing uniform activation of low-target genes by leaked ligand.

Conclusion

We have shown that, in the presence of extracellular binders, GFP can form a gradient in an epithelial tissue. Because GFP is inert in wing imaginal discs, it is unlikely to spread by a specialized transport mechanism, such as planar transcytosis. The low off-rate of Nb^{high}

($k_{\text{off}} = 1.7 \times 10^{-4} \text{ s}^{-1}$) also limits the contribution of ligands passing from one receptor to another. We therefore suggest that the GFP gradient forms by free diffusion, even though the readily detectable gradient is largely made up of bound GFP (Fig. 1C and fig. S5, H to K). In the presence of engineered GFP-responsive receptors (SR), diffusing GFP can act as a morphogen. One limitation of free diffusion is that it allows leakage into the circulation, a potential threat to positional information. As we have shown, signaling from leaked GFP can be reduced by increasing the level of SR. However, this was at the expense of a reduced range. Leakage can be reduced without a concomitant decrease in gradient range by adding GPI-anchored nonsignaling receptor (NR). We suggest that, by virtue of their labile association with cell membranes, GPI-anchored non-signaling receptors can undergo tissue-level diffusion and thus extend the gradient. Although this hypothesis remains to be demonstrated experimentally, our results so far show that a combination of free and NR-assisted diffusion suffices to emulate the range and activity of a natural morphogen.

REFERENCES AND NOTES

1. P. Müller, K. W. Rogers, S. R. Yu, M. Brand, A. F. Schier, *Development* **140**, 1621–1638 (2013).
2. S. Zhou et al., *Curr. Biol.* **22**, 668–675 (2012).
3. S. R. Yu et al., *Nature* **461**, 533–536 (2009).
4. A. D. Lander, Q. Nie, B. Vargas, F. Y. Wan, *J. Mech. Mater. Struct.* **6**, 321–350 (2011).
5. T. B. Kornberg, A. Guha, *Curr. Opin. Genet. Dev.* **17**, 264–271 (2007).
6. M. Affolter, K. Basler, *Nat. Rev. Genet.* **8**, 663–674 (2007).
7. E. V. Entchev, A. Schwabedissen, M. González-Gaitán, *Cell* **103**, 981–992 (2000).
8. S. Roy, H. Huang, S. Liu, T. B. Kornberg, *Science* **343**, 1244624–1244624 (2014).
9. U. Hacker, K. Nybakken, N. Perrimon, *Nat. Rev. Mol. Cell Biol.* **6**, 530–541 (2005).
10. H. Nakato, J. P. Li, *Int. Rev. Cell Mol. Biol.* **325**, 275–293 (2016).
11. D. Yan, X. Lin, *Cold Spring Harb. Perspect. Biol.* **1**, a002493–a002493 (2009).
12. P. Li et al., *Science* **360**, 543–548 (2018).
13. S. Toda et al., *Science* **370**, 327–331 (2020).
14. S. Harmansa, I. Alborelli, D. Bieli, E. Caussinus, M. Affolter, *eLife* **6**, e22549 (2017).
15. U. Rothbauer et al., *Nat. Methods* **3**, 887–889 (2006).
16. A. Kirchhofer et al., *Nat. Struct. Mol. Biol.* **17**, 133–138 (2010).
17. P. C. Fridy et al., *Nat. Methods* **11**, 1253–1260 (2014).
18. A. D. Lander, Q. Nie, F. Y. M. Wan, *Dev. Cell* **2**, 785–796 (2002).
19. T. Bollenbach, K. Kruse, P. Pantazis, M. González-Gaitán, F. Jülicher, *Phys. Rev. E Stat. Nonlin. Soft Matter Phys.* **75**, 011901 (2007).
20. S. J. Newfeld et al., *Development* **124**, 3167–3176 (1997).
21. B. Müller, B. Hartmann, G. Pyrowolakis, M. Affolter, K. Basler, *Cell* **113**, 221–233 (2003).
22. R. Barrio, J. F. de Celis, *Proc. Natl. Acad. Sci. U.S.A.* **101**, 6021–6026 (2004).
23. R. Sivasankaran, M. A. Vigano, B. Müller, M. Affolter, K. Basler, *EMBO J.* **19**, 6162–6172 (2000).
24. J. C. Tang et al., *Cell* **154**, 928–939 (2013).
25. P. S. Bosch, R. Ziukaite, C. Alexandre, K. Basler, J.-P. Vincent, *eLife* **6**, e22546 (2017).
26. C. J. Evans et al., *Nat. Methods* **6**, 603–605 (2009).
27. J. F. De Celis, *BioEssays* **25**, 443–451 (2003).
28. R. Ruppert, E. Hoffmann, W. Sebald, *Eur. J. Biochem.* **237**, 295–302 (1996).
29. S. Mayor, H. Riezman, *Nat. Rev. Mol. Cell Biol.* **5**, 110–120 (2004).
30. J. Schlessinger, I. Lax, M. Lemmon, *Cell* **83**, 357–360 (1995).
31. G. A. Müller, *Arch. Biochem. Biophys.* **656**, 1–18 (2018).
32. V. Greco, M. Hannus, S. Eaton, *Cell* **106**, 633–645 (2001).
33. C. Tempesta, A. Hijazi, B. Moussian, F. Roch, *PLOS ONE* **12**, e0185897 (2017).

ACKNOWLEDGMENTS

We thank C. Alexandre for generating *vg-Gal4* and *dally-attP* and advice on genome engineering and the Crick Fly Facility for DNA injections. We also acknowledge the technical and intellectual contributions of S. Crossman and I. McGough. J. Briscoe provided comments on the manuscript. We are also grateful to A. Lander for pointing out the possible relevance of GPI's loose anchorage to membranes. We thank H. Ashe, G. Pflugfelder, and A. Salzberg for the generous gift of antibodies. The Developmental Studies Hybridoma Bank also provided antibodies. Drosophila stocks obtained from the Bloomington Drosophila Stock Center (NIH P40OD018537) were used in this study. **Funding:** This work was supported by core funding from the Francis Crick Institute (FC001204 to J.-P.V. and FC001317 to G.S.) and a Wellcome Trust Investigator Award to J.-P.V. (206341/Z/17/Z). K.S.S. was the recipient of a PhD Studentship from the Wellcome Trust (109054/Z/15/Z). **Author contributions:** This project was conceived by K.S.S., J.-P.V., and G.S. K.S.S. designed and performed all the experiments. The results were analyzed by all authors. The model was conceived by G.S., M.d.G., and L.C., and numerical simulations were performed by M.d.G. and L.C. The main text was written by K.S.S., J.-P.V., and G.S. with comments from M.d.G. and L.C. **Competing interests:** The authors declare no competing or financial interests. All data are described in the main text or supplementary materials. **Data and materials availability:** All materials are available upon request. A link to the computer code can be found in the supplementary text.

SUPPLEMENTARY MATERIALS

science.sciencemag.org/content/370/6514/321/suppl/DC1
Materials and Methods
Supplementary Text
Figs. S1 to S13
Tables S1 to S3
References (34–61)
MDAR Reproducibility Checklist

[View/request a protocol for this paper from Bio-protocol.](#)

21 March 2020; accepted 21 August 2020
10.1126/science.abb8205

REPORT

MORPHOGENS

Engineering synthetic morphogen systems that can program multicellular patterning

Satoshi Toda^{1,*†}, Wesley L. McKeithan¹, Teemu J. Hakkinen², Pilar Lopez¹,
Ophir D. Klein^{2,3}, Wendell A. Lim^{1,*}

In metazoan tissues, cells decide their fates by sensing positional information provided by specialized morphogen proteins. To explore what features are sufficient for positional encoding, we asked whether arbitrary molecules (e.g., green fluorescent protein or mCherry) could be converted into synthetic morphogens. Synthetic morphogens expressed from a localized source formed a gradient when trapped by surface-anchoring proteins, and they could be sensed by synthetic receptors. Despite their simplicity, these morphogen systems yielded patterns reminiscent of those observed *in vivo*. Gradients could be reshaped by altering anchor density or by providing a source of competing inhibitor. Gradient interpretation could be altered by adding feedback loops or morphogen cascades to receiver cell response circuits. Orthogonal cell-cell communication systems provide insight into morphogen evolution and a platform for engineering tissues.

Development of multicellular organisms requires precise spatial control of cell fate. Morphogens are molecules that provide positional information. They diffuse from a source to form a concentration gradient that is interpreted by neighboring cells (1–4). In metazoans, a small set of specialized molecules, including sonic hedgehog (Shh), Wnt, fibroblast growth factor (FGF), and bone morphogenetic protein (BMP)—transforming growth factor- β (TGF β) family members, serve as morphogens (5). Reconstitution of morphogen signaling *in vitro* is a powerful approach to understand how morphogens encode positional information (6, 7). To define the minimal requirements for a functional morphogen, we asked whether it is possible to construct a synthetic morphogen signaling system that functions orthogonally to endogenous morphogens. Orthogonal morphogen signaling would enable the systematic exploration of patterning circuits, free from confounding cross-talk with endogenous systems.

To create synthetic morphogens, we modified the recently developed synthetic Notch (synNotch) system to detect user-defined soluble factors. SynNotch receptors are a modular platform for engineering orthogonal juxtacrine signaling (8), composed of an extracellular rec-

ognition domain [e.g., nanobody or single chain antibody (scFv)], the Notch core regulatory domain, and an intracellular transcriptional domain (e.g., TetR-VP64). When an anti-green fluorescent protein (GFP) synNotch receptor recognizes membrane-tethered GFP on a neighboring sender cell, the synNotch core undergoes cleavage, which releases its intracellular domain to enter the nucleus to activate target gene expression. Soluble GFP does not activate synNotch because exposure of the cleavage site requires the mechanical force of a membrane-tethered ligand (8). Here, we reengineered the synNotch system to detect soluble molecules by tethering the diffusible ligand to a complementary engineered anchor cell (Fig. 1A). In the case of GFP, we used two noncompetitive anti-GFP nanobodies: One serves as the anchor binding domain, and the other serves as the receptor binding domain (Fig. 1B). We designed this diffusible synNotch system with anti-GFP LaG2 nanobody fused to a transmembrane domain as the anchor molecule and anti-GFP LaG17 nanobody as the recognition domain of the synNotch receptor (fig. S1A). These nanobodies recognize different sites on GFP (9). SynNotch receiver cells were only activated by soluble GFP in the presence of anchor cells (Fig. 1C and fig. S1, B and C).

To test whether this soluble synNotch system allowed GFP to function as a morphogen, we reconstituted an *in vitro* model of L929 fibroblast cells organized into a pole and a body (fig. S2A) (culture well divided by insert wall; see materials and methods). The pole was composed of GFP secretor cells and the body of mixed anchor and receiver cells. To minimize disruptive convective flow, we used a solidified media containing 1% agarose (fig.

S2B). We observed the formation of a long-range gradient (~4 mm) of both secreted GFP and synNotch reporter gene expression (mCherry) in contrast to the narrow band of activation observed when pole cells expressed membrane-tethered GFP (Fig. 1D and fig. S2C). The GFP gradient formed within ~24 hours, whereas induced mCherry reporter expression reached steady state in ~96 hours (fig. S2, C and D, and movie S1). We found that another bivalently recognized protein—a fusion protein of mCherry with a PNE peptide (mCherry-PNE)—could also be recognized by an analogous anchor-receptor system (fig. S3 and supplementary text), which further supports the idea that arbitrary proteins can be converted into morphogens (Fig. 1B).

To investigate how the shape of a synthetic morphogen gradient could be modulated, we systematically perturbed different interaction parameters. Using the LaG2 anti-GFP nanobody as an anchor protein, we tested how anchor protein density can regulate gradient shape. We generated four different levels of anchor protein density by varying both the anchor protein expression level and the anchor cell number in the body. More specifically, we constructed high- or low-expressing anchor cells and mixed them at 50% (a 1:1 ratio) with receiver cells in the body (Fig. 2A and fig. S4). We also created a combination anchor-receiver L929 cell, which was used at 100% in the body, yielding an approximately twofold higher density of anchor proteins for a given expression level (fig. S4). These studies showed that when the overall density of anchor protein was reduced, the maximal signal amplitude close to the pole decreased, but the signal range extended a longer distance as morphogen diffused further before being trapped. The importance of anchor density as a determinant of morphogen gradient shape is consistent with trends predicted by a simple computational model (fig. S5B).

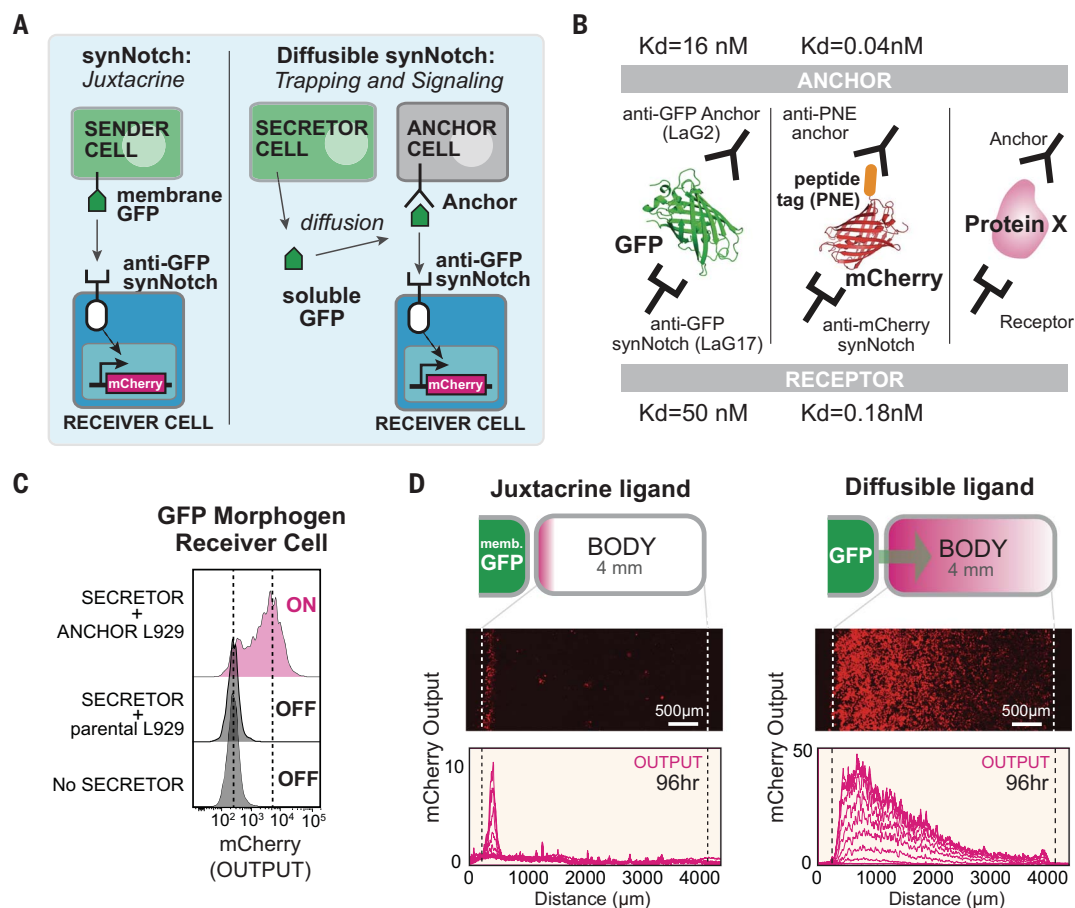
The spatial distribution of morphogens can also be regulated by antimorphogen inhibitors. For example, during *Xenopus* embryogenesis, BMP is secreted from a ventrally located pole, whereas Chordin—a BMP-binding inhibitor—is secreted from an opposing pole (10, 11). Such antagonism by an inhibitor is a common theme observed in development. Inspired by activator-inhibitor opposition, we designed a three-region configuration on the culture dish: a central body surrounded by a morphogen-secreting pole and an inhibitor-secreting pole on opposite sides (Fig. 2B; see fig. S6, A and B, and materials and methods for development of morphogen inhibitor). We tested both morphogen and inhibitor sets (GFP and mCherry-PNE) in the double-pole system. When the GFP inhibitor was secreted from the opposing pole, we observed a reduced amplitude of the activation gradient generated by the GFP morphogen (fig. S6C). The mCherry-PNE inhibitor showed

¹Cell Design Institute, Department of Cellular and Molecular Pharmacology, and Howard Hughes Medical Institute, University of California San Francisco, San Francisco, CA 94158, USA. ²Program in Craniofacial Biology and Department of Orofacial Sciences, University of California San Francisco, San Francisco, CA 94143, USA. ³Department of Pediatrics and Institute for Human Genetics, University of California San Francisco, San Francisco, CA 94143, USA. *Corresponding author. Email: wendell.lim@ucsf.edu (W.A.L.); satoshi.toda@staff.kanazawa-u.ac.jp (S.T.)

[†]Present address: WPI Nano Life Science Institute, Kanazawa University, Kanazawa 920-1192, Japan.

Fig. 1. Turning arbitrary proteins into synthetic morphogens.

(A) SynNotch receptors detect juxtacrine signals (e.g., membrane-tethered GFP). In the diffusible synNotch system, soluble GFP is produced from a secretor cell, then trapped by anti-GFP anchor protein, and finally presented to anti-GFP synNotch on a receiver cell. (B) Multiple arbitrary proteins with two recognition sites could be converted into synthetic morphogens (see fig. S3 for construction of mCherry-PNE peptide morphogen). K_d, dissociation constant. (C) Testing diffusible GFP synNotch system in L929 mouse fibroblasts. Anchor cell expresses anti-GFP LaG2 anchor protein. Receiver cell expresses anti-GFP LaG17 synNotch (induces mCherry reporter). 1×10^4 GFP-secreting cells, 0.5×10^4 anchor cells, and 0.5×10^4 receiver cells were cultured overnight, and mCherry induction in receiver cells was measured by flow cytometry. (D) Juxtacrine versus diffusible GFP signaling gradient. Left pole has 3×10^4 sender cells, and right body has 1.5×10^4 cells (100% receiver cells for juxtacrine; 50:50 anchor:receiver cells for diffusible GFP; see fig. S2, A and B). Images were taken by incuCyte system over 4 days when system reached steady state (movie S1). Individual lines show mCherry intensity every 12 hours.



a somewhat different pattern, reducing the signaling range of the activation gradient generated by mCherry-PNE morphogen with smaller effects on amplitude (Fig. 2B and supplementary text). Together, these results show that the signaling range and amplitude of a synthetic morphogen gradient can be tuned to generate a variety of shapes similar to those seen in embryos.

In natural morphogen systems, receiver cells can interpret a morphogen gradient in diverse, higher-order ways. We explored several mechanisms to reshape how the body cells interpret the synthetic morphogen gradient, taking advantage of the flexibility with which synNotch signaling can be engineered to drive any genetically encoded payload. We particularly focused on engineering intercellular positive and negative feedback loops among receiver cells (Fig. 3).

We first designed an intercellular positive feedback circuit in which the receiver cells sense the GFP morphogen and, in response, induce expression of more GFP (Fig. 3A). Cells with this positive feedback circuit did not trigger spontaneous activation with the

anchor cells when engineered with sufficiently low background expression of GFP (fig. S7A). By contrast, when a body of positive feedback receiver cells (with anchor cells) was placed next to a pole of GFP-producing cells, the positive feedback circuit caused rapid, high-amplitude spatial propagation of morphogen signal and reporter gene activation across the entire body (Fig. 3, B and C; fig. S7C; and movie S1).

We also constructed intercellular negative feedback receiver cells, in which the receiver cells sense the GFP morphogen and, in response, produce the soluble GFP inhibitor (Fig. 3A and fig. S7B). When negative feedback receiver cells (mixed with anchor cells) were placed in the body, the maximal amplitude of the response gradient was notably dampened. The negative feedback activity gradient reached a stable steady state far more rapidly (~30 versus 70 hours for negative feedback versus nonfeedback cells) (Fig. 3D and fig. S7D). Such stable gradient formation is similar to that which is observed in response to natural morphogens (e.g., wingless or hedgehog), with negative feedback

pathways involving self-induced morphogen degradation, endocytosis, or inhibition (6, 12). In these cases, the common principle of morphogen-induced negative feedback is thought to lead to higher levels of negative regulation in the vicinity of the morphogen source but lower levels of negative regulation at a greater distance from the source, which yields a more extended and stable gradient.

We have created a modular toolkit of intercellular signaling components that can flexibly reshape morphogen production and interpretation. We wanted to test whether these modules could be combined to program higher-order pattern formation, such as the formation of multiple distinct segments within a body plan (Fig. 4). We first asked whether we could create a body plan with two distinct domains (activated and unactivated). To do so, we combined the positive feedback morphogen circuit with a counteracting inhibitor pole on the opposite side of the body (Fig. 4A). This circuit yielded two distinct domains: receiver cells close to morphogen source triggered positive feedback to drive strong synNotch activation, whereas signal activation close to the

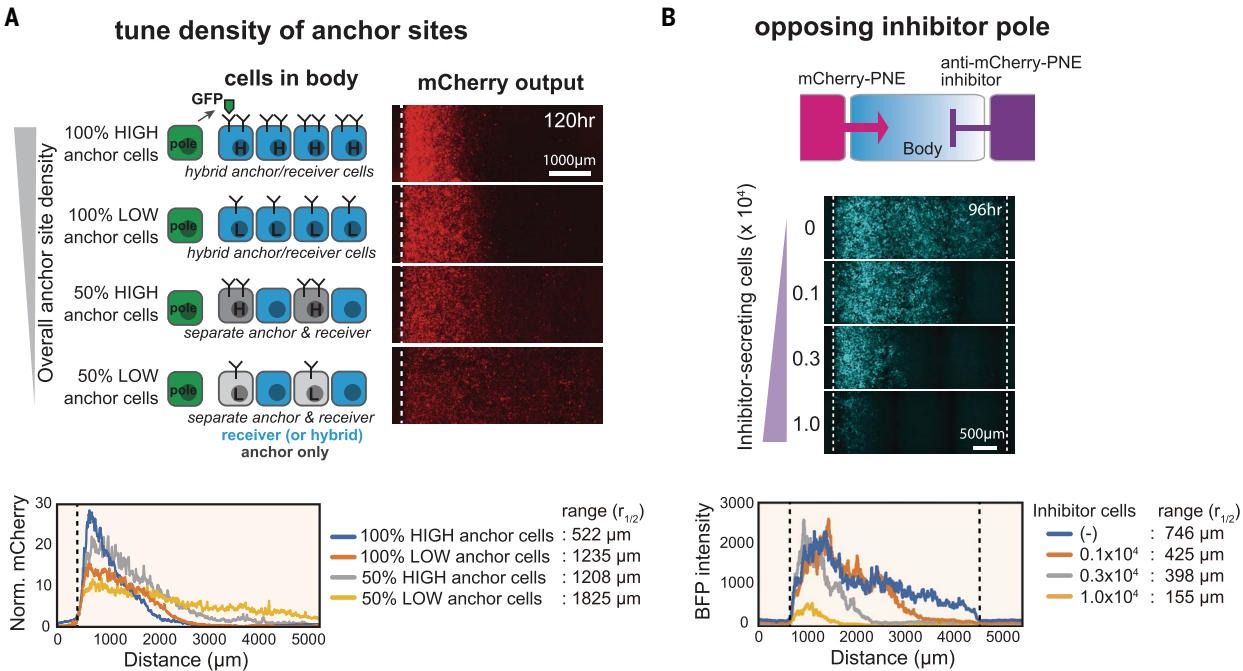


Fig. 2. Systematic control over distance range of synthetic morphogen gradient. (A) Anchor density can tune synthetic GFP morphogen gradient shape and signaling range. We constructed bodies with four different densities of LaG2-anchor by using two types of variations: anchor expression level (high or low) and fraction of cells in the body that express anchor (100 or 50%). See materials and methods for details. Norm., normalized. (B) Controlling signaling range of mCherry-PNE morphogen with inhibitor. We used a three-well insert wall to build three regions:

morphogen pole, body, and inhibitor pole. The morphogen pole has a mixture of 1×10^4 mCherry-PNE-secreting cells and 2×10^4 parental L929 cells. The body has a 1.5×10^4 mixture of anti-PNE anchor cells and anti-mCherry synNotch receiver cells (50:50 ratio). The inhibitor pole has cells expressing anti-mCherry-PNE inhibitor (total cell number: 3×10^4 of cells; varying number of inhibitor cells: 0, 0.1×10^4 , 0.3×10^4 , or 1.0×10^4 ; remaining cells were parental L929). BFP output was quantified by In Cell Analyzer 6000 at day 4 (see fig. S6 for GFP inhibitor analysis).

Fig. 3. Reshaping morphogen interpretation with positive or negative feedback. (A) In a positive feedback circuit, GFP morphogen activates receiver cells to induce the secretion of more GFP. In a negative feedback circuit, GFP morphogen induces the expression of antimorphogen inhibitor by receiver cells. TF, transcription factor. (B) Comparison of mCherry output in the body with and without positive feedback at 96 hours (see fig. S7C for time course). The pole has 3×10^4 GFP-secreting cells; the body has a 1.5×10^4 mixture of anchor cells and receiver cells engineered with a positive feedback circuit (50:50 ratio). Images were taken by incucyte system for 4 days (movie S1). (C) Activity gradient profiles at 96 hours, with and without positive feedback. Shaded area shows SD from multiple experiments. (D) The mCherry-positive area (integral of top plots) plotted over time shows that the body with negative feedback reaches steady state faster than it does without feedback. AU, arbitrary units.

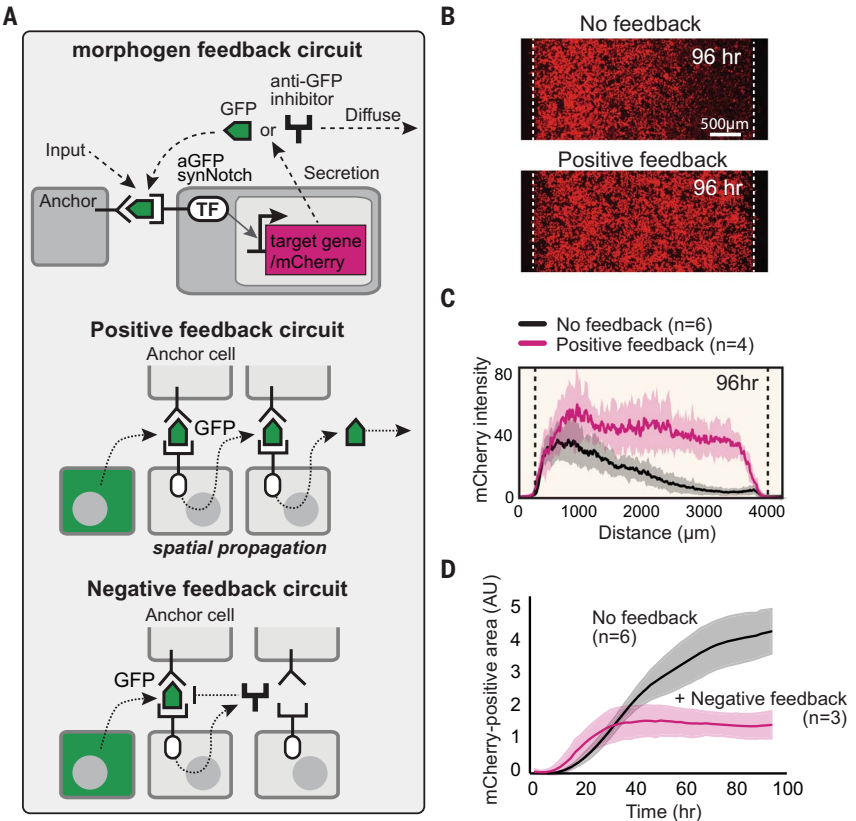
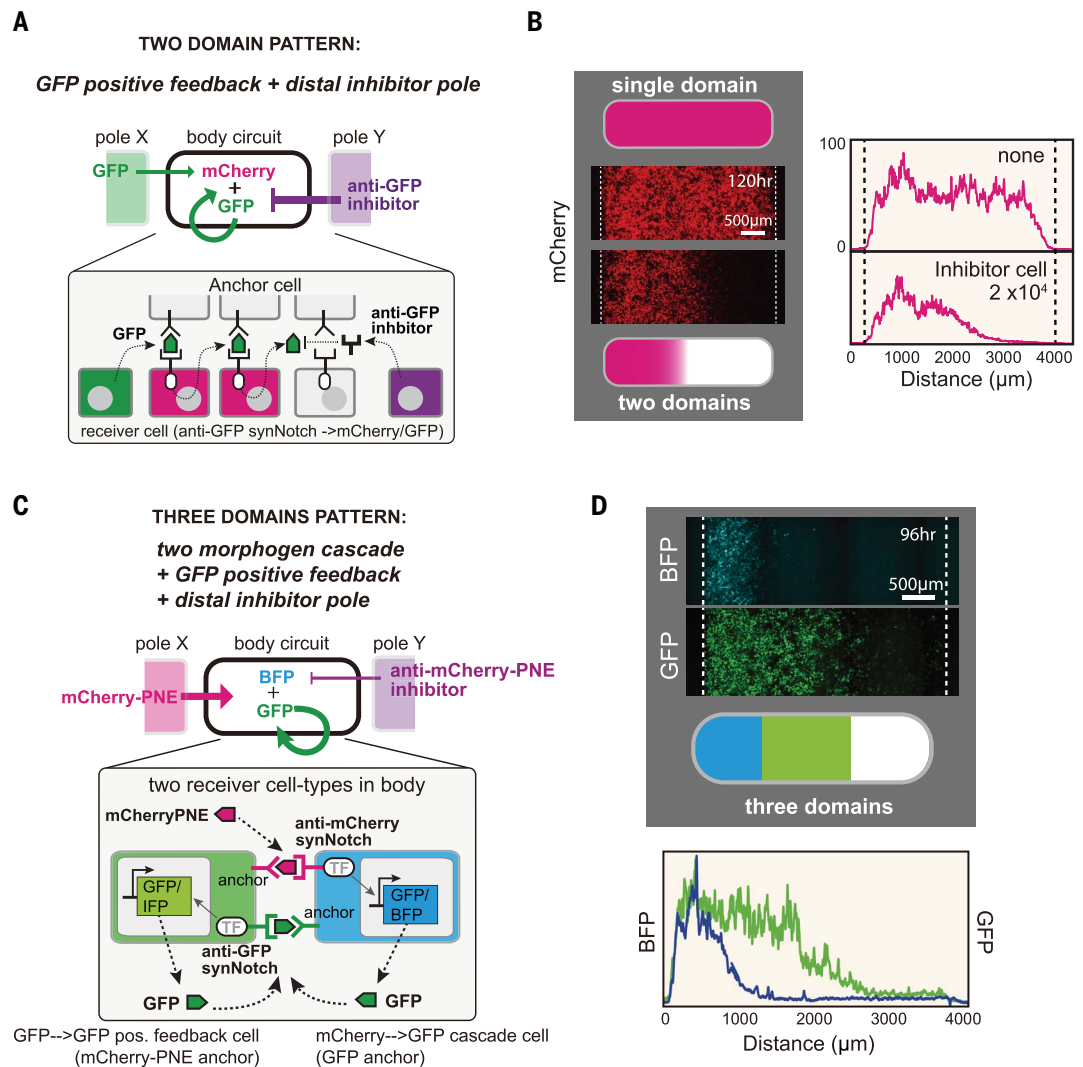


Fig. 4. Combining synthetic morphogen interpretation circuits to engineer multidomain spatial patterns. (A and B) Programming two-domain pattern by combining positive feedback circuit with opposing morphogen and inhibitor poles. Morphogen pole (X) has 3×10^4 GFP-secreting cells; the body has a 50:50 mixture of anchor cells and receiver cells with positive feedback (used in Fig. 3B) (1.5×10^4 total cells); and the inhibitor pole (Y) has 2×10^4 anti-GFP inhibitor-secreting cells. Images were taken by incuCyte at 120 hours (movie S1). See fig. S8B for variant circuits. (C and D) Programming three-domain pattern. We combined the two-morphogen cascade and positive feedback circuit with opposing morphogen and inhibitor poles. The body contains two types of cells: Cell A expresses anti-mCherry synNotch that induces BFP reporter and GFP morphogen (mCherry-PNE \rightarrow GFP cascade), and cell B expresses anti-GFP LaG17 synNotch that induces expression of GFP morphogen (GFP \rightarrow GFP positive feedback). See materials and methods for details. Image was taken at 96 hours by In Cell Analyzer 6000 (movie S2). IFP, infrared fluorescent protein.



inhibitor source was blocked, which lead to a nonlinear, switch-like transition from active to inactive domains (Fig. 4B). By changing the number of GFP inhibitor-secreting cells, we could tune the widths of the domains (fig. S8, A and B).

Finally, we set out to engineer a circuit that produces a three-domain body, akin to Wolpert's classic French Flag pattern (2). We designed a circuit that incorporates a two-morphogen cascade, positive feedback, and opposing pole inhibition (Fig. 4C). In this circuit, the left pole secretes mCherry-PNE morphogen. The body contains two types of uniformly mixed receiver cells (fig. S8C): receiver A cells that sense mCherry-PNE to induce the expression of a blue fluorescent protein (BFP) reporter and GFP morphogen (mCherry-PNE \rightarrow GFP two-morphogen cascade) and receiver B cells that sense GFP to induce the secretion of GFP (GFP \rightarrow GFP positive feedback) (cells A and B are engineered to serve as anchors for each other). To oppose morphogen signaling, the right pole secretes the anti-mCherry-PNE in-

hibitor to sharpen the initial morphogen gradient. With this composite circuit, we observe the robust formation of three distinct domains (Fig. 4D): a BFP⁺GFP⁺ domain closest to the mCherry-PNE morphogen pole; a BFP⁺GFP⁺ middle domain (where the GFP⁺ region is extended by GFP \rightarrow GFP positive feedback); and, furthest (closest to the inhibitor pole), a BFP⁺GFP⁻ domain (fig. S8D and movie S2). This toolkit of synthetic cell-cell communication components can be used to write spatial programs capable of encoding multiple, distinct body domains.

Although evolution has relied on a relatively small set of specialized morphogen families, we find that arbitrary proteins with no known history of functioning as morphogens can be converted into effective morphogens if they are deployed with a complementary system of receptors, anchoring interactions, and inhibitors. These synthetic morphogens differ from natural morphogens in that they explicitly require a distinct anchoring protein to constrain their distribution and mediate synNotch re-

ceptor activation. Whereas natural morphogens often function autonomously, most participate in weak tethering interactions that are analogous to anchoring—whether interacting with cell surface proteoglycans, extracellular matrix, or cell membranes through lipid modifications (fig. S9A) (13–15). These tethering interactions are proposed, in many cases, to constrain signaling range and to prevent the leakage of morphogens (16, 17) (supplementary text and fig. S10).

These synthetic morphogen platforms can program positional information without crosstalk to endogenous signaling pathways. Thus, it may be possible to deploy them in vivo as inert tools to probe or redirect development. Related studies (18) have shown that an analogous synthetic GFP morphogen can function in vivo in *Drosophila*. Thus, these synthetic morphogen systems could be used to facilitate controlled forward engineering of tissues and organs, both in a native-like or a modified fashion. We found that the diffusible synNotch system functioned in other cell types, including

immune cells (fig. S11), which provides further possibilities as to how such synthetic signaling systems could be deployed to shape spatially controlled functions in vivo.

REFERENCES AND NOTES

1. A. M. Turing, *Phil. Trans. R. Soc. Lond. B* **237**, 37–72 (1952).
2. L. Wolpert, *J. Theor. Biol.* **25**, 1–47 (1969).
3. K. W. Rogers, A. F. Schier, *Annu. Rev. Cell Dev. Biol.* **27**, 377–407 (2011).
4. A. D. Lander, *Science* **339**, 923–927 (2013).
5. T. Tabata, Y. Takei, *Development* **131**, 703–712 (2004).
6. P. Li *et al.*, *Science* **360**, 543–548 (2018).
7. R. Sekine, T. Shibata, M. Ebisuya, *Nat. Commun.* **9**, 5456 (2018).
8. L. Morsut *et al.*, *Cell* **164**, 780–791 (2016).
9. P. C. Fridy *et al.*, *Nat. Methods* **11**, 1253–1260 (2014).
10. E. M. De Robertis, H. Kuroda, *Annu. Rev. Cell Dev. Biol.* **20**, 285–308 (2004).
11. E. Bier, E. M. De Robertis, *Science* **348**, aaa5838 (2015).
12. A. Eldar, D. Rosin, B.-Z. Shilo, N. Barkai, *Dev. Cell* **5**, 635–646 (2003).
13. D. Yan, X. Lin, *Cold Spring Harb. Perspect. Biol.* **1**, a002493 (2009).
14. A. Parchure, N. Vyas, S. Mayor, *Trends Cell Biol.* **28**, 157–170 (2018).
15. Y. Wang, X. Wang, T. Wohland, K. Sampath, *eLife* **5**, e13879 (2016).
16. P. Müller, K. W. Rogers, S. R. Yu, M. Brand, A. F. Schier, *Development* **140**, 1621–1638 (2013).
17. T. B. Kornberg, A. Guha, *Curr. Opin. Genet. Dev.* **17**, 264–271 (2007).
18. K. S. Stapornwongkul, M. de Gennes, L. Cocconi, G. Salbreux, J.-P. Vincent, *Science* **370**, 321–327 (2020).

ACKNOWLEDGMENTS

We thank A. McMahon for Shh-GFP and L. Morsut, K. Roybal, J. Brunger, N. Frankel, and members of the Lim laboratory for discussion and assistance. We also thank members of the University of California San Francisco Center for Systems and Synthetic Biology and the NSF Center for Cellular Construction.

Funding: This work was supported by the Human Frontiers of Science Program (HFSP); the Senri Life Science Foundation; the Kato Memorial Bioscience Foundation; JSPS KAKENHI grant no. 20K15828 and World Premier International Research Center Initiative (WPI), MEXT, Japan (to S.T.); a Ruth L. Kirschstein National Research Service Award (NRSA) Individual Postdoctoral Fellowship F32DK123939 (to W.L.M.); the NSF DBI-1548297 Center for Cellular Construction; the DARPA Engineered Living Materials program; and the Howard Hughes Medical Institute (to W.A.L.). T.J.H. and O.D.K. were supported by NIH R01-DE028496 and R35-DE026602. **Author contributions:** S.T. developed and planned research; carried out design, construction, and testing of multicellular patterning circuits; and wrote the manuscript. W.L.M. planned research, carried out testing of multicellular patterning circuits, and edited the

manuscript. T.J.H. designed and tested simulation works, wrote methods for simulations, and edited the manuscript. P.L. helped with material construction. O.D.K. oversaw research and edited the manuscript. W.A.L. developed, planned, and oversaw research and wrote and edited the manuscript.

Competing interests: W.A.L. and S.T. have a financial interest in Gilead Biosciences. W.A.L. and S.T. are inventors on a patent application (PCT/US2016/019188) held by the Regents of the University of California that covers binding synthetic Notch receptors. **Data and materials availability:** All data are available in the main manuscript and supplementary materials. All plasmids developed in this study will be deposited at Addgene (www.addgene.org/Wendell_Lim/), where they will be publicly available.

SUPPLEMENTARY MATERIALS

science.sciencemag.org/content/370/6514/327/suppl/DC1
Materials and Methods
Supplementary Text
Figs. S1 to S11
Table S1
References (19–27)
MDAR Reproducibility Checklist
Movies S1 and S2

[View/request a protocol for this paper from Bio-protocol.](#)

31 March 2020; accepted 24 August 2020
10.1126/science.abc0033

ULTRACOLD CHEMISTRY

Coherently forming a single molecule in an optical trap

Xiaodong He^{1,2,*†}, Kunpeng Wang^{1,2,3,*}, Jun Zhuang^{1,2,3}, Peng Xu^{1,2}, Xiang Gao^{4,5}, Ruijun Guo^{1,2,3}, Cheng Sheng^{1,2}, Min Liu^{1,2}, Jin Wang^{1,2}, Jiaming Li^{6,7,8}, G. V. Shlyapnikov^{9,10,11}, Mingsheng Zhan^{1,2,†}

Ultracold single molecules have wide-ranging potential applications, such as ultracold chemistry, precision measurements, quantum simulation, and quantum computation. However, given the difficulty of achieving full control of a complex atom-molecule system, the coherent formation of single molecules remains a challenge. Here, we report an alternative route to coherently bind two atoms into a weakly bound molecule at megahertz levels by coupling atomic spins to their two-body relative motion in a strongly focused laser with inherent polarization gradients. The coherent nature is demonstrated by long-lived atom-molecule Rabi oscillations. We further manipulate the motional levels of the molecules and measure the binding energy precisely. This work opens the door to full control of all degrees of freedom in atom-molecule systems.

Many fundamental research topics related to ultracold molecules, such as ultracold collisions and chemistry (1–3), strongly correlated quantum systems (4, 5), quantum degenerate gases (6, 7), precision measurements (8), and quantum information processing (9, 10), are rapidly developing and attracting broad attention. After the work on producing coherent coupling between atoms and molecules in a ⁸⁵Rb Bose-Einstein condensate near a Feshbach resonance (11), various types of ultracold diatomic molecules in the gas phase (12–17) and in an optical lattice (18–20) have been formed via Feshbach resonances or photoassociation, leading to the observation of ultracold chemistry (21) and to the simulation of quantum spin models (22). At the same time, because of recent developments in high-level individual particle control and detection (23–27), bottom-up assembly of single molecules in optical tweezers (OTs) has attracted attention for ultracold molecule applications (28–30). However, the coherent formation of single mol-

ecules out of atoms and the full control over atom-molecule systems remain a challenge.

Here, we report an alternative approach that allows us to bypass the strong dephasing encountered (without Feshbach resonances) in the photoassociation of atoms. The idea is to couple the spin of one of the interacting atoms to the two-body relative motion. In this way, a noticeable displacement can be induced on the wave function of the relative motion under the action of a microwave spin-flip transition. The induced displacement could enhance the atom-molecule wave function overlap and thus the corresponding Franck-Condon (FC) factor in the molecule formation. Such spin-motion coupling (SMC) is mediated by the inherent polarization gradients in a strongly focused trapping laser, namely in an OT. We experimentally demonstrated the idea of engineering the quantized motion of a two-atom system and coherently binding two atoms, one ⁸⁵Rb atom and one ⁸⁷Rb atom, into a single molecule. We obtained long-lived atom-molecule Rabi oscillations and further manipulated the motional levels of the formed molecules. We measured their binding energy in free space as well as the differential light shifts between scattering and molecular states.

Optical tweezers are typically realized with strongly focused Gaussian beams to provide strong spatial confinements of laser-cooled atoms. When the beam waists ω_{OT} are comparable to the wavelength λ (here, $\omega_{OT} \approx 0.75 \mu\text{m}$ and $\lambda = 0.852 \mu\text{m}$), the tightly focused beams exhibit longitudinal polarization components (31), which give rise to spatially varying elliptical polarizations, even for linearly polarized input fields. The resulting polarizations function as magnetic field gradients (32, 33), and therefore atoms with different spin projections m_F of hyperfine state F have different equilibrium positions. Because of this effect, a spin-flip microwave transition between different m_F states could induce a displacement

of the spatial wave function (d_a), as illustrated in Fig. 1A. Thus, the atomic motion and the spin are coupled with each other, that is, there exists an SMC (34). Consequently, the wave function overlap $|\langle n | n' \rangle|$ ($n \neq n'$) between different motional states can become noticeable, where n' and n are vibrational quantum numbers in two spin states. SMC in the optical trap leads to the appearance of sidebands in the microwave transition, similar to the case of a state-dependent optical lattice (35, 36). For two isolated colliding atoms in a tight OT, the spatial displacement d_i of a given atom with mass m_i and position \vec{r}_i ($i = 1$ or 2) is straightforwardly transferred to the center-of-mass (c.m.) and relative (rel.) coordinates, $\vec{R} = (m_1\vec{r}_1 + m_2\vec{r}_2)/(m_1 + m_2)$ and $\vec{r} = \vec{r}_1 - \vec{r}_2$, respectively. This indicates that a microwave spin-flip transition of this atom in the presence of SMC also enables a possibility of manipulating the two-atom relative motion and even tuning the atom-molecule overlaps so as to reliably bind the targeted atom to the colliding partner, as schematically depicted in Fig. 1B. Specifically, for the ⁸⁵Rb⁸⁷Rb bound states with binding energy at the megahertz level, SMC could increase the atom-molecule overlap by a factor of 2 to 3 (37).

The starting point of the experiments was the preparation of one ⁸⁵Rb atom and one ⁸⁷Rb atom in internal hyperfine states $|\uparrow\rangle_{85} \equiv |3, -3\rangle_{85}$ and $|\downarrow\rangle_{87} \equiv |1, -1\rangle_{87}$, respectively, in which inelastic collisions between these two atoms are energetically forbidden. The microwave radiation can drive transitions between $|\uparrow\rangle_{85}$ and $|\downarrow\rangle_{85} \equiv |2, -2\rangle_{85}$ for the ⁸⁵Rb atom. Both atoms occupy the ground state in a linearly polarized OT. The details for preparing such a two-atom reservoir and the atomic state-resolved detection can be found in our previous work (38). After simultaneous Raman sideband cooling of ⁸⁵Rb and ⁸⁷Rb in two separate traps, the two atoms in spin-stretched states of $|\uparrow\rangle_{85}$ and $|\downarrow\rangle_{87}$ were merged into a single OT via species-dependent transport, by which these two atoms were split for imaging.

In the first set of experiments, we used SMC to probe the quantized motion of two atoms and deduce the displacements of the c.m. and rel. motions. To induce SMC, the axis of the guiding magnetic field of 2.0 G was switched on perpendicular to both the propagation direction of the OT laser (z axis) and the linear polarization vector (x axis). This arrangement initiated displacement predominantly along the x axis, which was measured to be 21.6(1) nm (fig. S1) (37, 39). The trap depth is set at 1.6 mK, corresponding to a radial trap frequency $\omega_x = 2\pi \times 165$ kHz and axial trap frequency $\omega_z = 2\pi \times 27$ kHz. We then used conventional Rabi spectroscopy to measure the two-atom vibrational transitions $|\psi_s\rangle|\varphi_0\rangle \rightarrow |\psi_s'\rangle|\varphi_{N_x}\rangle$ ($|\psi\rangle$ and $|\varphi\rangle$ are the rel. and c.m. motional states; $N_x = \{0, 1, \dots\}$ denotes the quantum number of

¹State Key Laboratory of Magnetic Resonance and Atomic and Molecular Physics, Wuhan Institute of Physics and Mathematics, APM, Chinese Academy of Sciences, Wuhan 430071, China. ²Center for Cold Atom Physics, Chinese Academy of Sciences, Wuhan 430071, China. ³School of Physical Sciences, University of Chinese Academy of Sciences, Beijing 100049, China. ⁴Institute for Theoretical Physics, Vienna University of Technology, A-1040 Vienna, Austria. ⁵Beijing Computational Science Research Center, Beijing 100193, China. ⁶Department of Physics and Center for Atomic and Molecular Nanosciences, Tsinghua University, Beijing 100084, China. ⁷Key Laboratory for Laser Plasmas (Ministry of Education), and Department of Physics and Astronomy, Shanghai Jiao Tong University, Shanghai 200240, China. ⁸Collaborative Innovation Center of Quantum Matter, Beijing 100084, China. ⁹LPTMS, CNRS, Univ. Paris-Sud, Université Paris-Saclay, 91405 Orsay, France. ¹⁰Russian Quantum Center, Skolkovo, Moscow 121025, Russia. ¹¹Van der Waals-Zeeman Institute, Institute of Physics, University of Amsterdam, 1098 XH Amsterdam, Netherlands.

*These authors contributed equally to this work.

†Corresponding author. Email: hexd@wipm.ac.cn (X.H.); mszhan@wipm.ac.cn (M.Z.)

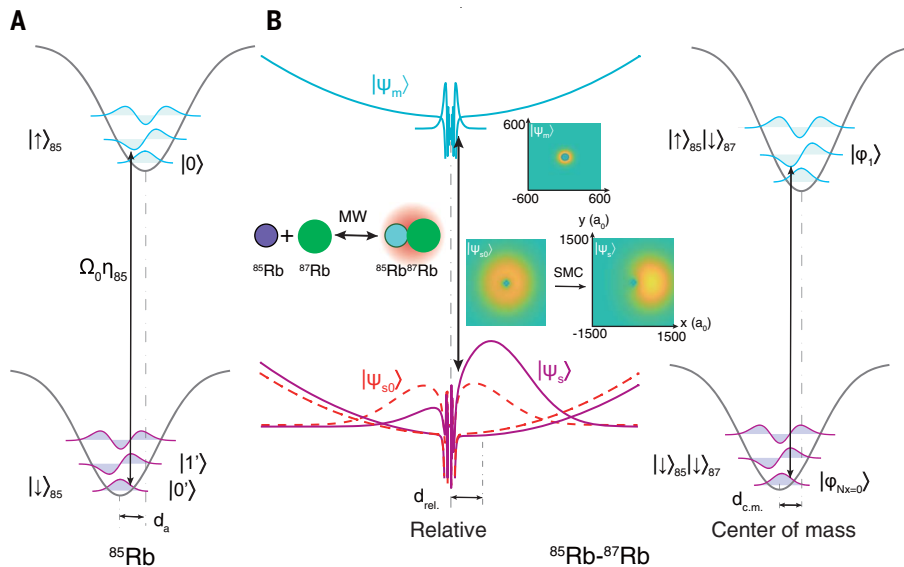


Fig. 1. Schemes of SMC and molecular association in a tight OT. (A) SMC of a single ^{85}Rb atom. The trapping potentials in the spin states of $|\uparrow\rangle_{85}$ and $|\downarrow\rangle_{85}$ are displaced in space by d_a , leading to the coupling between $|0\rangle$ and $|1\rangle$ with a strength of $\Omega_0\eta_{85}$ (Ω_0 is the bare spin-flip coupling, and η_{85} is an additional factor resulting from the wave function overlap). (B) Making one molecule via SMC. The wave functions are shown with two-dimensional density plots and the corresponding cross sections in the $y = 0$ plane, and the potential profiles include the trapping potential and the molecular potential. In an external trapping field without SMC (dashed red curve), the background overlap of the atomic rel. wave function $|\psi_{s0}\rangle$ (red wave packet) and the molecular wave function $|\psi_m\rangle$ is relatively low. While in the presence of SMC, a displacement (d_{rel}) between the atomic rel. wave function $|\psi_s\rangle$ (purple wave packet) and $|\psi_m\rangle$ along the x direction shows up, as well as a displacement $d_{\text{c.m.}}$ in the c.m. motion. The d_{rel} could enhance the FC factor for binding ^{85}Rb and ^{87}Rb into one molecule by implementing the microwave (MW) spin-flip transition $|\downarrow\rangle_{85}|\downarrow\rangle_{87} \rightarrow |\uparrow\rangle_{85}|\downarrow\rangle_{87}$. The $d_{\text{c.m.}}$ allows us to make the resulting molecule in the motional ground state $|\varphi_0\rangle$ ($N_x = 0$) or in the excited state $|\varphi_1\rangle$ ($N_x = 1$).

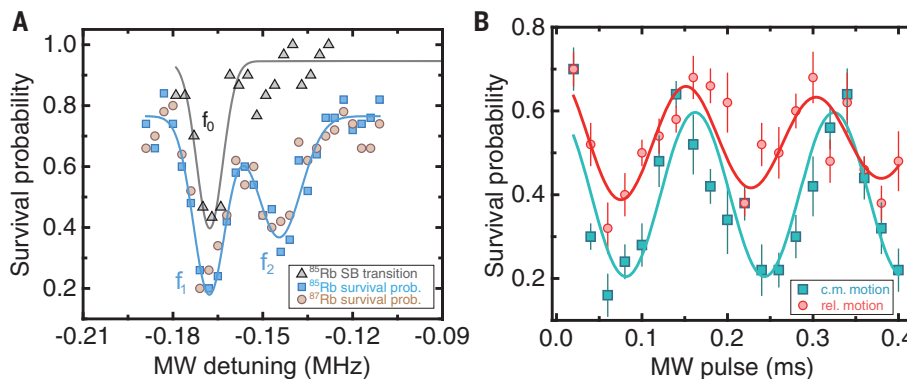


Fig. 2. Observation of sideband transitions of two atoms via SMC. (A) Microwave spectra of sideband (SB) transitions of ^{85}Rb in the presence (filled squares and circles) and absence (filled triangles) of ^{87}Rb . The detuning is given with respect to the carrier transition frequency of a single ^{85}Rb atom. The corresponding spin-flip coupling $\Omega_0 = 2\pi \times 17.4(1)$ kHz. All of the data points are averaged over 100 runs. The solid curves are Gaussian fits of the data, yielding resonant detunings of $f_1 = -167.9(5)$ kHz and $f_2 = -144.5(8)$ kHz for the two-atom case, and $f_0 = -167.7(5)$ kHz for the one-atom case. (B) The Rabi oscillations at detunings f_1 (filled squares) and f_2 (filled circles). The data points are averaged over 100 runs, and the error bars denote the standard deviation of the mean. The solid curves are damped sinusoidal fits of the oscillations, yielding the Rabi frequencies $\Omega_1 = 2\pi \times 6.1(1)$ kHz and $\Omega_2 = 2\pi \times 6.5(2)$ kHz.

the c.m. motion in the x direction) together with the spin-flip transition $|\uparrow\rangle_{85}|\downarrow\rangle_{87} \rightarrow |\downarrow\rangle_{85}|\downarrow\rangle_{87}$. When the ^{85}Rb spin was flipped, the resulting two atoms, $|\downarrow\rangle_{85}$ and $|\downarrow\rangle_{87}$, had vector light shifts of the same sign and moved together

after the species-dependent transport, leading to the disappearance of the atomic fluorescent signals. Compared with the $\Delta n_x = 1$ sideband transition of a single ^{85}Rb atom, the two-atom spectrum exhibited a double-peak structure

(Fig. 2A). The peak f_1 , closely resembling the single-atom transition f_0 , was identified as the spin-flip transition together with the motional transition $|\varphi_0\rangle \rightarrow |\varphi_{N_x=1}\rangle$ in the c.m. motion. The peak f_2 corresponds to the transition $|\psi_s\rangle = |m_p = 0\rangle \rightarrow |\psi_s'\rangle = |m_p = 1\rangle$ in the rel. motion, where m_p is the angular momentum quantum number of a two-dimensional harmonic oscillator describing the relative motion. For the contact interaction in the ultracold regime, the interaction potential was characterized by a pseudopotential that can only shift the quantized energy of states with $m_p = 0$ and even k , where k is the quantum number of the one-dimensional harmonic oscillator in the axial direction (z axis). The collisional shift $\epsilon_s(\vec{r})$ for all $m_p = 0$ states has been found analytically (40). In contrast, the wave functions of the states with $m_p \neq 0$ vanished at $r = 0$, and these states did not feel the s -wave interaction. Thus, the splitting between f_1 and f_2 was equal to the interaction shift of the initial two-atom state.

Next, we observed the coherent driving of the two-atom quantized motion, from which the displacements $d_{\text{c.m.}}$ and d_{rel} of the c.m. and rel. motions, respectively, were extracted. The coherent Rabi oscillations for these motions were obtained with the corresponding Rabi frequencies Ω_1 and Ω_2 , respectively. The resulting oscillations are shown in Fig. 2B. The lower contrast of the rel. motion resulted from a finite ground-state fidelity. Given the measured Ω_1 and Ω_2 , the displacements $d_{\text{c.m.}}$ and d_{rel} were estimated to be about 9 and 25 nm, respectively (37).

Having demonstrated the manipulation of quantized motion of two atoms with microwave radiation, we now describe the formation of a single least-bound molecule in the presence of SMC. We first considered the least-bound molecule for the channel $|\uparrow\rangle_{85}|\downarrow\rangle_{87}$, where the background scattering length was the largest among all collisionally stable channels (41). From coupled-channel calculations, the scattering length for this channel was $314.4 a_0$ (where a_0 is the Bohr radius) at a magnetic field of 2.0 G, and the calculated binding energy was -0.901 MHz (37).

To drive the molecule-formation transition $|\psi_s\rangle \rightarrow |\psi_m\rangle$, the corresponding spin-flip coupling was increased to $\Omega_0 = 2\pi \times 64.5(4)$ kHz by using high-power microwave radiation. Then we applied a sequence of three pulses: the first and third were resonant π pulses driving only the transitions $|\uparrow\rangle_{85}|\downarrow\rangle_{87} \rightarrow |\downarrow\rangle_{85}|\downarrow\rangle_{87}$ and $|\downarrow\rangle_{85}|\downarrow\rangle_{87} \rightarrow |\uparrow\rangle_{85}|\downarrow\rangle_{87}$ while leaving atoms in the scattering ground state $|\psi_s\rangle$ unchanged. The frequency f_m of the middle pulse was scanned in order to search for the molecular transition. When f_m was resonant with the molecular transition, the sequence resulted in the formation of a $^{85}\text{Rb}^{87}\text{Rb}$ molecule. Otherwise, the sequence would implement

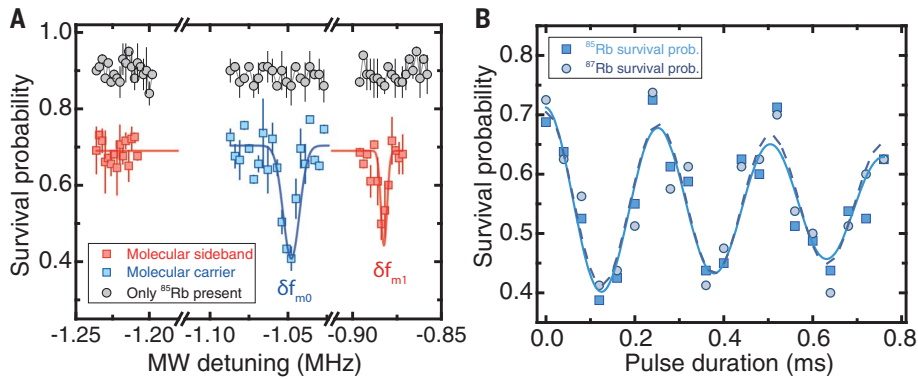


Fig. 3. Atom-molecule transitions and coherent Rabi oscillations. (A) Microwave spectra of the $|\psi_s\rangle|\downarrow_{85}\downarrow_{87}\rangle \rightarrow |\psi_m\rangle|\uparrow_{85}\downarrow_{87}\rangle$ transition at the trap frequency of $\omega_z = 2\pi \times 27$ kHz. The survival probability of ^{85}Rb atoms is measured as a function of detuning from the carrier transition of a single ^{85}Rb atom and the background signals are shown with filled gray circles. The pulse duration is 0.11 (0.22) ms for the carrier (sideband) transition. All the data points are averaged over 100 experimental runs, and the error bars denote the corresponding standard deviations. The solid curves are Gaussian fits of the peaks, yielding $\delta f_{m0} = -1.048(1)$ MHz and $\delta f_{m1} = -0.8825(5)$ MHz. (B) The atom-molecule Rabi oscillation for the molecular carrier transition at the trap depth of $\omega_z = 2\pi \times 18.5$ kHz. The detected ^{85}Rb signals oscillate similarly to ^{87}Rb ones, with decay times of 1.1 ± 0.6 ms and 1.7 ± 1.5 ms, respectively. The average Rabi frequency is $\Omega_m = 2\pi \times 3.95(5)$ kHz. The data points are averaged over 150 experimental runs.

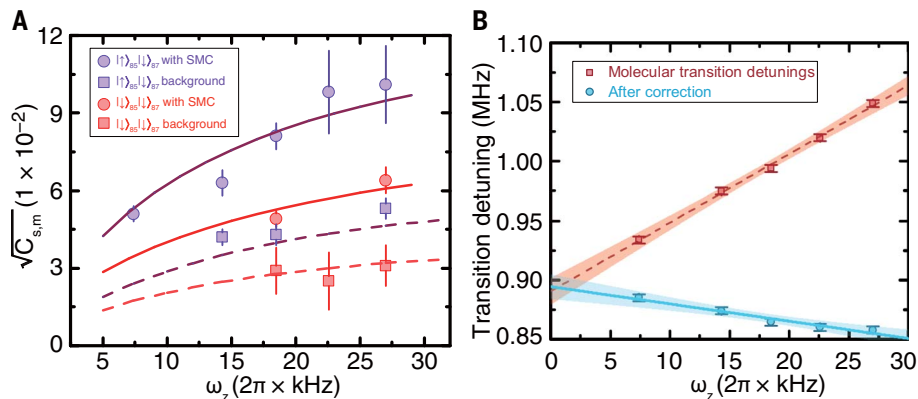


Fig. 4. Atom-molecule wave function overlap and molecular binding energy. (A) The dependence of the atom-molecule wave function overlap ($\sqrt{C_{s,m}}$) on the axial trapping frequency ω_z . The purple (red) filled circles are of measured overlap integrals for making $|\uparrow_{85}\downarrow_{87}\rangle$ ($|\downarrow_{85}\downarrow_{87}\rangle$) molecules in the presence of SMC, and the corresponding fitting with the pseudopotential model is shown with the solid purple (red) line. In the absence of SMC, the measured background overlap of $|\uparrow_{85}\downarrow_{87}\rangle$ ($|\downarrow_{85}\downarrow_{87}\rangle$) molecules is denoted via the purple (red) filled squares and the corresponding calculation with coupled-channel method is shown with the purple (red) dashed line. The error bars denote standard deviations. (B) Measurement of the binding energy E_b of the $|\uparrow_{85}\downarrow_{87}\rangle$ bound state. The transition detuning δf_{m0} (filled squares) is plotted as a function of the axial trapping frequency ω_z , and the error bars include the fitting errors (standard deviations) and fluctuations (± 3 kHz) induced by the magnetic field. After taking into account the zero-point energy $E_{n=0}$, the interaction shift $\epsilon_8(\vec{r})$, and the energy shift due to confinement ΔE_b , the resulting dependence of transition resonances (filled circles) on ω_z is obtained. The solid line is a linear fit, yielding $-E_b = 0.890(3)$ MHz.

an effective 2π rotation for ^{85}Rb . The species-dependent transport was unable to dissociate such a molecule that has binding energy on the order of megahertz. Thus, the molecule formation would manifest itself as the disappearance of the atomic ^{87}Rb and ^{85}Rb fluorescence signals. As shown in Fig. 3A, we observed two molecular resonances δf_{m0} and δf_{m1} at detunings of about -1 MHz with a

spacing of $165(1)$ kHz. This spacing, which amounted to $\omega_x/2\pi$ of the constituent atoms in the OT, originated from the resolved quantized motion of the formed molecules. Under the same spin-flip transition, $|\downarrow_{85}\downarrow_{87}\rangle \rightarrow |\uparrow_{85}\downarrow_{87}\rangle$, the recorded resonant vibrational transitions at detunings of δf_{m0} and δf_{m1} corresponded to $|\psi_s\rangle|\varphi_0\rangle \rightarrow |\psi_m\rangle|\varphi_0\rangle$ and $|\psi_s\rangle|\varphi_0\rangle \rightarrow |\psi_m\rangle|\varphi_{N_x=1}\rangle$, respectively (for the former, the

resulting single molecules were in the ground state of OT, and for the latter, the resulting single molecules were in the first excited motional states $|\varphi_{N_x=1}\rangle$). The difference in strength of these resonances was due to an additional FC factor of 0.35 for the quantized motion of the molecule.

Having confirmed the formation of a single molecule, we subsequently observed coherent atom-molecule Rabi oscillations. The time-resolved Rabi oscillations allowed full control of the final superposition state. Figure 3B shows the recorded Rabi oscillation for the transition starting from the two-atom ground state, at the resonant detuning of δf_{m0} . Slowly damped oscillating survival probabilities of atoms were obtained with technical noise-limited decay time of about 1 ms. We subsequently measured the lifetime of the resulting molecules, which was about $20(7)$ ms (37). To illustrate the range of adjustable coupling strengths, we measured the Rabi frequencies versus the trapping frequencies ω_z and deduced the associated FC factors for the atom-molecule transition $C_{s,m}$. The values of $\sqrt{C_{s,m}} = \Omega_m/\Omega_0$, which amounts to the wave function overlap between the scattering and the molecular state, are shown in Fig. 4A. The wave function overlap and thus the FC factor increased as the confinement got stronger. To measure the background atom-molecule overlap, the magnetic field was set along the x axis. The background overlap was measured as the Rabi frequency ratio of the atom-molecule transition and single-atom transition. As compared with the measured and calculated background overlap, SMC could enhance the overlap by a factor of more than two (Fig. 4A). The corresponding fitting with the pseudopotential model leads to a shift of the wave function of about 9 nm (37).

To deduce the binding energy in free space, E_b , we measured the molecular transition detuning δf_{m0} as functions of ω_z (Fig. 4B). The molecule formation was accompanied by a change in the energy of the relative motion, E_{rel} . For the initial state, the associated E_{rel} consisted of the zero-point energy $E_{n=0}$ and interaction shift $\epsilon_8(\vec{r})$. As for the molecular state, it included E_b and the energy shift due to the confinement, ΔE_b . The calculated ΔE_b and $\epsilon_8(\vec{r})$ as functions of ω_z can be found in fig. S2. After subtracting the contributions of trap-dependent energy values $\{E_{n=0}; \epsilon_8(\vec{r}); \Delta E_b\}$, we obtained the resulting dependence of the binding energy on ω_z . With this correction, E_b was determined to be $-0.890(3)$ MHz by linearly extrapolating $\omega_z \rightarrow 0$ (Fig. 4B). The evidently linear dependence has a strong connection with the separated external trapping potentials seen by the constituent atoms, which lifts the energy of the bound state (42). From the binding energy E_b measured with a kilohertz uncertainty, the scattering length can be calculated to be $316.9(4) a_0$ with an analytical

formula in the framework of multichannel quantum defect theory (43), which is slightly larger than the value $314.4 a_0$ from coupled-channel calculations (37). The slight difference may arise from a finite precision of the analytical formula (37, 41).

Aside from the production of the $|\uparrow\rangle_{85}|\downarrow\rangle_{87}$ least-bound molecule, we also created the $|\downarrow\rangle_{85}|\downarrow\rangle_{87}$ molecule. We then observed the corresponding coherent Rabi oscillations and measured the binding energy in free space, E_b (see fig. S5). With the determined value of $E_b = -2.224(6)$ MHz, we deduced the corresponding scattering length to be $230.5(2) a_0$, which is also slightly larger than the value $227.9 a_0$ from coupled-channel calculations (37). Compared with the case of the $|\uparrow\rangle_{85}|\downarrow\rangle_{87}$ bound state, the atom-molecule wave function overlap was smaller and amounted to $0.064(5)$ at the trap frequency of $\omega_z = 2\pi \times 27$ kHz (Fig. 4A), while, without SMC, the background overlap was only 0.032 (37). The fitting with the pseudopotential model leads to a wave function shift of about 23 nm (37).

The least-bound molecule can be further transferred to the rovibrational ground state via the two-photon stimulated Raman adiabatic passage. Our work opens the door to the studies of motional state controlled (44) state-to-state cold chemistry (45, 46) and few-body molecular dynamics. The SMC method demonstrated here is especially important for atom-molecule transfer between states of near-equal and large scattering lengths, where direct microwave transitions are weak, thus SMC enhancement plays a key role. This method may find applications in interesting systems such as alkali atom-alkaline-earth atom pairs (47, 48). Furthermore, SMC can be realized with optical near fields of nanoscale waveguides and nanophotonic structures (49), and our work may be directly applied to form molecules and to

control the molecule-photon interactions in these systems.

REFERENCES AND NOTES

- H. Yang *et al.*, *Science* **363**, 261–264 (2019).
- R. Chapurin *et al.*, *Phys. Rev. Lett.* **123**, 233402 (2019).
- M.-G. Hu *et al.*, *Science* **366**, 1111–1115 (2019).
- M. A. Baranov, M. Dalmonte, G. Pupillo, P. Zoller, *Chem. Rev.* **112**, 5012–5061 (2012).
- J. A. Blackmore *et al.*, *Quantum Sci. Technol.* **4**, 014010 (2018).
- L. De Marco *et al.*, *Science* **363**, 853–856 (2019).
- W. G. Tobias *et al.*, *Phys. Rev. Lett.* **124**, 033401 (2020).
- S. S. Kondov *et al.*, *Nat. Phys.* **15**, 1118–1122 (2019).
- J. W. Park, Z. Z. Yan, H. Loh, S. A. Will, M. W. Zwerlein, *Science* **357**, 372–375 (2017).
- K.-K. Ni, T. Rosenband, D. D. Grimes, *Chem. Sci.* **9**, 6830–6838 (2018).
- E. A. Donley, N. R. Claussen, S. T. Thompson, C. E. Wieman, *Nature* **417**, 529–533 (2002).
- K.-K. Ni *et al.*, *Science* **322**, 231–235 (2008).
- J. G. Danzl *et al.*, *Science* **321**, 1062–1066 (2008).
- T. Takekoshi *et al.*, *Phys. Rev. Lett.* **113**, 205301 (2014).
- P. K. Molony *et al.*, *Phys. Rev. Lett.* **113**, 255301 (2014).
- J. W. Park, S. A. Will, M. W. Zwerlein, *Phys. Rev. Lett.* **114**, 205302 (2015).
- M. Guo *et al.*, *Phys. Rev. Lett.* **116**, 205303 (2016).
- T. Rom *et al.*, *Phys. Rev. Lett.* **93**, 073002 (2004).
- F. Lang, K. Winkler, C. Strauss, R. Grimm, J. H. Denschlag, *Phys. Rev. Lett.* **101**, 133005 (2008).
- A. Chotia *et al.*, *Phys. Rev. Lett.* **108**, 080405 (2012).
- S. Ospelkaus *et al.*, *Science* **327**, 853–857 (2010).
- B. Yan *et al.*, *Nature* **501**, 521–525 (2013).
- P. Xu *et al.*, *Nat. Commun.* **6**, 7803 (2015).
- D. Barredo, S. de Léséleuc, V. Lienhard, T. Lahaye, A. Browaeys, *Science* **354**, 1021–1023 (2016).
- M. Endres *et al.*, *Science* **354**, 1024–1027 (2016).
- T.-Y. Wu, A. Kumar, F. Giraldo, D. S. Weiss, *Nat. Phys.* **15**, 538–542 (2019).
- J. P. Covey, I. S. Madjarov, A. Cooper, M. Endres, *Phys. Rev. Lett.* **122**, 173201 (2019).
- L. R. Liu *et al.*, *Science* **360**, 900–903 (2018).
- L. R. Liu *et al.*, *Phys. Rev. X* **9**, 021039 (2019).
- L. Anderegg *et al.*, *Science* **365**, 1156–1158 (2019).
- B. Richards, E. Wolf, *Proc. R. Soc. London Ser. A* **253**, 358–379 (1959).
- A. M. Kaufman, B. J. Lester, C. A. Regal, *Phys. Rev. X* **2**, 041014 (2012).
- J. D. Thompson, T. G. Tiecke, A. S. Zibrov, V. Vuletić, M. D. Lukin, *Phys. Rev. Lett.* **110**, 133001 (2013).
- A. Dareau, Y. Meng, P. Schneeweiss, A. Rauschenbeutel, *Phys. Rev. Lett.* **121**, 253603 (2018).
- L. Förster *et al.*, *Phys. Rev. Lett.* **103**, 233001 (2009).
- X. Li, T. A. Corcovilos, Y. Wang, D. S. Weiss, *Phys. Rev. Lett.* **108**, 103001 (2012).

- See supplementary materials for more details.
- K. P. Wang *et al.*, *Phys. Rev. A* **100**, 063429 (2019).
- K. P. Wang *et al.*, *Chin. Phys. Lett.* **37**, 044209 (2020).
- Z. Idziaszek, T. Calarco, *Phys. Rev. A* **74**, 022712 (2006).
- K. P. Wang *et al.*, arxiv:1907.12722 [quant-ph] (30 July 2019).
- M. Krych, Z. Idziaszek, *Phys. Rev. A* **80**, 022710 (2009).
- B. Gao, *J. Phys. At. Mol. Opt. Phys.* **37**, 4273–4279 (2004).
- L. Caldwell, M. R. Tarbutt, *Phys. Rev. Res.* **2**, 013251 (2020).
- J. Wolf *et al.*, *Science* **358**, 921–924 (2017).
- J. Wolf, M. Deib, J. Hecker Denschlag, *Phys. Rev. Lett.* **123**, 253401 (2019).
- P. S. Zuchowski, J. Aldegunde, J. M. Hutson, *Phys. Rev. Lett.* **105**, 153201 (2010).
- D. A. Brue, J. M. Hutson, *Phys. Rev. A* **87**, 052709 (2013).
- D. E. Chang, J. S. Douglas, A. González-Tudela, C.-L. Hung, H. J. Kimble, *Rev. Mod. Phys.* **90**, 031002 (2018).
- X. He *et al.*, Data for figures: Coherently forming a single molecule in an optical trap, Version 1, Zenodo (2020); <https://doi.org/10.5281/zenodo.3941379>.

ACKNOWLEDGMENTS

We thank P. Zhang for insightful discussions. **Funding:** This work was supported by the National Key R&D Program of China (grants 2017YFA0304501, 2016YFA0302800, 2016YFA0302002, and 2016YFA0302104), the Key Research Program of Frontier Science of the Chinese Academy of Sciences (CAS) (grant ZDBS-LY-SLH012), the National Natural Science Foundation of China (grants 11774389, 11774023, and U1930402), the Strategic Priority Research Program of CAS (grant XDB 21010100), and the Youth Innovation Promotion Association of CAS (grants 2019325 and 2017378). The work of G.V.S. was supported by the Russian Science Foundation (grant 20-42-05002). **Author contributions:** X.H. and M.Z. conceived of the experiments. K.W., X.H., J.Z., R.G., and C.S. established the setup and performed the experiment. X.G., X.H., K.W., and J.L. performed theoretical calculations. K.W., X.H., P.X., X.G., M.L., J.W., G.V.S., and M.Z. analyzed the data and discussed the results. X.H., K.W., G.V.S., and M.Z. wrote the manuscript. All authors reviewed the manuscript. X.H. and M.Z. supervised the project. **Competing interests:** None declared. **Data and materials availability:** All data needed to evaluate the conclusions in the paper are present in the paper or the supplementary materials and are deposited in (50).

SUPPLEMENTARY MATERIALS

science.sciencemag.org/content/370/6514/331/suppl/DC1
Materials and Methods
Figs. S1 to S6
Tables S1 and S2
References (51–58)

1 January 2020; accepted 27 August 2020
Published online 24 September 2020
10.1126/science.aba7468

HYDROGELS

Cartilage-inspired, lipid-based boundary-lubricated hydrogels

Weifeng Lin¹, Monika Kluzek¹, Noa Iuster¹, Eyal Shimoni², Nir Kampf¹, Ronit Goldberg^{1*†}, Jacob Klein^{1*}

The lubrication of hydrogels arises from fluid or solvated surface phases. By contrast, the lubricity of articular cartilage, a complex biohydrogel, has been at least partially attributed to nonfluid, lipid-exposing boundary layers. We emulated this behavior in synthetic hydrogels by incorporating trace lipid concentrations to create a molecularly thin, lipid-based boundary layer that renews continuously. We observed a 80% to 99.3% reduction in friction and wear relative to the lipid-free gel, over a wide range of conditions. This effect persists when the gels are dried and then rehydrated. Our approach may provide a method for sustained, extreme lubrication of hydrogels in applications from tissue engineering to clinical diagnostics.

Synthetic hydrogels are widely used in biomedical and other applications (1–3), and their lubricity is crucial for their efficient function whenever surfaces slide past each other. The lubrication is attributed to fluid interfacial layers intrinsic to the gels, such as exuded liquid films or solvated flexible polymers at their surfaces (4–7). By contrast, biological materials such as articular cartilage remain well lubricated over a lifetime of sliding and wear. The low friction of cartilage has been attributed to fluid pressurization supporting much of the load [an effect that does not apply in synthetic hydrogels (8)], whereas its boundary lubrication has been attributed to nonfluid boundary layers at its surface (9–13). These layers expose phosphatidylcholine (PC) lipids whose highly hydrated phosphocholine headgroups may reduce friction via the hydration lubrication mechanism (14, 15). The maintenance of such boundary layers after frictional wear occurs through cellular replenishment and self-assembly of their components (14, 16, 17), including hyaluronan, lubricin, and especially PC lipids (18–22), which reduce friction at the slip plane via their hydrated phosphocholine headgroups (12). These components are ubiquitous in both cartilage and the surrounding synovial fluid (16, 20, 21) and thus are readily available to maintain the lubricating layer at the articular surface.

We adapted this mechanism to lubricate synthetic hydrogels via the incorporation of small amounts of PC lipids to form microreservoirs throughout the gel bulk, by mixing a low concentration of PC lipids with the desired monomer solution, then polymerizing and cross-linking to form the hydrogel. The

reduction in friction and wear is attributed to a lipid-based boundary layer at the hydrogel surface, which is continually reconstructed as it wears, through progressive release of lipids, as indicated schematically in Fig. 1. We used this approach to create several different self-lubricating hydrogels of both biological and synthetic polymers (supplementary text section 1); here we focus on the widely exploited (1) poly(hydroxyethylmethacrylate) (pHEMA) hydrogel.

Hydrogels were prepared either without lipids or with low concentrations of the PC lipids dimyristoylphosphatidylcholine (DMPC) or hydrogenated soy phosphatidylcholine (HSPC) added in the form of multilamellar vesicles (MLVs) (though smaller unilamellar vesicles may also be present; materials and methods section 2). These lipids were chosen because they are respectively above and below their gel-to-liquid transition—known to affect lubrication (23)—at room and physiological temperatures. Their distribution is revealed by freeze-fracture cryo-scanning electron microscopy (cryo-SEM) and confocal fluorescence microscopy (materials and methods section 6), as depicted in Fig. 2 (see also supplementary text section 4). The lipid-free hydrogel (Fig. 2A) displays a featureless internal surface, as expected at this resolution. Figure 2, B to F, shows the incorporated DMPC and HSPC MLVs within the hydrogel bulk. These are sequestered in clusters, either as spherical microreservoirs filled with roughly spherical vesicles (DMPC; Fig. 2, B to D), whose size is consistent with dynamic light scattering measurements on the liposome dispersions (materials and methods section 2), or in less regular clusters (HSPC; Fig. 2, E and F). Rheometrically determined mechanical properties (materials and methods section 4) reveal that the hydrogel storage modulus G' ($>G''$, the loss modulus) varies, over a frequency (f) range of 0.1 to 10 Hz, by ~30% or less between lipid-free and PC-incorporating hydrogels (Fig. 2G).

The sliding friction F_s between the hydrogel and a polished stainless steel surface, as well as surfaces of other materials (supplementary text section 7), was examined over a range of loads F_n , corresponding to different mean contact stresses P and sliding velocities v_s (materials and methods section 7 and supplementary text section 12), yielding the coefficient of sliding friction $\mu = F_s/F_n$. Figure 3A shows the tribometer configuration, with representative directly recorded traces from which F_s , and thus μ , is determined, whereas panels B and C in Fig. 3 reveal and quantify the transfer of lipids between gel and steel surface during contact and sliding.

Figure 3, D and E, shows the variation of μ with load for the two lipids used, at room (25°C) and at physiological temperature (37°C). A reduction in friction is seen for the lipid-incorporating gels relative to the lipid-free gels. For the former, μ can range from ~0.02 at lower loads to 0.005 at higher loads; for the latter, at low loads and contact stresses $0.5 \leq \mu \leq 1$ was measured [similar to earlier measurements of high friction for steel sliding against pHEMA hydrogels (24)], whereas for P higher than ~0.5 MPa the metal surface would deform or tear the gel, without sliding (Fig. 3A; see materials and methods section 7). The reduction in friction (Fig. 3, D and E) arising from the lipid incorporation thus ranges from 95% to 99.3% at the higher loads and contact pressures. Although both lipids reduce the friction relative to that of the lipid-free gel, at room temperature DMPC is slightly more lubricious at low loads, whereas at 37°C the

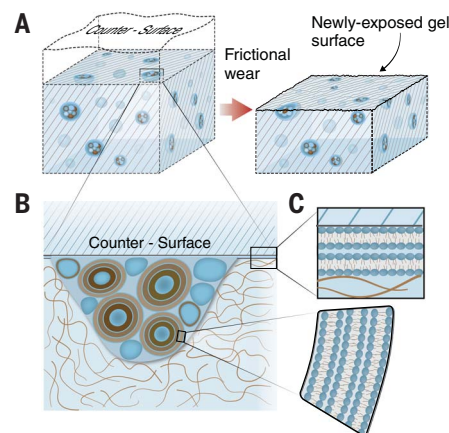


Fig. 1. Schematic illustrating the self-lubrication of lipid-incorporating hydrogels. As the surface of the hydrogel, incorporating lipids as vesicles in microreservoirs (A), wears away because of friction, additional microreservoirs of lipid are exposed. This enables boundary layers of lipids to form on the surfaces (B and C), leading to friction reduction via the hydration lubrication mechanism at the slip plane between the highly hydrated lipid headgroups.

¹Department of Materials and Interfaces, Weizmann Institute of Science, Rehovot 76100, Israel. ²Department of Chemical Research Support, Weizmann Institute of Science, Rehovot 76100, Israel.

*Corresponding author. Email: ronit.goldberg@lipo-sphere.com (R.G.); jacob.klein@weizmann.ac.il (J.K.)

†Present address: LipoSphere Ltd., Pinhas Sapir Street 3, Nes Ziona 7403626, Israel.

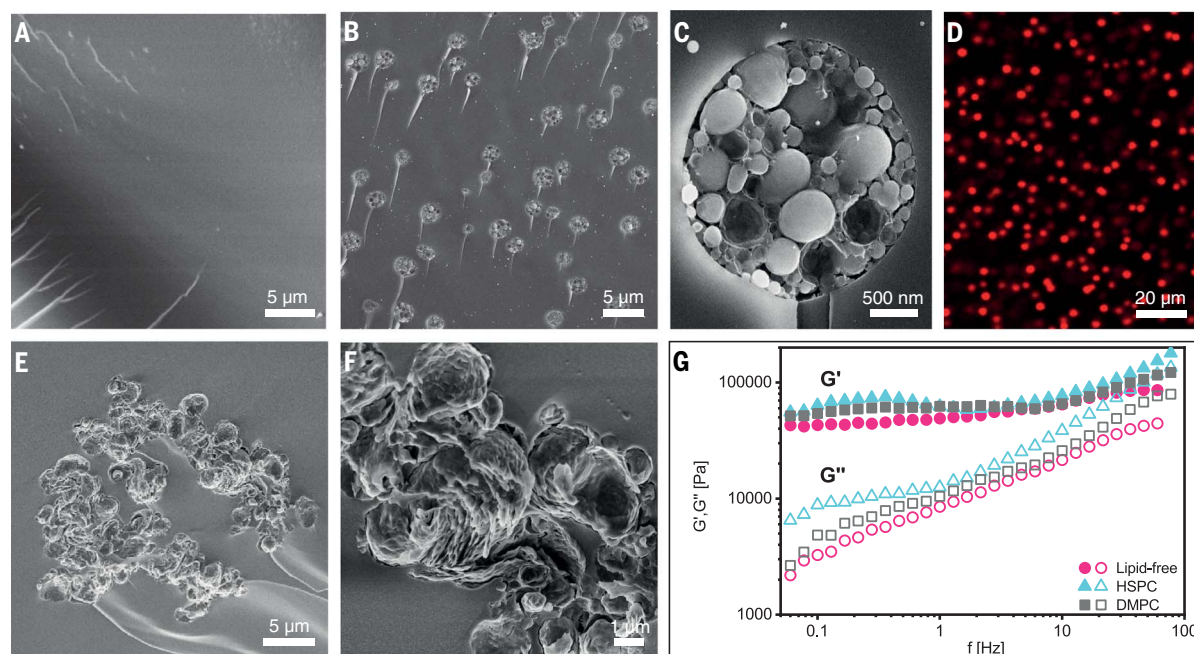


Fig. 2. Characterization of lipid-free and lipid-incorporating hydrogels. (A) Freeze fracture surface of lipid-free pHEMA hydrogel. (B) Freeze-fracture surface of the gel incorporating DMPC vesicles, showing the microreservoirs transected by the surface. (C) A single microreservoir from (B) at larger magnification. (D) Confocal

microscopy section of the hydrogel incorporating fluorescently labeled DMPC vesicles, showing the lipid microreservoir distribution. (E) Freeze-fracture surface of the gel incorporating HSPC vesicles. (F) Microreservoir from (E) at larger magnification. (G) Storage and loss moduli of lipid-free and lipid-incorporating pHEMA gels.

HSPC lipids reduce friction more effectively. We attribute this to the interplay between head-group hydration and bilayer robustness for the two lipids, arising from their different phase states (23). Figure 3F shows the near-constant value of μ with sliding velocity over some three orders of magnitude in v_s , a clear signature of boundary as opposed to fluid-film lubrication.

Incorporating lipids within the bulk hydrogel resulted in much lower friction than when the gels were exposed to lipids externally, as shown in Fig. 4A. For lipid-incorporating hydrogels sliding under water, $\mu \approx 0.01$, as compared with $\mu \approx 0.06$ to 0.08 for lipid-free gels sliding immersed in a PC-MLV dispersion, and $\mu \approx 0.08$ to 0.15 for lipid-free hydrogels incubated overnight in PC-MLV dispersions, then measured in water. In the latter case, the friction rises sharply with sliding time (supplementary text section 2). Thus, lubrication by such external application of lipids is far less effective than when the lipids are incorporated in the bulk hydrogel. For the case of sliding in a liposome dispersion, this observation is attributed to the lipids having poor access to the intersurface region, which arises from the very large distortion energy required for liposomes to enter the intersurface gap (supplementary text section 8). For the case of sliding after overnight lipid adsorption, the lubrication deteriorates rapidly through wear once the external PC source is removed (supplementary text section 2).

When the lipid-incorporating gels are fully dried and then rehydrated (materials and methods section 9), the friction returns to its low value, and the lubrication is once again self-sustaining (Fig. 4B). This robustness to drying and rehydration has particular implications for hydrogel coating and storage of hydrogels. Finally, friction as well as wear and surface damage were reduced by the incorporated lipids. Figure 4C compares wear of the lipid-free hydrogel with that of a DMPC-MLV-incorporating hydrogel after 2 hours of sliding. In these conditions, the wear of the lipid-free pHEMA gel surface was $57 \pm 3 \mu\text{m}$ for a 1-N load, whereas the wear of the lipid-incorporating gel (where $\mu \approx 0.01$ throughout the 2 hours of sliding) was below the detection limit ($\pm 3 \mu\text{m}$) of the tribometer, even for a load 10 times as large. This implies that such gels could resist substantial wear over many sliding cycles (supplementary text section 13). The effect of low surface wear and low damage manifests at a higher load, as shown in Fig. 4D. The lipid-free gel is damaged and torn after just a few seconds of back-and-forth motion of the steel countersurface. This phenomenon is attributed to the high friction strongly shearing the gel and arises because the shear stress σ_s at the gel surface—given by $\sigma_s = \mu P \approx 10^6 \text{ N/m}^2$, where the friction coefficient $\mu \approx 0.5$ to 1 and the mean pressure $P \approx 1.5 \text{ MPa}$ —greatly exceeds the gel shear modulus $G' \approx 6 \times 10^4 \text{ N/m}^2$. At the same time, the lipid-incorporating hydro-

gel (Fig. 4D, left, for which $\mu \approx 0.01$ and $\sigma_s = \mu P \approx 10^4 \text{ N/m}^2$ is much less than G') is barely affected after a full hour of sliding under this load. Notably, after 1 hour of sliding at this high load and contact stress (1.53 MPa), the surface of the liposome-containing gel has worn by $9 \pm 3 \mu\text{m}$ (materials and methods section 7 and supplementary text section 11), yet despite this removal-by-wear of the original gel surface, the frictional force remains unchanged, with $\mu \approx 0.01$ throughout. Because this extent of surface wear far exceeds the thickness of any boundary-lubricating layer or size of the microreservoirs (Fig. 2), it is clear that such layers are continuously renewing as friction abrades the surface, as indicated in Fig. 1. Hydrogels conform affinely when compressed by a countersurface already at very low contact stresses (higher than a fraction of an atmosphere; see supplementary text section 14). Thus the lubricating lipids are expected to spread over the entire hydrogel contact area, as long as the sliding amplitude exceeds the mean inter-microreservoir spacing of a few micrometers.

Sliding takes place through hydration-lubricated slip between the exposed hydrated headgroups of the lipid bilayers or liposomes (supplementary text section 6). These are extracted by interfacial shear, due to the sliding, from the surface-exposed microreservoirs (Figs. 1 and 2) and are thereby spread to coat the opposing (gel and metal) surfaces (supplementary

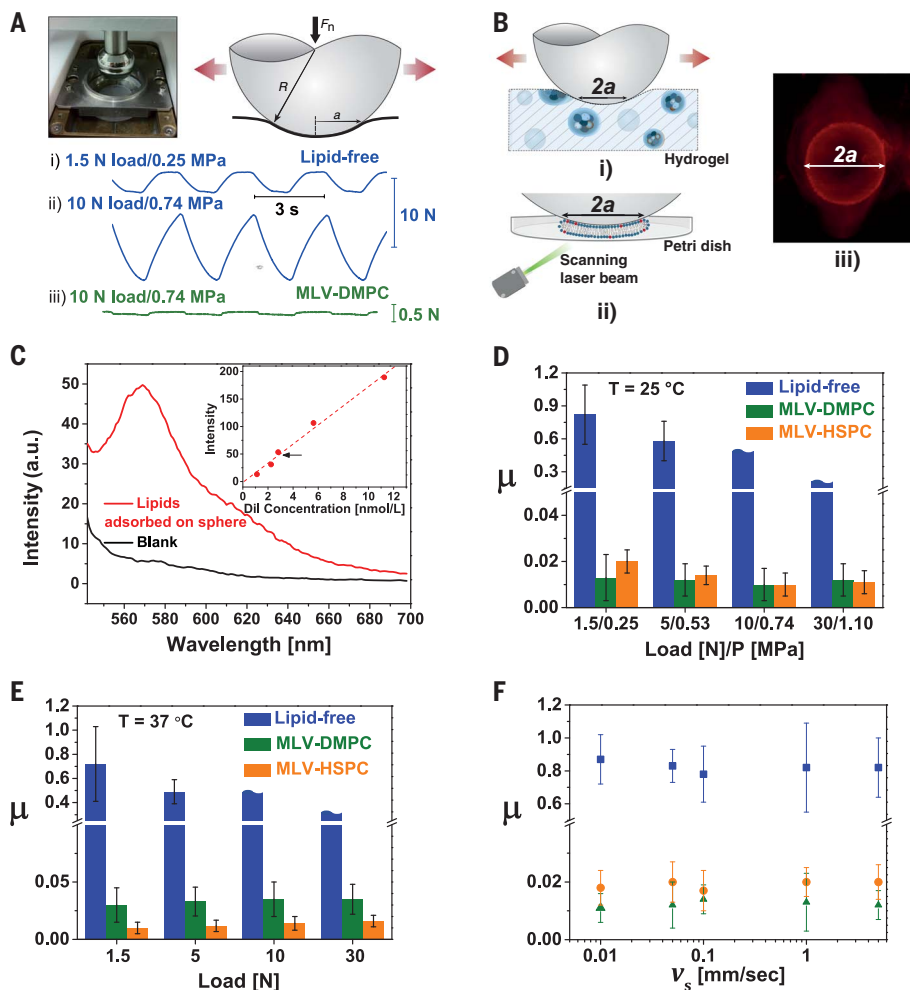


Fig. 3. Sliding between a steel sphere and pHEMA hydrogels. (A) UMT (Universal Mechanical Tester) tribometer and sliding configuration (materials and methods section 7) and typical friction-versus-time traces for lipid-free and lipid-incorporating gels, where F_s is taken as half of the amplitude between sliding plateaus. The middle trace (no sliding plateau) indicates that sliding is not achieved and that F_s must be larger than half of the amplitude between peaks. (B) Transfer of fluorescently labeled lipids incorporated in the gel to the contact area (radius a) with the sliding steel sphere, as in (i), is monitored as follows: After sliding, the steel sphere is placed in a Petri dish and the dye in the transferred lipid layer is excited with a scanning laser beam, as in (ii), and imaged with a photomultiplier tube to yield images, as in (iii), that show the lipid transfer after 5 min of sliding. The amount of transferred lipids is then quantified as in (C) (see also materials and methods section 11). a.u., arbitrary units. (D) and (E) show friction coefficient values μ at room and physiological temperatures, respectively, at a series of loads and corresponding contact stresses. “Wavy-topped” columns indicate that no sliding was achieved [see middle trace in (A)], so μ must be larger than the column height shown. Error bars indicate SD from at least six independent measurements. (F) Variation of μ with sliding velocity v_s for lipid-free (blue) and lipid-incorporating (HSPC, orange; DMPC, green) pHEMA gels. Error bars indicate SD from at least three measurements.

text section 5). The zwitterionic phosphocholine headgroups adhere to both the negatively charged (25) pHEMA surface, which is rich in dipolar hydroxyl groups (26) (such dipole-charge interactions may also help localize the vesicles within the microreservoirs), and the negatively charged stainless steel countersurface (27), as seen by atomic force microscopy imaging (supplementary text sections 3 and 4). More directly, we see trans-

fer of fluorescently labeled gel-incorporated lipids to the sliding steel sphere countersurface. The area covered by the transferred lipids can be imaged (Fig. 3B) and its thickness evaluated from their total calibrated fluorescence intensity (Fig. 3C and materials and methods section 11). This shows that the lipid layer on the metal surface is 1.5 ± 0.5 bilayers thick, consistent with hydration lubrication at the slip plane between metal-attached and gel-

attached bilayers, as indicated in Fig. 1. Similar hydration lubrication by PC boundary layers on model substrates (14, 28) yields even lower friction ($\mu \approx 0.001$ or less) than observed with our hydrogels (for which $\mu \approx 0.005$ to 0.02). This finding reflects the softer and rougher nature of our substrates, with consequent additional pathways for frictional dissipation, such as viscoelastic losses, relative to these earlier studies in which rigid and extremely smooth substrates were used (23, 28, 29). Evidence for this phenomenon is provided by the variation of μ for pHEMA gels of different moduli, induced by varying the cross-linker density within the lipid-incorporating gels, where softer gels have higher sliding friction (supplementary text section 9).

The self-renewal of the lubricating boundary layer, as the hydrogel abrades under friction, is attributed to its continuous healing through availability of lipids at the surface, as microreservoirs of the PC vesicles within the gel become progressively exposed and sheared by the countersurface (Fig. 1). A more detailed consideration (materials and methods section 10) shows that the total volume of lipids available at the gel surface from reservoirs transected by it would be sufficient to form a lipid film of thickness d given by

$$d \approx 2\phi R_0$$

where ϕ is the mean volume fraction of lipids incorporated in the bulk hydrogel, and R_0 is the radius of a microreservoir. R_0 could be varied by changing the concentration of lipids incorporated within the gel (supplementary text section 10). When $R_0 \approx 1.5 \mu\text{m}$ (Fig. 2, B and C) and $\phi = 0.012$ (materials and methods section 2), as in our experiments, $d \approx 36 \text{ nm}$, which is equivalent to the thickness of some seven to eight bilayers of DMPC. This is more than sufficient for hydration lubrication between a bilayer or even a compressed vesicle layer attached on each of the opposing surfaces (23, 29), indicating that the mechanism shown in Fig. 1 can amply account for the self-sustaining lubricating boundary layers as the gel surface wears away. It is also consistent with the thickness of the lipid layer transferred to the metal surface, as indicated above (Fig. 3, B and C).

We show that trace incorporation of PC lipids provides a simple route to create hydrogels that can continuously lubricate themselves as they wear, via the hydration lubrication mechanism attributed to PC-exposing boundary layers on articular cartilage. Such gels maintain very low friction and wear—up to contact stresses of several megapascals and sliding velocities up to the centimeter-per-second scale—while minimally perturbing their bulk mechanical properties. Our approach may provide a platform for creating self-lubricating hydrogels wherever low friction and low wear are required.

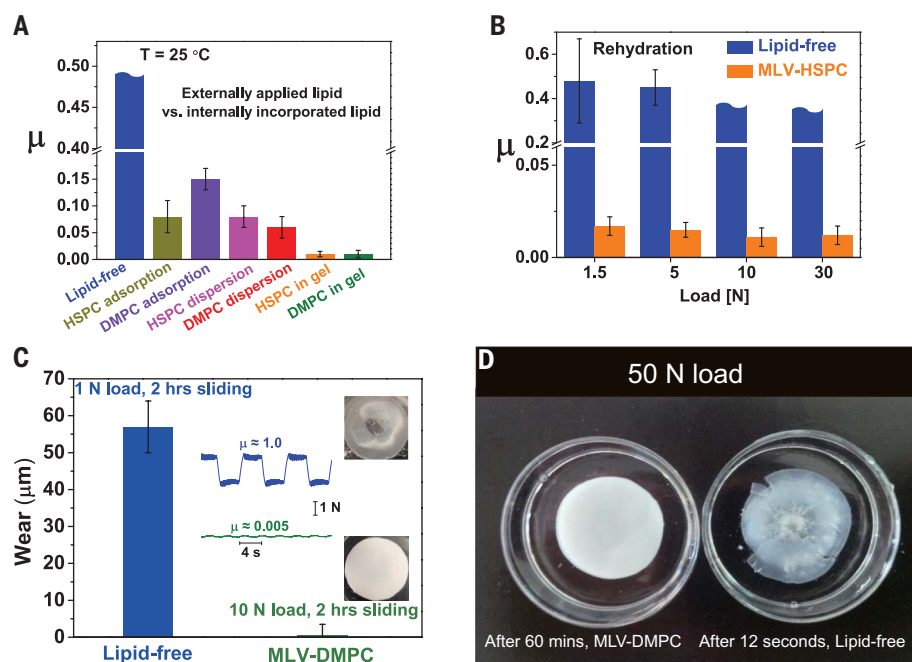


Fig. 4. Friction and wear of lipid-treated pHEMA gels. (A) Sliding friction between lipid-free gels (blue), between lipid-free gels after adsorption of HSPC (olive green) and DMPC (violet) followed by washing, after 30 min of sliding, and between lipid-free gels immersed in lipid dispersions (purple and red), compared with lipid-incorporating gels immersed in water (orange and green). Error bars indicate SD from at least three independent measurements. (B) Effect of rehydration after dehydration of lipid-free and HSPC-incorporating gels, showing retention of the characteristic self-lubricating ability for the latter. Wavy-topped columns represent a lower bound on μ (see also Fig. 3, D and E, and materials and methods section 7). Error bars indicate SD from at least three independent measurements. (C) Wear of lipid-free and DMPC-incorporating gels, showing typical friction traces as well as the visual appearance of the gel samples, after 2 hours of sliding of the steel sphere on the gels, at 1-N load for the lipid-free gel and 10-N load for the lipid-incorporating gel. (D) Appearance of gel samples under 50-N load (1.53-MPa contact stress) on the steel sphere. After 1 hour of sliding (corresponding to 9 μm of wear), the appearance of the DMPC-incorporated gel was unchanged, whereas the lipid-free gel was torn after 12 s of back-and-forth shear under the load.

REFERENCES AND NOTES

- N. A. Peppas, J. Z. Hilt, A. Khademhosseini, R. Langer, *Adv. Mater.* **18**, 1345–1360 (2006).
- J. J. Green, J. H. Elisseeff, *Nature* **540**, 386–394 (2016).
- M. Liu *et al.*, *Nature* **517**, 68–72 (2015).
- J. P. Gong, *Soft Matter* **2**, 544–552 (2006).
- A. A. Pitenis, J. Manuel Uruña, A. C. Cooper, T. E. Angelini, W. Gregory Sawyer, *J. Tribol.* **138**, 042103 (2016).
- X. Zhang, J. Wang, H. Jin, S. Wang, W. Song, *J. Am. Chem. Soc.* **140**, 3186–3189 (2018).
- J. Cui, D. Daniel, A. Grinthal, K. Lin, J. Aizenberg, *Nat. Mater.* **14**, 790–795 (2015).
- E. Porte, P. Cann, M. Masen, *J. Mech. Behav. Biomed. Mater.* **90**, 284–294 (2019).
- C. W. McCutchen, *Nature* **184**, 1284–1285 (1959).
- V. C. Mow, G. A. Ateshian, in *Basic Orthopaedic Biomechanics*, V. C. Mow, W. Hayes, Eds. (Lippincott-Raven, 1997), pp. 275–315.
- H. Forster, J. Fisher, *Proc. Inst. Mech. Eng. H* **210**, 109–119 (1996).
- S. Jahn, J. Seror, J. Klein, *Annu. Rev. Biomed. Eng.* **18**, 235–258 (2016).
- S. Lee, N. D. Spencer, *Science* **319**, 575–576 (2008).
- J. Seror, L. Zhu, R. Goldberg, A. J. Day, J. Klein, *Nat. Commun.* **6**, 6497 (2015).
- W. H. Briscoe *et al.*, *Nature* **444**, 191–194 (2006).
- J. A. Buckwalter, H. J. Mankin, A. J. Grodzinsky, *Instr. Course Lect.* **54**, 465–480 (2005).
- J. Klein, *Science* **323**, 47–48 (2009).
- D. P. Chang *et al.*, *Soft Matter* **5**, 3438–3445 (2009).
- A. Singh *et al.*, *Nat. Mater.* **13**, 988–995 (2014).
- M. K. Kosinska *et al.*, *Arthritis Rheum.* **65**, 2323–2333 (2013).
- A. V. Sarma, G. L. Powell, M. LaBerge, *J. Orthop. Res.* **19**, 671–676 (2001).
- B. A. Hills, B. D. Butler, *Ann. Rheum. Dis.* **43**, 641–648 (1984).
- R. Sorkin, N. Kampf, Y. Dror, E. Shimon, J. Klein, *Biomaterials* **34**, 5465–5475 (2013).
- M. E. Freeman, M. J. Furey, B. J. Love, J. M. Hampton, *Wear* **241**, 129–135 (2000).
- A. H. Hogt *et al.*, *J. Colloid Interface Sci.* **106**, 289–298 (1985).
- Q. Chen, D. Zhang, G. Somorjai, C. R. Bertozzi, *J. Am. Chem. Soc.* **121**, 446–447 (1999).
- L. Boulangé-Petermann, A. Doren, B. Baroux, M.-N. Bellon-Fontaine, *J. Colloid Interface Sci.* **171**, 179–186 (1995).
- A.-M. Trunfio-Starghiu, Y. Berthier, M.-H. Meurisse, J.-P. Rieu, *Langmuir* **24**, 8765–8771 (2008).
- R. Goldberg *et al.*, *Adv. Mater.* **23**, 3517–3521 (2011).

ACKNOWLEDGMENTS

We thank S. Safran and A. Butcher for useful discussions and M. Urbakh for comments on the manuscript. The electron microscopy studies were conducted at the Irving and Cherna Moskowitz Center for Nano and Bio-Nano Imaging at the Weizmann Institute of Science.

Funding: This project has received funding from the European Research Council (ERC) under the European Union's Horizon 2020 research and innovation program (grant 743016). We thank the McCutchen Foundation, the Israel Science Foundation (grant 1715/2014), the Israel Science Foundation–National Science Foundation China (grant 2577/17), the Israel Ministry of Science and Technology (grant 713272), and the Weizmann-EPFL Collaboration Program funded by the Rothschild Caesarea Foundation for support of this work. This work was made possible in part through the historic generosity of the Harold Perlman family. **Author contributions:** R.G. and J.K. conceived the project; R.G., W.L., M.K., N.I., and N.K. carried out experiments; E.S. and R.G. carried out cryo-SEM imaging; J.K., R.G., W.L., and M.K. wrote the manuscript and analyzed the data; and all authors commented on the manuscript. **Competing interests:** The Weizmann Institute has a patent on low-friction hydrogels (US20160175488A1). **Data and materials availability:** All data are available in the manuscript or the supplementary materials.

SUPPLEMENTARY MATERIALS

science.sciencemag.org/content/370/6514/335/suppl/DC1
Materials and Methods
Supplementary Text
Figs. S1 to S16
References (30–39)

23 July 2019; resubmitted 10 May 2020
Accepted 6 August 2020
10.1126/science.aay8276

SPECTROSCOPY

Zeptosecond birth time delay in molecular photoionization

Sven Grundmann^{1*}, Daniel Trabert¹, Kilian Fehre¹, Nico Strenger¹, Andreas Pier¹, Leon Kaiser¹, Max Kircher¹, Miriam Weller¹, Sebastian Eckart¹, Lothar Ph. H. Schmidt¹, Florian Trinter^{1,2,3}, Till Jahnke^{1*}, Markus S. Schöffler¹, Reinhard Dörner^{1*}

Photoionization is one of the fundamental light-matter interaction processes in which the absorption of a photon launches the escape of an electron. The time scale of this process poses many open questions. Experiments have found time delays in the attosecond (10^{-18} seconds) domain between electron ejection from different orbitals, from different electronic bands, or in different directions. Here, we demonstrate that, across a molecular orbital, the electron is not launched at the same time. Rather, the birth time depends on the travel time of the photon across the molecule, which is 247 zeptoseconds (1 zeptosecond = 10^{-21} seconds) for the average bond length of molecular hydrogen. Using an electron interferometric technique, we resolve this birth time delay between electron emission from the two centers of the hydrogen molecule.

Photoionization is a fundamental quantum process that has become a powerful tool to study atoms, molecules, liquids, and solids. Facilitated by the advent of attosecond technology, it can now even be addressed in the time domain. Timing in photoionization usually refers to the time it takes for an electron to escape to the continuum after absorption of the photon. This time depends, for example, on the electronic orbital (1, 2), on the energy band in solids (3, 4), or on the orientation (5) and handedness (6) of the target molecule. The escape time difference manifests as a phase shift of the electron wave in the far field. This relation is based on the concept of the Wigner delay, which is the energy derivative of the phase of a photoelectron wave at an asymptotic distance from the source (7). Typical numbers are, for example, 20 attoseconds (1 as = 10^{-18} s) for the Wigner delay between emission from the 2s and 2p shells in neon (1).

However, the Wigner delay does not cover another notable question about the timing in photoionization of extended systems—namely the temporal buildup of the photoelectron wave across its spatially extended source. Hereafter, we refer to these variations in the temporal structure of the electron wave as the birth time delay τ_b . Although the Wigner delay is caused during the travel of the electron to the continuum after its birth, τ_b relies on different birth times of the contributions to the total photoelectron wave along a molecular orbital. Accord-

ingly, the birth time delay quantifies to what extent a delocalized molecular orbital reacts simultaneously as a single unit on being hit by a photon. For example, it shows whether the part of the orbital facing toward an approaching photon reacts first and whether the part downstream of the photon beam has a retarded

response. Notably, the delays expected from that travel time of a photon across molecular orbitals are one to two orders of magnitude shorter than the Wigner delay—i.e., they manifest in the zeptosecond (1 zs = 10^{-21} s) domain. In the description of light-matter interactions, such ultrashort time differences are often ignored, and the dipole approximation is invoked. Doing so corresponds to neglecting the spatial dependence of the light wave, and the light's electric field is approximated to be present instantaneously with the same phase over the whole relevant region of space. Beyond this approximation, however, the birth time delay leads to a phase shift between the corresponding contributions to the overall photoelectron wave. Such relative phases—and hence the birth time delays across a molecular orbital—are accessible by experiments that exploit the interference between the different parts of the wave function. Figure 1 outlines our metrology to measure τ_b .

Our approach builds on the close analogy between a plane wave behind a double slit (Fig. 1, A and B) and the photoelectron wave emitted from a homonuclear diatomic molecule (Fig. 1, C and D). This analogy was proposed by Cohen and Fano (8) and is well established

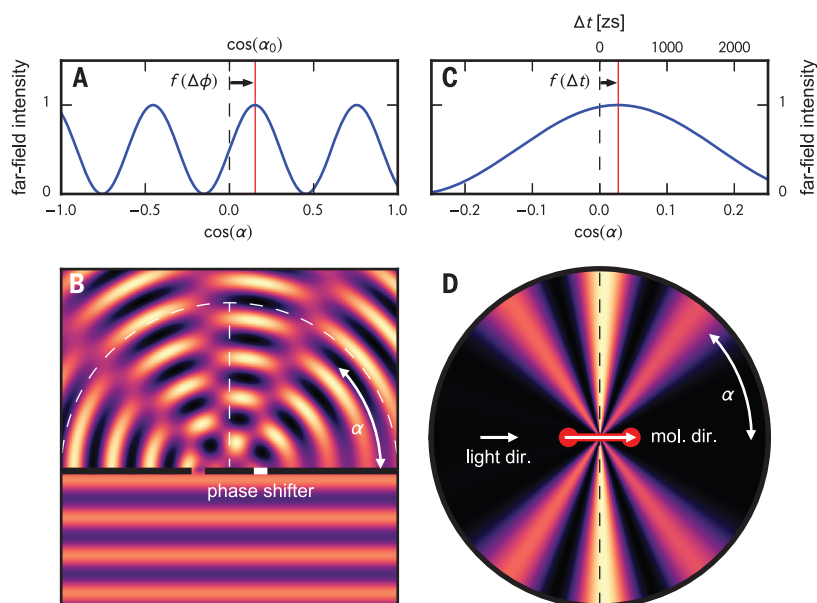


Fig. 1. Concept of birth time delay measurement. (A) Intensity distribution on a screen in the far field behind the double slit in (B). (B) A plane wave impinges on a double slit. The phase shift [$\Delta\phi$] in the right slit causes a tilt of the interference pattern. (C and D) Emission of a photoelectron wave from two indistinguishable atoms of a homonuclear diatomic molecule mimics the double-slit setup in (B). Here, the angle α is enclosed by the electron momentum vector and the molecular axis. A time delay (Δt) between the emission from one of the two centers—e.g., originating from the travel time of the photon impinging from the left side in (D)—leads to a shift of the interference fringes in (C). The ratio of slit distance (molecular bond length R , respectively) to wavelength is 1.65 in both cases [(B) and (D)]. In (B) the right-hand part of the wave is delayed by $\Delta\phi = \pi/2$, whereas in (D) a birth time delay of 247 zs causes $\Delta\phi \approx \pi/11$ for $R = 0.74$ Å. light dir., light direction; mol. dir., molecular direction.

¹Institut für Kernphysik, Goethe-Universität, Max-von-Laue-Strasse 1, 60438 Frankfurt, Germany. ²Photon Science, Deutsches Elektronen-Synchrotron (DESY), Notkestrasse 85, 22607 Hamburg, Germany. ³Molecular Physics, Fritz-Haber-Institut der Max-Planck-Gesellschaft, Faradayweg 4-6, 14195 Berlin, Germany.

*Corresponding author. Email: grundmann@atom.uni-frankfurt.de (S.G.); jahnke@atom.uni-frankfurt.de (T.J.); doerner@atom.uni-frankfurt.de (R.D.)

today (9, 10). It has been used, for example, to study the onset of decoherence of a quantum system (11) and entanglement in an electron pair (12). The angular emission pattern from a gerade orbital has a maximum that is perpendicular to the molecular axis, which corresponds to the zeroth-order interference maximum behind the double slit. If a constant phase shift $\Delta\phi$ is introduced to one of the slits, the interference pattern behind the double slit becomes asymmetric, and the angular position of the interference fringes moves as a function of $\Delta\phi$ on an intensity screen in the far field. In Fig. 1, A and B, we illustrate this relation. A corresponding shift may also occur when two interfering electron waves are emerging from the two indistinguishable centers of a homonuclear diatomic molecule upon photon absorption (Fig. 1, C and D). If the contributions to the photoelectron wave are launched simultaneously across an orbital of a diatomic molecule, the electron emission pattern in the molecular frame of reference is symmetric with respect to the normal of the bond axis. However, any initial phase shift between the waves emerging from one or the other center leads to an angular shift of the diffraction pattern—just as in the double-slit case. Hence, inspecting the angular emission distribution of photoelectrons emitted from a homonuclear diatomic molecule for such angular shifts offers a way to measure the birth time delay τ_b (13).

For an electron of kinetic energy E_e and momentum p_e , τ_b can be obtained from the measured angle α_0 —the angle to which the central interference maximum is shifted—in the following way: An electron wave is emitted and propagates with the phase velocity $v_{ph} = E_e/p_e$ for the time τ_b before a second electron wave is born at a distance R . The zeroth-order interference maximum occurs under the emission angle α_0 for which the path length difference between both electron waves vanishes

$$2\pi \left[\frac{\cos(\alpha_0) \cdot R}{\lambda} - \frac{\tau_b \cdot v_{ph}}{\lambda} \right] = 0 \quad (1)$$

where λ is the electron's de Broglie wavelength. Accordingly, the birth time delay τ_b can be inferred from the angular shift α_0 , and an angle of $\alpha_0 = 90^\circ$ corresponds to zero birth time delay (simultaneous emission)

$$\tau_b = \cos(\alpha_0) \frac{R}{v_{ph}} \quad (2)$$

We implemented this scheme by studying one-photon double ionization of H_2 using left-handed circularly polarized photons with an energy of 800 eV. Using a COLTRIMS reaction microscope (14), we measured the three-

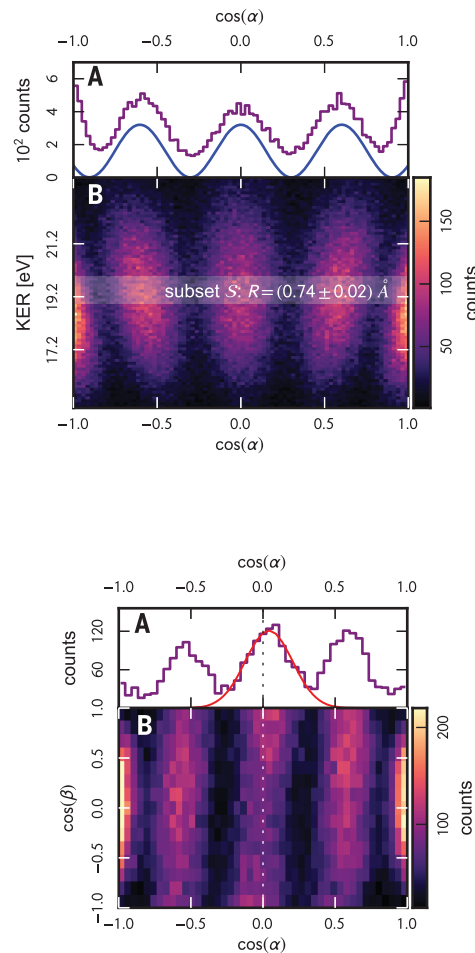


Fig. 2. Electron emission from H_2 mimics the double-slit experiment. (A and B) Interference pattern of fast electrons ($E_e = 735 \pm 15$ eV) from one-photon double ionization of H_2 by 800 eV circularly polarized photons for the average internuclear distance of $R = 0.74 \pm 0.02$ Å [purple line in (A)] and as function of R (B). The blue line in (A) models a double-slit interference pattern for a slit distance $R = 0.74$ Å and $\lambda = 0.45$ Å, which is the average de Broglie wavelength of the fast electron. The subset S of the data are used for (A) and for the subsequent analysis of the birth time delay.

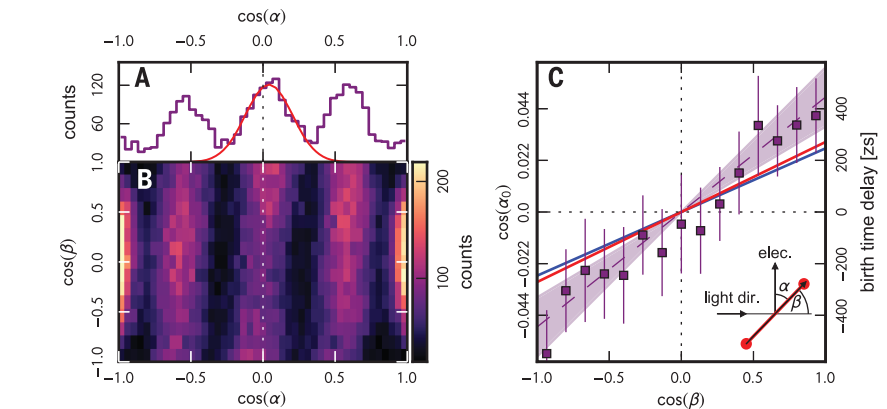


Fig. 3. Results of birth time delay measurement. Birth time delay of fast electrons ($E_e = 735 \pm 15$ eV) from one-photon double ionization of H_2 by 800 eV circularly polarized photons for the average internuclear distance of $R = 0.74 \pm 0.02$ Å (selected subset S as shown in Fig. 2B). (A) Electron angular distribution with respect to the molecular axis, which is aligned parallel to the light propagation direction [$\cos(\beta) > 0.87$, corresponding to the top row of bins in (B)]. Red curve is the Gaussian fit used to obtain the angular position of the zeroth-order maximum $\cos(\alpha_0)$. (B) Electron angular distribution in the molecular frame of reference as a function of $\cos(\beta)$. Dashed line is perpendicular to the molecular axis—i.e., the location of the zeroth-order maximum in the absence of birth time delays. (C) Location of the maxima of the zeroth-order interference fringe as a function of $\cos(\beta)$. The maxima are obtained with Gaussian fits, as indicated by the red line in (A). The error bars include statistical and systematic errors, and the purple-shaded error range indicates the systematical error (see supplementary materials for further details). Left axis: $\cos(\alpha_0)$; right axis: birth time delay calculated with Eq. 2. The blue line resembles a birth time delay given by the travel time of light across the molecule (Eq. 3). The red line is a prediction combining atomic nondipole effects and the travel time of the photon (see text for details). elec., electron.

dimensional momenta of both protons in coincidence with one electron. From the sum momentum of the three measured particles, we inferred the missing electron momentum vector by means of momentum conservation including the photon momentum. The molecules in the target gas jet were randomly oriented with respect to the light propagation. After ejection of the two electrons, the two protons were driven apart by their Coulomb repulsion. We obtained the orientation of the molecular axis and the kinetic energy release

(KER) from the relative momentum of the protons (15, 16). In the reflection approximation, the internuclear distance R at the moment of photoabsorption is related to the kinetic energy release through $KER = e^2/(4\pi\epsilon_0 R)$, where e is the elementary charge and ϵ_0 is the vacuum permittivity.

One-photon double ionization typically proceeds by means of one of two sequential processes. A primary photoelectron is set free by the absorption of the photon, and the second electron is either shaken off or knocked out to

the continuum (17). The fraction of the photon energy that exceeds the sum of the adiabatic double ionization energy of H₂ (31.03 eV) and the KER is shared between the two electrons. The symmetry of this energy sharing is a measure for the strength of the Coulomb interaction among the two electrons, which has the potential to destroy the single-particle quantum interference pattern (12). Therefore, we restricted our investigation to fast electrons that carried >96% of the excess energy (fig. S2). For such fast electrons, double-slit interference effects are well established on the single-particle level (11, 18). Corresponding slow electrons of the double ionization process had <4% of the excess energy and are not shown here (19).

In Fig. 2A, we display the electron angular distribution of those fast electrons for the average internuclear distance of 0.74 Å (purple line). The results show a rich structure, which—as expected—resembles the interference pattern of electrons emerging from a double slit. Figure 2B displays this measured interference pattern of the fast electron as a function of the internuclear distance. The results show how the number of interference fringes increased and how the angular separation of the maxima decreased with increasing internuclear distance R , which affirms the double-slit nature of the electron emission.

The data shown in Fig. 2 were averaged over all orientations of the molecular axis with respect to the light propagation and the light's polarization plane. Thus, the results must be symmetric. To search for possible shifts of the interference fringes resulting from birth time delays, we inspected the interference pattern of the fast electron for different angles β between the photon propagation direction and the molecular axis in Fig. 3 for the subset S (see Fig. 2B). Figure 3A shows the measured fringes for molecules aligned parallel to the light propagation direction (see fig. S3 for a corresponding polar plot). The zeroth-order maximum of the distribution was displaced to the right, which suggested the existence of a birth time delay. To confirm this assumption, we depicted the interference fringes as function of $\cos(\beta)$ in Fig. 3B. The histogram shows a clear dependence of the central fringe on the photon direction. For a quantitative analysis, we determined $\cos(\alpha_0)$ —i.e., the angular position of the central maximum—for each row of the histogram in Fig. 3B through a Gaussian fit (red curve in Fig. 3A). Figure 3C shows the results of these fits and the corresponding birth time delays (according to Eq. 2) on the right vertical scale. The birth time delay might be interpreted as a nondipole Wigner delay between photoionization from different locations of the spatially extended molecular orbital. However, the usual Wigner times—treated entirely within the dipole approximation so

far—would likely depend on α and β , but they are equal for the different pathways that interfere under a certain emission angle α and do not influence our measurement.

We compared our experimental findings with two simple models. First, we assumed that τ_b is given by the time difference with which a point of constant phase of the photon wave hits the two centers

$$\tau_b = \cos(\beta) \frac{R}{c} \quad (3)$$

where c is the speed of light. In the case of $\cos(\beta) = 0$, the photon wave hits both centers of the molecule simultaneously, and there cannot be any birth time delay between electrons emitted from one or the other center because the outgoing waves are exactly in phase. On the other hand, $\cos(\beta) = \pm 1$ resembles the maximum possible travel time of the photon from one molecular center to the other. For this case, the expected birth time delay was ± 247 zs for $R = 0.74$ Å. Between these extreme cases, the birth time delay showed a linear dependence on $\cos(\beta)$. For comparison to the experimental data, the blue line in Fig. 3C resembles this simple model. Note that the model agreed with the prediction from equation 12 of (20), if one neglects the ionization potential.

Second, the red line in Fig. 3C shows the result from a more refined model. This model accounted for the fact that—other than in the optical double slit—in photoionization, the two interfering waves are not simply spherical. At the high photon energy used here, the atomic nondipole effect tilts the electron angular distributions from each center slightly in the forward direction with respect to the photon propagation (21). This fact led to an additional angular shift of the interference pattern that slightly increased the slope of the red line compared with the blue one. The red line obtained from considering molecular photoionization in the time domain was in line with the prediction of calculations of molecular photoionization in the frequency domain if nondipole effects are included in full (22). This model is in reasonable agreement with the experimental results, but more theoretical work including electron-electron correlation is needed to clarify the deviation.

We have shown that the birth of a photoelectron wave from a molecular orbital did not occur simultaneously across the molecule. With an electron interferometric technique, we observed the resulting birth time delay, which was imprinted as a phase difference between the parts of the wave launching from the two sides of the H₂ molecule. The observed effect is general and does not only alter molecular photoionization, but it is also expected to be relevant for electron emission from solids and liquids.

The analogy between electron emission from the H₂ molecule and a classical double-slit experiment suggests that the birth time delay could be interpreted as the travel time of the photon from one molecular center to the other, which is up to 247 zs for the average bond length of H₂. Our experimental results support this picture, but studies targeting more-complex molecules and applying more-sophisticated theoretical models are necessary to further unveil the scope of birth time delay. This work can function as a benchmark for such studies.

REFERENCES AND NOTES

1. M. Schultze *et al.*, *Science* **328**, 1658–1662 (2010).
2. M. Isinger *et al.*, *Science* **358**, 893–896 (2017).
3. A. L. Cavalieri *et al.*, *Nature* **449**, 1029–1032 (2007).
4. Z. Tao *et al.*, *Science* **353**, 62–67 (2016).
5. J. Vos *et al.*, *Science* **360**, 1326–1330 (2018).
6. S. Beaulieu *et al.*, *Science* **358**, 1288–1294 (2017).
7. J. M. Dahlström, A. L'Huillier, A. Maquet, *J. Phys. B* **45**, 183001 (2012).
8. H. D. Cohen, U. Fano, *Phys. Rev.* **150**, 30–33 (1966).
9. J. Fernández, O. Fojón, A. Palacios, F. Martín, *Phys. Rev. Lett.* **98**, 043005 (2007).
10. S. E. Canton *et al.*, *Proc. Natl. Acad. Sci. U.S.A.* **108**, 7302–7306 (2011).
11. D. Akoury *et al.*, *Science* **318**, 949–952 (2007).
12. M. Waitz *et al.*, *Phys. Rev. Lett.* **117**, 083002 (2016).
13. This interferometric technique is insensitive to the length of the used synchrotron light pulses up to 100 ps.
14. J. Ullrich *et al.*, *Rep. Prog. Phys.* **66**, 1463–1545 (2003).
15. T. Weber *et al.*, *Nature* **431**, 437–440 (2004).
16. M. S. Schöffler *et al.*, *Phys. Rev. A* **78**, 013414 (2008).
17. C. Siedschlag, T. Pattard, *J. Phys. B* **38**, 2297–2310 (2005).
18. D. A. Horner *et al.*, *Phys. Rev. Lett.* **101**, 183002 (2008).
19. The emission of the second electron is mediated through the Coulomb interaction and is therefore subject to the retardation of the electromagnetic field. This possible additional delay of the double ionization process is symmetric with respect to the inversion of the two centers of the molecule. Therefore, our interferometric technique is blind to this absolute delay.
20. G. L. Yudin, S. Chelkowski, A. D. Bandrauk, *J. Phys. B* **39**, L17–L24 (2006).
21. S. Grundmann *et al.*, *Phys. Rev. Lett.* **124**, 233201 (2020).
22. S. Chelkowski, A. D. Bandrauk, *Phys. Rev. A* **97**, 053401 (2018).
23. S. Grundmann, Zeptosecond Birth Time Delay in Molecular Photoionization, version v1, Zenodo (2020); <http://doi.org/10.5281/zenodo.3899920>.

ACKNOWLEDGMENTS

We acknowledge DESY (Hamburg, Germany), a member of the Helmholtz Association HGF, for the provision of experimental facilities. Parts of this research were carried out at PETRA III, and we thank J. Seltmann and K. Bagschik for excellent support during the beam time. S.G. is grateful for discussions on the topic with A. Kheifets and H. Kremer. **Funding:** We acknowledge support by BMBF and by DFG. K.F. acknowledges support by the German National Merit Foundation. **Author contributions:** M.S.S., T.J., K.F., N.S., A.P., L.K., S.E., M.W., S.G., D.T., L.Ph.H.S., R.D., and F.T. designed, prepared, and performed the experiment. S.G. performed the data analysis. S.G. and M.K. created the figures. All authors contributed to the manuscript. **Competing interests:** None declared. **Data and materials availability:** Data presented in this study are available on Zenodo (23).

SUPPLEMENTARY MATERIALS

science.sciencemag.org/content/370/6514/339/suppl/DC1
Materials and Methods
Supplementary Text
Figs. S1 to S3
References (24–26)

28 April 2020; accepted 26 August 2020
10.1126/science.abb9318

THERMOGALVANICS

Thermosensitive crystallization-boosted liquid thermocells for low-grade heat harvesting

Boyang Yu^{1*}, Jiangjiang Duan^{1*}, Hengjiang Cong², Wenke Xie¹, Rong Liu¹, Xinyan Zhuang¹, Hui Wang¹, Bei Qi¹, Ming Xu³, Zhong Lin Wang⁴, Jun Zhou^{1†}

Low-grade heat (below 373 kelvin) is abundant and ubiquitous but is mostly wasted because present recovery technologies are not cost-effective. The liquid-state thermocell (LTC), an inexpensive and scalable thermoelectric device, may be commercially viable for harvesting low-grade heat energy if its Carnot-relative efficiency (η_r) reaches ~5%, which is a challenging metric to achieve experimentally. We used a thermosensitive crystallization and dissolution process to induce a persistent concentration gradient of redox ions, a highly enhanced Seebeck coefficient (~3.73 millivolts per kelvin), and suppressed thermal conductivity in LTCs. As a result, we achieved a high η_r of 11.1% for LTCs near room temperature. Our device demonstration offers promise for cost-effective low-grade heat harvesting.

A vast amount of low-grade heat (below 373 K) is distributed in industrial processes (waste heat), the environment (solar-thermal and geothermal energy), and the human body. Because present-day energy recovery technologies are not cost-effective, this heat is wasted (1). Thermoelectric devices convert heat to energy without moving parts, audible noise, or greenhouse emissions (2). The performance of thermoelectric devices is estimated by a device figure of merit ($Z = S_e^2 \sigma / \kappa$), which depends on the Seebeck coefficient (S_e), electrical conductivity (σ), and thermal conductivity (κ). Among thermoelectrics, traditional solid-state thermoelectric cells are the most intensively studied. However, their efficiency near room temperature has only modestly progressed because of the well-known strong interdependence of S_e , σ , and κ in solid thermoelectric materials. This is especially problematic for low-cost materials free of rare elements (3–10). Alternatively, liquid-state thermocells (LTCs) offer more ways to decouple the interdependence of S_e , σ , and κ (11). Furthermore, LTCs are inexpensive, scalable, and potentially commercially viable for harvesting low-grade heat energy if the Carnot-relative efficiency (η_r) reaches ~5% (12). That value has been challenging to achieve even with ideal laboratory devices (13). We achieved an η_r of 11.1% for LTCs near room temperature by using a thermosensitive crystallization process that highly enhances S_e and suppresses κ without scarifying σ synergistically. The cost-performance metric

of our LTC therefore substantially decreases and is comparable to that of current power generation technologies, indicating its potential for inexpensive and highly efficient harvesting of low-grade wasted heat energy.

The pristine LTC consists of two electrodes and electrolyte containing a redox couple (Fig. 1A). The electrodes and electrolyte are readily available and do not require complex manufacturing. The 0.4 M $K_3Fe(CN)_6/K_4Fe(CN)_6$ aqueous electrolyte with $S_e \sim 1.4$ mV K⁻¹ has been studied extensively as the benchmark for LTCs (13–22). When a temperature gradient is built between two electrodes, the balance of reversible reactions between the redox couple is broken, and the reactions at the electrodes will incline to the opposite direction, thus causing a potential difference. According to our theoretical analysis (23), the potential difference under a temperature difference (namely S_e) is associated with the solvent-dependent entropy difference (ΔS) between the redox anions (24) and the concentration ratio difference (ΔC_r) between the hot and cold sides of the LTC.

In general, the concentration gradient is thermodynamically unstable and spontaneously decays into a homogeneous and thermodynamically stable state (Fig. 1A and fig. S1). Namely, ΔC_r is equal to zero at stable state in the 0.4 M $K_3Fe(CN)_6/K_4Fe(CN)_6$ aqueous electrolyte. Therefore, the Seebeck effect for the LTC is only driven by ΔS . Specifically, $Fe(CN)_6^{4-}$ with a small solvation entropy is spontaneously oxidized into $Fe(CN)_6^{3-}$ with a high solvation entropy by releasing an electron to the hot electrode, and the electron through an external circuit is consumed at the cold cathode by the reduction of $Fe(CN)_6^{3-}$ to $Fe(CN)_6^{4-}$ (Fig. 1A).

In contrast to this paradigm, we achieved the Seebeck effect enhancement driven by both ΔS and ΔC_r by using guanidinium cations (Gdm^+) to selectively induce $Fe(CN)_6^{4-}$ crystallization (Fig. 1, A and B, and figs. S2

and S3). Relative to $Fe(CN)_6^{3-}$, $Fe(CN)_6^{4-}$ has a higher charge density and takes part in stronger interactions with Gdm^+ (18). If Gdm^+ is added to the LTC system, $Fe(CN)_6^{4-}$ crystallizes on the cold side (top) and then spontaneously precipitates and redissolves on the hot side (bottom). As a result, a low local concentration of $Fe(CN)_6^{4-}$ near the cold electrode enhances the reduction reaction of $Fe(CN)_6^{3-} \rightarrow Fe(CN)_6^{4-}$, and a high local concentration of $Fe(CN)_6^{4-}$ near the hot electrode also enhances the oxidation reaction of $Fe(CN)_6^{4-} \rightarrow Fe(CN)_6^{3-}$. We term this system a thermosensitive crystallization-boosted LTC (TC-LTC).

We directly measured and simulated the concentration ratio profile of $Fe(CN)_6^{4-}/Fe(CN)_6^{3-}$ in the TC-LTC under various temperature differences (Fig. 1C and figs. S4 and S5). $Fe(CN)_6^{4-}$ is almost completely crystallized on the cold side (293 K), resulting in a low $[Fe(CN)_6^{4-}/Fe(CN)_6^{3-}]_{cold}$ ratio of ~0.02. In contrast, the crystals rapidly dissolve with the increase in temperature on the hot side, boosting the $[Fe(CN)_6^{4-}/Fe(CN)_6^{3-}]_{hot}$ ratio to ~0.94 at 343 K. Therefore, a huge ΔC_r is built between the two electrodes, which increases with increasing temperature difference (ΔT). Because S_e is synergistically driven by ΔS and ΔC_r , the voltage output for the TC-LTC is intensively enhanced (Fig. 1D and fig. S6). The maximum S_e value of 3.73 mV K⁻¹ is more than 2.5 times that of the LTC (1.4 mV K⁻¹). Furthermore, the S_e of the TC-LTC is orientation-dependent and achieves the maximum value when the TC-LTC is laid with the cold electrode above the hot electrode (fig. S7), further proving that thermosensitive crystallization, precipitation, and dissolution processes induce a persistent concentration gradient and thus highly enhance the S_e of thermocells. In addition, we verified that the precipitates do not directly react on the bottom electrode (fig. S8), and the crystallization dissolution kinetics of precipitates are quick enough to ensure the continuous redox reaction in TC-LTC. The high voltage and current output can therefore hold constant during continuous operation for ~100 hours (fig. S9). We also investigated the optimized addition amount of Gdm^+ at which the largest ΔC_r is achieved, which is ~3 mol liter⁻¹ (Fig. 1E and fig. S10). If excess Gdm^+ is added, ΔC_r declines as a result of the accompanying crystallization of $Fe(CN)_6^{3-}$ (fig. S11).

To achieve the largest enhancement of the Seebeck effect, the cation additives need to meet two characteristics: (i) the strong ability to induce crystallization of $Fe(CN)_6^{4-}$, and (ii) the high thermosensitive solubility of $Fe(CN)_6^{4-}$ -associated crystals (Fig. 2A). Small monovalent cations, such as Li^+ , Na^+ , K^+ , and NH_4^+ (strongly hydrated cations) (25, 26), cannot induce crystallization of $Fe(CN)_6^{4-}$ (Fig. 2C) and thus produce no enhancement effect on S_e . Divalent cations, such as Ca^{2+} and Mg^{2+} (strong cations) (27), can

¹Wuhan National Laboratory for Optoelectronics, Huazhong University of Science and Technology, Wuhan 430074, China. ²College of Chemistry and Molecular Science, Engineering Research Center of Organosilicon Compounds and Materials, Ministry of Education, Wuhan University, Wuhan 430072, China. ³School of Materials Science and Engineering, Huazhong University of Science and Technology, Wuhan 430074, China. ⁴Beijing Institute of Nanoenergy and Nanosystems, Chinese Academy of Sciences, Beijing, China. *These authors contributed equally to this work. †Corresponding author. Email: jun.zhou@mail.hust.edu.cn

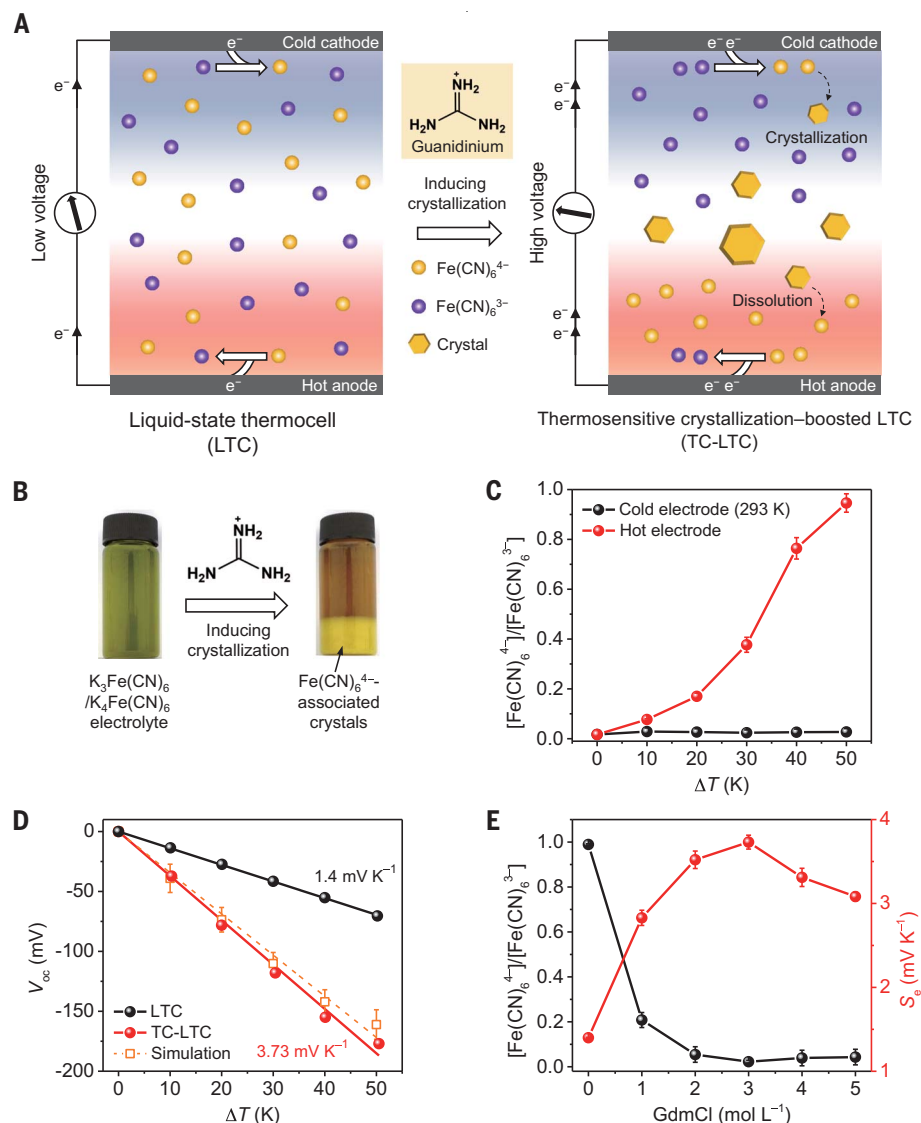


Fig. 1. Crystallization-inducing enhancement of the Seebeck effect in the TC-LTC. (A) Schematic of guanidinium cations (Gdm^+) inducing Fe(CN)_6^{4-} crystallization and enhancement of the Seebeck effect in the $0.4 \text{ M K}_3\text{Fe(CN)}_6/\text{K}_4\text{Fe(CN)}_6$ system. (B) Photographs of the $0.4 \text{ M K}_3\text{Fe(CN)}_6/\text{K}_4\text{Fe(CN)}_6$ electrolyte before and after the addition of Gdm^+ . The diameter of each bottle is 2.7 cm . (C) $\text{Fe(CN)}_6^{4-}/\text{Fe(CN)}_6^{3-}$ concentration ratio at the cold and hot electrodes with increasing temperature difference ΔT . The temperature of the cold electrode was controlled at 293 K . (D) Open-circuit voltage (V_{oc}) of the LTC and TC-LTC at different values of ΔT . The simulated result (dashed line) is consistent with the experimental result. The Seebeck coefficient (S_e) is calculated from the slope of the $V_{oc}-\Delta T$ curves. (E) $\text{Fe(CN)}_6^{4-}/\text{Fe(CN)}_6^{3-}$ concentration ratio in the $0.4 \text{ M K}_3\text{Fe(CN)}_6/\text{K}_4\text{Fe(CN)}_6$ electrolyte (293 K) and corresponding S_e values with the addition of Gdm^+ at different concentrations. Error bars in (C) to (E) denote SD from repeated measurements for three times at the same temperatures and Gdm^+ concentrations.

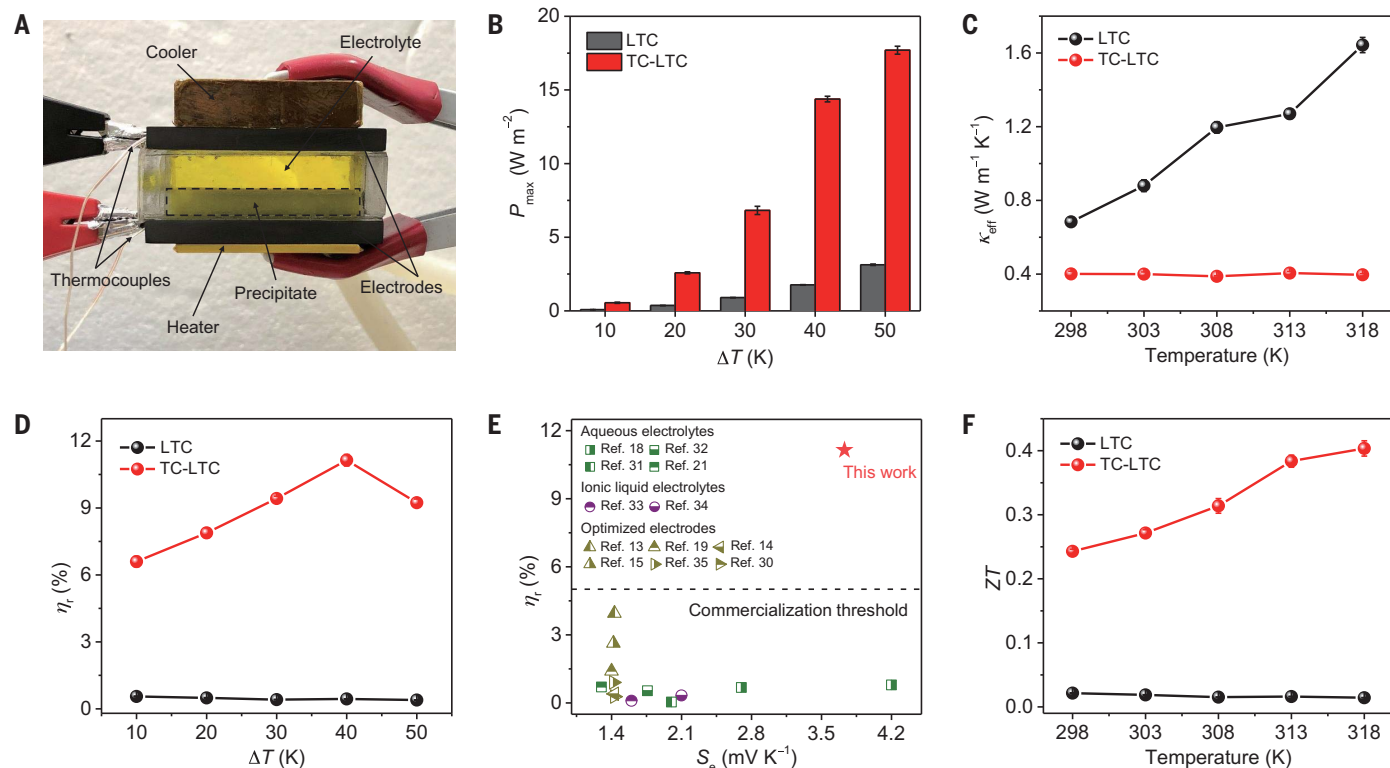
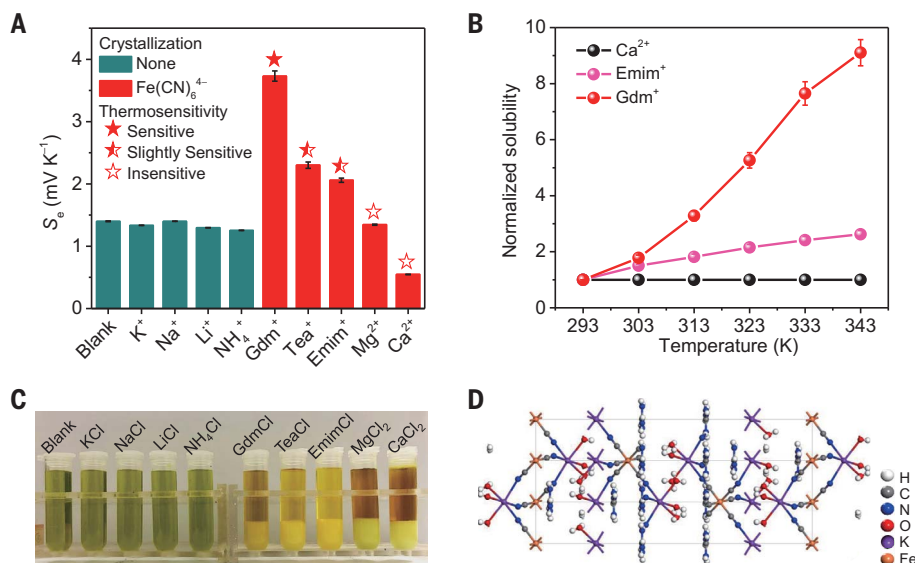
induce crystallization of Fe(CN)_6^{4-} (Fig. 2C), but their crystals have little temperature-dependent solubility, at least in the temperature range we are interested in (Fig. 2B and figs. S12, D and E, and S13). As a result, they also have no enhancement effect on S_e (fig. S14). Only large monovalent cations, such as Gdm^+ , tetraethylammonium (Tea^+), and 1-ethyl-3-methylimidazolium (Emim^+)—weak cations, weakly hydrated—possess the two characteristics and enable the enhancement of S_e (figs.

S12, A to C, and S14). Among them, the crystals formed by Gdm^+ exhibited the highest thermosensitivity, and the corresponding TC-LTC system achieved the highest S_e (Fig. 2, A and B, and fig. S14). To further explain the thermosensitivity difference of crystals induced by different cations, we analyzed the chemical structures of three typical crystals induced by Gdm^+ , Emim^+ , and Ca^{2+} with single-crystal x-ray diffraction; these are $\text{K}_2[\text{C}(\text{NH}_2)_3\text{Fe(CN)}_6] \cdot 6\text{H}_2\text{O}$, $\text{K}_4\text{Fe(CN)}_6 \cdot 3\text{H}_2\text{O}$, and $\text{K}_2\text{CaFe(CN)}_6$, respec-

tively (Fig. 2D and fig. S15). According to thermodynamic theory, $\Delta G = \Delta H - T\Delta S$; that is, the thermosensitivity of the crystal is associated with its enthalpy change (ΔH) and entropy change (ΔS) during the dissolution process. In general, crystals with a small ΔH and a large ΔS will achieve a substantial Gibbs free energy decrease (ΔG) at a small increase of the temperature and possess a high thermosensitivity. The crystal induced by Gdm^+ contains the most hydrated water molecules and possesses the highest structural complexity. The highly hydrated crystal is loose and has low lattice energy (28). The corresponding ΔH during the dissolution process is small. The highly complex crystal will also cause a large ΔS during the dissolution process.

We measured the thermoelectric performance of the TC-LTC with a typical planar cell (Fig. 3A). In brief, a plastic cell is filled with an electrolyte containing crystals and sealed first with commercial carbon fabric paper (thickness $\sim 600 \mu\text{m}$) and then with graphite plates, which serve as the electrodes. The porous carbon fabric paper, having high specific surface area, enhances the current density (13–15, 19). The temperature gradient in the TC-LTC is controlled by an electrical heating plate (on the bottom) and a water-cooled plate (on the top). In the steady state, crystals precipitate to the bottom, and the residual transparent electrolyte is on the top (Fig. 3A). Owing to the crystallization-induced enhancement of the Seebeck effect, the electrical output for the TC-LTC is much higher than that for the pristine LTC (Fig. 3B and fig. S16). The maximum power density (P_{max}) for the TC-LTC is 17.7 W m^{-2} at a ΔT of 50 K , which is more than five times the P_{max} of the pristine LTC (3.1 W m^{-2}). The enhancement effect is further verified by using other electrode materials including graphite sheet, pin graphite sheet, graphite felt, and carbon cloth in the LTC and TC-LTC, which demonstrates the universality of our strategy (fig. S17). Additionally, the thick precipitate layer in the TC-LTC clearly suppresses thermal convection of the liquid electrolyte (20, 29). The effective thermal conductivity (κ_{eff}) for the TC-LTC is therefore substantially lower than that of the pristine LTC (Fig. 3C and fig. S18). Thermal convection in the pristine LTC intensifies at a higher temperature, and the corresponding κ_{eff} increases from 0.67 to $1.64 \text{ W m}^{-1} \text{ K}^{-1}$. By contrast, the κ_{eff} for the TC-LTC is maintained at $\sim 0.4 \text{ W m}^{-1} \text{ K}^{-1}$ over the tested temperature range. In addition, a temperature difference of $\sim 50 \text{ K}$ in the TC-LTC holds constant during a continuous operation of ~ 10 hours (fig. S19), which indicates that the low thermal conductivity of TC-LTC is stable for long-term operation. In contrast to the traditional solid-state thermoelectric cells (TECs), the electrical conductivity for the LTC/TC-LTC is difficult to directly measure because of its complex dependence on the

Fig. 2. Various additive-induced enhancements of the Seebeck effect in the TC-LTC. (A) Optimized S_e for the TC-LTC induced by different cation additives. According to their ability to induce crystallization of $\text{Fe}(\text{CN})_6^{4-}$, cation additives are classified into two categories: Dark cyan indicates that no crystallization was observed, whereas red indicates crystallization of $\text{Fe}(\text{CN})_6^{4-}$. Furthermore, according to the temperature-dependent solubility (thermosensitivity) of $\text{Fe}(\text{CN})_6^{4-}$ -associated crystals, cation additives are classified as “sensitive” (solid star), “slightly sensitive” (half-solid star), and “insensitive” (open star). (B) Change in the normalized solubility of $\text{Fe}(\text{CN})_6^{4-}$ -associated crystals induced by Ca^{2+} , Emim^+ , and Gdm^+ with increasing temperature. (C) Photographs of the 0.4 M $\text{K}_3\text{Fe}(\text{CN})_6/\text{K}_4\text{Fe}(\text{CN})_6$ electrolyte with different additives. The diameter of each tube is 1.3 cm. (D) Chemical structure of the crystal $\text{K}_2[\text{C}(\text{NH}_2)_3]_2\text{Fe}(\text{CN})_6 \cdot 6\text{H}_2\text{O}$ induced by Gdm^+ . Error bars in (A) and (B) denote SD from repeated measurements for three times at the same temperatures and cation additive concentrations.



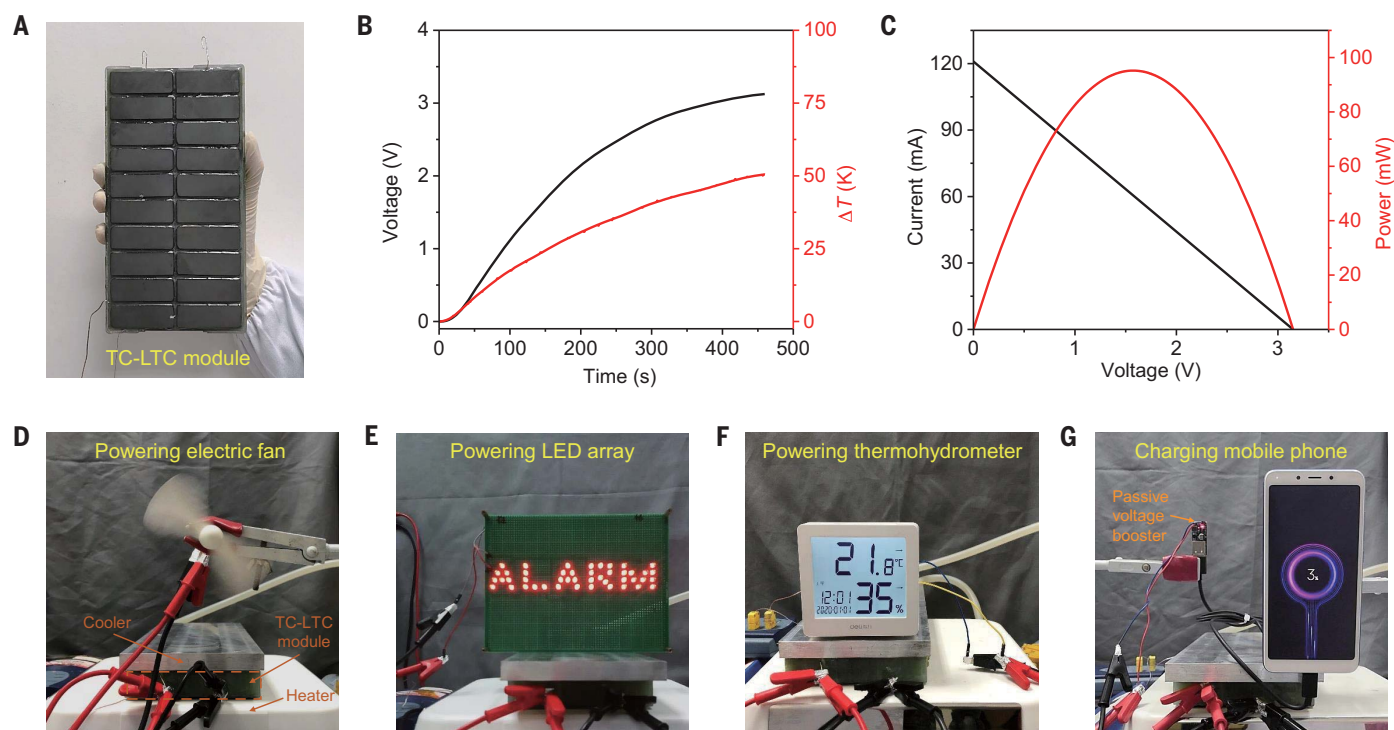


Fig. 4. Electricity generation and demonstration of using a TC-LTC module to power electronic devices. (A) Photograph of a TC-LTC module containing 20 units in series. (B) Real-time voltage curves (black) of the module with an increase in ΔT (red). (C) Current-voltage curve (black) and corresponding power output (red) at $\Delta T = 50$ K. (D to G) The module can directly power various electronic devices, including (D) an electric fan, (E) a LED array, (F) a thermohydrometer, and (G) a mobile phone using a passive voltage booster.

ionic conductivity of the electrolyte, electrical conductivity of the electrodes, and reaction kinetics of the redox species at the electrodes (30). Therefore, a more comprehensive parameter, the effective electrical conductivity (σ_{eff}), is used for the LTC/TC-LTC. This value is calculated from the slope of the current-voltage curve (12, 13). The σ_{eff} of the TC-LTC increases from 23 to 36 S m⁻¹ with increasing temperature, which is nearly consistent with that of the pristine LTC (fig. S20). Overall, the strategy of crystallization in the TC-LTC synergistically enhances S_e and reduces κ_{eff} without sacrificing σ_{eff} .

The conversion efficiency is one important standard for evaluating thermoelectric devices. Owing to the high power density (electricity output) and low thermal conductivity (heat input), the highest η_r for the TC-LTC is 11.1% at a ΔT of 40 K, which is 18.5 times that of the pristine LTC (Fig. 3D). In addition, the η_r for the TC-LTC substantially surpasses that for other optimized LTC systems in the literature (13–15, 18, 19, 21, 30–35) and the predicted commercialization threshold (~5%) (12) (Fig. 3E and table S2). Furthermore, the dimensionless figure of merit (ZT) of ~0.4 for the TC-LTC at 318 K is high relative to other LTCs and comparable to that of most TEC systems (Fig. 3F and table S3). In addition, for a typical thermoelectric module, gener-

ating a useful voltage (>1 V) under a small temperature difference requires a challenging integration of thousands or even tens of thousands of units (10). Because of the high S_e of 3.73 mV K⁻¹, integrating fewer TC-LTCs enables a considerable voltage output, which is beneficial to enhance the fill factor and reduce the manufacturing costs for the thermoelectric devices (36). To evaluate the potential for application to low-grade heat harvesting, we estimated the cost-performance metric (CPM) of various thermoelectric systems based on their raw material prices (table S3 and figs. S21 and S22). Relative to inorganic solid-state thermoelectric cells (ITECs) and organic solid-state thermoelectric cells (OTECS), our TC-LTC system may be more cost-effective; its estimated CPM (~\$1.56 W⁻¹) is closer to those of commercial power generation technologies (nuclear, \$5.34 W⁻¹; coal, \$2.84 W⁻¹; natural gas, \$0.98 W⁻¹) (9).

Finally, we designed a TC-LTC module by connecting 20 units (size ~1.4 cm × 5 cm × 2 cm) in series to demonstrate viability for scale-up (Fig. 4A and fig. S23). The module generated a V_{oc} of 3.1 V and a short-circuit current (I_{sc}) of 120 mA, and the corresponding P_{max} was 96 mW under a ΔT of 50 K between the heater and cooler plates (Fig. 4, B and C). Because of the considerable power output we achieved, the module could directly drive various electronic

devices including an electric fan, an LED array, and a thermohydrometer (Fig. 4, D to F, and movie S1). Furthermore, the module enabled a smart mobile phone to be charged through integration with a passive voltage booster (Fig. 4G and movie S1).

Unlike previous LTC strategies that enhanced S_e but sacrificed σ_{eff} (31), our thermosensitive crystallization-based TC-LTC strategy synergistically enhances S_e and reduces κ_{eff} without sacrificing σ_{eff} . We achieved attractive single-cell performance for Carnot-relative efficiency (11.1%) and current density (416 A m⁻²). We obtained a high power density (6.86 W m⁻²) for our module at a temperature difference of 50 K (fig. S24 and tables S4 and S5). These examples show that LTCs may be a viable technology for harvesting low-grade waste heat. Our approach can be expanded to other LTC systems by using thermosensitive crystals of corresponding redox species, as well as other thermal energy-harvesting systems, including thermally regenerative electrochemical cycles (37–39) and direct thermal charging cells (40), which also require a redox system of high S_e .

REFERENCES AND NOTES

1. C. Forman, I. K. Muritala, R. Pardemann, B. Meyer, *Renew. Sustain. Energy Rev.* **57**, 1568–1579 (2016).
2. J. He, T. M. Tritt, *Science* **357**, 1369 (2017).
3. J. P. Heremans, *Nature* **508**, 327–328 (2014).

4. R. Venkatasubramanian, E. Siivola, T. Colpitts, B. O'Quinn, *Nature* **413**, 597–602 (2001).
5. S. I. Kim *et al.*, *Science* **348**, 109–114 (2015).
6. B. Poudel *et al.*, *Science* **320**, 634–638 (2008).
7. J. Mao *et al.*, *Science* **365**, 495–498 (2019).
8. W. He *et al.*, *Science* **365**, 1418–1424 (2019).
9. S. LeBlanc, S. K. Yee, M. L. Scullin, C. Dames, K. E. Goodson, *Renew. Sustain. Energy Rev.* **32**, 313–327 (2014).
10. S. K. Yee, S. LeBlanc, K. E. Goodson, C. Dames, *Energy Environ. Sci.* **6**, 2561–2571 (2013).
11. M. F. Dupont, D. R. MacFarlane, J. M. Pringle, *Chem. Commun.* **53**, 6288–6302 (2017).
12. T. I. Quickenden, Y. Mua, *J. Electrochem. Soc.* **142**, 3985–3994 (1995).
13. H. Im *et al.*, *Nat. Commun.* **7**, 10600 (2016).
14. L. Zhang *et al.*, *Adv. Mater.* **29**, e1605652 (2017).
15. M. S. Romano *et al.*, *Adv. Mater.* **25**, 6602–6606 (2013).
16. Y. Mua, T. I. Quickenden, *J. Electrochem. Soc.* **143**, 2558–2564 (1996).
17. C. G. Han *et al.*, *Science* **368**, 1091–1098 (2020).
18. J. Duan *et al.*, *Nat. Commun.* **9**, 5146 (2018).
19. R. Hu *et al.*, *Nano Lett.* **10**, 838–846 (2010).
20. L. Jin, G. W. Greene, D. R. MacFarlane, J. M. Pringle, *ACS Energy Lett.* **1**, 654–658 (2016).
21. G. Li *et al.*, *Adv. Mater.* **31**, e1901403 (2019).
22. T. Kim *et al.*, *Nano Energy* **31**, 160–167 (2017).
23. See supplementary materials.
24. S. Sahami, M. J. Weaver, *J. Electroanal. Chem. Interfacial Electrochem.* **122**, 155–170 (1981).
25. Y. Marcus, *Chem. Rev.* **109**, 1346–1370 (2009).
26. H. Ohtaki, T. Radnai, *Chem. Rev.* **93**, 1157–1204 (1993).
27. Y. Marcus, G. Hefter, *Chem. Rev.* **106**, 4585–4621 (2006).
28. J. Sohr, H. Schmidt, W. Voigt, *Acta Crystallogr. C* **74**, 194–202 (2018).
29. P. Yang *et al.*, *Angew. Chem. Int. Ed.* **55**, 12050–12053 (2016).
30. T. J. Kang *et al.*, *Adv. Funct. Mater.* **22**, 477–489 (2012).
31. H. Zhou, T. Yamada, N. Kimizuka, *J. Am. Chem. Soc.* **138**, 10502–10507 (2016).
32. J. H. Kim *et al.*, *Sci. Rep.* **9**, 8706 (2019).
33. P. F. Salazar, S. T. Stephens, A. H. Kazim, J. M. Pringle, B. A. Cola, *J. Mater. Chem. A* **2**, 20676–20682 (2014).
34. K. Kim, H. Lee, *Phys. Chem. Chem. Phys.* **20**, 23433–23440 (2018).
35. W. Qian, M. Cao, F. Xie, C. Dong, *Nano-Micro Lett.* **8**, 240–246 (2016).
36. G. J. Snyder, A. H. Snyder, *Energy Environ. Sci.* **10**, 2280–2283 (2017).
37. S. W. Lee *et al.*, *Nat. Commun.* **5**, 3942 (2014).
38. Y. Yang *et al.*, *Proc. Natl. Acad. Sci. U.S.A.* **111**, 17011–17016 (2014).
39. Y. Ding *et al.*, *Energy Environ. Sci.* **12**, 3370–3379 (2019).
40. X. Wang *et al.*, *Nat. Commun.* **10**, 4151 (2019).

ACKNOWLEDGMENTS

We thank the reviewers whose comments have helped us to improve the manuscript significantly; N. S. Xu, S. Z. Deng, H. X. Deng, J. Tang, Y. Z. Pei, and J. Chen for their help; and the Center for Nanoscale Characterization and Devices, WNLO-HUST, and the Analysis and Testing Center of Huazhong University of

Science and Technology for their support. **Funding:** Supported by National Natural Science Foundation of China grant 51672097, the National Program for Support of Topnotch Young Professionals, the program for HUST Academic Frontier Youth Team (2017QYTD11), and the Director Fund of WNLO (J.Z.). **Author contributions:** J.Z. conceived the research; J.D., B.Y., and J.Z. designed the experiments; B.Y. and J.D. carried out the experiments; H.J.C. conducted the single-crystal x-ray characterization; B.Y., J.D., H.C., W.X., R.L., X.Z., H.W., B.Q., M.X., Z.L.W., and J.Z. analyzed the data; and J.Z., J.D., B.Y., Z.L.W., and M.X. wrote the paper. All authors discussed the results and approved the final version of the manuscript. **Competing interests:** The authors declare no competing interests. **Data and materials availability:** All data are available in the manuscript or the supplementary materials.

SUPPLEMENTARY MATERIALS

science.sciencemag.org/content/370/6514/342/suppl/DC1
Materials and Methods
Supplementary Text
Figs. S1 to S24
Tables S1 to S5
Movie S1
References (41–65)

5 July 2020; accepted 25 August 2020
Published online 10 September 2020
10.1126/science.abd6749

ECOLOGY

Species richness and redundancy promote persistence of exploited mutualisms in yeast

Mayra C. Vidal^{1,2*}, Sheng Pei Wang¹, David M. Rivers³, David M. Althoff^{1,2}, Kari A. Segraves^{1,2}

Mutualisms, or reciprocally beneficial interspecific interactions, constitute the foundation of many ecological communities and agricultural systems. Mutualisms come in different forms, from pairwise interactions to extremely diverse communities, and they are continually challenged with exploitation by nonmutualistic community members (exploiters). Thus, understanding how mutualisms persist remains an essential question in ecology. Theory suggests that high species richness and functional redundancy could promote mutualism persistence in complex mutualistic communities. Using a yeast system (*Saccharomyces cerevisiae*), we experimentally show that communities with the greatest mutualist richness and functional redundancy are nearly two times more likely to survive exploitation than are simple communities. Persistence increased because diverse communities were better able to mitigate the negative effects of competition with exploiters. Thus, large mutualistic networks may be inherently buffered from exploitation.

Mutualist communities are prevalent in every ecosystem (1–3), forming the core of food webs and providing critical ecosystem services. Like other communities, mutualist communities must be able to cope with constantly changing conditions, but the factors that help maintain their stability remain under debate (4–6). Recent efforts to understand mutualistic community dynamics by using network analysis suggest that high species richness could enhance persistence (4); however, experimental validations of this hypothesis are needed. Understanding the persistence of mutualist communities is paramount for the management and conservation of ecosystems (7), especially given the risk of species loss with climate change (8).

To persist, mutualisms need to resist exploitation by organisms that use the exchanged commodities of the mutualism without providing anything in return (9). These exploiters can be unrelated to the mutualists or they can be mutualistic species or individuals that have defected from the mutualism (“cheaters”) (10). Although there is debate about whether exploitation has strong negative fitness consequences in many mutualisms (11), exploitation can change the structure of communities (3, 12, 13), leading to local species loss (14). Despite the possible negative effects of exploitation, exploiters or cheaters are present in virtually all mutualistic communities; thus, how mutualistic communities are buffered from the effects of exploitation is unclear.

Similar to the proposed effect of species richness on mutualism persistence (4), rich-

ness could potentially enhance mutualism persistence under exploitation because rich communities have redundant species with similar functional roles (4, 5). Consequently, if a mutualist goes extinct after exploitation, the community can persist with fewer species because the remaining redundant mutualist species still provide the commodities to sustain the community (15, 16). Simultaneously, however, redundant species have similar niches and may compete strongly with one another for mutualistic commodities and/or other resources. Theory suggests that coexistence of redundant mutualists is hindered by competition for the mutualistic commodity (17). Competition could lead to removal of inferior competitors (17) and decreased species richness over time (5), and influence mutualism persistence. Considering these contrasting effects of species redundancy on communities, in this study we experimentally test how mutualist species richness and functional redundancy contribute to mutualism persistence with and without cheaters.

We created a synthetic mutualism using brewer's yeast, *Saccharomyces cerevisiae*, by engineering asexual strains to overproduce either lysine or adenine but not produce the other resource (Fig. 1A) (18). Adenine is required for cell division and lysine for cell growth, making these nutrients essential for yeast fitness. Because the overproduced nutrients are released into the medium and are freely available, the mutualism cannot involve sanctions or partner choice, which are mechanisms used in some mutualisms to restrict cheating, for example, by controlling the amount of commodities exchanged or by avoiding interactions (19). Thus, this mutualism is similar to common, diffuse mutualisms such as many generalized pollination systems (20). We genetically engineered the strains to function ecologically as different species; as such, the strains are

genetically distinct, reproductively isolated, and analogous to species. Additionally, within each mutualist type, the strains have small differences in genotype and phenotype (e.g., yield) (Fig. 1, B and C), making them analogous to closely related, ecologically similar species that would compete strongly with one another because of niche overlap.

We also engineered cheater strains that provide no resources but consume either adenine (hereafter, “adenine cheater”) or lysine (“lysine cheater”). We call them cheaters because they are derived from the mutualists, simulating cheaters that share recent evolutionary history with mutualists. Because no lysine or adenine is available in the medium except for that released by the mutualists, the cheaters cannot exist independently of the mutualists, and community persistence critically depends on the presence of both types of overproducing mutualists. Thus, when one or both mutualist types went extinct, we considered these communities as having collapsed. To test the hypothesis that species richness enhances mutualism persistence, we created symmetrical communities that varied in richness with and without the two types of cheaters (Fig. 1A). Communities were grown for 4 weeks, and we assessed their survival and community composition weekly (1679 communities) (18).

Persistence of mutualistic communities was highly dependent on community composition. All mutualist-only communities survived the entire experiment. Communities with cheaters, however, went extinct at different rates depending on the type of cheater. The lysine cheater led to the collapse of 55% of the mutualistic communities, whereas the adenine cheater caused <5% collapse (Fig. 2A), thus demonstrating that the effect of cheaters on mutualism persistence is context dependent. This context dependency may help explain why some cheaters, but not others, can have strong negative effects on natural mutualistic communities. The negative effect of the lysine cheater on community persistence was buffered by the higher initial number of mutualist strains in the community, as persistence rates nearly doubled in the richest communities (Fig. 2A). Because the richest communities were not independently replicated, as the mutualist strains were sampled from a pool of eight total strains, we also tested for changes in persistence by excluding the eight-strain communities, thus eliminating communities that were not independently replicated. This analysis confirmed that species richness buffers mutualist communities that are experiencing substantial negative effects from cheaters ($\chi^2 = 17.96$, $df = 2$, $P = 0.0001$).

The results suggest that species richness is an important component of persistence with cheaters, yet increasing richness also adds

¹Department of Biology, Syracuse University, Syracuse, NY 13210, USA. ²Biology Department, University of Massachusetts Boston, Boston, MA 02125, USA.

*Corresponding author. Email: mayracvidal@gmail.com (M.C.V.); dalthoff@syr.edu (D.M.A.); ksegraves@syr.edu (K.A.S.)

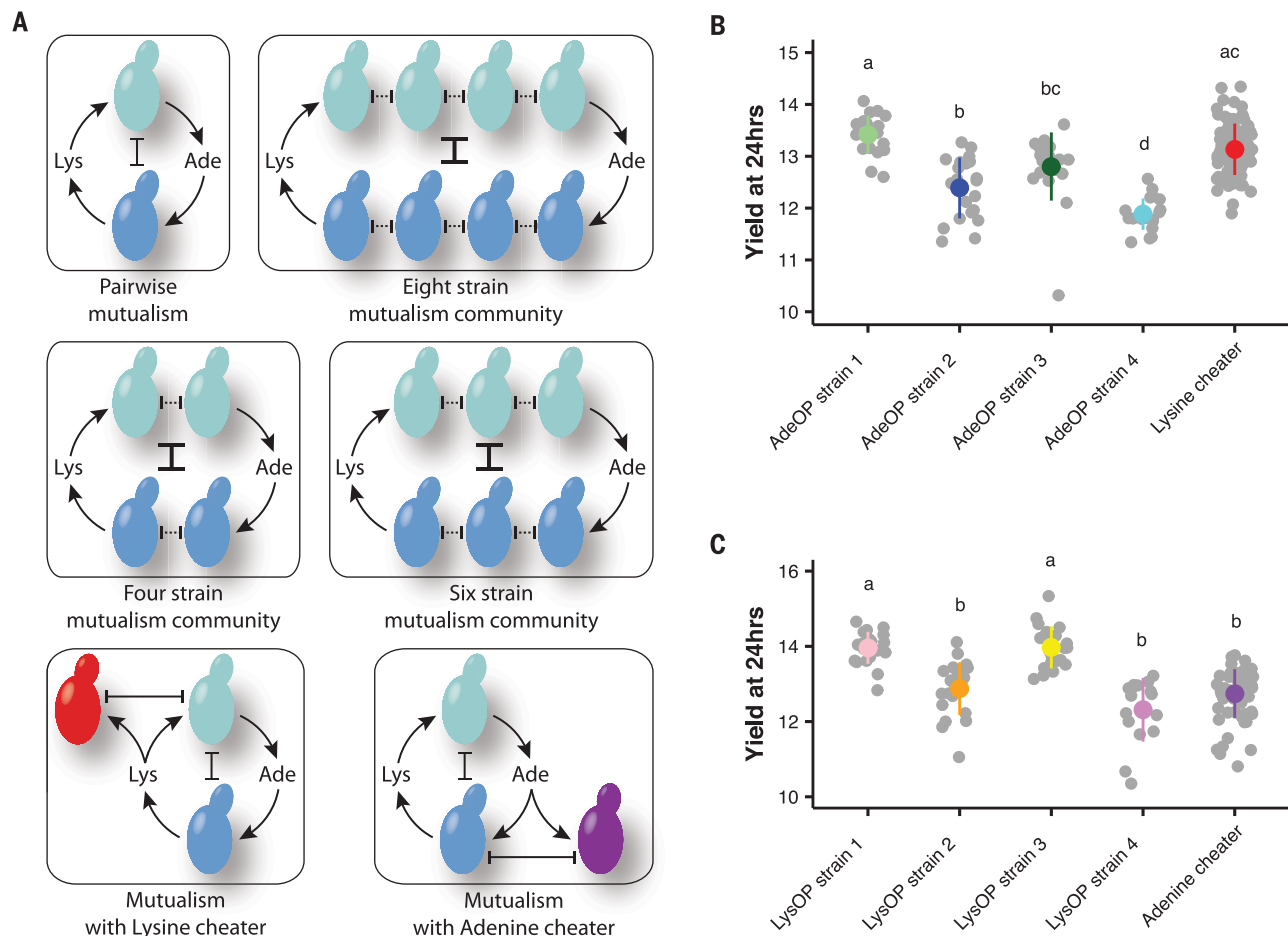


Fig. 1. Representation of symmetrical yeast communities and yield differences among strains used to build the communities. (A) Symmetrical mutualist communities. (Top left) Simplest community, with one strain of adenine (Ade) mutualist (top, green) that releases adenine into the medium, which is taken up by the lysine (Lys) mutualist (bottom, blue) that releases lysine, which is used by the adenine mutualist. Although these strains are mutualists, they compete for other resources (blunt-ended line). We added pairs of mutualist types to create symmetrical communities of up to eight strains (top right) in which there was also competition within mutualist

types (blunt-ended dashed lines). Besides mutualist-only communities, we created communities with a lysine cheater (red) that competed with the adenine mutualists for lysine and communities with an adenine cheater (purple) that competed for adenine with the lysine mutualists. **(B)** Yield at 24 hours of growth for the adenine overproducing mutualists (AdeOP) and the lysine cheater. **(C)** Yield at 24 hours of growth for the lysine overproducing mutualists (LysOP) and the adenine cheater. Yield was measured when strains were growing alone in complete medium. Letters represent Tukey's honest significant difference (HSD) comparisons.

functional redundancy of mutualists. To disentangle the effects of species richness and redundancy, we compared the persistence of asymmetrical communities with and without the lysine cheater. We created mutualist-only communities and a replicate set including the lysine cheater in which one adenine mutualist was matched with either two, three, or four lysine mutualists, as well as the converse (1431 total communities) (18).

Results from the asymmetrical communities showed that the positive effect of species richness on community persistence was driven by mutualist functional redundancy, and this redundancy was critical when mutualists use the same mutualistic commodity as the lysine cheater. For the mutualist-only communities, there was no change in persistence, with in-

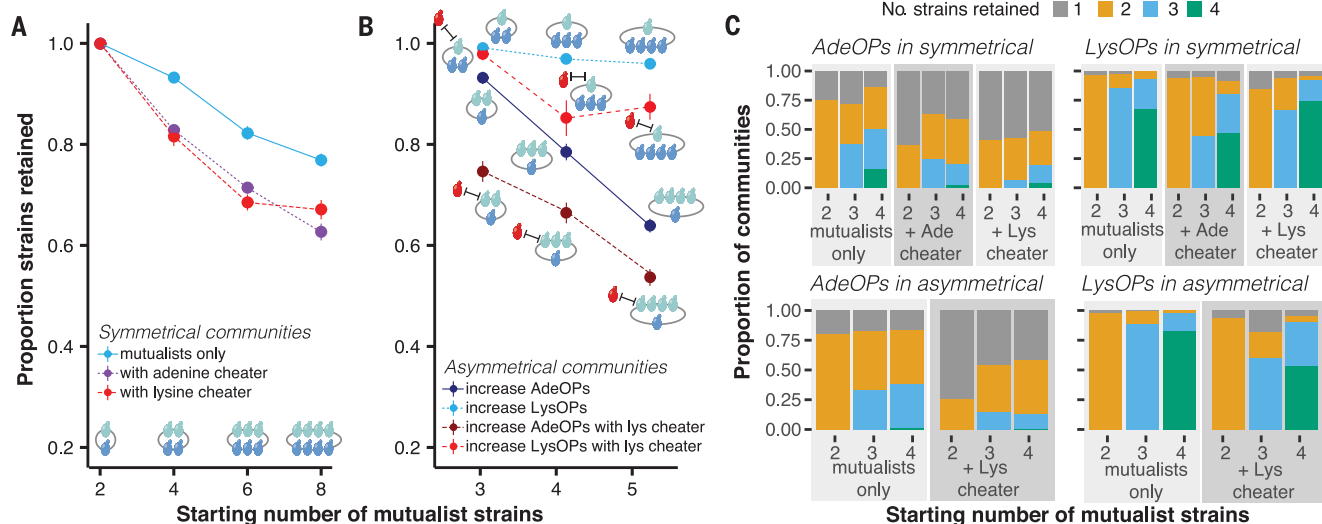
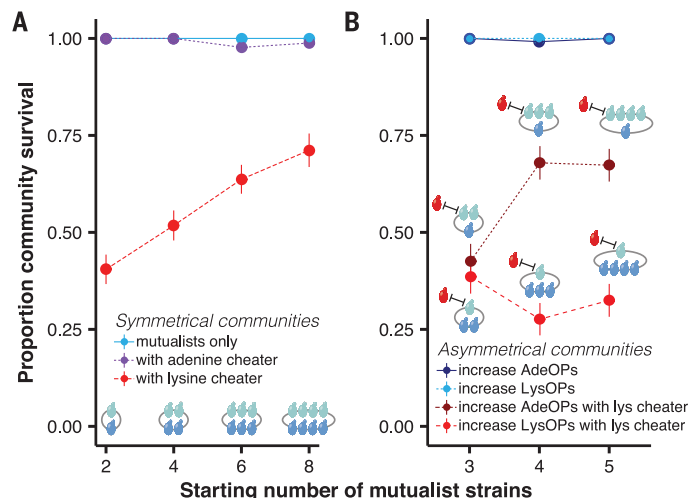
creasing redundancy of either mutualist type, as the communities did not experience collapse (Fig. 2B). Similarly, changes in redundancy of the lysine mutualists that do not compete for mutualistic commodities with the lysine cheater led to no change in persistence, as these communities suffered ~65% collapse regardless of the initial number of strains. By contrast, increases in functional redundancy of the adenine mutualists that compete with the lysine cheater led to a 25% increase in community persistence when we compared communities with two versus three or four adenine mutualists (from 43 to 67% survival) (Fig. 2B). Thus, functional redundancy of the mutualist type that directly competes with the cheater for the mutualistic resource had a notable impact on community persistence. These results

suggest a key role for functional redundancy in mutualism and that having a greater number of redundant mutualist species that compete with a strong cheater increases the likelihood that the mutualism will persist despite the negative effects of cheaters.

Although we found that functional redundancy can buffer the negative effects of a strong cheater (Fig. 2B), redundancy can be disadvantageous as well because similar mutualist species should also compete strongly with one another (17). Our results show that starting species richness had a negative effect on individual strain retention in all multimutualist communities (Fig. 3). Despite that, when we examined the final composition of surviving communities, we observed that coexistence among mutualists usually occurred in at least

Fig. 2. Effect of species richness and functional redundancy on community persistence.

(A) Symmetrical communities with mutualists only and with the adenine cheater had high survival, whereas communities with the lysine cheater had 40 to 75% survival rate, depending on the starting number of mutualistic strains ($\chi^2 = 27.47$, $df = 3$, $P < 0.0001$). (B) Asymmetrical communities containing only mutualists had high survival. By contrast, communities with the lysine cheater and variable numbers of strains of the adenine mutualist (AdeOPs) increased community persistence from ~40 to 70% as the number of adenine mutualists increased ($\chi^2 = 25.29$, $df = 2$, $P < 0.0001$; excluding the most diverse communities that were not independently replicated: $\chi^2 = 17.78$, $df = 1$, $P < 0.0001$). Communities with the lysine cheater and increasing numbers of lysine mutualists (LysOPs) did not differ ($\chi^2 = 2.94$, $df = 2$, $P = 0.23$). Points on graphs represent mean \pm SE.

**Fig. 3. Effect of richness on strain loss in persistent communities.**

(A) Mutualist strain retention in symmetrical communities decreased with the starting number of mutualistic strains (mutualists only: $t = -14.47$, $df = 1328$, $P < 0.0001$; with lysine cheater: $t = -14.8$, $df = 1328$, $P < 0.0001$, with adenine cheater: $t = -23.87$, $df = 1328$, $P < 0.0001$). Communities with cheaters had greater loss than communities with mutualists only (Tukey's test: mutualists only versus with lysine cheater: $t = 3.06$, $df = 1328$, $P = 0.006$; mutualists only versus with adenine cheater: $t = 6.02$, $df = 1328$, $P < 0.0001$; with lysine cheater versus with adenine cheater: $t = 2$, $df = 1328$, $P = 0.11$). (B) Strain retention decreased with the starting number of mutualist strains

in asymmetrical communities ($F_{2,992} = 100.9$, $P < 0.0001$); within each community type, all pairwise comparisons differed with increasing richness ($P < 0.001$) except for communities with increasing number of lysine mutualists (light red and light blue). In these communities, there was no difference in strain loss with starting numbers of four or five mutualists, regardless of the presence of the lysine cheater (with cheater: $z = 0.52$, $n = 123$, $P = 0.859$; without cheater: $z = -0.69$, $n = 285$, $P = 0.765$). Points on graphs (A) and (B) represent mean \pm SE. (C) Coexistence of mutualists as a proportion of communities, showing the number (No.) of strains of adenine mutualists (AdeOPs) and lysine mutualists (LysOPs) retained to the end of the experiment for each community type.

half of the communities and was even more frequent among lysine mutualists and in mutualist-only communities (Fig. 3C). In addition, strain loss was more pronounced when either cheater was present (Fig. 3), likely because cheaters removed mutualistic commodities without contributing any resources to the environment.

Together, the results suggest that competition for the shared resources among mutualists and between mutualists and cheaters is driving the patterns of strain loss. For instance, the

negative effect on community survival caused by the lysine cheater but not the adenine cheater suggests that there is likely a difference in the intensity of competition for the mutualistic commodities being exchanged. This idea is further supported by our finding that strain loss was higher among redundant adenine mutualists than among redundant lysine mutualists (Fig. 3B). Furthermore, in contrast to the adenine mutualists, the lysine mutualists were less likely to be excluded from communities (Fig. 3C). Competition for lysine could be

more intense than for adenine because lysine availability is delayed but adenine is readily available. Lysine is stored in vacuoles and is released as the lysine-producing mutualists die, whereas adenine is continuously secreted by the adenine mutualists (27). Consequently, lysine availability was nearly unmeasurable for the first 48 hours, whereas adenine availability increased over time (Fig. 4A). Thus, this difference in resource availability might be leading to stronger competition for lysine than for adenine, both among adenine mutualist strains

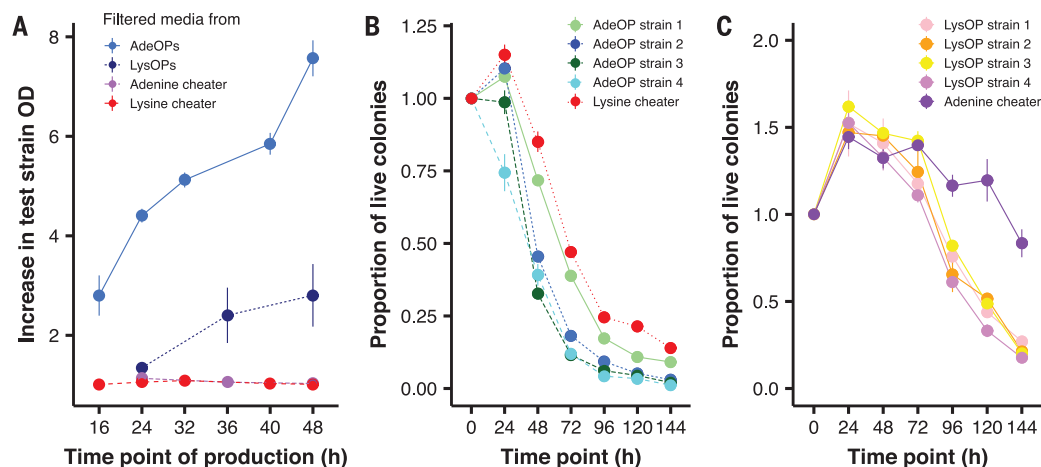


Fig. 4. Mechanism of strain loss and community collapse. (A) Estimates of lysine and adenine produced by mutualists and cheaters over time (compared with the first time point: 8 hours adenine mutualists and lysine cheater, 12 hours lysine mutualists and adenine cheater). Production of adenine by mutualists increases over time ($F_{4,35} = 40.4$, $P < 0.0001$), whereas production did not differ for cheaters and lysine mutualists (LysOPs: $F_{2,20} = 2.5$, $P = 0.107$; adenine cheater: $F_{4,5} = 2.36$, $P = 0.186$; lysine cheater: $F_{2,3} = 0.71$, $P = 0.56$). Production was measured indirectly by assessing the growth of a test strain

that could not produce adenine or lysine, and the only lysine or adenine available was that produced by the mutualists. OD, optical density. (B) Starvation resistance of adenine mutualists and the lysine cheater. The lysine cheater was more resistant to 48 hours of starvation than the adenine mutualists (Tukey's HSD between lysine cheater and AdeOPs had $P < 0.05$). (C) Starvation resistance of lysine mutualists and adenine cheater. All strains had similar starvation resistance at 48 hours ($F_{4,10} = 0.72$, $P = 0.6$). Points on graphs represent mean \pm SE.

as well as between the adenine mutualists and the lysine cheater.

One important competitive trait for the lysine cheater and adenine mutualists would be starvation resistance that would allow survival during periods when lysine is limiting. Strains that have more individuals surviving a period of starvation would have higher initial population density when the resource becomes available, leading to priority effects. If lysine cheaters are more resistant to starvation than the adenine mutualists, it could explain the severity of their impact on mutualist communities. To test this hypothesis, we grew the strains alone and measured starvation resistance to the mutualistic commodity that they require. At 48 hours, 85% (± 3.5 SE) of the lysine cheater population survived lysine starvation, whereas only 47.3% (± 4.6 SE) of the adenine mutualist populations survived (Fig. 4B). In comparison, the lysine mutualists and the adenine cheater had similar starvation resistance at 48 hours (Fig. 4C); however, these strains probably do not starve for adenine because adenine is continuously released in relatively high quantities (Fig. 4A). We hypothesized that the superiority in starvation resistance of the lysine cheater would cause shifts in composition ratios toward the lysine cheater, as would be expected under a model of priority effects. To test this, we assembled a small set of pairwise mutualist communities with and without cheaters and quantitatively tracked the population size of each species. Lysine cheaters quickly became

dominant in 25% of the communities, and these communities eventually went extinct (table S3). By contrast, communities containing the adenine cheater shifted in favor of the mutualists, and the cheater was eventually excluded, possibly because of a competitive trait other than starvation resistance (e.g., yield) (Fig. 1B). For the mutualist-only communities, the ratio of lysine and adenine mutualists remained constant. Thus, differences in starvation resistance appear to be linked to shifts in population ratio favoring the lysine cheater, ultimately resulting in community collapse.

Community persistence increased with richness regardless of strain composition (figs. S1 and S2), suggesting that the patterns of community survival were not driven by the presence of competitively superior strains. As more mutualist strains are added, there is an increased probability that one of those strains will be competitively superior to the lysine cheater. Consequently, we tested (i) whether communities containing the superior adenine mutualist competitor were more likely to survive, (ii) whether the strongest mutualist competitor was numerically dominant in the surviving communities, and (iii) whether coexistence with the cheater was rare. These tests showed that survival and abundance of different adenine mutualist strains varied from one community to the next (figs. S3 and S4), and there was no specific strain that dominated all of the communities. In addition, coexistence of the mutu-

alists and lysine cheater was as likely as the exclusion of the cheater for most of the surviving communities (fig. S5). Thus, the outcome of competition among mutualist strains and between mutualists and the lysine cheater was context dependent and was not solely predictable on the basis of the identity of the mutualist strains in the communities. These results show that although competition is an important factor in all communities, competitive exclusion alone does not determine the persistence of mutualist communities that are exploited.

Our results provide evidence for the feasibility of the coexistence of functionally redundant species in multimutualistic communities. In non-neutral models that assume niche differentiation, coexistence occurs either when intraspecific competition is stronger than interspecific competition, when there is a trade-off between colonization and competitive abilities, or when there is spatial or temporal heterogeneity in resource availability coupled with trade-offs in competitive abilities for different resources or for environmental tolerances (22, 23). The mutualist species that we used in our experiments closely resemble one another and were growing together in a mixed, homogenous, closed environment. These conditions should promote competitive exclusion, yet we commonly observed coexistence among mutualists as well as between mutualists and cheaters. Johnson and Bronstein (17) suggested that coexistence can be facilitated

in multimutualist communities if mutualist species can partition the shared mutualistic commodity as well as another nonmutualistic resource. The redundant mutualist strains in our system likely have trade-offs in their competitive ability for different resources, and this, combined with temporal resource heterogeneity due to mutualistic resource production and nonmutualistic resource consumption, may allow coexistence of multiple mutualist strains. How the temporal dynamics of competition and resource availability drive coexistence in mutualisms requires further experimentation. Our results, however, highlight the importance of context dependency in determining coexistence in multimutualist communities with and without exploitation.

Together, our results show that species richness can ameliorate mutualistic community collapse caused by cheaters. Mutualist functional redundancy allowed the mutualism to persist even with extinction of some mutualist species. The positive effect of functional redundancy was pronounced for mutualist species that directly competed with cheaters for the most limiting mutualistic commodity. Although only one type of cheater markedly affected community survival, both had negative effects on the communities in terms of species loss, possibly because they reduce the availability of the mutualistic resources. Thus, our results show that cheaters in general can have negative effects on mutualist communities even when they do not cause community collapse.

In terms of understanding the persistence of multispecies mutualistic communities, our results suggest three key findings. First, exploitation can have strong negative effects on multimutualist communities by affecting community persistence and species loss. However, the negative effects of cheaters are context dependent and vary greatly with the strength of

competition for mutualistic commodities [e.g., (24)]. Second, for mutualist communities experiencing exploitation, the fate of the community is determined largely by the effect of cheaters on mutualist population dynamics [e.g., (25)]. Cheaters that use resources more efficiently or that better survive periods of low resource availability will have an advantage over mutualists. Third, in complex, diffuse mutualistic networks, regulatory mechanisms such as host sanctions, partner choice, and positive partner feedbacks [e.g., (26,27)] may not be required to explain community stability. Regulatory mechanisms are unlikely to work in diffuse mutualisms because these communities have many species that differ in life history, behavior, and the benefit they provide. Competition, however, is one mechanism that is universal across species and communities and offers a general framework to explain the stability of diverse types of mutualistic communities under exploitation. In the face of inevitable competition among redundant mutualist species and exploiters, maintenance of high richness in natural systems is necessary to promote persistence of mutualist communities.

REFERENCES AND NOTES

1. J. Albrecht *et al.*, *Nat. Commun.* **5**, 3810 (2014).
2. J. Bascompte, P. Jordano, *Annu. Rev. Ecol. Evol. Syst.* **38**, 567–593 (2007).
3. E. Toby Kiers, T. M. Palmer, A. R. Ives, J. F. Bruno, J. L. Bronstein, *Ecol. Lett.* **13**, 1459–1474 (2010).
4. A. James, J. W. Pitchford, M. J. Plank, *Nature* **487**, 227–230 (2012).
5. U. Bastolla *et al.*, *Nature* **458**, 1018–1020 (2009).
6. E. Thébault, C. Fontaine, *Science* **329**, 853–856 (2010).
7. K. R. S. Hale, F. S. Valdivinos, N. D. Martinez, *Nat. Commun.* **11**, 2182 (2020).
8. M. C. Urban, *Science* **348**, 571–573 (2015).
9. J. L. Bronstein, *Ecol. Lett.* **4**, 277–287 (2001).
10. O. Pellmyr, J. Leebens-Mack, *Am. Nat.* **156** (S4), S62–S76 (2000).
11. E. I. Jones *et al.*, *Ecol. Lett.* **18**, 1270–1284 (2015).
12. M. C. Vidal, S. F. Sendoya, P. S. Oliveira, *Ecology* **97**, 1650–1657 (2016).
13. J. Genini, L. P. C. Morellato, P. R. Guimarães Jr., J. M. Olesen, *Biol. Lett.* **6**, 494–497 (2010).
14. C. E. Christian, *Nature* **413**, 635–639 (2001).
15. J. Memmott, N. M. Waser, M. V. Price, Tolerance of pollination networks to species extinctions. *Proc. R. Soc. London Biol. Sci.* **271**, 2605–2611 (2004).
16. S. D. Allison, J. B. Martiny, *Proc. Natl. Acad. Sci. U.S.A.* **105** (Suppl. 1), 11512–11519 (2008).
17. C. A. Johnson, J. L. Bronstein, *Ecology* **100**, e02708 (2019).
18. Materials and methods are available as supplementary materials.
19. J. L. Sachs, U. G. Mueller, T. P. Wilcox, J. J. Bull, *Q. Rev. Biol.* **79**, 135–160 (2004).
20. N. M. Waser, L. Chittka, M. V. Price, N. M. Williams, J. Ollerton, *Ecology* **77**, 1043–1060 (1996).
21. W. Shou, S. Ram, J. M. Vilar, *Proc. Natl. Acad. Sci. U.S.A.* **104**, 1877–1882 (2007).
22. D. Tilman, "Interspecific competition and multispecies coexistence" in *Theoretical Ecology: Principles and Application*, R. May, A. R. McLean, Eds. (Oxford Press, ed. 3, 2007), pp. 84–97.
23. P. Chesson, *Annu. Rev. Ecol. Evol. Syst.* **31**, 343–366 (2000).
24. E. I. Jones, J. L. Bronstein, R. Ferrière, *Ann. N. Y. Acad. Sci.* **1256**, 66–88 (2012).
25. J. N. Holland, D. L. DeAngelis, *Ecology* **91**, 1286–1295 (2010).
26. E. T. Kiers *et al.*, *Science* **333**, 880–882 (2011).
27. O. Pellmyr, C. J. Huth, *Nature* **372**, 257–260 (1994).
28. M. C. Vidal *et al.*, Data from: Species richness and redundancy promote persistence of exploited mutualisms in yeast. *Dryad* (2020); <https://doi.org/10.5061/dryad.pc866t1m6>.

ACKNOWLEDGMENTS

We thank J. Bronstein, T. Anneberg, A. Curé, and D. Luna for comments on earlier versions of the draft. Two anonymous reviewers provided insightful, detailed comments that greatly improved the manuscript. We thank W. Shou for providing the overproduction mutants and S. Erdman for access to equipment. We thank C. Moore, C. Ritchie, and M. Ritchie for insightful discussions. **Funding:** This research was funded by NSF-DEB 1655544. **Author contributions:** K.A.S. and D.M.R. modified the yeast strains. M.C.V., S.P.W., D.M.A., and K.A.S. designed the experiments and synthesized media. M.C.V., S.P.W., and K.A.S. conducted the experiments and collected data. M.C.V. and S.P.W. analyzed the data. M.C.V. wrote the first draft, and M.C.V., S.P.W., D.M.A., and K.A.S. contributed equally to editing. **Competing interests:** The authors declare no competing interests; **Data and materials availability:** Data are available in (28).

SUPPLEMENTARY MATERIALS

science.sciencemag.org/content/370/6514/346/suppl/DC1
Materials and Methods
Figs. S1 to S5
Tables S1 to S4
References (29–35)

26 March 2020; resubmitted 26 June 2020
Accepted 26 August 2020
10.1126/science.abb6703

SIGNAL TRANSDUCTION

The GATOR–Rag GTPase pathway inhibits mTORC1 activation by lysosome-derived amino acids

Geoffrey G. Hesketh¹, Fotini Papazotos¹, Judy Pawling¹, Dushyandi Rajendran¹, James D. R. Knight¹, Sebastien Martinez¹, Mikko Taipale^{2,3}, Daniel Schramek^{1,2}, James W. Dennis^{1,2,4}, Anne-Claude Gingras^{1,2,*}

The mechanistic target of rapamycin complex 1 (mTORC1) couples nutrient sufficiency to cell growth. mTORC1 is activated by exogenously acquired amino acids sensed through the GATOR–Rag guanosine triphosphatase (GTPase) pathway, or by amino acids derived through lysosomal degradation of protein by a poorly defined mechanism. Here, we revealed that amino acids derived from the degradation of protein (acquired through oncogenic Ras-driven macropinocytosis) activate mTORC1 by a Rag GTPase-independent mechanism. mTORC1 stimulation through this pathway required the HOPS complex and was negatively regulated by activation of the GATOR–Rag GTPase pathway. Therefore, distinct but functionally coordinated pathways control mTORC1 activity on late endocytic organelles in response to distinct sources of amino acids.

The mechanistic target of rapamycin complex 1 (mTORC1) coordinates cell growth with nutrient sufficiency. Exogenous amino acids (AAs), taken up through cell surface transporters, promote mTORC1 lysosomal recruitment and activation (1). AAs derived from exogenous protein, acquired through Ras-driven macropinocytosis and trafficked to lysosomes for degradation, also activate mTORC1 and can fuel cell growth in the absence of exogenous free AAs (2–7). Although the AA transporter SLC38A9 mediates arginine-dependent efflux of protein-derived essential AAs (EAAs) from lysosomes (8–10), whether this leads to mTORC1 activation through the canonical Rag guanosine triphosphatase (GTPase) pathway (11) remains unknown.

We developed a pair of “sensors” for proximity-dependent biotinylation (BioID) (12) characterization of the surface proteomes of late endocytic organelles in living cells, using VAMP7 (vesicle-associated membrane protein 7) and VAMP8 (Fig. 1A). VAMP7 and VAMP8 are two related R-SNARE (soluble NSF attachment protein receptors) proteins that traffic through late endocytic organelles (13). An N-terminal longin domain in VAMP7 binds adaptor protein complex 3 (AP-3) and enables its localization to lysosomes (14–16), the site of mTORC1 activation. Green fluorescent protein (GFP)-tagged wild-type VAMP7 (VAMP7-wt), a VAMP7 mutant deficient in AP-3 complex binding (15) (VAMP7-mut), and wild-type VAMP8 all localized to late endocytic organelles (VAMP7-mut and VAMP8 also partially localized to the plasma membrane; fig. S1, A and B). BioID

with each “sensor” captured >800 proximity interactors at a false discovery rate (FDR) $\leq 1\%$ relative to negative controls (Fig. 1, A and B; figs. S1C and S2, A and B; and table S1, A to C). Although VAMP7 and VAMP8 associated with a large common set of proteins, each also enriched sets of proteins representing their distinct trafficking itineraries (Fig. 1, C to F; fig. S2, C and D; and tables S2, A and B, and S3, A and B). VAMP8 enriched plasma membrane, cell junction, and endosomal recycling proteins, whereas VAMP7 enriched late endocytic trafficking complexes, including AP-3 and the homotypic fusion and vacuole protein sorting (HOPS) tethering complex (Fig. 1, D and E). In addition, multiple proteins known to regulate mTORC1 function were recovered with VAMP7-wt to a greater extent than with VAMP8 or VAMP7-mut (Fig. 1F; VAMP7-mut more closely resembled VAMP8, fig. S2E). This is consistent with AP-3 mediating the delivery of VAMP7 to a HOPS- and mTORC1-containing late endosomal domain.

To validate the role of AP-3 in localizing VAMP7 to this domain, we performed VAMP7 BioID after CRISPR-Cas9-mediated ablation of genes encoding individual complex subunits in pooled cell populations [referred to here as KO-BioID (fig. S3); estimated KO efficiencies ranged from 85 to 99% for all experiments (table S4)]. Upon ablation of the AP-3 δ -subunit (AP3D1), VAMP7-wt BioID more closely resembled VAMP7-mut and VAMP8 (fig. S4A), with gains in plasma membrane proteins (fig. S4B) and loss of HOPS and mTORC1 proteins (Fig. 2, A and B), confirming that AP-3 mediates VAMP7 lysosomal localization. By contrast, ablation of individual HOPS subunits had a milder impact on total VAMP7 proximity interactions (Fig. 2, A and B, and fig. S4, A to C), and a subset of proteins sensitive to AP-3 disruption was insensitive to HOPS disruption (Fig. 2C and fig. S4D), suggesting that VAMP7 trafficking by

AP-3 and HOPS are distinct events. The labeling of mTORC1-related proteins was strongly reduced in the absence of HOPS, but not after ablation of other tethering complex genes (Fig. 2, A and B, and fig. S4, A and C). The loss of labeling of mTORC1-related proteins upon AP-3 or HOPS disruption is not likely due to their dissociation from lysosome membranes, because they remained associated with an alternative lysosomal BioID “sensor,” GTP-locked RAB7A (fig. S5). Collectively, these data support a model (fig. S6) in which VAMP7 and VAMP8 partly coexist in a common late endosomal domain from which VAMP7 is trafficked (by AP-3) to a specific late endocytic domain where it encounters mTORC1-related proteins through a HOPS-dependent process. This model was supported by analyzing gene coessentiality across published genome-wide CRISPR screens in cancer cell lines (17, 18), which revealed correlations between multiple HOPS- and mTORC1-related components, suggesting common functions (19) (fig. S7). We therefore aimed to explore the functional contribution of the HOPS complex to mTORC1 activation.

By promoting macropinocytosis, activated Ras can drive exogenous protein uptake (20), resulting in the generation of lysosome-derived AAs that can fuel cell growth (2) and activate mTORC1 in the absence of exogenous free AAs (3). Human embryonic kidney 293 (HEK293) and engineered HEK293 cells expressing an inducible oncogenic KRAS^{G12V} allele (HEK293^{G12V}; fig. S8A) were deprived of AAs, then supplemented with exogenous free Leu or with exogenous protein [bovine serum albumin (BSA), added alone or in the presence of Gln]. mTORC1 was readily reactivated [measured by immunoblotting for ribosomal protein S6 kinase 1 (S6K1), phosphorylated at Thr³⁸⁹] in both cell types by Leu, and in HEK293^{G12V} by the synergistic addition of BSA and Gln, with partial activation by Gln alone and no activation by BSA alone (Fig. 3A). Steady-state mTORC1 activity in complete medium (fig. S8B) or after Leu stimulation alone (fig. S8C) was minimally affected by HOPS ablation (Fig. 3B and table S4), and there was a moderate reduction in mTORC1 activation by EAAs (Fig. 3, C and D). By contrast, there was a marked reduction in mTORC1 activation in cells treated with BSA and Gln (BSA+Gln; Fig. 3, E and F), suggesting reduced activation by lysosome-derived AAs.

Lysosome-derived AAs have been suggested to activate mTORC1 through the Rag GTPases (3), but whether this is mediated by the GAP toward Rags (GATOR)–Rag GTPase (here; GATOR–Rag) pathway (Fig. 4A) has not been thoroughly explored. HOPS and GATOR2 are evolutionarily related protocoatomer family complexes (21–23), which together exclusively possess C-terminal RING domains within

¹Lunenfeld-Tanenbaum Research Institute, Sinai Health System, Toronto, ON, Canada. ²Department of Molecular Genetics, University of Toronto, Toronto, ON, Canada. ³Donnelly Centre for Cellular and Biomolecular Research, Toronto, ON, Canada.

⁴Department of Laboratory Medicine and Pathobiology, University of Toronto, Toronto, ON, Canada.

*Corresponding author. Email: gingras@lunenfeld.ca

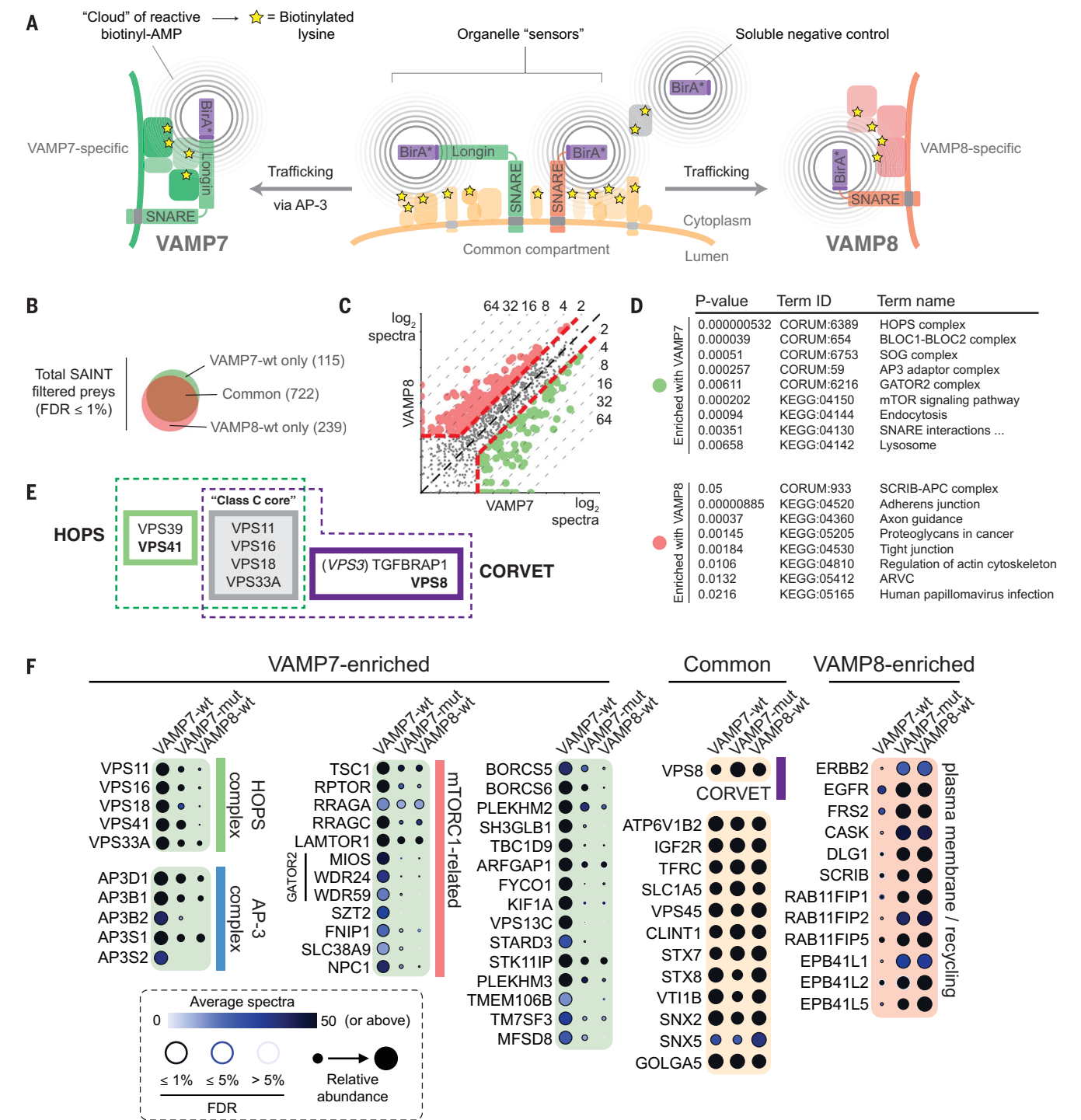


Fig. 1. VAMP7 and VAMP8 access distinct endosomal domains.

(A) Establishment of late endosomal BioID “sensors.” N-terminally BirA*-FLAG-tagged VAMP7 (a wild-type, VAMP7-wt, or AP-3 binding-deficient mutant VAMP7-mut) and VAMP8 traffic through both common and specific late endocytic compartment surfaces where they allow biotinylation of proximal proteins. (B) Venn diagram of proximity interactions with FDR ≤1% for VAMP7-wt and VAMP8-wt baits (see table S1, A and C, for complete list). (C) Bait versus bait plot of abundance (average spectral counts plotted as log₂ values) for all proximity interactions (FDR ≤1%). Enriched proximity interactions (≥2-fold enriched and with ≥10 spectral counts) are color-coded in green and red for

VAMP7 and VAMP8, respectively (see table S2, A and B). The black dashed diagonal line indicates equal abundance for both baits, with relative fold enrichment indicated by gray dashed lines. (D) g:Profiler analysis of CORUM complexes and KEGG pathway terms for VAMP7- and VAMP8-enriched proteins [as indicated in (C); see table S3, A and B]. (E) Organization of HOPS and CORVET multisubunit tethering complexes. The CORVET-specifying subunit VPS8 and the HOPS-specifying subunit VPS41, and in some instances VPS39, are studied here; “class C core” refers to the subunits common to both HOPS and CORVET. (F) Dot plots (columns show baits) of selected proximity interactors (rows; see legend inset and table S6, A and B, for complete dataset).

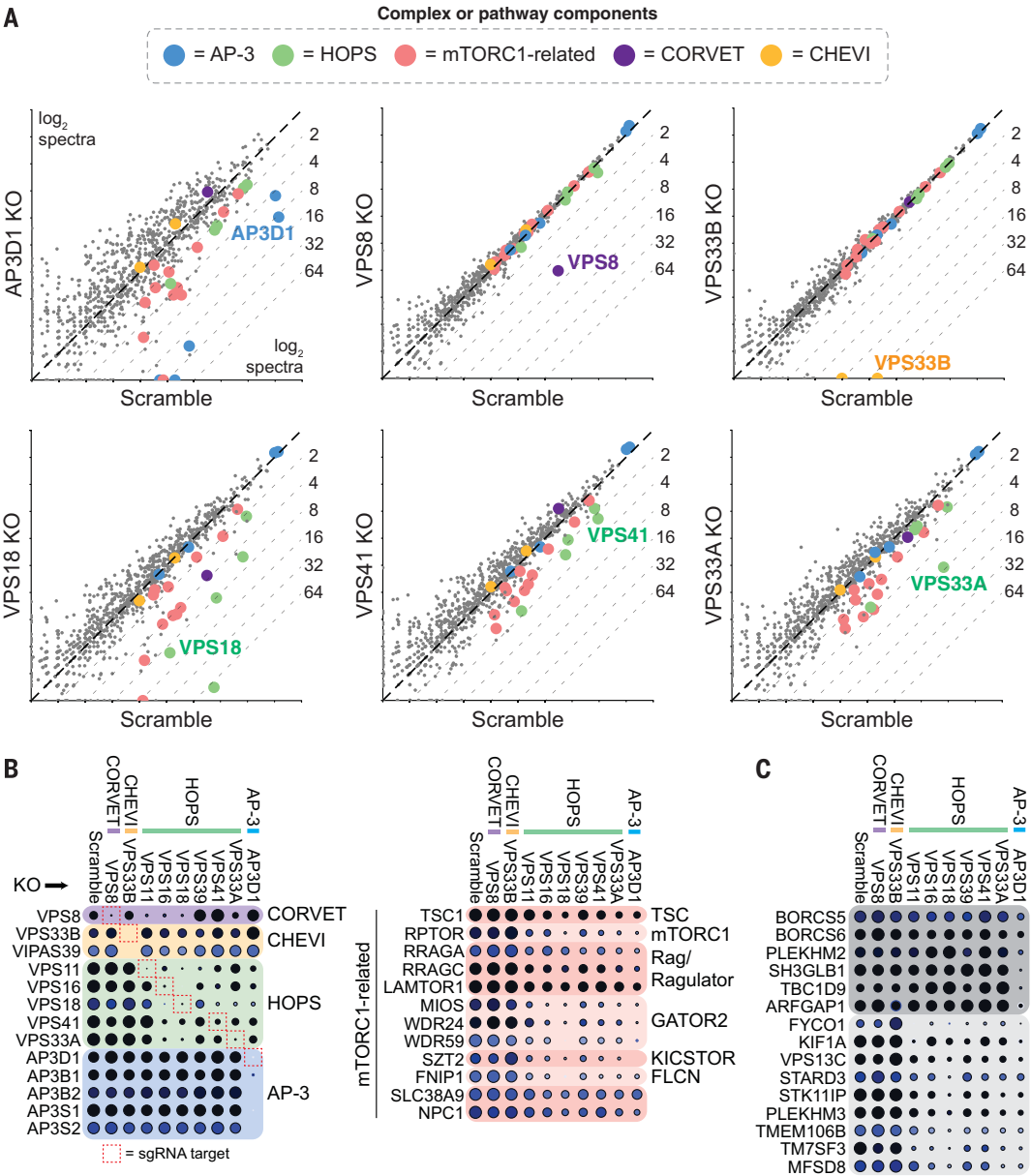


Fig. 2. mTORC1 access by VAMP7 is AP-3 and HOPS dependent. (A) Bait versus bait plots of VAMP7-wt Biold profiles comparing the scramble knockout condition (x axis) to different ablation conditions (y axis; display as in Fig. 1C). Members of the indicated protein complexes or pathways are colored as shown in the inset legend. CHEVI is a trafficking complex that comprises VPS33B and VIPAS39 and is used here as a negative control; see Fig. 1E for CORVET and

HOPS composition. (B) Dot plots of proximity interactors annotated by color coding in (A). Proteins that are components of defined complexes are indicated (see Fig. 1F for dot plot legend inset). (C) Dot plot of selected preys, highlighting differential behavior between AP-3 and HOPS ablation conditions. Darker shade indicates AP-3– but not HOPS-dependent proximity interactors; lighter shade indicates proximity interactors that depend on both AP-3 and HOPS.

three of their subunits (fig. S9A). We therefore tested if HOPS and GATOR2 share a functional as well as evolutionary relationship. KOs of individual GATOR2 or GATOR1 subunits (fig. S9B) displayed delayed mTORC1 inactivation when deprived of AAs in both HEK293^{G12V} and HEK293 cells (fig. S10, A and B), with GATOR1 acting as a strong negative regulator, as expected (11). Contrary to the effect of HOPS disruption, GATOR2-ablated cells displayed a marked increase in mTORC1 activation in cells

treated with BSA+Gln (fig. S11A). This potentiated signal was strongly blunted by concomitant HOPS ablation [Fig. 4B; effect also seen in VPS18 KO clones (fig. S11B)] and did not appear to result from increased protein-derived AA production (fig. S11, C to E) (6). GATOR complexes control the activation state of the Rag heterodimer (12). Consistent with this, ablation of RagA+RagB or RagC+RagD (or all Rags) strongly potentiated mTORC1 activation by BSA+Gln but blunted

activation by EAAs, as did ablation of the GATOR2 subunit MIOS (Fig. 4C). Similar results were observed after ablation of LAMTOR1, the membrane-anchored subunit of the Ragulator complex that docks the Rags on the lysosome surface (fig. S12, A to C). The potentiated signal was abolished in cells treated with either Torin-1 or rapamycin (fig. S12D) and in cells in which RPTOR (regulatory-associated protein of mTOR) is depleted (fig. S13), confirming that mTORC1 activity is responsible

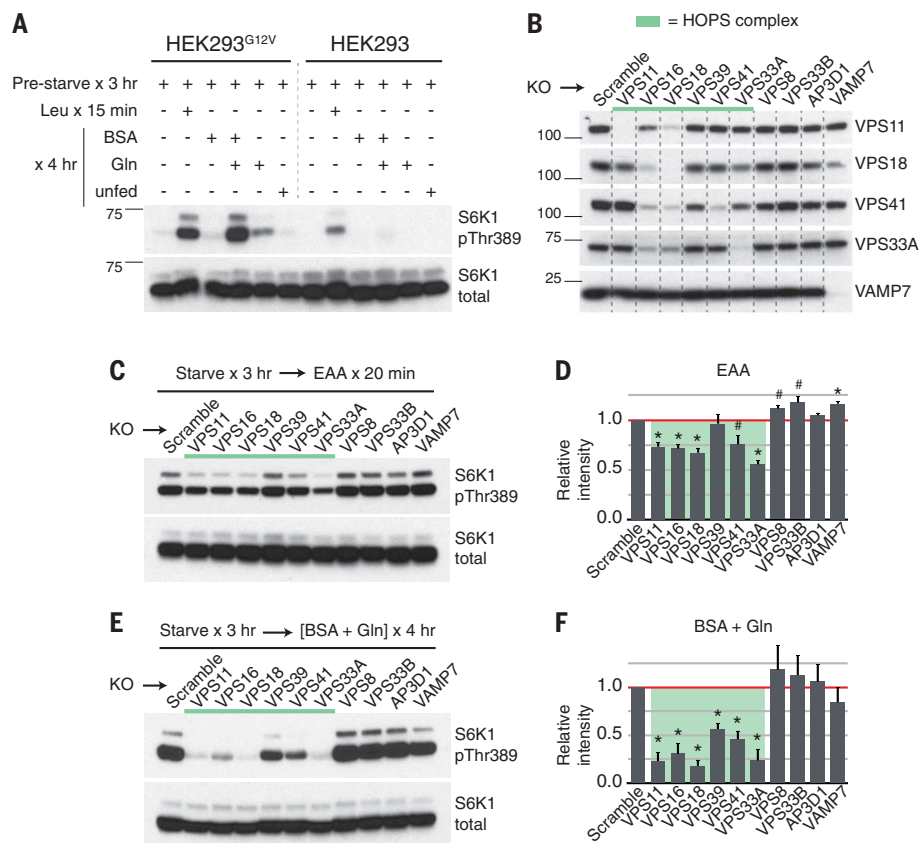


Fig. 3. mTORC1 activation by exogenous protein-derived AAs requires the HOPS complex.

(A) Immunoblots of HEK293^{G12V} or HEK293 cells starved in AA-free Dulbecco's modified Eagle medium–F12 medium for 3 hours and then treated as indicated (p85 and p70 splice variants are observed for S6K1). (B) Immunoblots of HOPS proteins in HEK293^{G12V} KO cell pools (see table S4 for KO efficiency). (C) Immunoblots of HEK293^{G12V} KO cell pools starved of AAs for 3 hours and stimulated with EAAs (1×; see materials and methods) for 20 min (see fig. S8D for complete blot, including starvation condition). (D) Quantification of S6K1-pThr³⁸⁹ immunoblots from three independent experiments (see fig. S8E for replicates) done as in (C). Values are means ± SD relative to scramble (**P* < 0.01, #*P* < 0.05; *n* = 3; two-tailed paired *t* test). (E) Immunoblots of HEK293^{G12V} KO cell pools starved of AAs for 3 hours and stimulated with BSA plus Gln for 4 hours. (F) Quantification of three independent experiments done as in (E); see (D) for details. (BSA = 3%, Gln = 2 mM).

for the phosphorylation events detected. Signal potentiation requires AA sensing by the GATOR-Rag pathway, as ablation of the sensors for Leu (the Sestrins SESN1, SESN2, and SESN3) (24) or Arg (CASTOR1 and CASTOR2) (25) also potentiated stimulation with BSA+Gln, albeit with differing magnitudes (fig. S14). By contrast, ablation of folliculin (FLCN), which promotes an active Rag dimer by a mechanism independent from the GATOR complexes (26, 27), had no potentiation effect (fig. S13). These results were confirmed with another mTORC1 substrate, the eukaryotic translation initiation factor 4E binding protein 1 (fig. S15). These data support a model in which activation of the GATOR-Rag signaling axis negatively regulates Rag-independent activation of mTORC1 by exogenous protein-derived AAs.

To better distinguish whether the effects observed were due to BSA-derived AAs and/or the Gln contribution, we explored these stimuli separately. Gln activates mTORC1 through a Rag-independent mechanism (28, 29), likely involving mTORC1 activation through autophagy (30). In HEK293^{G12V} cells (but not HEK293; Fig. 3A), Gln treatment induced gradual but transient mTORC1 activation (fig. S16A). The Gln signal was unaffected by HOPS (VPS18) depletion, but was reduced upon ablation of the autophagy-activating kinases ULK1 and ULK2, and was strongly potentiated by ablation of RagA and RagB, LAMTOR1, or all three Sestrins (fig. S16, B and C). Thus, mTORC1 activation by Gln is also negatively regulated by activation of the GATOR-Rag pathway. GATOR-Rag pathway disruption also potentiated mTORC1 activation in cells stimulated

with BSA alone, although the ability of BSA to synergize with Gln was maintained (Fig. 4D and figs. S13A and S15). Signal potentiation with BSA stimulation was blocked by concomitant ablation of VPS18 with GATOR-Rag pathway disruption, whereas potentiation with Gln stimulation alone was not (Fig. 4D and fig. S17). These data suggest that the GATOR-Rag pathway negatively regulates mTORC1 activation by protein-derived AAs, with AA production from exogenous or endogenous sources of protein being HOPS dependent and HOPS independent, respectively.

To further explore how Gln may enable Rag-independent mTORC1 activation by lysosome-derived AAs, we treated cells with a glutaminase inhibitor (CB-839), which partially reduced mTORC1 activation by BSA+Gln, suggesting that Gln may be acting primarily as a nitrogen source (fig. S18) (30). We therefore tested whether any of the other 20 proteinogenic AAs can enable Rag-independent mTORC1 activation (either in combination with BSA or alone). In addition to Gln, multiple AAs enabled Rag-independent mTORC1 activation (including Q, S, N, T, A, P, and G) largely aligned with those previously reported to synergize with EAA in activating mTORC1 (31), suggesting that these observations may be linked.

We revisited the role of additional lysosomal trafficking proteins in the activation of mTORC1 by BSA+Gln. HOPS function is coordinated with Rab7 (32), and ablation of RAB7A reduced activation of mTORC1 by BSA+Gln (and partially reduced activation by EAAs; fig. S21). Rab7 ablation both delayed the starvation response and inhibited activation by BSA+Gln, indicating that Rab7 likely underlies an important regulatory point for mTORC1 activation (33). We tested additional genes that coordinate Rab7 function (some of which correlated with HOPS through coessentiality analysis; see fig. S7). Ablation of vacuolar fusion protein CCZ1 homolog [a Rab7-GEF (34)] reduced activation, whereas TBC1 domain family member 5 [TBC1D5; a putative Rab7-GAP (33)] had a partial effect (Fig. 4F). Disrupting the Retromer complex [by ablating VPS35 or VPS29], which is coordinated with Rab7 function to mediate late endocytic recycling (35), reduced activation by BSA+Gln and induced a delayed starvation response, indicating a role in this pathway.

Taken together, our results demonstrate that GATOR-Rag pathway activation negatively regulates Rag-independent mTORC1 activation by lysosome-derived AAs, although a mechanistic explanation for this negative regulation is currently lacking (3, 6). How Rab7 function is coordinated with late endosomal trafficking complexes, including HOPS and Retromer,

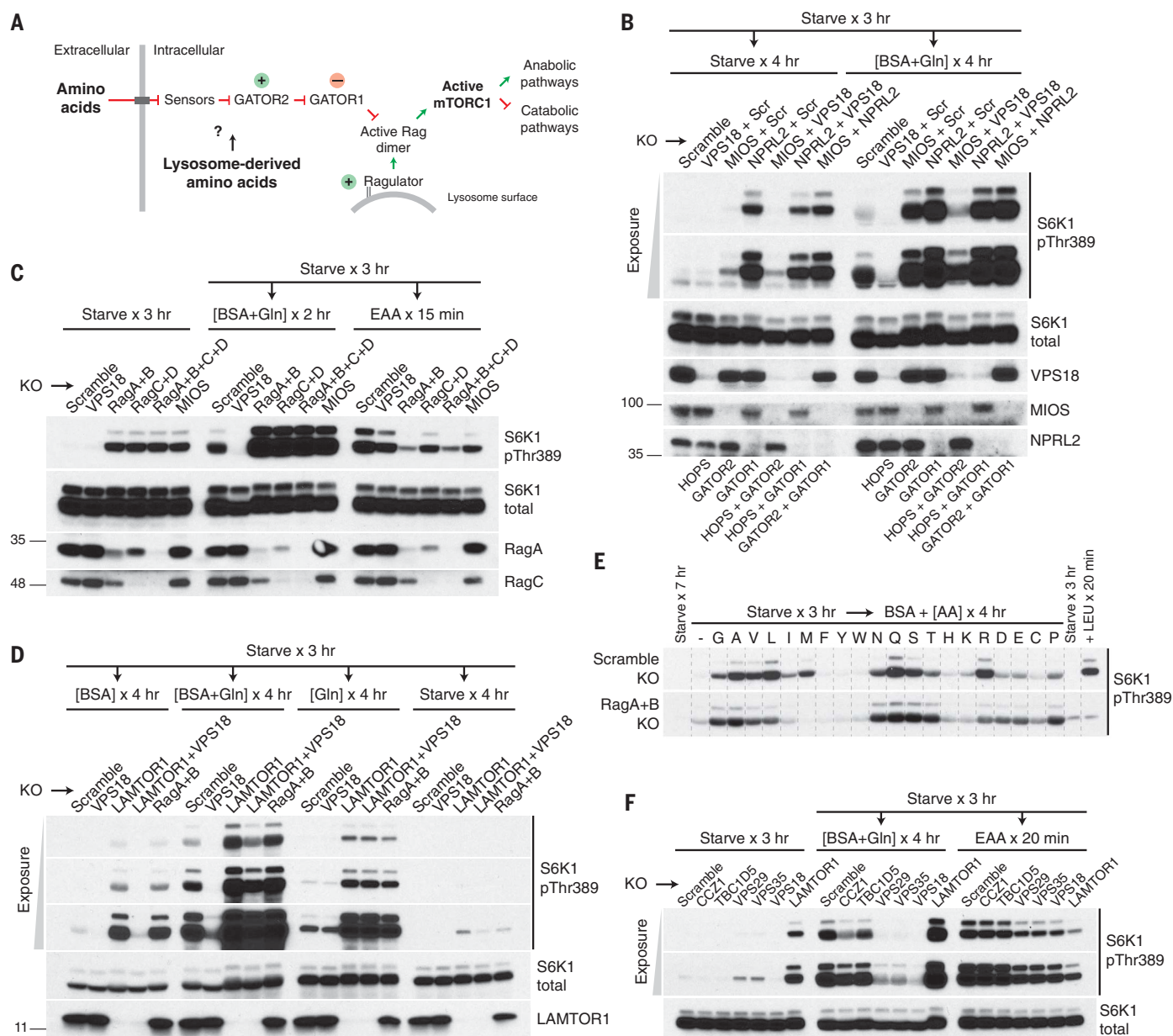


Fig. 4. The GATOR-Rag pathway negatively regulates Rag-independent mTORC1 activation by lysosome-derived AAs. (A) mTORC1 activation through the GATOR-Rag pathway: Sensing of free AA induces the regulation of the GATOR2-GATOR1 module, which controls the activation status of the Rag GTPases, enabling recruitment of mTORC1 to the lysosome and activation. Positive (+) and negative (−) pathway regulators and effect on downstream pathways are indicated (see fig. S9B for an expanded view listing

complex components). (B–F) Immunoblots of HEK293^{G12V} KO cell pools [either single or single guide RNA (sgRNA) combinations as indicated] starved and stimulated as shown. Additional blots and quantification associated with (E) are shown in fig. S19 (BSA = 3%, Gln = 2 mM, EAA = 1×). Abbreviations for the amino acid residues are as follows: A, Ala; C, Cys; D, Asp; E, Glu; F, Phe; G, Gly; H, His; I, Ile; K, Lys; L, Leu; M, Met; N, Asn; P, Pro; Q, Gln; R, Arg; S, Ser; T, Thr; V, Val; W, Trp; and Y, Tyr.

to control the switch between Rag-dependent and Rag-independent mTORC1 activation will require further study. Similarly, whether the HOPS complex contributes to mTORC1 activation purely through its function as a tether, or whether it regulates mTORC1 more directly [as proposed for the yeast HOPS subunit Vam6/Vps39, suggested to be a GEF for the yeast RagA and RagB paralog Gtr1 (36)], is also unknown. We propose that the evolutionary relation-

ship between HOPS and GATOR2 complexes may underlie related but divergent roles in activating mTORC1 in response to distinct nutrient inputs.

REFERENCES AND NOTES

- R. L. Wolfson, D. M. Sabatini, *Cell Metab.* **26**, 301–309 (2017).
- C. Commisso et al., *Nature* **497**, 633–637 (2013).
- W. Palm et al., *Cell* **162**, 259–270 (2015).
- J. J. Kamphorst et al., *Cancer Res.* **75**, 544–553 (2015).
- S. M. Davidson et al., *Nat. Med.* **23**, 235–241 (2017).
- M. Nofal, K. Zhang, S. Han, J. D. Rabinowitz, *Mol. Cell* **67**, 936–946.e5 (2017).
- R. M. Perera et al., *Nature* **524**, 361–365 (2015).
- M. Rebsamen et al., *Nature* **519**, 477–481 (2015).
- S. Wang et al., *Science* **347**, 188–194 (2015).
- G. A. Wyant et al., *Cell* **171**, 642–654.e12 (2017).
- L. Bar-Peled et al., *Science* **340**, 1100–1106 (2013).
- K. J. Roux, D. I. Kim, M. Raida, B. Burke, *J. Cell Biol.* **196**, 801–810 (2012).
- J. P. Luzio, P. R. Pryor, N. A. Bright, *Nat. Rev. Mol. Cell Biol.* **8**, 622–632 (2007).

14. P. R. Pryor *et al.*, *Cell* **134**, 817–827 (2008).
15. H. M. Kent *et al.*, *Dev. Cell* **22**, 979–988 (2012).
16. I. B. Schäfer *et al.*, *Nat. Struct. Mol. Biol.* **19**, 1300–1309 (2012).
17. R. M. Meyers *et al.*, *Nat. Genet.* **49**, 1779–1784 (2017).
18. M. Costanzo *et al.*, *Science* **353**, aaf1420 (2016).
19. E. Kim *et al.*, *Life Sci. Alliance* **2**, e201800278 (2019).
20. D. Bar-Sagi, J. R. Feramisco, *Science* **233**, 1061–1068 (1986).
21. S. Dokudovskaya *et al.*, *Mol. Cell. Proteomics* **10**, 006478 (2011).
22. R. Algret *et al.*, *Mol. Cell. Proteomics* **13**, 2855–2870 (2014).
23. M. P. Rout, M. C. Field, *Annu. Rev. Biochem.* **86**, 637–657 (2017).
24. R. L. Wolfson *et al.*, *Science* **351**, 43–48 (2016).
25. L. Chantranupong *et al.*, *Cell* **165**, 153–164 (2016).
26. R. E. Lawrence *et al.*, *Science* **366**, 971–977 (2019).
27. K. Shen *et al.*, *Cell* **179**, 1319–1329.e8 (2019).
28. J. L. Jewell *et al.*, *Science* **347**, 194–198 (2015).
29. D. Meng *et al.*, *J. Biol. Chem.* **295**, 2890–2899 (2020).
30. H. W. S. Tan, A. Y. L. Sim, Y. C. Long, *Nat. Commun.* **8**, 338 (2017).
31. J. Dyachok, S. Earnest, E. N. Iturraran, M. H. Cobb, E. M. Ross, *J. Biol. Chem.* **291**, 22414–22426 (2016).

32. H. J. K. Balderhaar, C. Ungermann, *J. Cell Sci.* **126**, 1307–1316 (2013).
33. A. Kvainickas *et al.*, *J. Cell Biol.* **218**, 3019–3038 (2019).
34. M. Nordmann *et al.*, *Curr. Biol.* **20**, 1654–1659 (2010).
35. K. E. Chen, M. D. Healy, B. M. Collins, *Traffic* **20**, 465–478 (2019).
36. M. Binda *et al.*, *Mol. Cell* **35**, 563–573 (2009).

ACKNOWLEDGMENTS

We thank C. Wong and B. Larsen for assistance with mass spectrometry; J. P. Luzio and D. Owen for VPS33A antiserum; and F. Zhang for the px459v2 plasmid (Addgene plasmid no. 62988). We thank J. P. Luzio, D. Owen, L. Wartosch, J. Brummell, and J.-Y. Youn for critical reading of the manuscript and discussions. **Funding:** This work was supported by Canadian Cancer Society Research Institute Innovation and i2I grants (CCSRI grants 704301 and 705938 to A.-C.G.) and a Canadian Institutes of Health Research Foundation Grant (CIHR FDN 143301 to A.-C.G.). Proteomics work was performed at the Network Biology Collaborative Centre at the Lunenfeld-Tanenbaum Research Institute, a facility supported by Canada Foundation for Innovation funding, by the Government of Ontario, and by Genome Canada and Ontario Genomics (OGI-139). A.-C.G. is the Canada Research Chair (Tier 1) in Functional Proteomics. G.G.H. was funded by a Basic Research fellowship from Parkinson Canada, and F.P. was funded by a Natural Sciences and Engineering Research Council

of Canada Undergraduate Student Research Award and BioTalent Canada. We thank the Glowinsky-Sandler family for financial support. **Author contributions:** Conceptualization: G.G.H., A.-C.G.; Investigation: G.G.H., F.P., J.P., D.R., J.D.R.K., S.M., M.T.; Supervision: D.S., J.W.D., A.-C.G.; Writing: G.G.H., A.-C.G. **Competing interests:** The authors declare no competing interests. **Data and materials availability:** All MS files used in this study were deposited at MassIVE (<http://massive.ucsd.edu>) and have been assigned the following accession number: MSV000084159. The scored proximity interactions associated with quantitative values are available for searching at prohits-web.lunenfeld.ca (project 43). All code will be made available upon request.

SUPPLEMENTARY MATERIALS

science.sciencemag.org/content/370/6514/351/suppl/DC1
Materials and Methods
Figs. S1 to S21
Tables S1 to S7
References (37–51)

[View/request a protocol for this paper from Bio-protocol.](#)

10 August 2019; resubmitted 18 April 2020
Accepted 27 August 2020
10.1126/science.aaz0863

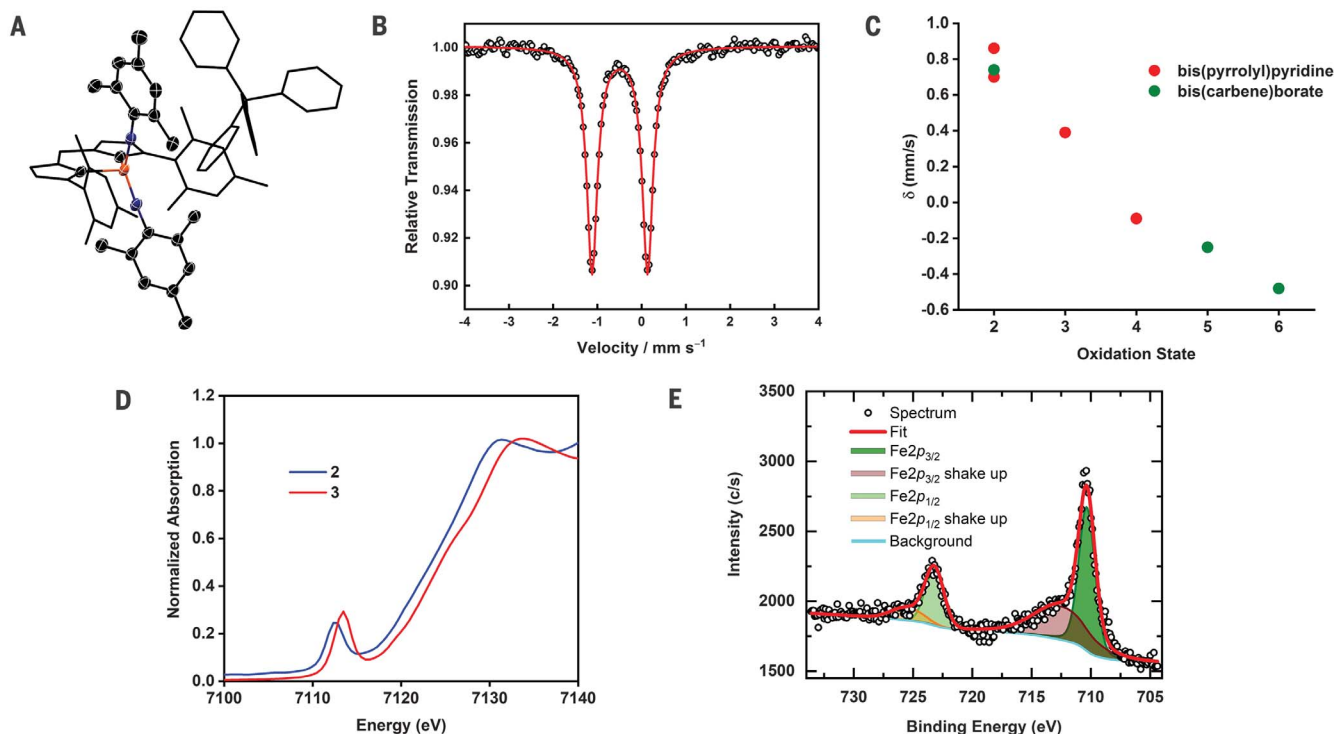
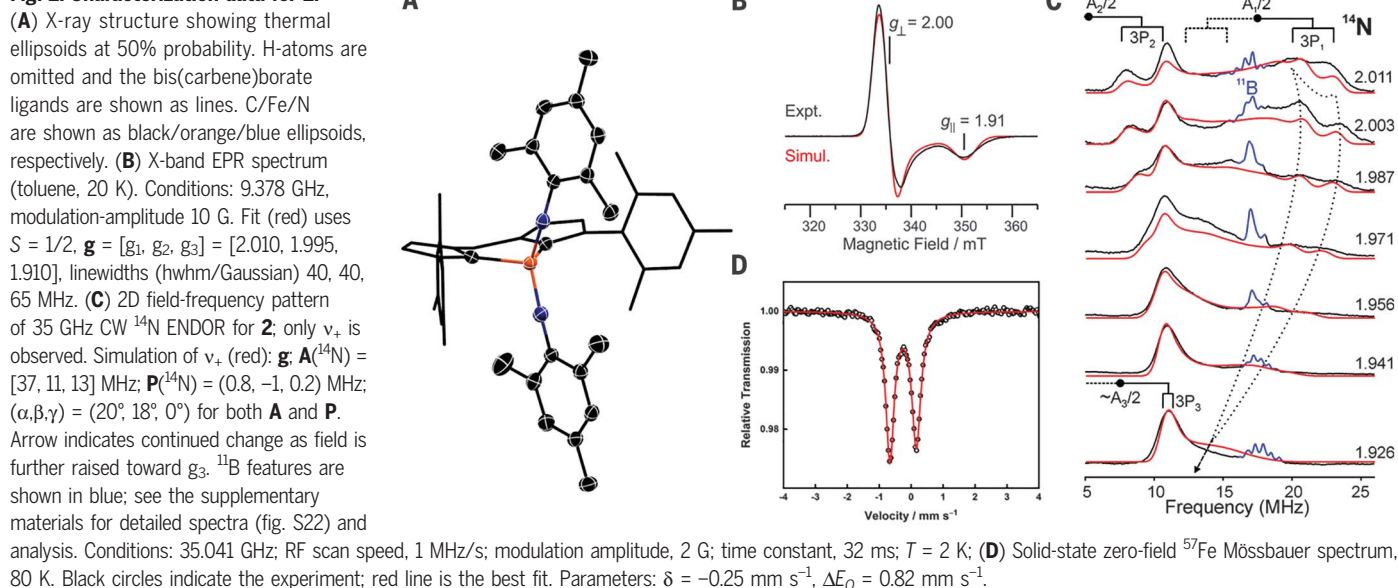
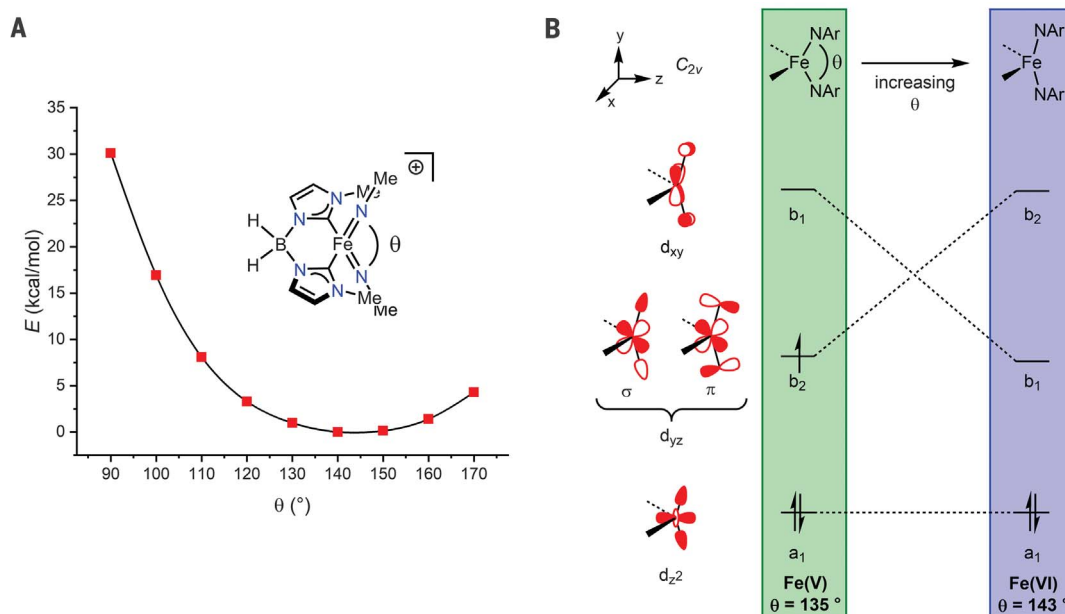
Fig. 2. Characterization data for 2.

Fig. 3. Characterization data for 3. **(A)** X-ray structure showing thermal ellipsoids at 50% probability. H-atoms are omitted and bis(carbene)borate ligands are shown as lines. One component of the disordered bis(carbene) borate ligand is shown. C/Fe/N are shown as black/orange/blue ellipsoids, respectively. **(B)** Solid-state zero-field ^{57}Fe Mössbauer spectrum, 80 K. Black circles indicate the experiment; red line is the best fit. Parameters: $\delta = -0.48 \text{ mm s}^{-1}$, $\Delta E_Q = 1.25 \text{ mm s}^{-1}$; **(C)** Isomer shift versus oxidation state for: $\text{H}_2\text{B}(\text{MesIm})_2\text{Fe}(\text{I})(\text{THF})$ (**1**), $\text{H}_2\text{B}(\text{MesIm})_2\text{Fe}(\text{=NMe})_2$ (**2**),

$[\text{H}_2\text{B}(\text{MesIm})_2\text{Fe}(\text{=NMe})_2]^+$ (**3**), $(\text{pyrr2py})\text{Fe}(\text{OEt}_2)$ (**30**), $(\text{pyrr2py})\text{Fe}(\text{CH}_2\text{PPh}_3)$ (**30**), $(\text{pyrr2py})\text{Fe}(\text{SCH}_2\text{PPh}_3)$ (**30**), $(\text{pyrr2py})\text{FeCl}$ (**29**), and $(\text{pyrr2py})\text{Fe}=\text{NAD}$ (**29**). See table S1 for data; **(D)** Normalized Fe K-edge XAS of **2** and **3**. See table S2 for fitting parameters; **(E)** High-resolution XPS Fe 2p spectrum of **3**. Black circles indicate the experiment; green and blue lines are the Fe $2p_{3/2}$ and Fe $2p_{1/2}$ components, respectively; and the red line is the resulting fit. Dark red and orange are the shake-up satellites; cyan is the background. See table S5 for fitting parameters.

Fig. 4. Electronic structure modeling.

(A) Angular dependence of the DFT-calculated electronic energy of the Fe(VI) model compound $[\text{H}_2\text{B}(\text{Melm})_2\text{Fe}(\text{=NMe})_2]^+$, **3'**. **(B)** Qualitative Fe-3d orbital diagram showing the effects of N-Fe-N bending and d-orbital occupancies for Fe(VI) and Fe(V). The z-axis lies on N-Fe-N and C-Fe-C bisector; x-axis is perpendicular to N-Fe-N plane. Note that the $3d_{yz}$ orbital can engage in both σ - and π -bonding interactions with the imido ligands, which are shown separately for clarity. The $3d_{x^2-y^2}$ and $3d_{xz}$ orbitals are at higher energy because of destabilizing interactions with the σ -donor orbitals of the imido and bis(carbene)borate ligands, respectively.



component corresponds to a semiempirically estimated minority spin density on each nitrogen of only $\rho(\text{N}) < 0.2 - 0.25$ (26), which is compatible with the even smaller values of $\rho(\text{N})$ given by the DFT computations. The quadrupole coupling constant, $e^2qQ/h = 2P_{\text{max}} \sim -2$ MHz is relatively small as the result of strong N \rightarrow Fe σ donation. (27)

The solid-state ^{57}Fe Mössbauer spectrum of **2** is an asymmetric doublet (Fig. 2D) the parameters of which ($\delta = -0.25$ mm s $^{-1}$; $\Delta E_Q = 0.82$ mm s $^{-1}$ at 80 K) are consistent with a high oxidation state complex having low orbital degeneracy, as expected for the relatively low symmetry structure. Although the parameters differ from other Fe(V) complexes (3, 13), e.g., $[(\text{TAML})\text{Fe}=\text{O}]^-$ ($S = 1/2$), $\delta = -0.42$ mm s $^{-1}$; $\Delta E_Q = 4.25$ mm s $^{-1}$; $[\text{PhB}(\text{BuIm})_3\text{Fe}=\text{N}]^+$ ($S = 1/2$), $\delta = -0.45$ mm/s; $\Delta E_Q = 4.78$ mm s $^{-1}$, the different coordination numbers and/or geometries make direct comparisons difficult. Complex **2** has been characterized by other spectroscopies (see the supplementary materials).

Unexpectedly, the cyclic voltammogram of **2** shows a reversible oxidative wave at low potential ($E_{1/2} = -0.73$ V vs Fc^+/Fc ; figs. S13 and S14), suggesting a stable higher-valent state. Chemical oxidation with Fc^+ (as Cp_2FeBF_4) afforded the dark blue diamagnetic complex **3-BF₄** in 81% yield (Fig. 1). The molecular structure of **3** has been determined by XRD for **3-BPh₄**, prepared analogously using $\text{Cp}_2\text{FeBPh}_4$ (Fig. 3A). The seesaw coordination environment around iron in **2** is retained upon oxidation, with a slight contraction in the Fe=N distances [1.630(2) Å and 1.638(2) Å], linearization of the imido ligands [Fe-N-C 175.1(2)° and 176.4(2)°], and increase in the N-Fe-N

angle [143.4(1)°]. Because the structural data provide no evidence for ligand-based oxidation in **3-BPh₄**, they therefore implicate the Fe(VI) oxidation state.

Solid-state ^{57}Fe Mössbauer spectroscopic data support the Fe(VI) assignment of this diamagnetic complex. The substantially decreased isomer shift of **3-BF₄** ($\delta = -0.48$ mm s $^{-1}$ at 80 K) and increased quadrupole splitting ($\Delta E_Q = 1.25$ mm s $^{-1}$) are both consistent with metal-centered oxidation (Fig. 3B). Although the isomer shift is not as negative as that of tetrahedral ($S = 1$) $[\text{FeO}_4]^{2-}$ ($\delta = -0.81$ mm s $^{-1}$ for K_2FeO_4 ; fig. S17) (28), it is substantially lower than that observed for six-coordinate ($S = 0$) $[(\text{MecyclamAc})\text{Fe}=\text{N}]^{2+}$ ($\delta = -0.29$ mm s $^{-1}$) (17). As noted for **2**, these comparisons are difficult because of the different geometries and electronic structures of these three Fe(VI) complexes. Because of this concern, we compared the isomer shift of **3-BF₄** with a series of structurally related iron complexes in a range of oxidation states (Fig. 3C). Because of the paucity of four-coordinate iron bis(carbene) borate complexes, we included bulky bis(pyrrolyl)pyridine complexes, which also stabilize four-coordinate iron in a seesaw geometry (29, 30). Notably, we observed a linear correlation between isomer shift and oxidation state for this series of complexes (Fig. 3C), further supporting the Fe(VI) assignment for **3-BF₄**. A similar analysis of six-coordinate iron cyclam complexes supported the Fe(VI) state assignment for $[(\text{MecyclamAc})\text{Fe}=\text{N}]^{2+}$, which was characterized in frozen solution. (17)

X-ray absorption spectroscopy (XAS) also supports metal-based oxidation. The pre-edge feature in the Fe K-edge XAS shifts from

7112.3(4) eV in **2** to 7113.5(4) eV in **3-BF₄** (Fig. 3D). This 1.2-eV increase in energy is similar to that when the Fe(V) species $[(\text{MecyclamAc})\text{Fe}=\text{N}]^+$ is oxidized to Fe(VI). (17) In addition, the intensity of the pre-edge feature increases upon oxidation, consistent with increased 4p-3d mixing from shorter metal-ligand bond distances (31). The x-ray photoelectron spectrum (XPS) of **3-BF₄** reveals that the Fe $2p_{3/2}$ binding energy (710.34 eV) increases by 1.3 eV from **2** (Fig. 3E, table S5, and figs. S26 to S28), as expected for oxidation at the metal center (32). The narrow linewidths and low-energy, low-intensity shake-up satellites are also consistent with a diamagnetic Fe(VI) metal center in a seesaw geometry (33). The structure of **3-BF₄** is maintained in solution, as supported by multinuclear NMR spectroscopy (figs. S6 to S8).

Complexes **2** and **3** are notable for their seesaw geometries, with relatively large N-Fe-N (θ) and small C-Fe-C angles, similar to other d 2 bis(imido) and bis(oxo) complexes (tables S13 and S14). DFT calculations (B3LYP/def2-TZVP) on the truncated Fe(VI) model compound $[\text{H}_2\text{B}(\text{MeIm})_2\text{Fe}(\text{=NMe})_2]^+$, **3'**, with bulky mesityl groups replaced by methyl, reveal a minimum energy for **3'** at $\theta \sim 140^\circ$ (Fig. 4A), matching the angle found for **3** by XRD (see above). Similar calculations for the analogous Fe(V) model $\text{H}_2\text{B}(\text{MeIm})_2\text{Fe}(\text{=NMe})_2$, **2'**, show its minimum energy at $\theta \sim 135^\circ$, which matches **2** (fig. S33). These results indicate that the geometries of **2** and **3** are electronically dictated.

These geometric preferences can be explained using a simple bonding analysis that considers the angular dependence of metal-ligand orbital overlap. Because of the low

d -electron count in these complexes, the relative energies and occupancies of the lowest-lying metal-based orbitals and their covalent interactions with the ligand-based orbitals are expected to play the greatest role in determining molecular geometry (Fig. 4B). The relevant iron-based orbitals are the $3d_{z^2}$ -derived a_1 orbital, lying along the bisector of $\angle\text{N-Fe-N}$ (θ), and the $3d_{xy}$ and $3d_{xz}$ orbitals, whose relative energies are determined by determined by θ .

The structure of **2** is determined by the highest singly occupied molecular orbital (SOMO), the $3d_{yz}$ -derived b_2 orbital (Fig. 4B, green). Here, $\theta = 135^\circ$ minimizes overlap between the iron $3d_{yz}$ and imido π -donor orbitals (fig. S34). Because overlap of the $3d_{yz}$ and imido σ -donor orbitals and of the $3d_{xy}$ and imido π -donor orbitals is less sensitive to θ , the energy of $3d_{yz}$ dictates the molecular geometry. This orbital description is quantitatively supported by the EPR/ENDOR results for **2**. The computed SOMO reveals most of the spin to be on Fe, with π delocalization of a small spin density into the imido nitrogen $2p\pi$ orbitals normal to the mesityl plane: Mulliken spin densities 0.756 on Fe and 0.134 on each imido nitrogen (fig. S31 and table S10). As noted above, the g -values are characteristic of a metal-centered spin, and the DFT-calculated \mathbf{g} -tensor has components and orientation in satisfactory agreement with the experimental results (table S11). The DFT and EPR/ENDOR analyses agree that the ^{14}N -ligand hyperfine tensors have near-axial symmetry, with small ^{14}N $2p\pi$ spin densities yielding small components [calculated, $\mathbf{A}(^{14}\text{N}) = (39.8, 11.4, 16.9)$ MHz]. Together, these results confirm the assignment of **2** as exhibiting an Fe(V) valency.

Similar analysis provides insight into the larger θ angle in **3**, where the relative energy of the highest occupied molecular orbital (HOMO) determines the molecular geometry. The a_1 HOMO is most stabilized at $\theta = 144.7^\circ$, which minimizes antibonding interactions between the Fe $3d_{z^2}$ and the imido σ -donor orbitals by placing the imido ligands in the $3d_{z^2}$ nodal cone (fig. S34). At this angle, b_1 is anticipated to be the lowest unoccupied molec-

ular orbital (LUMO) of **3** (Fig. 4B, blue) because of σ and π interactions between $3d_{yz}$ and the imido ligands that destabilize the antibonding b_2 orbital.

The combination of strongly donating bis(carbene)borate and imido ligands stabilize Fe(V) and Fe(VI), respectively, in complexes **2** and **3**, the unusual molecular structures and properties of which are dictated by the electronic structure requirements of their low d -electron count. This structural template provides the basis for a distinct class of high-valent iron complexes.

REFERENCES AND NOTES

- A. R. McDonald, L. Que Jr., *Coord. Chem. Rev.* **257**, 414–428 (2013).
- O. Y. Lyakin, K. P. Bryliakov, E. P. Talsi, *Coord. Chem. Rev.* **384**, 126–139 (2019).
- F. Tiago de Oliveira *et al.*, *Science* **315**, 835–838 (2007).
- M. Ghosh *et al.*, *J. Am. Chem. Soc.* **136**, 9524–9527 (2014).
- M. R. Mills, A. C. Weitz, M. P. Hendrich, A. D. Ryabov, T. J. Collins, *J. Am. Chem. Soc.* **138**, 13866–13869 (2016).
- R. Fan *et al.*, *J. Am. Chem. Soc.* **140**, 3916–3928 (2018).
- K. M. Van Heuvelen *et al.*, *Proc. Natl. Acad. Sci. U.S.A.* **109**, 11933–11938 (2012).
- S. Hong *et al.*, *J. Am. Chem. Soc.* **139**, 8800–8803 (2017).
- S. Hong *et al.*, *J. Am. Chem. Soc.* **139**, 14372–14375 (2017).
- K. Meyer, E. Bill, B. Mienert, T. Weyhermüller, K. Wieghardt, *J. Am. Chem. Soc.* **121**, 4859–4876 (1999).
- G. Sabenya *et al.*, *J. Am. Chem. Soc.* **139**, 9168–9177 (2017).
- H. C. Chang *et al.*, *J. Am. Chem. Soc.* **141**, 2421–2434 (2019).
- J. J. Scepaniak *et al.*, *Science* **331**, 1049–1052 (2011).
- C. Citek, P. H. Oyala, J. C. Peters, *J. Am. Chem. Soc.* **141**, 15211–15221 (2019).
- C. Ni, J. C. Fetting, G. J. Long, M. Brynda, P. P. Power, *Chem. Commun.* (45): 6045–6047 (2008).
- V. K. Sharma, *Coord. Chem. Rev.* **257**, 495–510 (2013).
- J. F. Berry *et al.*, *Science* **312**, 1937–1941 (2006).
- L. Wang, L. Hu, H. Zhang, H. Chen, L. Deng, *J. Am. Chem. Soc.* **137**, 14196–14207 (2015).
- E. R. King, E. T. Hennessy, T. A. Betley, *J. Am. Chem. Soc.* **133**, 4917–4923 (2011).
- D. A. Iovan, T. A. Betley, *J. Am. Chem. Soc.* **138**, 1983–1993 (2016).
- M. J. T. Wilding *et al.*, *J. Am. Chem. Soc.* **139**, 14757–14766 (2017).
- X. Wang, Z. Mo, J. Xiao, L. Deng, *Inorg. Chem.* **52**, 59–65 (2013).
- X. Wang, J. Zhang, L. Wang, L. Deng, *Organometallics* **34**, 2775–2782 (2015).
- Y. Dong *et al.*, *Chem. Sci.* **11**, 1260–1268 (2020).
- E. Kogut, H. L. Wiencko, L. Zhang, D. E. Cordeau, T. H. Warren, *J. Am. Chem. Soc.* **127**, 11248–11249 (2005).
- A. H. Cohen, B. M. Hoffman, *J. Phys. Chem.* **78**, 1313–1321 (1974).

- E. A. C. Lucken, *Nuclear Quadrupole Coupling Constants* (Academic, 1969).
- S. K. Dedushenko, Y. D. Perfiliev, M. G. Goldfeld, A. I. Tsapin, *Hyperfine Int.* **136/137**, 373–377 (2001).
- K. Searles *et al.*, *Angew. Chem. Int. Ed.* **53**, 14139–14143 (2014).
- D. Sorsche *et al.*, *Inorg. Chem.* **57**, 11552–11559 (2018).
- N. Aliaga-Alcalde *et al.*, *Angew. Chem. Int. Ed.* **44**, 2908–2912 (2005).
- R. D. Feltham, P. Brant, *J. Am. Chem. Soc.* **104**, 641–645 (1982).
- P. Brant, R. D. Feltham, *J. Electron. Spectrosc.* **32**, 205–221 (1983).
- J. L. Martinez *et al.*, Data for: Structural and spectroscopic characterization of an Fe(VI) bis(imido) complex, IUScholarWorks (2020); <https://doi.org/10.5967/vty9-rd36>.

ACKNOWLEDGMENTS

We thank the IU Nanoscale Characterization Facility for access to the XPS, M. Warren and J. Wright for assistance with XAS measurements at beamline APS 10-BM-A, B, and Y. Gao for assistance with experiments. **Funding:** Funding from the NSF is gratefully acknowledged by J.L.M., S.A.L., and J.M.S. (CHE-1566258) and B.M.H. (MCB-1515981). This material is based upon work supported by the U.S. Department of Energy (DOE), Office of Science, Office of Basic Energy Sciences under award nos. DE-SC0019466 (to J.M.S.) and DE-SC0019342 (to B.M.H.). The XPS instrument at the IU Nanoscale Characterization Facility was funded by the NSF (DMR MRI-1126394). Support for the acquisition of the Bruker Venture D8 diffractometer through the Major Scientific Research Equipment Fund from the President of Indiana University and the Office of the Vice President for Research is gratefully acknowledged. NSF's ChemMatCARS Sector 15 is supported by the NSF Divisions of Chemistry (CHE) and Materials Research (DMR) under grant no. CHE-1834750. Use of the Advanced Photon Source, an Office of Science User Facility operated for the DOE Office of Science by Argonne National Laboratory, was supported by DOE under contract no. DE-AC02-06CH11357. **Author contributions:** J.L.M. designed and performed the experiments, interpreted the results, and assisted with writing the manuscript. S.A.L. designed and performed the computational investigations and interpreted the results. J.T. and H.Y. collected and interpreted the EPR and ENDOR data. J.X. collected and interpreted the XAS data. V.C. and M.P. collected and refined the x-ray data. Y.L. collected and interpreted the XPS data. J.M.S. and B.M.H. discussed results and wrote the manuscript.

Competing interests: The authors declare no competing interests.

Data and materials availability: All x-ray structural data are available free of charge from the Cambridge Structural Database (CCDC 1990354-1990357). Computationally optimized structures as well as raw Mössbauer and XAS data has been deposited at IU Data CORE and are freely available (34). All other data are presented in the main text or supplementary materials.

SUPPLEMENTARY MATERIALS

science.sciencemag.org/content/370/6514/356/suppl/DC1
Materials and Methods
Figs. S1 to S40
Tables S1 to S18
References (35–68)

12 June 2020; accepted 31 August 2020
10.1126/science.abd3054

STRUCTURAL BIOLOGY

Structural and mechanistic bases for a potent HIV-1 capsid inhibitor

Stephanie M. Bester^{1*}, Guochao Wei^{1*}, Haiyan Zhao^{2*}, Daniel Adu-Ampratwum³, Naseer Iqbal², Valentine V. Courouble⁴, Ashwanth C. Francis⁵, Arun S. Annamalai¹, Parmit K. Singh^{6,7}, Nikoloz Shkriabai¹, Peter Van Blerkom², James Morrison¹, Eric M. Poeschla¹, Alan N. Engelman^{6,7}, Gregory B. Melikyan⁵, Patrick R. Griffin⁴, James R. Fuchs³, Francisco J. Asturias^{2,†}, Mamuka Kvaratskhelia^{1,†}

The potent HIV-1 capsid inhibitor GS-6207 is an investigational principal component of long-acting antiretroviral therapy. We found that GS-6207 inhibits HIV-1 by stabilizing and thereby preventing functional disassembly of the capsid shell in infected cells. X-ray crystallography, cryo-electron microscopy, and hydrogen-deuterium exchange experiments revealed that GS-6207 tightly binds two adjoining capsid subunits and promotes distal intra- and inter-hexamer interactions that stabilize the curved capsid lattice. In addition, GS-6207 interferes with capsid binding to the cellular HIV-1 cofactors Nup153 and CPSF6 that mediate viral nuclear import and direct integration into gene-rich regions of chromatin. These findings elucidate structural insights into the multimodal, potent antiviral activity of GS-6207 and provide a means for rationally developing second-generation therapies.

Long-acting antiretroviral therapy would substantially improve the care of people living with HIV and would mitigate a number of challenges including the necessity of daily administration of current HIV medications, suboptimal treatment adherence, and emergence of drug resistance. GS-6207 (Lenacapavir, Gilead Sciences) is the first-in-class long-acting ultrapotent HIV capsid (CA) inhibitor. Recently completed phase 1 clinical trials (NCT03739866) have suggested that a 6-month dosing interval may be possible. On the basis of these results, GS-6207 has advanced into phase 2/3 clinical trials (NCT04143594/NCT04150068). Initial mechanistic studies with GS-CA1, an archetypal predecessor of GS-6207, revealed its multistage mechanism of antiviral action (1). GS-CA1 potentially [half-maximal effective concentration (EC₅₀) = 87 pM] inhibited early steps of HIV-1 replication and also exhibited a second, less potent (EC₅₀ = 240 pM) antiviral activity during virus egress. Molecular modeling studies predicted that both GS-CA1 and GS-6207 bind to the hydrophobic pocket formed by two adjoining CA subunits within the hexamer (2). HIV-1 genotyping, after selection in cell cul-

ture in the presence of the inhibitor, identified a number of CA mutations positioned near the potential inhibitor binding site that conferred substantial resistance to GS-CA1 (1). However, the structural and mechanistic bases for how this class of compounds binds and alters the biological functions of HIV-1 CA remain unclear.

We synthesized GS-6207 (Fig. 1A) and examined its antiviral activities. GS-6207 inhibited HIV-1 replication in peripheral blood mononuclear cells (PBMCs) and various cell lines, with EC₅₀ values in the range of ~12 to 314 pM (Fig. 1B and table S1). PBMCs and MT4 T cells were fully viable in the presence of 50 μM GS-6207 (the highest concentration tested), indicating a selectivity index of >10⁶ (Fig. 1B). GS-6207 exhibited higher potency during early (EC₅₀ ≈ 55 pM) versus late (EC₅₀ ≈ 314 pM) steps of HIV-1 replication (Fig. 1B and table S1). Our subsequent efforts focused on understanding the structural and mechanistic bases for inhibition of incoming HIV-1 by GS-6207.

To dissect HIV-1 post-entry infection steps targeted by GS-6207, we monitored viral DNA intermediates, including total reverse transcripts, two-long terminal repeat (2-LTR) circles (a surrogate for nuclear import), and integrated proviruses (the viral copy DNA incorporated into the host cell DNA) (Fig. 1C). In parallel, we examined the effects of GS-6207 on viral DNA levels in the cytoplasm and nuclei of infected cells (fig. S1). In control experiments, the reverse transcriptase inhibitor azidothymidine (AZT) impaired viral DNA synthesis, whereas the integrase (IN) inhibitor dolutegravir (DTG) specifically blocked integration, as evidenced by marked reduction of proviral DNA and increased levels of 2-LTR circles. In contrast, GS-6207 affected multiple sequential steps of virus ingress in a dose-dependent

manner. At a comparatively high concentration (50 nM), GS-6207 effectively inhibited reverse transcription. At the pharmacologically relevant concentration of 5 nM (3), the inhibitor partly impaired viral DNA synthesis and effectively blocked formation of 2-LTR circles and integrated HIV-1 DNA. In line with these results (Fig. 1C), 5 nM GS-6207 markedly reduced viral DNA levels in both the cytoplasm and nucleus (fig. S1). At 0.5 nM, GS-6207 inhibited integration without detectably affecting reverse transcription. Although 0.5 nM GS-6207 and 1 μM DTG similarly inhibited integration, the former failed to increase 2-LTR circle formation, likely as a result of concomitant inhibition of nuclear import (Fig. 1C). Results of cellular fractionation indeed support this interpretation of the population-specific polymerase chain reaction assays (fig. S1). Relative to the dimethyl sulfoxide (DMSO) control, 0.5 nM GS-6207 increased and decreased viral DNA levels in the cytoplasm and nucleus, respectively (fig. S1). The multistep inhibition, which depends on the concentration of GS-6207, is likely due to the inhibitor affecting the multifaceted roles of CA during virus ingress (4).

We considered the following two scenarios to account for the observed inhibitions of viral DNA replication intermediates: (i) GS-6207 could adversely affect functional disassembly of the CA shell through stabilizing or destabilizing its architecture, which in turn would adversely affect reverse transcription, nuclear import, and integration; (ii) GS-6207 could interfere with CA interactions with cognate cellular cofactors needed for nuclear import, and/or could interfere with trafficking of pre-integration complexes inside the nucleus to preferred sites of integration.

To examine these possibilities, we imaged the effects of GS-6207 on incoming HIV-1 by using single-particle detection of virus cores colabeled with CypA-DsRed (a marker for CA) and INmNG (IN fused to NeonGreen protein) (fig. S2) (5). GS-6207 substantially increased levels of virus cores in the cytoplasm, which suggested a stabilizing effect of the inhibitor (Fig. 1D). Conversely, GS-6207 inhibited the formation of IN puncta in the nucleus with concomitant inhibition of HIV-1 infection (Fig. 1, E and F, and fig. S3). These findings indicate that GS-6207 stabilizes virus cores, leading to their accumulation in the cytoplasm and preventing nuclear import.

To explore the stabilizing role of the inhibitor on the CA shell, we conducted *in vitro* assays with isolated HIV-1 particles (6). In the absence of inhibitor, virus cores fully dissociated within 30 min, whereas picomolar concentrations of GS-6207 markedly enhanced the stability of native cores (Fig. 1G and fig. S4). Next, we tested the effects of GS-6207 on tubular assemblies made in the presence of 2 M NaCl (7) (Fig. 1H). The preassembled tubes

¹Division of Infectious Diseases, Anschutz Medical Campus, University of Colorado School of Medicine, Aurora, CO 80045, USA. ²Department of Biochemistry and Molecular Genetics, Anschutz Medical Campus, University of Colorado School of Medicine, Aurora, CO 80045, USA. ³Division of Medicinal Chemistry and Pharmacognosy, College of Pharmacy, The Ohio State University, Columbus, OH 43210, USA. ⁴Department of Molecular Medicine, The Scripps Research Institute, Jupiter, FL 33458, USA. ⁵Department of Pediatrics, Infectious Diseases, Emory University, Atlanta, GA 30322, USA. ⁶Department of Cancer Immunology and Virology, Dana-Farber Cancer Institute, Boston, MA 02215, USA. ⁷Department of Medicine, Harvard Medical School, Boston, MA 02115, USA.

*These authors contributed equally to this work.

†Corresponding author. Email: mamuka.kvaratskhelia@cuanschutz.edu (M.K.); francisco.asturias@cuanschutz.edu (F.J.A.)

dissociated immediately upon exposure to a buffer containing 150 mM NaCl (<1 min; Fig. 1H, lane 2). In sharp contrast, addition of GS-6207 to preassembled CA tubes rendered these tubular assemblies highly resistant to low ionic strength (150 mM NaCl) conditions. Strikingly, in the presence of GS-6207, tubular CA assemblies remained stable even after 96 hours of incubation under physiologically relevant conditions (Fig. 1H). The stabilizing effects correlated with a GS-6207:CA ratio of ~1:1 (fig. S5).

We tested the effects of the cellular CA binding partner CypA on GS-6207's activities. As expected (8, 9), the addition of increasing concentrations of CypA resulted in effective disassembly of the preformed CA tubes in the absence of the inhibitor (fig. S6). In sharp contrast, GS-6207-stabilized CA tubes remained intact in the presence of CypA (fig. S6). Furthermore, GS-6207's antiviral activities remained unaffected by depletion or overexpression of CypA in Jurkat and MT4 T cells (fig. S7).

Next, we examined whether GS-6207 affects CA interactions with the known cellular cofactors Nup153 and CPSF6 needed for nuclear import (10, 11). GS-6207 substantially reduced binding of cellular Nup153 and CPSF6 to preassembled CA tubes (fig. S8). Because CPSF6 is also known to regulate integration site selectivity (12, 13), we tested whether GS-6207 influences sites of HIV-1 integration. The inhibitor substantially reduced integration in gene-dense regions and, conversely, enhanced integration in lamina-associated domains (fig. S9). These GS-6207-mediated effects on integration targeting mimicked the CPSF6 depletion phenotype. However, the extent of inhibitor-induced changes was less than those seen with CPSF6 knockout, which suggests that GS-6207 may not fully displace the cellular cofactor. Taken together, our mechanistic studies reveal stabilizing effects of GS-6207 on viral cores, coupled with the ability of the inhibitor to interfere with CA binding to the cognate cellular cofactors CPSF6 and Nup153.

To understand the structural basis for GS-6207 interaction with CA, we solved a cocrystal structure of the inhibitor bound to a prestabilized CA_{A14C/E45C/W184A/M185A} hexamer (14) (Fig. 2 and table S2). The high-resolution structure (2.22 Å) revealed that GS-6207 binds in the hydrophobic pocket formed by two adjacent CA subunits (Fig. 2A and fig. S10) with a stoichiometry of six GS-6207 compounds bound per each CA_{A14C/E45C/W184A/M185A} hexamer. GS-6207 makes extensive van der Waals and hydrogen-bonding interactions with CA1-NTD (the N-terminal domain of CA subunit 1), CA2-CTD (the C-terminal domain of CA subunit 2), and CA2-NTD. Two ring systems, R3 and R4, primarily drive the van der Waals interactions with CA1-NTD and CA2-CTD (fig. S10). R1 and R2 also provide additional interactions with

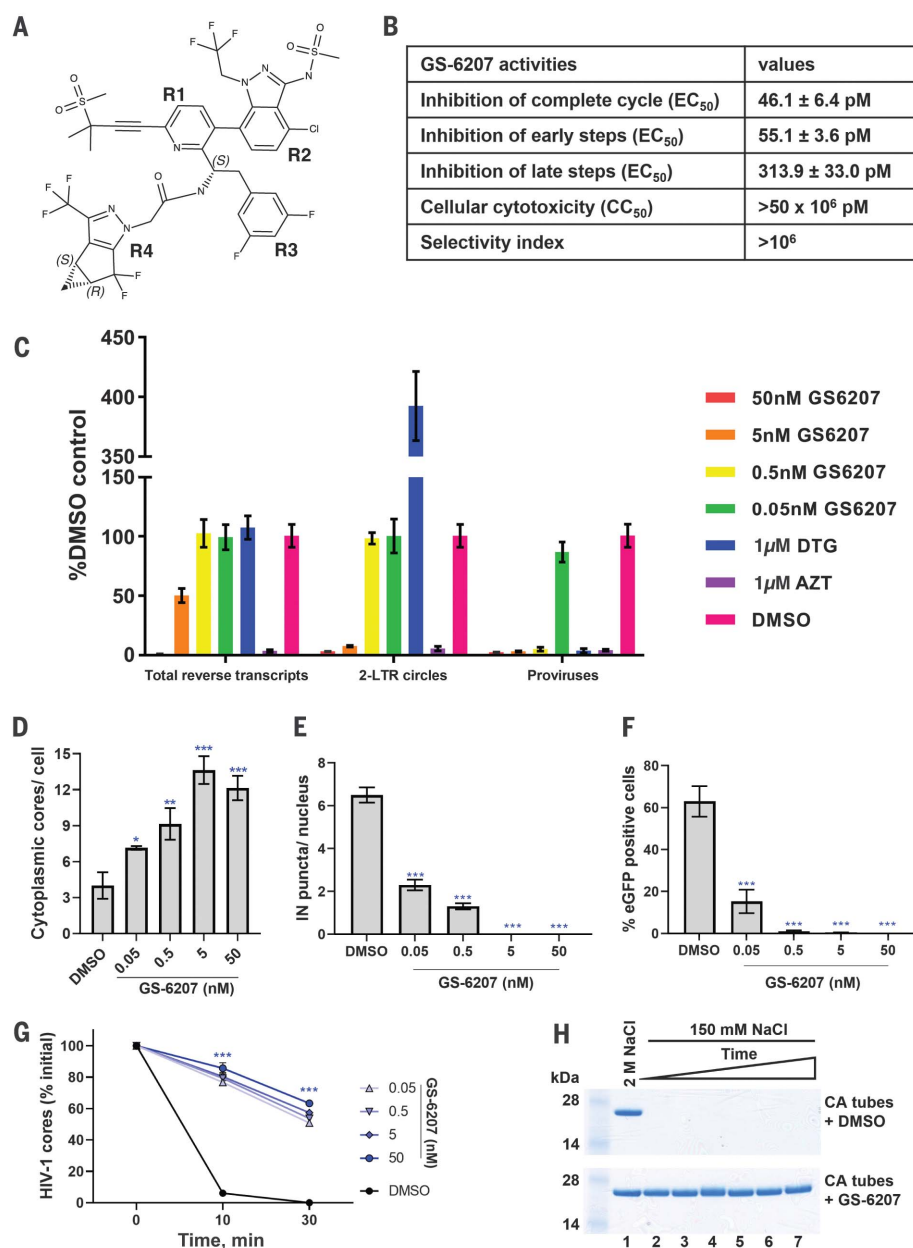


Fig. 1. Multimodal mechanism of action of GS-6207. (A) Chemical structure of GS-6207. (B) Antiviral activities and cytotoxicity of GS-6207 (see also table S1). (C) Effects of GS-6207 on formation of total reverse transcripts, 2-LTR circles, and proviruses. Error bars indicate SD for three independent experiments. (D) Effect of GS-6207 on the number of post-fusion HIV-1 cores in the cytoplasm (see also fig. S2). (E) Inhibition of nuclear import of HIV-1 (see fig. S3A). (F) Effect of GS-6207 on HIV-1 infectivity (see fig. S3B). eGFP, enhanced green fluorescent protein. (G) GS-6207 increases the stability of isolated HIV-1 cores in vitro (see fig. S4). Error bars in (D) to (G) represent SEM from four fields of view for a representative experiment of two independent experiments (**P* < 0.05, ***P* < 0.005, ****P* < 0.0001). (H) Effects of GS-6207 on the stability of recombinant CA tubes. Only pelleted fractions of CA from each reaction are shown. CA tubes were assembled in 2 M NaCl in the absence (top) or presence of GS-6207 (bottom) and then either directly pelleted (lane 1) or exposed to low ionic strength (150 mM NaCl) buffer for increasing periods of time (0, 1, 4, 24, 48, and 96 hours; lanes 2 to 7) and then pelleted.

CA1-NTD and CA2-NTD. GS-6207 establishes a hydrogen-bonding network with the side chains of Asn⁵⁷, Lys⁷⁰, and Asn⁷⁴ of CA1-NTD, Ser⁴¹ of CA2-NTD, and Gln¹⁷⁹ and Asn¹⁸³ of CA2-CTD (Fig. 2B, fig. S10, and table S3).

The interacting helices that predominantly form the GS-6207 binding pocket include αH3 and αH4 from CA1-NTD, αH8 and αH9 from CA2-CTD, and αH2* from CA2-NTD (Fig. 2C). Particularly noteworthy is that GS-6207 strongly

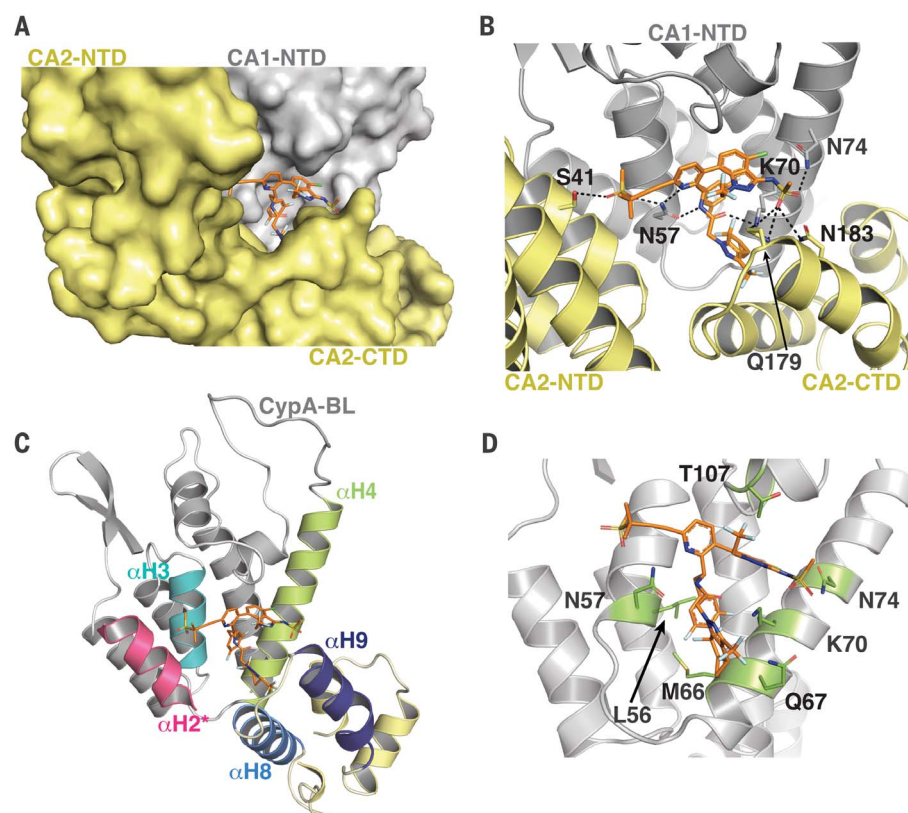


Fig. 2. Structural basis for GS-6207 interaction with CA hexamer. (A) X-ray crystal structure of GS-6207 (orange) bound to the prestabilized CA_{A14C/E45C/W184A/M185A} hexamer (PDB ID 6VKV). GS-6207 binds at the pocket formed by two adjoining CA subunits CA1 (light gray) and CA2 (pale yellow). Relative positions of CA1-NTD, CA2-NTD, and CA2-CTD are indicated. (B) Cartoon representation of the structure indicating GS-6207's interactions with the two subunits that form the binding pocket, CA1 and CA2. Hydrogen bonds are denoted by black dashed lines. (C) The main helices (α H2*, α H3, α H4, α H8, and α H9) that interact with GS-6207 are indicated. (D) Reported resistance mutations (green) for GS-CA1 (1) are shown in the context of GS-6207 bound to CA1-NTD.

influences the conformation and relative positioning of α H9 of CA2-CTD with respect to α H4 of CA1-NTD. For comparison, α H9 is seen to exhibit substantial conformational variation in the absence or presence of different cellular protein partners bound to CA_{A14C/E45C/W184A/M185A} or native CA hexamers (figs. S11 to S20).

Previously reported resistant mutations to predecessor compound GS-CA1 are within close proximity of the GS-6207 binding site (Fig. 2D). Met⁶⁶ is a key constituent of the hydrophobic pocket and forms strong van der Waals interactions with rings R3 and R4. The M66I substitution had the most profound effects on loss of GS-6207 potency, reducing activity by more than four orders of magnitude (table S4). N57S, Q67H, K70A, and N74D substitutions, which are expected to adversely affect direct interactions of CA with GS-6207, reduced potency by factors of ~60, ~10, ~45, and 14, respectively (table S4). Consistent with a previous report (1), infectivity of the M66I mutant virus, which conferred the greatest extent of GS-6207 resistance, was markedly com-

promised (fig. S21). The infectivity of N57S and K70A mutant viruses, which exhibited substantial resistance to the inhibitor, was severely and considerably reduced, respectively. Q67H and N74D, which exhibited lower levels of resistance, displayed wild-type HIV-1 infectivity (fig. S21).

Structural comparison of GS-6207 with the substantially less potent HIV-1 CA inhibitor PF74 (15–17) revealed both similarities and marked differences (fig. S22 and table S3). The resemblance between the two compounds is seen with respect to their interactions with CA1-NTD. The phenyl R1 and R2 rings and indole R3 ring of PF74 superimpose onto the indazole (R2), difluorobenzyl (R3), and cyclopentapyrazole (R4) rings of GS-6207, respectively. However, unlike PF74, which only makes limited hydrophobic contacts with CA2-CTD, GS-6207 establishes extensive hydrogen-bonding and hydrophobic interactions with adjoining CA2-NTD and CA2-CTD (Fig. 2 and figs. S10 and S22).

We also compared GS-6207 binding to known interactions of CPSF6 and Nup153 with CA

hexamers (15, 18). The backbone of Nup153 aligns along R1 and R3 of GS-6207, with Phe¹⁴¹⁷ of Nup153 closely superimposing on the difluorobenzyl moiety (R3) of GS-6207 (fig. S23). Similarly, there is substantial overlap between GS-6207 and the main chain of CPSF6, with Phe³²¹ of CPSF6 superimposing on R3 extremely well (fig. S24). Interestingly, the binding pockets for Nup153 and CPSF6 are more open, with CTD α H9 being positioned farther away from NTD α H4 than in the presence of GS-6207. In turn, the closer α H4- α H9 conformation imposed by GS-6207 creates steric clashes with Nup153 and CPSF6 (figs. S23 and S24). Collectively, these findings provide structural explanations for the displacement of Nup153 and CPSF6 by GS-6207 (fig. S8).

To understand the structural basis for GS-6207's interactions with curved CA assemblies, we used cryo-EM. GS-6207, but not a DMSO control, stabilized preformed tubes and resulted in well-defined tubular CA assemblies at physiological salt concentration (Fig. 3A and figs. S25 and S26). Imaging these structures allowed us to obtain a 6.3 Å map for GS-6207 bound to A92E CA tubes (Fig. 3B, figs. S27 and S28, and table S5); GS-6207 interacted similarly with wild-type and A92E CA tubes (fig. S25), and the latter protein was successfully used for prior cryo-EM studies (8, 19). A hexamer with pseudo-two-fold symmetry characteristic of CA tubes was readily identified (Fig. 3, C and D) and was further refined by analyzing helical tube patches with RASTR, a single-particle approach independent of helical parameter determination (fig. S29) (20). The mutually independent helical and RASTR approaches produced equivalent maps of a tube hexamer (fig. S30), further validating the map's accuracy (figs. S31 to S33). Rigid-body docking of individual crystallographic CA monomers in the presence of GS-6207 could account for all features in the cryo-EM hexamer, including the positions of well-defined α helices in the CTD (Fig. 3D and figs. S30 and S34). Density corresponding to bound GS-6207 could be identified by segmentation of the helical or RASTR cryo-EM maps (fig. S35). Thus, we were able to obtain a model of the GS-6207-bound tube hexamers under physiologically relevant conditions.

Comparisons of our cryo-EM structure with published cryo-EM- and cryo-electron tomography-derived structures of CA hexamers from tubes and native HIV-1 particles (19, 21) reveal the principal differences in formation of curved hexameric lattices in the absence and presence of GS-6207 (figs. S36 to S41). Normally, CA CTDs move away from the adjacent NTDs to accommodate inter-hexamer contacts in the context of a curved topology (19, 21). In sharp contrast, GS-6207 strongly restricts changes in the

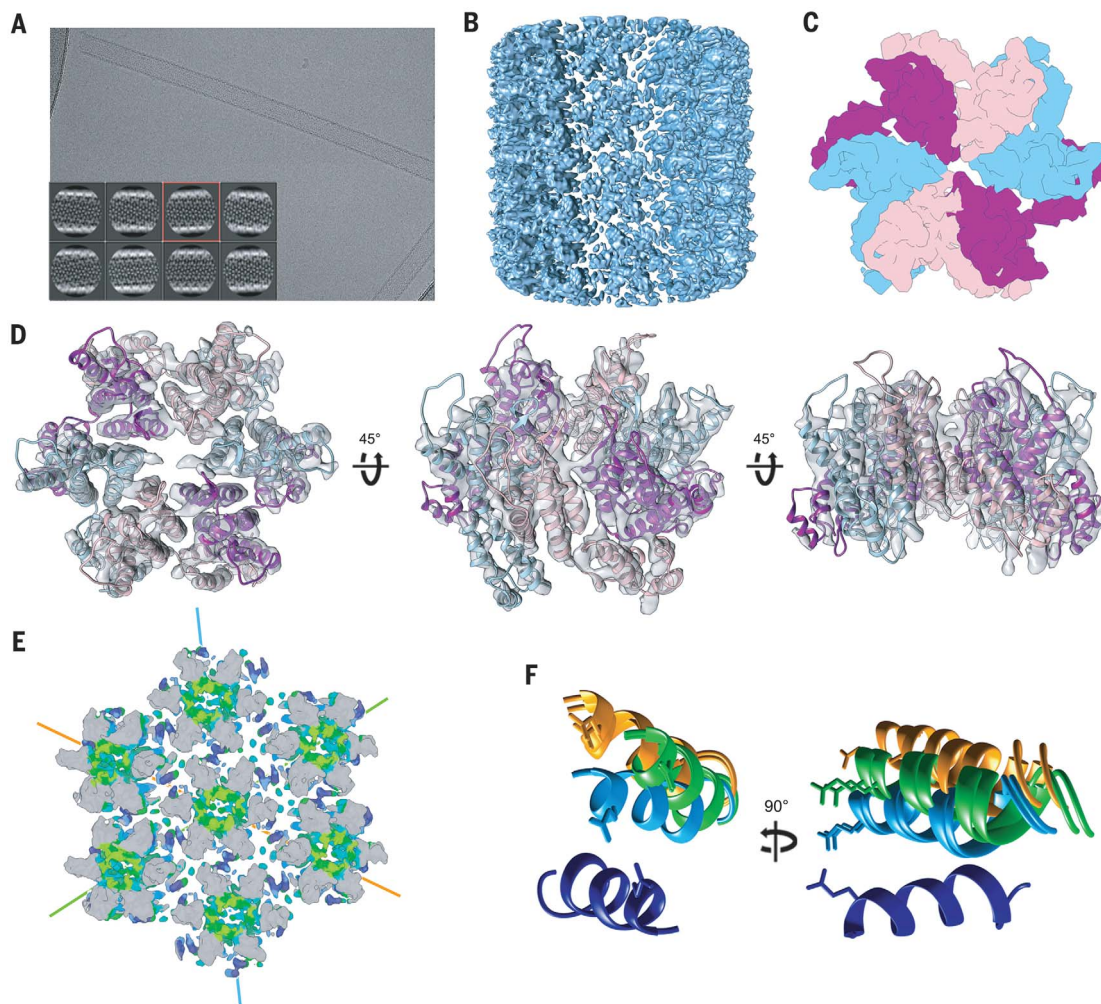
Fig. 3. Cryo-EM structure of GS-6207-stabilized CA tubes.

(A) Cryo-EM image of A92E CA tubes stabilized by GS-6207 in 150 mM NaCl. Inset shows a subset of the averages obtained by 2D clustering of tube segments.

(B) Cryo-EM map at 6.3 Å resolution from helical processing of GS-6207-stabilized A92E CA tubes.

(C) Diagram showing the pseudo-two-fold symmetric arrangement of monomers in a tube hexamer. **(D)** Atomic model of a hexamer in the GS-6207-stabilized CA tube generated by rigid-body fitting of six copies of the x-ray structure of a GS-6207-bound CA monomer into the RASTR map. **(E)** A portion of a tube showing interactions between seven hexamers. Coloring corresponds to HDX protection levels. The cyan, green, and orange lines indicate three helical directions.

(F) Close up of α H9- α H9 interactions involving a central hexamer. All six H9 helices in the central hexamer (dark blue) were superimposed. α H9 helices in neighboring hexamers are shown in cyan, green, and orange, matching the coloring of helical directions in (E). The absence of true two-fold symmetry results in slight differences in the positioning of the two helices along a specific helical direction. The visible side chain is Glu¹⁸⁰.



CTD position with respect to the adjoining NTD, and requirements for establishing inter-hexamer interactions on a curved surface are satisfied by repositioning of the comparatively rigid GS-6207-bound CA monomers in each hexamer (see movies S1 to S4; also compare movie S5 with movies S7 and S9, and movie S6 with movies S8 and S10). Accordingly, NTD α H4 and CTD α H9 from adjacent subunits are farther apart and closer together in the absence and presence of the inhibitor, respectively (figs. S37 and S39).

To further understand how GS-6207 affects tubular CA assemblies, we used hydrogen-deuterium exchange (HDX) (figs. S42 to S46). HDX experiments revealed strong protection in CA segments that directly interact with the inhibitor (figs. S47 and S48). Unexpectedly, we observed strong protection beyond the direct inhibitor binding sites. The NTDs that form the inner hexamer core and provide the binding site for IP6 [a natural cellular cofactor of

CA that also stabilizes virus cores (22)] showed strong protection (figs. S47 and S49) despite a lack of direct contacts with GS-6207. These findings suggest that GS-6207 stabilizes individual CA hexamers. This notion is further supported by thermal shift assays, which show that GS-6207 substantially increases the melting temperature of isolated CA hexamers (fig. S50). Collectively these biochemical findings are consistent with our cocrystal structure (Fig. 2), which shows that each GS-6207 connects two adjoining monomers in a hexamer, with the binding of six inhibitors resulting in a more stable hexamer.

Strikingly, the strongest GS-6207-induced protections were seen in α H9 (figs. S47 and S51), which suggests that the inhibitor stabilizes inter-hexamer α H9- α H9 contacts essential for curved lattice formation (Fig. 3, E and F) (19, 21). The E45A and E180A CA substitutions, which influence intra- and inter-hexamer interfaces, respectively (23–25), but do not di-

rectly interact with GS-6207 (fig. S47), conferred partial resistance to the inhibitor (fig. S52).

Pliability of intra- and inter-hexamer interactions is essential for both proper assembly of the CA shell during virion maturation and its subsequent disassembly during virus ingress (8, 23). GS-6207 disrupts this delicately balanced interplay by rigidifying the CTD conformation and stabilizing both intra-hexamer and α H9- α H9 inter-hexamer interactions (Figs. 2 and 3 and fig. S47). These findings provide structural clues as to how GS-6207 inhibits functional disassembly of virus cores and blocks incoming HIV-1 in infected cells (Fig. 1). Taken together, our results elucidate the structural and mechanistic bases for the multimodal, potent antiviral activity of GS-6207 and provide a platform for rationally developing improved long-acting therapies.

We note that during the revision of the present manuscript, an article describing clinical targeting of HIV CA by GS-6207, which also

includes synthesis of the inhibitor and a crystal structure of GS-6207 bound to CA hexamer (fig. S53), was published (26).

REFERENCES AND NOTES

1. S. R. Yant *et al.*, *Nat. Med.* **25**, 1377–1384 (2019).
2. K. Singh *et al.*, *Front. Microbiol.* **10**, 1227 (2019).
3. E. Daar *et al.*, paper presented at the Conference on Retroviruses and Opportunistic Infections, Boston, 8 to 11 March 2020; www.croiconference.org/abstract/dose-response-relationship-of-subcutaneous-long-acting-hiv-capsid-inhibitor-gs-6207/.
4. M. Yamashita, A. N. Engelman, *Trends Microbiol.* **25**, 741–755 (2017).
5. A. C. Francis, M. Marin, J. Shi, C. Aiken, G. B. Melikyan, *PLOS Pathog.* **12**, e1005709 (2016).
6. A. C. Francis, G. B. Melikyan, *Cell Host Microbe* **23**, 536–548.e6 (2018).
7. L. S. Ehrlich, B. E. Agresta, C. A. Carter, *J. Virol.* **66**, 4874–4883 (1992).
8. C. Liu *et al.*, *Nat. Commun.* **7**, 10714 (2016).
9. M. Grättinger *et al.*, *Virology* **257**, 247–260 (1999).
10. D. A. Bejarano *et al.*, *eLife* **8**, e41800 (2019).
11. K. A. Matreyek, A. Engelman, *J. Virol.* **85**, 7818–7827 (2011).
12. V. Achuthan *et al.*, *Cell Host Microbe* **24**, 392–404.e8 (2018).
13. G. A. Sowd *et al.*, *Proc. Natl. Acad. Sci. U.S.A.* **113**, E1054–E1063 (2016).
14. O. Pornillos *et al.*, *Cell* **137**, 1282–1292 (2009).
15. A. J. Price *et al.*, *PLOS Pathog.* **10**, e1004459 (2014).
16. A. Bhattacharya *et al.*, *Proc. Natl. Acad. Sci. U.S.A.* **111**, 18625–18630 (2014).
17. A. Saito *et al.*, *J. Virol.* **90**, 5808–5823 (2016).
18. A. J. Price *et al.*, *PLOS Pathog.* **8**, e1002896 (2012).
19. G. Zhao *et al.*, *Nature* **497**, 643–646 (2013).
20. P. S. Randolph, S. M. Stagg, *J. Struct. Biol.* **4**, 100023 (2020).
21. S. Mattei, B. Glass, W. J. Hagen, H. G. Kräusslich, J. A. Briggs, *Science* **354**, 1434–1437 (2016).
22. R. A. Dick *et al.*, *Nature* **560**, 509–512 (2018).
23. M. del Álamo, M. G. Mateu, *J. Mol. Biol.* **345**, 893–906 (2005).
24. J. Shi, J. Zhou, V. B. Shah, C. Aiken, K. Whitby, *J. Virol.* **85**, 542–549 (2011).
25. B. M. Forshey, U. von Schwedler, W. I. Sundquist, C. Aiken, *J. Virol.* **76**, 5667–5677 (2002).
26. J. O. Link *et al.*, *Nature* **584**, 614–618 (2020).

ACKNOWLEDGMENTS

We thank S. Rebersburg, P. Koneru, and other members of the participating laboratories for their help with data analysis and valuable suggestions. All cryo-EM data were collected at the Anschutz Medical Campus Cryo-EM Core Facility. **Funding:** Supported by NIH grants R01 AI062520 and R01 AI143649 (M.K.), R01 AI157802 (M.K., F.J.A., and J.R.F.), U54 AI150472 (M.K., P.R.G., A.C.F., G.B.M., and A.N.E.), R01 AI129862 (G.B.M.), R01 AI052014 (A.N.E.), and R01 AI77344 and DP1 DA043915 (E.M.P.). **Author contributions:** The following authors conducted experiments and interpreted the results: S.M.B. (x-ray crystallography); G.W., A.S.A., and J.M. (virology); N.S. (biochemistry); H.Z., N.I., P.V.B., and F.J.A. (cryo-EM); D.A.-A. and J.R.F. (medicinal chemistry); A.C.F. and G.B.M. (cell imaging); V.V.C. and P.R.G. (HDX); P.K.S. and A.N.E. (integration site sequencing). Separate aspects of the study were designed and supervised by E.M.P., A.N.E., A.C.F.,

G.B.M., P.R.G., J.R.F., F.J.A., and M.K. The entire project was conceived by M.K. with all authors providing intellectual input and contributing to preparation of the manuscript. **Competing interests:** A.N.E. declares fees from ViiV Healthcare Co. for work unrelated to this project. No other authors declare competing interests. **Data and materials availability:** The cocrystal structure and cryo-EM-derived atomic model are deposited in the Protein Data Bank under accession numbers 6VKV and 6VWS, respectively. The EM maps are deposited in the Electron Microscopy Data Bank under accession codes EMD-21423 and EMD-21424. DNA sequences for integration site mapping are deposited in the National Center for Biotechnology Information Sequence Read Archive (NCBI SRA) under accession code PRJNA608802. All other data are available in the manuscript or the supplementary materials. Materials are available from M.K.

SUPPLEMENTARY MATERIALS

science.sciencemag.org/content/370/6514/360/suppl/DC1
Materials and Methods
Figs. S1 to S53
Tables S1 to S5
¹H, ¹³C, and HSQC NMR Spectra of GS-6207 and Synthetic Intermediates
References (27–58)
Movies S1 to S10
MDAR Reproducibility Checklist
[View/request a protocol for this paper from Bio-protocol.](#)

26 February 2020; accepted 25 August 2020
10.1126/science.abb4808

PHYSIOLOGY

Comprehensive quantification of fuel use by the failing and nonfailing human heart

Danielle Murashige^{1*}, Cholsoon Jang^{2*†}, Michael Neinst^{1†}, Jonathan J. Edwards³, Alexis Cowan², Matthew C. Hyman⁴, Joshua D. Rabinowitz², David S. Frankel⁴, Zolt Arany^{1§}

The heart consumes circulating nutrients to fuel lifelong contraction, but a comprehensive mapping of human cardiac fuel use is lacking. We used metabolomics on blood from artery, coronary sinus, and femoral vein in 110 patients with or without heart failure to quantify the uptake and release of 277 metabolites, including all major nutrients, by the human heart and leg. The heart primarily consumed fatty acids and, unexpectedly, little glucose; secreted glutamine and other nitrogen-rich amino acids, indicating active protein breakdown, at a rate ~10 times that of the leg; and released intermediates of the tricarboxylic acid cycle, balancing anaplerosis from amino acid breakdown. Both heart and leg consumed ketones, glutamate, and acetate in direct proportionality to circulating levels, indicating that availability is a key driver for consumption of these substrates. The failing heart consumed more ketones and lactate and had higher rates of proteolysis. These data provide a comprehensive and quantitative picture of human cardiac fuel use.

The heart generates copious adenosine 5'-triphosphate (ATP), almost all through oxidative phosphorylation in mitochondria (1). A continuous supply of oxygen and nutrients is thus vitally needed. Heart failure is a leading cause of death worldwide, and the failing heart is often described as an “engine out of fuel” that fails to use circulating nutrients to satisfy its metabolic demands (2). Understanding how the heart handles fuels during health and disease is thus foundational to the rational development of new heart failure therapies.

We measured arteriovenous (A-V) gradients of circulating metabolites across the human heart and leg by simultaneously sampling blood from radial artery, coronary sinus, and femoral vein (Fig. 1A). We enrolled 87 patients who were undergoing elective percutaneous catheter ablation of atrial fibrillation, had a left ventricular ejection fraction (LVEF) >50%, and had no history of heart failure (fig. S1A). Patient characteristics were representative of the US middle-aged population (table S1). A total of 600 known metabolites were measured using liquid chromatography–mass spectrometry, 277 of which were reliably detected in the plasma. By comparing the abundance of

these metabolites in the artery (C_A) versus vein (C_{CS} or C_{FV} for coronary sinus and femoral vein, respectively) (Fig. 1A), we identified statistically significant uptake or release of 117 metabolites across the leg and 65 across the heart (Fig. 1B and fig. S1B). Our C_{FV}/C_A data confirmed all 10 previously reported metabolites taken up or released by the human arm without anesthesia (3). We further identified an additional 107 metabolites that were significantly altered across the human leg (table S2).

Table S3 lists cardiac- and leg-specific uptake and release of abundant, high-turnover fuels. Both organs efficiently extracted ketones, acetate, and glutamate (up to ~67%). Although the leg took up glucose, there was no net average glucose uptake by the heart, unlike prior reports (4, 5), and cardiac glucose uptake did not correlate with plasma insulin or insulin resistance (fig. S2), perhaps reflecting the fasted state of patients. The heart consumed all free fatty acid (FFA) species, whereas the leg primarily took up saturated FFAs and released unsaturated FFAs, likely from subcutaneous adipose depots (table S4 and fig. S3). The heart secreted most essential amino acids, indicating active proteolysis (table S3).

To quantify the net contribution of each metabolite to carbon balance, we measured absolute arterial concentrations of the most abundant metabolites (tables S5 to S7) and used publicly reported concentrations for the remaining ones (6). From the concentrations and molecular formula of each metabolite, we calculated the absolute carbon uptake or excretion of each metabolite, measured as micromoles per liter of blood passing through the heart or leg (Fig. 1, D and E). The leg obtained ~90% of carbons as glucose and ketone bodies, whereas it released most carbons as FFAs, lactate, and amino acids (Fig. 1D). About half of the released FFA was linoleate

(C18:2), an abundant essential FFA, indicative of active lipolysis from adipose depots. Many released amino acids were also essential, reflecting muscle proteolysis. The total release of carbons was 15% higher than uptake, indicating a net loss of leg mass during fasting.

In contrast to the leg, the heart obtained most carbons from FFAs (Fig. 1E), accounting for >70% of carbons (1750 μ M) extracted from the circulation [\sim 99 μ M FFA, similar to that previously measured by 13 C-palmitate and positron emission tomography (7) equivalent to \sim 1.4 μ mol/min/g of FFA-derived carbons (8)]. This rate may be underestimated because FFAs can also accumulate in venous plasma when liberated from lipoprotein particles (9). Only a negligible portion of FA carbons were converted to acylcarnitines and secreted (< 0.25 μ M carbons, ~0.01%), indicating nearly complete oxidation of FFAs. Ketones accounted for ~15% of myocardial carbon uptake (Fig. 1E). Acetate, the most abundant short-chain FA produced by gut microbiota (10), accounted for ~2% of myocardial carbon uptake and was avidly taken up by the heart (Fig. 1E and table S3). Acetate may be used as fuel and as an epigenetic modifier through histone acetylation (11, 12).

The heart secreted most amino acids (Fig. 1E and table S3), contributing to a large net negative nitrogen balance of 108 μ M ($P < 0.0001$) (fig. S4) and indicating active proteolysis. Glutamine and alanine were the most abundant amino acids secreted. Glutamine release was nearly equimolar to glutamate uptake, suggesting active exchange of glutamate for glutamine for nitrogen removal. Lactate uptake likely supports nitrogen release as alanine through pyruvate transamination (13). Amino acids with greater nitrogen content (i.e., the ratio of nitrogen to carbon atoms) were strongly excreted (fig. S5A), further supporting the notion that the heart actively releases nitrogen as amino acids (14–16). We calculated a net cardiac proteolysis rate of 81 μ M amino acid equivalents (AA-Eqs) (Fig. 2A; see the materials and methods for details of calculations), i.e., 0.06 μ mol of AA-Eqs/min/g cardiac tissue. By comparison, the rate of proteolysis in the leg was 0.006 μ mol of AA-Eqs/min/g. Cardiac proteolysis thus occurs at \sim 10 \times the rate in the leg, equivalent to \sim 1.5 g of protein over 12 hours, or just over 2% of that of cardiac protein (17, 18). Human cardiac protein is thus actively consumed and produced across fasting-feeding cycles.

Suppression of branched chain amino acid (BCAA) catabolism is implicated in maladaptive remodeling in heart failure (19–21). We calculate that BCAAs contribute 105 μ M carbon equivalents to overall carbon use, or just under 5% of total carbon combustion, similar to that measured in mice (22). Further reduction of BCAA

¹Perelman School of Medicine, Cardiovascular Institute, University of Pennsylvania, Philadelphia, PA 19104, USA.

²Department of Chemistry and Lewis-Sigler Institute for Integrative Genomics, Princeton University, Princeton, NJ 08544, USA. ³Department of Pediatrics, Division of Pediatric Cardiology, Children's Hospital of Philadelphia, Philadelphia, PA 19104, USA. ⁴Division of Cardiovascular Medicine, Perelman School of Medicine at the University of Pennsylvania, Philadelphia, PA 19104, USA.

*These authors contributed equally to this work.

[†]Present address: Department of Biological Chemistry, University of California Irvine, Irvine, CA 92697, USA.

[‡]Present address: Department of Chemistry and Lewis-Sigler Institute for Integrative Genomics, Princeton University, Princeton, NJ 08544, USA.

[§]Corresponding author. Email: zarany@penmedicine.upenn.edu

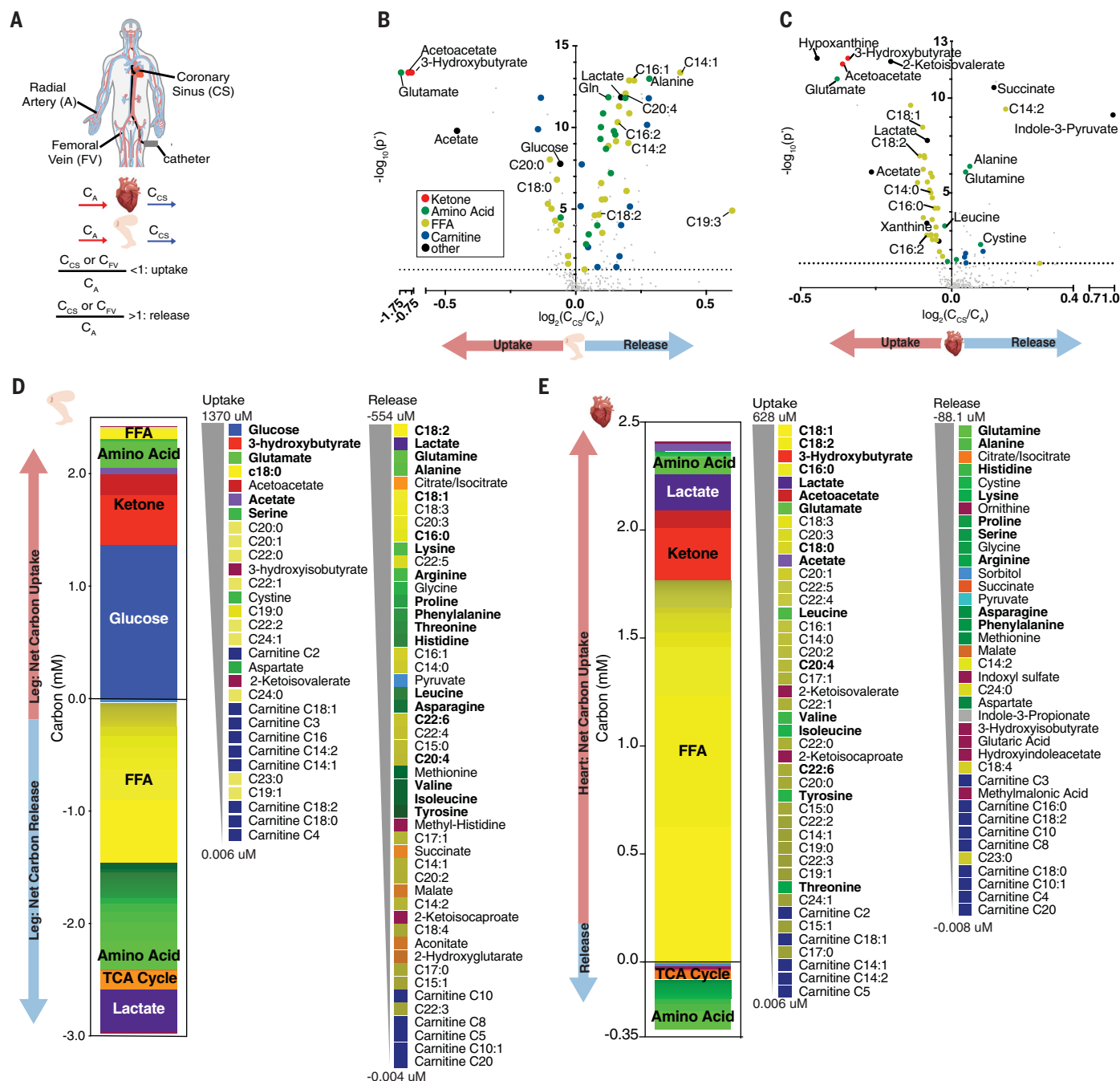


Fig. 1. Human A-V metabolomics reveal distinct fuel profiles of the heart and leg. (A) Blood was sampled simultaneously from the radial artery (A), coronary sinus (CS), and femoral vein (FV), and metabolite uptake or release was determined. (B and C) Volcano plot of metabolite abundance in the FV (B) or CS (C) relative to (A). *P* values were derived from one-sample Wilcoxon test and then Benjamini-Hochberg corrected (*P**). Dotted line indicates *P** = 0.05. (D and E) Net A-V carbon balance across the leg (D) and heart (E) shown in order of greatest to least average absolute carbon uptake or release.

catabolism in the failing heart would thus have only a small effect on overall accessible carbons for combustion, suggesting that BCAAs affect heart failure through other mechanisms. Histidine was the most highly secreted essential amino acid (Fig. 2A and figs. S5A and S5B), suggesting that the proteins being degraded were histidine rich. Myoglobin constitutes 5 to 10% of cytosolic cardiac protein, is dispensable for baseline cardiac function (23), and is

composed of 6% histidine, in contrast to most proteins, which contain only 1 to 2% histidine (24). Therefore, in addition to carrying oxygen, myoglobin may also serve as a reservoir of carbons. Other cardiac proteins may also contribute, as could sources exogenous to the heart, e.g., through macropinocytosis of albumin or other plasma proteins (25).

Paradoxically, despite high reliance on the tricarboxylic acid (TCA) cycle for ATP gener-

ation, the heart and leg release TCA cycle intermediates (Fig. 1, B to E). Tissues may export citrate, an allosteric inhibitor of FA oxidation and glycolysis (26), to prevent excessive suppression of these pathways. TCA intermediate secretion may also represent a means of clearing excess TCA cycle four-carbon units produced by amino acid breakdown. We calculated 140 μM (0.1 $\mu\text{mol}/\text{min}/\text{g}$) anaplerotic carbon flux from amino acid breakdown (Fig. 2B), well in excess

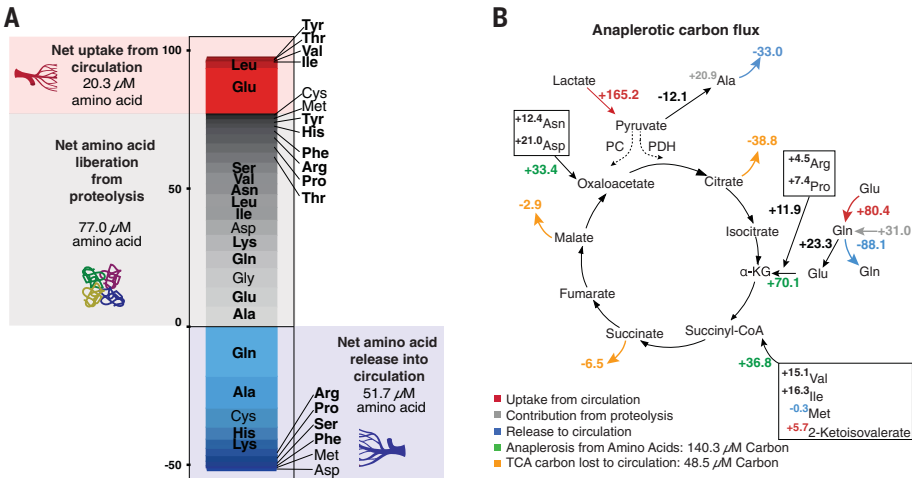


Fig. 2. Cardiac nitrogen release reveals net amino acid liberation from proteolysis. (A) Calculated cardiac sources of free amino acids (uptake from circulation is shown in red, liberation from proteolysis in gray) and released amino acids (shown in blue). Shading is proportional to the quantity of amino acid uptake or secretion. (B) Calculated anaplerotic carbon input from amino acid consumption exceeds carbon released as TCA cycle intermediates. Anaplerotic contribution from lactate through pyruvate carboxylase (PC) could not be determined (dashed lines). All numbers are micromoles of carbon. Non-anaplerotic amino acids (leucine) and amino acids not catabolized in heart (histidine, phenylalanine, and tyrosine) were excluded. PDH, pyruvate dehydrogenase.

of the $\sim 50 \mu\text{M}$ ($0.04 \mu\text{mol/min/g}$) loss of TCA intermediates to the circulation. This is a likely underestimate of total anaplerosis because we could not quantify the contribution from pyruvate carboxylase (27, 28). This suggests active internal catabolism of TCA four-carbon units, e.g., through malic enzyme.

Calculating the contribution of all metabolites to cardiac oxygen consumption and ATP production (Fig. 3, A and B) implied a cardiac requirement of 3.0 mM plasma oxygen, equivalent to 2.0 mM in whole blood after correction for plasma-to-blood volume. Measured oxygen consumption was 3.5 mM ($\sim 9.5 \text{ ml O}_2/\text{g/min}$). Thus, $\sim 60\%$ of measured oxygen consumption was accounted for by the measured metabolite A-V gradients (Fig. 3A). This is an underestimate because it does not account for FAs liberated from lipoproteins (29). Thus, the remaining $\sim 40\%$ oxygen consumption likely reflects a combination of lipoprotein-derived FAs (LpFAs) that are combusted by the heart and those that replace albumin-derived FFAs combusted by the heart. Consistent with this, unaccounted oxygen consumption correlated inversely with measured FA uptake (fig. S6, B and C). Other minor sources may include internal fuels such

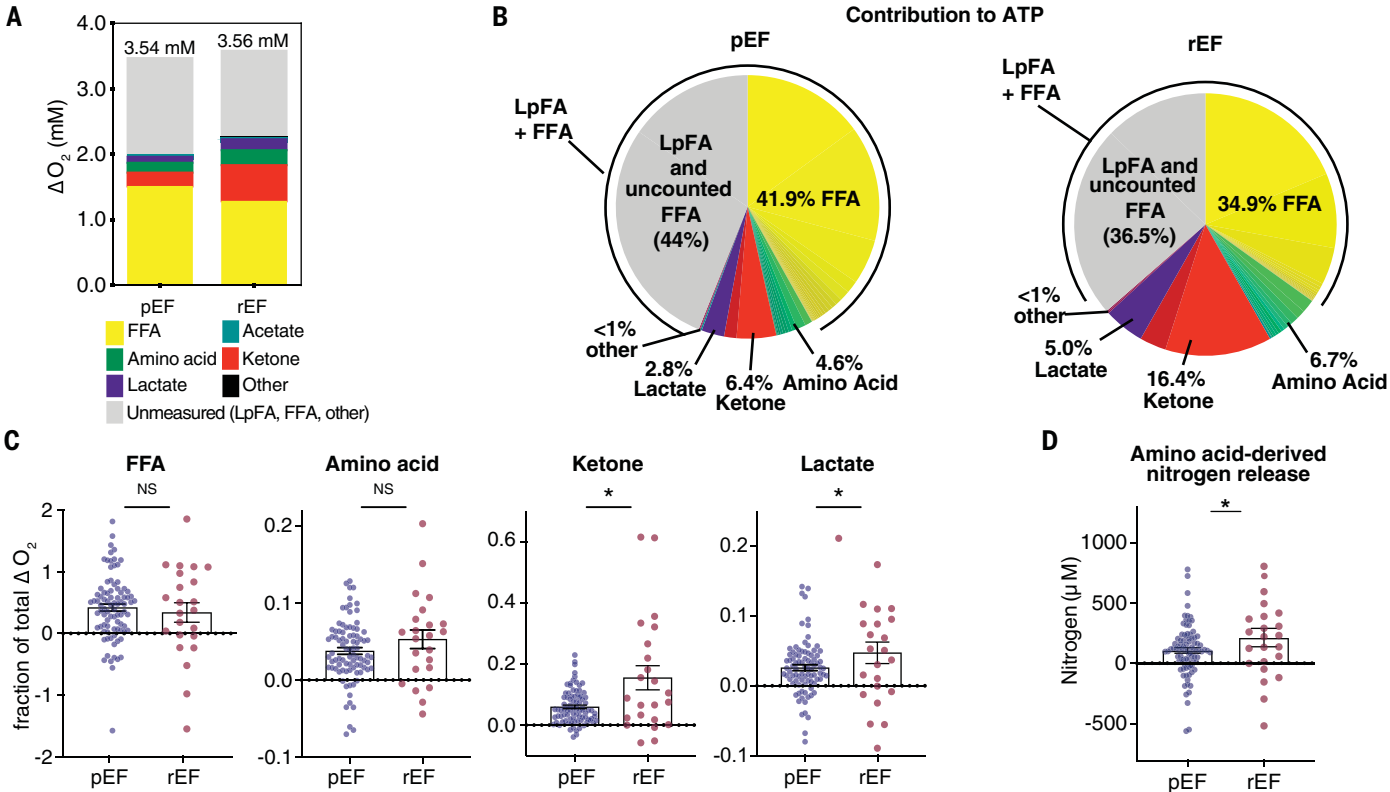


Fig. 3. Comparison of myocardial substrate use in patients with preserved versus reduced ejection fraction. (A) Calculated substrate-specific contribution to total cardiac oxygen consumption. Average measured myocardial O_2 consumption (ΔO_2) is indicated above each bar. (B) Substrate-specific contribution to cardiac ATP generation in patients with preserved ejection fraction (pEF) versus reduced ejection fraction (rEF). (C) Proportion of total ΔO_2 accounted for by the catabolism of each indicated substrate class in pEF versus rEF. (D) Net amino acid-derived nitrogen release in patients with pEF versus rEF. * $P < 0.05$ by t test.

as triglycerides (30), FFAs liberated from epicardial adipose tissue, or oxygen consumption that does not generate ATP (e.g., conversion of hypoxanthine to uric acid by xanthine oxidase) (table S7) (31). Combustion of glycogen is not thought to occur in the heart during fasting (32–34). Assuming that ~35% of LpFAs are released into the coronary sinus, we calculated that ~57% of cardiac ATP production derives from FFAs, 6.4% from ketones, 4.6% from amino acids, 2.8% from lactate, and ~28% from LpFAs (for a total of ~85% from FFAs) (Fig. 3B and table S8).

We evaluated in a similar fashion 23 patients diagnosed with cardiomyopathy with an LVEF <40. Other than reduced LVEF, the cohort was similar to that with preserved LVEF (table S1). Patients with reduced LVEF had nearly tripled consumption of ketones (16.4 versus 6.4%), doubled lactate consumption (5.0 versus 2.8%), and a doubled rate of net amino acid–derived nitrogen release (212 versus 106 μM), i.e., rate of proteolysis

(Fig. 3, B to D, and tables S5 to S8). Overall use of FFAs was suppressed. Increased plasma long-chain acylcarnitines have been associated with heart failure (35, 36), but tissue acylcarnitine amounts are decreased in failing hearts (37). We detected no increase in secretion of acylcarnitine by the failing heart (table S9), indicating that (i) any putative defect in FA consumption in heart failure occurred upstream of acylcarnitine production and (ii) a tissue other than the heart increases systemic acylcarnitine production.

To gain insight into factors affecting fuel choice, we looked for correlations between metabolite concentrations and their use as fuel (Fig. 4A), between fractional extraction of different metabolites (fig. S8, A and B), and between fractional extraction and clinical or demographic parameters (fig. S9). Uptake of acetate, 3-hydroxybutyrate, and glutamate (but not that of glucose, lactate, or FFA) was directly proportional to circulating concentrations in both heart and leg (Fig. 4, A to C, and fig. S10C),

suggesting that consumption of these three fuels is driven by substrate availability without the need for overt regulation. Moreover, their fractional uptake correlated strongly with each other (fig. S8, A and B), suggesting that it depends on tissue perfusion. In patients with reduced LVEF, all three fuels were extracted ~20% more by the heart (fig. S10, A and B), consistent with the longer transit times of blood through the heart vasculature allowing increased uptake. Thus, the increased consumption of ketones and glutamate in heart failure reflects higher plasma concentrations and lower rates of cardiac perfusion, as opposed to an inherent change in cardiac capacity to combust these fuels.

In summary, we measured the uptake and secretion of 277 circulating metabolites by the human nonfailing and failing heart during fasting. FFAs were the predominant cardiac fuel source. Unexpectedly, we observed little glucose uptake, perhaps a response to fasting or to general anesthesia, limitations of our

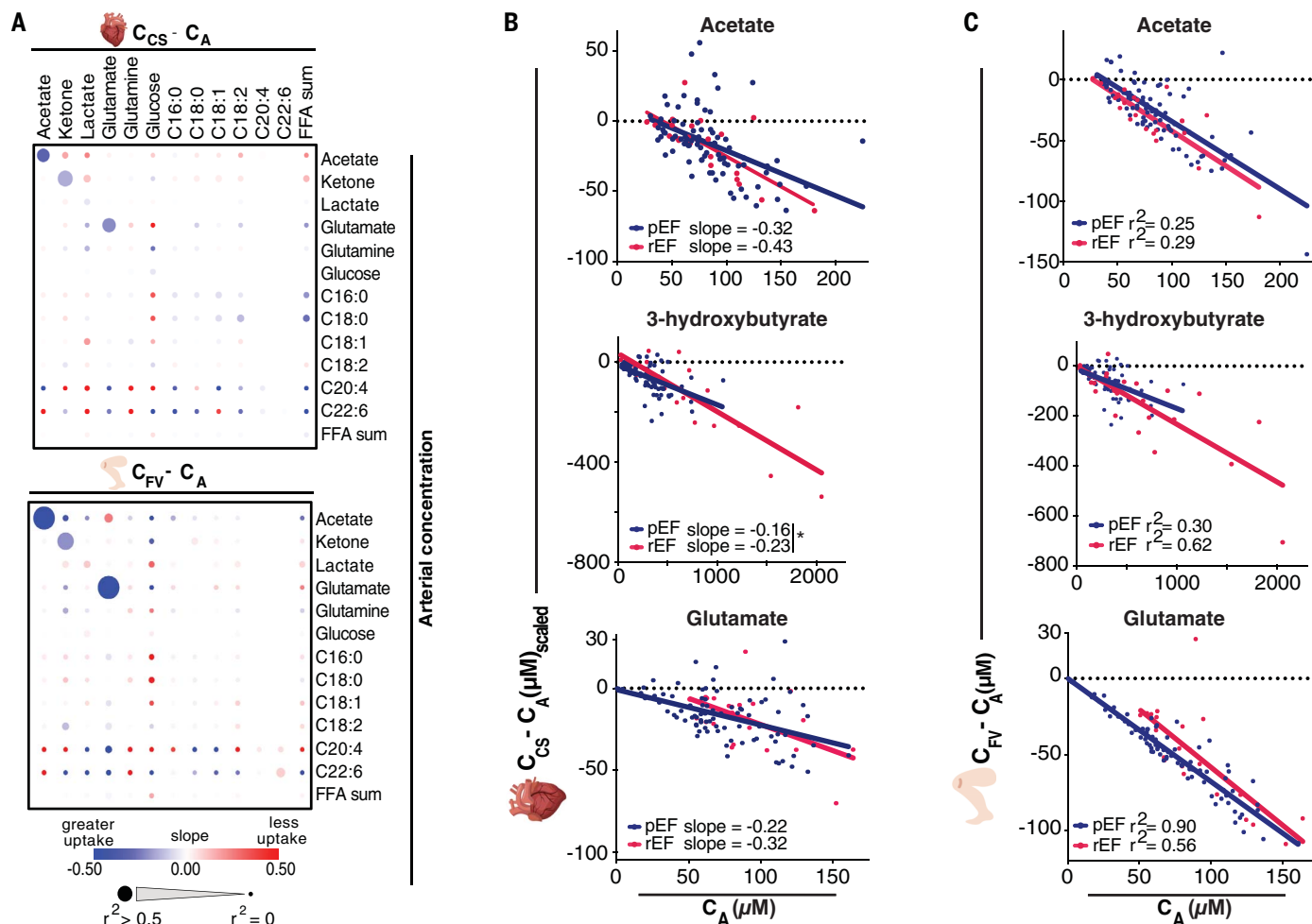


Fig. 4. Cardiac uptake of acetate, ketones, and glutamate primarily depends upon circulating concentrations in pEF and rEF. (A) Relationship of A-V metabolite gradient ($C_V - C_A$) with arterial concentration of indicated metabolites by linear regression. (B) C_A versus uptake of indicated metabolites by the heart after adjustment for acetate extraction [$(C_{CS} - C_A)_{scaled}$; see the supplementary data]. * $P < 0.05$ by analysis of covariance. (C) C_A versus uptake of the indicated metabolites by the leg.

study that were imposed by clinical necessity. Uptake of ketones was substantial and accentuated in heart failure. Ketone consumption has been suggested to be protective in heart failure (38), and our data suggest that delivery of ketones to the heart should be readily achievable. There was evidence of cardiac proteolysis despite the availability of circulating amino acids, which was markedly accentuated in heart failure. Whether this increased proteolysis in heart failure is adaptive or maladaptive will require further studies. The present data provide a framework of fuel use in the beating human heart and a foundation for understanding aberrant cardiac metabolism in disease.

REFERENCES AND NOTES

1. M. F. Allard, B. O. Schönekeß, S. L. Henning, D. R. English, G. D. Lopaschuk, *Am. J. Physiol.* **267**, H742–H750 (1994).
2. S. Neubauer, *N. Engl. J. Med.* **356**, 1140–1151 (2007).
3. J. Ivanisevic *et al.*, *Sci. Rep.* **5**, 12757 (2015).
4. Y. Mizuno *et al.*, *Metabolism* **77**, 65–72 (2017).
5. J. A. Wisneski *et al.*, *J. Clin. Invest.* **76**, 1819–1827 (1985).
6. D. S. Wishart *et al.*, *Nucleic Acids Res.* **46** (D1), D608–D617 (2018).
7. L. R. Peterson *et al.*, *Diabetes* **57**, 32–40 (2008).
8. G. D. Hutchins *et al.*, *J. Am. Coll. Cardiol.* **15**, 1032–1042 (1990).
9. R. H. Nelson, A. Prasad, A. Lerman, J. M. Miles, *Diabetes* **56**, 527–530 (2007).
10. R. J. Perry *et al.*, *Nature* **534**, 213–217 (2016).
11. M. L. Soliman, T. A. Rosenberger, *Mol. Cell. Biochem.* **352**, 173–180 (2011).
12. P. B. Taylor, C. C. Liew, *Basic Res. Cardiol.* **71**, 27–35 (1976).
13. K. J. Peuhkurinen, I. E. Hassinen, *Biochem. J.* **202**, 67–76 (1982).
14. T. Takala, J. K. Hiltunen, I. E. Hassinen, *Biochem. J.* **192**, 285–295 (1980).
15. H. Taegtmeyer, A. G. Ferguson, M. Lesch, *Exp. Mol. Pathol.* **26**, 52–62 (1977).
16. O. I. Pisarenko, E. S. Solomatina, I. M. Studneva, *Biochim. Biophys. Acta* **885**, 154–161 (1986).
17. G. H. A. Clowes Jr., H. T. Randall, C.-J. Cha, *JPEN J. Parenter. Enteral Nutr.* **4**, 195–205 (1980).
18. V. R. Preedy, L. Paska, P. H. Sugden, P. S. Schofield, M. C. Sugden, *Biochem. J.* **250**, 179–188 (1988).
19. H. Sun *et al.*, *Circulation* **133**, 2038–2049 (2016).
20. T. Li *et al.*, *Cell Metab.* **25**, 374–385 (2017).
21. W. Wang *et al.*, *Am. J. Physiol. Heart Circ. Physiol.* **311**, H1160–H1169 (2016).
22. M. D. Neinast *et al.*, *Cell Metab.* **29**, 417–429.e4 (2019).
23. D. J. Garry *et al.*, *Nature* **395**, 905–908 (1998).
24. A. E. Romero-Herrera, H. Lehmann, *Proc. R. Soc. London Ser. B* **186**, 249–279 (1974).
25. C. Commisso *et al.*, *Nature* **497**, 633–637 (2013).
26. P. B. Garland, P. J. Randle, E. A. Newsholme, *Nature* **200**, 169–170 (1963).
27. B. Comte *et al.*, *J. Biol. Chem.* **272**, 26125–26131 (1997).
28. A. R. Panchal *et al.*, *Am. J. Physiol. Heart Circ. Physiol.* **279**, H2390–H2398 (2000).
29. H.-L. Noh, K. Okajima, J. D. Molkentin, S. Homma, I. J. Goldberg, *Am. J. Physiol. Endocrinol. Metab.* **291**, E755–E760 (2006).
30. N. H. Banke *et al.*, *Circ. Res.* **107**, 233–241 (2010).
31. Y. Xia, J. L. Zweier, *J. Biol. Chem.* **270**, 18797–18803 (1995).
32. M. R. Laughlin, W. A. Petit Jr., R. G. Shulman, E. J. Barrett, *Am. J. Physiol.* **258**, E184–E190 (1990).
33. C. A. Schneider, H. Taegtmeyer, *Circ. Res.* **68**, 1045–1050 (1991).
34. G. Evans, *J. Physiol.* **82**, 468–480 (1934).
35. T. Ahmad *et al.*, *J. Am. Coll. Cardiol.* **67**, 291–299 (2016).
36. W. G. Hunter *et al.*, *J. Am. Heart Assoc.* **5**, e003190 (2016).
37. K. C. Bedi Jr. *et al.*, *Circulation* **133**, 706–716 (2016).
38. R. Nielsen *et al.*, *Circulation* **139**, 2129–2141 (2019).

ACKNOWLEDGMENTS

We thank the staff of the University of Pennsylvania Electrophysiology Section for their enthusiastic support of this

study, in particular M. Gnap, K. Conn, L. Tomczuk, and L. Czerniawski, as well as members of the Arany and Rabinowitz laboratories for insightful comments, in particular N. Yücel and S. Yang. **Funding:** D.M. was supported by the NHLBI (F30 HL142186-01A1) and the Blavatnik Family Foundation, C.J. was supported by the American Diabetes Association (1-17-PDF-076), J.J.E. was supported by NIH 5T32HL007915, J.D.R. was supported by an NIH Pioneer grant (1DP1DK113643) and an NIH Diabetes Research Center grant (P30 DK019525), and Z.A. was supported by the NHLBI (HL126797) and the NIDDK (DK114103). **Author contributions:** This study was conceived and designed by D.M., C.J., J.D.R., D.F., and Z.A. Patients were identified and recruited by D.F. and M.H. Samples were collected by D.M., M.H., and D.F. Mass spectrometry was performed by C.J. Data analysis was performed by D.M. with input from C.J. and M.N. Quantification of metabolites by the YSI Biochemistry Analyzer was performed by A.C. ELISAs were performed by J.E. Figures were prepared by D.M. The original draft was written and revised by D.M., C.J., and Z.A. and reviewed by all authors. **Competing interests:** J.D.R. is a member of the Rutgers Cancer Institute of New Jersey and the University of Pennsylvania Diabetes Research Center, cofounder of VL54, stakeholder in Colorado Research Partners, and consultant to Pfizer, Inc. The remaining authors declare no competing interests. **Data and materials availability:** All data are available in the main text or the supplementary materials.

SUPPLEMENTARY MATERIALS

science.sciencemag.org/content/370/6514/364/suppl/DC1
Materials and Methods
Figs. S1 to S10
Tables S1 to S10
Captions for Data S1 to S2
References (39–43)
MDAR Reproducibility Checklist
Data S1 and S2

[View/request a protocol for this paper from Bio-protocol.](#)

19 May 2020; accepted 25 August 2020
10.1126/science.abc8861



2D-Barcoded NMR Tube Scanner

The Express Scanner from Ziath delivers an industry-leading fast scan and decode time of under 3 s for a full rack of 2D-barcode nuclear magnetic resonance (NMR) sample tubes. 2D-barcode NMR tubes are usually difficult to read with a conventional scanner, as the caps are on top of the tubes and most scanners are designed to read from underneath. Designed in collaboration with a leading European NMR spectrometry lab,

the Express Scanner operates on top of the sample tubes without applying any weight (which could damage the tubes). In addition, for Bruker NMR spectrometer users, Ziath provides a dedicated slide for their tube carriers that can only be inserted in one orientation—thereby conserving the origin position (“A1” position) each time. The Express Scanner is supplied with a controller that regulates scanning and data processing using Ziath industry-standard DataPac software (version 3.17) or new DP5 web-enabled software that allows exporting of tube barcodes as tables or text, or in JPEG, XML, XLS, or JSON file formats. For convenience, the unit can be separated and positioned under your lab bench.

Ziath

For info: 858-880-6920
www.ziath.com

Water-Soluble Lipofuscin Autofluorescence Quencher

Lipofuscin autofluorescence is a common source of background in human and aged animal tissues, particularly brain and eye, which can make specific fluorescence imaging virtually impossible. Common quenchers such as Sudan Black B have been used to reduce lipofuscin autofluorescence, however these reagents often introduce nonspecific red and far-red fluorescence. TrueBlack Plus is a next-generation lipofuscin autofluorescence quencher that offers the lowest far-red background of all available quenchers, including Sudan Black B and our original TrueBlack. In addition, TrueBlack Plus is water-soluble, making it the only lipofuscin quencher that can be used in aqueous buffer instead of ethanol. Quenching in phosphate buffered saline allows longer incubation times for thicker samples without shrinkage and can be performed with hydrophobic stains.

Biotium

For info: 510-265-1027
www.biotium.com

Primary Kupffer Cells

BioIVT's high-purity Kupffer cells are ideal for in vitro screening assays, toxicity studies, disease models, and predicting inflammation-induced adverse drug reactions. Researchers often use these cells in plated monocultures, cocultures, and liver microtissue configurations. The cells are cryopreserved immediately after isolation at passage zero. Their purity is assessed using flow-cytometric analysis of CD68⁺ cells, and their function is measured based on interleukin-6 release in response to lipopolysaccharide. Each vial of BioIVT's high-purity Kupffer cells contains a minimum of 1 million viable cells. The cells can be thawed and plated in coculture with BioIVT's cryoplateable human hepatocytes using InVitroGRO CP NPC Medium.

BioIVT

For info: 516-483-1196
bioivt.com

Sterile Deep-Well Plates

Porvair Sciences offers an extensive range of sterile deep-well microplates for sensitive biological and drug discovery applications. These high-quality deep-well plates are made from virgin polypropylene and are available in several different sizes, well shapes, plate formats (the most commonly used being 96- and 384-well plates), and volumes (240 μ L–2.2 mL). With qualified low-extractables and low-leachables characteristics, they contain no contaminants that can leach out and affect stored sample or bacterial or cell growth. They are precisely manufactured to ANSI/SLAS dimensions to ensure they are completely automation compatible. Porvair Sciences deep-well plates are designed with raised well rims to facilitate reliable heat-seal closure—critical for long-term integrity of stored samples at -80°C . Used in conjunction with a support mat, the plates can be routinely centrifuged at up to 6,000 g.

Porvair Sciences

For info: 800-552-3696
www.microplates.com

Dye for Flow Cytometry

Bio-Rad Laboratories announces the launch of StarBright Violet 515 (SBV515) Dye, the first of a new range of unique fluorescent nanoparticles for use in flow cytometry. StarBright Dyes are conjugated to a growing range of antibodies and are compatible with most flow cytometers and experimental protocols. With an excitation maximum of 401 nm and emission maximum of 516 nm, SBV515 offers researchers improved brightness to resolve rare and low-antigen-density populations more easily. It has a narrow emission profile to reduce spillover into neighboring filters and minimal excitation by other lasers, making it suitable for inclusion in multicolor panels. The dye is not susceptible to photobleaching, delivers high lot-to-lot reproducibility, and is stable at 4°C with no loss of signal, ensuring consistent staining and reliable results. It has been tested in many common staining buffers and does not require a special staining buffer, permitting easy integration into common experimental protocols without compromising performance.

Bio-Rad Laboratories

For info: 800-424-6723
www.bio-rad-antibodies.com/flow-cytometry-starbrightviolet515.html

SARS-CoV-2 rRT-PCR Kit

The Quick SARS-CoV-2 rRT-PCR Kit is a real-time reverse transcription PCR (rRT-PCR) test for the qualitative detection of RNA from the severe acute respiratory syndrome coronavirus 2 (SARS-CoV-2), which is responsible for the coronavirus disease (COVID-19). It targets three different regions of the viral nucleocapsid (N) gene and a host-specific target region (human ribonuclease P gene) to assess sample quality. The kit also includes coefficient of variation (CV) Positive Control to enable assay performance monitoring as well as a No-Template Control to confirm the absence of contamination in the reagents. It can be used on purified RNA samples isolated from upper respiratory and lower respiratory systems. The Quick SARS-CoV-2 rRT-PCR Kit has high sensitivity with a limit of detection as low as 15 viral genome equivalent copies per reaction, a fast turnaround time of less than 1.5 h, and a simple workflow in which RNA is simply added to the kit reagents and directly analyzed. Due to its simplicity, the kit can be set up with a manual or automated system and is compatible with high-throughput platforms.

Zymo Research

For info: 888-882-9682
www.zymoresearch.com/products/quick-sars-cov-2-rrt-pcr-kit

Electronically submit your new product description or product literature information! Go to www.sciencemag.org/about/new-products-section for more information.

Newly offered instrumentation, apparatus, and laboratory materials of interest to researchers in all disciplines in academic, industrial, and governmental organizations are featured in this space. Emphasis is given to purpose, chief characteristics, and availability of products and materials. Endorsement by *Science* or AAAS of any products or materials mentioned is not implied. Additional information may be obtained from the manufacturer or supplier.



FACULTY POSITION IN STEM CELLS AND REGENERATIVE MEDICINE

We invite applications for faculty position at the **Assistant or Associate Professor** levels in the STaR Center at Baylor College of Medicine.

We are seeking motivated investigators in all areas of stem cells and regenerative medicine including embryonic and adult stem cell biology, organoids, developmental biology, cancer stem cells (hematologic, glioma, and others).

BCM is the premier medical school of Texas and has the top-ranked Genetics and Cell Biology Departments in the U.S. based on NIH funding. BCM has internationally recognized strengths in structural biology and biochemistry, a long-standing NIH human genome sequencing center, cutting edge Advanced Technology Cores, exceptional Ph.D. graduate programs, a commitment to technology transfer for faculty discoveries, and a rich history of translating basic science into clinical implementation.

Applications received by **November 1st, 2020** will receive priority.

Please send Cover Letter, CV and a two-page summary of research interests as a single PDF file to:

STAR@bcm.edu

http://www.bcm.edu/star/

*Baylor College of Medicine is an Equal Opportunity/Affirmative Action/
Equal Access Employer*



Research Leaders and Principal Investigators

The Agency for Science, Technology and Research (A*STAR) is Singapore's lead public sector science and technology agency. A*STAR has a strategic R&D agenda, driving use-inspired basic research, spearheading economic growth and advancing social well-being through scientific discovery, technological innovation and talent development. A*STAR is consistently ranked world's top 10 in the Reuters Innovative Institutions, and top 30 in the Nature Index of Top Government Institutions for the last 5 years. It averaged about 3,000 international publications annually in recent years, and filed over 2,000 patents in the past decade. At A*STAR, we Impact, Invest, and Inspire, to bring out the best in you.

One Organisation. Multiple Careers

A*STAR is seeking established and potential research leaders and principal investigators in the following areas: • Artificial Intelligence & data science (e.g. machine learning) • Decarbonization & urban technology (e.g. CO₂ capture and utilization) • Diagnostics & therapeutics (e.g. gene therapy; immunotherapy; medical devices) • Neuroscience & cognitive analytics • Other emerging technologies (e.g. food security; industrial biotechnology; quantum engineering)

We are particularly interested in candidates who are creative and impactful in their works, able to deliver outcomes in a highly competitive environment, and share our ideals in delivering scientific & technological outcomes and benefits to the society and its people. We value cross-disciplinary ideas in a strongly collaborative setting. Suitable candidates will be appointed as Senior Scientists/Principal Scientists (or Engineers) typically in one of the research institutes of A*STAR, with responsibilities depending on experience, aptitude and research areas. Researchers with leadership experience may also be appointed as centre directors, programme managers or team leaders. At A*STAR, there are multiple career track options, from research to planning and from enterprise development to institutional management. A*STAR offers competitive remuneration and benefits, commensurate to experience and research qualities and potential. We are seeking research leaders and performers with at least 10 years of relevant experience (in academia or industry), but emerging talent with less experience are welcome to apply.

We invite all interested applicants to visit bit.ly/joinastar to submit your CV and contact details by **7 November 2020**. All enquiries can be directed to talent@hq.a-star.edu.sg with the subject title "CAREER" For ongoing news and latest research developments, visit www.a-star.edu.sg and <https://research.a-star.edu.sg/print-magazine/>.

U.S. POSTAL SERVICE

Statement required by the Act of 12 August 1970, Section 3685, Title 39, United States Code, showing the ownership, management, and circulation of:

1–9. Science, Publication No. 0036-8075, is published weekly on Friday, except the last week in December, at 1200 New York Avenue, N.W., Washington, DC 20005. Date of filing: 29 September 2020. This is also the address of the publisher, the editor, and the managing editor, who are, respectively, Bill Moran, Holden Thorp, and Monica M. Bradford.

10. The owner is the American Association for the Advancement of Science, 1200 New York Avenue, N.W., Washington, DC 20005. Stockholders: None.

11. Known bondholders, mortgages, and other security holders owning or holding 1 percent or more of total amount of bonds, mortgages, or other securities: None.

12. The purpose, function, and nonprofit status of this organization and the exempt status for federal income tax purposes have not changed during the preceding 12 months.

13–15. The average number of copies of each issue during the preceding 12 months is (A) Total number of copies printed: 57,397; (B) Paid circulation: 52,808; (1) Paid/Requested outside-county mail subscriptions stated on form 3541: 46,515; (2) Paid/Requested in-county subscriptions stated on form 3541: 0; (3) Sales through dealers and carriers, street vendors, counter sales: 6,288. (4) Other classes mailed through USPS: 5; (C) Total paid circulation: 52,808; (D) Free distribution: samples, complimentary, and other free copies: 3,275; (1) Outside-county as stated on form 3541: 2,776; (2) In-county as stated on form 3541: 0; (3) Other classes mailed through the USPS: 2; (4) Free distribution outside of mail carrier or other means: 497; (E) Total free distribution: 3,275; (F) Total distribution: 56,083; (G) Copies not distributed: 1,315; (H) Total: 57,398; (I) Percent paid and/or Requested Circulation: 94.2%.

Actual number of copies of single issue (9/25/2020) published nearest to filing date are (A) Total number of copies printed: 54,671; (B) Paid circulation: 50,214; (1) Paid/Requested outside-county mail subscriptions stated on form 3541: 44,328; (2) Paid/Requested in-county subscriptions stated on form 3541: 0; (3) Sales through dealers and carriers, street vendors, counter sales: 5,881; (4) Other classes mailed through USPS: 5; (C) Total paid circulation: 50,214; (D) Free distribution: Samples, complimentary, and other free copies: 3,207; (1) Outside-county as stated on form 3541: 2,863; (2) In-county as stated on form 3541: 0; (3) Other classes mailed through the USPS: 2; (4) Free distribution outside of mail: Carrier or other means: 342; (E) Total free distribution: 3,207; (F) Total distribution: 53,421; (G) Copies not distributed: 1,250; (H) Total: 54,671; (I) Percent paid and/or Requested Circulation: 94.0%.

I certify that the statements made above are correct and complete. (signed) Bill Moran, Publisher.

**Independent Research
Fellowships Leading to Tenured
Faculty Positions at the
John Innes Centre**



The John Innes Centre (JIC), Norwich, UK is a world leading centre of excellence in plant and microbial sciences based on the Norwich Research Park. We are inviting applications from outstanding researchers who either hold or wish to apply for Independent Research Fellowships [such as a UKRI Future Leaders Fellowship (<https://www.ukri.org/funding/funding-opportunities/future-leaders-fellowships/>), or a Royal Society University Research Fellowship (<http://royalsociety.org/grants/schemes/university-research/>)]. Shortlisted candidates will be invited to give a seminar at a virtual Fellows Conference, which will be held on 01, 02 and 03 February 2021. During the conference, you will be able to discuss your proposals, the development of your group and your future career plans in depth with JIC Faculty in virtual one-to-one meetings.

After the conference, we will select and mentor outstanding candidates in writing Fellowship applications and/or offer the opportunity to move existing Fellowships to the JIC. Candidates who win Fellowships will be considered for transfer onto tenure-track at 3 years, and if transferred, for tenure at 5 years. Considerable additional resources will be provided to Fellows by the Centre. For further information, contact mark.buttner@jic.ac.uk

Further details and particulars can be found at <https://www.jic.ac.uk/vacancies/>

To apply: please e-mail a 2-page summary of your research plan, a copy of your CV and arrange for three letters of recommendation to be e-mailed to fellows@jic.ac.uk by Friday 04 December 2020. Before applying please read our Privacy Notice.



The John Innes Centre is a registered charity (No223852) grant-aided by the Biotechnology and Biological Sciences Research Council and is an Equal Opportunities Employer and supports flexible working.



The University of Missouri (MU) invites applications for a tenure-track faculty position in the School of Medicine (SOM) and Department of Biochemistry. Responsibilities will include contributions to medical, graduate and undergraduate education. We seek applications in areas of including gene/genome regulation, gene delivery and transgenic technology, synthetic biology, medicinal biochemistry, structural biology and imaging, including development of new molecular markers and reporters. Of particular interest are areas of fundamental science that might relate to emerging strengths in biomedical translation, precision health and/or electron microscopy (see below).

Qualifications: An earned doctorate and a record of research in an area of biomedically-relevant biochemistry that complements departmental strengths. Applications for this position at the Assistant Professor level are encouraged, but candidates at a higher level will be considered if there is evidence of continuous extramural research funding, high impact publications and excellence in teaching and service expected of tenured faculty at a research-intensive university.

About MU and Biochemistry: MU is the flagship campus of the University of Missouri System. Current strengths of the Department of Biochemistry include medical biochemistry, plant biochemistry and biophysical, structural and mechanistic biochemistry. The department forms a bridge between fundamental molecular science and translation into biomedical and agricultural applications. Biomedical advances will be anchored by the \$225M NextGen Precision Health Institute, opening Fall 2021, that will house an Electron Microscopy center with multiple state-of-art instruments.

Application: To apply, visit <https://biochem.missouri.edu/open-positions/>, click on Open Positions and submit: (1) a cover letter; (2) a curriculum vitae; (3) a one-page summary of research accomplishments with two pages of future plans; (4) a narrative of teaching philosophy and diversity inclusion; and (5) names and contact information of four references. Review of applications will begin on **November 16, 2020** and will continue until the position is filled. For information, contact Dr. Jack Tanner, Chair of the Search Committee (tannerjj@missouri.edu).

The University of Missouri is an Equal Access, Equal Opportunity, and Affirmative Action Employer. We are fully committed to achieving the goal of a diverse and inclusive academic community of faculty, staff and students. We seek individuals who are committed to this goal and our core campus values of respect, responsibility, discovery and excellence.



CO-FOUNDED BY:
American Heart Association



WITH SIGNIFICANT SUPPORT FROM:



AND PILLAR SUPPORT FROM:



Postdoctoral Fellow & Staff Scientist Positions

One Brave Idea and the laboratories of Dr. Calum MacRae and Dr. Rahul Deo are seeking Postdoctoral Fellows & Staff Scientists interested in studying the earliest molecular and phenotypic changes during cardiovascular disease development in order to design novel, more efficacious therapies and gain insight into disease mechanisms. One Brave Idea combines innovative participant phenotyping, large scale genetic, genomic and proteomic characterization, and mechanistic cell biology to enable novel discoveries and drive their application to clinical practice.

The successful candidate would join our international team of data scientists, staff scientists, postdocs and MD/PhDs and will be part of the highly inclusive and collaborative research community at the Brigham and Women's Hospital & Harvard Medical School. We have generous core-funding support and access to state-of-the-art facilities and technology platforms.

We're seeking candidates who are interested in combining interdisciplinary approaches to gain further knowledge on the initial events happening at the earliest stages of cardiovascular disease using an integration of zebrafish models and mammalian fixed and fresh samples, including those collected through a high-volume human translational program. The suitable candidates will apply both genetic and high-resolution imaging approaches with metabolic, transcriptional, and chromatin profiling assays to elucidate the core pathological mechanisms at play in cardiovascular disease.

Qualifications: PhD in molecular and cellular biology, molecular genetics, or related field. Previous experience with zebrafish research is preferred for postdoc applicants. Applicants interested in the staff scientist position should have 3-5 years of academic or industry experience. We are committed to support candidates' transition to academic positions or industry.

Interested candidates should email their CV and cover letter to Evan Wilson – ewilson17@bwh.harvard.edu

For more information, please visit

www.onebraveidea.org

and

<https://macraelab.bwh.harvard.edu/>



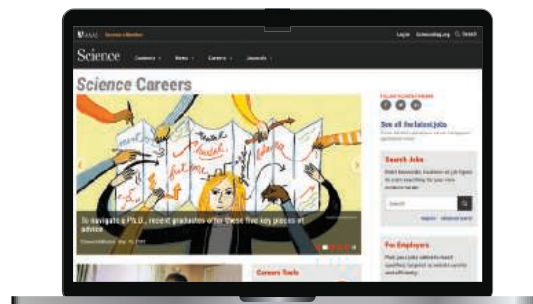
Science Careers helps you advance your career. Learn how !

- Register for a free online account on **ScienceCareers.org**.
- Search hundreds of job postings and find your perfect job.
- Sign up to receive e-mail alerts about job postings that match your criteria.
- Upload your resume into our database and connect with employers.
- Watch one of our many webinars on different career topics such as job searching, networking, and more.
- Download our career booklets, including Career Basics, Careers Beyond the Bench, and Developing Your Skills.
- Complete an interactive, personalized career plan at "my IDP."
- Visit our Employer Profiles to learn more about prospective employers.
- Read relevant career advice articles from our library of thousands.

Visit **ScienceCareers.org**
today — all resources are free

ScienceCareers

FROM THE JOURNAL SCIENCE 



SCIENCECAREERS.ORG



PROFESSOR/NOOYI ENDOWED CHAIR

POSITION ID: F00119P

The College of Engineering, on behalf of the University of Texas at Arlington, invites applications for the **Nooyi Endowed Chair position**, with starting employment date early in **2021**. This position will be at the **full professor level**, with an appointment in the College of Engineering or the College of Nursing and Health Innovation or in the College of Science with possible secondary appointments in a variety of supporting disciplines across the University. It is preferred that the candidate's primary appointment be in the Department of Bioengineering. The search is part of the University's strategic hiring plan within the four thematic research thrusts of UTA's Strategic Plan Health and the Human Condition, Sustainable Urban Communities, Global Environmental Impact, and Data-Driven Discovery. A key objective is to hire faculty members with outstanding qualifications who share the University's core values of high standards of excellence in teaching, innovative and collaborative research, and service, combined with fostering an open and inclusive environment.

In this prestigious role, this individual is expected to lead at least one of the university's efforts to establish research clusters at the intersection of human health and data-driven discovery. Major emphasis will be placed on creating and realizing potentials for a major bioinformatics-related research and education powerhouse in North Texas by collaborating across UTA and with premier medical schools in DFW area. Indications of success will include a stimulating environment that supports development of joint degree-granting programs in areas such as bioinformatics, medical informatics, or more broadly in biocomputation.

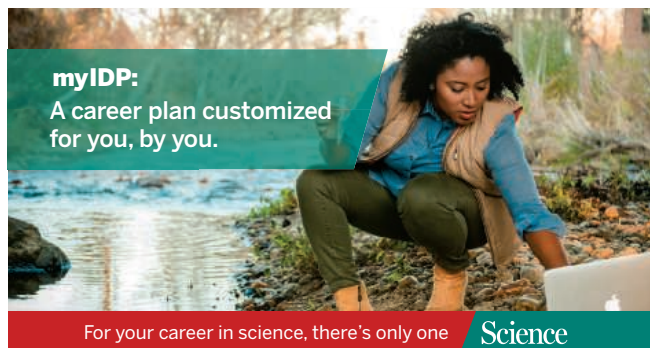
The University of Texas at Arlington is a Carnegie Research-1 "highest research activity" institution. With a student enrollment of close 60,000, UTA is rapidly becoming one of the largest institutions in the University of Texas System. Guided by its Strategic Plan Bold Solutions | Global Impact, UTA fosters interdisciplinary research and teaching to enable the sustainable megacity of the future within four broad themes: health and the human condition, sustainable urban communities, global environmental impact, and data-driven discovery. UTA was cited by U.S. News & World Report as having the second lowest average student debt among U.S. universities in 2017. U.S. News & World Report also ranks UTA fifth in the nation for undergraduate diversity. The University is a Hispanic-Serving Institution and is ranked as the top four-year college in Texas for veterans on Military Times' 2017 Best for Vets list.

The successful candidate will have demonstrated internationally recognized research programs in one or more areas including, but not limited to, big data analytics, bioinformatics, molecular and computational modeling, and systems biology. The successful candidate will be expected to teach and develop graduate courses in these areas, supervise graduate students, and serve on departmental, college and university committees. Applicants must have earned a Ph.D. or M.D./Ph.D. degree in an engineering, science or health care related discipline and have a significant level of research and scholarship accomplishments commensurate with the rank of full professor with tenure and Nooyi Endowed Chair.

Application Instructions

To apply, applicants should go to <https://uta.peopleadmin.com/> and submit their application, including a cover letter, curriculum vitae, statements of research and teaching objectives, and contact information for at least five references. Questions about the position should be addressed to michael.cho@uta.edu. Review of applications will continue until the positions are filled.

UTA is an Equal Opportunity/Affirmative Action Employer. All qualified applicants will receive consideration for employment without regard to their race, color, national origin, religion, age, sex, disabilities, or sexual orientation.



myIDP:
A career plan customized for you, by you.

For your career in science, there's only one **Science**

Features in myIDP include:

- Exercises to help you examine your skills, interests, and values.
- A list of 20 scientific career paths with a prediction of which ones best fit your skills and interests.



Visit the website and start planning today!
myIDP.sciencecareers.org

ScienceCareers
NIAAS

In partnership with:



WAYNE STATE
UNIVERSITY
SCHOOL OF MEDICINE



TENURE TRACK FACULTY POSITIONS DEPARTMENT OF PHYSIOLOGY

The Department of Physiology at Wayne State University (WSU) School of Medicine (SOM) (<http://physiology.med.wayne.edu>) in Detroit, Michigan invites applications for **two tenure-track Assistant/Associate Professor positions**. We seek candidates that employ molecular, cellular or systems approaches to explore research interests in cardiovascular, respiratory or metabolic physiology/pathophysiology and biophysics. WSU SOM is a state-of-the-art research environment, rated in the top third of all US Research Institutions by the Carnegie Foundation. The Department of Physiology, has one of the most active research programs among the basic science departments at WSU-SOM and is presently ranked #40 out of ~120 Departments of Physiology in the USA. The start-up package and salary are highly competitive.

Candidates should hold a Ph.D., M.D. or equivalent from a relevant area. The selected candidates are expected to establish an extramurally funded active research program and participate in teaching medical and graduate students. Please apply to https://jobs.wayne.edu/applicants/jsp/shared/Welcome_css.jsp, posting 043648 and 043757, by uploading a curriculum vitae, a detailed future research plan, and names/contact information of three references. Please submit inquiries with a CV to Physiologyfacultysearch@wayne.edu. Review of applications will begin after **October 30, 2020** and continue until the positions are filled.

WSU is an affirmative action/equal opportunity employer and encourages applications from women, people of color or other underrepresented backgrounds.

By John C. Ayers

My last drop

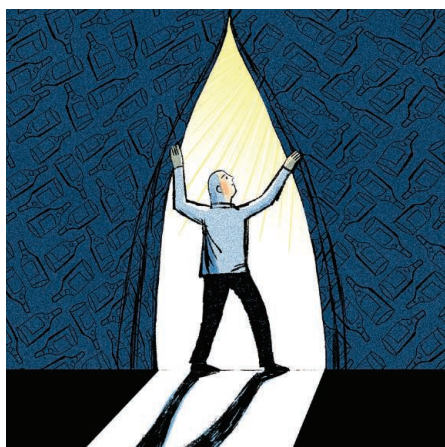
was looking back in my diary, trying to find clues to why I was struggling with severe insomnia. I had just begun to take new antidepressant medications, and something wasn't right. I'd experienced insomnia before, and now I saw the common thread. In both cases, my psychiatrist had started me on new medications and had recommended that I temporarily stop drinking alcohol. Suddenly it hit me: The insomnia was a symptom of alcohol withdrawal. I was a functioning alcoholic. It was the wake-up call I needed, and I've been sober ever since. But now I worry that others, facing the stresses and sadness of the pandemic, may be starting down a similar path. Here's my cautionary tale.

Alcohol had long been a respite for me. During high school and into college, I drank heavily to cope with anxiety. Part of me knew this wasn't a healthy approach, but it seemed to work. When I discovered a love of geochemistry, I eased up on my drinking. On weekdays, I chose to study rather than go to the bars. I still enjoyed drinking on weekends, but it was social drinking—nothing I was concerned about. Throughout grad school and my early years as a professor, I still sometimes drank too much. But it didn't cause problems.

That started to change roughly 11 years into my faculty position, when my father died. Devastated by his loss, I began to suffer from depression, which in turn led to weight gain and sleep apnea. I became chronically sleep deprived and could no longer think clearly, which made it challenging to meet the intellectual demands of my job. I suffered from a short temper and strained relationships. I started to self-medicate with alcohol, which reduced my anxiety in the short term. But eventually I became so depressed that I no longer tried to restrain my drinking. I took up mixology as a hobby and started to drink cocktails every night.

Years passed, and I still felt deeply unhappy. I decided to see a psychiatrist, who began to treat me for chronic depression at first. It took me several more years to recognize I was an alcoholic.

An important clue came one morning when I awoke after an awards dinner at a conference feeling so hungover I wasn't able to co-chair a session that morning as planned; I had to ask colleagues to go on without me. I had vowed not to drink too much. But my anxiety got the best of me. After multiple bottles of wine were placed on the table in front of me, I started to drink heavily, the conversation distracting



“It was the wake-up call I needed, and I’ve been sober ever since.”

me from realizing how much I consumed. Afterward, I was frustrated and confused by my lack of control, but I wasn't quite ready to admit I had a serious problem.

That changed a few months later when I looked back on my diary and finally, with the help of my psychiatrist, named my problem. I immediately committed to abstinence. The first 6 weeks were especially hard, but I got through them by exercising regularly and spending time with my family. I was fortunate that I was on a sabbatical at that time, which gave me space to focus on my health and recovery. I started to practice mindfulness and meditation and attend Alcoholics Anonymous meetings. I also took time to learn about a new scientific

discipline and start a new collaboration, which got my creative juices flowing again and helped me rediscover my thirst for research.

Now, nearly 10 years later, I live with less stress, have healthier relationships, and am happier and more productive. I still suffer from anxiety, but I find that regular exercise and meditation help me cope. When I attend conferences—at least, when I used to do so in person, before COVID-19—I avoid alcohol-centered events or decline the free alcohol tickets. Occasionally, I get odd looks from colleagues, but they quickly understand when I tell them I'm a recovered alcoholic. No one I've confided in has made me feel bad.

If you're one of the many people who are currently struggling in the midst of the pandemic, take it from me: Alcohol may make you feel better temporarily, but it's not a healthy way to cope with stress and anxiety. Ask for help instead. ■

John C. Ayers is a professor at Vanderbilt University in Nashville, Tennessee. Send your career story to SciCareerEditor@aaas.org.